

1 2 9 0



UNIVERSIDADE D
COIMBRA

Bernardo Albuquerque Nogueira

**GENERATION AND CHARACTERIZATION OF
NOVEL MATERIALS EXHIBITING
COLOR POLYMORPHISM**

**Tese no âmbito do Doutoramento em Química - Ramo de
Espectroscopia Molecular, orientada pelo Professor Doutor Rui
Fausto Martins Ribeiro da Silva Lourenço, coorientada pela
Professora Doutora Chiara Castiglioni, e apresentada ao
Departamento de Química da Faculdade de Ciências e Tecnologia
da Universidade de Coimbra.**

Maio de 2022

Departamento de Química
Faculdade de Ciências e Tecnologia da Universidade de Coimbra

GENERATION AND CHARACTERIZATION OF NOVEL MATERIALS EXHIBITING COLOR POLYMORPHISM

Bernardo Albuquerque Nogueira

Tese no âmbito do Doutoramento em Química – Ramo de Espectroscopia Molecular, orientada pelo Professor Doutor Rui Fausto Martins Ribeiro da Silva Lourenço, coorientada pela Professora Doutora Chiara Castiglioni, e apresentada ao Departamento de Química da Faculdade de Ciências e Tecnologia da Universidade de Coimbra.

Maio de 2022



UNIVERSIDADE D
COIMBRA

I am utterly convinced that Science and Peace will triumph over Ignorance and War, that nations will eventually unite not to destroy but to edify, and that the future will belong to those who have done the most for the sake of suffering humanity.

Louis Pasteur

We were wanderers from the beginning.

Carl Sagan

Acknowledgements

Science is a collective venture. The quest for better understanding the universe we live in is one of the most distinctive aspects of our kind. Hence, Science is made from human beings to human beings. In other words, there is not science without humankind. Moreover, the developments in science are always built over the work of other people, being thus a cumulative endeavor.

In fact, with the degree of technical sophistication we have presently achieved, Science is more and more a teamwork, rather than an individual task. Therefore, there is a vast number of people I must acknowledge, which were absolutely fundamental for this PhD project to be completed.

First of all, I must show all my gratitude to Professor Rui Fausto, the Laboratory for Molecular Cryospectroscopy and Biospectroscopy's group leader and supervisor of this work. Professor Rui Fausto has been my supervisor since my BSc studies. I have also performed my MSc thesis studies under his supervision and started my researching career in his research group. For this reason, I have been learning personally and scientifically from him for the past 8 years and I could not be more grateful. Above all, I must emphasize the rigor and the determination I have witnessed in every work, which were absolutely inspiring. Everything I have accomplished scientifically with this work was only possible with Professor Rui Fausto's help, and I only wish that this apprenticeship with him can continue in the next years.

To Professor Chiara Castiglioni, co-supervisor of this PhD project, I want to endorse my most sincere gratefulness. During this PhD project I had the chance to live the most challenging moment of my life so far. Living in a different country, away from home and during an unusual pandemics' situation, but without feeling the common homesickness. That was only possible because Professor Chiara Castiglioni received me in her research group at Politecnico di Milano in such a way that I always felt that I belonged there. I am also very grateful for all the scientific guidance and all the learning moments lived in Italy under *Professoressa's* supervision. It was a unique development period, both personally and scientifically. For this once-in-a-lifetime opportunity, I am most grateful to Professor Chiara Castiglioni.

I am also absolutely grateful to Alberto Milani, who guided me through the computational studies at the Politecnico di Milano. For all the patience and the knowledge shared with me, I could not wish for more. Additionally, all the tips regarding visiting sites in lovely Italy were super valuable for a very

well spent year abroad, even with the complications due to the pandemics. To the rest of the research group, especially to Matteo Tommasini, Gigi Brambilla and Andrea Lucotti, my thanks for the warm reception, the support, and for always making me feel one of the group.

To Timur Nikitin, Susy Lopes, Alcides Simão, Maria Carvalho and all the group members of the Laboratory for Molecular Cryospectroscopy and Biospectroscopy, I am grateful for all the laboratorial assistance and for the supportive environment that is present every day in the research group.

To Professor Ermelinda Eusébio I am very grateful for all the guidance in the thermal analysis studies and for the fruitful discussions about the collected results. Additionally, to Professor João Canotilho, João Baptista and all the other members of the CQC-IMS Thermodynamics and Solid State Chemistry Lab, I owe a sincere acknowledgement for all the scientific discussions and for all the help inside the lab.

To Professor Teresa Pinho e Melo and to Susana Lopes, I want to acknowledge the opportunity to perform my first chemical synthesis work, which I consider of fundamental importance to get a rich and complete chemistry training. To Susana I also thank the patience in the laboratory and the kindness to complete the synthetical route investigations, when I went to Italy, and to obtain all the compounds in significant quantities to allow the subsequent studies performed in this Thesis.

To Professor José António Paixão, I want to show my appreciation for the X-ray diffraction studies and for all the enlightening conversations that we have had over the past few years. This collaboration, which started in my MSc studies, has been a source of enriching know-how that deeply boosted my vision on molecular structure. For this great opportunity, I am profoundly grateful to Professor José António Paixão.

To Ana Clara Rodrigues, I am grateful for the help in the UV-visible absorption studies performed in the context of this Thesis, some of which produced interesting results.

To Professor Teresa Duarte and to Vânia André, from the Instituto Superior Técnico, I wish to show my appreciation for the availability to run some of the X-ray diffraction studies, with little advance time, at the end of this project. Such results were crucial to finish this thesis.

Additionally, I am mostly grateful to Roberto Dovesi, Michel Rérat and Fabien Pascale, for their critical help to overcome the unexpected hardware complications that emerged in the final part of this project.

To Fundação para a Ciência e Tecnologia, which funded this PhD research program, I want to thank for this opportunity, which was not only a possibility to obtain a university degree, but also to begin my the career of my dreams.

I would also like to present some personal acknowledgments: to all my family and friends, who understood my decision to endeavor an arduous path, which originated some absences over the last four years, and nonetheless always supported me. To my parents, for all the opportunities proportionated during my childhood and adolescence, which allowed me to acquire fundamental tools to fight for my future. To my mother, for being a safe harbor when mostly needed. To my brothers and sister, for all the companionship and happy moments lived together, which were essential to make me who I am today. Finally, to Inês, for all the comprehension during the past years and, most importantly, for making this path to have a higher purpose and meaning.

Abstract

Color polymorphism, a fascinating property of chemical systems presenting polymorphs of different colors, is the main subject of this Thesis. Color polymorphic organic molecular systems are rare, with only a few examples reported previously. However, in theory, these systems have an immense potential for applications in different areas, such as pigment, sensor, and technology industries. In the first part of this work, a comprehensive review of the color polymorphic systems reported in the literature is presented and some of the fundamental concepts related to the subject that have been frequently imprecisely used in the scientific literature are discussed and clarified.

Five different molecular systems based on two known color polymorphic compounds were designed, synthesized for the first time, and studied in the context of this PhD project: 3-((2,4,6-trinitrophenyl)amino)phenol (TAP) and 2,4,6-Trinitro-*N*-(*m*-tolyl)aniline (TMA), which belong to the *N*-picryl-*p*-toluidine family of compounds, and 2-(4-((3-cyanothiophen-2-yl)amino)-3-nitrophenyl)acetic acid (ROY-CAM), 5-acetyl-2-((2-nitrophenyl)amino)thiophene-3-carbonitrile (AcROY), and 2-((4-hydroxy-2-nitrophenyl)amino)thiophene-3-carbonitrile (ROY-ol), which are ROY analogues. In total, from the recrystallization processes employed in this project, thirteen colored solid-state crystal forms of the studied compounds were obtained, ten of which were possible to characterize structurally.

These systems were studied by both computational and experimental approaches. The first included the study of the isolated molecules of the compounds and focused on the study of the conformational landscape of the molecules and on the investigation of the solid-state vibrational characteristics of the polymorphs, taking advantage of state-of-the-art fully periodic quantum chemical calculations. Density Functional Theory (DFT) was chosen as theoretical approach to be employed in both cases. Experimentally, the core techniques employed in this PhD. research project included vibrational spectroscopy (IR and Raman spectroscopies), single crystal X-ray diffraction and thermal analysis methods (DSC and PLTM).

The outcome of the PhD project led to the preparation of seven manuscripts, which have already been published or submitted for publication in international peer-reviewed scientific journals, as well as to the establishment of a set of general rules regarding the ability of these systems to exhibit polymorphism in general, and color polymorphism in particular, besides the detailed structural investigation of the

selected chemical systems. These results and the respective conclusions that were drawn will allow a better comprehension of the rare color organic molecular polymorphic systems, which is essential for the evaluation and exploration of potential applications of such systems, especially the ones where thermal conversion between polymorphs is observed.

Resumo

O polimorfismo de cor, uma propriedade fascinante de sistemas químicos que apresentam polimorfos com diferentes cores, constitui o tema principal desta Tese. Compostos orgânicos que possuem polimorfismo de cor são raros, existindo apenas alguns exemplos reportados anteriormente. Contudo, em teoria, este tipo de sistemas tem um imenso potencial para aplicação em diferentes áreas, como nas indústrias de pigmentos, sensores e tecnológica. Na primeira parte deste trabalho, é apresentada uma revisão profunda dos sistemas orgânicos moleculares que possuem polimorfismo de cor reportados na literatura, e são discutidos e clarificados alguns dos conceitos fundamentais relacionados com o tema e que têm sido frequentemente utilizados incorretamente na literatura científica.

Foram desenhados cinco sistemas moleculares diferentes a partir de dois compostos conhecidos que possuem polimorfismo de cor, de forma a serem sintetizados pela primeira vez e estudados no contexto deste projeto de Doutorado: 3-((2,4,6-trinitrofenil)amino)fenol (TAP) and 2,4,6-Trinitro-*N*-(*m*-tolil)anilina (TMA), que são compostos pertencentes à família da *N*-picril-*p*-toluidina, e 2-(4-((3-cianotiofen-2-il)amino)-3-nitrofenil)carboximetil (ROY-CAM), 5-acetil-2-((2-nitrofenil)amino)-tiofeno-3-carbonitrilo (AcROY) e 2-((4-hidroxi-2-nitrofenil)amino)tiofeno-3-carbonitrilo (ROY-ol), que são compostos derivados do composto usualmente conhecido por ROY e que é o mais bem conhecido (e famoso) sistema químico que exibe polimorfismo de cor. No total, a partir dos processos de recristalização realizados durante este projeto, foram obtidas treze formas cristalinas de estado sólido com cor dos compostos estudados, dez das quais foram caracterizadas estruturalmente.

Os compostos escolhidos foram estudados tanto por abordagens computacionais como experimentais. As primeiras incluíram o estudo das moléculas isoladas dos compostos, tendo como objetivos principais o estudo do seu perfil conformacional, e o estudo das propriedades vibracionais dos polimorfos, neste último caso usando cálculos mecânico-quânticos do estado-da-arte para sistemas periódicos. A Teoria do Funcional da Densidade (DFT, do inglês, *Density Functional Theory*) foi o método teórico utilizado em ambos os casos. Experimentalmente, as principais técnicas utilizadas foram a espectroscopia vibracional (espectroscopias de infravermelho e de Raman), a difração de raios-X de monocristal e métodos de análise térmica (calorimetria diferencial de varrimento e termomicroscopia de luz polarizada – abreviadas em DSC e PLTM, respetivamente, do inglês: *differential scanning calorimetry* e *polarized light thermomicroscopy*).

O resultado deste projeto de Doutorado levou à preparação de sete manuscritos, já publicados ou submetidos para publicação em revistas internacionais com revisão por pares, e à elaboração de um conjunto de regras gerais relativamente à capacidade destes sistemas apresentarem polimorfismo, em particular polimorfismo de cor, para além do estudo detalhado da estrutura dos compostos selecionados. Estes resultados e as respetivas conclusões permitirão uma melhor compreensão dos incomuns sistemas orgânicos moleculares que exibem polimorfismo de cor, o que é essencial para que possa ser feita uma avaliação e exploração das suas potenciais aplicações, nomeadamente nos casos em que se observa conversão térmica entre polimorfos.

Table of Contents

Acknowledgements.....	i
Abstract.....	iv
Resumo	vi
Table of Contents.....	viii
List of Figures.....	x
List of Tables	xvii
Abbreviations.....	xxi
1. Introduction.....	1
1.1. Problem Statement and General Approach.....	2
1.2. Color Polymorphism: State-of-the-art	5
1.3. Specific Objectives and Structure of the Work.....	32
2. Theory and Methodology.....	34
2.1. Computational Methods.....	34
2.1.1. Density Functional Theory (DFT)	34
2.1.2. Basis Sets	37
2.1.3. DFT Calculations with Periodic Boundary Conditions	39
2.1.4. Hirshfeld Surfaces.....	40
2.2. Vibrational Spectroscopy: Infrared Absorption and Raman Scattering Spectroscopies.....	45
2.3. Computational vs. Experimental Polarized Raman Spectra.....	56
2.4. Thermal analysis.....	79
2.4.1. Differential Scanning Calorimetry.....	79
2.4.2. Polarized Light Thermomicroscopy.....	80
2.5. X-ray diffraction	83

2.6. Synthesis and Polymorph screening	88
3. <i>N</i> -picryl- <i>p</i> -toluidine Analogues	90
3.1. TMA.....	92
3.2. TAP & TMA – Polarized Raman Study	123
4. ROY Analogues	148
4.1. Ac-ROY	151
4.2. ROY-ol.....	181
4.3. ROY-CAM.....	210
5. Conclusions and Perspectives for the Future	235
Annexes	243

List of Figures

1. Introduction

1.2. Color Polymorphism: State-of-the-art

Figure 1 – Schematic illustration of the two different classes of polymorphism: packing and conformational polymorphism. 10

Figure 2 – Structures of the parent molecules that give rise to color polymorphs: N-(4-methyl-2-nitrophenyl)acetamide, dimethyl 2,5-dichloro-3,6-dihydroxy-terephthalate, 5-methyl-2-((2-nitrophenyl)amino)thiophene-3-carbonitrile (ROY), 2,4,6-trinitro-N-(p-tolyl)aniline, dimethyl-5-benzoyl-3-phenylindolizine-1,2-dicarboxylate and 1,4,7,10-tetrabutyltetracene. 11

Figure 3 – Polymorphs of 5-methyl-2-((2-nitrophenyl)amino)thiophene-3-carbonitrile and their melting point (m.p.). 18

Figure 4 – Relative energy as a function of the C-C-N-S torsion angle (θ) for the 5-methyl-2-((2-nitrophenyl)amino)thiophene-3-carbonitrile monomer. 21

Figure 5 – Structures of 2-((2-nitrophenyl)amino)thiophene-3-carbonitrile, 5-methyl-2-((4-methyl-2-nitrophenyl)amino)thiophene-3-carbonitrile and 2,2'((ethyne-1,2-diylbis(2-nitro-4,1-phenylene))bis(azanediyl)) bis(5-methylthiophene-3-carbonitrile). 22

Figure 6 – Relative energy as a function of the (NO₂)C-C-N-C torsion angle for the 2,4,6-trinitro-N-(p-tolyl)aniline monomer. 24

Figure 7 – Structure of picryl aniline and N-(2,4-dinitrophenyl)-o-anisidine. 25

2. Theory and Methodology

2.2. Vibrational Spectroscopy: Infrared Absorption and Raman Scattering Spectroscopies

Figure 1 – Illustration of the derivatives of dipole moment and polarizability, which determines the activity of a given vibration in infrared and Raman spectroscopy, respectively. 46

Figure 2 – Morse potential energy curve, which reproduces the general shape of a molecular potential energy. 49

Figure 3 – Thermo Scientific Nicolet iS50 FTIR spectrometer equipped with an MCT/A detector and a KBr beam splitter, mounted together with the ARS Cryogenics closed-cycle helium refrigeration system cryostat. 51

Figure 4 – Thermo Scientific Nicolet iS5 FTIR system, equipped with an iD7 ATR accessory. 51

Figure 5 – Schematic illustration of the IR absorption, the Rayleigh scattering and the Stokes and anti-Stokes Raman scattering phenomena. 53

Figure 6 – BWTEK i-Raman Pro system. 54

Figure 7 – Micro-Raman Horiba LabRam HR Evolution instrument. 54

2.3. Computational vs. Experimental Polarized Raman Spectra

Figure 1 – Schematic representation of the geometric configurations determining the polarization of the laser beam relatively to the sample in the used instrument. 65

Figure 2 – Experimental polarized Raman spectra of LiNbO₃ crystal (X-cut; Y-cut and Z-cut) collected for the different possible configurations in the back-scattering mode. 67

Figure 3 – CRYSTAL B3LYP/pob-TZVP calculated spectra of the LiNbO₃ crystal, considering the whole and individual components of the Raman tensors. 68

Figure 4 – Top panel: Experimental $X(ZZ)\bar{X}$ and $Y(ZZ)\bar{Y}$ spectra of LiNbO₃ crystal. Bottom panel: CRYSTAL B3LYP/pob-TZVP calculated spectrum based on the α'_{zz} Raman tensors component values. 69

Figure 5 – Top panel: Experimental $X(YZ)\bar{X}$, $X(ZY)\bar{X}$, $Y(XZ)\bar{Y}$ and $Y(ZX)\bar{Y}$ spectra of LiNbO₃ crystal. Bottom panel: CRYSTAL B3LYP/pob-TZVP calculated spectrum based on the α'_{xz} and α'_{yz} components of the Raman tensors. 70

Figure 6 – Top and middle panels: Experimental $X(YY)\bar{X}$ and $Y(XX)\bar{Y}$ spectra of LiNbO₃ crystal, respectively. Bottom panel: CRYSTAL B3LYP/pob-TZVP calculated spectrum based on the α'_{xx} and α'_{yy} components of the Raman tensors. 72

Figure 7 – Top panel: Experimental $Z(XX)\bar{Z}$ and $Z(YY)\bar{Z}$ spectra of LiNbO_3 crystal. Middle: Experimental $Z(XY)\bar{Z}$ and $Z(YX)\bar{Z}$ spectra of LiNbO_3 crystal. Bottom panel: CRYSTAL B3LYP/pob-TZVP calculated spectrum based on the α'_{xy} component of the Raman tensors. 73

2.4. Thermal analysis

Figure 1 – Perkin-Elmer DSC Pyris 1 with liquid nitrogen cooling system. 80

Figure 2.2 – Linkam DSC-600 hot stage and Leica DMRB microscope with a Sony CCD-IRIS/RGB video camera. 81

2.5. X-ray diffraction

Figure 1 – X-ray diffraction from crystal lattice planes, illustrating Bragg's law. 84

Figure 2 – Bruker D8 Advance diffractometer. 86

Figure 3 – Bruker APEX II diffractometer. 86

3. N-picryl-p-toluidine Analogues

3.1. TMA

Figure 1 – Computed B3LYP/6-311++G(d,p) relaxed potential energy scans corresponding to the internal rotation around the 1N–7C bond, as defined by the 4C–1N–7C–12C torsion angle. 102

Figure 2 – Geometries of the two conformers of TMA, with atom numbering. 103

Figure 3 – Computed B3LYP/6-311++G(d,p) relaxed potential energy profile for internal rotation of the methyl group in conformers A and B. 103

Figure 4 – Experimental infrared spectrum of monomeric TMA isolated in an argon matrix at 15 K, calculated spectra of conformers A and B and the simulated sum-spectrum of the conformational mixture according to the predicted room temperature Boltzmann populations 104

Figure 5 – Photographs of yellow (recrystallized in carbon tetrachloride), orange (recrystallized in DMF) and red (recrystallized in DMSO) crystals of TMA, with 20× magnification. 107

Figure 6 – Benchmark regions of the Raman spectra of the yellow (Y), orange (O) and red (R) crystals of TMA.	107
Figure 7 – Benchmark regions of the IR-ATR spectra of the yellow (Y), orange (O) and red (R) polymorphs of TMA.	107
Figure 8– ORTEP plots of the monoclinic (Y), orthorhombic (O) and triclinic (R) polymorphs of TMA.	110
Figure 9 – Hydrogen-bonding network in the monoclinic (Y), orthorhombic (O) and triclinic (R) polymorphs of TMA.	112
Figure 10 – d_{norm} mapping on the Hirshfeld surfaces of the molecules in the crystals of the three polymorphs of TMA.	113
Figure 11 – DSC curves of the Y, O and R polymorphs of TMA.	115
Figure 12 – PLTM images of the heating process of the O polymorph of TMA.	116
Figure 13 – DSC devitrification curve of a melted sample of TMA.	117
Figure 14 – Normalized solid-state UV-vis absorption spectra of the three polymorphs of TMA, in the 250–750 nm range, and the corresponding color parameters in the CIE 1931 chromaticity scale.	117

3.2. TAP & TMA – Polarized Raman Study

Figure 1 – Conformers of TAP with adopted atom numbering. Two perspectives are shown for each form.	130
Figure 2 – DFT(B3LYP)/6-311++G(d,p) calculated potential energy profiles for internal rotation about the N1–C7 bond of the amine bridge of TAP molecule.	132
Figure 3 – DFT(B3LYP)/6-311++G(d,p) calculated potential energy profiles for internal rotation of the phenolic OH group in the pairs of conformers A and C, and B and D of TAP molecule.	133
Figure 4 – ORTEP plots depicting the anisotropic displacement ellipsoids drawn at the 50 % probability level.	134
Figure 5 – Hydrogen-bonding network in TAP crystal showing the 1D-chains running along the crystallographic direction $[1\ 0\ -1]$.	135
Figure 6 – Hydrogen-bonding network showing the TAP crystal packing.	136

Figure 7 – Experimentally obtained single crystal polarized Raman spectra compared with the simulated spectra resulting from fully periodic first principles calculations on the crystal of the orthorhombic polymorph of TMA 138

Figure 8 – Experimentally obtained single crystal polarized Raman spectra compared with the simulated spectra resulting from fully periodic first principles calculations on the crystal of the triclinic polymorph of TMA. 139

Figure 9 – Experimentally obtained single crystal polarized Raman spectra compared with the simulated spectra resulting from fully periodic first principles calculations on the crystal of the monoclinic polymorph of TMA. 141

Figure 10 – Experimentally obtained single crystal polarized Raman spectra compared with the simulated spectra resulting from fully periodic first principles calculations on the crystal of the TAP. 142

4. ROY Analogues

4.1. AcROY

Figure 1 – Geometries of the four low-energy intramolecularly H-bonded conformers of AcROY with the adopted atom numbering. 161

Figure 2 – Potential energy profiles associated with the internal rotation θ , as defined by the dihedral angle C8–N2–C1=C2. 163

Figure 3 – Potential energy profiles associated with the internal rotation φ , as defined by the dihedral angle C3–C4–C5=O1. 163

Figure 4 – The three different AcROY crystalline materials obtained in the polymorph screening experiments. Images are 10× amplified. 164

Figure 5 – Room temperature Raman spectra of the three observed AcROY polymorphs. 165

Figure 6 – FTIR spectra (ATR mode) of the three observed AcROY polymorphs. 166

Figure 7 – Hydrogen-bonding network in polymorph 1. 169

Figure 8 – Hydrogen-bonding network in polymorph 2. 170

Figure 9 – Powder X-ray diffractograms for the polymorphs of AcROY. 171

Figure 10 – d_{norm} mapping on the Hirshfeld surfaces of the molecules in polymorphs 1 and 2 of AcROY.	173
Figure 11 – DSC heating curves of polymorphs 1 and 3 of AcROY.	174
Figure 12 – Temperature variation Raman spectra obtained for a sample of polymorph 2 of AcROY.	175
Figure 13 – PLTM images showing the 2 → 1 solid-solid transition.	176

4.2. ROY-ol

Figure 1 – ROY-ol polymorphs-1 and -2. Images are amplified 50×.	189
Figure 2 – IR and Raman spectra of polymorphs 1 and 2 of ROY-ol.	190
Figure 3 – ORTEP plots depicting the anisotropic displacement ellipsoids drawn at the 50 % probability level and the atom numbering schemes for polymorph-1 and polymorph-2.	192
Figure 4 – Hydrogen-bonding network in polymorph-1 of ROY-ol showing the 1D-chains running along the crystallographic direction b-axis with molecules joined by strong N–H··O hydrogen bonds.	193
Figure 5 – Hydrogen-bonding network in polymorph-2 of ROY-ol showing the 1D-chains running along the [1 1 0] and [1 –1 0] crystallographic direction joined by strong N–H··O hydrogen bonds.	194
Figure 6 – Maps of d_{norm} on the Hirshfeld surfaces of the crystallographic asymmetric units of polymorphs 1 and 2 of ROY-ol, also showing the neighboring molecules which account for the strongest interactions.	195
Figure 7 – DSC heating curves of two samples of ROY-ol, one corresponding to pure polymorph-2 and the other to a mixture of polymorphs 1 and 2.	197
Figure 8 – PLTM images obtained along the heating of a crystal of the polymorph-2 of ROY-ol.	198
Figure 9 – PLTM images obtained along the heating of a crystal of the polymorph-1 of ROY-ol.	199
Figure 10 – Raman spectra of ROY-ol polymorphs 1, 2 and 3.	200
Figure 11 – PLTM images obtained along the heating of ROY-ol amorphous material on a crystal of polymorph-2.	201

Figure 12 – Geometries of the four low-energy conformers of ROY-ol.	202
Figure 13 – DFT calculated potential energy profiles (gas phase) associated with the internal rotation θ , as defined by the dihedral angle C–N–C–S, for ROY-ol, AcROY and ROY compounds, and corresponding dihedral angles observed experimentally for the different polymorphs.	204
4.3. ROY-CAM	
Figure 1 – Red and green polymorphs of ROY-CAM, obtained from the polymorph screening experiments.	217
Figure 2 – ATR mode FTIR spectra of ROY-CAM green and red polymorphs.	219
Figure 3 – Raman spectra of ROY-CAM green and red polymorphs.	219
Figure 4 – ORTEP plots depicting the anisotropic displacement ellipsoids drawn at the 50 % probability level and the atom numbering schemes for the red and green) polymorphs of ROY-CAM.	220
Figure 5 – Hydrogen-bonding network in the red polymorph of ROY-CAM showing the stacking of molecular planes joined <i>via</i> weak C–H \cdots O and C–H \cdots N hydrogen bonds.	221
Figure 6 – Hydrogen-bonding network in the green polymorph of ROY-CAM showing the main hydrogen bond interactions.	222
Figure 7 – DSC heating curves of ROY-CAM red and green polymorphs and of a sample containing both polymorphs.	223
Figure 8 – PLTM images obtained from the heating of ROY-CAM red polymorph.	224
Figure 9 – PLTM images obtained from the heating of ROY-CAM green polymorph.	224
Figure 10 – B3LYP/6-311++G(2d,p) calculated relaxed potential energy scan corresponding to the rotation around the σ internal rotation axis.	229
Figure 11 – Geometry representation of the 11 low-energy carboxylic acid <i>cis</i> conformers of ROY-CAM (two different perspectives).	229
Figure 12 – B3LYP/6-311++G(2d,p) calculated relaxed potential energy scan corresponding to the rotation around the θ dihedral angle.	231

List of Tables

2. Theory and Methodology

2.3. Computational vs. Experimental Polarized Raman Spectra

Table 1 – Experimental wavenumbers of the LiNbO_3 vibrational modes (A_1 and E symmetries) and their assignment. 63

Table 2 – Phonon modes expected to be visible in the different polarized Raman spectra of LiNbO_3 , for back-scattering mode, and their respective experimental wavenumbers. 64

Table 3 – Correspondence between experimental configurations according to Porto notation and the used experimental set ups. 66

Table 4 – Wavenumbers of the phonons observed in the $X(ZZ)\bar{X}/Y(ZZ)\bar{Y}$ experimental spectra of LiNbO_3 crystal, CRYSTAL B3LYP/pob-TZVP calculated wavenumbers with non-null intensities according to the α'_{zz} Raman tensors component, and comparison with literature data. 69

Table 5 – Wavenumbers of the phonons observed in the $X(YZ)\bar{X}/X(ZY)\bar{X}/Y(XZ)\bar{Y}/Y(ZX)\bar{Y}$ experimental spectra of LiNbO_3 crystal, CRYSTAL B3LYP/pob-TZVP calculated wavenumbers with non-null intensities according to the α'_{xz} and α'_{yz} Raman tensors components, and comparison with literature data. 71

Table 6 – Wavenumbers of the phonons observed in the experimental $X(YY)\bar{X}$ and $Y(XX)\bar{Y}$ spectra of LiNbO_3 crystal, CRYSTAL B3LYP/pob-TZVP calculated wavenumbers with non-null intensities according to the α'_{xx} and α'_{yx} Raman tensors components, and comparison with literature data. 72

Table 7 – Wavenumbers of the A_1 (LO) phonons observed in the experimental $Z(XX)\bar{Z}$ and $Z(YY)\bar{Z}$ spectra of LiNbO_3 crystal and comparison with literature data. 73

Table 8 – Comparison between the Raman intensities (areas under the bands) of the calculated spectrum based on the α'_{zz} Raman tensor components and the $X(ZZ)\bar{X}$ experimental configuration spectrum (A_1 symmetry modes). 74

Table 9 – Comparison between the Raman intensities (areas under the curve) of the calculated spectrum based on the α'_{xz} and α'_{yz} Raman tensor components and the $Y(XZ)\bar{Y}$ experimental configuration spectrum (E symmetry modes). 75

Table 10 – Comparison between the Raman intensities (area under the curve) of the calculated spectrum based on the α'_{xy} and α'_{yx} components of the Raman tensors and the $Z(XY)\bar{Z}$ experimental configuration spectrum (E symmetry modes). 75

Table 11 – Comparison between the Raman intensities (area under the curve) of the calculated spectrum based on the α'_{yy} component of the Raman tensors and the $X(YY)\bar{X}$ experimental configuration spectrum (A_1 and E symmetry modes). 76

3. N-picryl-p-toluidine Analogues

3.1. TMA

Table 1 – Summary of the single-crystal X-ray data collection and crystal structure refinement. 98

Table 2 – Assignment of the infrared spectrum of matrix isolated (Ar, 15 K) TMA. 105

Table 3 – Valence angles in the picryl ring of the three polymorphs of TMA. 111

Table 4 – Relevant dihedral and torsion angles for the three polymorphs of TMA. 111

Table 5 – Hydrogen bonds and short intermolecular contacts for the polymorphs of TMA. 112

Table 6 – Percent areas of the Hirshfeld surface assigned to the different types of intermolecular interactions in the three polymorphs of TMA. 114

Table 7 – Melting point and enthalpy of fusion for the three polymorphs of TMA. 115

3.2. TAP & TMA – Polarized Raman Study

Table 1 – Summary of the single-crystal X-ray data collection and crystal structure refinement. 129

Table 2 – Valence angles in the picryl ring of TAP crystal. 135

Table 3 – Relevant dihedral and torsion angles for the TAP crystal. 135

Table 4 – Hydrogen bonds and short intermolecular contacts in TAP crystal.	136
--	-----

4. ROY Analogues

4.1. Ac-ROY

Table 1 – Summary of the single-crystal X-ray data collections and crystal structure refinements.	158
---	-----

Table 2 – Values of the C8–N2–C1=C2 (θ) and C3–C4–C5=O1 (φ) dihedral angles and relative energies (ΔE) of the four low-energy conformers of AcROY.	161
---	-----

Table 3 – Relevant dihedral and torsion angles for the two polymorphs.	168
--	-----

Table 4 – Hydrogen bonds and short intermolecular contacts in polymorph 1.	169
--	-----

Table 5 – Hydrogen bonds and short intermolecular contacts in polymorph 2.	170
--	-----

Table 6 – Fractional areas of the Hirshfeld surface assigned to the different intermolecular interactions in AcROY polymorphs 1 and 2.	174
--	-----

4.2. ROY-ol

Table 1 – Summary of the single-crystal X-ray data collections and crystal structure refinements.	188
---	-----

Table 2 – Valence angles in the thiophene and nitrophenyl rings of the two polymorphs of ROY-ol.	192
--	-----

Table 3 – Relevant dihedral and torsion angles for the two polymorphs of ROY-ol.	192
--	-----

Table 4 – Hydrogen bonds and short intermolecular contact distances and angles for the two polymorphs of ROY-ol.	193
--	-----

Table 5 – Fractional areas of the Hirshfeld surface assigned to the different intermolecular contacts in ROY-ol polymorphs 1 and 2.	195
---	-----

4.3. ROY-CAM

Table 1 – Summary of the single-crystal X-ray data collections and crystal structure refinements.	221
---	-----

Table 2 – Relevant dihedral and torsion angles for the red and green polymorphs of ROY-CAM. 222

Table 3 – Hydrogen bonds and short intermolecular contact distances and angles for the two polymorphs of ROY-CAM. 222

Table 4 – Fractional areas of the Hirshfeld surface assigned to the different intermolecular contacts in ROY-CAM green and red polymorphs. 226

Table 5 – Dihedral angle values and relative energies of the different ROY-CAM optimized conformers. 228

Abbreviations

AcROY: 5-Acetyl-2-((2-nitrophenyl)amino)thiophene-3-carbonitrile

ATR: Attenuated Total Reflection

BZ: Brillouin Zone

CCD: Charge-coupled Device

CCDC: Cambridge Crystallographic Data Centre

CIE: Commission Internationale de l'Eclairage Proceedings

CPKS: Coupled Perturbed Kohn Sham

CSD: Cambridge Structural Database

DFT: Density Functional Theory

DMF: Dimethylformamide

DMSO: Dimethyl Sulfoxide

DSC: Differential Scanning Calorimetry

ESI: Electrospray Ionization

FTIR: Fourier Transform Infrared Spectroscopy

IR: Infrared

HOMO: Highest Occupied Molecular Orbital

HRMS: High-resolution Mass Spectrometry

LCAO: Linear Combination of Atomic Orbitals

LO: Longitudinal Optical

LUMO: Lowest Unoccupied Molecular Orbital

m.p.: Melting Point

NMR: Nuclear Magnetic Resonance

PhD: Doctor of Philosophy

PLTM: Polarized Light Thermal Microscopy

ROY: 5-Methyl-2-((2-nitrophenyl)amino)thiophene-3-carbonitrile

ROY-CAM: 2-(4-((3-Cyanothiophen-2-yl)amino)-3-nitrophenyl)acetic Acid

ROY-ol: 2-((4-Hydroxy-2-nitrophenyl)amino)thiophene-3-carbonitrile

RT: Room Temperature

TAP: 3-((2,4,6-Trinitrophenyl)amino)phenol

T_{fus} : Temperature of Fusion

TLC: Thin Layer Chromatography

TO: Transverse Optical

TMA: 2,4,6-Trinitro-*N*-(*m*-tolyl)aniline

THF: Tetrahydrofuran

UV: Ultraviolet

$\Delta_{\text{fus}}H$: Enthalpy of Fusion

λ : Wavelength

1. Introduction

In this Chapter, the general scientific problem that was chosen as the main topic of this PhD project is presented, alongside the main research strategies followed in this work and an overview of the state-of-the-art on the subject at the time the project was designed.

Section 1.1 briefly introduces the topic under investigation and the chosen investigation tools, presenting a general overview of the performed studies and of the contents of this Thesis. It highlights the relevance of the developed work and prepares the reader for the more in-deep description of the matter and objectives of this study that are presented in Sections 1.2 and 1.3.

Section 1.2 focus on *Color Polymorphism* in organic molecular systems, providing its fundamentals, underlining the most relevant studies appearing in the scientific literature before the present investigation and emphasizing its relevance in the fields of physical chemistry and materials science. As it is the case of other sections throughout this Thesis, this section consists of an original article on the subject we have recently published in a high-impact factor international scientific peer-reviewed journal. For this reason, we have decided to include the list of references relative to each section of this Thesis at the end of the corresponding section, as in the original publication. For the same reason, the Figures, Schemes and Tables throughout the text are numbered from the beginning in every section. On the first page of each section, all the details regarding the publication are provided, including the number of citations it has collected. The supplementary material to the original publications is not included in this Thesis, but the hyperlinks to the webpages where this material can be consulted are indicated in the first page of each section. In the case of a section presenting results that have not yet been published, the supplementary material is provided in the Annexes section of the Thesis.

Section 1.3 describes the main specific objectives of this research project, presenting the topics initially selected to guide the project and the adjustments made along its implementation, as well as the general structure of the following chapters. The first part of this information will be further developed in the last chapter of the Thesis (Conclusions and Perspectives for the Future).

1.1. Problem Statement and General Approach

Color polymorphism is a very interesting property of chemical systems that present polymorphs of different colors. Color polymorphism in molecular organic systems is a rare phenomenon, exhibited only by a small number of systems, but it has the potential to be used in a wide variety of applications. Rather surprisingly, only a few studies dealing with this type of polymorphism have been reported hitherto. For these reasons and taking advantage of the know-how developed in our research group in the past few years on the subject of polymorphism and on the properties of crystalline systems in general, this topic was chosen as main subject of this PhD research program.

As discussed in detail in the next section, until the beginning of this project (November 2017) only six families of organic compounds were known to exhibit color polymorphism.¹⁻⁶ In total, less than a dozen of different compounds had been reported to possess molecular polymorphs with different colors. Moreover, this rather uncommon property was not yet fully understood. In particular, the impact of conformational and packing polymorphisms on the different colors displayed by the different crystals was still a matter of intense discussion by the scientific community.

Hence, we have decided to synthesize and characterize a series of new compounds that appeared to be good candidates for exhibiting color polymorphism. For the design of these compounds, we considered two basic structural units that had already been shown to give rise to compounds that exhibit color polymorphism: the *N*-picryl-*p*-toluidine³ and 2-(2-nitrophenyl)aminothiophene moieties, the latter being the structural unit of the famous compound known as ROY (from the Red, Orange, Yellow colors of its polymorphs),⁴ the compound of which the largest number of polymorphs is known.⁷ It was also our intention to try to increase the wavelength difference of the colors displayed by the polymorphs of the same compound, which appears as an interesting property for possible future applications of these systems.

The general approach followed in the present research program was the following:

(i) The initial step consisted in the identification of the compounds to be investigated. These compounds were selected by preliminary computational screening, using density functional theory (DFT) calculations. A large number of molecules bearing different substituents attached to different positions of the two selected molecular basic frameworks was tested, regarding the dependence of their electronic absorption spectra with the molecular conformation. Among those, the five molecules

Introduction

exhibiting more distinct electronic spectra in the visible region for different minimum energy conformations (2 molecules belonging to *N*-picryl-*p*-toluidine family, and 3 molecules to the ROY family) were chosen for synthesis and subsequent work, which included their detailed structural and vibrational theoretical study.

(ii) The selected compounds were then synthesized in the Organic Chemistry Laboratory of the Coimbra Chemistry Centre - Institute of Molecular Sciences (CQC-IMS).

(iii) For each synthesized compound, a polymorph screening was performed using classical procedures to generate the crystalline forms, including crystallization from the melt, from different solutions and by sublimation.

(iv) The obtained crystalline materials were then characterized spectroscopically, by infrared (IR) and Raman spectroscopies, and thermally, by differential scanning calorimetry (DSC) and polarized-light thermomicroscopy (PLTM), the latter two techniques being used to determine the thermodynamic relationships between each group of polymorphs. The DSC and PLTM studies were performed in the Thermodynamics and Solid State Chemistry Lab of the CQC-IMS. Moreover, the structure of the polymorphs whose crystals were suitable for structural determination by single crystal X-ray diffraction, were solved and interpreted in terms of the conformations assumed by the molecules in the crystal, as well as the characteristics and determining factors of the molecular packing, with focus on the intermolecular interactions. These studies were done in collaboration with the X-Ray Group of the Center of Physics of the University of Coimbra (CFisUC; Trace Analysis and Imaging Laboratory – TAIL) and with the BioMol group of the Centre for Structural Chemistry – Institute of Molecular Sciences (CQE-IMS; IST - University of Lisbon).

(v) The structural results obtained by X-ray diffraction were then used as input data for periodic boundary conditions DFT calculations, which were undertaken in order to computationally predict the vibrational spectra of each polymorph and to assess the impact of the different conformations and/or the different intermolecular environments on the vibrational properties. These studies were carried out at the Politecnico di Milano.

(vi) Finally, the crystal structures were subjected to a detailed analysis regarding intermolecular interactions, mainly using the Hirshfeld surface analysis method, to better evaluate the factors responsible for the different stabilities of each polymorphic structure and specific characteristics that determine its color.

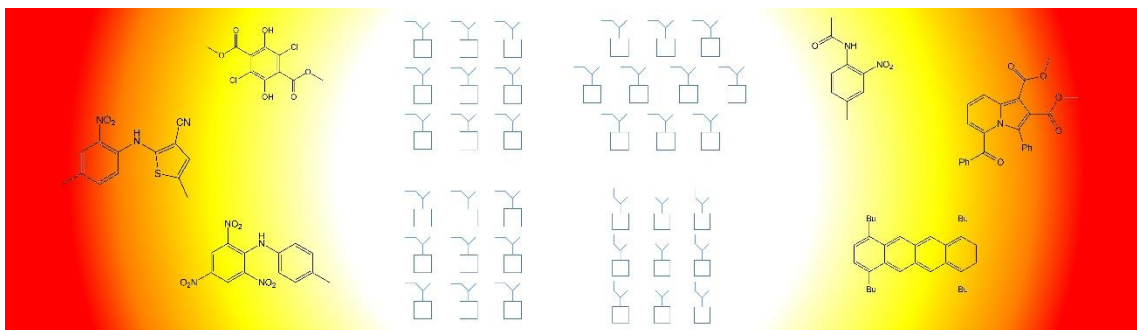
The approach used in this investigation corresponds to an integrated multidisciplinary research project, which resulted in the generation of a large amount of information used in a synergistic way during the performed analyses. This will be clearly evidenced in Chapters 3 and 4 of the Thesis, where the results obtained for the different molecular systems investigated will be presented and discussed.

References

- 1 J. Swiatkiewicz and P. N. Prasad, Spectroscopic Studies of the Thermal Rearrangement Reaction of Dimethyl 3,6-Dichloro-2,5-dihydroxyterephthalate in the Solid State, *J. Am. Chem. Soc.*, 1982, **104**, 6913–6918.
- 2 J. C. Moore, A. Yeadon and R. A. Palmer, Crystal and molecular structures of two polymorphs of 4-methyl-2-nitroacetanilide (MNA), *J. Crystallogr. Spectrosc. Res.*, 1983, **13**, 279–292.
- 3 D. E. Braun, T. Gelbrich, R. K. R. Jetti, V. Kahlenberg, S. L. Price and U. J. Griesser, Colored Polymorphs: Thermochemical and Structural Features of *N*-Picryl-*p*-toluidine Polymorphs and Solvates, *Cryst. Growth Des.*, 2008, **8**, 1977–1989.
- 4 L. Yu, Polymorphism in Molecular Solids: An Extraordinary System of Red, Orange, and Yellow Crystals, *Acc. Chem. Res.*, 2010, **43**, 1257–1266.
- 5 C. Kitamura, Y. Abe, T. Ohara, A. Yoneda, T. Kawase, T. Kobayashi, H. Naito and T. Komatsu, Synthesis and crystallochromy of 1, 4, 7, 10-tetraalkyltetracenes: Tuning of solid-state optical properties of tetracenes by alkyl side-chain length, *Chem. - A Eur. J.*, 2010, **16**, 890–898.
- 6 C. Dohmen, H. Ihmels, R. Kreienmeier and B. O. Patrick, Synthesis of a crystallochromic indolizine dye by a base- and catalyst-free photochemical route, *Chem. Commun.*, 2019, **55**, 11071–11074.
- 7 L. R. Warren, E. McGowan, M. Renton, C. A. Morrison and N. P. Funnell, Direct evidence for distinct colour origins in ROY polymorphs, *Chem. Sci.*, 2021, **12**, 12711–12718.

1.2. Color Polymorphism: State-of-the-art

The review article that constitutes this section is entitled *Color Polymorphism in Organic Crystals* and was published golden open access in Springer Nature's *Communications Chemistry* (Vol. 3; Art. 34) on 17th March 2020. On the day of submission of this Thesis, according to CrossRef, the article has been accessed 8186 times and cited by 26 other peer-reviewed scientific publications. The article is in the 1st percentile (ranked 1st) among the articles of similar age in the journal. It has received 541 reads in Research Gate.



Authors: Bernardo A. Nogueira, Chiara Castiglioni and Rui Fausto.

Corresponding author: Bernardo A. Nogueira.

Author contributions: Bernardo A. Nogueira conducted the literature research, discussed literature examples with Chiara Castiglioni and Rui Fausto, and wrote the first draft of the manuscript. All the authors wrote and edited the paper.

Synopsis:

As mentioned before, there are not many organic compounds known to exhibit color polymorphism. However, the interest of the scientific community for this topic has been growing consistently and, especially in the last 20 years, several articles have been published on the subject. In our article, we have surveyed the publications focusing on color polymorphism, describing systems which exhibit this property and the reasons for that. Also, since some of the concepts related to color polymorphism have been frequently used imprecisely in the scientific literature, in our article concise systematic definitions for these concepts were provided.

Color Polymorphism in Organic Crystals

Bernardo A. Nogueira,^{1,2,*} Chiara Castiglioni² and Rui Fausto^{1,3}

¹ *CQC, Department of Chemistry, University of Coimbra, P-3004-535 Coimbra, Portugal.*

² *CMIC, Dipartimento di Chimica, Materiali e Ingegneria Chimica "G. Natta", Politecnico di Milano, Piazza Leonardo da Vinci 32, 20133, Milano, Italy.*

³ *Department of Chemistry, King Fahd University of Petroleum and Minerals, 31261 Dhahran, Saudi Arabia.*

ABSTRACT

Color polymorphism is a very interesting property of chemical systems which present crystal polymorphs of different colors. It is a rare phenomenon, with only a few examples reported in the literature hitherto. Nevertheless, systems exhibiting color polymorphism have many potential applications in different domains, such as pigment, sensor, and technology industries. Here, known representative chemical systems showing color polymorphism are reviewed, and the reasons for them to present such property discussed. Also, since some of the concepts related to color polymorphism have been frequently used imprecisely in the scientific literature, this article provides concise, systematic definitions for these concepts.

Keywords: polymorphism, color polymorphism, conformational polymorphism, packing polymorphism

* Corresponding author e-mail: ban@qui.uc.pt

Introduction

This article focuses on color polymorphism, a fascinating property exhibited by chemical systems which present polymorphs showing different colors. In the first sections, unambiguous definitions of the structural properties and of the relevant physical concepts related with this subject will be provided, since some of them have been frequently used in an imprecise way in the scientific literature. Then, the physicochemical reasons leading to color polymorphism will be described briefly using an essentially phenomenological approach. The last sections of this article will survey representative chemical systems showing color polymorphism.

Terminology

Polymorphism

In the crystallographic context, *polymorphism*, from the Greek *poly* (many) and *morphe* (form), also known as crystal polymorphism, refers to the ability of a certain compound to exist in different crystallographic structures, resulting from different packing arrangements of its molecules in the crystal structure.¹ It is worth to differentiate between polymorphism and *allotrophism*. While the latter term describes the existence of different crystal structures of the same element, polymorphism is used regarding different crystalline structures of compounds. It is also important to mention that in this review one will not consider solvates, hydrates or dynamic isomers (including geometric isomers and tautomers) as polymorphic phases but, instead, as pseudopolymorphic states. Hence, a safe criterion for the classification of a system as polymorphic would be if the crystal structures are different but give rise to the same liquid and vapor states.

Why is polymorphism so important? The main reason is that, although being composed by the same compound, different polymorphic structures can behave as different materials.² Indeed, in general different polymorphs present different physical, chemical and mechanical properties. Among others, such properties may include different melting temperature, solubility, vibrational transitions (*e.g.*, different infrared and Raman spectra), electronic transitions (distinct UV-visible spectra), density, surface tension, crystal shape, kinetic stability, crystal hardness and color. These differences in the properties of crystals of the same compound have important practical implications, and result in a wide range of applications in many domains. Nevertheless, they are not only relevant in the context of the production and commercialization of crystalline materials as pharmaceuticals, agrichemicals, food additives, pigments and explosives, for example,¹ but they have also been shown to be important from the view point of fundamental research. They help scientists understanding some fundamental chemical aspects related to intra and intermolecular interactions, the driving forces leading to their occurrence,

and their structural implications. Polymorphs are also important in the context of intellectual and industrial property, since a new polymorphic structure can sometimes originate new or further legal commercialization protection regarding one compound.³

Conformational polymorphism

Conformational polymorphism can be described as the existence of different conformers of the same molecule in different polymorphic crystal structures.¹ In order to make clear the above statement, it is relevant to clearly define what is a conformer. In simple terms, a new *conformation* can be defined as the result of a variation of any torsion angle in a molecule. On the other hand, a new *conformer* only exists if this variation of the torsion angle, implies the appearance of structure defining a new potential energy well, which corresponds to a different stable structure of the molecule. Therefore, not every pair of conformations are conformers, but only the ones that correspond to distinct minima on the potential energy surface.⁴

Another pair of concepts that are worth to distinguish are *conformational arrangement* and *conformational change*. The first one happens always for a flexible molecule in a crystal, even if in a minimal extent. This means that, due to the flexibility of the molecule, the optimal geometry in the gas phase is, in the crystal, slightly modified by the intermolecular interactions in order to minimize the lattice energy. Therefore, conformational arrangements give rise to a new molecular structure, because of the modulation of the intramolecular potential by interactions occurring in solid state. Instead, conformational changes require a change of conformer, *i.e.*, a change of the molecular structure from one minimum of the intramolecular potential energy surface to another one. This change will result often in a markedly different molecular geometry (different conformer), which will also be adjusted (it relaxes) in the crystal by the intermolecular forces so that it differs somehow from that corresponding to the geometry of the gas-phase minimum energy structure. Thus, conformational arrangements do not give rise to different conformational polymorphs, while conformational changes do.⁴

Notice, moreover, that intermolecular interactions in solid state are not merely responsible of molecular structure relaxation, but they can remarkably modify the relative energy of two (or more) different conformations, and eventually stabilize a conformer characterized by a relatively high energy in gas phase, as indeed happens in different solvents.

Packing polymorphism

When two crystalline polymorphs are constituted by a non-flexible molecule or by the same conformer of a flexible molecule, then the type of polymorphism present in the system is designated by *packing polymorphism*. In this case, the different crystallographic structures arise at the intermolecular level, being determined by different intermolecular interactions that are, in this case, comparatively weaker than the intramolecular interactions defining the adopted conformational geometry.

Non-covalent interactions, acting both at intermolecular as well as intramolecular level, include van der Waals interactions (including steric repulsion), hydrogen and halogen bonding, charge-transfer forces and coulombic interactions, among others.¹ They can be roughly organized into three different categories: (1) non-bonded, non-coulombic (*e.g.*, van der Waals dispersion forces, charge-transfer), (2) coulombic and (3) hydrogen and halogen bonding. The energy range of interactions for group (1) is about 5-20 kJ mol⁻¹ (between 5-8 kJ mol⁻¹ for dispersion interactions and less than 20 kJ mol⁻¹ for charge-transfer interactions),⁵⁻⁸ while for the hydrogen and halogen bonds the energy is usually comprised between 4 and 42 kJ mol⁻¹. The wide range of energy characteristic of the last type of interactions is due to their strong dependence of the distance and relative orientation between the participating atoms.⁹ The long-range coulombic interactions exist on an even wider energy range, depending essentially on the distance between the charged molecules or groups involved.¹⁰

The energies associated with intermolecular interactions are, thus, in most of the cases, of the same order of magnitude of those required to distort the molecular geometry in their absence, and are, consequently, likely to affect torsion angles around single bonds, which correspond in general to the most flexible molecular internal coordinates. How much these coordinates are effectively affected by the intermolecular interactions is the key property leading to the two different types of polymorphism, conformational and packing polymorphism. As mentioned in the previous section, when intermolecular interactions are strong enough to overcome intramolecular interactions and result in a *conformational change*, the type of polymorphism displayed is conformational polymorphism. When they are weaker compared to the intramolecular forces acting to stabilize the conformer that is present in the different crystalline structures, one is facing a case of *packing polymorphism*. Figure 1 schematically represents the difference between the two described types of polymorphism.

Introduction

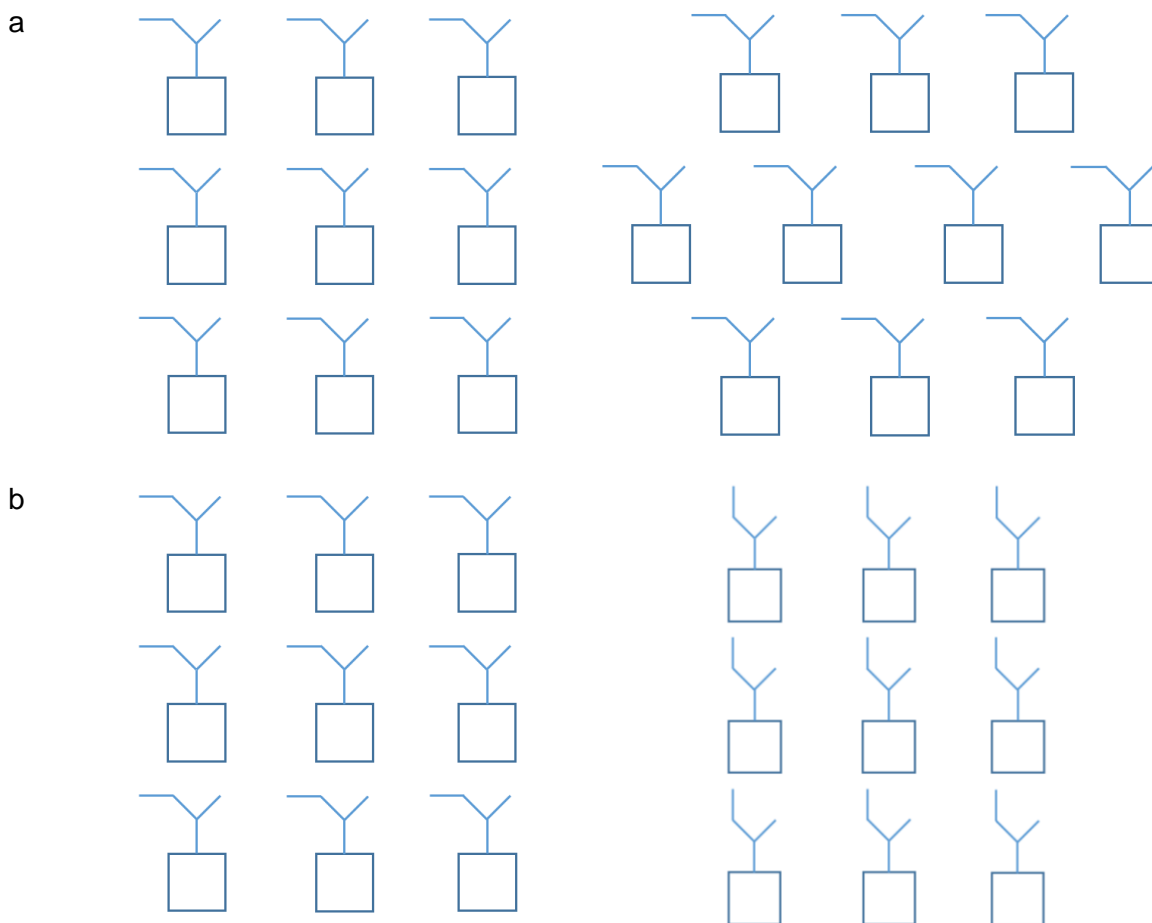


Figure 1 – Schematic illustration of the two different classes of polymorphism: packing and conformational polymorphism. In the top of the Figure (a) packing polymorphism is depicted schematically, while conformational polymorphism is represented in the lower part of Figure (b).

Color polymorphism

It is of fundamental importance to distinguish between *color polymorphism* and *crystallochromism*, two terms often mistakenly employed as synonyms. In fact, the correct term to define a molecule that presents polymorphs (either packing or conformational) with different color is *color polymorphism*. This means that one of the physical properties that varies with the different crystallographic structures of the same compound is, indeed, the color. On the other hand, *crystallochromism* is correctly defined as the dependence of the solid-state color resulting from small changes in molecular structure specifically related with the length, shape, number, pattern of substitution and kind of substituent groups.^{11,12} This means that different molecules, having the same backbone structure but different substituents, can present considerably different solid-state colors, despite presenting very similar colors in solution.¹² The misunderstanding between the two definitions appears to have begun in 1994, when Kazmaier and Hoffmann explicitly defined crystallochromism as

Introduction

the dependence of color on crystal packing,¹³ a much wider definition where both terms that we are trying to distinguish would fit. It must be stressed that, despite of the referred broad definition, the authors use the term for the correct purpose, as we suggest here. Nevertheless, this wide-ranging definition of crystallochromism leads to the misuse of the term, sometimes appearing as synonym of color polymorphism,¹⁴ sometimes being used simultaneously for both meanings that are being discussed here.¹¹ Therefore, and to summarize, color polymorphism should be used when one is dealing with different solid-state colored systems of the same compound, and crystallochromism when referring to crystals that present different colors but are formed by distinct, yet structurally related compounds (such as compounds belonging to the same family bearing different substitutions on the parent molecule), which present similar colors in solution.

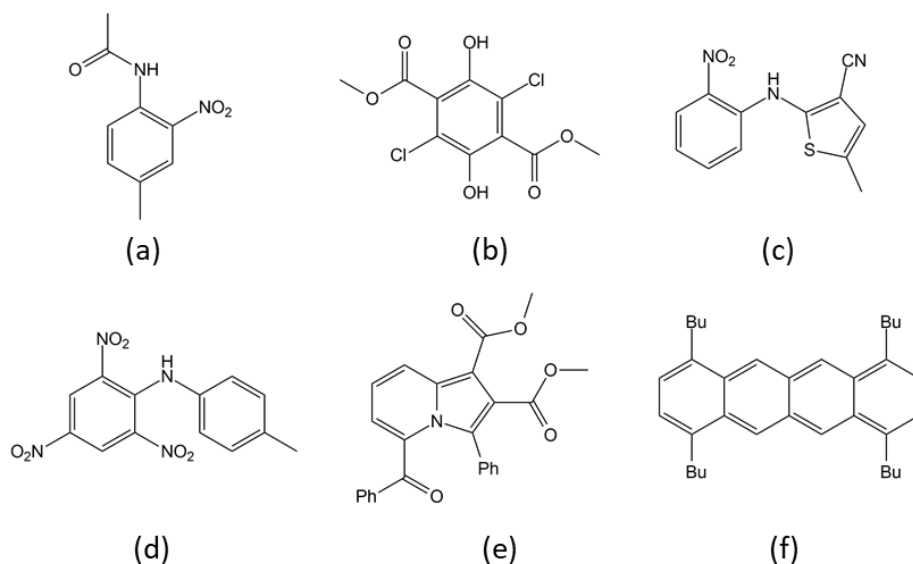


Figure 2 – Structures of the parent molecules that give rise to color polymorphs and that are discussed here: (a) N-(4-methyl-2-nitrophenyl)acetamide,^{20–26} (b) dimethyl 2,5-dichloro-3,6-dihydroxy-terephthalate,^{27–35} (c) 5-methyl-2-((2-nitrophenyl)amino)thiophene-3-carbonitrile (ROY),^{36–53} (d) 2,4,6-trinitro-N-(p-tolyl)aniline,^{54–61} (e) dimethyl-5-benzoyl-3-phenylindolizine-1,2-dicarboxylate¹⁴ and (f) 1,4,7,10-tetrabutyltetracene.^{62–64} The structures of related compounds exhibiting also color polymorphs are presented in the relevant section.

Different polymorphs may also exhibit different fluorescence colors, and several fluorescent polymorphic materials whose altered emission between two states under stimuli can be controlled and reversibly switched through interconversion between polymorphs have been reported.^{15–19} Despite of many potential applications in different areas, such as pigment, sensor, and technology industries, there are only few examples of systems displaying color polymorphism reported in the literature. Specifically, among other technological applications,¹⁵ color polymorphic materials can be used as time-temperature sensors, as described by Cavallini et al.,^{16,17} or used in photoelectronic devices with multiplex capabilities, as suggested by Lin et al.¹⁸ In fact, to the best of our knowledge, there are no more than ten

different compound families already synthesized and characterized, and not much more different compounds exhibiting this special type of polymorphism. In this article, one will focus on the six most representative families of compounds displaying color polymorphism, whose most famous members are represented in Figure 2: *N*-(4-methyl-2-nitrophenyl)acetamide,^{20–26} dimethyl 2,5-dichloro-3,6-dihydroxyterephthalate,^{27–35} 5-methyl-2-((2-nitrophenyl)amino)tiophene-3-carbonitrile (ROY),^{36–53} 2,4,6-trinitro-*N*-(*p*-tolyl)aniline,^{54–61} dimethyl-5-benzoyl-3-phenylindolizine-1,2-dicarboxylate¹⁴ and 1,4,7,10-tetrabutyltetracene.^{62–64}

Mechanisms for polymorphs' color variation

The difference in the color of different polymorphs is caused by a dissimilar electron distribution within the chromophore of their constituting molecules, which affect the electronic energy levels and, consequently, the photons' frequencies the materials are able to absorb when exposed to light. The distinct electron distributions can be due to the different packing interactions existing in the polymorphs, by the different geometry of the conformers present in the crystals, or by both.

To understand the change of color induced by a conformational change, one can think in a molecule exhibiting a π -delocalized system in two conformations where the extension of the delocalization is different. This can be varied by performing an internal rotation about a bond, so that for example an initially more planar conformation with an extended π -delocalized system transforms into a less planar conformation where the π -electrons overlap in the neighborhood of the rotated bond is weakened. In practical terms, the conformational change reduces the length of the π -delocalized system, which leads to increase the energy difference between the excited and the ground electronic states, *i.e.*, to a decrease of the wavelength associated with the electronic absorption responsible for the color of the system. Let us suppose that the molecule, in the initial conformation absorbs in the green and that, after the conformational change it absorbs in the violet. Since one perceives the color of the materials as the complementary color to that associated with the absorption, the initial material would be perceived as being red, while after the conformational change it would look yellow. A similar reasoning can be applied when the conformational change would work in the opposite way, so that the π -delocalization within the chromophore increases.

The effects on color strictly associated with packing are also easy to conceptualize. A change in the intermolecular potential felt by the molecules might affect the charge distribution, which in turn will result in a change on the spacing of the energy levels. In this case, the direction of the changes is not easy to predict, so that both red or blue shifts may result. Moreover, peculiar intermolecular interactions

Introduction

which determines charge polarization and/or electron charge transfer (*e.g.*, in the presence of strong H bonds), are expected to be the most effective in terms of color changes.

In the next sections one will consider the relative importance of the two factors (packing and conformational changes) for the specific systems herein addressed (see Figure 2). In brief, for *N*-(4-methyl-2-nitrophenyl)acetamide, the chromophore, which in this case is the whole molecule, is sensitive to changes in both the intermolecular interactions and conformational arrangements, generating three different polymorphs of white, yellow and amber colors; the last two are packing polymorphs, while the first one is a conformational polymorph of the previous ones. A similar situation occurs for 2,5-dichloro-3,6-dihydroxyterephthalate, where yellow, light-yellow, and white crystals appear as a result of a combination of changes in the intermolecular interactions, in particular hydrogen bonding (for white *versus* the two yellow polymorphs), and conformation (for all three polymorphs). In the case of ROY, the dissimilarity in the color of the different polymorphs is mainly due to conformational differences, in particular the different values of the dihedral angles defining the relative orientation of the nitrophenyl and thiophene rings (specifically the arrangement about the N–C_(thiophenyl) bond]. However, these values are themselves determined in large extent by the different intermolecular forces present in the different crystals, and all the polymorphs of the compound whose crystallographic structure is known are based on only two conformers, with the red and orange polymorphs forming a group and the yellow polymorphs defining a second group, with only one exception. Within each group, differences in the color shall be characterized as packing color polymorphism, associated to different crystal architectures, where molecules exhibit non-negligible conformational relaxation. The difference in the color of the 2,4,6-trinitro-*N*-(*p*-tolyl)aniline polymorphs is attributed to the different degree of charge delocalization from the amino group lone electron-pair into the aromatic rings. This depends on the strength of the N–H···O intramolecular hydrogen bond that is dissimilar in the orange-yellow and dark red polymorphs of the compound. Since the conformer present in the two polymorphs is the same, this is then a case of packing-induced color polymorphism. For dimethyl-5-benzoyl-3-phenylindolizine-1,2-dicarboxylate, the difference in the color of the orange and the green crystals results from the different degree of π -conjugation between the indozolidine chromophore and the carbonyl groups of its benzoyl substituents, which assume different orientations in the two polymorphs. This is a clear case of conformationally-driven color polymorphism. Similarly, the 1,4,7,10-tetrabutyltetracene system exhibits conformational color polymorphism: while in the red crystals the alkyl groups are perpendicularly oriented in relation to the aromatic chromophoric moiety, in the yellow polymorph the same alkyl groups are essentially coplanar with the chromophore; the distinct alignment of the alkyl chains in the different conformers leads to significantly different electronic distributions throughout the tetracene chromophore and changes in the crystal packing, giving rise to the color difference.

Representative chemical systems showing color polymorphism

N-(4-methyl-2-nitrophenyl)acetamide

N-(4-methyl-2-nitrophenyl)acetamide (Figure 2), also known as 4'-methyl-2'-nitroacetanilide, is a compound that exhibits color polymorphism firstly reported in 1885, by Gattermann.²⁰ It is the first known example of a compound presenting this property. Gattermann first identified white and yellow crystals of the compound, while almost a century later a third form, amber colored, was isolated and structurally characterized by Moore *et al.*²¹ In 1963, Skulski reported that the white and yellow polymorphs give rise to the same ultraviolet (UV) solution spectrum but considerably different UV and infrared (IR) solid-state spectra.¹⁷ Based on these, he proposed that the white polymorph (stable, m.p. 95 °C) should present intermolecular hydrogen bonding, while the yellow polymorph (metastable, m.p. 93.5 °C) should, instead, exhibit intramolecular hydrogen bonds.²²

This proposal was confirmed in 1983, when Moore, Yeadon and Palmer solved the crystallographic structure of these two polymorphs.²³ Those authors showed that the white crystals (tabular shaped, obtained by recrystallization in aqueous ethanol) are monoclinic ($P2_1/c$ space group) and present strong $C=O \cdots H-N$ intermolecular hydrogen bonds between adjacent molecules, which are identical and *c*-glide plane related, forming chains along the *c* direction. In this polymorph, the NH amide bond points towards the opposite direction relatively to the nitro substituent of the aromatic ring. On the other hand, the yellow crystals (filamentary shaped, obtained by light petroleum and carbon disulfide recrystallization) are triclinic ($P\bar{1}$), showing two non-equivalent molecules, both exhibiting the NH amide bond pointing towards the nitro substituent with which an $N-O \cdots H-N$ intramolecular hydrogen bond is established. The molecules form a columnar-type structure, with each column presenting only one of the two different molecular conformations existing in the crystal.

One year later, the same authors published¹⁶ the crystal structure of the amber polymorph (needle shaped, obtained by the partial evaporation of a hot solution: petrol containing about 10% v/v of carbon tetrachloride). The crystals are monoclinic ($P2_1/c$), with the molecules related by a *c*-glide axis and stacked along the *c* direction in a very distinct columnar form. The conformer present in this polymorph is the same present in the yellow form and does also show a weak $N-O \cdots H-N$ intramolecular hydrogen bond.

In 1986, Fletton *et al.* presented a study revealing the distinctive solid-state infrared and the high-resolution solid-state nuclear magnetic resonance (NMR) spectra of the three polymorphs,²⁴ and more recently Krivoruchka and co-workers^{25,26} reported on the ability of *N*-(4-methyl-2-nitrophenyl)acetamide to form bifurcated hydrogen bond complexes with several different protophilic solvents (since solvation is not the theme of this article, the specific structure of these complexes are not here described), thus confirming once again the flexibility of the molecule in relation to H-bonding.

Introduction

To conclude, the *N*-(4-methyl-2-nitrophenyl)acetamide system is a paradigmatic example where color polymorphism is determined essentially either by packing (between yellow and amber forms) or conformational (between white and the other two forms) polymorphism.

Dimethyl 2,5-dichloro-3,6-dihydroxyterephthalate

Dimethyl 2,5-dichloro-3,6-dihydroxyterephthalate (Figure 2), also referred in the literature as dimethyl 3,6-dichloro-2,5-dihydroxyterephthalate, and its white and yellow polymorphic crystals were firstly reported by Hantzsch, respectively in 1908 and 1915.^{27,28} About 50 years later, Curtin and Byrn²⁹ suggested, based on ³⁵Cl nuclear quadrupole resonance and IR spectroscopic data, that in the yellow polymorph the molecules should exhibit two C=O \cdots H–O intramolecular hydrogen bonds involving the phenolic groups and the carbonyl moiety of the closest located carbomethoxyl substituents, while in the white form the intramolecular H-bonds were suggested to be established with the chlorine atoms. They have also reported that a solid-state transformation of the yellow into the white crystals takes place at around 125 °C, and that the melting point of the latter is *ca.* 185 °C.²⁹

In a subsequent investigation, the same authors, alongside Paul, were able to solve the crystallographic structures of the two polymorphs. The yellow crystals (thin plates, obtained from ethanol recrystallization) are triclinic ($P\bar{1}$), with one molecule in the unit cell, and exhibit the predicted²⁴ strong C=O \cdots H–O intramolecular hydrogen bonds. The molecules are practically planar (with the exception of the methyl hydrogen atoms) and are arranged in stacks or columns along the *b* axis. Along the columns, each molecule is placed in such a way that the center of its ring lies almost precisely over the phenolic oxygen atom of the adjacent molecule in the stack. When viewed down the axis through the ring centers, all molecules in a stack show the same sequence of substituents (chloro, hydroxyl, carbomethoxyl) proceeding clockwise around the ring. The principal intermolecular forces acting in this crystal are van der Waals interactions. The structure of the white crystals (needles, obtained from ether) was also found to confirm the previous structural conclusions extracted from the spectroscopic data, in particular the involvement of the chlorine atoms in intramolecular Cl \cdots H–O hydrogen bonds.²⁹ The crystals are triclinic ($P\bar{1}$), and show two molecules in the unit cell, form the asymmetric unit whose planes of the aromatic rings are inclined at an angle of 12.4° with respect to each other. Like for the yellow polymorph, the molecules in the crystal of the white polymorph are also arranged in stacks along the *b* axis. However, in this case, for a given stack, the order of attachment of groups around the ring is clockwise in one molecule and counterclockwise in the molecules above and below it (and vice-versa). These geometric features allow for the establishment of intermolecular C=O \cdots H–O hydrogen bonds between pairs of adjacent molecules, but both the relatively long O \cdots H distances and small O \cdots H–O angles of these intermolecular hydrogen bonds³⁰ are consistent with the participation of the phenolic hydrogen atoms also in an intramolecular hydrogen bond to the neighbor chlorine atoms (thus giving

Introduction

rise to a bifurcated intra/intermolecular H-bond type interaction), as suggested by the previously obtained spectroscopic data.³⁰

The major structural difference of the molecules of the compound in the yellow and white polymorphs concerns the dihedral angle between the plane of the aromatic ring and the plane of the carbomethoxyl groups ($\sim 4^\circ$ in the yellow crystals and around 70 and 85° in the case of the two non-equivalent molecules present in crystals of the white polymorph).^{30,31} In 1982, Swiatkiewicz and Prasad reported the Raman and the electronic emission spectra of these two polymorphs.³²

A third, light-yellow polymorph of dimethyl 2,5-dichloro-3,6-dihydroxyterephthalate has been more recently described by Yang, Richardson and co-workers.³³⁻³⁵ The crystals of this polymorph contain centrosymmetric molecules with the carbomethoxyl group neither coplanar (as in the firstly reported yellow crystals) nor nearly perpendicular (like in the white form) to the aromatic ring. In the light-yellow crystals, the dihedral angle between the aromatic ring and the carbomethoxyl group is about 40° . As in the case of the yellow polymorph, the molecules in the new light-yellow form show intramolecular $C=O \cdots H-O$ hydrogen bonds between the phenolic group and the neighbor carbonyl moiety, and the global molecular packing is also comparable to that of the first reported yellow polymorph. The light-yellow, rounded edged crystals were found to undergo a phase transition into the stable white form at around $100^\circ C$ (sometimes they transform at lower temperatures into the yellow polymorph),²⁸ and are obtained concomitantly with the other two forms by slow evaporation of the compound from ethanol and ether solutions, being easily isolated by hand separation according to color and morphology.

In conclusion, dimethyl 2,5-dichloro-3,6-dihydroxyterephthalate is an interesting system where, though it shall be clearly defined as a case of conformational color polymorphism, differences in the major intermolecular interactions present in the known polymorphs (for white *versus* the two yellow polymorphs), in particular hydrogen bonding, are also very important in structural terms and in determining the color of the polymorphs.

5-Methyl-2-((2-nitrophenyl)amino)thiophene-3-carbonitrile

5-Methyl-2-((2-nitrophenyl)amino)thiophene-3-carbonitrile, or 5-methyl-2-[(2-nitrophenyl)amino]-3-thiophenecarbonitrile (Figure 2), better known as ROY due to the red, orange and yellow colors of its polymorphs, is undoubtedly the most famous and the most extensively studied compound that exhibits color polymorphism.

Introduction

ROY was firstly reported in 1995 by Stephenson *et al.*, in a paper where five different polymorphs were identified, and the crystallographic structures of three of them (one red, one orange and one yellow) were described.³⁶ These three polymorphs were subsequently studied by two-dimensional ¹³C solid-state NMR (2D-SSNMR) by Smith and co-workers, in the first published study where 2D-SSNMR was employed to study conformational polymorphism.³⁷ In the year 2000, Yu *et al.* disclosed a sixth polymorph of ROY and presented its crystallographic structure, alongside with those of the two other already known polymorphs of the compound whose structure had not yet been solved.⁴⁶ At that time, ROY was the only compound with more than five reported polymorphic structures in the Cambridge Structural Database (CSD). One year later, Mitchell, Yu and Ward published an article about the selective nucleation of ROY polymorphs through epitaxy with single crystal substrates, reporting also the evidence of a seventh polymorphic form.⁴⁷ In 2002, Yu presented optical-crystallography, single-crystal spectroscopy and computational chemistry results for all the seven ROY polymorphs known at the time.⁴⁸ Three years later, Chen, Guzei and Yu discovered two new polymorphs of the compound and reported the crystal structure of one of them.⁴⁹

More recently, a very interesting study also authored by Yu's group focused on the effects of cross-nucleation during formation of the ROY crystals, and showed that certain polymorphs cannot nucleate without the presence of others.⁵⁰ That study also led to the identification of the tenth polymorph of the compound.⁵⁰ In 2018, Tan *et al.* reported the crystallographic structure of one of the polymorphs that had not been yet solved before, employing X-ray powder diffraction with Crystal Structure Prediction algorithms,⁵¹ increasing to eight the number of ROY polymorphs present in the CSD. Finally, in the first semester of 2019, Gushurst *et al.* described the eleventh polymorph (PO13). Its structure was also determined recurring to quantum calculations. Specifically, it was done by matching the experimental powder pattern with one of the previously predicted crystal structures by Vasileiadis *et al.*,⁵² since no single crystal of the PO13 polymorph was obtained.⁵³

With the ninth structure reported, ROY became, once again, at the top of the list of compounds with most polymorphic structures determined, together with flufenamic acid⁶⁵ and aripiprazole.^{66,67} However, in the second semester of 2019, two compounds were reported having ten determined crystallographic structures, galunisertib and R-encenicline hydrochloride, overtaking ROY, flufenamic acid and aripiprazole at the top of the list.^{68,69} The eleven different polymorphs of ROY are illustrated in Figure 3.

Introduction

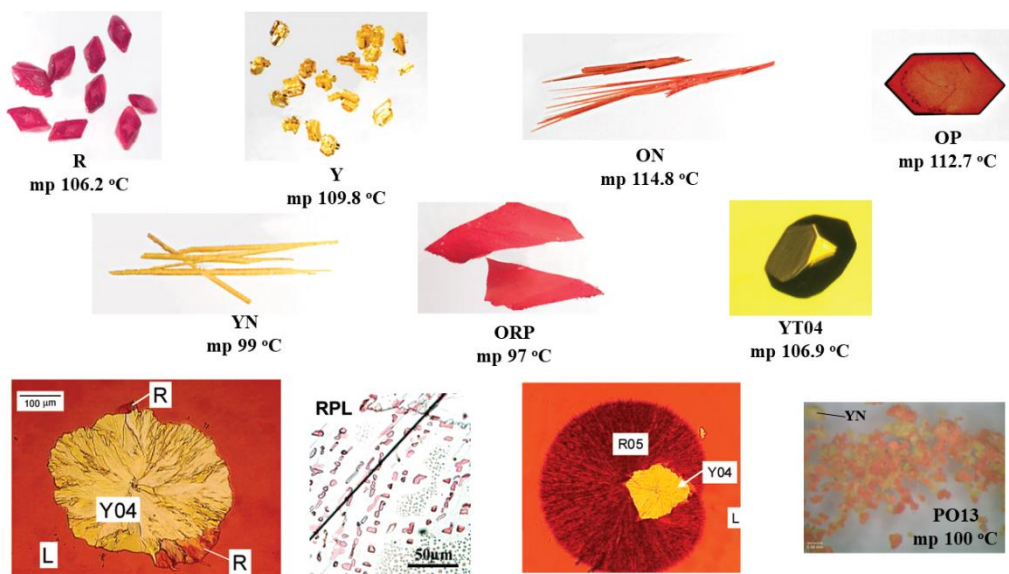


Figure 3 – Polymorphs of 5-methyl-2-((2-nitrophenyl)amino)thiophene-3-carbonitrile and their melting point (m.p.). Reprinted (adapted) with permission from Acc. Chem. Res. 2010, 43, 9, 1257-1266. Copyright 2010 American Chemical Society and also from CrystEngComm, 2019, 21, 1363.

The rich polymorphism of ROY results from a combination of favorable thermodynamics and kinetics. The abundance of molecular crystals primarily arises from the conformational flexibility associated with the C–N–C–S torsion angle between the amine and the thiophene moieties, θ . The nine different polymorphs of ROY whose crystallographic structures are known are designated as R (red prism), Y (yellow prism), ON (orange needle), OP (orange plate), YN (yellow needle), ORP (orange-red plate), YT04 (yellow prism), R05 (red 2005) and PO13 (pumpkin-orange 2013), while the two polymorphs whose structure is still unknown are designated by RPL (red plate) and Y04 (yellow prism). The crystallization of the different polymorphs is a rather complex process. Polymorphs R, Y, ON, OP, YN and ORP were obtained by solution crystallization, and RPL by vapor deposition on single-crystal substrates.^{38,46,48} Near room temperature, ROY was found to crystallize spontaneously into YN, Y04, ON and R05.^{46,48,49} YT04 was identified after a solid-solid transition of the metastable polymorph Y04,^{38,49} while other several cross-nucleation processes were also described.^{38,46,50} Polymorph PO13 was isolated by recrystallization from a supercooled melt of form YN (previously recrystallized in 2-propanol), at 60 °C.⁵³

Every ROY polymorph with solved structure presents one crystallographically independent molecule ($Z' = 1$) in centrosymmetric packing and, hence, two molecules with mirror-related conformations in the unit cell, with the exception of polymorph R05 that displays two molecules in the asymmetric unit cell without a center of symmetry. In each crystal polymorph the ROY molecule adopts

Introduction

a different structure, the largest conformational difference being observed in the torsion angle θ (C–N–C–S), which ranges from 21.7° (R) to 122.1° (PO13). It is also interesting to note that the values of this torsion angle roughly correlate with the color of the polymorphs. $\theta = \pm 21.7, \pm 39.4, +44.9(-34.0), \pm 46.1$ and $\pm 52.6^\circ$ for the red and orange crystals (R, ORP, R05, OP and ON, respectively), all showing a structure of the ROY molecule, which can be described as the same gas phase conformer, after a non-negligible structure relaxation driven by intermolecular forces. $\theta = \pm 104.1, \pm 104.7$ and $\pm 112.8^\circ$ for the yellow polymorphs (YN, Y and YT04, respectively), also sharing a common parent conformer different from that associated to the red and orange polymorphs. The above observations suggests that a correlation does exist among the torsional angle values and the trend in colors: values of θ closer to 0° correspond to species characterized light absorption at lower energy, while increasing the torsional angle, the absorption maximum is blue shifted. Apparently, polymorph PO13 is an exception, since it shows a pumpkin-orange color, but it has the highest torsion angle θ value of all the nine structures (122.1°); moreover, it can be considered the result of the relaxation of the same conformer giving rise to the yellow varieties. This apparent discrepancy can be easily justified considering that the θ value of PO13 exceeds 90° , namely the θ value characteristic of a hypothetical molecular conformation where the planes of the phenyl ring and of the thiophene ring are nearly orthogonal. There are two choices of θ , which makes the two rings nearly coplanar: $\theta = 0^\circ$ and $\theta = 180^\circ$. So, if we want to describe effectively the “distortion from planarity” (irrespective to a trans or cis configuration of the two rings) we must refer to the smaller value among $|\theta|$ and $|\phi| = |180^\circ - \theta|$. Namely, for a torsional θ angle larger than 90° we should consider the corresponding ϕ value.

In this way one can classify the ROY polymorphs in the following way:

- red polymorphs of ROY, corresponding to $|\theta| = 21.7^\circ$ (R), 39.4° (ORP) and 44.9° (or 34.0°) (R05);
- orange polymorphs, with $|\theta| = 46.1^\circ$ and 52.6° (OP and ON), and $|\phi| = 57.9^\circ$ (PO13);
- yellow polymorphs, with $|\phi| = 75.9^\circ$ (YN), 75.3° (Y) and 67.2° (YT04).

The above observations clearly indicate the primary factor responsible for the color of the ROY polymorphs. Indeed, the variety of color of ROY polymorphs highlights the relevance of the degree of conjugation between the substituted phenyl and thiophene rings in determining the relative energies of the electronic states of the molecule. A more effective conjugation correlates with an angle between the planes of the two rings approaching to zero, what in fact happens both in the case of $|\theta|$ (or $|\phi|$) near 0° .

Introduction

As discussed above, a more extended conjugation leads to a red shift in the visible absorption spectrum and, accordingly, the polymorphs seen as red absorb in the green (the complementary color of red) while those perceived as orange and yellow absorb in the blue and in the violet, respectively.

Nonetheless, it shall be stressed that intermolecular forces also play an important role in determining the color of the different polymorphs of ROY. In all polymorphs whose structure is known, the arrangement about the N–C_(phenyl) bond of the amino-bridge is the same (this corresponds to the geometry shown in Figure 2), which is justified by the fact that the assumed geometry allows for the establishment of a strong intramolecular hydrogen bond between the amine group and the nitro substituent of the phenyl ring. Since this intramolecular hydrogen bond consumes the best H-bond donor in the molecule, the intermolecular forces presented in ROY polymorphs are essentially of the van der Waals type, which stabilize the different conformations found in the crystals. The relative free energies of seven of the structurally characterized ROY polymorphs have been determined from melting and eutectic melting data obtained by differential scanning calorimetry (DSC), and found to follow the order, over a range of 4 kJ mol⁻¹: Y < YT04 < R < OP < ON < YN < ORP.^{46,49-51} This order contrasts with the order of the relative energy for the isolated monomeric structures corresponding to the conformations found in the crystals, which is OP < ON < ORP < YT04 < Y < YN < R (Figure 4), demonstrating the relevance of intermolecular interactions. Different interactions in the different crystal polymorphs are indeed responsible for the displacement of the potential energy minima, namely for the stabilization of torsional angles values different from those of gas phase equilibrium structures, but they are also responsible of remarkable changes in energy, resulting in a trend totally unpredictable simply considering the isolated molecule.

In conclusion, despite the major importance of the conformational flexibility of the ROY molecule to its extraordinary rich polymorphism, and though it has been mistakenly said many times, ROY is not just a case of conformational color polymorphism, but also an outstanding case of packing polymorphism. Figure 4 presents the DFT(B3LYP)/6-311+G(2d,p) calculated relative energy of the isolated ROY molecule as a function of the C-N-C-S dihedral angle (line). The angles and specific energy (for the isolated molecule) of each monomeric unit present in the different crystals are represented by the squares. It is clear from this figure that there are only two different conformers (minima at 50° and 120° respectively) present in the eight polymorphs of ROY whose crystallographic structure is known. Polymorphs R, ORP, R05, OP and ON are conformational polymorphs regarding polymorphs YN, Y, YT04 and PO13. On the other hand, these two groups are formed by 5 and 4 packing polymorphs, respectively.

Introduction

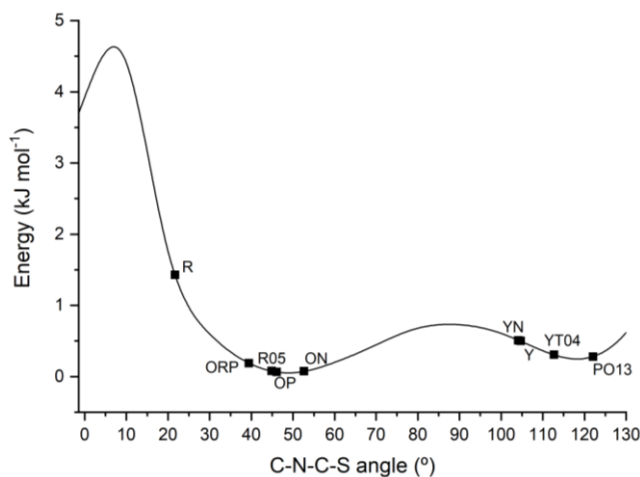


Figure 4 – Relative energy as a function of the C-C-N-S torsion angle (θ) for the 5-methyl-2-((2-nitrophenyl)amino)thiophene-3-carbonitrile monomer. The values of this torsion angle in the monomers present in each of the polymorphs of the compound are indicated by the solid squares on the energy profile. The calculations were performed at the DFT(B3LYP)/6-311+G(d,p) level of approximation.

Three molecules closely related structurally with ROY have also been shown to give rise to color polymorphs, specifically, 2-((2-nitrophenyl)amino)thiophene-3-carbonitrile, 5-methyl-2-((4-methyl-2-nitrophenyl)amino)thiophene-3-carbonitrile and 2,2'((ethyne-1,2-diylbis(2-nitro-4,1-phenylene))bis(azane diyl))bis(5-methylthiophene-3-carbonitrile) (Figure 5).³⁹⁻⁴²

2-((2-Nitrophenyl)amino)thiophene-3-carbonitrile (Figure 5), also known as 2-[(2-nitrophenyl)amino]-3-thiophenecarbonitrile, is a molecule differing from ROY just because it does not possess the methyl substituent in position 5 of the thiophene moiety, was studied by Li *et al.*⁴² Like for ROY, a red (obtained from tetrahydrofuran solution), an orange (obtained from ethanol) and a yellow (only observed during synthesis) polymorph were observed and the first two characterized structurally. The single crystal structural data revealed a similar behavior compared to ROY, with the stable red polymorph presenting the thiophene and phenyl rings more coplanar (θ closer to 0°) than the metastable orange form.

5-Methyl-2-((4-methyl-2-nitrophenyl)amino)thiophene-3-carbonitrile, or 5-methyl-2-[(4-methyl-2-nitrophenyl)amino]-3-thiophenecarbonitrile (Figure 5), was synthesized and investigated by He *et al.*,³⁹ who found four different polymorphs of the compound (red R, dark red DR, light red LR, and orange O). Although only the DR crystal structure was determined, the thermodynamic relationships between all the polymorphs were determined. Polymorph R was found to be the most stable form above 60 °C, O the most stable form between room temperature and 60 °C, and LR the most stable polymorph below -15 °C, while polymorph DR is metastable throughout the entire studied temperature range. In a subsequent paper from the same group the solid-solid transformation between the DR and R polymorphs was investigated in details, allowing to conclude that it is defect driven and accelerated by presence of

Introduction

water, which can serve as a nucleation catalyst by binding to the crystal surface, especially at defect sites, thus increasing the molecular mobility of these sites and increasing the transformation rate.⁴⁰

Finally, in the case of 2,2'((ethyne-1,2-diylbis(2-nitro-4,1-phenylene))bis(azanediyl))bis(5-methylthiophene-3-carbonitrile) (Figure 5), also referred to as bis(5-methyl-2-[(2-nitrophenyl)amino]-3-thiophenecarbonitrilyl)acetylene (or simply as el-ROY), which is a dimeric ROY derivative that possesses two chromophores electronically coupled through a triple bond, Lutker, Tolstyka and Matzger concluded about the existence of at least three different polymorphs.⁴¹ One polymorph (I) was obtained as red needles from evaporation of toluene solution, the second (II) as red-orange plates from dichloromethane, and the third (III) as red-orange rice-shaped needles using polymer-induced heteronucleation. Only the crystal structures of polymorphs I and II were solved, the results showing that, as for ROY and the other ROY derivatives investigated so far, the molecules show the usual intramolecular hydrogen bond between the amino and the nitro groups. The θ torsion angles are the smallest ones found hitherto for polymorphs of ROY and ROY derivatives, with the values of 0.1 and 3.3° for polymorphs I and II, respectively.⁴¹ These small angles lead to an almost planar molecular configuration in the crystals, with a high-degree of π -conjugation, which is consistent with the red color.

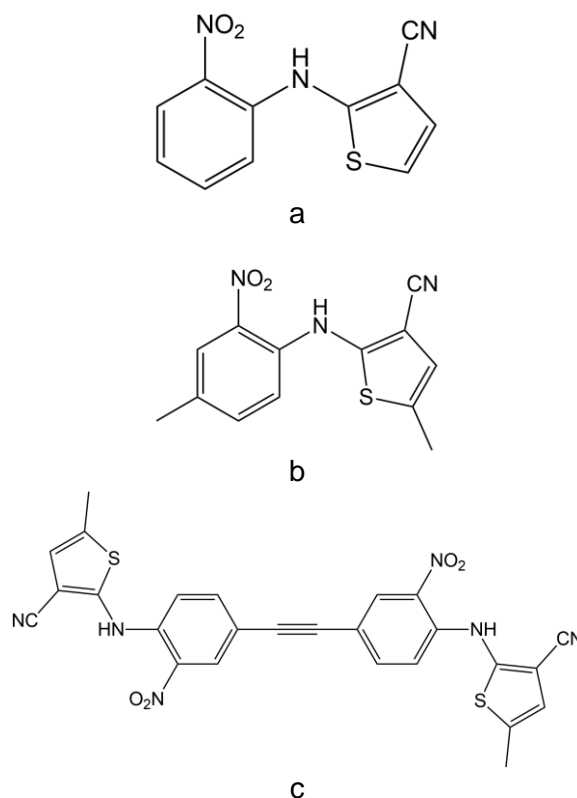


Figure 5 – Structures of 2-((2-nitrophenyl)amino)thiophene-3-carbonitrile (a, top), 5-methyl-2-((4-methyl-2-nitrophenyl)amino)thiophene-3-carbonitrile (b, middle) and 2,2'((ethyne-1,2-diylbis(2-nitro-4,1-phenylene))bis(azanediyl)) bis(5-methylthiophene-3-carbonitrile) (c, bottom).

2,4,6-trinitro-*N*-(*p*-tolyl)aniline

2,4,6-Trinitro-*N*-(*p*-tolyl)aniline, or *N*-picryl-*p*-toluidine (Figure 2) was firstly reported as a color polymorphic system by Busch and Pungs in 1909, in an article that claimed existence of three different forms, yellow, orange-yellow and dark red colored.⁵⁴

The system was further investigated by Cullinane, Embrey and Davis⁵⁵ and by Wood, Ayliffe and Cullinane,⁵⁶ the X-ray crystallographic structures for the orange-yellow and the dark red polymorphs being reported in the later study. Yasui, Taguchi and Iwasaki⁵⁷ reported the transformation of the orange-yellow form into the more stable dark red polymorph through the liquid phase. According to their study, the orange-yellow polymorph melts at 163-164 °C, and then starts to recrystallize into the dark red polymorphic form, which finally melts at 167 °C. The dark red form is also the sole one that was possible to obtain by cooling the liquid phase, while the orange-yellow polymorph could only be obtained by recrystallization from solutions.⁵⁷ In the more recent study of Braun *et al.*,⁵⁸ the dark red and orange-yellow polymorphs (together with five different solvates) were investigated by a combined multi-technique approach (single-crystal X-ray diffractometry, hot stage microscopy, DSC, thermal gravimetric analysis, and IR and Raman spectroscopies). In that work, the dark red crystals were obtained by slow evaporation of the solvent in different solutions (acetone, acetonitrile, ethyl acetate, methanol, isopropanol, *n*-butanol, methanol/water) and the orange-yellow form upon recrystallization from acetone/water, chloroform, and mesitylene. The thermal analysis data allow concluding that the dark red polymorph is the thermodynamically stable form in the entire temperature range investigated (room temperature to 167 °C), as suggested by the earlier study of Yasui, Taguchi and Iwasaki.⁵⁷ It is also worth noticing that each polymorph was found to sublime into itself, and the transformation of the orange-yellow form into the dark red polymorph was only observed in the presence of dark red seed crystals.

Both dark red and orange-yellow polymorphs crystallize in the monoclinic space group $P2_1/a$, but the values of the two dihedral angles (τ_1 and τ_2) between the aromatic rings are somewhat different in the two polymorphs (respectively 23.80° and 43.07° for the dark red polymorph, and -12.52° and -54.35° for the orange-yellow form).⁵⁸ In both polymorphs the molecules adopt a herring-bone arrangement, with neighboring molecules arranged in a head-to-head fashion in the dark red form and head-to-tail in the orange-yellow one.^{58,59} Though the authors classify the two crystalline varieties as conformational polymorphs, this is in fact a case of packing polymorphism. In fact, as it can be seen in Figure 6, where the potential energy profile for internal rotation about τ_1 [as defined by the (NO₂)C-C-N-C torsion angle] is represented, the molecule exhibits four minima on the potential energy surface that are equivalent by symmetry and thus define the same conformer.

Introduction

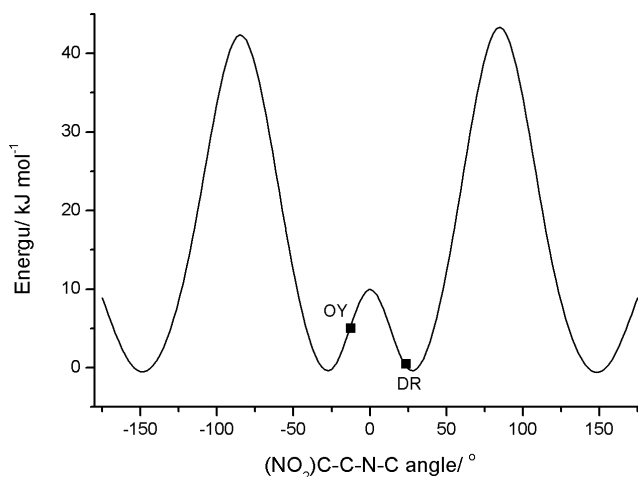


Figure 6 – Relative energy as a function of the (NO₂)C-C-N-C torsion angle for the 2,4,6-trinitro-*N*-(*p*-tolyl)aniline monomer. The values of this torsion angle in the monomers present in both dark red (DR) and orange yellow (OY) polymorphs of the compound are indicated by the solid squares on the energy profile. The calculations were performed at the DFT(B3LYP)/6-311+G(d,p) level of approximation..

In both crystalline structures, an intramolecular N–H···O bond between the H atom of the amine and one O atom of the nitro group adjacent to the amine is present. The different colors are attributed to the variation of the length/strength of this H-bond, or more specifically, to the associated intramolecular effects leading to an increased delocalization of the secondary amino nitrogen lone-pair electrons into the aromatic rings' moiety. The N–H···O intramolecular bond is stronger in the orange-yellow form than in the dark red polymorph, as the geometrical parameters for the H-bond confirm ($d(\text{H}\cdots\text{O}) = 1.98$ vs. 1.88 Å in the dark red vs. orange-yellow polymorph).

The two structurally characterized polymorphs have also been studied computationally. Yatsenko and Paseshnichenko demonstrated through their calculations that in the dark red form the polarization effect of crystal packing is stronger than the effect of a highly polar solvent, and that under the effect of the crystal electrostatic potential the LUMO-HOMO energy gap decreases. In the case of the orange-yellow form, the effect of the crystal field is nearly the same as that of a moderately polar solvent, so that the authors predicted a color blue-shift for this polymorph when compared to the dark red form, in consonance with the observations, and also in agreement with the packing-nature of the observed color polymorphism.⁶⁰

Interestingly, the putative yellow polymorph of the compound has not been described in the literature since the original work of Busch and Pungs.⁵⁴ To the best of our knowledge, only the 2001 paper by Ilyina *et al.*⁵⁹ refers to this species, but the authors suggest that the obtained material might correspond to a water solvate instead of a polymorph of the compound.⁵⁹ The precise nature of yellow phase is still awaiting a definitive answer.

Introduction

There are also some reports on other compounds related to 2,4,6-trinitro-*N*-(*p*-tolyl)aniline, namely on 2,4,6-trinitro-*N*-phenylaniline (also known as picryl aniline)⁵⁶ and *N*-(2-methoxyphenyl)-2,4-dinitroaniline (or *N*-(2,4-dinitrophenyl)-*o*-anisidine)^{57,61} (Figure 7) but the collected information on these systems is still scarce.



Figure 7 – Structure of picryl aniline (left) and *N*-(2,4-dinitrophenyl)-*o*-anisidine (right).

We have also recently started an investigation on this type of compounds. A new 2,4,6-trinitro-*N*-(*p*-tolyl)aniline related compound with the methyl group bonded in a different position was synthesized and found to exhibit color polymorphism likewise the original compound. The two identified polymorphs have reddish and yellow-orange colors, respectively. Very interestingly, contrarily to what happens for 2,4,6-trinitro-*N*-(*p*-tolyl)aniline, the new compound presents conformational color polymorphism. Also very interestingly, the higher-energy conformer for the isolated molecule gives rise to the most stable polymorph (at room temperature), which is stabilized by the presence of a bifurcated inter- and intramolecular hydrogen bond, while the most stable conformer is present as constituting unit of the less stable polymorph, which only presents intramolecular H-bonding.

Dimethyl-5-benzoyl-3-phenylindolizine-1,2-dicarboxylate

Dimethyl-5-benzoyl-3-phenylindolizine-1,2-dicarboxylate (Figure 2) is a recently synthesized compound that was found to crystallize either as orange cubes (from cyclohexane and hexane/ethyl acetate solutions) or as green needles (from the same solutions, but with longer crystallization time).¹⁴

The green polymorph crystallizes in the monoclinic space group $C2/c$, and the orange polymorphic form crystallizes in the monoclinic space group $P2_1/n$. In both crystal lattices, there are pairs of molecules arranged in an anti-head-to-tail orientation. The bond lengths and angles of the molecules in both structures are almost the same, with one big exception, which is the orientation of the benzoyl group relative to the indolizine part of the molecule. Specifically, the carbonyl bond of the benzoyl group points away from the indolizine core in the green polymorph, whereas it is aligned in the opposite

direction in the orange polymorphic structure. This conformational difference is the main reason of the distinct color of the polymorphs, since it causes a different degree of π -conjugation of the carbonyl group with the chromophore (indolizine), which is confirmed by the dissimilar frequencies of the benzoyl C=O stretching vibrational mode in the two crystals.¹⁴ Therefore, dimethyl-5-benzoyl-3-phenylindolizine-1,2-dicarboxylate presents conformational color poly-morphism (designated as crystallochromism in the original paper; see section 2.3).

1,4,7,10-tetrabutyltetracene

In 2007, Kitamura *et al.*⁶² described the synthesis of 1,4,7,10-tetrabutyltetracene (or 1,4,7,10-tetra(*n*-butyl)tetracene), and the discovery of two different color polymorphs of the compound: one red (m.p. 128–130 °C, obtained from recrystallization in chloroform) and one yellow (m.p. 114–116 °C, obtained by recrystallization in *n*-hexane) (Figure 2). The solid fluorescence spectra of both polymorphs were reported in this study and are substantially different. Additionally, the polymorphic structures were studied by X-ray crystallography. The red polymorph crystallizes in the monoclinic space group $C2/c$ ($Z = 4$) and the yellow crystals in the triclinic space group $P\bar{1}$ ($Z = 1$). The most striking difference between the two polymorphs is the conformation assumed by the alkyl groups. While in the red form the alkyl zigzag chain planes are practically perpendicular to the tetracene backbone, in the yellow polymorph, the alkyl groups are almost coplanar to the tetracene ring. Hence, the molecules in the red polymorph present a chair-shaped structure, while in the yellow form they are nearly planar. Consequently, being in the presence of distinct conformers in the polymorphs this system should be classified as a case of conformational color polymorphism, and not as a system displaying packing color polymorphism as it has been suggested in the original work.⁶²

Other members of the 1,4,7,10-alkyl substituted tetracene family were also studied by the Kitamura group both experimentally and computationally, in particular a series of compounds where the length of the alkyl side chains was varied (from methyl to hexyl derivatives).^{63,64} The solid-state colors of the synthesized tetracenes range through yellow, orange, and red, and depend upon the alkyl side-chains length: methyl, propyl, and pentyl derivatives are orange, ethyl is yellow, and hexyl is red (as already mention the butyl-substituted compound exists in two conformational color polymorphs, red and yellow). Structural information for all molecules was obtained, revealing that different alkyl side-chain lengths orient preferentially in different directions leading to distinct molecular shapes: nearly planar, semi-chair, or chair form, although all the alkyl chains assume an all-*trans* planar conformation. The packing arrangements for solids of the same color are similar to one another: herringbone-like in the red solids and slipped-parallel in the orange and yellow solids. With exception of the butyl derivative, described above, only one crystal variety was found for the studied compounds. The mechanism of the

Generation and Characterization of Novel Materials Exhibiting Color Polymorphism

observed crystallochromy in the studied series of compounds was discussed by the authors in terms of molecular structure, crystal packing, and calculations that take into account exciton coupling.^{63,64}

Concluding remarks and outlook

In this article representative chemical systems showing color polymorphism were discussed, and the reasons for them to present such property addressed. Examples were given where the change of conformation is the clearly dominant driven-force determining the different color of the polymorphs (as, for example in the case of dimethyl-5-benzoyl-3-phenylindolizine-1,2-dicarboxylate and the 1,4,7,10-tetrabutyltetracenes). In all these cases, the distinct electron distributions in the polymorphs leading to color variation result from subtle modifications in the strengths of specific intramolecular interactions associated with conformational changes. It was noticed that, in these cases, intramolecular hydrogen bonds are efficient determining factors to modulate the geometric characteristics that lead to color changes in the solid state. In other cases, packing is clearly the major cause of the color polymorphism (*e.g.*, as in 2,4,6-trinitro-*N*-(*p*-tolyl)aniline). However, even in these cases intramolecular bonding appears as a relevant factor in the most striking examples reported hitherto, the packing forces affecting the structures of the molecular units of the crystal in such a way that the H-bonding gains or reduces importance.

Examples where both types of color polymorphism (conformational and packing) are observed, such as in *N*-(4-methyl-2-nitrophenyl)acetamide, dimethyl 2,5-dichloro-3,6-dihydroxyterephthalate and ROY, have also been discussed, revealing the interplay between the two factors in determining the considered macroscopic property. As a whole, the cited examples, which cover most of the hitherto known chemical systems exhibiting color polymorphism, highlight the general complexity and interrelation of the factors determining this fascinating property.

As in many other cases along the history of science, color polymorphism is nowadays more than just an interesting academic curiosity. Indeed, the applications of color polymorphism in time-temperature sensors and multiplex photoelectronic devices have already given this phenomenon a dimension which goes beyond the academic serendipity. Nevertheless, there is still a world to explore in the field. To design cheap, affordable polymorphic materials that can experience easy controllable color changes is in fact still an open field of research. Moreover, to use a change of color as a visible indicator of a simultaneous change in other relevant property of solid materials, for example for magnetic or photonic applications, appears also as an avenue to explore. For this, organometallic materials appear *a priori* as the most promising chemical systems, but investigation on this subject still needs to give the first steps. Finally, integration of these materials in suitable supports that may make them easier to handle is also a field yet to be developed.

Acknowledgements

This work was supported by the Portuguese “Fundação para a Ciência e a Tecnologia” (FCT): research project PTDC/QUI-QFI/3284/2014, co-funded by QREN-COMPETE2020-UE. The Coimbra Chemistry Centre (CQC) is also supported by the FCT, through the projects UIDB/00313/2020 and UIDP/00313/2020. B.A.N also acknowledges FCT for the SFRH/BD/129852/2017 PhD Scholarship.

Competing interests

The authors declare no competing interests.

References

1. J. Bernstein, *Polymorphism in Molecular Crystals. Polymorphism in Molecular Crystals*, Oxford University Press, 2010.
2. F. Grepioni, Themed issue: Polymorphism and crystal forms. *New J. Chem.*, 2008, **32**, 1657–1658.
3. G. R. Desiraju, *Crystal Engineering: The Design of Organic Solids*, Elsevier, 1989.
4. A. J. Cruz-Cabeza and J. Bernstein, Conformational polymorphism. *Chem. Rev.*, 2014, **114**, 2170–2191.
5. D. Braga, F. Grepioni and P. Sabatino, On the factors controlling the crystal packing of first-row transition-metal binary carbonyls. *J. Chem. Soc. Dalton Trans.*, 1990, **10**, 3137–3142.
6. D. Braga, and F. Grepioni, Crystal Construction and Molecular Interplay in Solid Ferrocene, Nickelocene, and Ruthenocene. *Organometallics*, 1992, **11**, 711–718.
7. D. Braga, F. Grepioni, L. Maini, and M. Polito, Crystal Polymorphism and Multiple Crystal Forms. in *Molecular Networks* (ed. M. W. Hosseini), Springer Berlin Heidelberg, 2009, 25-50.
8. R. Foster, *Organic charge-transfer complexes*, Academic Press, 1969.
9. G. Desiraju and T. Steiner, *The Weak Hydrogen Bond. The Weak Hydrogen Bond*, Oxford University Press, 2010.
10. P. Popelier, A. T. H. Lenstra, C. Van Alsenoy and H. J. Geise, An ab initio study of crystal field effects: Solid-state and gas-phase geometry of acetamide. *J. Am. Chem. Soc.*, 1989, **111**, 5658–5660.
11. C. Kitamura, Synthesis, Crystal Structures, and Solid-State Optical Properties of Substituted Tetracenes, in *Chemical Science of Electron Systems* (ed. T. Akasaka, A. Osuka, S. Fukuzumi, H. Kandori and Y. Aso), Springer Japan, 2015, 69–87.
12. G. Klebe, F. Graser, E Hädicke and J. Berndt, Crystallochromy as a solid-state effect: correlation of molecular conformation, crystal packing and colour in perylene-3,4:9,10-bis(dicarboximide) pigments. *Acta Crystallogr. Sect. B*, 1989, **45**, 69–77.
13. P. M. Kazmaier and R. A. Hoffmann, Theoretical Study of Crystallochromy. Quantum Interference Effects in the Spectra of Perylene Pigments. *J. Am. Chem. Soc.*, 1994, **116**, 9684–9691.
14. C. Dohmen, H. Ihmels, R. Kreienmeier and B. O. Patrick, Synthesis of a crystallochromic indolizine dye by a base- and catalyst-free photochemical route. *Chem. Commun.*, 2019, **55**, 11071–11074.
15. D. Gentili, M. Gazzano, M. Melucci, D. Jones and M. Cavallini, Polymorphism as an additional

- functionality of materials for technological applications at surfaces and interfaces. *Chemical Society Reviews*, 2019, **48**, 2502–2517.
16. M. Cavallini, A. Calò, P. Stoliar, J. C. Kengne, S. Martins, F. C. Maticotta, F. Quist, G. Gbabode, N. Dumont, Y. H. Geerts and F. Biscarini, Liquid-Crystal Patterning: Lithographic Alignment of Discotic Liquid Crystals: A New Time-Temperature Integrating Framework. *Adv. Mater.*, 2009, **21**, 4688–4691.
 17. D. Gentili, M. Durso, C. Bettini, I. Manet, M. Gazzano, R. Capelli, M. Muccini, M. Melucci and M. Cavallini, A time-temperature integrator based on fluorescent and polymorphic compounds. *Sci. Rep.*, 2013, **3**, 2581.
 18. Z. Lin, X. Mei, E. Yang, X. Li, H. Yao, G. Wen, C.-T. Chien, T. J. Chow and Q. Ling, Polymorphism-dependent fluorescence of bithienylmaleimide with different responses to mechanical crushing and grinding pressure. *CrystEngComm*, 2014, **16**, 11018–11026.
 19. N. Zhao, Z. Yang, J. W. Y. Lam, H. H. Y. Sung, N. Xie, S. Chen, H. Su, M. Gao, I. D. Williams, K. S. Wong and B. Z. Tang, Benzothiazolium-functionalized tetraphenylethene: An AIE luminogen with tunable solid-state emission. *Chem. Commun.*, 2012, **48**, 8637–8639.
 20. L. Gattermann, Ueber einige Derivate des m-Nitro-p-Toluidins. *Berichte der Dtsch. Chem. Gesellschaft*, 1885, **18**, 1483–1488.
 21. J. C. Moore, A. Yeadon and R. A. Palmer, Crystal and molecular structure of an amber polymorph of 4-methyl-2-nitroacetanilide (MNA). *J. Crystallogr. Spectrosc. Res.*, 1984, **14**, 283–291.
 22. L. Skulski, The Ultraviolet and Infrared Spectra of Some o-Nitroamides. *J. Org. Chem.*, 1963, 3565–3567.
 23. J. C. Moore, A. Yeadon and R. A. Palmer, Crystal and molecular structures of two polymorphs of 4-methyl-2-nitroacetanilide (MNA). *J. Crystallogr. Spectrosc. Res.*, 1938, **13**, 279–292.
 24. R. A. Fletton, R. W. Lancaster, R. K. Harris, A. M. Kenwright, K. J. Packer, D. N. Waters and A. Yeadon, A comparative spectroscopic investigation of two polymorphs of 4'-methyl-2'-nitroacetanilide using solid-state infrared and high-resolution solid-state nuclear magnetic resonance spectroscopy. *J. Chem. Soc. Perkin Trans.*, 1986, **2**, 1705–1709.
 25. I. G. Krivoruchka, A. I. Vokin and V. K. Turchaninov, Molecular structure of complexes with bifurcated hydrogen bond: I. N-(4-methyl-2-nitrophenyl)acetamide. *Russ. J. Org. Chem.*, 2002, **38**, 1456–1461.
 26. I. G. Krivoruchka, A. I. Vokin, T. N. Aksamentova, A. M. Shulunova, M. S. Sorokin, E. I. Dubinskaya and V. K. Turchaninov, Solvatochromism of Heteroaromatic Compounds: XXII.1 Effect of Bifurcate Hydrogen Bond on the IR Spectrum and Dipole Moment of N-(4-Methyl-2-nitrophenyl)acetamide in Solution. *Russ. J. Org. Chem.*, 2004, **74**, 120–127.
 27. A. Hantzsch, Über Chromoisomerien. *Zeitschrift für Angew. Chemie*, 1907, **20**, 1889–1892.
 28. A. Hantzsch, Über chromoisomere Salze von Acetessigester-ähnlichen Phenol- und Enol-Derivaten. *Berichte der Dtsch. Chem. Gesellschaft*, 1915, **48**, 785–797.
 29. D. Y. Curtin, and S. R. Byrn, Stereoisomerism at the Oxygen-Carbon Single Bond due to Hydrogen Bonding. Structures of the Yellow and White Crystalline Forms of Dimethyl 3,6-Dichloro-2,5-dihydroxyterephthalate. *J. Am. Chem. Soc.*, 1969, **91**, 1865–1866.
 30. S. R. Byrn, D. Y. Curtin and I. C. Paul, The X-Ray Crystal Structures of the Yellow and White Forms of Dimethyl 3,6-Dichloro-2,5-dihydroxyterephthalate and a Study of the Conversion of the Yellow Form to the White Form in the Solid State. *J. Am. Chem. Soc.*, 1972, **94**, 890–898.
 31. M. Strohmeier, A. M. Orendt, D. W. Alderman and D. M. Grant, Investigation of the polymorphs of dimethyl-3,6-dichloro-2,5-dihydroxyterephthalate by ¹³C solid-state NMR spectroscopy. *J. Am. Chem. Soc.*, 2001, **123**, 1713–1722.
 32. J. Swiatkiewicz and P. N. Prasad, Spectroscopic Studies of the Thermal Rearrangement Reaction of Dimethyl 3,6-Dichloro-2,5-dihydroxyterephthalate in the Solid State. *J. Am. Chem. Soc.*, 1982, **104**, 6913–6918.
 33. R. Hi, Q. Yang and M. F. Richardson, Internal molecular motion as forerunner of a phase change involving conformational isomerization. *J. Am. Chem. Soc.*, 1985, **107**, 5535–5537.
 34. Q.-C. Yang, M. F. Richardson and J. D. Dunitz, Conformational polymorphism of dimethyl 3,6-dichloro-2,5-dihydroxyterephthalate. I. Structures and atomic displacement parameters between

- 100 and 350 K for three crystal forms. *Acta Crystallogr. Sect. B*, 1989 **45**, 312–323.
35. M. F. Richardson, Q.-C. Yang, E. Novotny-Bregger and J. D. Dunitz, Conformational polymorphism of dimethyl 3,6-dichloro-2,5-dihydroxyterephthalate. II. Structural, thermodynamic, kinetic and mechanistic aspects of phase transformations among the three crystal forms. *Acta Crystallogr. Sect. B*, 1990, **46**, 653–660.
 36. G. A. Stephenson, T. B. Borchardt, S. R. Byrn, J. Bowyer, C. A. Bunnell, S. V. Snorek and L. Yu Conformational and color polymorphism of 5-methyl-2-[(2-nitrophenyl)amino]-3-thiophenecarbonitrile. *J. Pharm. Sci.*, 1995, **84**, 1385–1386.
 37. J. Smith, E. MacNamara, D. Raftery, T. Borchardt and S. Byrn, S. Application of two-dimensional ¹³C solid-state NMR to the study of conformational polymorphism. *J. Am. Chem. Soc.*, 1998, **120**, 11710–11713.
 38. L. Yu, Polymorphism in Molecular Solids: An Extraordinary System of Red, Orange, and Yellow Crystals. *Acc. Chem. Res.*, 2010, **43**, 1257–1266.
 39. X. He, U. J. Griesser, J. G. Stowell, T. B. Borchardt and S. R. Byrn, Conformational color polymorphism and control of crystallization of 5-methyl-2-[(4-methyl-2-nitrophenyl)amino]-3-thiophenecarbonitrile. *J. Pharm. Sci.*, 2001, **90**, 371–388.
 40. H. Li, J. G. Stowell, X. He, K. R. Morris and S. R. Byrn, Investigations on solid-solid phase transformation of 5-methyl-2-[(4-methyl-2-nitrophenyl)amino]-3-thiophenecarbonitrile. *J. Pharm. Sci.*, 2007, **96**, 1079–1089.
 41. K. M. Lutker, Z. P. Tolstyka and A. J. Matzger, Investigation of a Privileged Polymorphic Motif: a Dimeric ROY Derivative. *Cryst. Growth Des.*, 2008, **8**, 136–139.
 42. H. Li, J. G. Stowell, T. B. Borchardt and S. R. Byrn, Synthesis, conformational polymorphism, and construction of a G-T diagram of 2-[(2-nitrophenyl)amino]-3-thiophenecarbonitrile. *Cryst. Growth Des.*, 2006, **6**, 2469–2474.
 43. J. D. Dunitz and A. Gavezzotti, Toward a quantitative description of crystal packing in terms of molecular pairs: Application to the hexamorphic crystal system, 5-methyl-2-[(2-nitrophenyl)amino]-3-thiophenecarbonitrile. *Cryst. Growth Des.*, 2005, **5**, 2180–2189.
 44. K. Adrjanowicz, K. Kaminski, M. Paluch, K. L. Ngai and L. Yu, Study of dynamics and crystallization kinetics of 5-methyl-2-(2-nitrophenyl)amino-3-thiophenecarbonitrile at ambient and elevated pressure. *J. Chem. Phys.*, 2012, **136**, 234509.
 45. T. B. Borchardt, J. G. Stowell and S. R. Byrn, The crystallization of 5-methyl-2-[(2-nitrophenyl)amino]-3-thiophenecarbonitrile in the presence of structurally similar compounds. *Mol. Cryst. Liq. Cryst. Sci. Technol. Sect. A Mol. Cryst. Liq. Cryst.*, 1998, **313**, 271–276.
 46. L. Yu, G. A. Stephenson, C. A. Mitchell, C. A. Bunnell, S. V. Snorek, J. J. Bowyer, T. B. Borchardt, J. G. Stowell and S. R. Byrn, Thermochemistry and Conformational Polymorphism of a Hexamorphic Crystal System. *J. Am. Chem. Soc.*, 2000, **122**, 585–591.
 47. C. A. Mitchell, L. Yu and M. D. Ward, Selective nucleation and discovery of organic polymorphs through epitaxy with single crystal substrates. *J. Am. Chem. Soc.*, 2001, **123**, 10830–10839.
 48. L. Yu, Color Changes Caused by Conformational Polymorphism: Optical-Crystallography, Single-Crystal Spectroscopy, and Computational Chemistry. *J. Phys. Chem. A*, 2002, **106**, 544–550.
 49. S. Chen, I. A. Guzei and L. Yu, New polymorphs of ROY and new record for coexisting polymorphs of solved structures. *J. Am. Chem. Soc.*, 2005, **127**, 9881–9885.
 50. S. Chen, H. Xi and L. Yu, Cross-nucleation between ROY polymorphs. *J. Am. Chem. Soc.*, 2005, **127**, 17439–17444.
 51. M. Tan, A. G. Shtukenberg, S. Zhu, W. Xu, E. Dooryhee, S. M. Nichols, M. D. Ward, B. Kahr and Q. Zhu, ROY revisited, again: the eighth solved structure. *Faraday Discuss.*, 2018, **211**, 477–491.
 52. M. Vasileiadis, A. V. Kazantsev, P. G. Karamertzanis, C. S. Adjiman and C. C. Pantelides, The polymorphs of ROY: Application of a systematic crystal structure prediction technique. *Acta Crystallogr. Sect. B Struct. Sci.*, 2012, **68**, 677–685.
 53. K. S. Gushurst, J. Nyman and S. X. M. Boerrigter, The PO13 crystal structure of ROY. *CrystEngComm*, 2019, **21**, 1363–1368.

54. M. Busch and E. Pungs, Über isomere Verschiedenfarbige Pikrylamine. *J. für Prakt. Chemie*, 1909, **79**, 546–554.
55. N. M. Cullinane, O. E. Embrey and D. R. Davis, Investigation of the Differently Colored Forms of Certain Derivatives of Diphenylamine. *J. Phys. Chem.*, 1932, **36**, 1434–1448.
56. R. G. Wood, S. H. Ayliffe and N. M. Cullinane, XXXIII. A crystallographic and x-ray investigation of some diphenylamine derivatives, *Lond. Edinb. Dublin Phil. Mag.*, 1935, **19**, 405–416.
57. M. Yasui, K. Taguchi and F. Iwasaki, Dynamic Behavior of *N*-(2,4-Dinitrophenyl)-*o*-Anisidine Crystals. *Mol. Cryst. Liq. Cryst. Sci. Technol. Sect. A. Mol. Cryst. Liq. Cryst.*, 1996, **277**, 167–176.
58. D. E. Braun, T. Gelbrich, R. K. R. Jetti, V. Kahlenberg, S. L. Price and U. J. Griesser, Colored Polymorphs: Thermochemical and Structural Features of *N*-Picryl-*p*-toluidine Polymorphs and Solvates. *Cryst. Growth Des.*, 2008, **8**, 1977–1989.
59. I. G. Ilyina, O. V. Mikhalev, K. P. Butin, B. N. Tarasevich and B. M. Uzhinov, Differently coloured crystalline modifications of organic autocomplexes of the nitroaromatic type. *Synthetic Metals*, 2001, **120**, 1067–1068.
60. A. V. Yatsenko and K. A. Paseshnichenko, A semi-empirical electrostatic potential in the studies of molecular crystals. *Chem. Phys.*, 2000, **262**, 293–301.
61. T. Yaji, S. Isoda, T. Kobayashi, K. Taguchi, K. Takada, M. Yasui and F. Iwasaki, Color Change Due to Phase Transition in *N*-(2,4-Dinitrophenyl)-*o*-Anisidine. *Mol. Cryst. Liq. Cryst. Sci. Technol. Sect. A Mol. Cryst. Liq. Cryst.*, 1999, **327**, 57–60.
62. C. Kitamura, T. Ohara, N. Kawatsuki, A. Yoneda, T. Kobayashi, H. Naito, T. Komatsu and T. Kitamura, Conformational polymorphism and optical properties in the solid state of 1,4,7,10-tetra(*n*-butyl)tetracene. *CrystEngComm*, 2007, **9**, 644–647.
63. C. Kitamura, Y. Abe, T. Ohara, A. Yoneda, T. Kawase, T. Kobayashi, H. Naito and T. Komatsu, Synthesis and crystallochromy of 1, 4, 7, 10-tetraalkyltetracenes: Tuning of solid-state optical properties of tetracenes by alkyl side-chain length. *Chem. - A Eur. J.*, 2010, **16**, 890–898.
64. K. J. Fujimoto and C. Kitamura, A theoretical study of crystallochromy: Spectral tuning of solid-state tetracenes. *J. Chem. Phys.*, 2013, **139**, 084511.
65. V. López-Mejías, J. W. Kampf and A. J. Matzger, Nonamorphism in flufenamic acid and a new record for a polymorphic compound with solved structures. *J. Am. Chem. Soc.*, 2012, **134**, 9872–9875.
66. S. P. Delaney, D. Pan, S. X. Yin, T. M. Smith and T. M. Korter, Evaluating the roles of conformational strain and cohesive binding in crystalline polymorphs of aripiprazole. *Cryst. Growth Des.*, 2013, **13**, 2943–2952.
67. T. A. Zeidan, J. T. Trotta, P. A. Tilak, M. A. Oliveira, R. A. Chiarella, B. M. Foxman, Ö. Almarsson and M. B. Hickey, An unprecedented case of dodecamorphism: The twelfth polymorph of aripiprazole formed by seeding with its active metabolite. *CrystEngComm*, 2016, **18**, 1486–1488.
68. R. M. Bhardwaj, J. A. McMahon, J. Nyman, L. S. Price, S. Konar, I. D. H. Oswald, C. R. Pulham, S. L. Price and S. M. Reutzel-Edens, A Prolific Solvate Former, Galunisertib, under the Pressure of Crystal Structure Prediction, Produces Ten Diverse Polymorphs. *J. Am. Chem. Soc.*, 2019, **141**, 13887–13897.
69. A. Kons, A. Bērziņš, A. Actiņš, T. Reķis, S. van Smaalen and A. Mishnev, Polymorphism of R-Encenicline Hydrochloride: Access to the Highest Number of Structurally Characterized Polymorphs Using Desolvation of Various Solvates. *Cryst. Growth Des.*, 2019, **19**, 4765–4773.

1.3. Specific Objectives and Structure of the Work

The main goal of this work was the study of two groups of compounds that were selected from two families of compounds that were known to exhibit color polymorphism, specifically *N*-picryl-*p*-toluidine and 5-methyl-2-((2-nitrophenyl)amino)thiophene-3-carbonitrile (ROY).

The *N*-picryl-*p*-toluidine analogues that were selected to be synthesized and studied are the compounds 3-((2,4,6-trinitrophenyl)amino)phenol (TAP) and 2,4,6-Trinitro-*N*-(*m*-tolyl)aniline (TMA). On the other hand, the chosen ROY analogues are 2-(4-((3-cyanothiophen-2-yl)amino)-3-nitrophenyl)acetic acid (ROY-CAM), 5-acetyl-2-((2-nitrophenyl)amino)thiophene-3-carbonitrile (AcROY), and 2-((4-hydroxy-2-nitrophenyl)amino)thiophene-3-carbonitrile (ROY-ol). All these compounds were newly synthesized in this work and no information of any kind was previously available in the scientific literature for any of them.

After the synthesis of the five referred compounds, the ultimate purpose of this research project was to study their propensity to form polymorphs, followed by the determination of relevant physicochemical properties of the different polymorphs. As mentioned in Section 1.1, the selected methods to study these systems rely both on computational and experimental approaches. Computationally, isolated molecule oriented DFT methods were employed to study the conformational behavior of the molecules, while state-of-the-art fully-periodic DFT calculations were used to study the crystalline structures obtained experimentally. The core experimental methods used in this Thesis were vibrational spectroscopy techniques (Raman and IR), X-ray diffraction, and thermodynamics methods (DSC and PLTM). Additional techniques were occasionally employed, such as matrix-isolation IR spectroscopy, solid-state UV-vis absorption spectroscopy and thermogravimetric analysis.

This Thesis includes one chapter (Chapter 2) where the fundamental aspects and general apparatus conditions of the main computational and experimental methods used in this work are introduced, two chapters (3 and 4) where the main results obtained throughout the 4 years of the project are described, and a concluding section (Chapter 5) where the main conclusions of the combined results produced in Chapters 3 and 4 are highlighted, and perspectives for the future development of this program of studies are presented.

Throughout this work, in total, from the two different compound families, 12 different color polymorphs were identified, and 10 crystal structures were determined. From this starting point, the

Introduction

used computational and experimental approaches were applied to characterize the polymorphs of the five new compounds and to further the knowledge on color polymorphic systems in general.

2. Theory and Methodology

In this Chapter, a brief introduction to the fundamentals of the most important theoretical and experimental methods used throughout this PhD project is presented. Additionally, the general experimental conditions and instrumentation used are concisely described. Further information on the applied theoretical and experimental procedures, in particular the details about the specific conditions used in each laboratorial or computational experiment, will be provided in the respective sections of Chapters 3 and 4.

2.1. Computational Methods

2.1.1. Density Functional Theory (DFT)

Density Functional Theory (DFT) is one of the most used methods for electronic structure determination in computational chemistry due to the generally highly-accurate results it provides and its computational efficiency.¹⁻⁴ Indeed, DFT represents a very effective tool both to predict and to characterize, at the molecular level, numerous properties of materials.⁵⁻⁷

Differently to the *ab initio* wavefunction-based methods, as the Hartree-Fock (HF) and post-HF methods, such as the Moller and Plesset (MP) perturbational theory (e.g., the popular second order Moller and Plesset method – MP2), the density functional theory methods are based on the existence of a functional that determines the exact electronic energy of the ground-state from the electron density (ρ), according to the Hohenberg-Kohn theorems.⁸

The computational efficiency of the DFT methods, which is one of its main advantages, derives from the simplicity of the calculation of the electronic probability density, $\rho(\vec{r})$, which depends only on three coordinates (the spatial coordinates of a particular point in space r), while the wavefunction-based approaches use, for a molecule with N electrons, a total of $4N$ coordinates (three spatial coordinates plus an extra coordinate for the spin, for every electron). Hence, in DFT, the electronic energy (E) is calculated as a functional of the electron density: $E[\rho]$.⁹⁻¹²

Based on the Hohenberg-Kohn theorems, it is possible to correlate not only the energy of the system but also other properties with the electron density. The first Hohenberg-Kohn theorem, known as the *Existence Theorem*, demonstrates that the ground-state energy of a molecular system is exclusively defined by the electronic density of that system, which means that the ground-state energy and the respective electronic properties are a functional of the electron density. However, the *Existence Theorem* does not provide any information regarding the form of this functional. In a second theorem, the *Variational Theorem*, the authors demonstrated that it is possible to use a variational approach in order to calculate the energy and the electron density of the system, which means that, if the exact functional form is used, the electron density can be varied until the energy of the functional is fully minimized.¹³

Nowadays, Kohn and Sham approach, which allowed to deal the fundamental difficulties related with the kinetic energy functional in the DFT method, is employed in the DFT calculations. Kohn and Sham approach acts dividing the kinetic energy functional in two components, one that reflects the non-interacting electrons and that can be calculated exactly, and a second relatively small correction term, which considers the electron-electron interaction. The energy functional can then be divided in different contributions:

$$E(\rho) = E^T(\rho) + E^V(\rho) + E^J(\rho) + E^{XC}(\rho) \quad (2.1)$$

where E^T represents the electronic kinetic energy term, E^V denotes the nuclear-electronic interaction potential energy term, and E^J is the Coulomb electronic repulsion term. The latter term of Eq. 2.1, E^{XC} , is designated as the electron exchange-correlation energy term; it includes the quantic effects of exchange and correlation, as well as the correction of the classic interelectronic energy and the difference between the kinetic energy of an ideal system of non-interacting electrons and the real system.¹⁴

Amongst the vast number of approximated approaches to calculate the electron exchange-correlation energy functional, E^{XC} , the Local Density Approximation (LDA) is the simplest one. The LDA approach, based on the concept of a uniform electron gas, considers that the electronic density is uniform throughout the molecular system, and is given by:

$$E_{XC}^{LDA}[\rho] = \int \rho(\vec{r}) \varepsilon_{XC}(\rho(\vec{r})) d\vec{r} \quad (2.2)$$

where $\varepsilon_{XC}(\rho(\vec{r}))$ is the exchange-correlation energy per particle of the uniform electron gas of density $\rho(\vec{r})$. Additionally, the exchange-correlation energy, ε_{XC} , can be divided in two individual terms, the exchange energy, ε_X , and the correlation energy, ε_C .¹⁵⁻¹⁷

The Local Spin Density Approximation (LSDA) is a more general approximation than the LDA one. In the LSDA approximation, the spin density is introduced in the functionals, and the total

electronic density is given by the sum of the α spin electronic density and the β spin electronic density. This approach has replaced LDA for the treatment of open shell systems. However, both the LDA and LSDA approaches only give good results for particular systems where the electron density is approximately uniform, which is not the case for the vast majority of the chemical systems. Thus, other functionals were created to combine the electron density with a gradient correction. The Generalized Gradient Approximation (GGA), which is on the basis of the so called non-local methods, is one of the methods that takes into account the gradient correction effect. It is given by:

$$E_{XC}^{GGA}[\rho^\alpha, \rho^\beta] = \int f(\rho^\alpha(\vec{r}), \rho^\beta(\vec{r}), \nabla\rho^\alpha(\vec{r}), \nabla\rho^\beta(\vec{r})) d\vec{r} \quad (2.3)$$

where f represents any given function of the spin densities and the respective corrected gradients, and ∇ is the Laplace operator. Similarly to the LDA approach, the exchange-correlation energy in the GGA, E_{XC}^{GGA} , might also be split in two components, the exchange energy and the correlation energy.¹⁻⁴

Furthermore, hybrid methods combining functionals of the previous referred approximations with parts of a HF calculation, typically the exchange integrals, have also been developed. The exchange functional developed by Becke in 1988 (known as B or B88)¹⁸, that introduced by Perdew and Wang in 1986 (PW86)¹⁹ and modified later by the same authors in 1991 (PW91),²⁰ and the correlation functionals of Vosko, Wilk and Nusair (VWN)²¹ or that of Lee, Yang and Parr (LYP),²² both developed in the 1980s, are the most popular ones, with the hybrid functional designated as B3LYP, which combines the Becke exchange functional with the Lee, Yang and Parr correlation functional, being by far the most used functional in electronic structure computational science nowadays. This is also the functional that was mostly used throughout the present work. It is given by:

$$E_{XC}^{B3LYP} = (1 - a)E_X^{LSDA} + aE_X^{HF} + b\Delta E_X^B + (1 - c)E_C^{VWN} + cE_C^{LYP} \quad (2.4)$$

where E_X^{HF} , the exchange energy term from HF calculations, is also referred as the exact exchange energy functional, E_X^{exact} . The semi-empirical numerical parameters a , b and c (which constitute the origin of the number 3 in the acronym B3LYP) assume the values attributed by Becke for the B3PW91 functional, where a is 0.2, b is 0.72 and c is 0.81. E_X^B is the exchange functional developed by Becke, and is given by:

$$E_X^B = E_X^{LSDA} - b \sum_{\sigma=\alpha,\beta} \int \frac{(\rho^\sigma)^{\frac{4}{3}} \chi_\sigma^2}{1+6b\chi_\sigma \sinh^{-1}\chi_\sigma} d\vec{r} \quad (2.5)$$

where $\chi_\sigma \equiv |\nabla\rho| / (\rho^\sigma)^{4/3}$, σ denotes either *up* or *down* electron spin, and b is an empirical parameter, which value is usually 0.042 (in atomic units). In turn, the E_C^{LYP} term appearing in Eq. 2.4 corresponds to the correlation functional developed by Lee, Yang and Parr, which is given by:

$$E_C^{LYP} = -a \int \frac{\rho + b\rho^{\frac{2}{3}}[t_{HF} - 2t_W] e^{c\rho^{\frac{1}{3}}}}{1 + d\rho^{\frac{1}{3}}} \quad (2.6)$$

where the constants a , b , c and d are 0.049, 0.132, 0.2533 and 0.349, respectively, and t_{HF} and t_W represent the kinetic energy density calculated by Hartree-Fock and Weizsacker methods, respectively.

The B3LYP method provides generally very good results for organic molecules, namely for geometries, relative energies of isomeric forms and vibrational spectra predictions.^{23,24}

In the present work, the isolated molecule calculations were performed using the Gaussian 09 (revision D.01) software,²⁵ and the results were analysed using both GaussView²⁶ and Chemcraft.²⁷

2.1.2. Basis Sets

To perform electronic structure computational calculations, employing for example the DFT method, we need to choose an appropriate basis set. A basis set is a set of functions that are used to build the molecular orbitals of the systems under investigation. These functions are typically centred on the atomic nuclei and, *a priori*, can be any type of mathematical functions that might be useful to manipulate and provide practical representations of the molecular orbitals and the electronic distribution throughout the molecular system.

There are two main types of basis functions usually employed in electronic structure calculations on molecules: Slater type orbitals, or simply STOs, given by:

$$\chi_{\xi,n,l,m}(r, \theta, \varphi) = NY_{l,m}(\theta, \varphi)r^{n-1}\exp(-\xi r) \quad (2.7)$$

and Gaussian type orbitals (GTOs), represented by:

$$\chi_{\xi,n,l,m}(r, \theta, \varphi) = NY_{l,m}(\theta, \varphi)r^{2n-2-l}\exp(-\xi r^2) \quad (2.8)$$

In Eqs. 2.7 and 2.8, ξ represents the orbital exponent, n , l and m are, respectively, the principal, angular momentum and magnetic quantum numbers, r , θ and φ represent the spherical coordinates centred at the nucleus, N is a normalization constant, and $Y_{l,m}$ denotes the spherical harmonic functions. The STOs act as good approximations to atomic orbitals and they would be the best functions to be used to form the basis sets for electronic structure calculations if their calculation were not so complex and time-consuming. For this reason, they are not commonly employed, except in calculations performed on atomic and diatomic systems. The GTOs differ from the STOs in the exponential term, which involves the square of the distance from the electron to the point where the function is centred (in general a nucleus). As a result of the r^2 dependence, the Gaussian type orbitals are much easier to manipulate

mathematically, but, on the other hand, are less appropriate to represent properly the radial shape of the electron distribution both close to and far from the nucleus. To overtake this problem, linear combinations of several GTOs are commonly used to represent, as correctly as possible, a given Slater function. Therefore, when a basis function is defined as a linear combination of Gaussian orbital functions, it is denominated as a contracted basis function, whereas the individual Gaussian functions are referred to as primitive GTOs.

The correct selection of a size-adequate basis set is of fundamental importance due to its impact on the compromise between accuracy and computational cost. Nowadays, there are many basis sets available in computational chemistry software packages. The simplest ones, the so-called minimal basis sets, contain exclusively the number of basis functions required to accommodate the electrons existing in each atom of the molecule. Hence, in this case, a single 1s-type basis function is required for hydrogen and helium atoms, while for the elements of the first row of the periodic table 1s-, 2s- and 2p-type functions are required. Double-zeta, triple-zeta and quadruple-zeta basis sets are basis set with the double, triple or quadruple number of functions compared to the minimal basis sets, respectively. Since the chemical bonding occurs between valence orbitals, the core orbitals do not affect greatly the chemical properties, and single functions can be used to represent the core orbitals without compromising the quality of the calculations. On the other hand, valence orbitals are critical for the structure and reactivity of a molecular system and shall be represented by means of a more flexible function. The simplest way to implement such requirement is to use more than one basis function in the representation of valence orbitals. The basis sets built this way are named n-zeta split-valence basis sets and are the most commonly used basis sets in calculations performed on molecules. Examples of split valence basis sets are the Pople-type basis sets (developed by the Nobel prize winner John Pople). The designations of this type of basis follow a specific set of rules. For example, the double-zeta split-valence 3-21G basis set corresponds to a basis set constituted by 3 primitive contracted Gaussian functions for representation of each orbital of the atomic core, and two sets of Gaussian functions, one including 2 contracted GTOs and the other including a single GTO, for representation of the valence orbitals.^{28,29}

Additionally, basis sets can include the so-called polarization and diffuse functions. The first correspond to functions of higher angular momentum than that associated with the electrons in the atom they are centred on (*e.g.*, p-type orbitals for hydrogen and helium atoms, d-type orbitals for first and second row elements, etc.), and give additional flexibility to the wavefunction by allowing the electron distribution to be distorted along a particular direction. In Pople's basis sets notation, this type of functions might be represented either by the symbol * or by the letter p, d, f, ..., which are written between parenthesis after the letter G. If polarization functions are introduced both to heavy atoms (non-hydrogen) and to hydrogen atoms, the letters must be introduced in this order inside the parenthesis,

separated by a comma. The diffuse functions are spherical (s-type) functions with small exponents, which allow the electron distribution to be spread into a larger volume and are used to better describe molecular systems that contain lone pairs of electrons or electrons that are unusually far from the nuclei. These functions are notated by the symbol + in Pople's basis sets notation. A single + symbol indicates that the basis set contains diffuse functions for heavy atoms, while two + symbols indicate the addition of diffuse functions for both heavy and hydrogen atoms. For instance, the 6-311++G(d,p) basis set is composed of 6 primitive Gaussian functions to represent each core atomic orbital, three sets of valence orbitals (one combination of three primitive Gaussian functions plus two single primitive Gaussians), a set of d-type polarization Gaussian function for heavy atoms and a set of p-type polarization Gaussian for hydrogen atoms, and a diffuse function for each atom (both non-hydrogen and hydrogen atoms). The 6-311++G(d,p) basis set has been extensively used in computations performed on organic molecules and has shown to be of excellent quality for calculation of molecular geometries, relative conformational energies and vibrational spectra, in particular when used with the B3LYP functional in DFT-based calculations. This basis set has been selected as main basis set for the calculations presented in this Thesis.

2.1.3. DFT Calculations with Periodic Boundary Conditions

The quantum mechanical condensed matter simulations presented in this work were performed using the CRYSTAL17 software.³⁰ The CRYSTAL17 code adopts atom-centred Gaussian functions as basis sets and permits the treatment of systems of any periodicity: from 0D molecules, to 1D polymers or nanotubes, 2D monolayers and 3D bulk crystals.^{31,32} It allows the use of hybrid functionals at a modest computational cost, because of the efficient implementation of the exact non-local Fock exchange. Other feature that drastically reduces the computational cost of CRYSTAL17 calculations is the translational and point-symmetry properties being exploited in all steps of the calculations. Among many other properties, CRYSTAL17 3D structures predictions include the calculation of the electronic structure, geometry optimization (both full and constrained optimizations are accessible), and calculation of the vibrational properties, which embrace frequencies, symmetry of vibrations, infrared intensities and Raman activities, the latter encompassing polarizability differentiation and giving access to the individual contributions of the polarizability tensor to the Raman activities (a particularly useful feature for interpretation of polarized Raman spectra of single crystals).³² Additionally, CRYSTAL17 also presents an input parameter-free and user-friendly implementation of Grimme's correction to include weak dispersive interactions in the DFT functionals, which is also a particularly interesting feature in the study of molecular organic crystals.³³⁻³⁶

The DFT calculations with periodic boundary conditions carried out for every system studied along this work included the full optimization of the atomic positions and the lattice parameters, where the first guess input structures were those obtained experimentally by X-ray diffraction in this project. Also, for each molecular crystal system studied, different combinations of functionals and basis sets were benchmarked regarding their ability to properly predict the atomic positions in the crystal and the lattice parameters. The selected combinations were specific for each considered system and are provided in the proper sections of this Thesis, together with other particular details of each calculation performed.

As referred above, the CRYSTAL17 code allows accurate simulation of the vibrational properties of crystalline molecular materials. Conveniently, in CRYSTAL17 the electronic calculations and the simulation and analysis of IR and Raman spectra are undertaken within the MO-LCAO approach (instead of the most commonly used plane-wave functions) and take advantage of the explicit consideration of the space group symmetry of the crystals. CRYSTAL17 also provides infrared absorption intensities and Raman activities, thus allowing a direct comparison between the predicted results and the experimentally obtained intensity patterns. Specifically, the IR intensities and Raman activities are predicted in CRYSTAL17 through the Coupled Perturbed Kohn Sham (CPKS) method,³² as it will be discussed in further detail in Section 2.3. In the present study, all normal frequencies calculations at the Γ point ($k = 0$, the center of the first Brillouin zone – BZ) have been performed for the optimized geometries by diagonalization of the numerically calculated Hessian matrix (H):

$$W_{ai,bj}^{\Gamma} = \frac{H_{ai,bj}^0}{\sqrt{M_a M_b}} \quad \text{with} \quad H_{ai,bj}^0 = \left(\frac{\partial^2 E}{\partial u_{ai}^0 \partial u_{bj}^0} \right) \quad (2.9)$$

where E represents the total energy per cell, and atoms a and b in the reference cell are displaced along the i th and j th Cartesian directions from the equilibrium configuration, u_{ai} and u_{bj} representing the Cartesian components of the displacement vectors u_a and u_b respectively, and with M_a and M_b being their respective atomic mass. The first-order derivatives were obtained analytically, while the second-order derivatives were computed numerically.^{37,38}

2.1.4. Hirshfeld Surfaces

One of the most popular tools available for detailed analysis of the structure of molecular crystals is based on Hirshfeld surfaces. The Hirshfeld surface analysis method is a powerful approach to analyze the internuclear distances and angles relevant to the crystal packing, which are then used to identify, evaluate, and somehow quantify the most important intermolecular interactions in the crystal. These are inferred from the shorter interatomic contacts between the structural units present in the

crystal.³⁹ This semi-empirical computational method was introduced by Spackman and Byrom, in 1997, who presented it as a simple and aesthetically appealing technique that offered potential value in “*routine partitioning of crystalline electron densities and in computer graphics to provide additional insight into molecular packing in crystals*”.⁴⁰ The Hirshfeld surface emerged originally from the effort to define the space occupied by a molecule in a crystal for the purpose of partitioning the crystal into molecular fragments, in order to try to overcome some difficulties or limitations of other somehow similar methods (at least regarding some of their purposes), such as the quantum theory of atoms in molecules (QTAIM).⁴¹

The Hirshfeld surfaces are obtained from electron distributions that are calculated as the sum of spherical atomic electron densities. Briefly, the Hirshfeld surface of a molecule in a crystal defines the region where the electron distribution given by the sum of the electron densities of the spherical atoms of a given molecule (the so-called promolecule) exceeds that from all other promolecules in the crystal. Subsequently, structure-related properties can be mapped on the Hirshfeld surface. The normalized contact distances (d_{norm}) are calculated taking into consideration the distance from a point on the surface to the nearest nucleus outside the surface (d_e) and the distance from a point on the surface to the nearest nucleus inside the surface (d_i), normalized by the corresponding van der Waals radii (vdW), as defined by Eq. 2.10. The calculated d_{norm} values allow the identification of the regions of the molecule where intermolecular contacts are more important to the crystal lattice.⁴² Furthermore, the combination of d_e and d_i in the form of a 2D-fingerprint plot allows to condense the information about the intermolecular interactions that define the crystal contacts in an appealing visual format.^{43–45} These 2D-fingerprint plots offer a graphical summary of the frequency of each combination of d_e and d_i across the surface of a molecule, thus indicating not just which intermolecular contacts are present in the crystal structure, but also the relative importance of each interaction in the lattice as measured by the relative area of the surface assigned to each type of interaction.

$$d_{norm} = \frac{d_i - r_i^{vdW}}{r_i^{vdW}} + \frac{d_e - r_e^{vdW}}{r_e^{vdW}} \quad (2.10)$$

In this work, the Hirshfeld surfaces and their 2D fingerprint plots were generated using the CrystalExplorer 17.5 software,⁴⁶ with the structure input files (with the structures obtained by X-ray diffraction) being provided in the CIF format.

References

- 1 A. Szabo and N. S. Ostlund, *Modern quantum chemistry : introduction to advanced electronic structure theory*, Dover Publications, 1996.
- 2 F. Jensen, *Introduction to Computational Chemistry*, John Wiley & Sons, 2007.

- 3 E. G. Lewars, *Computational Chemistry*, Springer Netherlands, Dordrecht, 2011.
- 4 R. G. Parr and W. Yang, *Density-functional theory of atoms and molecules*, Oxford University Press, 1989.
- 5 J. Landers, G. Y. Gor and A. V. Neimark, Density functional theory methods for characterization of porous materials, *Colloids Surfaces A Physicochem. Eng. Asp.*, 2013, **437**, 3–32.
- 6 J. Hafner, C. Wolverton and G. Ceder, Toward Computational Materials Design: The Impact of Density Functional Theory on Materials Research, *MRS Bull.*, 2006, **31**, 659–668.
- 7 A. Jain, G. Hautier, C. J. Moore, S. Ping Ong, C. C. Fischer, T. Mueller, K. A. Persson and G. Ceder, A high-throughput infrastructure for density functional theory calculations, *Comput. Mater. Sci.*, 2011, **50**, 2295–2310.
- 8 W. Koch and M. C. Holthausen, *A chemist's guide to density functional theory*, Wiley-VCH Verlag GmbH, 2001.
- 9 S. F. Sousa, P. A. Fernandes and M. J. Ramos, General Performance of Density Functionals, *J. Phys. Chem. A*, 2007, **111**, 10439–10452.
- 10 K. E. Riley, B. T. Op't Holt and K. M. Merz, Critical Assessment of the Performance of Density Functional Methods for Several Atomic and Molecular Properties, *J. Chem. Theory Comput.*, 2007, **3**, 407–433.
- 11 Y. Zhao and D. G. Truhlar, Density Functionals with Broad Applicability in Chemistry, *Acc. Chem. Res.*, 2008, **41**, 157–167.
- 12 Y. Zhao and D. G. Truhlar, Applications and validations of the Minnesota density functionals, *Chem. Phys. Lett.*, 2011, **502**, 1–13.
- 13 P. Hohenberg and W. Kohn, Inhomogeneous Electron Gas, *Phys. Rev. B*, 1964, **136**, 864–871.
- 14 W. Kohn and L. J. Sham, Self-Consistent Equations Including Exchange and Correlation Effects, *Phys. Rev. A*, 1965, **140**, 1133–1138.
- 15 L. H. Thomas, The calculation of atomic fields, *Math. Proc. Camb. Philos. Soc.*, 1927, **23**, 542–548.
- 16 E. Fermi, Un metodo statistico per la determinazione di alcune proprietà dell'atomo., *Rend. Accad. Lincei.*, 1927, **6**, 602–607.
- 17 P. Dirac, Note on exchange phenomena in the Thomas atom, *Math. Proc. Camb. Philos. Soc.*, 1930, **26**, 376–385.
- 18 A. D. Becke, Density-functional exchange-energy approximation with correct asymptotic behavior, *Phys. Rev. A*, 1988, **38**, 3098–3100.
- 19 J. P. Perdew and Y. Wang, Accurate and simple density functional for the electronic exchange energy: Generalized gradient approximation, *Phys. Rev. B*, 1986, **33**, 8800–8802.
- 20 J. P. Perdew and Y. Wang, Accurate and simple analytic representation of the electron-gas correlation energy, *Phys. Rev. B*, 1992, **45**, 13244–13249.
- 21 S. H. Vosko, L. Wilk and M. Nusair, Accurate spin-dependent electron liquid correlation energies for local spin density calculations: a critical analysis, *Can. J. Phys.*, 1980, **58**, 1200–1211.
- 22 C. Lee, W. Yang and R. G. Parr, Development of the Colle-Salvetti correlation-energy formula into a functional of the electron density, *Phys. Rev. B*, 1988, **37**, 785–789.
- 23 A. A. El-Azhary and H. U. Suter, Comparison between Optimized Geometries and Vibrational Frequencies Calculated by the DFT Methods, *J. Phys. Chem.*, 1996, **100**, 15056–15063.
- 24 J. A. Montgomery, M. J. Frisch, J. W. Ochterski and G. A. Petersson, A complete basis set model chemistry. VI. Use of density functional geometries and frequencies, *J. Chem. Phys.*, 1999, **110**, 2822–2827.
- 25 Gaussian 09, Revision A.02, M. J. Frisch, G. W. Trucks, H. B. Schlegel, G. E. Scuseria, M. A. Robb, J. R. Cheeseman, G. Scalmani, V. Barone, G. A. Petersson, H. Nakatsuji, X. Li, M. Caricato, A. Marenich, J. Bloino, B. G. Janesko, R. Gomperts, B. Mennucci, H. P. Hratchian, J. V. Ortiz, A. F. Izmaylov, J. L. Sonnenberg, D. Williams-Young, F. Ding, F. Lipparini, F. Egidi, J. Goings, B. Peng, A. Petrone, T. Henderson, D. Ranasinghe, V. G. Zakrzewski, J. Gao, N. Rega, G. Zheng, W. Liang, M. Hada, M. Ehara, K. Toyota, R. Fukuda, J. Hasegawa, M. Ishida, T. Nakajima, Y. Honda, O. Kitao, H. Nakai, T. Vreven, K. Throssell, J. A. Montgomery, Jr., J. E. Peralta, F. Ogliaro, M. Bearpark, J. J. Heyd, E. Brothers, K. N. Kudin, V. N. Staroverov, T.

- Keith, R. Kobayashi, J. Normand, K. Raghavachari, A. Rendell, J. C. Burant, S. S. Iyengar, J. Tomasi, M. Cossi, J. M. Millam, M. Klene, C. Adamo, R. Cammi, J. W. Ochterski, R. L. Martin, K. Morokuma, O. Farkas, J. B. Foresman, and D. J. Fox, Gaussian, Inc., Wallingford CT, 2016.
- 26 GaussView, Version 6.1, Roy Dennington, Todd A. Keith, and John M. Millam, Semichem Inc., Shawnee Mission, KS, 2016.
- 27 Chemcraft (version 1.8) - Graphical software for visualization of quantum chemistry computations. <https://www.chemcraftprog.com>
- 28 R. Ditchfield, W. J. Hehre, J. A. Pople, R. Ditchfield, W. J. Hehre and J. A. Pople, Self-Consistent Molecular-Orbital Methods. IX. An Extended Gaussian-Type Basis for Molecular-Orbital Studies of Organic Molecules, *J. Chem. Phys.*, 1971, **54**, 724–728.
- 29 W. J. Hehre, K. Ditchfield and J. A. Pople, Self—Consistent Molecular Orbital Methods. XII. Further Extensions of Gaussian—Type Basis Sets for Use in Molecular Orbital Studies of Organic Molecules, *J. Chem. Phys.*, 2003, **56**, 2257–2261.
- 30 R. Dovesi, V. R. Saunders, C. Roetti, R. Orlando, C. M. Zicovich-Wilson, F. Pascale, B. Civalleri, K. Doll, N. M. Harrison, I. J. Bush, P. D’Arco, M. Llunell, M. Causà, Y. Noël, L. Maschio, A. Erba, M. Rerat and S. Casassa, CRYSTAL17 User's Manual (University of Torino, Torino, 2017).
- 31 R. Dovesi, R. Orlando, A. Erba, C. M. Zicovich-Wilson, B. Civalleri, S. Casassa, L. Maschio, M. Ferrabone, M. De La Pierre, P. D’Arco, Y. Noël, M. Causà, M. Rérat and B. Kirtman, CRYSTAL14: A program for the ab initio investigation of crystalline solids, *Int. J. Quantum Chem.*, 2014, **114**, 1287–1317.
- 32 R. Dovesi, A. Erba, R. Orlando, C. M. Zicovich-Wilson, B. Civalleri, L. Maschio, M. Rérat, S. Casassa, J. Baima, S. Salustro and B. Kirtman, Quantum-mechanical condensed matter simulations with CRYSTAL, *Wiley Interdiscip. Rev. Comput. Mol. Sci.*, 2018, **8**, e1360.
- 33 S. Grimme, Accurate description of van der Waals complexes by density functional theory including empirical corrections, *J. Comput. Chem.*, 2004, **25**, 1463–1473.
- 34 S. Grimme, Semiempirical GGA-type density functional constructed with a long-range dispersion correction, *J. Comput. Chem.*, 2006, **27**, 1787–1799.
- 35 B. Civalleri, C. M. Zicovich-Wilson, L. Valenzano and P. Ugliengo, B3LYP augmented with an empirical dispersion term (B3LYP-D*) as applied to molecular crystals, *CrystEngComm*, 2008, **10**, 405–410.
- 36 S. Grimme, J. Antony, S. Ehrlich and H. Krieg, A consistent and accurate ab initio parametrization of density functional dispersion correction (DFT-D) for the 94 elements H-Pu, *J. Chem. Phys.*, 2010, **132**, 154104.
- 37 F. Pascale, C. M. Zicovich-Wilson, F. López Gejo, B. Civalleri, R. Orlando and R. Dovesi, The calculation of the vibrational frequencies of crystalline compounds and its implementation in the CRYSTAL code, *J. Comput. Chem.*, 2004, **25**, 888–897.
- 38 C. M. Zicovich-Wilson, F. Pascale, C. Roetti, V. R. Saunders, R. Orlando and R. Dovesi, Calculation of the vibration frequencies of α -quartz: The effect of hamiltonian and basis set, *J. Comput. Chem.*, 2004, **25**, 1873–1881.
- 39 M. A. Spackman and D. Jayatilaka, Hirshfeld surface analysis, *CrystEngComm*, 2009, **11**, 19–32.
- 40 M. A. Spackman and P. G. Byrom, A novel definition of a molecule in a crystal, *Chem. Phys. Lett.*, 1997, **267**, 215–220.
- 41 R. F. W. Bader, *Atoms in Molecules: A Quantum Theory*, Oxford University Press, 1990.
- 42 J. J. McKinnon, A. S. Mitchell and M. A. Spackman, Hirshfeld Surfaces: A New Tool for Visualising and Exploring Molecular Crystals, *Chem. - A Eur. J.*, 1998, **4**, 2136–2141.
- 43 M. A. Spackman and J. J. McKinnon, Fingerprinting intermolecular interactions in molecular crystals, *CrystEngComm*, 2002, **4**, 378–392.
- 44 A. Parkin, G. Barr, W. Dong, C. J. Gilmore, D. Jayatilaka, J. J. McKinnon, M. A. Spackman and C. C. Wilson, Comparing entire crystal structures: Structural genetic fingerprinting, *CrystEngComm*, 2007, **9**, 648–652.
- 45 A. L. Rohl, M. Moret, W. Kaminsky, K. Claborn, J. J. McKinnon and B. Kahr, Hirshfeld Surfaces Identify Inadequacies in Computations of Intermolecular Interactions in Crystals:

- 46 Pentamorphic 1,8-Dihydroxyanthraquinone, *Cryst. Growth Des.*, 2008, **8**, 4517–4525.
Crystal Explorer17, version 17.5, S. K. Wolff, D. J. Grimwood, J. J. McKinnon, M. J. Turner,
D. Jayatilaka, M. A. Spackman, University of Western Australia: Crawley (AUS), 2017.

2.2. Vibrational Spectroscopy: Infrared Absorption and Raman Scattering Spectroscopies

The atoms in a molecule vibrate constantly around their equilibrium positions, continuously changing the bonds lengths and the bond and dihedral angles. For a molecular geometry close to the potential energy minimum, the harmonic approximation can be used and the potential energy (V) for a single diatomic molecular oscillator can be approximately given by:^{1,2}

$$V = \frac{1}{2}k (R - R_e)^2 \quad (2.11)$$

where R_e and R are the equilibrium and actual bond lengths, respectively, and k is the force constant of the bond, which corresponds to the second derivative of energy in order to the bond distance taken at the equilibrium position.

The Schrödinger equation for the motion of two atoms of masses m_1 and m_2 , with the potential energy given by Eq. 2.11 is:

$$-\frac{\hbar^2}{2\mu} \frac{d^2\psi}{dR^2} + V\psi = E\psi \quad (2.12)$$

where μ is the reduced mass, which is given by $\mu = \frac{m_1 m_2}{m_1 + m_2}$, E is the energy, ψ is the wave function and \hbar the Planck's constant divided by 2π .

If the previous equation is solved under the harmonic approximation and separating the relative motion of the atoms (vibration) from the motion of the molecule as a whole (rotations and translations):

$$E_v = \left(v + \frac{1}{2}\right) \hbar\omega \quad \text{with } v = 0, 1, 2, \dots \text{ and } \omega = \left(\frac{k}{\mu}\right)^{1/2} \quad (2.13)$$

where E_v is the energy of the vibrational level v for the molecule and ω the angular frequency of the vibration. Hence, the separation between adjacent vibrational levels is:

$$\Delta E = E_{v+1} - E_v = \hbar\omega \quad (2.14)$$

which is the same for all v values.

The generalization of the problem to polyatomic molecules, in keeping the harmonic approximation, leads to a system of $3N-6$ equations ($3N-5$ in the case of linear molecules), where N is

the number of atoms in the molecule, that is usually solved using a matrix method commonly known by Wilson and Decius method.³⁻⁶ The $3N-6$ independent vibrations of a molecule ($3N-5$ for a linear molecule) are designated by normal modes (Q_i) and possess characteristic energies given by equations similar to Eq. 2.13, where the angular frequency ω assumes *a priori* a specific value for each vibration (in practice, the symmetry of the molecule may lead to equal values of ω for different vibrations, which are related by symmetry and are designated as symmetry-degenerated modes).

Symmetry criteria are used to determine the activity of a vibrational transition both in infrared and Raman spectroscopies, the two major vibrational spectroscopy techniques. Under the double harmonic (mechanical and electrical) approximation, the molecular dipole and the molecular polarizability are described as linear functions of the normal coordinates Q_i .⁶ As a consequence, if the motion corresponding to a specific vibration results in a change in the dipole moment, this vibration is IR active. In contrast, a vibrational mode is active in Raman spectroscopy if its motion implies a change in the molecular polarizability. In Figure 1, simple examples of vibrations that are either infrared or Raman active are illustrated. The given examples also show that if a given molecule has a symmetry inversion center, then none of the normal modes can be simultaneously IR and Raman active, a rule that is known as the *mutual exclusion principle*. On the other hand, a mode can be inactive in both techniques, if neither the dipole moment or the molecular polarizability change along the vibration in the vicinity of the equilibrium geometry.⁷

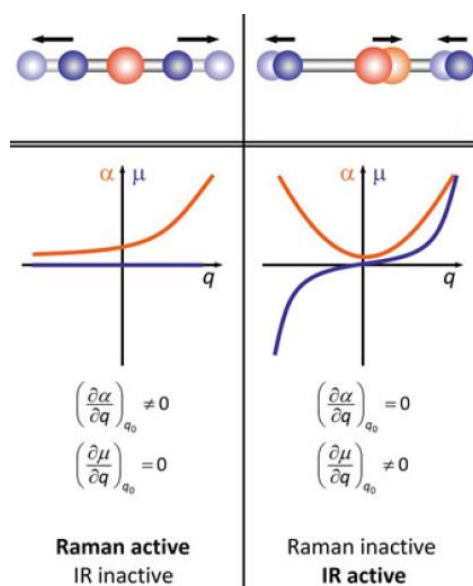


Figure 1 – Illustration of the derivatives of dipole moment (μ , in blue) and polarizability (α , in red), which determines the activity of a given vibration in infrared and Raman spectroscopy, respectively. See Eq. 2.18 and 2.22 for α and μ description. Figure adapted from *Confocal Raman Microscopy*.⁸

For systems in condensed phase, intermolecular interactions became important and affect the intramolecular potential, leading to changes in the values of the vibrational frequencies relative to the isolated molecule. For a crystalline material, the spatial symmetry of the crystal (which defines the symmetry space group) must also be considered for the definition of the vibrations of the system. It shall be noticed that intermolecular interactions and space group symmetry in crystalline phase affect not only the frequencies of the vibrations but also the intensities and profiles of the bands. For example, an intramolecular hydrogen bond makes the frequency of the stretching vibration of the H-bond donor ($\nu(\text{X-H})$) to reduce (due to the reduction of the electron density in the X-H bond after the formation of the H-bond, *i.e.*, due to the reduction of the force constant of the stretching vibration, see Eq. 2.11), while both the intensity and broadness of the band increase, the first due to an increased polarity/polarizability of the bond associated to the X-H bond after H-bond formation, and the second due to the heterogeneity of the X-H \cdots Y moieties in the condensed phase that leads to a dispersion of the vibrational energy levels associated with the vibration (this last effect is more noticeable in liquids and in amorphous solids, where the non-equivalence of the hydrogen bonds is more pronounced, but it is still relevant in crystals).

In practical terms, the most important consequence of intermolecular interactions for the vibrational spectra is that the differences in the spectra obtained in condensed phase relative to that of the isolated molecule (or gas phase spectra) allow to extract information on the type and strength of the intermolecular interactions. They also allow to extract information about the symmetry of the crystal, in particular when Raman spectroscopy of single crystals is used, taking advantage from the polarization characteristics of the incident and scattered light. These observable effects of intermolecular interactions on the vibrational spectra makes vibrational spectroscopy a powerful technique to study the structure of crystals. In some cases, the vibrational spectroscopic techniques (IR or Raman) are even more sensitive to structural effects than the X-ray diffraction technique, in particular when we are considering hydrogen bonding interactions, since hydrogen atoms do not efficiently diffract X-rays. For this reason, infrared and Raman spectroscopies are particularly useful for polymorphs distinction, even in the absence of X-ray structural information. Being also much more economical approaches in terms of time required for undertaking the experiments (compared to X-ray diffraction), Raman and infrared spectroscopies can be used very efficiently as techniques for preliminary polymorphs' screening, and in the present study, these techniques were used systematically for such task.

It shall be noticed that the analysis of a vibrational spectrum is generally convoluted by other factors than intermolecular interactions. For example, the presence of different conformers of a molecule in the sample leads to the appearance of bands due to the different conformers (different conformers possess different intramolecular potentials), while different isotopes existing in significant percentages in nature also give rise to band splitting (a good example occurs with chlorine which has

two abundant isomers, ^{35}Cl and ^{37}Cl). However, the main factor complicating the analysis of vibrational spectra is anharmonicity, either mechanical or electrical.

Mechanical anharmonicity invalidates the harmonic oscillator mechanic approach, and it is frequently important, particularly in vibrations involving hydrogen atoms and low-frequency torsional modes. Electrical anharmonicity determines the possibility of observation of transitions between vibrational levels that are not consecutive, i.e., transitions violating the selection rule which obliges the change in the vibrational quantum number to be equal to ± 1 that applies when electric anharmonicity is neglected. In practice, electrical and mechanical anharmonicity modify the selection rules and allow the experimental observation of overtones and combination tones. A remarkable evidence of the mechanical anharmonicity is the unequal spacing (in frequency) of the transitions of the same oscillator (Q). For example, for a stretching-type anharmonic oscillator coordinate, the spacing between consecutive vibrational levels (e.g. v and $v+1$) decreases as the quantum number (v) increases.

The mechanical anharmonicity for the typical case of a stretching coordinate can be considered if a Morse-type function is used to describe the vibrational potential energy of an oscillator:

$$V = D_e \{1 - e^{-a(R-R_e)}\}^2 \quad (2.15)$$

where D_e is the depth of the potential minimum, which roughly represents the bond dissociation energy (if the zero-point energy contribution is ignored), and $a = \left(\frac{\mu}{2D_e}\right)^{1/2} \omega$

In this case, the allowed energy levels are:

$$E(v) = \left(v + \frac{1}{2}\right) \hbar \sqrt{\frac{k}{\mu}} - \frac{\left(v + \frac{1}{2}\right)^2 \hbar \sqrt{\frac{k}{\mu}}}{4D_e} \quad (2.16)$$

Where k , which is the force constant is given in terms of the Morse potential's parameters, is given by $k = 2 D_e a^2$

Note that the Morse potential near the minimum of the potential energy well resembles a parabola (like in the harmonic approximation), whilst far from the minimum, unlike a parabola, the Morse function allows for dissociation (Figure 2). It can be seen that, according to Eq. 2.16, the anharmonicity term subtracts from the first term, leading to a decrease in the separation of the energies of consecutive vibrational levels at higher quantum numbers and to its convergence in the limit to the dissociation energy, as mentioned above.⁹

The mid-infrared (mid-IR) is the electromagnetic spectrum region with energy of the same order of magnitude as the fundamental vibrational transitions of the molecular systems. Therefore, mid-IR light can induce excitation of these vibrations, promoting a molecular system to a state of higher vibrational energy. As it has been stated, the IR selection rule implies that only absorptions

corresponding to vibrational motions that result in a change of the dipole moment of the molecule are infrared active, as they generate an oscillating dipole that is able to interact with the oscillating electric field of the incident radiation, when the resonance condition is verified (equal frequency of the molecular oscillator and of the external electric field).

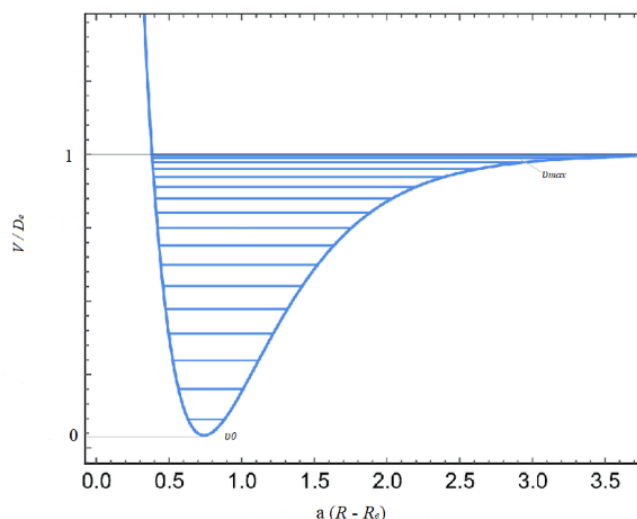


Figure 2 – Morse potential energy curve, which reproduces the general shape of a molecular potential energy. The vibrational fundamental energy state (v_0) and the vibrational highest energy level before the bond dissociation (v_{\max}) are stressed in the figure.

In infrared absorption spectroscopy, an infrared light-beam is focused on the molecular sample and collected after the light-matter interaction. Most of the times, the spectra are obtained in transmission mode, meaning that the IR beam must pass through the sample, though spectra can also be obtained in reflection mode. After the interaction with the sample, the IR light is converted into a spectrum, where the bands corresponding to the absorbed energies are related with the molecular vibrations that are able to interact with the excitation light.^{10,11}

The ratio between the incident light intensity, I_0 , the transmitted light intensity, I (in a transmission IR spectroscopy setup) defines the absorbance, A , of the sample at a given frequency, and is equal to the product of the absorption cross section by the number of absorbing entities, which for a molecule in solution can be stated in terms of the sample concentration, c , and the thickness of the sample, l , according to the Beer-Lambert equation:

$$A = \frac{I_0}{I} = \epsilon cl \quad (2.17)$$

The infrared absorption, in terms of quantum mechanics, is an electric operator mediated transition, where μ represents the variation in the dipole moment with respect to a change in the vibrational displacement, Q , which must be greater than zero to be effective, and thus, IR active as established in the selection rule:

$$\left(\frac{\partial\mu}{\partial Q}\right)_0 \neq 0 \quad (2.18)$$

For an isotropic sample, the measured infrared absorption, namely the integrated band area I , of a given normal mode Q , is directly proportional to the square of the change in the dipole moment during the respective vibrational motion:

$$I \propto \left(\frac{\partial\mu_x}{\partial Q}\right)_0^2 + \left(\frac{\partial\mu_y}{\partial Q}\right)_0^2 + \left(\frac{\partial\mu_z}{\partial Q}\right)_0^2 \quad (2.19)$$

It is important to notice that the referred change of the dipole moment during a vibration might not be enough for a vibration to be clearly observed in an infrared spectrum. The intensity of the IR absorption must be enough to be detected and differentiated from the instrumental noise. Additionally, there are several factors that can contribute to make the analysis of an infrared spectrum more complex. Examples of these factors are the appearance of overtones, combination tones and Fermi resonance bands. The overtone frequencies are multiples of the fundamental transition ($\nu_0 \rightarrow \nu_1$) frequency, which appear at slightly inferior integer multiple frequencies regarding the fundamental transition, due to the anharmonic nature of the vibrations (as explained above), and combination tones are vibrations involving changes in the vibrational quantum number associated with different vibrational coordinates. On the other hand, the Fermi resonances represent new transitions resulting from the mixing of a fundamental and an overtone or combination tone that have to be nearly degenerate and belong to the same symmetry species. From such mixing a characteristic Fermi resonance doublet band develops.¹²

The Fourier transform infrared spectroscopy (FTIR) experiments performed in this Thesis were acquired in two different instruments, with different sampling modes. The matrix isolation spectra, presented in Section 3.1, were obtained using a Thermo Scientific Nicolet iS50 FTIR spectrometer, equipped with an MCT/A detector and a KBr beam splitter, with 0.5 cm^{-1} spectral resolution (Figure 3). The condensed phase FTIR spectra presented in this Thesis were collected in the attenuated total reflectance (ATR) mode, on a Thermo Scientific Nicolet iS5 FTIR system, equipped with an iD7 ATR accessory, with an angle of incidence of 45° , on a diamond crystal (Figure 4). Further details of the experiments are provided in the corresponding sections of the Thesis.



Figure 3 – Thermo Scientific Nicolet iS50 FTIR spectrometer equipped with an MCT/A detector and a KBr beam splitter, mounted together with the ARS Cryogenics closed-cycle helium refrigeration system cryostat used in Section 3.1.



Figure 4 – Thermo Scientific Nicolet iS5 FTIR system, equipped with an iD7 ATR accessory.

In the case of the Raman spectra, as stated above, the spectral features are the result of the interaction between the induced transition dipole moment with the oscillating electrical field of the excitation radiation. The induced transition dipole moment is dependent on the molecular polarizability, $\bar{\alpha}$.

The classical picture of the interaction between an oscillating electromagnetic field and a molecular system is generally described as the disturbance of the electronic charge distribution in a molecular system by a primary incident light, which causes a dipole moment even for the case of a non-

polar molecular system.¹³ Then, the sum of the induced dipole moment acts as a microscopic polarization that represents the source for a secondary electric field irradiated by the molecular system, which represent the scattered light. The classical description for the induced dipole moment ($\boldsymbol{\mu}'$), is given by:

$$\boldsymbol{\mu}' = \bar{\boldsymbol{\alpha}} \mathbf{E}' \quad (2.20)$$

where $\boldsymbol{\mu}'$ represents the molecule dipole induced by the external electric field (\mathbf{E}') that is characterized by the respective amplitude vector (\mathbf{E}'_0) and the respective oscillation frequency (ω_0), as given by:

$$\mathbf{E}' = \mathbf{E}'_0 \cos(\omega_0 t) \quad (2.21)$$

In the induced dipole moment classical formula, the molecular polarizability tensor ($\bar{\boldsymbol{\alpha}}$) act as the proportionality factor between $\boldsymbol{\mu}'$ and the external field. $\bar{\boldsymbol{\alpha}}$ is physically related to the extension of which the incident field is able to disturb the electron density of the molecular system from the equilibrium configuration in the absence of the external field. Nonetheless, the polarizability of an electronic system is not a static quantity. Within the electrical harmonic approximation:

$$\boldsymbol{\mu}'(t) = \bar{\boldsymbol{\alpha}}_0 \mathbf{E}'_0 \cos(\omega_0 t) + \frac{1}{2} \left(\frac{\partial \bar{\boldsymbol{\alpha}}}{\partial Q} \right)_0 \cdot Q_0 \mathbf{E}'_0 \cos[(\omega_0 - \omega_Q)t] + \frac{1}{2} \left(\frac{\partial \bar{\boldsymbol{\alpha}}}{\partial Q} \right)_0 \cdot Q_0 \mathbf{E}'_0 \cos[(\omega_0 + \omega_Q)t] \quad (2.22)$$

where Q represents the individual normal modes.

Eq. 2.22 constitutes the conceptual core of Raman scattering, and includes also the more common phenomenon known as Rayleigh scattering. Indeed, the first of the three terms, oscillates at the same frequency ($\omega_0 t$) as the incident light and, therefore, the scattered light will have the same frequency as the incident, resulting in an elastic phenomenon, which does not contain information on the vibrational modes of the molecular system. The second term in the equation above, oscillates with the difference between the excitation light and the vibration frequencies. Thus, the emitted light is red-shifted regarding the incident light, which means that there is an inelastic scattering containing information about the vibrations of the molecular system due to the dependence of the term on ω_Q . This is usually known as Stokes scattering, and it represents the information commonly presented in a Raman spectrum. In the final term, the time dependence is given by the sum $\omega_0 + \omega_Q$, which represents a blue-shifted radiation with respect to the incident light, known as anti-Stokes scattering. As in the case of the Stokes scattering, this is also an inelastic process that is informative regarding the molecular vibrations. It is different from the Stokes scattering because the emitted light is more energetic than the incident light. Due to the Boltzmann factor, which describes the relative populations of the vibrational states, the anti-Stokes scattering, at room temperature, is much less intense than the Stokes scattering. The Rayleigh scattering phenomenon, together with the Raman Stokes and anti-Stokes scattering processes are schematic illustrated in Figure 5, which also depicts an infrared absorption process.

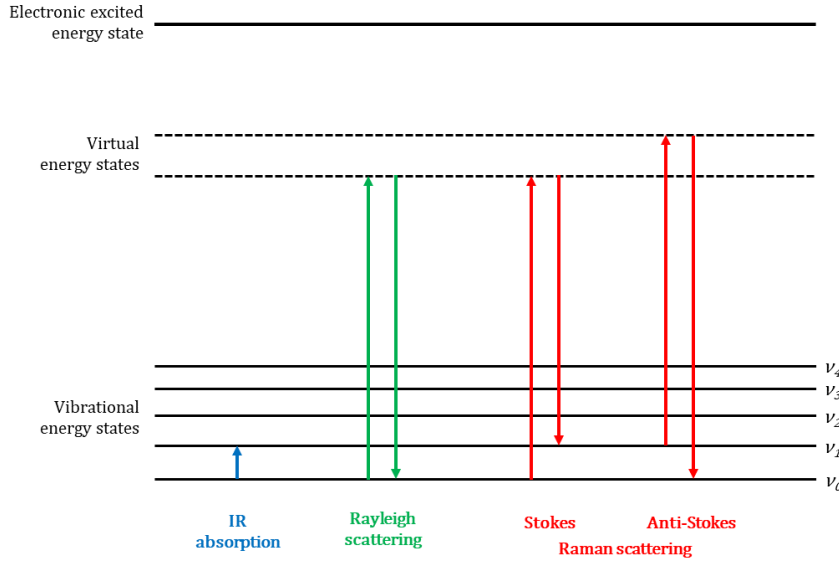


Figure 5 – Schematic illustration of the IR absorption (in blue), the Rayleigh scattering (in green) and the Stokes and anti-Stokes Raman scattering (in red) phenomena.

The intensities of the Raman Stokes scattering spectral features (generally known as Raman bands) are related with the oscillation induced dipole moment that gives rise to the Stokes radiation, as described by:

$$\boldsymbol{\mu}'^{Stokes}(t) \propto \left(\frac{\partial \bar{\alpha}}{\partial Q}\right)_0 \cdot Q_0 \mathbf{E}'_0 \cos[(\omega_0 - \omega_Q)t] \quad (2.23)$$

Every oscillating induced dipole acts as a Hertzian dipole emitting the referred secondary light, whose total power is given by:

$$P = \frac{|\boldsymbol{\mu}'|^2}{6\pi \cdot \epsilon_0 \cdot c^3} = \frac{Q_0^2}{12\pi \cdot \epsilon_0 \cdot c^3} \cdot \left(\frac{\partial \bar{\alpha}}{\partial Q}\right)_0^2 \cdot (\omega_0 - \omega_Q)^4 \mathbf{E}'_0^2 \quad (2.24)$$

where a temporal average over the oscillating part is made ($|\boldsymbol{\mu}'|^2 \propto \cos^2(\omega t)$). The Raman scattered intensity is proportional to the overall power emitted by the induced dipole moment, as given by:

$$I_{Stokes} \propto \left(\frac{\partial \bar{\alpha}}{\partial Q}\right)_0^2 \cdot (\omega_0 - \omega_Q)^4 \mathbf{E}'_0^2 \quad (2.25)$$

Considering the k normal mode, the quantity $\bar{\alpha}'_k = \left(\frac{\partial \bar{\alpha}}{\partial Q_k}\right)_0$ is called “Raman tensor of Q_k ”. The shape of $\bar{\alpha}'_k$ is determined by the symmetry species to which it belongs; for instance, all the normal modes belonging to symmetry species different from the totally symmetric ones have null trace. As shown in Section 2.3, the Raman intensities of macroscopically oriented samples (e.g., single-crystals) depend on the scattering geometry and on the polarization of the incident and scattered beam. Indeed,

the experimental set-up determines the component(s) of $\bar{\alpha}'_k$ involved in the Raman scattering at $(\omega_0 - \omega_{Q_k})$.

The Raman experiments presented in Chapters 3 and 4 were collected in a BWTEK i-Raman Pro system, equipped with a CCD detector, a BAC151C microscope, and a 785 nm solid-state laser (Figure 6) or in a micro-Raman Horiba LabRam HR Evolution instrument, equipped with a CCD detector and 532 nm solid-state laser, a 633 HeNe laser and a 785 nm solid-state laser (Figure 7). As for the FTIR spectra, the specific conditions of recording of the Raman spectra (e.g., acquisition time, number of accumulations, laser spot area, laser power, optical objective used, wavenumber range, spectra resolution) used in the different experiments are provided in the correspondent sections of Chapters 3 and 4.

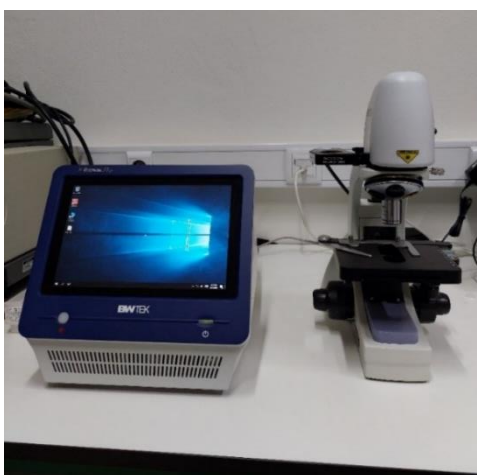


Figure 6 – BWTEK i-Raman Pro system.



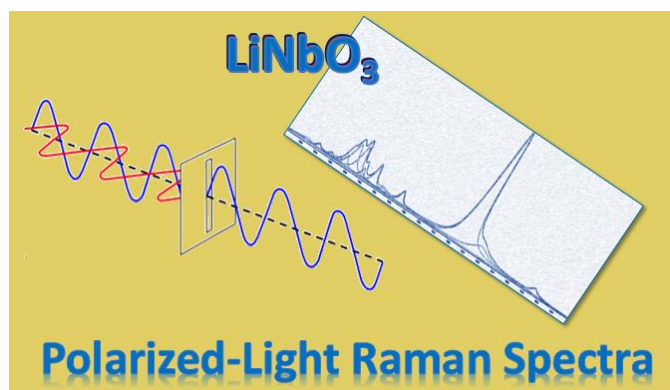
Figure 7 – Micro-Raman Horiba LabRam HR Evolution instrument.

References

- 1 C. N. Banwell, *Fundamentals of molecular spectroscopy*, McGraw-Hill London, 1972.
- 2 P. Atkins and R. Friedman, *Molecular Electronic Transitions*, Oxford University Press, 2011.
- 3 E. B. Wilson, Note on a Form of the Secular Equation for Molecular Vibrations, *J. Chem. Phys.*, 1947, **15**, 736-738.
- 4 J. C. Decius, A Tabulation of General Formulas for Inverse Kinetic Energy Matrix Elements in Acyclic Molecules, *J. Chem. Phys.*, 1948, **16**, 1025-1034.
- 5 J. C. Decius, Complete Sets and Redundancies among Small Vibrational Coordinates, *J. Chem. Phys.*, 1949, **17**, 1315-1318.
- 6 E. B. Wilson, J. C. Decius and P. C. Cross, *Molecular vibrations*, McGraw-Hill, 1955.
- 7 B. Schrader and D. Bougeard, *Infrared and Raman spectroscopy: methods and applications*, VCH, 1995.
- 8 T. Dieing, O. Hollricher and J. Toporski, Eds., *Confocal Raman Microscopy*, Springer, 2011.
- 9 P. W. Atkins, *Physical Chemistry*, Oxford University Press, 1992.
- 10 B. H. Stuart, *Infrared Spectroscopy: Fundamentals and Applications*, Wiley, 2004.
- 11 P. J. Larkin, *Infrared and Raman Spectroscopy: Principles and Spectral Interpretation*, Elsevier, 2011.
- 12 R. Fausto, *Espectroscopia Vibracional*, in *Química Síntese e Estrutura* (ed. M. M. Pereira and H. D. Burrows), Escolar Editora, 2006, 109–168.
- 13 B. Dietzek, D. Cialla, M. Schmitt and J. Popp, Introduction to the Fundamentals of Raman Spectroscopy, *Springer Ser. Opt. Sci.*, 2010, **158**, 21–42.

2.3. Computational vs. Experimental Polarized Raman Spectra

The article that constitutes this section is entitled *The Correlation Between Experimental Polarized Raman Spectra and Their DFT Prediction in the LCAO Framework: The R3c LiNbO₃ Crystal as a Test Case* and was published in the *Journal of Raman Spectroscopy* (John Wiley & Sons Ltd; Vol 52, pp. 995-1010) on 11th March 2021. On the day of the submission of this Thesis, according to the Google Scholar, the article has been cited three times by other peer-reviewed scientific publications. It has received 35 reads in Research Gate.



Supporting Information:

<https://analyticalsciencejournals.onlinelibrary.wiley.com/action/downloadSupplement?doi=10.1002%2Fjrs.6091&file=jrs6091-sup-0001-Figure+S1.pdf>

Authors: Bernardo A. Nogueira, Alberto Milani, Chiara Castiglioni and Rui Fausto.

Corresponding author: Bernardo A. Nogueira.

Author contributions: Bernardo A. Nogueira conducted the literature research, performed the Raman experiments, part of the periodic calculations and wrote the first draft of the manuscript. Alberto Milani performed the periodic calculations on the crystal. Chiara Castiglioni supervised the interpretation of the periodic calculations results. Rui Fausto wrote the final draft version of the manuscript. All the authors performed the analysis of the data and work on the final version of the paper.

Synopsis:

This work has been conducted with the main goal to correlate the information obtained from the fully periodic DFT vibrational predictions (normal mode frequencies and intensities obtained from the proper elements of the calculated Raman tensor) with the experimental results obtained by polarized Raman spectroscopy on a test model system (R_{3c} lithium niobate crystals).

The correlation between experimental polarized Raman spectra and their DFT prediction in the LCAO framework: the *R3c* LiNbO₃ crystal as a test case

Bernardo A. Nogueira,^{1,2,*} Alberto Milani,² Chiara Castiglioni² and Rui Fausto¹

¹ *University of Coimbra, CQC, Department of Chemistry, P-3004-535 Coimbra, Portugal.*

² *CMIC, Dipartimento di Chimica, Materiali e Ingegneria Chimica "G. Natta", Politecnico di Milano, Italy.*

Abstract

In this study, the polarized Raman spectra of the *R3c* LiNbO₃ crystal is used as a benchmark test for DFT full periodic boundary conditions LCAO calculation of the Raman tensors, according to the implementation in the CRYSTAL software. The theoretical approach used proved to provide excellent results regarding wavenumbers and relative intensities predictions for the transverse optical modes of both A₁ and E symmetry, considerably improving over previously reported data based on the plane-waves approach. Overall, the present investigation demonstrates that the LCAO approach, as implemented in the CRYSTAL software, gives excellent results regarding the calculation of Raman tensors and polarized Raman spectra. The possibility to put in correspondence the individual Raman tensors components and bands intensities in the different back-scattering experimental configurations revealed that the computed Raman tensors are very accurate, not only considering their average values (tensors invariant in the combination suitable for the description of Raman scattering of isotropic materials), but also when the tensors individual components are considered. Based on the present results, a reassignment of the E (TO) modes of the *R3c* LiNbO₃ crystal is proposed, in particular for the 2 E and 9 E modes, which have been a matter of discussion in the recent years.

Keywords: *R3c* LiNbO₃ crystal, Fully periodic CRYSTAL LCAO calculations, Polarized Raman spectra

* Corresponding author e-mail: ban@qui.uc.pt

1. Introduction

Lithium niobate (LiNbO_3) is a synthetic dielectric material,¹ belonging to the ferroelectric oxides class,² which is regularly used in various applications in nonlinear electro-optics²⁻⁷ and acoustics,^{1,8} because of its large elastic-optic, electro-optic, nonlinear optical and piezoelectric coefficients.^{1,8} At room temperature, LiNbO_3 exists as an uniaxial crystal that belongs to the trigonal system (space group $R3c$ and symmetry point group $3m$), with two formula units per cell. Below the ferroelectric Curie temperature (*ca.* 1210 °C) the crystal structure of LiNbO_3 comprises planar sheets of oxygen atoms in a distorted hexagonal close-packed configuration, the octahedral interstices in the structure being filled by lithium or niobium atoms (one third each) or being vacant (one third), in a continuous intercalated sequence.¹ The compound has been extensively studied due to the availability of large macroscopic single crystals suitable for investigation. This feature is particularly useful for polarized-light Raman experiments, and several studies on this subject have been reported.^{2,5-8} Nevertheless, as discussed below in detail, there is still no consensus regarding assignment of some Raman bands to specific vibrations, and the analysis of the band intensities of the polarized-light Raman spectra of LiNbO_3 obtained for different geometric arrangements at the light of contemporary LCAO-based electronic structure calculations has not yet been conveyed.

In the present article we present a comprehensive analysis of the Raman band intensities of the room temperature polarized-light Raman spectra of LiNbO_3 based on the detailed comparison of the experimental data with those resulting from start-of-the-art full periodic electronic structure calculations. In contrast to the standard theoretical predictions mimicking the non-polarized spectrum of an isotropic sample, where the Raman intensities are determined by averages of the elements of the polarizability tensor, we exploit here complementary experiments that probe the individual tensor components one at a time. This allows evaluating the reliability of present-day Density Functional Theory (DFT) simulations in predicting these components, as well as expanding our understanding of the experimental Raman data of crystalline LiNbO_3 . The analysis presented here considers the assignment of the transverse optical (TO) Raman active phonons, and allowed to address still open questions, such as the assignment of the fundamental transitions associated to TO phonons 2 E and 9 E.^{2,6-10} Full periodic boundary conditions electronic structure DFT calculations were used, following the LCAO approach as implemented in the CRYSTAL code,^{11,12} in order to reproduce the polarized-light Raman pattern associated with the excitation of the TO modes in the limit of static exciting field. As shown below, the obtained results highlight the suitability of the theoretical approach used for the investigation of the structure and phonons properties of the LiNbO_3 crystal, as a benchmark test for the application of the method to crystalline materials.

2. Material and methods

Computational approaches

The full optimization of the $R3c$ crystal structure of LiNbO_3 and the calculation of its Raman spectra have been carried out with the CRYSTAL software package, in the DFT framework,^{11,12} using the B3LYP functional¹³ and the pob-TZVP basis set.^{14–16} For all calculations, the atomic positions as well as the lattice parameters were optimized. The input structure for the calculations was that experimentally determined by Abrahams *et al.*¹⁷ The vibrational frequencies calculations were performed for the optimized geometries using the same method and basis set.

The CRYSTAL code has been used in the past to simulate the properties of other systems similar to LiNbO_3 ,¹⁸ and presents relevant advantages for the simulations of polarized Raman spectra. Indeed, by using a Gaussian basis set in the LCAO description of crystal orbitals, hybrid exchange-correlation functionals can be managed much easier than in plane-waves codes, thus allowing a more accurate prediction of vibrational spectra. Vibrational frequencies were computed by the diagonalization of the dynamical matrix at the Γ point of the first Brillouin zone (BZ) and the Cartesian force constants (*i.e.*, the elements of the Hessian of the potential energy, expressed in mass-weighted atomic Cartesian coordinates) were computed by numerical evaluation of the first derivatives of the analytical atomic gradients.

In CRYSTAL, Raman and infrared (IR) intensities can be predicted accurately through the Coupled Perturbed Kohn Sham (CPKS) method.^{11,12} Based on the different components of the Raman tensor, computed as second derivatives of the energy with respect to the electric field, intensities can be calculated and, then, used to predict polarized Raman spectra. The Raman activity of the k normal mode, A_{ij}^k , corresponding to incident and scattered beams with i and j polarization direction respectively, is computed as $A_{ij}^k = (\alpha_{ij}^k)^2$, where α_{ij}^k is the i,j component of the Raman tensor associated to mode k . In the limit of static exciting field ($\lambda_{\text{exc}} \rightarrow \infty$), Raman intensities I_{ij}^k can then be computed as $I_{ij}^k = \frac{A_{ij}^k}{\omega_k}$, where ω_k is the vibrational frequency of the normal mode k .

The correspondence between the different components of the CRYSTAL calculated polarized Raman spectra and the experimental spectra obtained using the back-scattering mode in a Horiba LabRam HR Evolution Raman spectrometer, was established as described below.

Experimental spectra collection

The LiNbO_3 crystal samples (X -cut, Y -cut and Z -cut; $10 \times 10 \times 0.5$ mm) were bought from PI-KEM, Ltd. X -cut, Y -cut and Z -cut mean that the crystal face cut is perpendicular to the x , y and z direction of the crystal, respectively, with z being the polar axis, *i.e.*, the direction of the crystal dipole.

The single crystal Raman spectra were obtained in the 50–1000 cm^{-1} Raman shift range, with accuracy better than 0.5 cm^{-1} , using a micro-Raman Horiba LabRam HR Evolution system. The excitation was provided by a solid-state laser at $\lambda = 532 \text{ nm}$ (horizontally polarized; laser power $\sim 50 \text{ mW}$ at the sample). In order to collect the polarized spectra, a half-wave polarization rotator (Horiba-Jobin-Yvon) was used to change the polarization of the incident light by 90° , and a CorePol P-500-1000 polarizer (Horiba-Jobin-Yvon) was used to select the component of the scattered light to collect. The collection time varied between 2 and 20 seconds, with 100 accumulations being averaged to produce the final spectra. A $50\times$ objective lens was used, the laser spot diameter being $1 \mu\text{m}$ at the sample. The wavenumber calibration was performed using the characteristic Si wafer band at 520.5 cm^{-1} .

3. General concepts and an overview of previous studies on the Raman spectrum of LiNbO_3

The classical theory of Raman scattering is based on the concept that the light scattered by a molecule is generated by oscillating electric dipoles induced by the electric field of the incident (exciting) light beam.¹⁹ The relation between the induced dipole moment vector, $\boldsymbol{\mu}'$, and the external electric field vector, \boldsymbol{E} , can be written in a simplified way (ignoring non-linear terms in the expansion)¹⁹ as:

$$\boldsymbol{\mu}' = \bar{\boldsymbol{\alpha}}\boldsymbol{E} \quad (2.26)$$

where $\bar{\boldsymbol{\alpha}}$ is the molecular polarizability tensor.

In the double harmonic approximation,¹⁹ the dipole component responsible for the k -th Raman line can be expressed as:

$$\boldsymbol{\mu}'_k = \bar{\boldsymbol{\alpha}}'_k \boldsymbol{E} Q_k \quad (2.27)$$

namely:

$$\begin{bmatrix} \mu_x \\ \mu_y \\ \mu_z \end{bmatrix}_k = \begin{bmatrix} \alpha'_{xx} & \alpha'_{xy} & \alpha'_{xz} \\ \alpha'_{yx} & \alpha'_{yy} & \alpha'_{yz} \\ \alpha'_{zx} & \alpha'_{zy} & \alpha'_{zz} \end{bmatrix}_k \begin{bmatrix} E_x \\ E_y \\ E_z \end{bmatrix} Q_k \quad (2.28)$$

where the coefficients α'_{ij} correspond to the components of the Raman polarizability tensor $\bar{\boldsymbol{\alpha}}'_k$, which contains the first derivatives of $\bar{\boldsymbol{\alpha}}$ with respect to a Raman active normal mode Q_k evaluated at the equilibrium geometry of the molecule. In the case of non-resonant Raman scattering, $\bar{\boldsymbol{\alpha}}'$ can be described by a real, symmetric matrix where $\alpha'_{ij} = \alpha'_{ji}$ and, therefore, it has, at maximum, six independent components.

In the case of a crystal, the Raman polarizability tensor is commonly referred to the matter belonging to the unit cell.

The contribution of the Raman polarizability tensor to the Raman scattering intensity of the k -th normal mode is determined by $|\mathbf{e}_i \bar{\alpha}'_k \mathbf{e}_s|^2$ where \mathbf{e}_i and \mathbf{e}_s represent, respectively, the polarizations of the incident and scattered photons.²⁰ The shape of the Raman tensor $\bar{\alpha}'_k$ depends on the symmetry of the k -th vibrational mode according to the point group of the molecule or of the crystal, so that the knowledge of the symmetry species to which a given vibrational normal mode belongs allows determining null tensor components and the possible existence of components with identical (or opposite) values.

In the case of a macroscopically oriented sample, $|\mathbf{e}_i \bar{\alpha}'_k \mathbf{e}_s|^2$ might be equal to zero for a given specific combination of photon polarizations: in this case, the vibrational mode k is not Raman active for that particular scattering configuration. Hence, by analyzing the shape of the Raman tensor $\bar{\alpha}'_k$ it is possible to obtain Raman selection rules for the vibrational modes in different scattering geometries.²¹ On the other hand, by careful controlling the polarization of both the incident and scattered photons, the selection rules experimentally determined allow identifying the symmetry of the vibrational modes, thus facilitating vibrational assignments.²¹

It is worth mentioning that also for isotropic samples (*e.g.*, molecules in solution) Raman measurements with polarized light allow to distinguish between totally symmetric and non-totally symmetric modes. Playing with two different experimental set-ups, where \mathbf{e}_i and \mathbf{e}_s are parallel (parallel-parallel polarization) or orthogonal (parallel-perpendicular polarization), Raman dichroic ratios can be obtained, which immediately sort polarized totally symmetric transitions from unpolarized ones.

When samples showing macroscopic orientation of the matter are investigated, the orientation of the sample in the laboratory frame, together with the polarization directions selected for the incident and scattered light beams, makes it possible to determine - from different complementary Raman experiments - the individual components of the Raman tensor. In particular, this can be done in the case of macroscopic single crystals. However, the determination of these data from experimental Raman intensity measurements is a cumbersome task: from *relative* bands intensities of judiciously chosen polarized Raman spectra one can extract information only on the *relative* values of the relevant individual polarizability components for the different Raman active modes. On the other hand, thanks to the current accuracy of the state-of-the-art computational approaches to predict Raman intensities, this problem can be overcome by exploiting the synergic use of theory and experiments. In turn, the evaluation of the quality of the computed Raman spectral patterns mimicking experiments performed with polarized light allows to assess the performance of the theory adopted in describing individual elements of the Raman tensors, thus providing a sound validation of the theoretical Raman activities obtained by calculations.

The $\Gamma = 0$ phonons of the room temperature phase ($R3c$) crystal of LiNbO_3 are classified in the irreducible representation as $4A_1$, $5A_2$ and $9E$, where the A_1 (polarized along Z) and the E (polarized in

the XY plane) modes are Raman active, whereas the A_2 modes are silent.^{2,6} By choosing the reference Cartesian XYZ system in such a way that Z is aligned along the polar axis of the LiNbO_3 crystal and X is aligned along the crystallographic axis a , the Raman polarizability tensors of the E and A_1 modes show the following general form:²²

$$A_1(Z) = \begin{pmatrix} a & 0 & 0 \\ 0 & a & 0 \\ 0 & 0 & b \end{pmatrix}, \quad E(X) = \begin{pmatrix} c & 0 & d \\ 0 & -c & 0 \\ d & 0 & 0 \end{pmatrix}, \quad E(Y) = \begin{pmatrix} 0 & -c & 0 \\ -c & 0 & d \\ 0 & d & 0 \end{pmatrix} \quad (2.29)$$

where a , b , c , $-c$ and d represent non-null Raman polarizability tensors component values.

Each phonon at $\Gamma = 0$ gives rise to a pair of observable Raman transitions at different frequencies, corresponding to longitudinal optical (LO) and transverse optical (TO) phonons.^{7,20} As discussed by Parlinski and Li,¹⁰ calculation of the forces at $\Gamma = 0$ according to the direct method allows to predict the wavenumbers corresponding to TO phonons, while a reliable calculation of LO phonon frequencies requires that explicit consideration of the interactions with the macroscopic electric field generated by lattice polar vibrations and are not accessible by direct method calculations.

Vibrational assignments for LiNbO_3 crystal have already been proposed in the literature, both experimentally and theoretically.^{2,6,8-10,23-27} Table 1 shows the experimentally measured Raman wavenumbers and the vibrational assignment of TO e LO phonons of LiNbO_3 according to the recent review by Fontana and Bourson.⁸ Note that the 2 E and 9 E modes (see Table 1 – in bold) have been assigned differently in the literature.^{2,6-10,23-27} As described below, the present study will add evidence for settling this point.

Table 1 – Experimental wavenumbers of the LiNbO_3 vibrational modes (A_1 and E symmetries) and their assignment, according to ref. 8. The assignments for the 2 E and 9 E modes (wavenumbers highlighted in bold) have been debated.

Vibrational mode	Wavenumber/ cm^{-1}		Assignment (motions)
	TO	LO	
1 A_1	254	272	$\text{Nb}_{(z)}$, $\text{O}_{(z)}$
2 A_1	275	332	$\text{Nb}_{(z)}$, $\text{Li}_{(z)}$
3 A_1	332	419	$\text{O}_{(x,y)}$
4 A_1	631	871	$\text{O}_{(x,y)}$
1 E	152	186	} $\text{Nb}_{(x,y)}$, $\text{O}_{(x,y)}$ } all atoms(all directions)
2 E	186	194	
3 E	236	238	
4 E	263	295	
5 E	322	366	
6 E	369	425	
7 E	432	456	
8 E	578	625	
9 E	738	880	

Fontana and Bourson⁸ reported also the expected modes that could be seen in polarized Raman spectra of an oriented single crystal of LiNbO₃, exploiting different experimental polarization set-ups, which are summarized for the back-scattering geometry in Table 2. In this table, the Porto notation is used to describe the geometry adopted in the polarized Raman experiments. According to this notation, a set of four symbols is used, $K_1(P_1, P_2)K_2$, where K_1 and K_2 are the directions of the incident and scattered waves (for the back-scattering collection mode, K_2 is equal to \bar{K}_1 , where the trace over the letter means opposite direction), while P_1 and P_2 denote the direction of the polarization of each wave.

Table 2 –Phonon modes expected to be visible in the different polarized Raman spectra of LiNbO₃, for back-scattering mode, and their respective experimental wavenumbers according to ref. 8.

Experimental configuration (Porto notation)	Expected visible modes	Wavenumber/ cm ⁻¹
$X(YY)\bar{X}$	A_1 (TO) + E (TO)	152, 186, 236, 254, 263, 275, 322, 332, 369, 432, 578, 631, 738
$X(YZ)\bar{X}$	E (TO)	152, 186, 236, 263, 322, 369, 432, 578, 738
$X(ZY)\bar{X}$	E (TO)	152, 186, 236, 263, 322, 369, 432, 578, 738
$X(ZZ)\bar{X}$	A_1 (TO)	254, 275, 332, 631
$Y(XX)\bar{Y}$	A_1 (TO) + E (LO)	186, 194, 238, 254, 275, 295, 332, 366, 425, 456, 625, 631, 880
$Y(XZ)\bar{Y}$	E (TO)	152, 186, 236, 263, 322, 369, 432, 578, 738
$Y(ZX)\bar{Y}$	E (TO)	152, 186, 236, 263, 322, 369, 432, 578, 738
$Y(ZZ)\bar{Y}$	A_1 (TO)	254, 275, 332, 631
$Z(YX)\bar{Z}$	E (TO)	152, 186, 236, 263, 322, 369, 432, 578, 738
$Z(XY)\bar{Z}$	E (TO)	152, 186, 236, 263, 322, 369, 432, 578, 738
$Z(XX)\bar{Z}$	A_1 (LO) + E (TO)	152, 186, 236, 263, 272, 322, 332, 369, 419, 432, 578, 738, 871
$Z(YY)\bar{Z}$	A_1 (LO) + E (TO)	152, 186, 236, 263, 272, 322, 332, 369, 419, 432, 578, 738, 871

In the theoretical work by Parlinski and Li,¹⁰ phonon dispersion curves for LiNbO₃ were obtained in the framework of DFT, according to the local-density approximation with ultrasoft pseudopotentials and a plane-wave basis set, and the LO and TO phonon wavenumbers for the Raman active transitions were reported. Using the same theoretical framework, Hermet *et al.*² predicted the polarized Raman spectra of LiNbO₃ (wavenumbers and intensities) by calculating the derivatives of the linear optical susceptibility with respect to atomic displacements. In turn, Caciuc *et al.*⁹ reported accurate TO Γ phonon wavenumbers from first-principles calculations using the full-potential linearized augmented plane-waves method within the frozen phonon approximation.

In the present work, the TO phonon wavenumbers and Raman activities have been calculated at $\Gamma = 0$, and a comparison between the experimental frequencies determined in this work and those reported by Fontana and Bourson⁸ will be presented in the next section. The theoretically obtained wavenumbers will be compared with the results reported by Caciuc *et al.*,⁹ and with the experimentally

obtained data. Finally, the intensity patterns (relative intensities of the bands) predicted for selected experimental polarization set-ups and its correlation with the experimental data will be discussed in detail.

4. Results and discussion

In the present study, the Raman spectra have been obtained using three different crystal orientations with respect to the laser beam direction, namely at incidence normal to the three cut surfaces of the crystal, identified by their normal vector as *X*-cut, *Y*-cut and *Z*-cut. For each crystal orientation, four different combinations of polarization of the incident and scattered radiation were selected, thus providing a total number of twelve experimental spectra. Figure 1 presents the geometric configurations determining the polarization of the laser beam relatively to the sample in the used instrument (Horiba LabRam HR evolution).

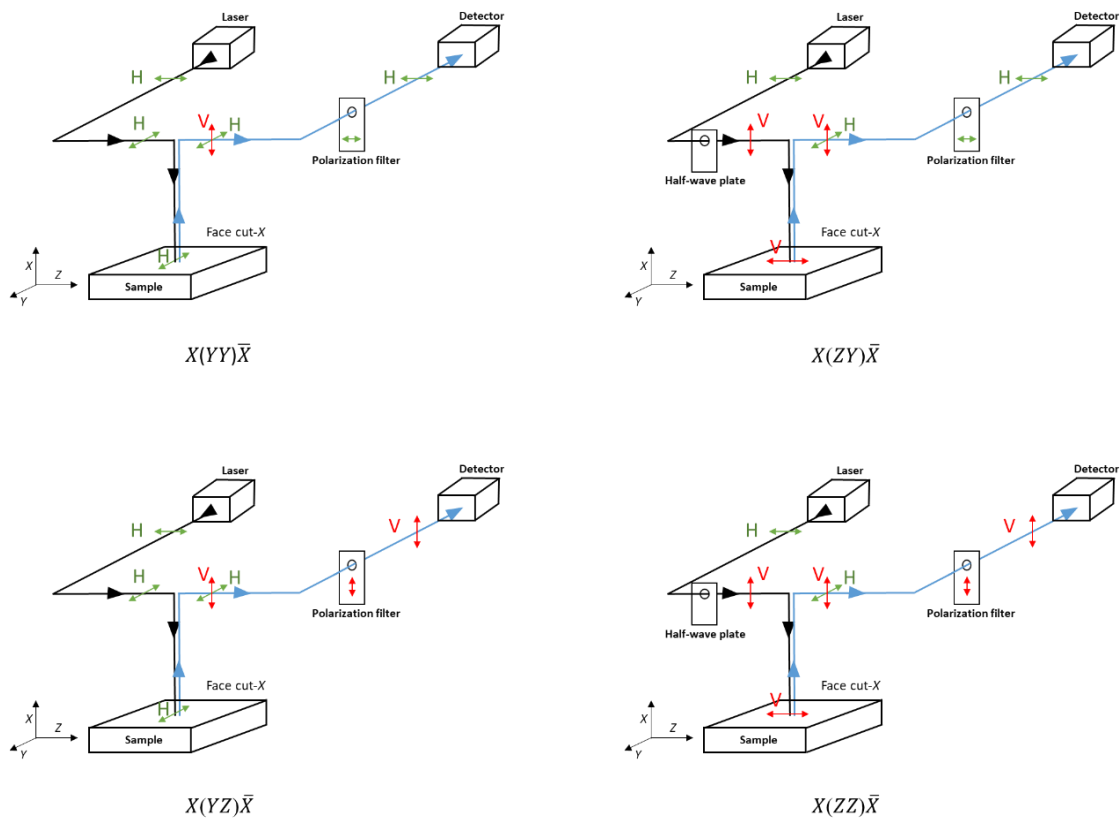


Figure 1 – Schematic representation of the geometric configurations determining the polarization of the laser beam relatively to the sample in the used instrument (Horiba LabRam HR evolution). The black and blue traces correspond to the incident and scattered beams, respectively. The double arrows represent the direction of the polarization of the beam, classified as horizontal (H) and vertical (V) in the reference frame of the laboratory. The depicted Cartesian vectors, *X*, *Y*, *Z*, refer to the crystal sample reference frame and vary for the different crystal cuts. The shown examples correspond to the four different configurations for the crystal cut-*X* (the corresponding Porto notations are also given).

Table 3 provides the equivalence of the used geometries to the experimental configurations according to Porto notation. As shown in the table, $X(Y\bar{Y})\bar{X}$, $X(YZ)\bar{X}$, $X(ZY)\bar{X}$ and $X(ZZ)\bar{X}$ correspond to the X -cut collection with the incident-scattered light polarizations horizontal-horizontal, horizontal-vertical, vertical-horizontal and vertical-vertical, respectively, while the Y -cut slide spectra collected with the incident-scattered polarizations horizontal-horizontal, horizontal-vertical, vertical-horizontal and vertical-vertical correspond to $Y(XX)\bar{Y}$, $Y(XZ)\bar{Y}$, $Y(ZX)\bar{Y}$ and $Y(ZZ)\bar{Y}$ Porto notations, respectively. In the Z -cut analysis, $Z(XY)\bar{Z}$ and $Z(YX)\bar{Z}$ correspond to horizontally-vertically and vertically-horizontally polarized waves and $Z(XX)\bar{Z}$ and $Z(YY)\bar{Z}$ to horizontally-horizontally and vertically-vertically polarized light experiments, respectively.

Table 3 –Correspondence between experimental configurations according to Porto notation and the used experimental set ups.

Porto Notation	Horiba LabRam HR Evolution experimental configurations		
	Crystal cut	Incident light polarization	Scattered light polarization
$X(Y\bar{Y})\bar{X}$	X-cut	horizontal	horizontal
$X(YZ)\bar{X}$		horizontal	vertical
$X(ZY)\bar{X}$		vertical	horizontal
$X(ZZ)\bar{X}$		vertical	vertical
$Y(XX)\bar{Y}$	Y-cut	horizontal	horizontal
$Y(XZ)\bar{Y}$		horizontal	vertical
$Y(ZX)\bar{Y}$		vertical	horizontal
$Y(ZZ)\bar{Y}$		vertical	vertical
$Z(XY)\bar{Z}$	Z-cut	horizontal	vertical
$Z(YX)\bar{Z}$		vertical	horizontal
$Z(XX)\bar{Z}$		horizontal	horizontal
$Z(YY)\bar{Z}$		vertical	vertical

The experimental spectra of the studied LiNbO_3 crystal, collected for all possible back-scattering configurations, are presented in Figure 2. Because of the crystal symmetry at Γ , in the absence of any external electric field the set of spectra corresponding to X - and Y -cuts should be superimposable. However, in presence of a macroscopic electric field the degeneracy of E modes is removed,^{7,10} giving rise to different spectra in correspondence to the $X(Y\bar{Y})\bar{X}$ set up ($A_1(\text{TO}) + E(\text{TO})$) and $Y(XX)\bar{Y}$ set up ($A_1(\text{TO}) + E(\text{LO})$). As expected, geometries related by simple exchange of X and Y indexes in the Porto notation give superimposable spectra in all the other cases, namely: all four spectra corresponding to X -cut and Y -cut spectra (ii) and (iv) in Figure 2 practically coincide; spectra (iii) in these two crystal cut orientations do also coincide; and the Z -cut set-up provides only two different spectra, corresponding to the pairs (i)/(iii) and (ii)/(iv). These results provide evidence that good control of the experimental set up (crystal orientation and light polarization) was achieved in the performed experiments.

Figure 3 shows the calculated LiNbO_3 spectrum constructed taking into account the whole Raman tensor (spectrum (v) in the figure, mimicking an isotropic distribution of LiNbO_3 crystals), and the spectra built using the individual components of the Raman tensor (spectra (i) to (iv) in the figure). As

already mentioned, according to the capabilities of the used theoretical approach in all the calculated spectra only the TO modes are considered.

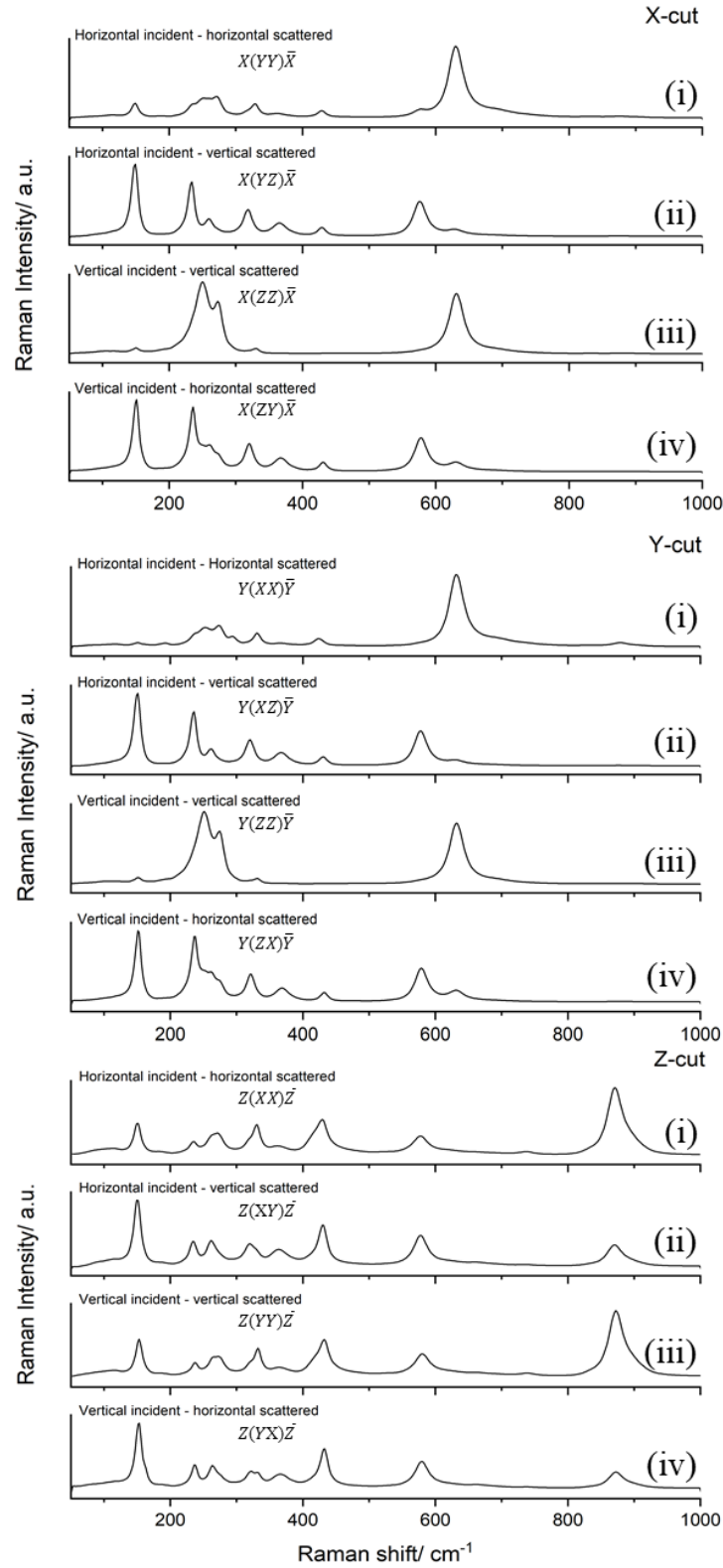


Figure 2 – Experimental polarized Raman spectra of LiNbO₃ crystal (X-cut: top; Y-cut: middle; Z-cut: bottom) collected for the different possible configurations in the back-scattering mode.

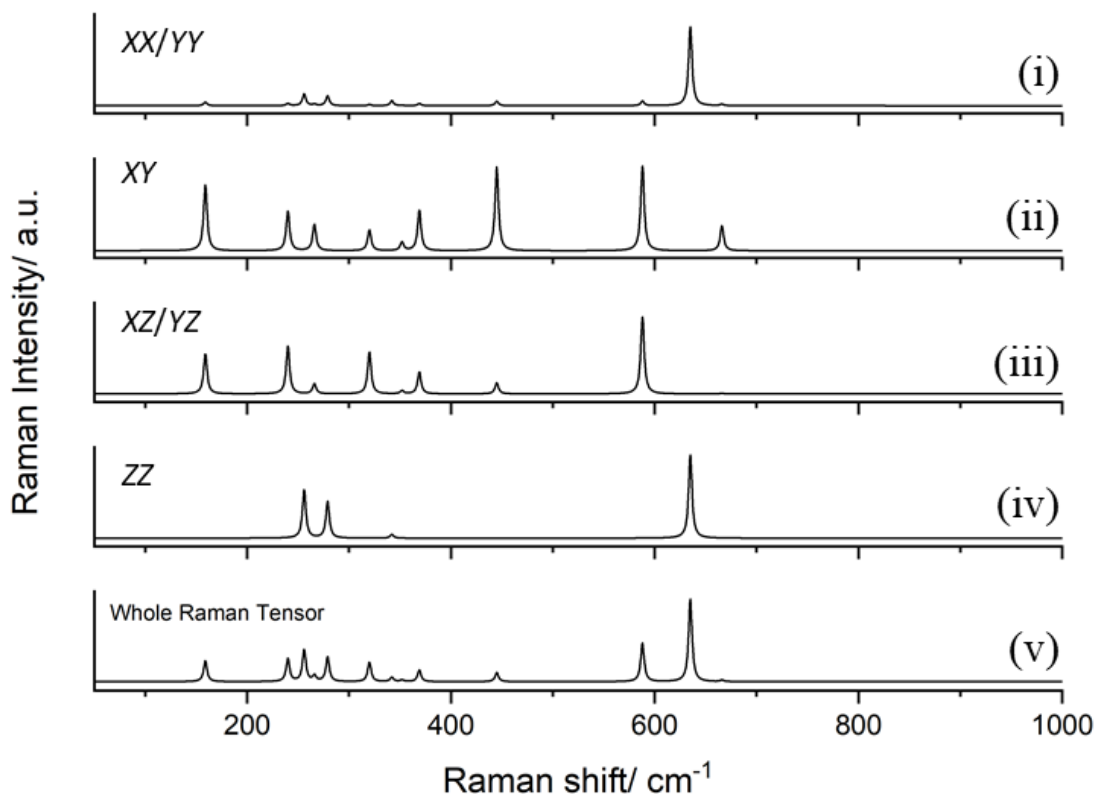


Figure 3 – CRYSTAL B3LYP/pob-TZVP calculated spectra of the LiNbO_3 crystal, considering the whole and individual components of the Raman tensors (abbreviated in the figure using only their Cartesian indexes). All spectra are normalized by their highest intensity peak.

Wavenumbers

Figure 4 allows to compare the spectra collected in the $X(ZZ)\bar{X}$ and $Y(ZZ)\bar{Y}$ experimental set ups (which probe only A_1 phonons) with that of the calculated spectrum obtained using the α'_{zz} component of the Raman tensors (the b values in Eq. 2.29). The wavenumbers are collected in Table 4. As it can be seen by comparing both the spectral patterns and wavenumbers, the agreement between our experimental and calculated results is remarkable. The appearance of a small peak in the experimental spectra at 152 cm^{-1} , which is not predicted by the calculations, is an evidence of the excitation of a phonon of E species, which should be not allowed by symmetry in this configuration (see Table 3). Its presence in the experimental spectrum might be ascribed to some crystal misalignment, or, more probably, to the actual efficiency of the polarizer that might have not completely filtered the scattered light with horizontal polarization. Indeed, the $X(ZY)\bar{X}$ and $Y(ZX)\bar{Y}$ spectra both show E (TO) transitions, among which 1 E at 152 cm^{-1} is the most intense one (see Figure 5 and Table 5). The A_1 phonons experimental wavenumbers we have measured are in very good agreement with the data reported in the work by Fontana and Bourson.⁸ Moreover, it is also clear that the wavenumbers prediction by the present calculations - showing errors not exceeding 3% - is much more accurate than that reported previously by Caciuc *et al.*⁹ (errors between 1% and 17%), who also focused on the prediction on the TO vibrations.

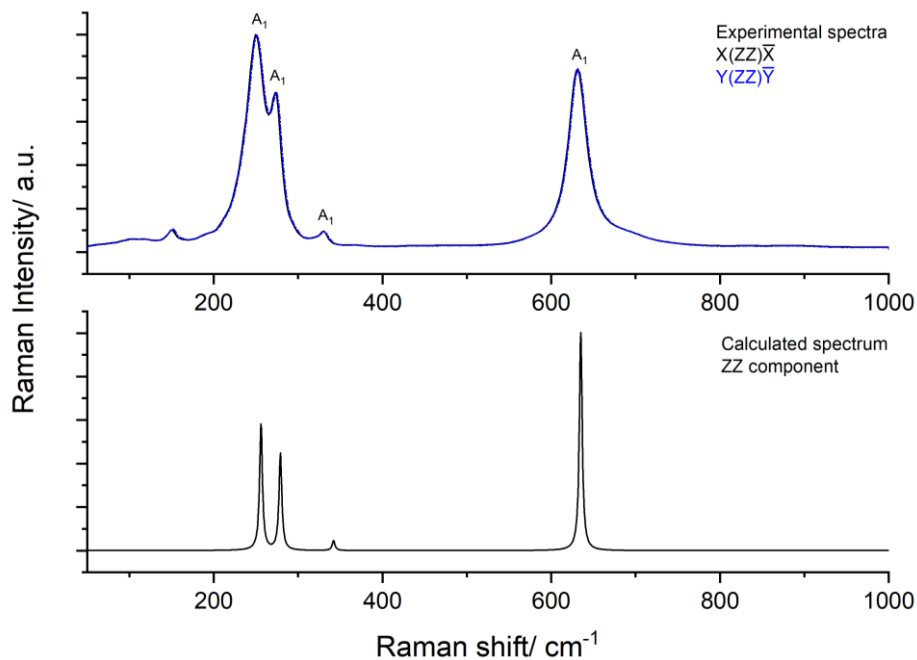


Figure 4 – *Top panel:* Experimental $X(ZZ)\bar{X}$ (black) and $Y(ZZ)\bar{Y}$ (blue) spectra of LiNbO_3 crystal. *Bottom panel:* CRYSTAL B3LYP/pob-TZVP calculated spectrum based on the α'_{zz} Raman tensors component values.

Table 4 – Wavenumbers (cm^{-1}) of the phonons observed in the $X(ZZ)\bar{X}/Y(ZZ)\bar{Y}$ experimental spectra of LiNbO_3 crystal, CRYSTAL B3LYP/pob-TZVP calculated wavenumbers with non-null intensities according to the α'_{zz} Raman tensors component, and comparison with literature data.

Experimental (this work) ^a	Ref. 8	Calculated (this work)	Ref. 9	Assignment
252	254	256	208	1 A_1 (TO)
274	275	280	279	2 A_1 (TO)
331	332	342	344	3 A_1 (TO)
632	631	635	583	4 A_1 (TO)

^a An additional minor band was observed in the experimental spectra, at 152 cm^{-1} , which is ascribable to the 1 E vibration (see text).

The experimental spectra collected in the $X(YZ)\bar{X}$, $X(ZY)\bar{X}$, $Y(XZ)\bar{Y}$ and $Y(ZX)\bar{Y}$ arrangements are compared in Figure 5 with the theoretical spectrum displaying intensities computed using the α'_{xz} and α'_{yz} components of $E(X)$ and $E(Y)$ Raman tensors respectively, which are identical because of symmetry (d values in Eq. 2.29). The experimental spectra showing deconvolution of the individual bands are presented in Figure S1, in the Supporting Information. The agreement between the experimental and calculated data is noteworthy, with all experimentally observed bands being well predicted by the calculations both regarding wavenumber and intensity. The attained accuracy in the wavenumbers improves on those of previous works.⁹ The calculated bands at 352 and 369 cm^{-1} merge

into a single broad band at 366 cm^{-1} in the experimental spectra, which after deconvolution reveals two components at 359 and 369 cm^{-1} (see Figure S1), also in good agreement with the calculated values.

It is important to underline that only seven among the nine E symmetry TO modes assigned to fundamental transitions in the last published experimental work on LiNbO_3 ⁸ can be reasonably correlated to the present predicted values (see Table 5). Indeed, the previously reported very weak feature at 186 cm^{-1} does not find any correspondence with our predicted Raman transitions. This band has been assigned before⁸ to both TO and LO E phonons, and the present results strongly suggest it is only due to the LO mode. Considering also the fact that the feature observed at 366 cm^{-1} corresponds, as already mentioned above, to the two E (TO) modes predicted at 352 and 369 cm^{-1} , a reassignment of the lowest frequency E (TO) modes is proposed here that fits all these evidence (see Table 5). Moreover, we propose also to reassign the 9 E phonon to the feature observed at 670 cm^{-1} , which fits both our prediction (666 cm^{-1}) and that of Cauciuc *et al.*⁹ (617 cm^{-1}) better than the weaker feature observed at 738 cm^{-1} by Fontana and Bourson⁸ and that could not be observed in our spectra.

Note also that, as above, the present experimental spectra also show one weak extra band (632 cm^{-1}), which shall be ascribed to an A_1 mode (strictly not allowed by symmetry in these experimental configurations). This band is the most intense band in the $X(YZ)\bar{X}$ spectrum (see Figure 6) and partially overlap the 9 E band, which is, however, clearly visible in the deconvoluted spectrum shown in Figure S1.

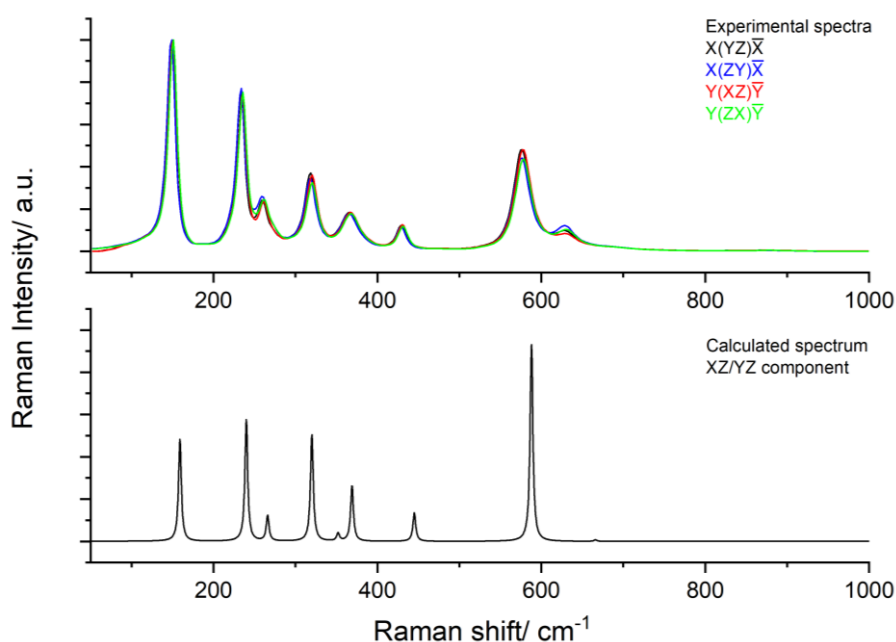


Figure 5 – *Top panel*: Experimental $X(YZ)\bar{X}$ (black), $X(ZY)\bar{X}$ (blue), $Y(XZ)\bar{Y}$ (red) and $Y(ZX)\bar{Y}$ (green) spectra of LiNbO_3 crystal. *Bottom panel*: CRYSTAL B3LYP/pob-TZVP calculated spectrum based on the α'_{xz} and α'_{yz} components of the Raman tensors.

Table 5 – Wavenumbers (cm^{-1}) of the phonons observed in the $X(YZ)\bar{X}/X(ZY)\bar{X}/Y(XZ)\bar{Y}/Y(ZX)\bar{Y}$ experimental spectra of LiNbO_3 crystal, CRYSTAL B3LYP/pob-TZVP calculated wavenumbers with non-null intensities according to the α'_{xz} and α'_{yz} Raman tensors components, and comparison with literature data.

Experimental (this work) ^a	Ref. 8 ^b	Calculated (this work)	Ref. 9	Assignment ^c
152	152	159	151	1 E (TO)
<i>237</i>	236	240	167	2 E (TO)
<i>261</i>	263	266	236	3 E (TO)
<i>320</i>	322	320	307	4 E (TO)
<i>359</i>	–	352	334	5 E (TO)
<i>369</i>	369	369	352	6 E (TO)
<i>432</i>	432	445	432	7 E (TO)
<i>579</i>	578	588	526	8 E (TO)
<i>670</i>	738	666	617	9 E (TO)

^a An additional minor band was observed in the experimental spectra, at 632 cm^{-1} , which is ascribable to the 4 A_1 vibration (see text); wavenumbers in italic correspond to the bands for whom reassignment is proposed. ^b In ref 8 the 2 E mode has been assigned to a very weak band at 186 cm^{-1} (also ascribed to a E (LO) mode), so that the next 4 observed E bands were assigned to 3 E, 4 E and 5 E (see discussion in the text) ^c The numbering of the vibrations follows an increasing order of the wavenumbers and strictly applies only to our own assignment.

The patterns of the $X(YY)\bar{X}$ Raman and $Y(XX)\bar{Y}$ spectra are quite complex, because of the simultaneous presence of A_1 (TO) and E (TO) or A_1 (TO) and E (LO) transitions, respectively. The spectra are determined by the α'_{yy} and α'_{xx} components of the Raman tensors (a and $c/-c$ values in Eq. 2.29 for A_1 and E modes, respectively). The results are shown in Figure 6 and Table 6 (and also in Figure S2, in the Supporting Information, which presents the bands deconvolution results). In the case of the $Y(XX)\bar{Y}$ spectrum, the present experimental results generally agree with those reported previously (see Table 6).^{8,26,27} Our calculations do not provide wavenumber values for the E (LO) modes, but the calculated data for the A_1 phonons fit nicely the experimental results. The results of the calculations by Parlinski and Li¹⁰ regarding the wavenumbers of the E (LO) modes are shown in Table 6, but one can see that the general agreement of the calculated values with the experimental data is modest.

The results for the case of the $X(YY)\bar{X}$ arrangement are particularly interesting, since all transitions of TO type (both of A_1 and E symmetries) are expected to contribute to the Raman spectrum, so that the data allow a more general comparison between the calculated and experimental results than when each set of bands (A_1 or E) is considered in separate (as in Figures 4 and 5). It can be seen that the general agreement between the experimental and calculated data obtained in the present investigation is remarkable, independently of the symmetry of the vibrations. In the $X(YY)\bar{X}$ experimental spectrum, the two pairs of bands predicted at $320/342 \text{ cm}^{-1}$ and $352/369 \text{ cm}^{-1}$ appear as two broad bands with maxima at 329 and 361 cm^{-1} , respectively. These bands could be successfully deconvoluted (see Figure S2), resulting in components with maxima at $320/331 \text{ cm}^{-1}$ and $359/369 \text{ cm}^{-1}$, respectively, which are in good agreement with the theoretically predicted values.

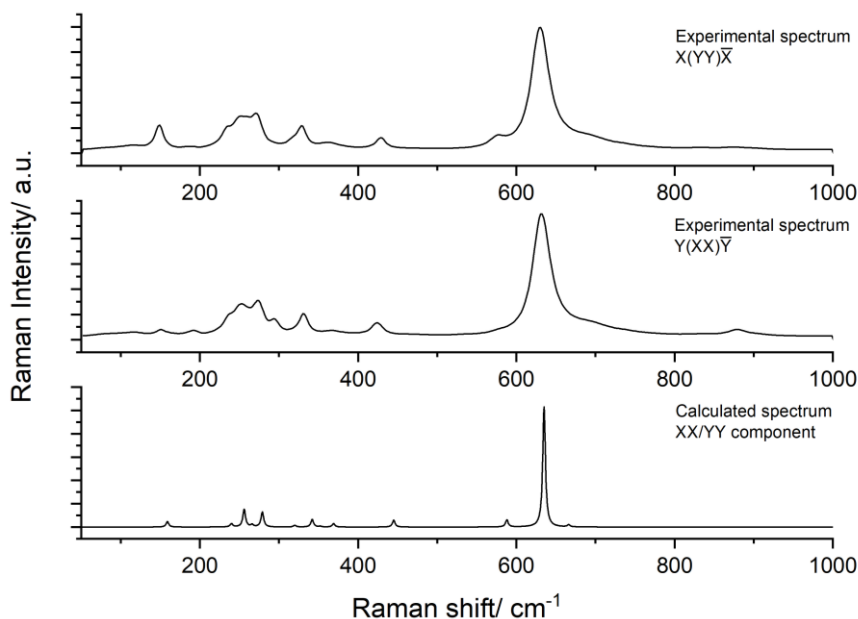


Figure 6 – *Top and middle panels:* Experimental $X(Y\bar{Y})\bar{X}$ and $Y(XX)\bar{Y}$ spectra of LiNbO_3 crystal, respectively. *Bottom panel:* CRYSTAL B3LYP/pob-TZVP calculated spectrum based on the α'_{xx} and α'_{yy} components of the Raman tensors.

Table 6 – Wavenumbers (cm^{-1}) of the phonons observed in the experimental $X(Y\bar{Y})\bar{X}$ and $Y(XX)\bar{Y}$ spectra of LiNbO_3 crystal, CRYSTAL B3LYP/pob-TZVP calculated wavenumbers with non-null intensities according to the α'_{xx} and α'_{yy} Raman tensors components, and comparison with literature data.

Experimental (this work)		Ref. 8 ^a		Calculated (this work)	Refs. 9,10 ^b	Assignment ^c
$X(Y\bar{Y})\bar{X}$	$Y(XX)\bar{Y}$	$X(Y\bar{Y})\bar{X}$	$Y(XX)\bar{Y}$			
152		152		159	151	1 E (TO)
	150		186	–	204	1 E (LO)
	191		194	–	216	2 E (LO)
237		236		240	167	2 E (TO)
	237		238	–	316	3 E (LO)
252	252	254	254	256	208	1 A ₁ (TO)
261		263		266	236	3 E (TO)
274	274	275	275	280	279	2 A ₁ (TO)
	295		295	–	372	4 E (LO)
320		322		320	307	4 E (TO)
331	331	332	332	342	334	3 A ₁ (TO)
359		–		352	344	5 E (TO)
	368		366	–	422	5 E (LO)
369		369		369	352	6 E (TO)
	423		425	–	445	6 E (LO)
432		432		445	432	7 E (TO)
	575		456 ^d	–	570	7 E (LO)
579		578		588	526	8 E (TO)
	689		625 ^e	–	677	8 E (LO)
632	632	631	631	635	583	4 A ₁ (TO)
670		738		666	617	9 E (TO)
	880		880	–	856	9 E (LO)

^a In ref 8 the 2 E mode has been assigned to a very weak band at 186 cm^{-1} (also ascribed to the 1 E (LO) mode), so that the next 4 observed E bands were assigned to 3 E, 4 E and 5 E (see discussion in the text) ^b Ref. 9 for TO modes; ref 10 for LO modes. ^c The numbering of the vibrations follows an increasing order of the wavenumbers and strictly applies only to our own assignment. ^d In ref 27 this mode was assigned to a band reported at 530 cm^{-1} . ^e In ref 26, this mode was assigned to a band reported at 668 cm^{-1} .

Figure 7 presents the comparison of the Raman spectra obtained using the pairs $Z(XX)\bar{Z} / Z(YY)\bar{Z}$ and $Z(XY)\bar{Z} / Z(YX)\bar{Z}$ of experimental configurations, together with the predicted spectrum built using the α'_{xy} component of the Raman tensors for the E modes ($-c$ value, Eq. 2.29). Band deconvolution of the experimental bands is presented in Figure S3 (Supporting Information). According to Table 2, both A_1 (LO) and E (TO) modes should be seen in the first pair of configurations, while only the E (TO) modes should be observed in the second one. All E (TO) vibrations are observed in the two pairs of experimental configurations, as expected. The A_1 (LO) modes are observed at 273, 331, 412 and 872 cm^{-1} , in good agreement with previous data (see Table 7).⁸ The calculated wavenumbers reported by Parlinski and Li¹⁰ for these modes are also included in Table 7, showing a relatively modest agreement with the experimental values. In the case of the $Z(XY)\bar{Z} / Z(YX)\bar{Z}$, besides the expected bands due to E (TO) vibrations, a band ascribable to residual intensity of the most intense LO A_1 mode at 872 cm^{-1} (observed in the $Z(XX)\bar{Z}$ and $Z(YY)\bar{Z}$ configurations) is also observed, most probably due to a minor crystal misalignment or incomplete filtering of the scattered light.

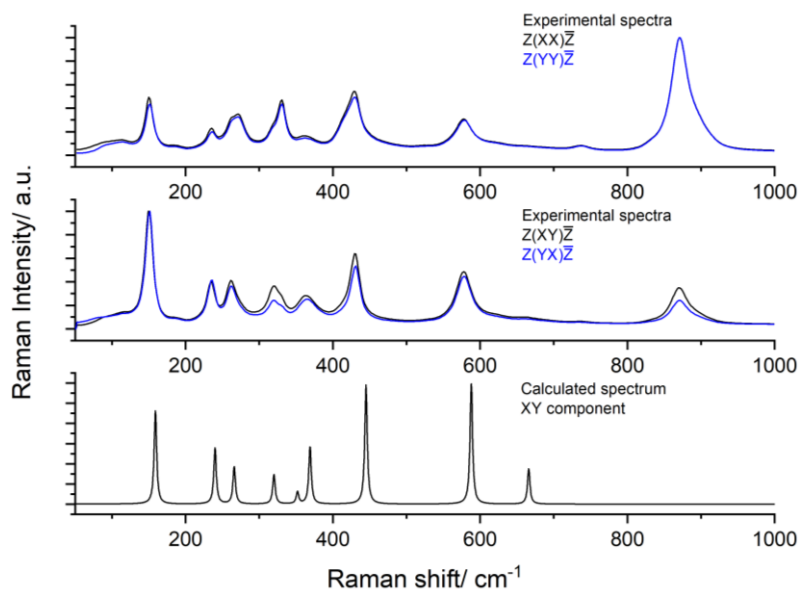


Figure 7 – *Top panel:* Experimental $Z(XX)\bar{Z}$ (black) and $Z(YY)\bar{Z}$ (blue) spectra of LiNbO_3 crystal. *Middle:* Experimental $Z(XY)\bar{Z}$ (black) and $Z(YX)\bar{Z}$ (blue) spectra of LiNbO_3 crystal. *Bottom panel:* CRYSTAL B3LYP/pop-TZVP calculated spectrum based on the α'_{xy} component of the Raman tensors.

Table 7 – Wavenumbers (cm^{-1}) of the A_1 (LO) phonons observed in the experimental $Z(XX)\bar{Z}$ and $Z(YY)\bar{Z}$ spectra of LiNbO_3 crystal and comparison with literature data.

Experimental (this work)	Ref. 8	Calculated (Ref. 10)	Symmetry
273	272	309	1 A_1 (LO)
331	332	381	2 A_1 (LO)
412	419	548	3 A_1 (LO)
872	871	831	4 A_1 (LO)

Intensities

In this Section, the comparison between the Raman intensity patterns of the calculated and experimental spectra is presented. The data is summarized in Tables 8-11: Table 8 for the A_1 (TO) modes (comparison between the calculated spectrum based on the α'_{zz} Raman tensor components and the $X(ZZ)\bar{X}/Y(ZZ)\bar{Y}$ experimental configuration spectra; the first experimental configuration was used for quantitative measurements of intensities), Tables 9 and 10 for the E (TO) modes (comparison between the calculated spectrum based on the α'_{xz} and α'_{yz} components of the Raman tensors and the $Y(XZ)\bar{Y}$, $X(ZY)\bar{X}$, $Y(XZ)\bar{Y}$ and $Y(ZX)\bar{Y}$ experimental spectra, and between that calculated based on the α'_{xy} and α'_{yx} components of the Raman tensors and the $Z(XY)\bar{Z}$ and $Z(YX)\bar{Z}$ experimental spectra, respectively, Table 11 for both A_1 (TO) and E (TO) modes (comparison between the calculated spectrum based on the α'_{yy} – equal to α'_{xx} – components of the Raman tensors and the $X(YY)\bar{X}$ experimental spectrum). For the comparison of the relative intensities of the bands, a well-isolated band was chosen as reference in each spectrum (bands ascribable to 3 A_1 and 7 E (TO) modes satisfy this criterion and were then selected) and the intensities of the other bands were compared with that of the reference band. Experimental intensities were obtained by band area determination.

The correspondence between the Raman relative intensities of the experimental spectra and of the spectra calculated in the present study is quite remarkable, strongly improving on previous results² where only a very modest agreement was obtained (in the present study, the average error in the calculated relative intensities, compared to experimental ones, is ~10%, while from the graphical data presented in ref. 2 an error larger than twice the one obtained in this study can be estimated).

Table 8 – Comparison between the Raman intensities (areas under the bands) of the calculated spectrum based on the α'_{zz} Raman tensor components and the $X(ZZ)\bar{X}$ experimental configuration spectrum (A_1 symmetry modes).

Mode	Calculated wavenumber (cm ⁻¹)	Relative intensity ^b			
		Calculated a.u.		Experimental a.u.	
1 A_1	256	13.4	<i>23.4</i>	16.1	<i>24.3</i>
2 A_1	280	10.0		8.2	
3 A_1	342	1		1	
4 A_1	635	<i>22.4</i>		<i>22.2</i>	

^a The band due to the 3 A_1 mode was chosen as reference. Intensities in relative arbitrary units (a. u.). ^b Values in italic correspond to sums for bands whose individual intensities resulted from band deconvolution.

Comparison of the A_1 Raman intensities presented in Table 8 (see also Figure 4) allows to conclude that there is an almost perfect correspondence regarding the experimental and calculated relative intensities for mode 4 A_1 (22.2 vs. 22.4) regarding the 3 A_1 mode, set as reference, and also a very good agreement between those of modes 1 A_1 (16.1 vs. 13.4) and 2 A_1 (8.2 vs. 10.0). It must be

noticed that for the two later modes, the individual intensities resulted from band deconvolution (which is particularly difficult in this case due to the close proximity of the two maxima), and that the agreement between the total experimental and calculated intensity of this pair of bands is in fact excellent (24.3 vs. 23.4).

An excellent correspondence is also observed in the case of the more complex spectra of the E (TO) modes (see Figures 5 and 7 and Tables 9 and 10). In fact, with the exception of 3 E mode in the XZ/YZ spectrum, whose calculated relative intensity is about one half the experimental value, the intensity pattern is remarkably well predicted by the calculations.

Table 9 – Comparison between the Raman intensities (areas under the curve) of the calculated spectrum based on the α'_{xz} and α'_{yz} Raman tensor components and the $Y(XZ)\bar{Y}$ experimental configuration spectrum (E symmetry modes).

Mode	Calculated wavenumber (cm ⁻¹)	Relative intensity			
		Calculated (a.u.)		Experimental (a.u.)	
1 E	159	3.7		3.8	
2 E	240	4.2		3.7	
3 E	266	1.0		1.8	
4 E	320	3.7		3.9	
5 E	352	0.4	2.3	0.3	2.7
6 E	369	1.9		2.4	
7 E	445	1		1	
8 E	588	7.0		7.6	
9 E	666	0.1		0.1	

^a The band due to the 7 E mode was chosen as reference. Intensities in relative arbitrary units (a. u.). ^b Values in italic correspond to sums for bands whose individual intensities resulted from band deconvolution.

Table 10 – Comparison between the Raman intensities (area under the curve) of the calculated spectrum based on the α'_{xy} and α'_{yx} components of the Raman tensors and the $Z(XY)\bar{Z}$ experimental configuration spectrum (E symmetry modes).

Mode	Calculated wavenumber (cm ⁻¹)	Relative intensity			
		Calculated (a.u.)		Experimental (a.u.)	
1 E	159	0.7		0.8	
2 E	240	0.4		0.5	
3 E	266	0.3		0.3	
4 E	320	0.3		0.3	
5 E	352	0.2	0.5	0.1	0.6
6 E	369	0.3		0.5	
7 E	445	1		1	
8 E	588	1.0		1.0	
9 E	666	0.2		0.3	

^a The band due to the 7 E mode was chosen as reference. Intensities in relative arbitrary units (a. u.). ^b Values in italic correspond to sums for bands whose individual intensities resulted from band deconvolution.

Similarly, the intensity pattern of the full set of A₁ and E modes observed in X(Y \bar{Y}) \bar{X} experimental spectrum is very well predicted by the XX/YY calculated spectrum. The biggest difference on the relative intensity of the most intense band in both experimental and theoretical spectra, the 4 A₁ mode. In both cases, this is the clearly the highest peak, see Figure 6 and Table 11, meaning that the difference in the relative intensity of this particular vibration is not significant to alter the structure of the spectra, which is in fact very similar. Therefore, our calculations predict well both A₁ and E modes intensity when they appear in simpler spectra where transitions of phonons belonging to only one symmetry species are allowed by symmetry, but also when both of them appear in the same spectrum.

Table 11 – Comparison between the Raman intensities (area under the curve) of the calculated spectrum based on the α'_{yy} component of the Raman tensors and the X(Y \bar{Y}) \bar{X} experimental configuration spectrum (A₁ and E symmetry modes).

Mode	Calculated frequency (cm ⁻¹)	Relative intensity			
		Calculated (a.u.)		Experimental (a.u.)	
1 E	159	0.8		0.8	
2 E	240	0.5		0.5	
1 A ₁	256	2.2		2.5	
3 E	266	0.4		0.5	
2 A ₁	280	1.8		2.2	
4 E	320	0.2		0.2	
3 A ₁	342	0.9	<i>1.1</i>	1.1	<i>1.3</i>
5 E	352	0.2		0.2	
6 E	369	0.4	<i>0.6</i>	0.5	<i>0.7</i>
7 E	445	1		1	
8 E	588	1.1		1.0	
4 A ₁	635	13.7		16.9	
9 E	666	0.5		0.4	

^a The band due to the 7 E mode was chosen as reference. Intensities in relative arbitrary units (a. u.). ^b Values in italic correspond to sums for bands whose individual intensities resulted from band deconvolution.

5. Conclusion

In this study, we propose a reassignment of the E (TO) modes of the R3c LiNbO₃ crystal, in particular for the 2 E and 9 E modes, which have been a matter of discussion in the recent years. The investigation of the vibrational properties of this system was carried out based on a new series of DFT calculations with full periodic boundary conditions, using the CRYSTAL software and the comparison of these results with the polarized Raman experimental spectra of the crystal. This comparison demonstrated the excellent ability of the theoretical approach used to calculate the wavenumbers of the A₁ and E (TO) modes. In addition, it was shown that the relative Raman intensities for both types of vibrations in the different experimental configurations are remarkably well predicted. Overall, the

present investigation demonstrates that the LCAO approach, as implemented in the CRYSTAL software gives excellent results regarding the calculation of Raman tensors and polarized Raman spectra. The possibility to put in correspondence the individual Raman tensor components and bands intensities in the different back-scattering experimental configurations allowed to demonstrate that the computed Raman tensors are very accurate, not only considering their average values (tensors invariant in the combination suitable for the description of Raman scattering of isotropic materials), but also considering the tensors individual components.

Supporting Information

Figures S1-S3, with the results of band deconvolutions.

Acknowledgements

The authors acknowledge financial support from the Portuguese Science Foundation (“Fundação para a Ciência e a Tecnologia” - FCT) – Projects CQC UIDB/00313/2020 and UIDP/00313/2020, also co-funded by FEDER/COMPETE 2020-EU. Access to instruments from Laser-Lab Coimbra facility funded under QREN-Mais Centro is gratefully acknowledged. B.A.N. also acknowledges FCT for the SFRH/BD/129852/2017 PhD Scholarship.

References

1. R. S. Weis and T. K. Gaylord, Lithium niobate: summary of physical properties and crystal structure, *Appl. Phys. A Solids Surfaces*, 1985, **37**, 191-203.
2. P. Hermet, M. Veithen and P. Ghosez, First-principles calculations of the nonlinear optical susceptibilities and Raman scattering spectra of lithium niobate, *J. Phys. Condens. Matter*, 2007, **19**, 456202.
3. K. Buse, A. Adibi and D. Psaltis, Non-volatile holographic storage in doubly doped lithium niobate crystals, *Nature*, 1998, **393**, 665-668.
4. L. Hesselink, S. S. Orlov, A. Liu, A. Akella, D. Lande and R. R. Neurgaonkar, Photorefractive materials for nonvolatile volume holographic data storage, *Science*, 1998, **282**, 1089-1094.
5. I. Noiret, J. Lefebvre, J. Schamps, F. Delattre, A. Brenier and M. Ferriol, New structural transformations in congruent ferroelectric LiNbO₃ fibres evidenced by Raman spectroscopy, *J. Phys. Condens. Matter*, 2000, **12**, 2305-2316.
6. Y. Repelin, E. Husson, F. Bennani and C. Proust, Raman spectroscopy of lithium niobate and lithium tantalate. Force field calculations, *J. Phys. Chem. Solids*, 1999, **60**, 819-825.
7. R. F. Schaufele and M. J. Weber, Raman scattering by lithium niobate, *Phys. Rev.*, 1966, **152**, 705-708.
8. M. D. Fontana and P. Bourson, Microstructure and defects probed by Raman spectroscopy in lithium niobate crystals and devices, *Applied Physics Reviews*, 2015, **2**, 040602.
9. V. Caciuc, A. Postnikov and G. Borstel, *Ab initio* structure and zone-center phonons in LiNbO₃, *Phys. Rev. B - Condens. Matter Mater. Phys.*, 2000, **61**, 8806-8813.
10. K. Parlinski, Z. Li and Y. Kawazoe, *Ab initio* calculations of phonons in LiNbO₃, *Phys. Rev. B - Condens. Matter Mater. Phys.*, 2000, **61**, 272-278.
11. R. Dovesi, A. Erba, R. Orlando, C. M. Zicovich-Wilson, B. Civalleri, L. Maschio, M. Rérat, S.

- Casassa, J. Baima, S. Salustro and B. Kirtman, Quantum-mechanical condensed matter simulations with CRYSTAL, *Wiley Interdiscip. Rev. Comput. Mol. Sci.*, 2018, **8**, e1360.
12. R. Dovesi, V. R. Saunders, C. Roetti, R. Orlando, C. M. Zicovich-Wilson, F. Pascale, B. Civalleri, K. Doll, N. M. Harrison, I. J. Bush, P. D'Arco, M. Llunell, M. Causà, Y. Noël, L. Maschio, A. Erba, M. Rerat and S. Casassa, CRYSTAL17 User's Manual (University of Torino, Torino, 2017).
 13. C. Lee, W. Yang and R. G. Parr, Development of the Colle-Salvetti correlation-energy formula into a functional of the electron density, *Phys. Rev. B*, 1988, **37**, 785-789.
 14. M. F. Peintinger, D. V. Oliveira and T. Bredow, Consistent Gaussian basis sets of triple-zeta valence with polarization quality for solid-state calculations, *J. Comput. Chem.*, 2013, **34**, 451-459.
 15. D. V. Oliveira, J. Laun, M. F. Peintinger and T. Bredow, BSSE-correction scheme for consistent gaussian basis sets of double-and triple-zeta valence with polarization quality for solid-state calculations, *J. Comput. Chem.*, 2019, **40**, 2364-2376.
 16. J. Laun, D. V. Oliveira and T. Bredow, Consistent gaussian basis sets of double-and triple-zeta valence with polarization quality of the fifth period for solid-state calculations, *J. Comput. Chem.*, 2018, **39**, 1285-1290.
 17. S. C. Abrahams, J. M. Reddy and J. L. Bernstein, Ferroelectric lithium niobate. 3. Single crystal X-ray diffraction study at 24 °C, *J. Phys. Chem. Solids*, 1966, **27**, 997-1012.
 18. S. Dall'Olivo, R. Dovesi and R. Resta, Spontaneous polarization as a Berry phase of the Hartree-Fock wave function: The case of KNbO₃, *Phys. Rev. B - Condens. Matter Mater. Phys.*, 1997, **56**, 10105-10114.
 19. G. Keresztury, *Raman Spectroscopy: Theory*, in *Handbook of Vibrational Spectroscopy*, John Wiley & Sons, 2006.
 20. R. Loudon, The Raman effect in crystals, *Adv. Phys.*, 1964, **13**, 423-482.
 21. J. Kim, J. U. Lee and H. Cheong, Polarized Raman spectroscopy for studying two-dimensional materials, *J. Phys. Condens. Matter*, 2020, **32**, 343001.
 22. H. Kuzmany, *Solid-State Spectroscopy*, Springer, 1998.
 23. A. Ridah, P. Bourson, M. D. Fontana and G. Malovichko, The composition dependence of the Raman spectrum and new assignment of the phonons in LiNbO₃, *J. Phys. Condens. Matter*, 1997, **9**, 9687-9693.
 24. I. P. Kaminow and W. D. Johnston, Quantitative Determination of Sources of the Electro-Optic Effect in LiNbO₃ and LiTaO₃, *Phys. Rev.*, 1967, **160**, 519-522.
 25. A. S. Barker and R. Loudon, Dielectric Properties and Optical Phonons in LiNbO₃, *Phys. Rev.*, 1967, **158**, 433-445.
 26. R. Claus, G. Borstel, E. Wiesendanger and L. Steffan, Assignments of Optical Phonon Modes in LiNbO₃, *Physical Review B*, 1972, **6**, 4878-4879.
 27. X. Yang, G. Lan, B. Li and H. Wang, Raman Spectra and Directional Dispersion in LiNbO₃ and LiTaO₃, *Phys. status solidi*, 1987, **142**, 287-300.

2.4. Thermal analysis

Thermal analysis methods are used for determination of thermodynamic data, being a group of analytical techniques that allow to investigate the relationship between a change in a property of a given sample and the temperature, when the sample is submitted to a controlled temperature variation program.^{1,2}

2.4.1. Differential Scanning Calorimetry

Differential scanning calorimetry (DSC) allows the study of phenomena that take place with an energy change, such as melting, crystallization, devitrification and solid-solid transition processes, among others.³ According to the International Confederation for Thermal Analysis and Calorimetry (ICTAC), DSC is defined as *a technique where the difference between the electric powers (the flow rates) into a sample and a reference material is measured.*

In power-compensation differential scanning calorimetry, the purpose is to keep both the sample and the reference material at the same temperature, all along the controlled temperature variation program. The differences in the independent power supplies to the sample and to the reference are measured as a function of the temperature and represent thermal events in the sample. They are used to build the DSC curves and appear as deviations from the DSC baseline in opposite directions depending on being endothermic (where more energy needs to be provided to the sample than to the reference) or exothermic processes (where less energy must be delivered to the sample relative to the reference material). Conventionally, endothermic responses (*e.g.*, melting processes, solid-solid transitions, devitrification events) are represented above the baseline, as positive deviations from the baseline.¹

The DSC experiments presented in this Thesis were performed in a Perkin Elmer Pyris-1 power compensation calorimeter (see Figure 1), equipped with a 1:1 v/v ethylene glycol:water cooler at -25 °C and a 20 mL min^{-1} nitrogen purge flow. In these experiments, hermetically sealed aluminium pans were used (samples weighting between 0.5 and 2 mg) and an empty pan used as reference.



Figure 1 – Perkin-Elmer DSC Pyris 1 with liquid nitrogen cooling system.

2.4.2. Polarized Light Thermomicroscopy

Polarized light thermomicroscopy (PLTM) is a thermal analytic technique that involves the merging of two separate methods: polarized light microscopy and thermomicroscopy (which is also referred to as thermal microscopy, optical thermal analysis, and hot-stage microscopy – HSM). The latter, according to ICTAC, is *a technique where the optical properties of the sample are observed and measured through a microscope.*²

In PLTM, the main optical property that is analyzed is the interaction of the sample with polarized light. The use of polarized light in the microscope gives access to unique information regarding the sampled material, in particular allowing to characterize the sample (or its different components, when a heterogeneous material is under analysis) as being isotropic or anisotropic.

When light passes through a polarizer, a specific direction of its electric field is selected. The polarized light can then be aimed towards the sample. When a second polarizing filter is placed in the optical path after the sample and perpendicular to the first polarizer, cross-polarization is achieved. Under cross-polarized light, crystalline samples in general (cubic crystals are the exception to the general rule) appear as birefringent, because the two different components of the polarized light that are transmitted through the sample recombine in a way that, although both components are initially travelling at the same speed, due to the different interaction with the crystalline material (where properties as the crystal thickness and the refractive index play important roles) one component of the

polarized light emerges slightly retarded relatively to the other.⁴ Visually, these anisotropic materials appear white or colored-shades under cross-polarization. On the other hand, isotropic materials such as liquids, amorphous solids or cubic crystals do not exhibit birefringence, thus being clearly distinguishable from anisotropic materials. Such difference between isotropic and anisotropic materials at optical observation under polarized light microscopy is particularly useful when the samples under investigation undergo phase transitions involving the two types of materials, such as, for instance, during crystallization or melting processes. However, birefringence is also very much affected by the different characteristics of the crystals. For this reason, PLTM is also a very powerful technique to distinguish transitions between different anisotropic crystalline phases, such as in the case of crystalline solid-solid transitions.^{5,6}

PLTM is then a valuable complementary technique to DSC when the information obtained from the calorimetric technique cannot be fully understood, since the data collected during the visual analysis of the sample, such as changes in birefringence of the particles under cross-polarization filters when a controlled temperature program is applied, as well as the information of the homogeneity of the sample, are extremely valuable in confirming the physical properties of materials.⁵

The PLTM experiments performed in this study were conducted using a Linkam DSC600 hot stage, a Leica DMRB microscope, and a Sony CCD-IRIS/RGB video camera (see Figure 2.2). The produced images (both at 50× or 200× magnification) were collected in heating runs carried out at a scanning rate of 10 °C min⁻¹ and analyzed with the LinkSys software (Linkam).



Figure 2 – Linkam DSC-600 hot stage and Leica DMRB microscope with a Sony CCD-IRIS/RGB video camera.

References

- 1 M. E. Brown, Ed., *Introduction to Thermal Analysis*, Kluwer Academic Publishers, 2004.
- 2 T. Lever, P. Haines, J. Rouquerol, E. L. Charsley, P. Van Eckeren and D. J. Burlett, ICTAC nomenclature of thermal analysis (IUPAC Recommendations 2014), *Pure Appl. Chem.*, 2014, **86**, 545–553.
- 3 D. Giron, Applications of Thermal Analysis and Coupled Techniques in Pharmaceutical Industry, *J. Therm. Anal. Calorim.*, 2002, **68**, 335–357.
- 4 R. Oldenbourg, Polarized Light Microscopy: Principles and Practice, *Cold Spring Harb. Protoc.*, 2013, **11**, 1023-1036.
- 5 D. Q. M. Craig and M. Reading, *Thermal Analysis of Pharmaceuticals*, CRC PRESS, 2007.
- 6 R. A. Carlton, *Polarized light microscopy*, in *Pharmaceutical Microscopy*, Springer, 2011, 7–64.

2.5. X-ray diffraction

X-ray diffraction is the most common experimental method that allows the direct determination of molecular structures at the atomic (or near atomic) level. The diffraction phenomenon can be defined as the interference caused by an entity in the path of electromagnetic radiation waves, with the resulting intensity pattern being known as the diffraction pattern. Diffraction occurs when the dimensions of the diffracting object are of the same order of magnitude of the wavelength of the radiation. X-rays have wavelengths with comparable orders of magnitude to bond lengths and to the spacing of atoms in molecular crystals (around 1 Å) and, hence, X-rays can be diffracted by molecular crystals.^{1,2}

The unit cell of a crystal is the fundamental unit from which the whole crystal may be constructed by purely translational displacements. Since there are virtually infinite different possible unit cells to describe the same crystal, the elected one has the shortest dimensions and defining axes that are closest to perpendicularity. The asymmetric unit is the smallest part of a crystal unit cell that can generate this latter by application of symmetry operations of the space group of the crystal. The unit cells can be classified in seven different crystal systems, depending on the rotation symmetry elements they possess: triclinic (no essential symmetry), monoclinic (one C_2 axis), orthorhombic (three perpendicular C_2 axes), rhombohedral (one C_3 axis), tetragonal (one C_4 axis), hexagonal (one C_6 axis) and cubic (four C_3 axes in a tetrahedral arrangement). The periodicity characteristic of the crystals allows that the determination of only the contents of the asymmetric unit (or the whole unit cell in the exceptional case of space group $P1$ systems) is sufficient to discover the position of all the atoms in a molecular crystal.

A simple approach to the analysis of crystal diffraction patterns considers the crystal as a stack of reflecting lattice planes (conventionally defined as h , k and l) with separation d . This model is useful as it helps the calculation of the crystal angle needed to generate constructive interferences of the X-ray beam (see Figure 1), in order to produce crystallographic structural information. When the path length difference of two X-ray rays inside the crystalline sample ($AB + BC = 2d_{hkl} \sin \theta$, with θ being the glancing angle, which is also known as the Bragg angle) is a multiple of the wavelength (λ), the reflected waves are in phase and the interference is constructive. Thus, a bright reflection might be observed when the glancing angle satisfies the condition known as the Bragg's law:

$$\lambda = 2d_{hkl} \sin \theta \quad (2.30)$$

The major use of Bragg's law is the determination of the separation distance between the lattice planes, so that once the glancing angle corresponding to a reflection is determined, the d value can be obtained.^{1,3}

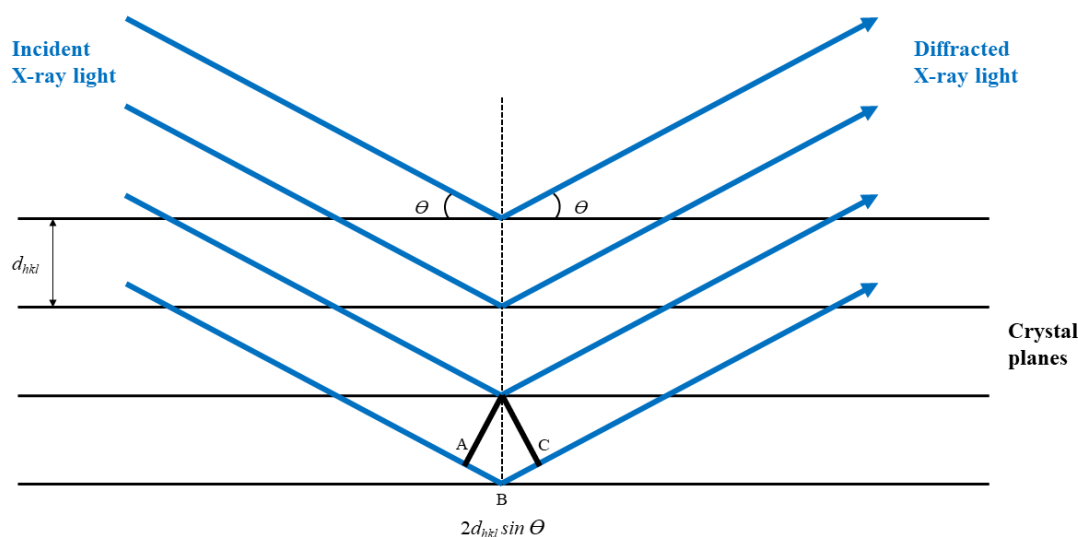


Figure 1 – X-ray diffraction from crystal lattice planes, illustrating Bragg's law.

The original X-ray method, developed by Laue, consisted in passing a broad beam of X-rays into a single crystal and to record the diffraction pattern (photographically as the technology, at that time, compelled). The concept of this scheme was that the Bragg's law would be satisfied for at least one of the wavelengths of the used broad range, even if the crystal was not suitably oriented to diffract a single pre-selected wavelength. Alternatively, Peter Debye and Paul Scherrer and, independently, Albert Hull, developed a monochromatic radiation technique to analyze powdered samples. In a powder sample, some of the crystallites that compose the powder will always be oriented in a way to satisfy the Bragg's law and the diffracted beams by the sample will lie on a cone around the incident beam of half angle 2θ . The main application of this technique is the qualitative analysis of the samples because the diffraction pattern acts as a fingerprint of each molecular system, if pure. Additionally, monochromatic powder diffraction can also be used, in certain molecular systems, to determine the dimensions and the symmetries of the unit cells.¹

To determine the crystallographic structure from single crystal samples, the method developed by the Nobel prize winners William and Lawrence Bragg, which consisted in the use of a monochromatic beam of X-rays into a single crystal that is rotated until a reflection is detected, is still the basis of modern X-ray crystallography. Since there are several different sets of planes in a crystal, there are also several different angles at which a reflection occurs, and the complete set of crystallographic data is made of the list of angles at which the reflections occur and their respective intensities.

In a unit cell containing different atoms with scattering factors (which are related to the electron density distribution in the atom via a Fourier transform) f_i and coordinates $x_i a$, $y_i b$, $z_i c$, the overall diffracted amplitude of the wave, which is defined as the structure factor (F_{hkl}), is given by:

$$F_{hkl} = \sum_i f_i e^{2\pi i(hx_i + ky_i + lz_i)} \quad (2.31)$$

The intensity of the diffracted beam reflected from the set of planes defined by hkl is proportional to the square of the structure factor.^{1,3} Thus, the single crystal X-ray experiments consist in measuring the diffracted intensity as a function of the glancing angle. The two key crystallographic parameters that essentially define the structure of a diffraction pattern are the unit cell and its atomic filling. Briefly, the diffraction pattern can be constructed from the positions of the Bragg peaks (which are established from the Bragg's law as a function of λ and d) and the intensities of these Bragg peaks (which depend on the coordinates of the atoms in the unit cell).^{4,5}

In the studies performed within the research program of this Thesis, the X-ray powder diffraction data were collected using a Bruker D8 Advance diffractometer (Figure 2), equipped with a LYNXEYE linear position sensitive detector and using Ni-filtered Cu $K\alpha$ radiation ($\lambda = 1.54059 \text{ \AA}$). The single crystal diffraction experiments were performed using graphite monochromated Mo $K\alpha$ ($\lambda = 0.71073 \text{ \AA}$) radiation in a Bruker APEX II diffractometer (Figure 3) or in a Bruker AXS-KAPPA D8 - QUEST diffractometer. The structures were solved by the dual-space algorithm implemented in SHELXT-2018/2, and full-matrix least-squares refinement of the structural model was performed using SHELXL-2018/3. All non-hydrogen atoms were refined anisotropically. Hydrogen atoms were placed at calculated idealized positions and refined as riding using SHELXL-2018/3 default values,⁶ with few expectations that are indicated in the proper sections of Chapters 3 and 4. All the single crystal X-ray measurements were performed at room temperature.



Figure 2 – Bruker D8 Advance diffractometer. Image adapted from Bruker’s website.⁷



Figure 3 – Bruker APEX II diffractometer.

References

- 1 P. W. Atkins, *Physical Chemistry*, Oxford University Press, 1992.
- 2 F. C. Phillips, *An introduction to crystallography*, Longman, 1979.
- 3 M. Ladd and R. Palmer, *Structure determination by X-ray crystallography: Analysis by X-rays and neutrons*, Springer, 2013.
- 4 A. Clearfield, J. H. Reibenspies and N. Bhuvanesh, *Principles and applications of powder diffraction*, John Wiley and Sons, 2008.
- 5 J. P. Glusker and K. N. Trueblood, *Crystal structure analysis*, Oxford University Press, 2010.
- 6 G. M. Sheldrick, Crystal structure refinement with SHELXL, *Acta Crystallogr. Sect. C Struct. Chem.*, 2015, **71**, 3–8.
- 7 D8 Advance Eco diffractometer | Bruker, <https://www.bruker.com/pt/products-and-solutions/diffractometers-and-scattering-systems/x-ray-diffractometers/d8-advance-family/d8-advance-eco.html>, (accessed 18 February 2022).

2.6. Synthesis and Polymorph screening

All the compounds investigated here (and presented in Chapters 3 and 4) are new and were synthesized in the Organic Chemistry Laboratory of the CQC-IMS. The main reagents used were either purchased from specialized companies or synthesized from the corresponding precursors following standard literature methods. The synthetic routes were adapted from the literature.¹⁻⁸ The synthetic steps involved protection of the functional groups and the subsequent cleavage of the protecting groups (in the case of ROY-ol), condensation reactions (for TMA and TAP), nucleophilic aromatic substitution reactions (for AcROY, ROY-ol and ROY-CAM) and Friedel–Crafts acylation reactions (AcROY), and are described in detail in the specific sections of Chapters 3 and 4. Thin-layer chromatography (TLC) analyses, which were executed with precoated silica gel plates, were performed throughout the synthetic steps to follow the extension of each reaction. The purification of the synthetic products involved filtrations, aqueous solution washings, dryings under vacuum, liquid-liquid extractions, solvent evaporations, flash chromatography and crystallization processes, as described in Chapters 3 and 4.

The synthesized precursors and final products were initially characterized by ¹H NMR and ¹³C NMR (recorded on a Bruker Avance III instrument, operating at 400 MHz and at 100 MHz, respectively), FTIR spectroscopy (performed on a Agilent Cary 630 FTIR spectrometer, with a diamond-based attenuated total reflection Smart Orbit cell and also on a Thermo Scientific FT-IR Nicolet iS5 system, with an iD7 ATR accessory, with a diamond crystal), melting point determination (in an open glass capillary system), elemental analysis (performed on an Elemental Vario MicroCube analyser) and high resolution electrospray ionization mass spectrometry (on an orbitrap q-exactive focus mass spectrometer).

The crystal growth of the different polymorphs of the synthesized compounds was achieved using different recrystallization techniques: recrystallization from the melted compound, recrystallization from different solutions, whose solvent was left to evaporate at room temperature, and sublimation of the solid material. The polymorphic screening of the obtained crystals was performed visually, in the cases where solids of very different colors were obtained, and also by Raman and FTIR spectroscopies, in particular when the colors of the obtained products appeared similar at visual inspection. When more than one of the described methods yielded the same polymorph, only the methods who produced crystals with enough quality for structure determination by X-ray diffraction were chosen to be reported in Chapters 3 and 4.

References

- 1 U. T. Bhalerao, B. C. Raju and P. Neelakantan, A Simple Debenzylation of O-Substituted Phenol Ethers Using Hydrobromic Acid in Presence of Phase Transfer Catalyst, *Synth. Commun.*, 1995, **25**, 1433–1439.
- 2 X. He, U. J. Griesser, J. G. Stowell, T. B. Borchardt and S. R. Byrn, Conformational color polymorphism and control of crystallization of 5-methyl-2-[(4-methyl-2-nitrophenyl)amino]-3-thiophenecarbonitrile, *J. Pharm. Sci.*, 2001, **90**, 371–388.
- 3 L. Shi, J. X. Wu, M. Z. Fu and Q. T. Yong, A novel, efficient, and highly selective O-Bn bond cleavage reaction via a rare K-induced electron transfer process, *Synlett*, 2002, **2002**, 1505–1507.
- 4 B. S. Rathore, V. Gupta, R. R. Gupta and M. Kumar, Synthesis of 7-chloro-9-trifluoromethyl-7-fluorophenothiazines, *Heteroat. Chem.*, 2007, **18**, 81–86.
- 5 M. Gao, Z. Shi, M. Wang and Q. H. Zheng, [¹¹C]Olanzapine, radiosynthesis and lipophilicity of a new potential PET 5-HT₂ and D₂ receptor radioligand, *Bioorg. Med. Chem. Lett.*, 2013, **23**, 1953–1956.
- 6 Synthetic method of intermediate of olanzapine - CN103524529A.
- 7 A. A. Thomas, K. W. Hunt, M. Volgraf, R. J. Watts, X. Liu, G. Vigers, D. Smith, D. Sammond, T. P. Tang, S. P. Rhodes, A. T. Metcalf, K. D. Brown, J. N. Otten, M. Burkard, A. A. Cox, M. K. G. Do, D. Dutcher, S. Rana, R. K. Delisle, K. Regal, A. D. Wright, R. Groneberg, K. Scarce-Levie, M. Siu, H. E. Purkey, J. P. Lyssikatos and I. W. Gunawardana, Discovery of 7-tetrahydropyran-2-yl chromans: β -site amyloid precursor protein cleaving enzyme 1 (BACE1) inhibitors that reduce amyloid β -protein (A β) in the central nervous system, *J. Med. Chem.*, 2014, **57**, 878–902.
- 8 P. I. Abronina, K. G. Fedina, N. M. Podvalnyy, A. I. Zinin, A. O. Chizhov, N. N. Kondakov, V. I. Torgov and L. O. Kononov, The use of O-trifluoroacetyl protection and profound influence of the nature of glycosyl acceptor in benzyl-free arabinofuranosylation, *Carbohydr. Res.*, 2014, **396**, 25–36.

3. *N*-picryl-*p*-toluidine Analogues

N-picryl-*p*-toluidine (IUPAC name: 2,4,6-trinitro-*N*-(*p*-tolyl)aniline; C₁₃H₁₀N₄O₆) was first described in the beginning of the 20th century, in 1909, by Busch and Pungs,¹ as a colored polymorphic system, with three different colored polymorphs, which were described as being yellow, orange-yellow and dark-red colored. In 1935, Wood *et al.*² presented the crystallographic structures for the orange-yellow and dark-red polymorphs. Six decades later, in 1996, the system was still matter of study and Yasui and co-workers³ described the conversion of the orange-yellow form into the more stable dark-red polymorph through the liquid phase. In 2008, Braun *et al.*⁴ revisited the orange-yellow and dark-red polymorphs, in a work where several analytical methods were employed and where the production of the two different polymorphs was thoroughly described. Intriguingly, the yellow polymorph reported in the 1909's original work has not been observed in any other published article since then. In 2001, Ilyina *et al.*⁵ proposed that the reported material corresponded to a water solvate and not to a color polymorph of *N*-picryl-*p*-toluidine.

The different colors of the two polymorphs of *N*-picryl-*p*-toluidine have been attributed to the variation of the length (and corresponding strength) of the intramolecular N–H··O bond between the hydrogen atom of the amine moiety and one of the oxygen atoms belonging to the nitro group of the molecule, induced by crystal packing.⁴ In particular, this color dependence is associated with intramolecular effects affected by the strength of the hydrogen bond that lead to an increased delocalization of the secondary amino nitrogen lone-pair electrons into the aromatic rings' moiety in the dark-red polymorph.⁴ This is an interesting case of color packing polymorphism where both polymorphs present the same conformer of *N*-picryl-*p*-toluidine, with different degrees of conformational relaxation due to intermolecular interactions.

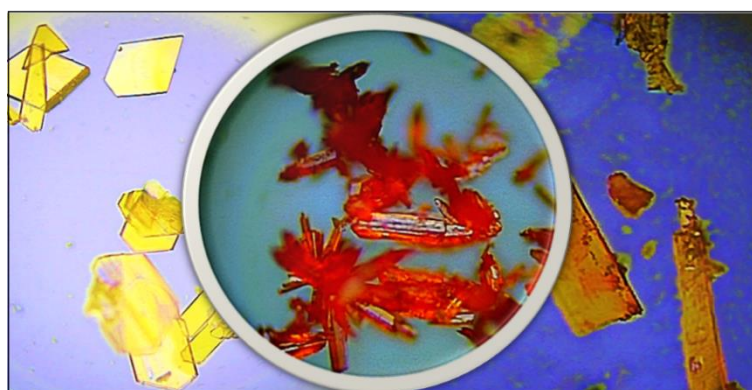
In this work, two *N*-picryl-*p*-toluidine analogue compounds were studied: 2,4,6-trinitro-*N*-(*m*-tolyl)aniline (TMA; C₁₃H₁₀N₄O₆ – Sections 3.1 and 3.2), which presented the methyl group in the *meta* position of the toluidine ring, rather than in the *para* position as in the parent compound, and 3-((2,4,6-trinitrophenyl)amino)phenol (TAP; C₁₂H₈N₄O₇ – Section 3.2), which has a hydroxyl group in the same *meta* ring position as in TMA.

References

- 1 M. Busch and E. Pungs, Über isomere Verschiedenfarbige Pikrylamine, *J. für Prakt. Chemie*, 1909, **79**, 546–554.
- 2 R. G. Wood, S. H. Ayliffe and N. M. Cullinane, XXXIII. A crystallographic and x-ray investigation of some diphenylamine derivatives, *London, Edinburgh, Dublin Philos. Mag. J. Sci.*, 1935, **19**, 405–416.
- 3 M. Yasui, K. Taguchi and F. Iwasaki, Dynamic Behavior of *N*-(2,4-Dinitrophenyl)-*o*-Anisidine Crystals, *Mol. Cryst. Liq. Cryst. Sci. Technol. Sect. A. Mol. Cryst. Liq. Cryst.*, 1996, **277**, 167–176.
- 4 D. E. Braun, T. Gelbrich, R. K. R. Jetti, V. Kahlenberg, S. L. Price and U. J. Griesser, Colored Polymorphs: Thermochemical and Structural Features of *N*-Picryl-*p*-toluidine Polymorphs and Solvates, *Cryst. Growth Des.*, 2008, **8**, 1977–1989.
- 5 I. G. Ilyina, O. V. Mikhalev, K. P. Butin, B. N. Tarasevich and B. M. Uzhinov, Differently coloured crystalline modifications of organic autocomplexes of the nitroaromatic type, *Synth. Met.*, 2001, **120**, 1067–1068.

3.1. TMA

The article that composes this subsection is entitled *2,4,6-Trinitro-N-(m-tolyl)aniline: A New Polymorphic Material Exhibiting Different Colors* and was published online in ACS Publications' *Crystal Growth & Design* (Vol. 21; Issue 12; Pages 7269-7284) on 18th November 2021. On the day of the submission of this Thesis, according to the Google Scholar, this article has been cited twice by other peer-reviewed published works and has received 42 reads in Research Gate.



Supporting Information:

https://pubs.acs.org/doi/suppl/10.1021/acs.cgd.1c01123/suppl_file/cg1c01123_si_001.pdf

Authors: Bernardo A. Nogueira, Susana M. M. Lopes, Susy Lopes, Timur Nikitin, Ana Clara B. Rodrigues, Maria Ermelinda S. Eusébio, José A. Paixão, Teresa M. V. D. Pinho e Melo, Alberto Milani, Chiara Castiglioni and Rui Fausto

Corresponding author: Bernardo A. Nogueira

Author contributions: Bernardo A. Nogueira conceptualized the study, wrote a preliminary version of the manuscript and participated in most of the experimental work and in the fully periodic theoretical studies. Rui Fausto contributed to the conceptualization of the study, took responsibility for its supervision and wrote the final version of the manuscript. Susana M. M. Lopes and Teresa M. V. D. Pinho e Melo were responsible for the development of the synthetic route and its implementation. Susy Lopes and Timur Nikitin. participated in part of the theoretical studies and performed the experimental study of the monomeric compound. Ana Clara B. Rodrigues was responsible for the absorption spectroscopy experiments and its interpretation. Alberto Milani and Chiara Castiglioni participated in

the full periodic theoretical calculations and the respective interpretation and conclusions. Maria Ermelinda S. Eusébio participated in the design of the DSC studies. José A. Paixão performed the XRD studies and wrote the first version of the corresponding section of the manuscript. All authors have participated in the discussion of the results and agreed with the final version of the manuscript.

Synopsis:

This was the first work published by us concerning the development and the physical and chemical characterization of a novel compound exhibiting color polymorphism. 2,4,6-Trinitro-*N*-(*m*-tolyl)aniline (TMA) was designed to be compared with its parent compound, and constitutional isomer, 2,4,6-trinitro-*N*-(*p*-tolyl)aniline, which presents the methyl group of the toluidine ring in the *para* position, regarding to the amine group that links the two aromatic rings, whereas TMA presents the same CH₃ group in the *meta* position. In this article, we present the structural, spectroscopic, and thermodynamic characterization of three identified polymorphs of TMA: one yellow, one orange and one red. Very interestingly, unlike 2,4,6-trinitro-*N*-(*p*-tolyl)aniline, TMA system presents both conformational and packing color polymorphism, which gives rise to the wider-ranging differences in the colors presented by the different crystal structures.

2,4,6-Trinitro-*N*-(*m*-tolyl)aniline: A New Polymorphic Material Exhibiting Different Colors

Bernardo A. Nogueira,^{1,2,*} Susana M. M. Lopes,¹ Susy Lopes,¹ Timur Nikitin,¹

Ana Clara B. Rodrigues,¹ Maria Ermelinda S. Eusébio,¹ José A. Paixão,³

Teresa M. V. D. Pinho e Melo,¹ Alberto Milani,² Chiara Castiglioni² and Rui Fausto¹

¹ *University of Coimbra, CQC-IMS, Department of Chemistry, P-3004-535 Coimbra, Portugal.*

² *CMIC, Dipartimento di Chimica, Materiali e Ingegneria Chimica "G. Natta", Politecnico di Milano, Italy.*

³ *University of Coimbra, CFisUC, Department of Physics, P-3004-516 Coimbra, Portugal*

Abstract

2,4,6-Trinitro-*N*-(*m*-tolyl)aniline or *N*-picryl-*m*-toluidine (abbreviated as TMA), exhibiting color polymorphism, was synthesized and characterized structurally, spectroscopically and thermodynamically. The studies consider both the isolated molecule of the compound (studied theoretically at the DFT(B3LYP)/6-311++G(d,p) level, and experimentally by matrix isolation infrared spectroscopy) and its polymorphic crystalline phases. The investigations on the isolated molecule allowed to evaluate the major intramolecular interactions determining the conformational preferences of the compound and characterize it in detail from the vibrational point of view. Two conformers were found (A and B), which differ in the relative orientation of the ring moieties of the molecule. Polymorph screening, by recrystallization of the compound using different solvents, allowed to identify three different polymorphs, exhibiting red, orange and yellow colors, which were subsequently characterized structurally by single crystal X-ray diffraction, vibrationally, by infrared and Raman spectroscopies (complemented by fully-periodic DFT calculations on the crystals), electronically, using solid state ultraviolet-visible absorption spectroscopy, and thermodynamically, by differential scanning calorimetry and polarized light thermomicroscopy. The yellow polymorph was found to be a conformational polymorph of the orange and red ones, while the last two are packing polymorphs. Mechanistic insights on the causes of the different colors of the polymorphs are presented. On the whole, the reported investigation constitutes a comprehensive structural (for both the isolated molecule and crystalline phases), spectroscopic and thermal analysis of the newly prepared compound, with particular emphasis on the rare color polymorphism it exhibits.

Keywords: 2,4,6-trinitro-*N*-(*m*-tolyl)aniline, color polymorphism, molecular structure, crystal structure, thermal analysis, infrared, Raman and UV-Vis spectroscopies

* Corresponding author e-mail: ban@qui.uc.pt

1. Introduction

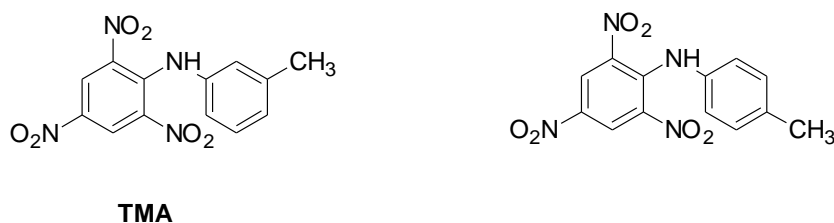
From the Greek *poly* (many) and *morph* (form), polymorphism refers, in the crystallographic context, to the ability of a compound to exist in more than one crystalline structure.^{1,2} Polymorphs, despite being composed by the same compound, present different physical, chemical and mechanical properties. This fact makes polymorphic materials interesting (and challenging) chemical systems from a fundamental perspective (*e.g.*, as ideal objects to investigate crystallization and the factors affecting crystallization), while it is also on the basis of their attractiveness for application in various fields, in particular in dyes, agrochemicals, pigment and pharmaceutical industries.¹⁻³

There are two main types of polymorphism, the conformational polymorphism, and the packing polymorphism. The first implies the existence of different conformers of the same compound in the different polymorphs (a new conformer is obtained every time the variation of torsion angles in a molecule leads to a region of the molecule's potential energy surface that is associated with a new minimum that is structurally not equivalent to the original one).^{1,4} On the other hand, packing polymorphism relates to polymorphs that are constituted by the same conformer.^{1,4} In the case of conformational polymorphism, the intermolecular forces are strong enough to supersede the intramolecular forces and stabilize, in the crystalline state, conformers that are not the conformational ground state for the isolated molecule. In contrast, in the case of the packing polymorphism, most frequently intramolecular forces determine the conformer which is present in the different polymorphs. This is in general the most stable conformer found for the isolated molecule, but the selection of a higher-energy form upon crystallization is not a rare phenomenon. In both types of polymorphism (conformational and packing), intermolecular interactions are distinct in the different polymorphs; in the case of conformational polymorphism, both inter- and intramolecular interactions are essentially different from polymorph to polymorph and, together, determine the dissimilar properties of the polymorphs.^{1,2,5-7}

Color polymorphism is the term used to define a compound presenting either conformational or packing polymorphs that display different color.¹ It is a rather uncommon property of polymorphic systems, and that is why, in spite of their relevant potential applications in several areas, like in pigments and sensors industries, for example,⁸⁻¹¹ the number of known compounds exhibiting color polymorphism is still very limited.¹²⁻²¹

In this work, we describe a compound that presents color polymorphism. The compound, 2,4,6-trinitro-*N*-(*m*-tolyl)aniline (C₁₃H₁₀N₄O₆, or *N*-picryl-*m*-toluidine; Scheme 1, abbreviated TMA) is made by the combination of a picryl moiety with a *meta*-toluidine ring, and it is a close parent of the previously investigated *para*-toluidine analogue, 2,4,6-trinitro-*N*-(*p*-tolyl)aniline (or *N*-picryl-*p*-toluidine; Scheme 1). *N*-picryl-*p*-toluidine was reported for the first time in 1909, by Busch and Pungs, and its color polymorphism is known since then.¹⁸ Subsequent studies on this compound allowed for the determination of the crystal structures of its orange-yellow and dark-red polymorphs, and the

investigation of their interconversion.^{22–26} The color polymorphism in *N*-picryl-*p*-toluidine is a typical case of packing polymorphism, where the same conformer is present in the different polymorphs.¹ Very interestingly, as it is shown in the present article, the synthesized *N*-picryl-*m*-toluidine analogue gives rise to 3 different polymorphs, which show both packing and conformational types of color polymorphism. The different position of the methyl group in the toluidine ring, which favors a larger number of conformers resulting from the rotation about the N–C_(tolyl) bond in the case of the presently studied *m*-substituted molecule, compared to the *p*-substituted compound previously investigated, is the main structural reason justifying the different behavior of the two compounds regarding the number of polymorphs and type of structural relation between them.



Scheme 1 – 2,4,6-Trinitro-*N*-(*m*-tolyl)aniline (TMA; left), and 2,4,6-trinitro-*N*-(*p*-tolyl)aniline (right).

In the next sections of this article, we will present the details of the synthesis of TMA, followed by the theoretical characterization of its conformational space using the DFT method, and the subsequent investigation of the isolated molecules of the compound trapped into a cryogenic inert matrix, by infrared spectroscopy. The interpretation of the spectroscopic results is supported by the comparison of the experimentally obtained spectra with those predicted theoretically for the experimentally relevant conformers. These investigations on the isolated molecule shed light on the major intramolecular interactions determining the conformational preferences of the compound. Then, the results of the performed polymorph screening, by recrystallization of the compound using different solvents, are presented. Three different polymorphs, exhibiting red, orange and yellow colors, were obtained, which were afterward characterized structurally by single crystal X-ray diffraction, vibrationally, by infrared and Raman spectroscopies (complemented by fully periodic DFT calculations on the crystals), electronically, using solid state ultraviolet-visible (UV-visible) absorption spectroscopy, and thermodynamically, by differential scanning calorimetry (DSC) and polarized light thermomicroscopy (PLTM). On the whole, the reported investigation constitutes a comprehensive structural (for both the isolated molecule and crystalline phases), spectroscopic and thermal analysis of the studied compound, with particular emphasis on the rare color polymorphism it exhibits.

2. Experimental and Computational Methods and Instrumentation

2.1. Experimental methods and instrumentation

The reagents and solvents were obtained commercially with analytical grade. For the initial characterization of the synthesized compound, the ¹H and ¹³C NMR spectra (Figure S1, in the

Supporting Information) were recorded on a Bruker Avance III instrument, operating at 400 MHz and at 100 MHz, respectively. The solvent used was deuteriochloroform. The infrared (IR) spectrum (Figure S2) was recorded on an Agilent Cary 630 FTIR Fourier transform spectrometer, with a diamond-based attenuated total reflection (ATR) cell (Smart Orbit). Melting point (uncorrected) was determined in an open glass capillary. Elemental analysis was carried out with an Elemental Vario MicroCube analyzer. Thin-layer chromatography (TLC) analyses were performed using precoated silica gel plates.

The cryogenic matrices were prepared by co-deposition of vapors of the studied compound together with a large excess of the matrix host-gas [Ar (N60) obtained from Air Liquide] onto a CsI substrate placed at the cold (15 K) tip of the cryostat (ARS Cryogenics closed-cycle helium refrigeration system, with a DE-202SI expander). The solid compound was sublimated from a homemade Knudsen cell, the calve nozzle being kept at room temperature. The temperature of the CsI window was measured directly at the sample holder by a silicon diode sensor, connected to a digital temperature controller (LakeShore 335 Temperature Controller), which provides an accuracy of 0.1 K. The IR spectrum of the matrix-isolated compound, in the 4000–400 cm^{-1} range, was obtained using a Thermo Nicolet iS50 Fourier transform infrared spectrometer equipped with an MCT/A detector and a KBr beam splitter, with 0.5 cm^{-1} spectral resolution and 256 scans. To avoid interference from atmospheric H_2O and CO_2 , a stream of dry CO_2 -filtered air was continuously purging the optical path of the spectrometer.

The different polymorphs of TMA were obtained by recrystallization with the slow evaporation of different solvents at room temperature. 30 mg of the compound were dissolved in 5–10 mL of the solvent, depending on the solubility, the solutions were filtered to prevent any crystal seed and the solvent left to evaporate at room temperature. The solvents used were toluene, 1,4-dioxane, tetrahydrofuran (THF), dichloromethane, chloroform, carbon tetrachloride, acetone, butanone, dimethyl sulfoxide (DMSO), ethyl acetate, formic acid, acetic acid, methanol, ethanol, 1-propanol, dimethylformamide (DMF) and acetonitrile.

The IR spectra of the polymorphs were collected in the attenuated total reflectance (ATR) mode, using a Thermo Scientific FT-IR Nicolet iS5 system, with an iD7 ATR accessory (angle of incidence: 45; crystal: diamond). The spectra were recorded in the wavenumber range of 400–4000 cm^{-1} , with spectral resolution of 1 cm^{-1} , being the average of 512 scans. The Raman spectra were obtained with 4 cm^{-1} resolution, in the 50–3350 cm^{-1} wavenumber range, with 785 nm excitation provided by a solid-state laser, using a BWTEK i-Raman Pro instrument, equipped with a CCD detector. The spectra were collected using a 20 \times magnification objective, the exposure time of 10 seconds, with 10 accumulations, and a laser power at the sample of \sim 4 mW, to prevent thermal degradation of the sample.

The single crystal X-ray diffraction experiments were performed at room temperature using graphite monochromated $\text{MoK}\alpha$ ($\lambda = 0.71073 \text{ \AA}$) radiation in a Bruker APEX II diffractometer. The structure was solved by the dual-space algorithm implemented in SHELXT-2018/2, and full-matrix least-squares refinement of the structural model was performed using SHELXL-2018/3. All non-

hydrogen atoms were refined anisotropically. Hydrogen atoms were placed at calculated idealized positions and refined as riding using SHELXL-2018/3 default values,²⁷ except for those of the N–H group that were refined isotropically with a displacement parameter constrained to 1.2x their parent atoms.

Full details on data collection and structure refinement are provided in the Supporting Information (Crystallographic Data). A summary of the data collection and refinement details is given in Table 1. CIF files containing the supplementary crystallographic data were deposited at the Cambridge Crystallographic Data Centre, with reference CCDC 2100574 (yellow polymorph), 2100587 (red polymorph) and 2100671 (orange polymorph).

Table 1 – Summary of the single-crystal X-ray data collection and crystal structure refinement.

Chemical formula	C ₁₃ H ₁₀ N ₄ O ₆		
Formula weight	318.25		
Color, shape	yellow/plate	orange/plate	red/block
Space group	<i>P</i> 2 ₁ / <i>c</i>	<i>P</i> na2 ₁	<i>P</i> -1
Temperature(K)	292(2)	294(2)	292(2)
Cell volume (Å ³)	681.42(4)	1388.0(3)	681.42(4)
Crystal system	monoclinic	orthorhombic	triclinic
<i>a</i> (Å)	12.5800(7)	29.971(3)	7.5195(2)
<i>b</i> (Å)	8.0014(4)	9.0537(10)	8.3723(3)
<i>c</i> (Å)	15.0156(8)	5.1150(6)	12.2263(4)
α (deg)	90	90	81.0389(19)
β (deg)	110.794(2)	90	81.9157(18)
γ (deg)	90	90	64.0565(17)
<i>Z</i> / <i>Z'</i>	4/1	4/1	2/1
<i>D</i> _c (Mg m ⁻³)	1.496	1.523	1.551
Radiation (Å) (graphite, monochromated)	0.71073	0.71073	0.71073
Max. crystal dimensions (mm)	0.53×0.45×0.18	0.43×0.35×0.19	0.25×0.19×0.17
Θ range (deg)	1.732-27.496	2.350-27.497	3.257-27.482
Range of <i>h, k, l</i>	-16,16;-10,10;-19,19	-38,38;-11,11;-6,6	-9,9;-10,10;-15,15
Reflections measured/independent	26093/3250	39121/3190	53896/3125
Reflections observed (<i>I</i> > 2 σ)	1931	2141	2031
Data/restraints/parameters	3250/0/212	3190/1/212/	3125/0/212
GOF	1.029	1.046	1.035
<i>R</i> ₁ (<i>I</i> > 2 σ)	0.0532	0.0448	0.0556
<i>wR</i> ₂	0.1613	0.1054	0.1714
Function minimized	$\Sigma w (F_o ^2 - S F_c ^2)$	$\Sigma w (F_o ^2 - S F_c ^2)$	$\Sigma w (F_o ^2 - S F_c ^2)$
Diff. density final max/min (e Å ⁻³)	0.255, -0.253	0.202, -0.176	0.426, -0.269

DSC experiments were performed using a PerkinElmer Pyris-1 power compensation calorimeter, with a 1:1 v/v ethylene glycol-water cooler at $-25\text{ }^{\circ}\text{C}$ and a 20 mL min^{-1} nitrogen purge flow. Hermetically sealed aluminum pans were used (samples weighting between 1 and 2 mg), with an empty pan used as reference. Indium (PerkinElmer, 99.99%, $T_{\text{fus}} = 156.60\text{ }^{\circ}\text{C}$) and biphenyl (CRM LGC, $T_{\text{fus}} = 68.93\text{ }^{\circ}\text{C} \pm 0.03\text{ }^{\circ}\text{C}$) were used for temperature and enthalpy calibrations. In the experiments, the samples were scanned from 25 to $140\text{ }^{\circ}\text{C}$ at a scan rate of $10\text{ }^{\circ}\text{C min}^{-1}$. Polarized light thermal microscopy (PLTM) images ($200\times$) were obtained within the range of temperature of the DSC experiments on a system that includes a DSC600 Linkam hot stage attached to a Leica DMRB microscope.

The absorption spectra of the crystalline samples were recorded by collecting diffuse reflectance using an Agilent Cary 5000 DRA UV-vis-NIR spectrometer, with an integrating sphere accessory with detection in the 200–2500 nm range. The background correction was performed by collecting the baseline with 0% and 100% reflectance (using a blocked beam and a polytetrafluoroethylene reference sample, respectively) before the collection of the spectra of the investigated samples. The conversion to absorption was performed assuming the Kubelka-Munk function.²⁸ The color parameters were determined according to the CIE (Commission Internationale de l’Eclairage proceedings) 1931 scale diagram.²⁹ The x and y color parameters were determined from the transmittance spectra acquired on the Agilent Cary 5000 DRA UV-Vis-NIR spectrometer.

2.2. Computational details

The density functional theory (DFT) calculations performed on the isolated molecule of the compound, including the geometry optimization, the dihedral coordinate scan, and the vibrational spectra of the different conformers of the studied molecule were carried out using the Gaussian 09 program.³⁰ Specifically, the three-parameter B3LYP density functional, with the Becke’s gradient exchange correction³¹ and the Lee, Yang and Parr correlation functional,³² was used together with the 6-311++G(d,p) basis set.³³ Calculated frequencies for the monomeric species were scaled by 0.982.

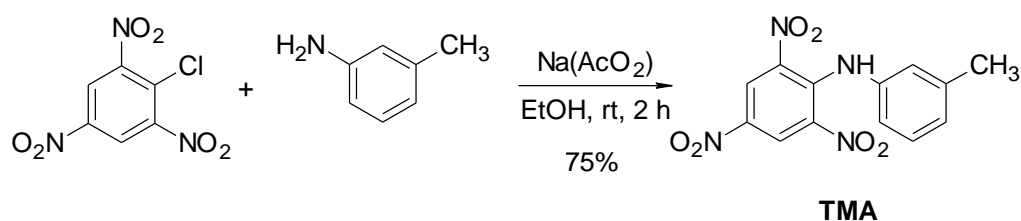
The full geometry optimization of the crystal structures and prediction of IR and Raman spectra of the three polymorphs of the studied compound were carried out using the CRYSTAL17^{34,35} code, within the DFT framework. To test the accuracy of different functionals and basis sets, the B3LYP^{31,32} and PBE0³⁶ hybrid exchange–correlation functionals were used, together with the 6-31G(d,p) basis set. The empirical correction for dispersion interaction (DFT-D) developed by Grimme^{37–39} was also employed to consider van der Waals and other dispersion attractive interaction forces. In all calculations, the atomic positions and the lattice parameters were fully optimized. The input structures for the calculations were those experimentally determined and presented in this work. The vibrational frequencies calculations at the Γ point have been performed on the optimized geometries, as achieved

by the diagonalization of the numerically calculated Hessian matrices. All predicted frequencies were scaled by a single empirical factor (0.9512)⁴⁰ to allow a better comparison with the experimental data.

3. Results and Discussion

3.1. Synthesis of the compound and characterization of the obtained material

2,4,6-Trinitro-*N*-(*m*-tolyl)aniline (TMA) was prepared by the condensation of *m*-toluidine with 1-chloro-2,4,6-trinitrobenzene (Scheme 2), under conditions adapted from literature.⁴¹ Sodium acetate anhydrous (0.170 g, 2.07 mmol) and *m*-toluidine (0.222 mL, 2.07 mmol) were added to a stirred solution of 1-chloro-2,4,6-trinitrobenzene (0.512 g, 2.07 mmol) in ethanol (15 mL). The reaction mixture was stirred at room temperature for 2 h (monitored by TLC). The precipitated product was filtered, washed with 30% aqueous solution of ethanol and dried under vacuum to give an orange solid (0.490 g, 75%). mp 120.0–121.8 °C (from ethanol). IR (ATR) ν 735, 1090, 1173, 1293, 1336, 1507, 1530, 1591, 1602, 1620 and 3293 cm^{-1} . ¹H NMR δ (CDCl₃): 2.34 (s, 3H), 6.87–6.88 (m, 2H), 7.10 (d, $J=7.6$ Hz, 1H), 7.25–7.29 (m, 1H), 9.09 (s, 2H), 10.28 (br s, 1H). ¹³C NMR δ (CDCl₃): 21.4, 118.0, 121.5, 127.2, 128.6, 129.8, 137.2, 137.9, 139.0, 140.3. Anal. Calc. for C₁₃H₁₀N₄O₆: C 49.06, H 3.17, N 17.61. Found: C 49.07, H 3.03, N 17.59. Only one polymorph, of orange color, was obtained directly from the synthetic procedure.



Scheme 2 – Synthesis of 2,4,6-trinitro-*N*-(*m*-tolyl)aniline (TMA).

3.2. DFT calculations and matrix-isolation IR investigation of the TMA isolated molecule

The molecule of the studied compound has three *a priori* conformationally relevant coordinates, which are associated with the internal rotations about the C_(picryl)–N and N–C_(tolyl) bonds of the bridge, and the rotation of the methyl group. However, the presence of the two nitro groups in the picryl moiety *ortho* to the C_(picryl)–N bond leads to a strong conformational preference for structures where the picryl–NH fragment is nearly planar, due to the establishment of an intramolecular hydrogen bond of N–H \cdots O type, forming a *pseudo*-6-membered ring. Since the conformation of the picryl–NH moiety is determined by this reason, the internal rotation around the N–C_(tolyl) bond becomes the single conformationally relevant coordinate associated with the bridging group.

A series of relaxed scan calculations was then performed, where the 4C–1N–7C–12C dihedral angle was chosen as driving coordinate, varying by increments of $\pm 10^\circ$, while all other internal

coordinates were optimized. Potential energy profiles corresponding to rotations in the two directions (clockwise and anti-clockwise) were computed and are depicted in Figure 1. The starting geometry and the direction of the rotation influence the obtained energy profiles by the reasons explained below. Altogether, the obtained energy profiles allowed for identification of two pairs of equivalent-by-symmetry conformers (herein-after referred to as conformers A/A' and B/B', or just A and B when there are no doubts of the meaning of the abbreviated version; see Figure 2). Figure 3 shows the potential energy profiles for methyl group rotation in each one of the conformers.

The potential energy plots shown in Figure 1 are very interesting. Along the rotation of the tolyl moiety around the 1N–7C bond, the orientation of the non-hydrogen-bonded *ortho*-nitro group has to change, in order to avoid steric hindrance when the tolyl group tries to approach co-planarity with the picryl moiety. Inversion at the amino bridge nitrogen atom also occurs during the scans. Hence, when the scan starts at the geometry of the minimum B, corresponding to a 4C–1N–7C–12C dihedral angle of 144.0°, using steps of –10°, the molecule first crosses the B→A isomerization barrier (which amounts to 13.0 kJ mol⁻¹), and reaches the global minimum (conformer A; 4C–1N–7C–12C of 40.4°), which stays 0.5 kJ mol⁻¹ below the energy conformer B. Then, the energy progressively raises to a value of 37.5 kJ mol⁻¹, which occurs for a dihedral angle of ca. –56.0°, where the change of orientation of the non-hydrogen-bonded *ortho*-nitro group takes place together with the inversion at the nitrogen of the amine bridge, so that energy reduces abruptly. Continuation of the scan after this point, leads to the B' minimum by overcoming the A'→B' conformational transition. The subsequent scan from B' in the direction of B follows a similar pattern, with the energy growing progressively till reaching the position at which an abrupt energy decrease takes place due to the change of the conformation of the non-hydrogen-bonded *ortho*-nitro group and inversion at the nitrogen of the amine bridge, at a position corresponding to a 4C–1N–7C–12C dihedral angle of ca. 124.0°, which is already smaller than that of B. Hence, the scan starting from B for decreasing values of the 4C–1N–7C–12C dihedral angle does not allow to reach the minimum A', but only A and B', and it does not return to the initial minimum B when moving from B'. However, it shall be noticed that these findings do not mean that the different minima do not interconvert. Indeed, for example, after the abrupt change in the geometry taking place at ca. –56.0°, the molecule still reaches the potential energy well of A', so that the conversion between A and A' can effectively occur in practice (the same can be stated for the conversion between B' and B). If the scan is performed in the opposite direction, identical conclusions can be drawn, both regarding the format of the potential energy profile along the scan, and about the real possibility of conversion between A' and A, on one side, and B and B' on the other. The scans starting at the position of the global minimum A yield identical results.

Taking into account the results discussed above, the barrier for interconversion between conformer A and B (and their equivalent forms, A' and B') is of 13.5 kJ mol⁻¹ (13.0 kJ mol⁻¹ in the reverse direction) and those between the symmetry-related forms of both conformers, A and A', and B

and B', are 37.5 and 30 kJ mol⁻¹, respectively. Conformer A is predicted to be only 0.5 kJ mol⁻¹ more stable than conformer B, which in practical terms means that they are nearly iso-energetic. In both conformers, the *para* and the *ortho*-hydrogen bonded nitro groups are nearly coplanar with the aromatic ring to which they are bound (these two groups are tilted out of the plane of the ring by 0.1 and 11.0° respectively, in both conformers), while the second *ortho* nitro group is tilted by -40.2 and -41.2° from the ring in conformers A and B, respectively, leading to a geometry where this group is nearly parallel to the tolyl moiety. The geometry around the intramolecular hydrogen bond is identical in both conformers, with the 5C-4C-1N-7C and 5C-4C-1N-1H dihedral angles being 154.4° and -13.4°, respectively, and the 1N-1H bond length being 1.017 Å in both conformers, and the 1H...5O distance being 1.813 and 1.811 Å in conformers A and B, respectively. The 4C-1N and 1N-7C bond lengths are also equal in the two conformers, the first being considerably shorter (1.348 Å) than the latter (1.425 Å) due to the π-electron delocalization from 1N to the picryl ring, which awards the 4C-1N a substantial double bond character.

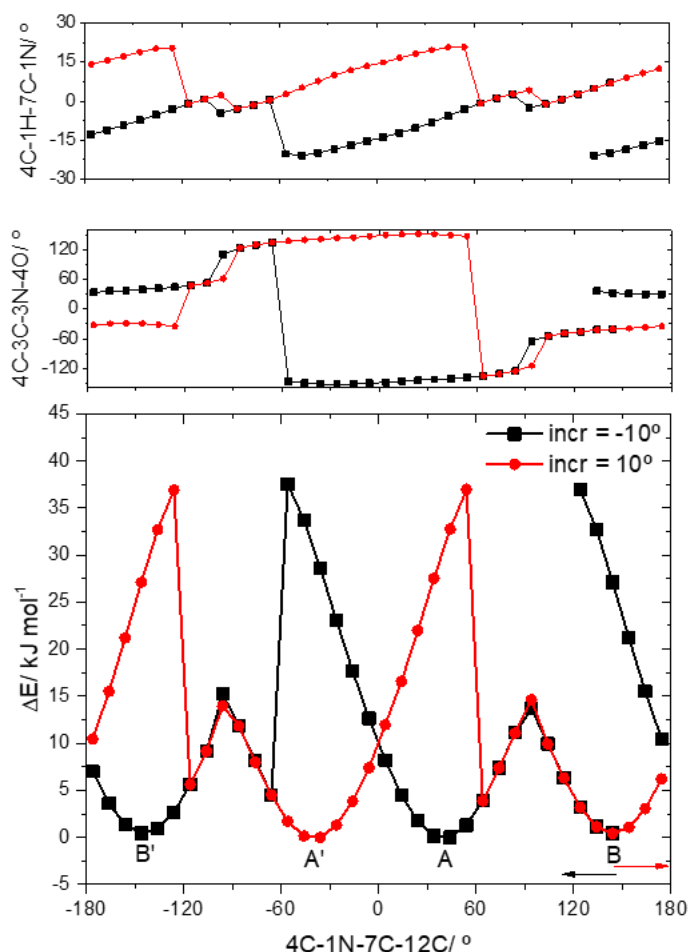


Figure 1 – Computed B3LYP/6-311++G(d,p) relaxed potential energy scans corresponding to the internal rotation around the 1N-7C bond, as defined by the 4C-1N-7C-12C torsion angle. The minima A/A' and B/B' correspond to the two pairs of symmetry-equivalent minima. The increment (incr) in the driving coordinate is equal to ±10°. The arrows indicate the direction of the scans. The top and middle panels show the variation of the pyramidalization degree at the bridging nitrogen atom (as expressed by the dihedral 4C-1H-7C-1N) and of the orientation of the non-hydrogen-bonded *ortho* nitro group along the scans.

N-picryl-p-toluidine analogues

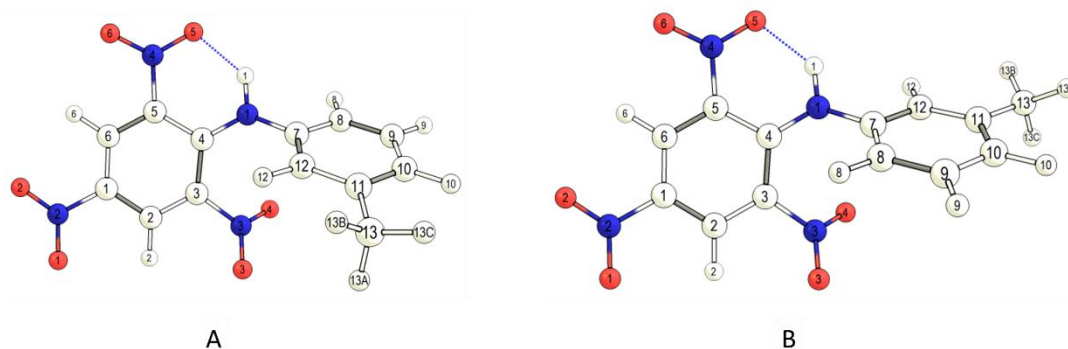


Figure 2 – Geometries of the two conformers of TMA, with atom numbering. Each of the represented structures have a symmetry-equivalent form (see Figure 1).

The orientation of the methyl group in the two conformers is slightly different (see Figure 3), though in both cases one of the hydrogen atoms stays nearly perpendicular to the ring and points roughly to the non-hydrogen-bonded *ortho* nitro group. However, in conformer A the 10C–11C–13C–H angle (97.3°) is larger than the 12C–11C–13C–H angle (i.e., the nearly perpendicular methyl hydrogen atom is turned to inside the molecule), while in conformer B the opposite trend is observed (the 10C–11C–13C–H angle is, in this case 80.6°). This structural feature is most probably due to the different importance in the two conformers of the long-range attractive interactions between the methyl group and the closest located nitro group, motivated by the rather distinct H...O(NO) distances in the two conformers (3.87 \AA in conformer A vs. 5.01 \AA in conformer B). It is also worth noticing that the barrier for the methyl internal rotation, though being very low in both conformers, is predicted to be nearly two-fold higher in conformer A than in conformer B (0.39 vs. 0.18 kJ mol^{-1}). This result is in consonance with the explanation given above for the different orientations of the methyl group in the two conformers, in particular the attractive nature of the long-range H...O(NO) interaction, which is stronger in conformer A, thus reducing in some extent the mobility of the methyl group.

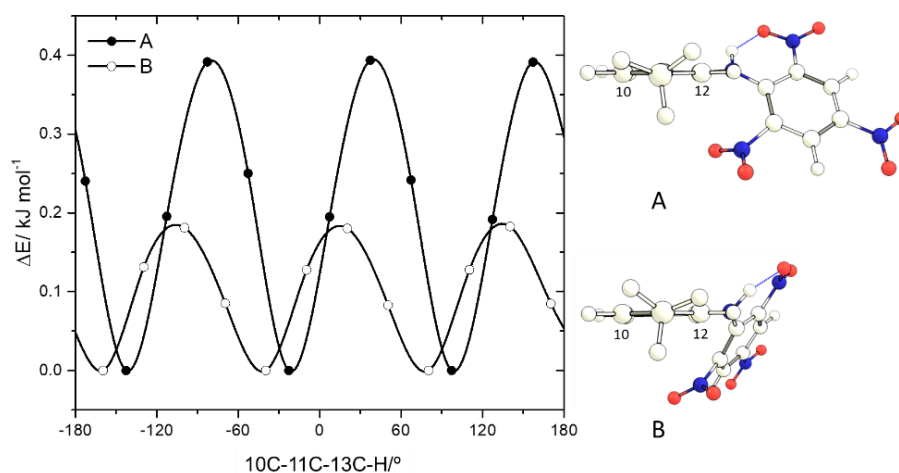


Figure 3 – Computed B3LYP/6-311++G(d,p) relaxed potential energy profile for internal rotation of the methyl group in conformers A and B.

Taking into account the results of the calculations, the populations of the two conformers in the room temperature (RT, 298.15 K) gas phase equilibrium are estimated as 54% (A) and 46% (B). The infrared spectrum of the TMA molecules trapped from the RT vapor of the compound into an argon matrix at 15 K was obtained. The registered data in the full 3600–600 cm^{-1} spectral range is provided in the Supporting Information Figure S3, while Figure 4 shows the 1700–1400 cm^{-1} region, whose analysis allows to conclude on the presence of the two conformers in the matrix in populations that match well the predicted ones.

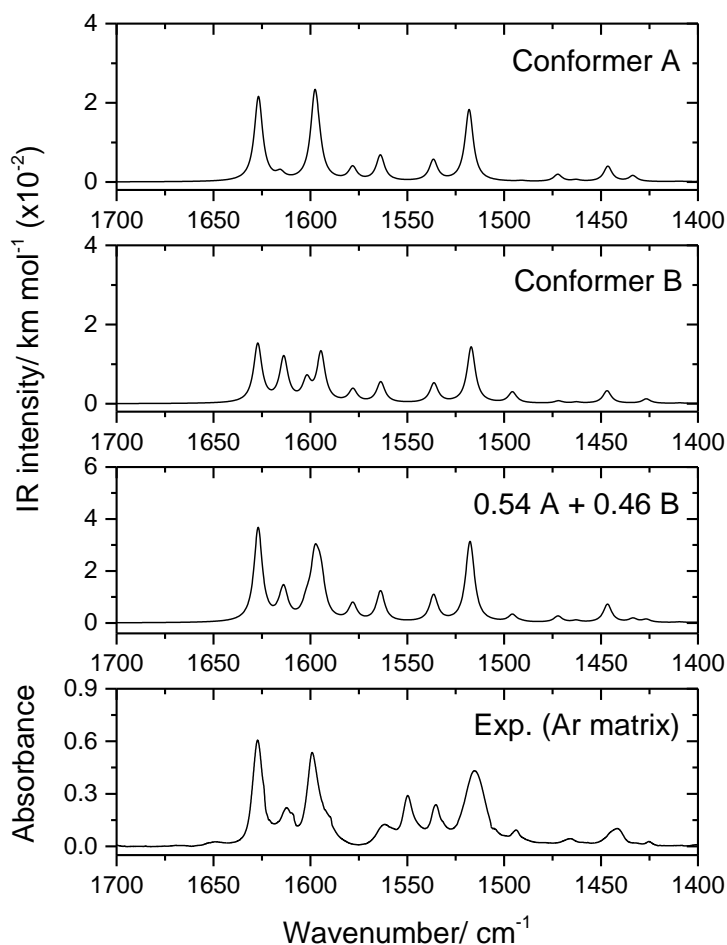


Figure 4 – Experimental infrared spectrum of monomeric TMA isolated in an argon matrix at 15 K (*bottom*), calculated spectra of conformers A and B (*top spectra*) and the simulated sum-spectrum of the conformational mixture according to the predicted room temperature Boltzmann populations. In the calculated spectra bands are represented by Lorentzian functions centered at the scaled B3LYP/6-311++G(d,p) calculated wavenumbers.

In Figure 4, the experimental spectrum can be compared with the calculated spectra of the two conformers and a spectrum built by adding these spectra with intensity scaled proportionally to the predicted relative populations of the conformers in the deposited RT equilibrium gaseous beam. It is considered here that this equilibrium is retained upon deposition, since the energy barriers separating the conformers are all large enough to prevent their interconversion during deposition.⁴² Though the

spectra of the two conformers are very similar, in the spectral region depicted in Figure 4 it is clear that the population weighted spectrum fits much better the experimental spectrum than the individual spectra of each conformer. The relative intensity of the feature appearing at ca. 1611 cm^{-1} (comparing it with the neighbor bands at 1627 and 1599 cm^{-1}) is predicted for conformer A to be much less intense than that observed experimentally, while for conformer B it is too intense. On the other hand, the population weighted spectrum fits nicely to the relative intensities of these bands in the experimental spectrum. Indeed, the reproduction of the experimental data by the sum spectrum is remarkable regarding both frequencies and relative intensities (see Figure 4), even for the low intensity bands, which does not happen for the spectra of the individual conformers. For example, the band at 1494 cm^{-1} , is absent from the spectrum of conformer A, and it is then a mark-band for the less stable conformer B. Below 1400 cm^{-1} , the reproduction of the experimental spectrum by the calculated sum-spectrum is also very good, though some bands ascribable mostly to vibrations of the nitro groups have been comparatively less well predicted by the calculations (the comparatively less good prediction of the frequencies associated with the vibrations of the nitro groups can also be noticed in the spectral region depicted in Figure 4, where the experimental bands at 1562 and 1550 cm^{-1} , which have significant contributions from the NO_2 anti-symmetric stretching modes, appear slightly overestimated by the calculations.)

The good overall agreement between the experimental and calculated spectra allowed a reliable assignment of the experimental bands, which is given in Table 2 (the full calculated vibrational data for the conformers are given in the Supporting Information Tables S1 and S2). In Table 2, the bands that are ascribable to the individual conformers are highlighted.

Table 2 – Assignment of the infrared spectrum of matrix isolated (Ar, 15 K) TMA.^a

Experimental ^c	Calculated ^b				Approximate description ^d
	Ar matrix	Conformer A		Conformer B	
ν	ν	I	ν	I	
3316 A/ 3308 B	3405.4	184.2	3402.0	178.2	νNH
3107	3178.0	30.7	3179.0	30.8	νC6H
3096	3170.0	20.0	3170.2	20.7	νC2H
3056	3137.8	7.4	3136.2	4.7	$\nu\text{C8/9/10H s}$
3048	3124.9	11.3	3122.7	11.0	$\nu\text{C8/9/10H as}$
3034	3112.2	3.2	3110.3	4.4	$\nu\text{C8/9/10H as}'$
3034	3111.7	5.1	3116.1	3.3	νC12H
2989	3052.6	14.7	3052.5	12.6	$\nu\text{CH}_3\text{ as}$
2967	3027.1	13.7	3027.6	14.6	$\nu\text{CH}_3\text{ as}'$
2934 ^e	2973.0	17.0	2973.5	23.5	$\nu\text{CH}_3\text{ s}$
1627	1626.8	397.2	1627.2	319.5	$\nu\text{CC ring1}$
1612 A/ 1610 B	1615.5	30.5	1613.7	241.6	$\nu\text{CC ring2}, \delta\text{NH}$
1599	1597.8	376.3	1601.9	113.2	$\nu\text{2NO}_2\text{ as}, \nu\text{CC ring1}, \delta\text{NH}$
1592 (sh)	1595.8	82.9	1594.5	268.0	$\nu\text{CC ring2}, \nu\text{2NO}_2\text{ as}$
1562	1578.2	62.6	1578.1	70.8	$\delta\text{NH}, \nu\text{1/2/3NO}_2\text{ as}$
1550	1563.9	120.8	1563.7	113.1	$\nu\text{3NO}_2\text{ as}, \delta\text{NH}$
1535	1536.5	98.5	1536.2	106.8	$\nu\text{CC ring1}, \nu\text{1NO}_2\text{ as}, \nu\text{2NO}_2\text{ as}$
1515, 1505 (sh)	1518.1	337.6	1517.0	306.5	$\nu\text{CC ring1}, \nu\text{1N4C}, \delta\text{C2H}$
1490 (sh) A/ 1494 B	1490.9	3.3	1495.7	59.5	$\delta\text{CH ring2}$
1466	1472.3	33.5	1472.0	12.7	$\delta\text{CH}_3\text{ as}$
1457	1462.9	7.1	1462.7	6.4	$\delta\text{CH}_3\text{ as}'$
1445 (sh), 1442	1446.5	71.9	1446.9	69.0	$\nu\text{CC ring1}, \delta\text{NH}$

N-picryl-*p*-toluidine analogues

1432 A/ 1425 B	1433.5	26.7	1426.6	24.2	vCC ring2
1400	1409.6	1.8	1409.3	2.5	δC6H, vCC ring1
1382	1391.1	3.6	1391.0	1.7	δCH ₃ s
1356	1349.6	38.7	1349.7	50.2	v3NO ₂ s, δC2H, vC3N
1341	1346.6	102.3	1344.8	96.7	δC6H, v3NO ₂ s, vC3N
n .obs.	1329.9	732.1	1330.0	747.6	v2NO ₂ s, vC2N
1317	1322.0	1.2	1322.9	1.2	δCH ring2
1300, 1290	1307.1	99.1	1309.6	72.6	δCH ring2
1280	1287.3	263.8	1287.7	288.7	v4NO ₂ s, δCH ring2
1255	1269.3	127.1	1269.1	124.2	v4NO ₂ s, δC2/6H, δNH
1188	1246.4	5.1	1248.9	2.4	δCC ring2, v1N7C, v11C13C
1188	1172.8	4.9	1174.4	3.9	δCH ring2
1188	1170.7	13.4	1171.2	14.9	δCH ring2
1172 A/ 1176 (sh) B	1156.5	119.8	1157.3	97.9	δCC ring1, vC2/3/4N s
1167 A/ 1160 B	1154.6	25.1	1152.7	48.9	δC2/6H, δC12H
1094	1096.6	16.6	1099.1	3.4	δC8/10H
1082	1077.1	84.2	1077.6	94.2	δC2/6H
1040	1043.3	5.0	1042.5	6.9	γCH ₃
n. obs.	1012.0	0.5	1006.5	3.4	γCH ₃ '
1002	997.7	3.4	996.6	6.3	δCC ring2
982 (?)	976.1	0.0	976.5	1.0	γC8/9/10H as
956	955.2	2.5	955.4	4.1	γC2/6H as
949	951.6	13.1	947.7	19.5	δring2, γCH ₃ ', v1N7C
943	939.6	18.2	939.3	14.6	γC3/6H s
940	933.2	27.2	931.8	26.6	vC2N, vC3N, δC2H
924 A/ 931 B	917.3	46.8	921.2	46.6	vC4N, δ4NO ₂
897	901.4	9.7	902.6	9.5	γC8/10H as
868	871.4	8.0	871.4	8.2	γC12H
842 A/ n. obs. B	839.5	5.7	830.9	3.8	δCC ring1
826	827.8	6.5	827.5	10.4	δ2/3/4NO ₂ s
793	791.5	22.8	791.7	18.2	γC8/9/10H s
774	769.5	21.6	773.6	30.7	γ3NO ₂ , γC8/9/10H s
751 A/ 756(?) B	748.8	13.0	753.7	7.8	γ3NO, τring1, δCC ring1
747	742.5	9.3	741.7	6.0	γ4NO, γ3NO, τring1
739	730.4	17.2	728.8	15.6	γNH, δCC ring1, δ4NO ₂
722 ^f	717.1	19.2	717.7	19.1	γ4NO ₂ , τring1
727 ^f	709.6	39.8	708.9	35.8	γ2NO ₂ , γNH
694	696.6	20.8	695.8	20.2	γNH, τring2
680	683.6	16.3	681.7	12.1	γNH
680 A/ 670 B	680.1	17.6	674.8	25.9	τring2, γ3NO ₂ , δCC ring1, γNH

^a Frequencies (ν) in cm^{-1} ; calculated IR intensities (I) in km mol^{-1} . ^b A scaling factor of 0.982 was used for calculated frequencies. ^c sh, shoulder; n. obs, not observed; ?, uncertain. ^d ν , stretching; δ , bending, τ , torsion, γ , rocking; s, symmetric, as, anti-symmetric, ring1 and ring2 refer to the picryl and tolyl rings, respectively. ^e This is the main band ascribable to the νCH_3 s mode, while the weak bands between 2908–2947 cm^{-1} are overtones and combinations of the methyl bending vibrations in Fermi resonance with the νCH_3 s mode. ^f The proposed assignment is based on relative intensities; frequencies would lead to the opposite assignment.

3.3. Polymorphs screening, IR/Raman fingerprints of the polymorphs and X-ray structures

For polymorph screening, TMA was dissolved in different solvents, as described in Section 2.1, and the different solutions were left to slow solvent evaporation at room temperature. The crystals that were obtained in the different patches were first observed at the microscope and then analyzed by Raman and IR-ATR spectroscopies.

Crystals of different colors were obtained from the recrystallizations. Yellow crystals were obtained in the recrystallizations using carbon tetrachloride, toluene, butanone, 1-propanol and ethanol, orange crystals from dimethyl formamide (DMF), acetonitrile, acetic acid, 1,4-dioxane, ethyl acetate, chloroform, and tetrahydrofuran (THF), and red crystals from dimethyl sulfoxide (DMSO). Recrystallization from acetone yielded both yellow and red crystals, while recrystallization from methanol produced red and orange crystals, and a mixture of yellow and orange crystals was obtained

in the recrystallization using formic acid. The attempt to produce crystals upon recrystallization in dichloromethane failed and, instead, amorphous droplets of TMA were obtained. The crystals of the different polymorphs exhibit different habits (Figure 5), the yellow (Y) and orange (O) crystals appearing as plaques (elongated in the case of the orange variety), and the red ones (R) being block shape. The Raman and IR-ATR spectra of the three polymorphs were obtained and are provided Figures S4 and S5 (Supporting Information). Selected regions where the spectra of the polymorphs differ more are presented in Figures 6 and 7.

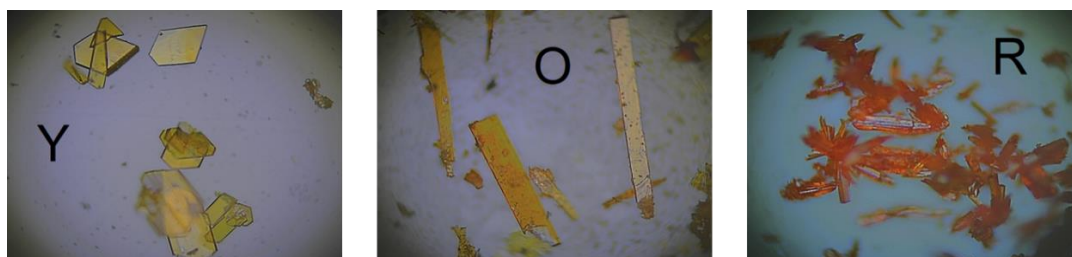


Figure 5 – Photographs of yellow (recrystallized in carbon tetrachloride), orange (recrystallized in DMF) and red (recrystallized in DMSO) crystals of TMA, with 20× magnification.

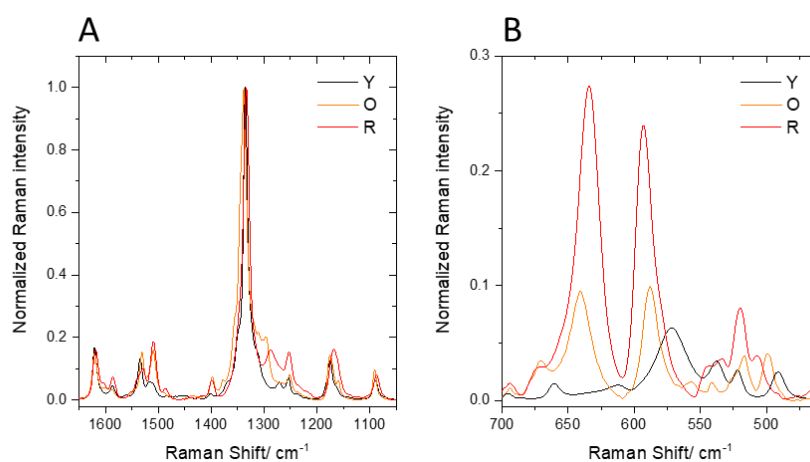


Figure 6 – Benchmark regions of the Raman spectra of the yellow (Y), orange (O) and red (R) crystals of TMA. Spectra were normalized to the peak intensity of the most intense band near 1335 cm^{-1} .

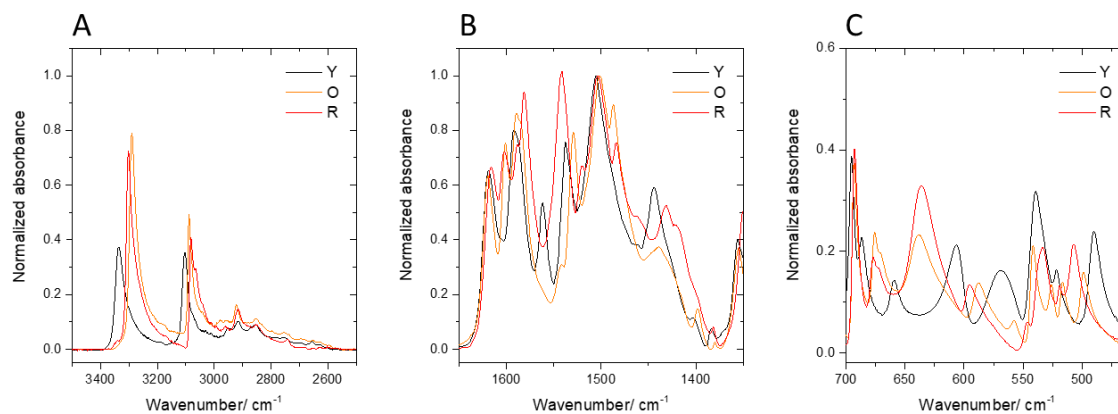


Figure 7 – Benchmark regions of the IR-ATR spectra of the yellow (Y), orange (O) and red (R) polymorphs of TMA. Spectra were normalized to the peak intensity of the band near 1505 cm^{-1} .

Both the Raman and IR-ATR spectra of the different polymorphs are significantly distinct, allowing for their simple discrimination, with the spectra of the yellow polymorph differing more from those of the orange and red polymorphs than the spectra of these latter from each other. This latter result can be taken as an indication of the greater structural similarity of the orange and red polymorphs, compared to the yellow form.

The most intense band observed in the Raman spectra of the three polymorphs is due to the NO₂ symmetric stretching mode of the nitro group in *para* position to the picryl moiety. The band is observed at clearly distinguishable frequencies in the three polymorphs: 1335 (Y), 1338 (O) and 1333 (R) cm⁻¹. Considering its much higher intensity compared to all the other bands in the Raman spectra of the polymorphs (see Figure 6 A), this band is the best possible marker for polymorph fast identification, even in experimental conditions that might not allow spectra of good quality to be obtained. The bands appearing as low-frequency satellites of this band are also good indicators for polymorph identification, with the yellow polymorph showing two bands in this region (at 1271 and 1254 cm⁻¹), the orange polymorph a group of three bands at 1311, 1297 and 1252 cm⁻¹, and the red polymorph a pair of bands centered at 1287 and 1253 cm⁻¹. In addition, the bands at ca. 1510 and 1400 cm⁻¹ show similar profiles and intensities in the O and R polymorphs but are very much less intense in the Y polymorph, thus allowing easy distinction of this latter species from the other two polymorphs.

The most intense Raman bands appearing in the 700–450 cm⁻¹ spectral range (see Figure 6 B) are also very much discriminative. The spectrum of the Y polymorph shows a single intense band at 572 cm⁻¹, while in the spectra of both the O and R forms two intense bands are observed in this region, at 641 and 589 cm⁻¹ (O) and 635 and 593 cm⁻¹ (R). Noteworthy, the pair of bands observed in the spectrum of R polymorph is more than twice as intense as that observed in the spectrum of the O form.

In the case of the IR-ATR spectra, the high-frequency region (see Figure 7 A), where the NH and CH stretching vibrations absorb, is very much appropriate for discrimination of the polymorphs. The NH stretching is observed at 3339, 3293 and 3304 cm⁻¹, respectively for the yellow, orange, and red crystals, while the highest intensity CH stretching band ($\nu_{6\text{CH}}$) appears at 3105 (Y), 3090 (O) and 3083 (R) cm⁻¹. It is also interesting to note that the relative intensity of these two bands is very much different in the yellow polymorph, compared to the orange and red polymorphs. While in the former the bands are of nearly equal intensity, in the latter two polymorphs the NH stretching band is almost twice as intense as that due to the CH stretching vibration.

The 1650-1350 cm⁻¹ region of the IR-ATR spectra is rather congested, but globally quite distinct in the different polymorphs (see Figure 7 B). In this spectral region the bands can be roughly grouped in 3 sets: a high frequency group, above 1570 cm⁻¹; a low frequency group, below 1520 cm⁻¹; and an intermediate set of bands, between 1570 and 1520 cm⁻¹. This grouping is very much arbitrary, but, in a certain perspective, it is a “picture” of the structure of the molecule, which has two ring-fragments linked by a small bridge that appears as the structurally most relevant element. In this

analogy, the spectroscopic bridging region between 1570 and 1520 cm^{-1} is also the most relevant of the 3 sub-regions for polymorphs distinction: between 1570 and 1520 cm^{-1} , the spectrum of the yellow polymorph exhibits two intense bands at 1563 and 1538 cm^{-1} , while those of the orange and red polymorphs show only one intense band at 1531 and 1540 cm^{-1} , respectively.

In the 700–450 cm^{-1} region, the IR-ATR spectrum of the yellow polymorph is also very much different from those of the orange and red forms (see Figure 7 C). Just to mention the most evident differences: (i) around 690 cm^{-1} , the yellow polymorph gives rise to a doublet of bands (at 696 and 687 cm^{-1}), whereas the orange and red polymorphs show a single band (at 693 and 692 cm^{-1} , respectively); and (ii) the most intense bands appearing below 650 cm^{-1} are observed at 607, 579, 540 (most intense) and 490 cm^{-1} for the yellow polymorph, and at 640/636 (most intense), 588/596, 542/533 and 499/508 cm^{-1} for the orange and red crystals, respectively.

On the whole, it can be concluded that both Raman and IR-ATR spectra are good fingerprints of the polymorphs of TMA, the spectra of the orange and red polymorphs being more similar to each other than to the spectra of the yellow polymorph, which is an indication that the first two polymorphs should share more common structural features.

To perform a detailed assignment of the spectra, a computational study relying on state-of-the-art first principles fully periodic calculations was performed on all polymorphs using the X-ray determined structures discussed below. The model to be used in these calculations was first chosen by testing different combinations of functional and empirical corrections for dispersion interaction, DFT-D proposed by Grimme,^{37–39} to predict the unit cell parameters. The results of this benchmarking are shown in Table S3 (Supporting Information), and led us to select the PBE0 functional with the 6-31G(d,p) basis set. The theoretically obtained spectra are shown in Figures S6-S9 and the tentative assignments are given in Tables S4 and S5, in the Supporting Information. It is worth noticing the general good description of the experimental spectra by the computations (in particular in the case of the Raman spectra). For example, the highest intensity Raman bands in the experimental spectra (Y: 1335; O: 1338; R: 1333 cm^{-1}) correspond in the calculated spectra to pairs of bands at 1380/1369 (Y), 1378/1365 (O) and 1382/1365 (R) cm^{-1} , with intensity-weighted gravity centers at 1373, 1369 and 1371 cm^{-1} , while the mark-bands observed at 572 (Y), 641 and 589 (O), and 635 and 593 (R) cm^{-1} are predicted at 579 (Y), 652 and 590 (O) and 659/640 and 584 (R) cm^{-1} , respectively.

The structures of the three polymorphs were determined by single crystal X-ray diffraction. The crystals of the yellow, orange, and red polymorphs were found to belong to the monoclinic, orthorhombic, and triclinic crystal systems, respectively. The monoclinic and triclinic polymorphs belong, respectively, to the centrosymmetric $P2_1/c$ and $P\bar{1}$ space groups, whereas the orthorhombic one crystallizes in the non-centrosymmetric $Pna2_1$ space group. The X-ray analysis confirmed that the polymorphs feature notorious differences in both molecular conformation, molecular packing, and intermolecular interactions.

The molecular conformation found in the crystal structure of the yellow polymorph is close to that of conformer A described for the isolated molecule, whereas conformer B is present in both orange and red polymorphs (Figure 8), thus confirming the indication obtained from the IR-ATR and Raman data that the yellow polymorph should have fundamental unique structural features compared to the remaining two polymorphs. As described in detail below, distinct hydrogen bonding networks are observed in the polymorphs, thus contributing to the observed preferential stabilization of a specific conformer (either A or B) in the different crystalline states.

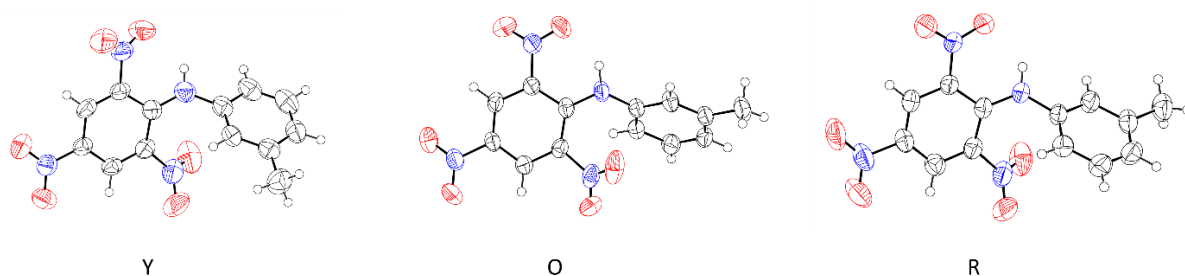


Figure 8– ORTEP plots of the monoclinic (Y, left), orthorhombic (O, centre) and triclinic (R, right) polymorphs of TMA. The anisotropic displacement ellipsoids are drawn at the 50% probability level.

Valence angles and bond distances in the molecule determined in the X-ray study are unexceptional for all polymorphs, falling within the range of expected values. The internal ring angles adjacent to the carbon atoms attached to the strong electron withdrawing NO₂ groups are significantly larger than those adjacent to unsubstituted carbon atoms (Table 3).⁴³ The N–O bond distances are in the range of 1.203–1.233 Å, a small lengthening being observed for the bonds involved in hydrogen-bonding, as described below.

In the three polymorphs, the angle between the least-squares planes of the two phenyl rings is similar, ranging from 53.93±0.12° (Y) up to 56.97±17° (O). The differences in molecular conformation are best put into evidence by an analysis of the torsion angles of the molecule (Table 4). Notorious differences are seen in both those angles involving rotation of the nitro groups around the N–C_(aryl) bonds and those corresponding to the conformational flexibility of the molecule around the 1N–7C and 4C–1N bonds. As shown below, not only steric effects but also the different involvement of the NO₂ groups in the hydrogen-bonding networks of these polymorphs explain the observed differences in the torsion angles of these groups in the three polymorphs, as well as the differences to the corresponding angles calculated for the A and B conformers of the isolated molecule.

N-picryl-p-toluidine analogues

Table 3 – Valence angles in the picryl ring of the three polymorphs of TMA.

Angle/ °	Monoclinic (Y)	Orthorhombic (O)	Triclinic (R)
6C–1C–2C	120.5(2)	121.5(3)	121.5(2)
4C–5C–6C	123.8(2)	123.3(3)	123.2(2)
2C–3C–4C	123.5(2)	123.8(3)	124.1(2)
1C–2C–3C	119.8(2)	118.8(3)	118.8(6)
5C–6C–1C	119.1(2)	119.0(3)	119.2(2)
3C–4C–5C	113.2(2)	113.3(3)	113.4(2)

Table 4 – Relevant dihedral and torsion angles for the three polymorphs of TMA.

Angle/ °	Monoclinic (Y)	Orthorhombic (O)	Triclinic (R)
<i>Torsion angle</i>			
<(1C...6C)/(7C...12C)	53.93(12)	56.97(17)	57.85(12)
<(1C...6C)/2NO ₂	–1.5(3)	17.0(4)	8.3(3)
<(1C...6C)/3NO ₂	41.5(3)	40.3(5)	48.2(4)
<(1C...6C)/4NO ₂	31.4(3)	18.9(4)	13.6(3)
<i>Dihedral angle</i>			
2C–1C–2N–1O	1.2(3)	15.6(5)	7.8(4)
4C–3C–3N–4O	–38.9(4)	38.6(5)	–44.8(4)
6C–5C–4N–6O	30.3(5)	–16.6(5)	12.8(3)
5C–4C–1N–7C	147.8(3)	–150.7(4)	153.0(2)
4C–1N–7C–12C	152.8(3)	–142.4(4)	143.5(3)

The three polymorphs show quite distinct hydrogen-bonding patterns, depicted in Figure 9, with details given in Table 5. Like for the isolated molecule of the compound, in the three polymorphs a strong intramolecular hydrogen bond is established between the amine 1N–1H group of the bridge and the neighbor *ortho* NO₂ group (with the 5O atom acting as proton acceptor). Notoriously, in the red polymorph this hydrogen bond is bifurcated, the 1N–1H proton being shared by two 5O atoms, one pertaining to the same molecule (intramolecular bond) and the other to a symmetry related 5O atom of a neighbor molecule, the intermolecular bond being much weaker than the intramolecular bond as inferred from the observed D–H and D...A distances (D and A representing the proton donor and acceptor atoms). In addition to the hydrogen bonds involving the bridging N–H group, inspection of the intermolecular distances shows several short C–H...O distances with a suitable geometry that may qualify them as weak hydrogen bond interactions (see Table 5).

In the monoclinic polymorph (Y), the molecules are joined by these weak hydrogen bonds in an extensive 3D pattern (see Figure 9). In the orthorhombic (O) polymorph, the hydrogen bond pattern joins the molecules in chains running along the crystallographic *b*-axis, the structure consisting of a stacking of these chains. In the case of the triclinic (R) polymorph, centrosymmetric pairs of molecules joined by the bifurcated 1N–1H...5O bonds propagate in chains running along the [111] direction, the dimers being joined by weaker C–H...O bonds.

Table 5 – Hydrogen bonds and short intermolecular contacts for the polymorphs of TMA.^a

Polymorph	D–H···A	D–H/ Å	H···A/ Å	D···A/ Å	< D–H···A/ °
Y	1N–1H···5O	0.83(3)	2.07(3)	2.701(4)	133(3)
Y	6C–6H···2O ^a	0.93	2.46	3.222(3)	139
Y	11C–11H···3O ^b	0.93	2.42	3.325(5)	163
Y	13C–13 _B H···5O ^c	0.96	2.60	3.415(5)	144
O	1N–1H···5O	0.90(4)	1.89(4)	2.649(4)	141(3)
O	1N–1H···1O ^f	0.90(4)	2.42(4)	3.085(4)	131(3)
O	6C–6H···5O ^g	0.93	2.56	3.480(5)	169
O	8C–8H···4O ^h	0.93	2.56	3.373(5)	147
R	1N–1H···5O	0.85(3)	1.97(3)	2.633(3)	135(3)
R	1N–1H···5O ^d	0.85(3)	2.56(3)	3.197(3)	151(3)
R	6C–6H···2O ^e	0.93	2.43(3)	3.322(3)	163

Symmetry codes: a) $1-x, -y, 1-z$; b) $-x, -1/2+y, 3/2-z$; c) $x, 1+y, z$; d) $-x, 2-y, 1-z$; e) $2-x, 1-y, 1-z$; f) $x, -1+y, z$; g) $1/2-x, 1/2+y, 1/2+z$; h) $x, y, 1+z$

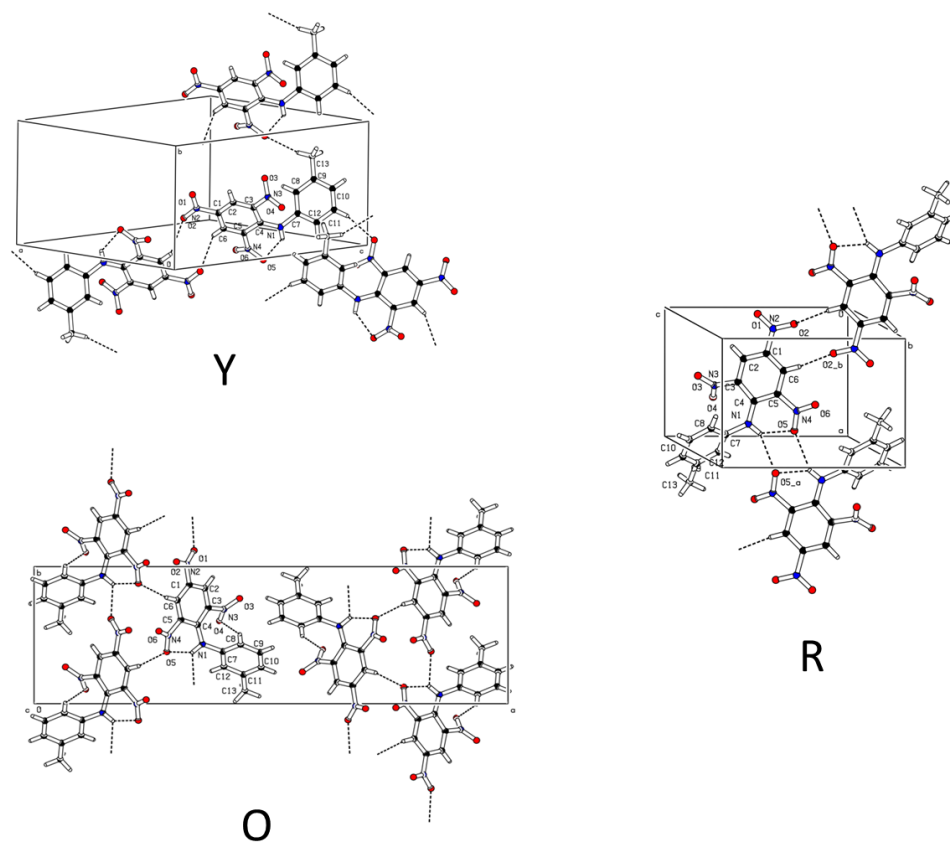


Figure 9 – Hydrogen-bonding network in the monoclinic (Y), orthorhombic (O) and triclinic (R) polymorphs of TMA. In the case of the orthorhombic crystal, the view is a projection of the structure along the *c*-axis.

3.4. Hirshfeld surfaces analysis of the polymorphs

The analysis of molecular crystal structures based on Hirshfeld surfaces, developed by Spackman and co-workers, is a powerful, elegant way to interpret intermolecular interactions in a crystal and to analyze crystal packing.^{44,45} In this study, we used this approach to compare the structures of the three polymorphs of TMA. The analysis was performed using CrystalExplorer 17.5,⁴⁶ based on the structure input files of the polymorphs (in CIF format). The results are summarized using maps of the normalized contact distance, d_{norm} , on the calculated Hirshfeld surfaces, and the corresponding 2D-

fingerprint plots. d_{norm} is calculated from the distances of a given point of the surface to the nearest atom outside, d_e , and inside, d_i , the surface, as defined by Eq. 1 (where r_i^{vdW} are the van der Waals radii), and allows the identification of the regions of the molecule where intermolecular interactions are more relevant.^{45–47} The 2D-fingerprint plots allow to condense the information about the relative importance of the different combinations of d_e and d_i throughout the surface of the molecule, indicating the types of intermolecular interactions present in the system and also their relative importance, as given by the associated percent areas of the surface.^{45,48–50}

$$d_{norm} = \frac{d_i - r_i^{vdW}}{r_i^{vdW}} + \frac{d_e - r_e^{vdW}}{r_e^{vdW}} \quad (1)$$

Figure 10 shows the calculated Hirshfeld surfaces for the Y, O and R polymorphs of TMA, with the respective intermolecular contacts, as given by the d_{norm} values, which vary from -0.25 to 1.31 in the Y polymorph, from -0.15 to 1.38 in the O polymorph, and from -0.25 to 1.18 in the R polymorph. The magnitude of the intervals of d_{norm} values follow the order 1.56 (Y) > 1.53 (O) > 1.43 (R), which is in agreement with the relative densities (Mg m^{-3}) of the crystals 1.496 (Y) < 1.523 (O) < 1.551 (R) (see Table 1). The red spots on the surfaces shown in Figure 10 represent the most important intermolecular interactions (see also Table 5).

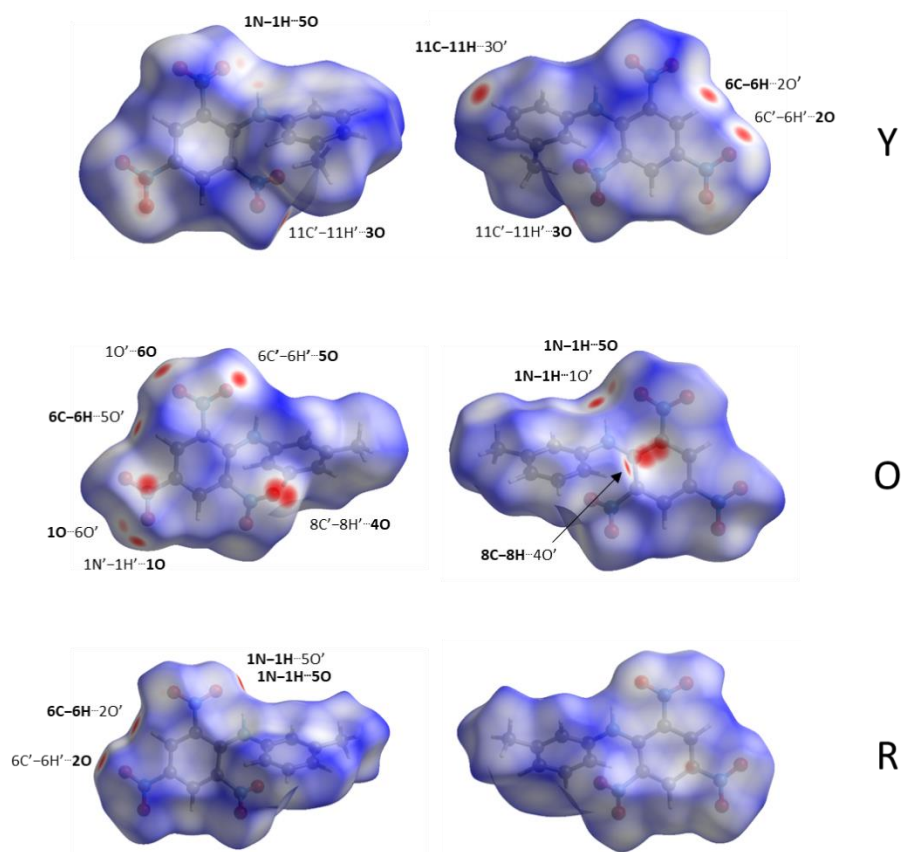


Figure 10 – d_{norm} mapping on the Hirshfeld surfaces of the molecules in the crystals of the three polymorphs of TMA. Two different viewpoints are shown for each molecule (in the left column, with the nitrobenzene group on the left-hand side, and in the right column with the nitrobenzene group on the right-hand side). Atoms participating in the indicating interactions that belong to neighbor molecules are notated using a plica.

Table 6 presents the relative percentages of the Hirshfeld surfaces assigned to the different types of intermolecular interactions, while the corresponding d_e vs. d_i 2D-fingerprint plots are provided as Supporting Information (Figures S10-S12). The H \cdots O/O \cdots H interactions are the prevalent ones in all polymorphs, accounting for ca. 40% of the total interactions. In the O and R polymorphs, where the molecules of TMA are in the B conformation, this type of interaction amounts to 42.7% and 38.6%, respectively, while in the Y polymorph (made by molecules in the A conformation) it represents 38.2% of the total interactions. The H \cdots C/C \cdots H interactions are also comparatively more important in the O and R polymorphs (12.8% and 14.7%, respectively) than for the Y form (8.9%). On the other hand, the H \cdots H interactions (the second most relevant ones) are more significant in the Y polymorph (22.1%), compared to the O (20.6%) and R (18.2%) forms. These data indicate that the crystal stabilization of the O and R polymorphs is ensured in a higher level both by conventional (H \cdots O/O \cdots H) and non-conventional (H \cdots C/C \cdots H) hydrogen bonding, when compared with the Y form (which is in consonance with the higher density of these crystals as well as with the shorter intervals of their d_{norm} values), while in the Y polymorph dispersive forces are comparatively more important. This latter conclusion is further supported by the larger contributions in the Y polymorph also of O \cdots O and C \cdots C interactions (11.6 and 4.7%, respectively), compared to the O (9.4 and 0.4%) and R (9.7 and 1.7%) forms.

Table 6 – Percent areas of the Hirshfeld surface assigned to the different types of intermolecular interactions in the three polymorphs of TMA.

Interactions	Y	O	R
H \cdots O/O \cdots H	38.2%	38.6%	42.7%
H \cdots H	22.1%	20.6%	18.2%
O \cdots O	11.6%	9.4%	9.7%
H \cdots C/C \cdots H	8.9%	12.8%	14.7%
C \cdots O/O \cdots C	7.3%	10.9%	5.6%
C \cdots C	4.7%	0.4%	1.7%
O \cdots N/N \cdots O	3.8%	3.7%	3.1%
H \cdots N/N \cdots H	2.3%	2.7%	2.3%
C \cdots N/N \cdots C	1.0%	0.7%	1.9%

3.5. Thermal analysis and thermodynamic relationship between the polymorphs

The thermal behavior of the three polymorphs was studied by differential scanning calorimetry (DSC) and by polarized light thermomicroscopy (PLTM). The powder X-ray diffractograms of the polymorphs are shown in Figure S13, where they can be compared with the simulated ones obtained from the single crystal X-ray diffraction data. The two sets of data agree very well, showing that the used materials correspond to the pure polymorphs. The DSC curves are presented in Figure 11 and the values of melting temperature and respective melting enthalpy for each polymorph are presented in Table 7.

From the heat of fusion rule,^{51–53} one can conclude that the three TMA polymorphs are enantiotropically related, which means that the orange polymorph is the most stable crystal at the lower temperatures (with all probability including room temperature), and the red and yellow forms correspond to the most stable forms in intermediate and high temperature ranges. Despite of this enantiotropic relationship, after more than two years of storage at room temperature the transformation of either the Y or R forms into the O polymorph was not observed, which points to a kinetic restriction for such processes at this temperature.

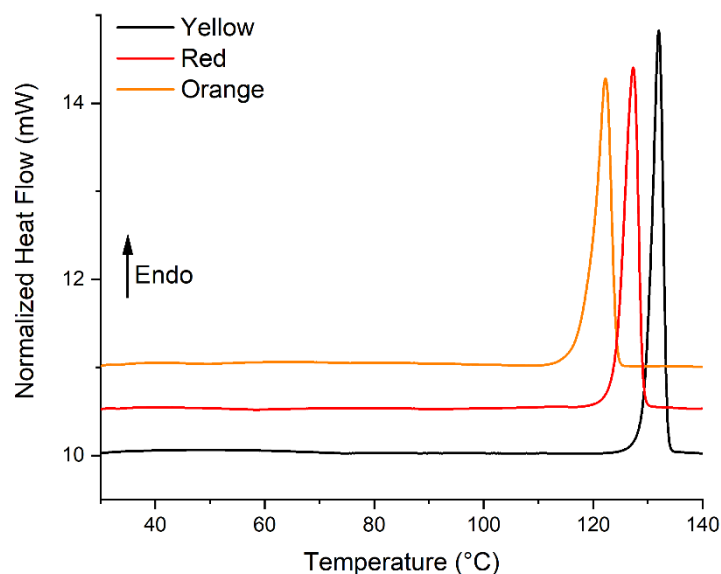


Figure 11 – DSC curves of the Y, O and R polymorphs of TMA (heating rate: 10 °C min⁻¹). Masses: 2.10 mg (Y), 1.10 mg (O), 2.16 mg (R).

Table 7 – Melting point and enthalpy of fusion for the three polymorphs of TMA.

Polymorph	Melting point/ °C	Enthalpy of fusion/ kJ mol ⁻¹
Y	129.5 ± 0.1	23.1 ± 0.3
O	120.2 ± 0.1	24.6 ± 0.5
R	124.7 ± 0.4	23.7 ± 0.3

The DSC curve of the O polymorph (see Figure 11) is relatively broad, compared to the curves obtained for the other two forms. For that reason, it was decided to study the heating process by PLTM, to visually investigate the melting process of this polymorph. The PLTM images are presented in Figure 12. At 118–120 °C the sample starts to melt, but the melting process is rather long, with small crystals growing from the melt and then melting again. The temperature of melting of the newly formed crystals (ca. 130 °C) indicates that they correspond to the yellow TMA polymorph (see Table 7). The formation

and subsequent melting of small crystals of either the Y or R polymorphs (or of both) alongside the melting of the O polymorph crystals could *a priori* explain a broadening of the DSC melting feature observed for the O polymorph. As mentioned above, the PLTM experiments doubtlessly demonstrated that, under the experimental conditions of the thermomicroscopy essays, polymorph Y crystallizes from the melt, while the formation of the R polymorph is uncertain. On the other hand, the observed profile of the DSC melting peak of the O polymorph sample, in particular its end-temperature (ca. 125 °C; see Figure 11), indicates that in the DSC experiments it is the R polymorph that crystallizes from the melt instead of the Y polymorph.

It is also interesting to note that the melted compound did not crystallize during cooling down till 0 °C, while the formed glassy phase devitrifies upon heating at around 29 °C (Figure 13).

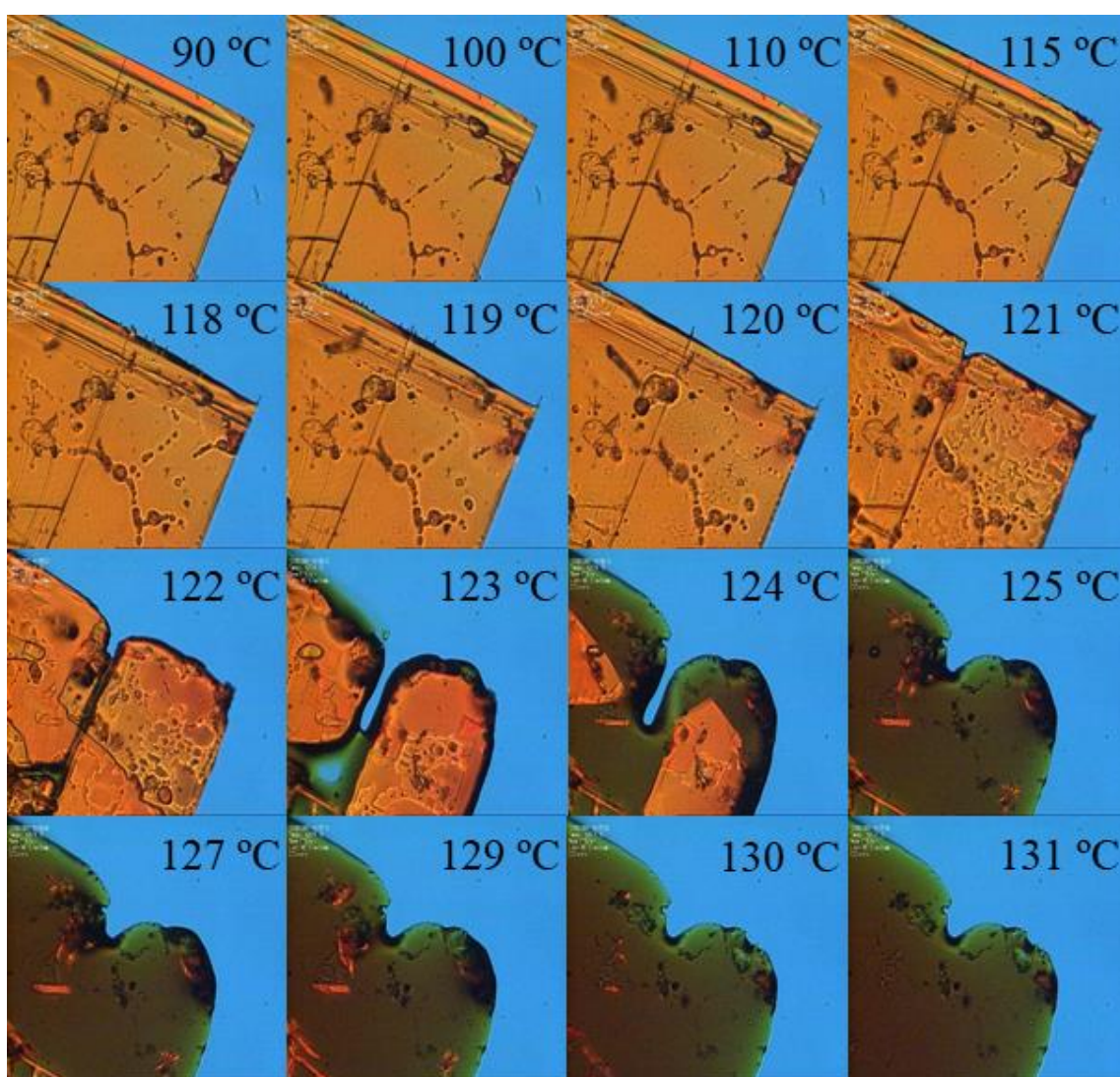


Figure 12 – PLTM images of the heating process of the O polymorph of TMA (heating rate: 10 °C min⁻¹).

N-picryl-p-toluidine analogues

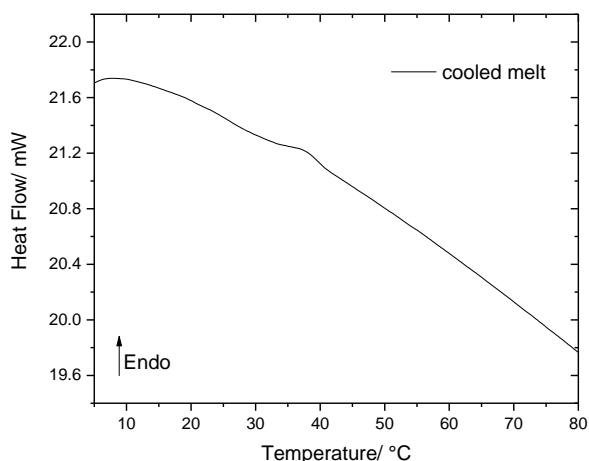


Figure 13 – DSC devitrification curve of a melted sample of TMA (heating rate: 10 °C min⁻¹).

3.6. Electronic absorption spectra and color of the polymorphs

In order to better understand the origin of the different colors in the three polymorphs of TMA, their UV-vis absorption spectra were collected (Figure 14 A). It is clear from the figure that the spectrum of the Y polymorph is considerably different from those of the other two polymorphic forms, which present an overall similar profile. The spectrum of the Y polymorph presents bands with maxima at 274 (UV), 447 (indigo) and 581 (green) nm and shoulders at 330 (UV) and 639 (red) nm, whereas the spectra of the O and R forms show bands with maxima respectively at 316 (UV) and 454 (indigo) nm (O; the band at longer wavelength clearly showing a profile compatible with the coalescence of two bands) and 322 (UV), 446 (violet) and 506 (green) nm (R). In the visible region, the spectral profiles of the different polymorphs have absorption regions compatible with the colors they exhibit (see Figure 5), the color parameters (x , y) obtained based on the absorption spectra using the CIE 1931 chromaticity scale being (0.338, 0.334), (0.393, 0.367) and (0.432, 0.366) for Y, O and R, respectively (Figure 14 B).

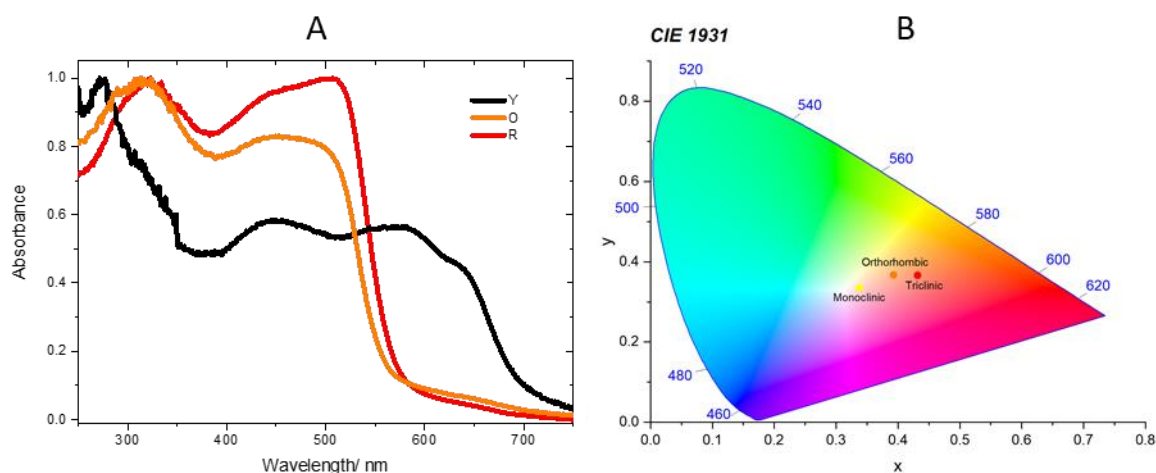


Figure 14 – Normalized solid-state UV-vis absorption spectra of the three polymorphs of TMA, in the 250–750 nm range (A), and the corresponding color parameters in the CIE 1931 chromaticity scale (B).²⁹

Considering all the results presented in this study, in particular the spectroscopic data, which are more similar for the O and R polymorph, where the TMA molecules exist in the same (B) conformer, compared to the Y polymorph in which the TMA molecules adopt the A conformation, the different colors of the polymorphs have to be determined in large amount by intramolecular structural features that affect the electronic structure of the chromophore, which corresponds essentially to the picryl moiety. A greater electron donation to the picryl ring shall take place in the R polymorph, and a more reduced one in the Y polymorph, the O form being an intermediate case. The key to understanding the mechanism leading to the different colors is the comparison between the 1N–4C bond lengths in the molecules constituting the different polymorphs. In the Y, O and R polymorphs, this bond length is 1.354, 1.348 and 1.341 Å, respectively, which shows that the extension of the electron donation from 1N to the picryl moiety follows the order $R > O > Y$, thus explaining the different colors of the polymorphs. The N–C bond length in aniline is 1.355 Å, which is indicative of an increased donation from 1N to 4C in all polymorphs of TMA, due to the presence of the three nitro substituents in the picryl ring of the molecule. On the other hand, the 1N–7C bond in all the TMA polymorphs (Y: 1.421, O: 1.434, R: 1.430 Å) is much longer than that found in aniline and closer to a typical N–C bond length in an amine (ca. 1.469 Å), which indicates that the electron delocalization from 1N to the tolyl moiety of TMA is unimportant. This result is also relevant because, under these conditions, the 1N atom is more available to donate to the picryl ring. Very interestingly, for the conformers of the isolated molecule of TMA, the 1N–4C bond length follows the opposite trend compared to what is observed in the crystals, being shorter in conformer A (1.337 Å) than in conformer B (1.371 Å). This points to the relevance of intermolecular interactions as a major factor in determining the extension of the electron donation from 1N to the picryl ring in the TMA crystals and, thus, ultimately also determining their color even when they correspond to conformational polymorphs (like Y vs. O and R; O and R are packing polymorphs).

4. Conclusion

The color polymorphism exhibited by *N*-picryl-*m*-toluidine (TMA) appears as a fascinating case where both conformational and packing polymorphs exist. As determined by single crystal X-ray diffraction, the yellow polymorph is formed by TMA molecules assuming the conformation of the most stable conformer (A) observed for the isolated molecule of the compound, while both the orange and red polymorphs are formed by conformer B. Interestingly, despite the yellow polymorph presents spectroscopic properties that differ more from those of the orange and red polymorphs, packing appears to be the ultimate cause determining the different colors of all polymorphs, modulating the electronic properties of the chromophore, in particular the electron donation from the amine bridge nitrogen atom to the picryl moiety. This conclusion results from the analysis of the structural data obtained for the isolated molecule and for the crystals, in particular the N–C_(picryl) bond length, which is a measure of the

electron delocalization from the bridging N atom to the picryl ring: this bond length correlates inversely with the electron delocalization and it follows the expected order $R < O < Y$, but it is longer in the isolated conformer B than in conformer A. Also, in agreement with this conclusion, the structural data show that the electron delocalization involving the tolyl moiety and the bridge is reduced and that the angle between the two rings (picryl and tolyl) is nearly the same in all crystals.

The Hirshfeld surface analysis for the crystals demonstrates that stabilization of the O and R polymorphs is ensured in a higher level both by conventional ($H\cdots O/O\cdots H$) and non-conventional ($H\cdots C/C\cdots H$) hydrogen bonding when compared with the Y polymorph, while in this latter form dispersive forces are comparatively more important. These differences might be in the origin of the different influence of the crystal packing on the electronic properties of the chromophore.

The investigations performed on the TMA isolated molecule allowed to evaluate the major intramolecular interactions determining the conformational preferences of the compound and characterize its two conformers (A and B) in detail both structurally and vibrationally. The information obtained from these studies were instrumental for the understanding of the structure and properties of the crystals of the different polymorphs.

The infrared and Raman spectra of the different polymorphs were investigated in a comparative basis and fully assigned with help of contemporary fully periodic DFT calculations on the crystals, while the DSC and PLTM studies allowed to identify the enantiotropic thermodynamic relationship between the polymorphs at normal pressure.

On the whole, this investigation constitutes a comprehensive structural (for both the isolated molecule and crystalline phases), spectroscopic and thermal analysis of TMA, with particular emphasis on the color polymorphism it exhibits.

Supporting Information

Figures S1-S13, with the 1H and ^{13}C NMR spectra of TMA, IR-ATR spectrum of the synthesized material, IR spectrum of the matrix isolated (Ar, 15 K) compound and B3LYP/6-311++G(d,p) calculated spectra its conformers, IR-ATR and Raman spectra of the polymorphs of the corresponding calculated spectra obtained from fully periodic calculations, results of Hirshfeld analysis of the studied crystals, and powder diffractograms (experimental and calculated) for the three polymorphs; Tables S1-S5, with calculated IR spectra of conformers A and B of TMA, and results of the fully-periodic quantum chemical calculations performed on the studied crystals (unit cell parameters of TMA polymorphs, and their IR and Raman spectra). Tables S6-S32 provide structural X-Ray data for the three polymorphs. CIF files containing the supplementary crystallographic data were deposited at the Cambridge Crystallographic Data Centre, with reference CCDC 2100574 (yellow polymorph), 2100587 (red polymorph) and 2100671 (orange polymorph).

Acknowledgements

The CQC-IMS is financially supported by the Portuguese Science Foundation (“Fundação para a Ciência e a Tecnologia” - FCT) – Projects CQC UIDB/00313/2020 and UIDP/00313/2020 (National Funds). CFisUC is funded by FCT through the projects UIDB/04564/2020 and UIDP/04564/2020. Access to instruments from Laser-Lab Coimbra and TAIL-UC (ICT_2009_02_012_1890) facilities funded under QREN-Mais Centro is gratefully acknowledged. B.A.N. also acknowledges FCT for the SFRH/BD/129852/2017 PhD Scholarship.

References

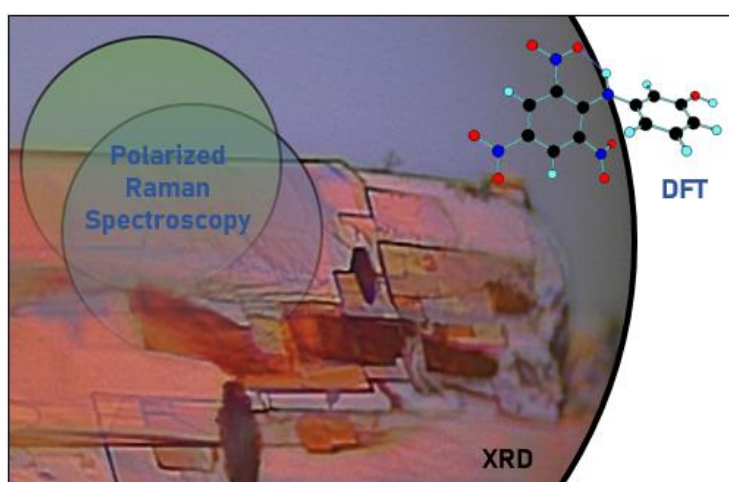
1. B. A. Nogueira, C. Castiglioni and R. Fausto, Color Polymorphism in Organic Crystals, *Commun. Chem.*, 2020, **3**, 1–12.
2. J. Bernstein, *Polymorphism in Molecular Crystals*, Oxford University Press, 2010.
3. G. R. Desiraju, *Crystal Engineering: The Design of Organic Solids*, Elsevier, 1989.
4. A. J. Cruz-Cabeza and J. Bernstein, Conformational Polymorphism, *Chem. Rev.*, 2014, **114**, 2170–2191.
5. D. Braga, F. Grepioni, L. Maini and M. Polito, *Crystal Polymorphism and Multiple Crystal Forms. in Molecular Networks, Structure and Bonding*, Springer, 2009, 87–95.
6. G. Desiraju and T. Steiner, *The Weak Hydrogen Bond: In Structural Chemistry and Biology*, Oxford University Press, 2010.
7. P. Popelier, A. T. H. Lenstra, C. Alsenoy and H. J. Van Geise, An Ab Initio Study of Crystal Field Effects: Solid-state and Gas-phase Geometry of Acetamide, *J. Am. Chem. Soc.*, 1989, **111**, 5658–5660.
8. M. Cavallini, A. Calò, P. Stoliar, J. C. Kengne; S. Martins, F. C. Maticotta, F. Quist, G. Gbabode, N. Dumont, Y. H. Geerts and F. Biscarini, Liquid-Crystal Patterning: Lithographic Alignment of Discotic Liquid Crystals: A New Time-Temperature Integrating Framework, *Adv. Mater.*, 2009, **21**, 4688–4691.
9. D. Gentili, M. Durso, C. Bettini, I. Manet, M. Gazzano, R. Capelli, M. Muccini, M. Melucci and M. Cavallini, A Time-temperature Integrator Based on Fluorescent and Polymorphic Compounds, *Sci. Rep.* 2013, **3**, 2581.
10. Z. Lin, X. Mei, E. Yang, X. Li, H. Yao, G. Wen, C.-T. Chien, T. J. Chow and Q. Ling, Polymorphism-dependent Fluorescence of Bisthiénylmaleimide with Different Responses to Mechanical Crushing and Grinding Pressure, *CrystEngComm*, 2014, **16**, 11018–11026.
11. D. Gentili, M. Gazzano, M. Melucci, D. Jones and M. Cavallini, Polymorphism as an Additional Functionality of Materials for Technological Applications at Surfaces and Interfaces, *Chem. Soc. Rev.*, 2019, **48**, 2502–2517.
12. L. Gattermann, Ueber Einige Derivate des *m*-Nitro-*p*-Toluidins, *Ber. Dtsch. Chem. Gesel.*, 1885, **18**, 1483–1488.
13. I. G. Krivoruchka, A. I. Vokin, T. N. Aksamentova, A. M. Shulunova, M. S. Sorokin, E. I. Dubinskaya and V. K. Turchaninov, Solvatochromism of Heteroaromatic Compounds: XXII.1 Effect of Bifurcate Hydrogen Bond on the IR Spectrum and Dipole Moment of *N*-(4-Methyl-2-nitrophenyl)acetamide in Solution, *Russ. J. Org. Chem.*, 2004, **74**, 120–127.
14. A. Hantzsch, Über Chromoisomerien, *Zeitsch. Angew. Chem.*, 1907, **20**, 1889–1892.
15. M. F. Richardson, Q.-C. Yang, E. Novotny-Bregger and J. D. Dunitz, Conformational Polymorphism of Dimethyl 3,6-dichloro-2,5-dihydroxyterephthalate. II. Structural, Thermodynamic, Kinetic and Mechanistic Aspects of Phase Transformations among the Three Crystal Forms, *Acta Cryst. B*, 1990, **46**, 653–660.
16. G. A. Stephenson, T. B. Borchardt, S. R. Byrn, J. Bowyer, C. A. Bunnell, S. V. Snorek and L. Yu, Conformational and Color Polymorphism of 5-Methyl-2-[(2-nitrophenyl)amino]-3-

- thiophenecarbonitrile, *J. Pharm. Sci.*, 1995, **84**, 1385–1386.
17. X. Li, X. Ou, H. Rong, S. Huang, J. Nyman, L. Yu, and M. Lu, The Twelfth Solved Structure of ROY: Single Crystals of Y04 Grown from Melt Microdroplets, *Cryst. Growth Des.*, 2020, **20**, 7093–7097.
 18. M. Busch and E. Pungs, E. Über Isomere Verschiedenfarbige Pikrylamine, *J. Prakt. Chem.*, 1909, **79**, 546–554.
 19. T. Yaji, S. Isoda, T. Kobayashi, K. Taguchi, K. Takada, M. Yasui and F. Iwasaki, Color Change Due to Phase Transition in *N*-(2,4-Dinitrophenyl)-*o*-Anisidine, *Mol. Cryst. Liq. Cryst.*, 1999, **327**, 57–60.
 20. C. Dohmen, H. Ihmels, R. Kreienmeier and B. O. Patrick, Synthesis of a Crystallochromic Indolizine Dye by a Base- and Catalyst-free Photochemical Route, *Chem. Commun.*, 2019, **55**, 11071–11074.
 21. C. Kitamura, T. Ohara, N. Kawatsuki, A. Yoneda, T. Kobayashi, H. Naito, T. Komatsu and T. Kitamura, Conformational Polymorphism and Optical Properties in the Solid State of 1,4,7,10-Tetra(*n*-butyl)tetracene, *CrystEngComm*, 2007, **9**, 644–647.
 22. N. M. Cullinane, O. E. Embrey and D. R. Davis, Investigation of the Differently Colored Forms of Certain Derivatives of Diphenylamine, *J. Phys. Chem.*, 1932, **36**, 1434–1448.
 23. R. G. Wood, S. H. Ayliffe and N. M. Cullinane, XXXIII. A Crystallographic and X-ray Investigation of Some Diphenylamine Derivatives, *Mag. J. Sci.*, 1935, **19**, 405–416.
 24. M. Yasui, K. Taguchi and F. Iwasaki, Dynamic Behavior of *N*-(2,4-Dinitrophenyl)-*o*-anisidine Crystals. *Mol. Cryst. Liq. Cryst.*, 1996, **277**, 167–176.
 25. D. E. Braun, T. Gelbrich, R. K. R. Jetti, V. Kahlenberg, S. L. Price and U. J. Griesser, Colored Polymorphs: Thermochemical and Structural Features of *N*-Picryl-*p*-toluidine Polymorphs and Solvates, *Cryst. Growth Des.*, 2008, **8**, 1977–1989.
 26. I. G. Ilyina, O. V. Mikhalev, K. P. Butin, B. N. Tarasevich and B. M. Uzhinov, Differently Colored Crystalline Modifications of Organic Autocomplexes of the Nitroaromatic Type, *Synth. Metals*, 2001, **120**, 1067–1068.
 27. G. M. Sheldrick, Crystal Structure Refinement with SHELXL, *Acta Cryst. C*, 2015, **5**, 3–8.
 28. D. P. Law, A. B. Blakeney and R. Tkachuk, The Kubelka–Munk Equation: Some Practical Considerations, *J. Near-Infrared Spectrosc.*, 2017, **4**, 189–193.
 29. T. Smith and J. Guild, The C.I.E. Colorimetric Standards and their Use, *Trans. Opt. Soc.*, 1931, **33**, 73–134.
 30. Gaussian 09, Revision A.02, M. J. Frisch, G. W. Trucks, H. B. Schlegel, G. E. Scuseria, M. A. Robb, J. R. Cheeseman, G. Scalmani, V. Barone, G. A. Petersson, H. Nakatsuji, X. Li, M. Caricato, A. Marenich, J. Bloino, B. G. Janesko, R. Gomperts, B. Mennucci, H. P. Hratchian, J. V. Ortiz, A. F. Izmaylov, J. L. Sonnenberg, D. Williams-Young, F. Ding, F. Lipparini, F. Egidi, J. Goings, B. Peng, A. Petrone, T. Henderson, D. Ranasinghe, V. G. Zakrzewski, J. Gao, N. Rega, G. Zheng, W. Liang, M. Hada, M. Ehara, K. Toyota, R. Fukuda, J. Hasegawa, M. Ishida, T. Nakajima, Y. Honda, O. Kitao, H. Nakai, T. Vreven, K. Throssell, J. A. Montgomery, Jr., J. E. Peralta, F. Ogliaro, M. Bearpark, J. J. Heyd, E. Brothers, K. N. Kudin, V. N. Staroverov, T. Keith, R. Kobayashi, J. Normand, K. Raghavachari, A. Rendell, J. C. Burant, S. S. Iyengar, J. Tomasi, M. Cossi, J. M. Millam, M. Klene, C. Adamo, R. Cammi, J. W. Ochterski, R. L. Martin, K. Morokuma, O. Farkas, J. B. Foresman, and D. J. Fox, Gaussian, Inc., Wallingford CT, 2016.
 31. A. D. Becke, Density-functional Exchange-energy Approximation with Correct Asymptotic Behavior, *Phys. Rev. A*, 1988, **38**, 3098–3100.
 32. C. Lee, W. Yang, and R. G. Parr, Development of the Colle-Salvetti Correlation-energy Formula into a Functional of the Electron Density, *Phys. Rev. B*, 1988, **37**, 785–789.
 33. A. D. McLean and G. S. Chandler, Contracted Gaussian Basis Sets for Molecular Calculations. I. Second Row Atoms, *Z = 11–18*, *J. Chem. Phys.*, 1980, **72**, 5639–5648.
 34. R. Dovesi, A. Erba, R. Orlando, C. M. Zicovich-Wilson, B. Civalleri, L. Maschio, M. Rérat, S. Casassa, J. Baima, S. Salustro and B. Kirtman, Quantum-mechanical Condensed Matter Simulations with CRYSTAL, *Wiley Interdiscip. Rev. Comput. Mol. Sci.*, 2018, **8**, e1360.
 35. R. Dovesi, V. R. Saunders, C. Roetti, R. Orlando, C. M. Zicovich-Wilson, F. Pascale, B. Civalleri, K. Doll, N. M. Harrison, I. J. Bush, P. D’Arco, M. Llunell, M. Causà, Y. Noël, L.

- Maschio, A. Erba, M. Rerat and S. Casassa, CRYSTAL17 User's Manual (University of Torino, Torino, 2017).
36. C. Adamo and V. Barone, Toward Reliable Density Functional Methods without Adjustable Parameters: The PBE0 Model, *J. Chem. Phys.*, 1999, **110**, 6158–6170.
 37. S. Grimme, Accurate Description of van der Waals Complexes by Density Functional Theory Including Empirical Corrections, *J. Comput. Chem.*, 2004, **25**, 1463–1473.
 38. S. Grimme, Semiempirical GGA-type Density Functional Constructed with a Long-range Dispersion Correction, *J. Comput. Chem.*, 2006, **27**, 1787–1799.
 39. B. Civalleri, C. M. Zicovich-Wilson, L. Valenzano and P. Ugliengo, B3LYP Augmented with an Empirical Dispersion Term (B3LYP-D*) as Applied to Molecular Crystals, *CrystEngComm*, 2008, **10**, 405–410.
 40. J. P. Merrick, D. Moran and L. Radom, An Evaluation of Harmonic Vibrational Frequency Scale Factors, *J. Phys. Chem. A*, 2007, **111**, 11683–11700.
 41. B. S. Rathore, V. Gupta, R. R. Gupta and M. Kumar, Synthesis of 7-Chloro-9-trifluoromethyl-7-fluorophenothiazines, *Heteroat. Chem.*, 2007, **18**, 81–86.
 42. I. D. Reva, S. G. Stepanian, L. Adamowicz and R. Fausto, Missing Conformers: Comparative Study of Conformational Cooling in Cyanoacetic Acid and Methyl Cyanoacetate Isolated in Low Temperature Inert Gas Matrixes, *Chem. Phys. Lett.*, 2003, **374**, 631–638.
 43. A. Domenicano, A. Vaciago and C. A. Coulson, Molecular Geometry of Substituted Benzene Derivatives. I. On the Nature of Ring Deformations Induced by Substitution, *Acta Cryst.*, 1975, **B31**, 221–234.
 44. M. A. Spackman and P. G. Byrom, A Novel Definition of a Molecule in a Crystal, *Chem. Phys. Lett.*, 1997, **267**, 215–220.
 45. M. A. Spackman and D. Jayatilaka, Hirshfeld Surface Analysis, *CrystEngComm*, 2009, **11**, 19–32.
 46. S. K. Wolff, D. J. Grimwood, J. J. McKinnon, M. J. Turner, D. Jayatilaka and M. A. Spackman, Crystal Explorer17 (version 17.5), University of Western Australia, Crawley (AUS), 2017.
 47. J. J. McKinnon, A. S. Mitchell and M. A. Spackman, Hirshfeld Surfaces: A New Tool for Visualising and Exploring Molecular Crystals, *Chem. - A Eur. J.*, 1998, **4**, 2136–2141.
 48. M. A. Spackman and J. J. McKinnon, Fingerprinting Intermolecular Interactions in Molecular Crystals, *CrystEngComm*, 2002, **4**, 378–392.
 49. A. L. Rohl, M. Moret, W. Kaminsky, K. Claborn, J. J. McKinnon and B. Kahr, Hirshfeld Surfaces Identify Inadequacies in Computations of Intermolecular Interactions in Crystals: Pentamorphic 1,8-Dihydroxyanthraquinone, *Cryst. Growth Des.*, 2008, **8**, 4517–4525.
 50. A. Parkin, G. Barr, W. Dong, C. J. Gilmore, D. Jayatilaka, J. J. McKinnon, M. A. Spackman and C. C. Wilson, Comparing Entire Crystal Structures: Structural Genetic Fingerprinting, *CrystEngComm*, 2007, **9**, 648–652.
 51. A. Burger and R. Ramberger, On the Polymorphism of Pharmaceuticals and other Molecular Crystals. I - Theory of Thermodynamic Rules, *Mikrochim. Acta*, 1979, **72**, 259–271.
 52. A. Burger and R. Ramberger, On the Polymorphism of Pharmaceuticals and other Molecular Crystals. II - Applicability of Thermodynamic Rules, *Mikrochim. Acta*, 1979, **72**, 273–316.
 53. L. Yu, Inferring Thermodynamic Stability Relationship of Polymorphs from Melting Data, *J. Pharm. Sci.*, 1995, **84**, 966–974.

3.2. TAP & TMA – Polarized Raman Study

The manuscript that constitutes this subsection is entitled *Molecular and Crystal Structures of N-Picryl-m-phenolidine and Investigation of Single Crystal Polarized Raman Spectra* and was published online on Elsevier's Journal of Molecular Structure, as a part of the Special Issue in honor of István Pálinkó, on 17th April 2022. To the date of the submission of this Thesis, the article remains uncited, and has received 23 reads in Research Gate.



Supporting Information:

<https://doi.org/10.1016/j.molstruc.2022.133111>

Authors: Bernardo A. Nogueira, Susana M. M. Lopes, Teresa M. V. D. Pinho e Melo, José A. Paixão, Alberto Milani, Chiara Castiglioni and Rui Fausto

Corresponding author: Bernardo A. Nogueira

Author contributions: Bernardo A. Nogueira and Rui Fausto conceptualized the study. Bernardo A. Nogueira wrote a preliminary version of the manuscript, performed the Raman experimental work and part of the theoretical studies; Rui Fausto took responsibility for supervision, analysed and interpreted the Raman and the theoretical data and wrote the final version of the manuscript; Susana M. M. Lopes and Teresa M. V. D. Pinho e Melo were responsible for the development of the synthetic route and its implementation; José A. Paixão performed the XRD studies and wrote the first version of the corresponding section of the manuscript; Alberto Milani and Chiara Castiglioni performed the fully-

periodic quantum chemical calculations on the different crystals. All authors have participated in the discussion of the results and agreed with the final version of the manuscript.

Synopsis:

In this work, we have reported the second *N*-picryl-*p*-toluidine derivative developed during this Thesis. *N*-picryl-*m*-phenolidine, or simply TAP, bears a hydroxyl group in the same position as TMA presents a methyl moiety. Though the large potential to present polymorphism, as its referred relative compounds, only one crystallographic structure was identified for this molecular system. A possible justification for the lack of easy-accessible polymorphs of TAP has been suggested. Nonetheless, TAP was studied by quantum chemical calculations (both the isolated molecule and the identified crystal structure) and also experimentally, specifically by single crystal X-ray diffraction and by polarized Raman spectroscopy. Additionally, the three colored polymorphs of TMA, presented in the previous subchapter, were also studied by polarized Raman spectroscopy, complemented with periodic DFT calculations, which revealed to be a combined powerful technique to identify and thoroughly investigate polymorphs and to characterize vibrationally organic crystals in general, due to the fact that it allows to expand the obtained information, when compared to regular Raman spectroscopy.

Molecular and Crystal Structures of *N*-Picryl-*m*-phenolidine and Investigation of Single Crystal Polarized Raman Spectra

Bernardo A. Nogueira,^{1,2,*} Susana M. M. Lopes,¹ Teresa M. V. D. Pinho e Melo,¹

José A. Paixão,³ Alberto Milani,² Chiara Castiglioni² and Rui Fausto¹

¹ University of Coimbra, CQC-IMS, Department of Chemistry, P-3004-535 Coimbra, Portugal.

² CMIC, Dipartimento di Chimica, Materiali e Ingegneria Chimica "G. Natta", Politecnico di Milano, Italy.

³ University of Coimbra, CFisUC, Department of Physics, P-3004-516 Coimbra, Portugal

Abstract

The molecular and crystal structures of *N*-picryl-*m*-phenolidine (or, 3-(2,4,6-trinitrophenylamino)phenol; TAP) were investigated by quantum chemical electronic structure calculations (including state-of-the-art fully-periodic DFT calculations for the crystal) and single crystal X-ray diffraction. The molecule of the compound has four low-energy conformers, which have calculated relative energies within 0.7 kJ mol⁻¹. In all conformers, an N–H···O intramolecular hydrogen bond exists, which is established between the bridging amine moiety and one of the nitro groups of the picryl fragment, and an average angle between the two rings of ca. 55°. The crystals of the compound are monoclinic, *P*2₁/*n* space group, with *a* = 11.8098(3), *b* = 6.5706(2) and *c* = 16.5172(4) Å, β = 91.5640(10)°, *Z* = 4 and *Z'* = 1, and is constituted by molecules assuming a geometry similar to that of the second most stable conformer of the isolated molecule. In the crystal, besides the N–H···O intramolecular hydrogen bond already present for the isolated molecule, a strong intermolecular H-bond exists where the OH group works as proton donor. The geometric constraints resulting from the establishment of this strong intermolecular H-bond is suggested to be the main factor precluding the existence of easily obtainable additional crystalline phases, contrarily to what has been found for similar molecules.

Single crystal polarized Raman spectra of TAP and of the three polymorphs exhibiting different colors of its analogue *N*-picryl-*m*-toluidine (2,4,6-trinitro-*N*-(*m*-tolyl)aniline; TMA), where the phenol OH group is replaced by a methyl group, were also studied at light of fully periodic first principle calculations. Both TAP and TMA belong to the family of the prominent *N*-picryl-*p*-toluidine compound, which is well-known for showing color polymorphism, the obtained results thus being also a contribution for the available knowledge about this rare and interesting phenomenon.

Keywords: *N*-picryl-*m*-phenolidine, *N*-picryl-*m*-toluidine, molecular and crystal structure, single-crystal polarized Raman spectra, quantum chemical calculations.

Corresponding author e-mail: ban@qui.uc.pt

interest of this study. In addition, the conformational space of the isolated molecule of the compound proved also to be worth to investigation.

In the present study, we have also explored the single crystal polarized Raman spectra of TAP, in comparison with those of the three different color polymorphs of TMA, whose structures we had reported before.⁷ Raman spectroscopy is one of the most authoritative techniques to differentiate between polymorphs, due to its sensitivity to structural characteristics of both the materials and individual molecules (i.e., inter- and intra- molecular interactions), besides the easiness of sample preparation it requires, speed of data acquisition and the fact that it is essentially non-destructive.^{26–28} When combined with confocal microscopy, Raman spectroscopy is indeed a very suitable (and powerful) tool allowing for a rapid analysis of individual crystals, in particular when advantage is taken from the polarization characteristics of the laser light used to generate the Raman effect. In fact, for single crystals the use of polarized light (laser) as excitation source may result in different outcoming spectra, depending on the specific components of the polarizability Raman tensors associated with the different vibrations.^{29–33} These characteristics can be used to exploit further information regarding the specific structural characteristics of the different crystallographic species. In the analysis of the experimental polarized Raman spectra of crystalline TAP and of the three polymorphs of TMA, state-of-the-art fully periodic quantum chemical calculations, as implemented in the CRYSTAL17 code,^{32,34} were used.

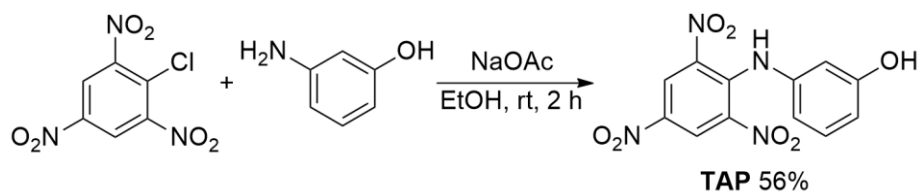
2. Experimental and Computational Methods

2.1. Experimental Methods

The reagents and solvents were obtained commercially as analytical grade. TAP was synthesized via nucleophilic aromatic substitution reaction of 1-chloro-2,4,6-trinitrobenzene with *m*-aminophenol (Scheme 2), following the general procedure described elsewhere.^{7,35} Anhydrous sodium acetate (2.07 mmol, 0.170 g) and *m*-aminophenol (2.07 mmol, 0.189 mL) were added to a solution of 1-chloro-2,4,6-trinitrobenzene (2.07 mmol, 0.512 g) in ethanol (15 mL). The reaction mixture is stirred at room temperature for 2 h (monitored by TLC). The product precipitates and was filtered, washed with 30% aqueous solution of ethanol and dried under vacuum to give a reddish-orange solid (0.360 g, 56%).

The characterization of the synthesized TAP material was undertaken by nuclear magnetic resonance (NMR) and infrared (IR) spectroscopies, melting point determination, and elemental analysis. The ¹H- and ¹³C-NMR spectra (Figure S1 in the Supporting Information) were obtained in DMSO-*d*₆ solution in a Bruker Avance III instrument, operating at 400 MHz and at 100 MHz, respectively. The IR spectrum (Figure S2) was recorded (512 scans; 1 cm⁻¹ resolution) using a Thermo Scientific Fourier transform IR Nicolet iS5 spectrometer, with an iD7 ATR (attenuated total reflectance) accessory (angle of incidence: 45; crystal: diamond). The melting point (uncorrected) was determined in an open-glass capillary. The elemental analysis was performed with an Elemental Vario MicroCube

analyser. TLC analyses were performed with precoated silica gel plates. Characterization results: m.p. 206.0–206.9 °C; elemental analysis: calc. for C₁₂H₈N₄O₇, C 45.01, H 2.52, N 17.50, found, C 45.05, H 2.18, N 17.52; ¹H-NMR: δ (DMSO-*d*₆): 6.54–6.59 (m, 3H), 7.09 (t, *J* = 8.4 Hz 1H), 8.93 (s, 2H), 9.63 (s, 1H), 10.10 (s, 1H); ¹³C-NMR δ (DMSO-*d*₆): δ 108.0, 111.2, 113.1, 126.8, 129.9, 135.5, 137.8, 139.1, 140.2, 158.1; IR (ATR): ν 426, 464, 504, 531, 563, 594, 616, 647, 683, 694, 729, 738, 746, 763, 798, 827, 873, 925, 935, 984, 1000, 1089, 1155, 1165, 1180, 1233, 1280, 1320, 1430, 1479, 1498, 1525, 1587, 1607, 1623, 3088, 3281, 3384 cm⁻¹.



Scheme 2 – Synthetic route to TAP.

The crystals of TAP to be used in the single crystal X-ray diffraction and polarized Raman spectroscopy experiments were obtained by slow recrystallization from ethanol. In search for different polymorphs of the compound, recrystallizations were also attempted using other solvents with different characteristics (polar protic and aprotic, and non-polar), covering a range of dielectric constant values (1.84, in *n*-pentane, to 46.68, in dimethyl sulfoxide), but in all cases the same crystalline material was obtained.

The single crystal X-ray diffraction (XRD) measurements were performed using graphite monochromated MoK α ($\lambda = 0.71073$ Å) radiation in a Bruker APEX II diffractometer, at room temperature. The structure was solved by the dual-space algorithm implemented in SHELXT-2018/2,³⁶ and full-matrix least-squares refinement of the structural model was performed using SHELXL-2018/3.³⁷ All non-hydrogen atoms were refined anisotropically. Hydrogen atoms were placed at calculated idealized positions and refined as riding using SHELXL-2018/3 default values,³⁷ except for those of the hydroxyl and amine groups that was refined isotropically with a displacement parameter constrained to 1.5 \times (hydroxyl) or 1.2 \times (amine) of the U_{iso} value of the parent atom. Full details of the data collection and structure refinement procedures are provided in the Supporting Information (Crystallographic Data). A summary of the data collection and refinement is provided in Table 1. The CIF file containing the supplementary crystallographic data for TAP was deposited at the Cambridge Crystallographic Data Centre, with the reference CCDC 2116365.

The polarized single crystal Raman spectra of TAP and TMA polymorphs (selected crystals obtained from solvent recrystallization, with approximate size of 1 \times 1 \times 0.5 mm) were obtained using a micro-Raman Horiba LabRam HR Evolution system. A half-wave polarization rotator (Horiba-Jobin-

Yvon) was used to change the polarization of the excitation beam by 90°, and a CorePol P-500-1000 polarizer (Horiba-Jobin-Yvon) was employed to select the polarization component of the scattered light for collection. The excitation was provided by a 633 nm HeNe laser, with approximate power of 1 mW at the sample, to prevent photodegradation. The final spectra resulted from 100 to 1000 accumulations of 1 s acquisition time single spectra, obtained using a 50× long working distance objective (~1 μm laser spot diameter at the sample). The wavenumber calibration was performed using a Si crystal as reference (characteristic intense band at 520.5 cm⁻¹).

Table 1 – Summary of the single-crystal X-ray data collection and crystal structure refinement.

Chemical formula	C ₁₂ H ₈ N ₄ O ₇
Formula weight	320.22
Color, shape	dark orange/plate
Space group	<i>P</i> 2 ₁ / <i>n</i>
Temperature(K)	293(2)
Cell volume (Å ³)	681.42(4)
Crystal system	monoclinic
<i>a</i> (Å)	11.8098(3)
<i>b</i> (Å)	6.5706(2)
<i>c</i> (Å)	16.5172(4)
<i>α</i> (deg)	90
<i>β</i> (deg)	91.5640(10)
<i>γ</i> (deg)	90
<i>Z</i> , <i>Z'</i>	4,1
<i>D</i> _c (Mg m ⁻³)	1.660
Radiation (Å) (graphite; monochromated)	0.71073
Max. crystal dimensions (mm)	0.33×0.25×0.18
<i>θ</i> range (deg)	3.337 – 27.497
Range of <i>h</i> , <i>k</i> , <i>l</i>	–15,15; –8,8; –21,21
Reflections measured/independent	119711/2942
Reflections observed (<i>I</i> > 2 <i>σ</i>)	2117
Data/restraints/parameters	2942/0/214
GOF	1.016
<i>R</i> ₁ (<i>I</i> > 2 <i>σ</i>)	0.0421
<i>wR</i> ₂	0.1283
Function minimized	Σ <i>w</i> (<i>F</i> _o ² – <i>S</i> <i>F</i> _c ²)
Diff. density final max/min (<i>e</i> Å ⁻³)	0.582, –0.223

2.2. Computational Methods

The calculations performed on the isolated TAP molecule were undertaken within the density functional theory (DFT) framework, with the three-parameter B3LYP density functional,^{38,39} and the 6-311++G(d,p) basis set.⁴⁰ These calculations were carried out using the Gaussian 09 (revision D.01) software.⁴¹

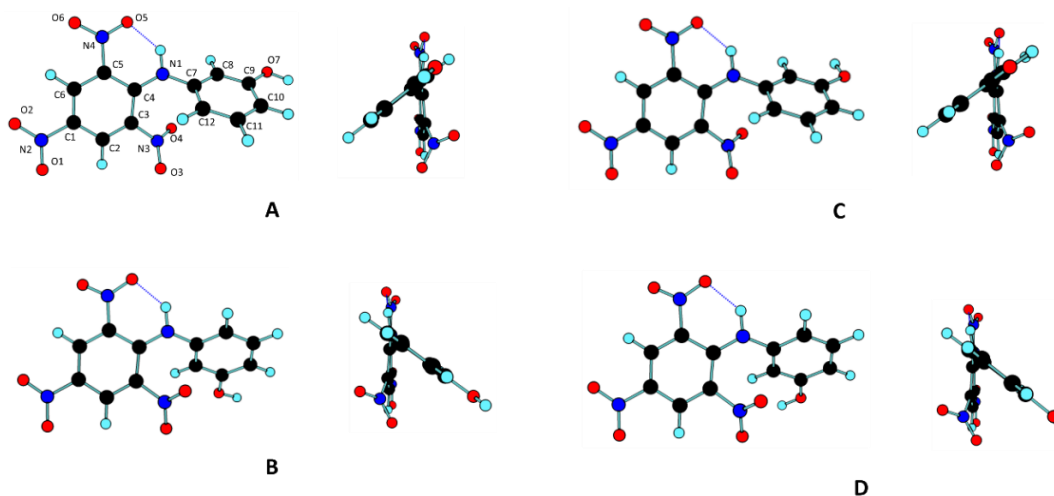
The computations on the crystal of TAP were performed using CRYSTAL17,^{32,34} with the PBE0 functional⁴² and the 6-31G(d,p) basis set.⁴³ The atomic positions and the lattice parameters were fully optimized, the input structure being that experimentally determined in this work (see Table S1, in the Supporting Information). The calculated structural data for the crystals of the three TMA polymorphs were those we have reported previously.⁷ The calculation of the vibrational frequencies at the Γ point

has been performed on the optimized geometries of all crystals studied was achieved by the diagonalization of the numerically calculated Hessian matrices, the predicted frequencies being subsequently scaled by a single empirical factor (0.9512),⁴³ for better comparison with the experimental data. Raman intensities were obtained from the calculated Raman activities as described in ref 44 for the complete set of individual Raman tensor contributions, and the appropriate contributions were then used to predict the intensities for comparison with the experimentally obtained single crystal Raman spectra. The orientation of the crystals and identification of the Miller indices of the crystal faces probed in the Raman experiment were determined from the XRD orientation matrix using the crystal orientation and face indexing algorithms implemented in the APEX3 software (Bruker).

3. Results and Discussion

3.1. Theoretical Investigation of the Conformational Space of the TAP molecule

The investigation of the potential energy surface of TAP at the DFT(B3LYP)/6-311++G(d,p) level of theory yields four different conformers, with calculated relative energies that differ to within 0.7 kJ mol⁻¹ (Figure 1). These four conformers (all of them being double-degenerated by symmetry) differ in the orientation of the two rings and/or orientation of the phenolic OH group. In all conformers, an N–H···O intramolecular hydrogen bond exists, which is established between the bridging amine moiety and one of the nitro groups of the picryl fragment. This last, is a common structural feature to all similar molecules previously investigated, as TMA and *N*-picryl-*p*-toluidine, for example.^{5,7} The H-bond geometry in all the four conformers of TAP is very much similar, with the calculated N–H bond length equal to 1.017 Å, and the H···O distance and N–H···O angle in the narrow ranges of 1.809-1.816 Å and 134.0-134.5°, respectively. The C4–N1 and N1–C7 bond lengths are also equal in the two conformers, the first being considerably shorter (1.349 Å) than the latter (1.423 Å) due to the π -electron delocalization from N1 to the picryl ring, which ensures the C4–N1 a substantial double bond character.



In the lowest energy conformer (**A**) the average angle between the two rings (ϕ) is 54.5° , the C4–N1–C7–C12 dihedral angle being $\pm 145.0^\circ$, while the OH group is oriented towards the opposite direction of the amine bridging group (*trans* orientation). In conformer **B**, which is only $0.097 \text{ kJ mol}^{-1}$ higher in energy than conformer **A**, the orientation of the OH group is also *trans*, while ϕ is equal to 55.3° and the C4–N1–C7–C12 dihedral angle is $\pm 39.4^\circ$. These conformers can be interconverted by internal rotation about the N1–C7 bond of the bridge. Figure 2 shows the results of relaxed scan calculations, where the C4–N1–C7–C12 dihedral angle was chosen as driving coordinate, while all other internal coordinates were optimized. Potential energy profiles corresponding to rotations in the two directions (clockwise and anti-clockwise, matching to an increase and to a decrease of the value of the dihedral angle, respectively) were computed, the starting geometry being that of conformer **A**. As seen in the figure, the direction of the rotation influences the obtained energy profile. Along the rotation around the N1–C7 bond, in order to avoid steric hindrance when the two rings of the molecule approach co-planarity the orientation of the non-hydrogen-bonded *ortho*-nitro group changes. In the transition states, this nitro group is near perpendicular to the picryl ring. When the scan starts at the geometry of the minimum **A** (C4–N1–C7–C12 dihedral angle equal to 145.0°) in the anti-clockwise direction, the molecule first crosses the **A**→**B** isomerization barrier (which amounts to $\sim 15 \text{ kJ mol}^{-1}$) and reaches the minimum **B** (C4–N1–C7–C12 of 39.4°). Then, the energy progressively raises to a value of ca. 37 kJ mol^{-1} , which occurs for a dihedral angle of ca. -53.0° , where the change of orientation of the non-hydrogen-bonded *ortho*-nitro group takes place, so that energy reduces abruptly. At this point, the conformation is close to that of the **B'** minimum (whose position has, however, already been surpassed), the symmetry-equivalent structure to minimum **B**. Continuation of the scan after this point, leads to the overcome of the **B'**→**A'** barrier (ca. 15 kJ mol^{-1}), **A'** being the symmetry-equivalent minimum of the initial structure **A**. On the other hand, when the scan is performed in the clockwise direction, starting from **A**, the energy grows continuously until ca. 37 kJ mol^{-1} , when it suddenly decreases abruptly, once again due to the change of the conformation of the non-hydrogen-bonded *ortho*-nitro group. At this point, the C4–N1–C7–C12 dihedral angle of ca. 238° , which is already larger than that of **A'**. Continuing the scan, the **B'** minimum is attained. Then, a similar profile is obtained for larger values of the scanned dihedral angle, a maximum of energy is observed at ca. 417° ($\sim 37 \text{ kJ mol}^{-1}$), overpassing the minimum **B** and proceeding till the minimum **A** is attained. Hence, the scan starting from **A** for increasing values of the C4–N1–C7–C12 dihedral angle does not allow to reach neither the minimum **B**, nor **A'**, but interconverts directly **A** into **B'** via effective barriers of ca. 37 kJ mol^{-1} . It shall, however, be stressed that the anti-clockwise rotation does allow easy interconversion between the minima **A** and **B** (and in a similar way between **A'** and **B'**) through a low energy transition state of only ca. 15 kJ mol^{-1} . In practical terms, this means that the effective barrier for interconversion between conformers **A** and **B** (and between their equivalent forms, **A'** and **B'**) is low, amounting to only ca. 15 kJ mol^{-1} , thus conferring to the molecule a considerably degree of conformational flexibility.

Conformers **C** and **D**, have energies 0.62 and 0.69 kJ mol⁻¹ higher than conformer **A**, respectively, and correspond to the two forms with the OH group in the *cis* orientation (i.e., having the OH group oriented towards the amine bridging group). Besides the different orientation of the OH group, conformers **C** and **D** are essentially identical to conformers **A** and **B**, respectively. The potential energy profile for interconversion between **C** and **D** is identical to that between **A** and **B** and it can be explained in the same way as above for this latter case and leads to the same implications.

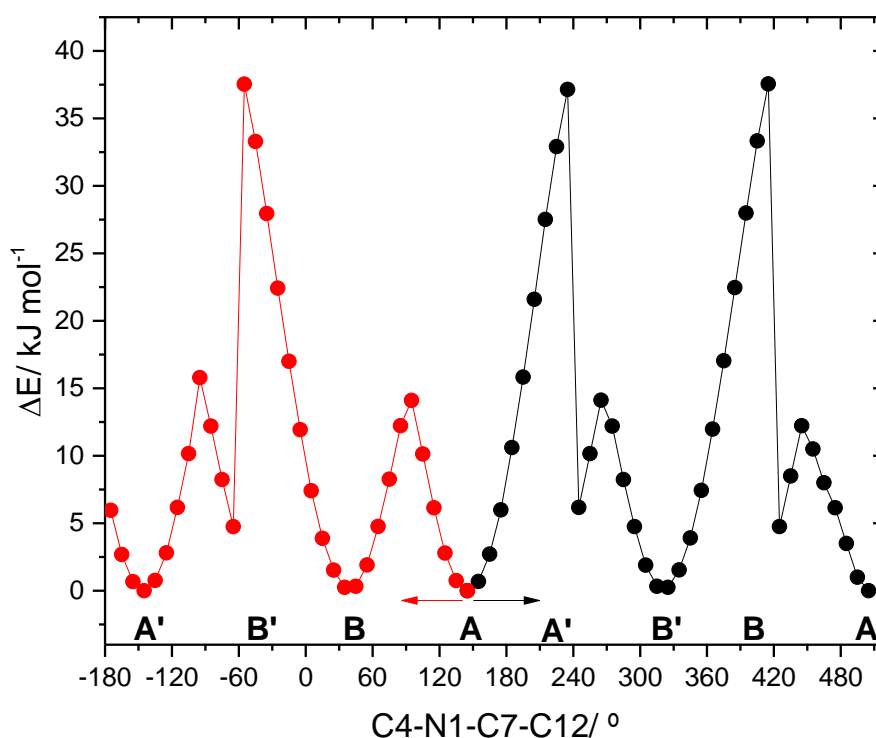


Figure 2 - DFT(B3LYP)/6-311++G(d,p) calculated potential energy profiles for internal rotation about the N1–C7 bond of the amine bridge of TAP molecule. The two curves correspond to interconversions between the pairs of conformers **A** and **B** and their symmetry-related forms **A'** and **B'**. The arrows indicate the directions of the scans. See Figure 1 for atom numbering and structures of the conformers.

The interconversions between the two pairs of conformers, **A** and **C**, and **B** and **D**, take place through internal rotation about the C–O phenolic bond. This rotation can take place in two ways, which considering the representations of the conformers shown in Figure 1, correspond to the cases where the phenolic hydrogen atom moves up (positive values of the C12–C–O–H dihedral angle in Figure 3) or down (negative values of the C12–C–O–H dihedral angle). These two paths have different energy barriers (see Figure 3), with that corresponding to the latter being lower than the first, because in the corresponding transition state structure the positively-charged rotating hydrogen atom points to the negatively-charged oxygen atoms of the closest nitro group (–N3O₂; see Figure 1). For the **A** → **C** conversion, the two energy barriers were predicted to be 15.3 and 17.3 kJ mol⁻¹, respectively, while in the case of the **B** → **D** rotamerization the corresponding barriers were calculated as 13.6 and 17.8 kJ mol⁻¹.

Another interesting structural feature shared by all TAP conformers is the deviation of the nitro group located closer to the phenolic ring from the plane of the picryl ring by ca. 40°, in order to reduce the steric interactions between this nitro group and the phenolic moiety. This structural feature has also been noticed before for TMA and *N*-picryl-*p*-toluidine and can be considered a general trend for this type of molecules.^{5,7}

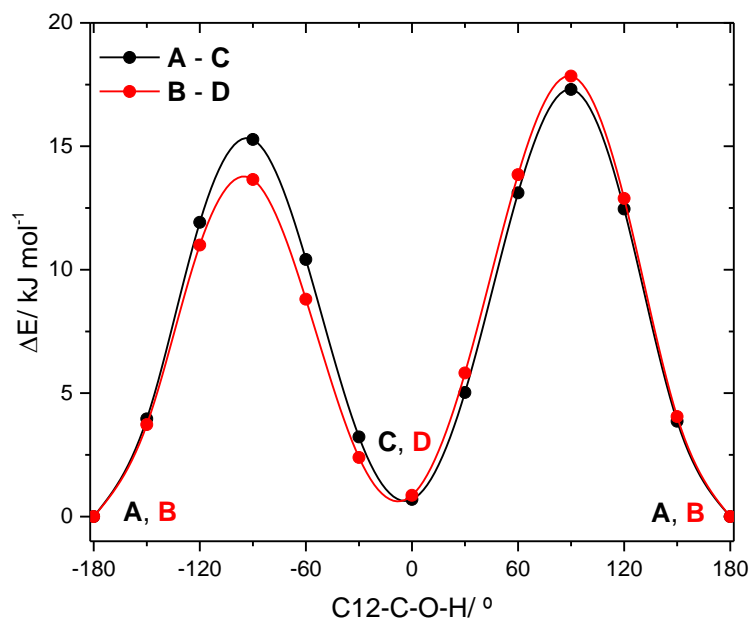


Figure 3 - DFT(B3LYP)/6-311++G(d,p) calculated potential energy profiles for internal rotation of the phenolic OH group in the pairs of conformers A and C, and B and D of TAP molecule. See Figure 1 for atom numbering and structures of the conformers.

3.2 Crystal Structure of TAP

Single crystal X-ray diffraction indicates that the plate-shape dark-orange crystals of TAP belong to the monoclinic, centrosymmetric, $P2_1/n$ space group, with $a = 11.8098(3)$, $b = 6.5706(2)$ and $c = 16.5172(4)$ Å, $\beta = 91.5640(10)^\circ$, $Z = 4$ and $Z' = 1$.

In the crystal, the molecules assume a geometry similar to that of the second most stable conformer **B** of the isolated molecule (Figure 4), the angle between the average planes of the two phenyl rings being $52.14(6)^\circ$, very close to that calculated for conformer **B** (55.26°). The intramolecular N–H \cdots O hydrogen bond established between the amine N–H bridging group and the O5 atom of the neighbouring *ortho* nitro group and found in the isolated molecule persists in the crystal. The measured N1 \cdots O5 distance in crystalline phase is $2.644(2)$ Å, which does not differ much from that calculated for the isolated molecule (2.627 Å), which indicates that this intramolecular H-bond is not disturbed strongly by the intermolecular interactions. Valence angles and bond distances in the molecule determined in the X-ray study fall within the range of expected values of similar compounds,^{5,7} and are also similar to those calculated for the isolated molecule. Noteworthy, the internal ring angles of the picryl ring where the apical C atom is attached to the strong electron withdrawing NO₂ groups are

significantly larger than those adjacent to unsubstituted C atoms, as it has already been noticed for TMA and nitrobenzene,^{7,45} and also in agreement with the theoretical calculations performed on the isolated TAP molecule (Table 2). The N–O bond distances are in the range 1.210–1.226 Å and are also similar to those calculated for the isolated molecule (1.220–1.238 Å), the longer values corresponding to those bonds involved in hydrogen-bonding. As a whole, the conformations of the nitro groups in the crystal are determined by their participation in hydrogen bonding and steric effects. These groups are not coplanar with the ring, the largest deviation from the plane of the ring being observed in the N3O₂ group, due to the steric interaction with the phenolic ring, as it was also found for the isolated molecule of the compound. For this nitro group, the angle of deviation from the ring in the crystal is 39.6(2)°, which matches exactly to the one calculated for conformer **B** (Table 3). The deviation of the intramolecularly H-bonded nitro group from the ring in the crystal is also similar to that calculated for the isolated molecule (13.5(3)° vs. 10.4°), while the deviation from the ring in the crystal for the last nitro group (C1NO₂) is considerably larger (9.5(3)°) than in the isolated molecule, where it is practically co-planar with the ring (the calculated deviation is only 1.6°), indicating that intermolecular packing influences more the geometry of this nitro group. In fact, a strong hydrogen bond occurs between the N2O₂ group and the hydroxyl group of a neighbouring molecule exists in the crystal. As shown in Figure 5, this hydrogen bond links molecules in 1D chains running parallel to the crystallographic [1 0 –1] axis.

In addition to the hydrogen bonds involving the hydroxyl and amine groups as proton donors, inspection of the intermolecular distances shows that the 1D chains also exhibit several short C–H···O distances with a suitable geometry that may qualify them as weak hydrogen bond interactions (Table 4). The structure consisting of a stacking of these chains is depicted in Figure 6. Connection between the chains occurs mainly through the weak C2–H2···O4ⁱ (*i*: 3/2–*x*, –1/2+*y*, 3/2–*z*) intermolecular hydrogen bond.

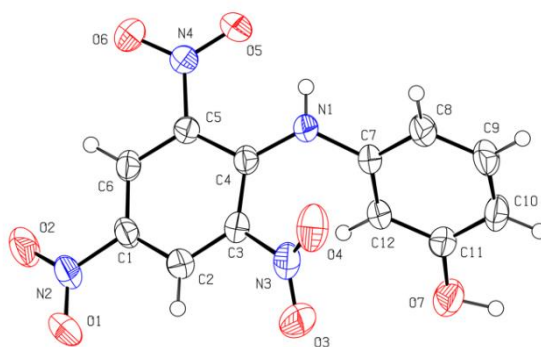


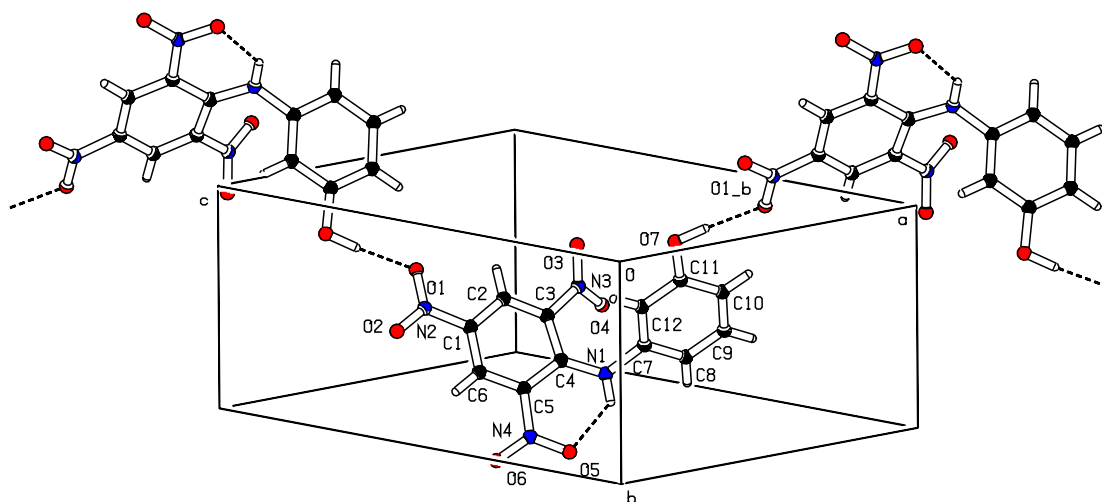
Figure 4 – ORTEP plots depicting the anisotropic displacement ellipsoids drawn at the 50 % probability level.

Table 2 – Valence angles in the picryl ring of TAP crystal.

Angle	Crystal (X-ray)/ °	Isolated molecule Form B (calculated)/ °
C6–C1–C2	121.21(16)	120.77
C4–C5–C6	122.96(17)	122.49
C2–C3–C4	124.10(16)	123.36
C1–C2–C3	118.41(18)	119.29
C5–C6–C1	119.10(17)	119.74
C3–C4–C5	113.32(15)	114.07

Table 3 – Relevant dihedral and torsion angles for the TAP crystal.

Dihedral/torsion angle	Crystal (X-ray)/ °	Isolated molecule Form B (calculated)/ °
< (C1...C6)/(C7–C12)	52.14(6)	53.8
< (C1...C6)/N2O ₂	9.5(3)	1.6
< (C1...C6)/N3O ₂	42.67(8)	43.1
< (C1...C6)/N4O ₂	13.5(3)	10.4
C2–C1–N2–O1	8.5(3)	2.2
C4–C3–N3–O4	39.6(2)	39.6
C6–C5–N4–O6	13.3(2)	10.3
C5–C4–N1–C7	–150.77(19)	–153.2
C4–N1–C7–C12	34.7(3)	39.5

Figure 5 – Hydrogen-bonding network in TAP crystal showing the 1D-chains running along the crystallographic direction $[1\ 0\ -1]$.

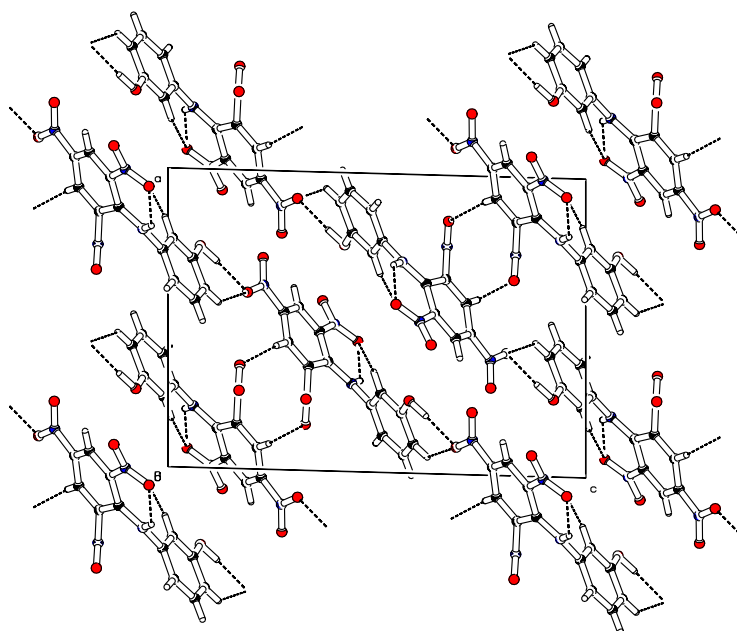


Figure 6 – Hydrogen-bonding network showing the TAP crystal packing. The view is a projection of the structure along the *b*-axis.

Table 4 – Hydrogen bonds and short intermolecular contacts in TAP crystal. *

D-H...A	D-H	H-A	D...A	< D-H...A
O7–H7A...O1 ^a	0.97(3)	1.85(3)	2.822(2)	176(3)
N1–H1...O5	0.84(2)	2.01(2)	2.644(2)	132(2)
C2–H2...O4 ^b	0.93	2.54	3.455(3)	168.8
C10–H10...O1 ^c	0.93	2.54	3.251(3)	133.1
C12–H12...O5 ^d	0.93	2.54	3.311(2)	141.0

*Distances and angles are given in Å and degrees, respectively. Symmetry codes: a) $1/2+x, 1/2-y, -1/2+z$; b) $3/2-x, -1/2+y, 3/2-z$; c) $x, 1+y, z$; d) $x, -1+y, z$

As mentioned in the introduction, we expected that TAP would present easily accessible distinct polymorphs due to its structural similarity with *N*-picryl-*p*-toluidine and TMA. Additionally, the extra conformational degree of freedom resulting from the presence of an OH group (with two possible different orientations) instead of the methyl group was also expected to increase the polymorphism potential of the compound. Nevertheless, despite our attempts, only one crystalline phase was identified. Considering the structural results, we can now propose that, contrarily to our initial predictions, the presence of the OH group in the molecule resulted as the main factor preventing the existence of easily obtainable additional crystalline phases. As described above, this group is involved in a strong intermolecular H-bond with a neighbouring molecule, and this intermolecular interaction affects considerably the geometry of the proton acceptor nitro group, which is fundamental in determining the overall structure of the crystal. Hence, the geometric constraints resulting from the establishment of this

H-bond strongly apparently reduce the possibility of formation of other energetically favored crystalline structures.

3.3. Single Crystal Polarized Raman Spectra of TAP and Polymorphs of TMA

Unlike the Raman spectra of powder samples, where the size of the randomly oriented individual grains is orders of magnitude smaller than the optical resolution in standard confocal Raman spectroscopy, the Raman spectra of single crystals depends directly on the relative orientation of the crystallographic axes of the samples (ultimately, on the polarizability Raman tensors of the vibrational modes) and the polarization direction of the excitation and collected light.²⁹⁻³³

As indicated before, TAP crystal is monoclinic, $P2_1/n \equiv C_{2h}^5$ (no. 14) space group, with $a = 11.8098(3)$, $b = 6.5706(2)$ and $c = 16.5172(4)$ Å, $\beta = 91.5640(10)^\circ$, $Z = 4$ and $Z' = 1$. The yellow, orange and red polymorphs of TMA are monoclinic, $P2_1/c \equiv C_{2h}^5$ (no. 14) space group, with $a = 12.5800(7)$, $b = 8.0014(4)$ and $c = 15.0156(8)$ Å, $\beta = 110.794(2)^\circ$, $Z = 4$ and $Z' = 1$, orthorhombic, $Pna2_1 \equiv C_{2v}^9$ (no. 33) space group, with $a = 29.971(3)$, $b = 9.0537(10)$ and $c = 5.1150(6)$ Å, $Z = 4$ and $Z' = 1$, and triclinic, $P\bar{1} \equiv C_1^1$ (no. 2) space group, with $a = 7.5195(2)$, $b = 8.3723(3)$ and $c = 12.2263(4)$ Å, $\alpha = 81.0389(19)^\circ$, $\beta = 81.9157(18)^\circ$, $\gamma = 64.0565(17)^\circ$, $Z = 2$ and $Z' = 1$, respectively.⁷ Both TAP and TMA molecules are non-symmetric, C_1 symmetry point group, and in the crystals the molecules are located in sites of symmetry C_1 . Altogether, these crystals constitute a set of samples that can be expected to show considerable differences regarding their behaviour when studied by single crystal polarized Raman spectroscopy.

Figure 7 shows the experimentally obtained single crystal Raman spectra of the orthorhombic polymorph of TMA. The spectra were obtained with the direction of the laser beam parallel to the c axis (face-cut ab), with the horizontal (H) polarization plane of the laser beam corresponding to the direction of the a axis, and the vertical (V) to the b axis. In the figure, the predicted spectra obtained from fully-periodic first principles calculations (see Section 2.2 for details of the calculations) are also presented. In the calculations, coordinates x , y and z correspond to the orientations of the axes a , b and c , respectively, so that the HH, VV and HV (or VH) experimental Raman spectra correlate directly with the calculated spectra built based on the Raman tensors' components xx , yy and xy/yx (Porto's notation for the HH, VV and VH spectra are $z(xx)\bar{z}$, $z(yy)\bar{z}$ and $z(xy)\bar{z}$, respectively). The symmetry of the vibrations spawn the symmetry species of the C_{2v} factor group (crystallographic point group), A_1 , A_2 , B_1 , B_2 , for which the nonvanishing components of the Raman tensors are xx , yy and zz (for A_1 modes), xy (A_2), yz (B_1) and xz (B_2). This means that in the performed experiments, only the A_1 modes should be observed in both the HH and VV spectra, and only the A_2 modes contribute to the HV (or VH) spectrum, while the B_1 and B_2 modes are silent. It can be seen in Figure 7 that the general concordance between the experimental and the simulated spectra based on the theoretical data is rather good, noteworthy also regarding intensities. For this crystal, the calculations predicted small Davydov splittings, which are

within 2 cm^{-1} for most of the modes, and attain the maximum of 5 cm^{-1} for the set of vibrations ascribed to one of the CC stretching modes of the phenolic ring whose frequencies span from 1322 cm^{-1} (A_1 mode), to 1327 cm^{-1} (A_2), the frequency of both the B_1 and B_2 modes being 1323 cm^{-1} . This result indicates a small perturbation of the intramolecular vibrational potential due to intermolecular interactions.

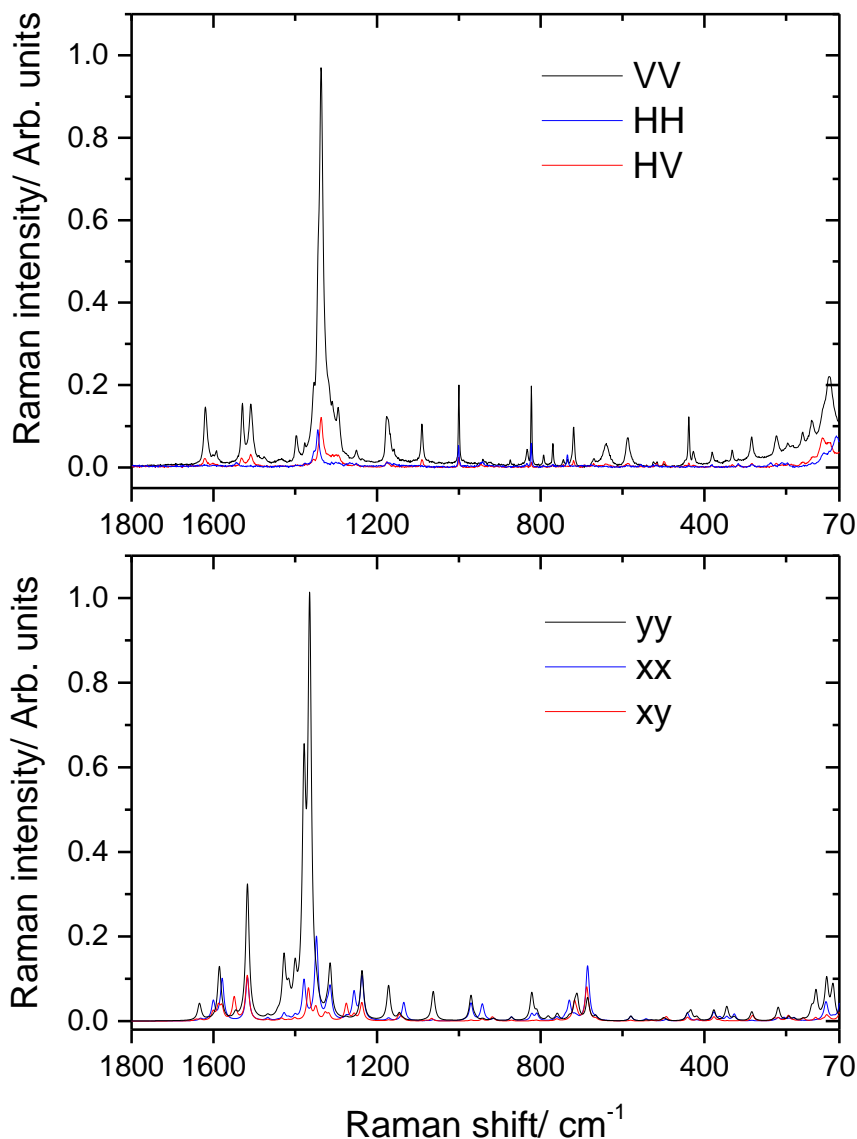


Figure 7 – Experimentally obtained single crystal polarized Raman spectra (*top panel*) compared with the simulated spectra resulting from fully periodic first principles calculations on the crystal of the orthorhombic polymorph of TMA (*bottom panel*). See text for details. The two groups of spectra were normalized to unity by the corresponding most intense band.

The analysis of the single crystal polarized Raman data obtained for the triclinic polymorph of TMA resulted trivial, since all spectra obtained (HH, UV and HV (or VH)) were identical. The face-cut used in the experiments was the *ac* plane, with the laser beam making an angle of 30.2° with the *b* axis, Generation and Characterization of Novel Materials Exhibiting Color Polymorphism 138

so that the contributions to the Raman intensities due to the yy , xy/yx and yz/xz can be anticipated to be small. The symmetry of the vibrations spawns the symmetry species of the C_i factor group, A_g , A_u , the latter being silent in Raman spectroscopy, while all components of the Raman tensors should contribute to the intensity of the A_g modes, making these vibrations observable in all HH, VV and HV (or VH) spectra. Noteworthy, the xx component of the Raman tensors strongly dominate (see Figure S3 in the Supporting Information), with the remaining contributions being comparatively negligible. The fairly good reproduction of the experimental Raman spectra by the simulated spectra based on the intensities calculated from the xx component of the Raman tensors (see Figure 8) shall be highlighted.

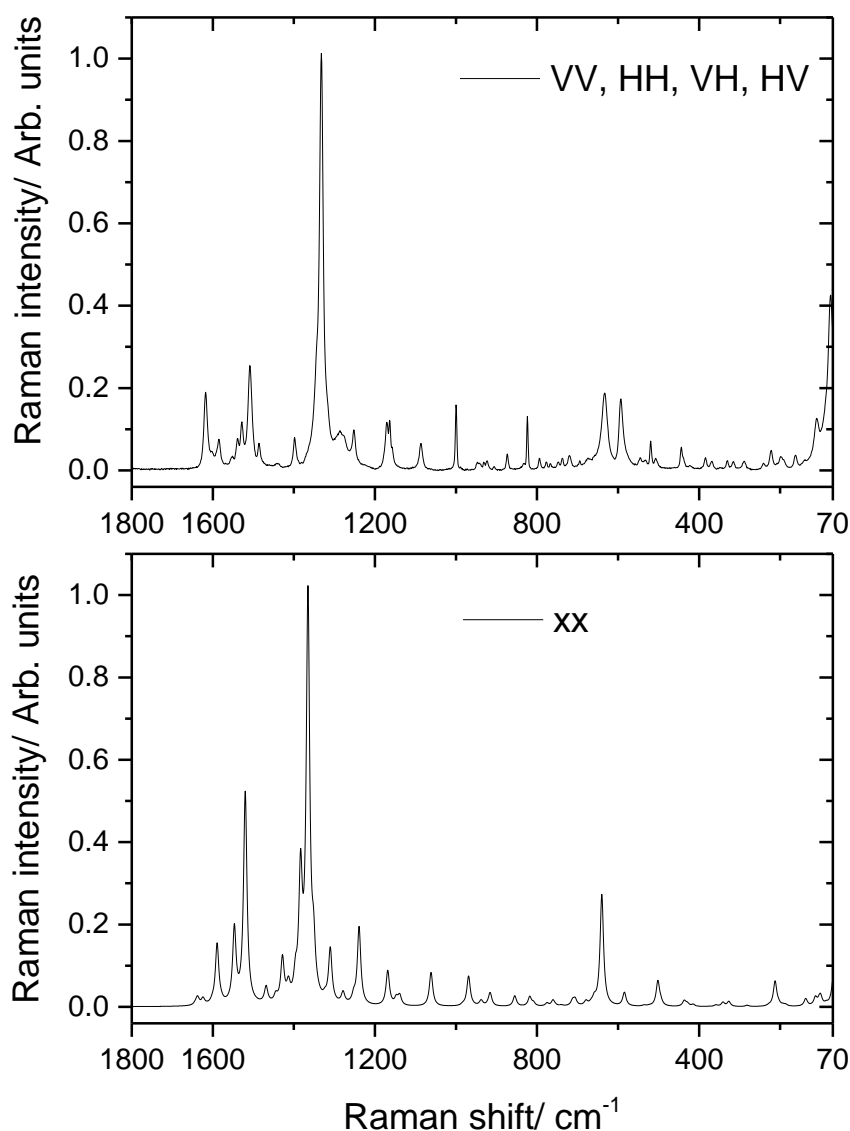


Figure 8 – Experimentally obtained single crystal polarized Raman spectra (*top panel*) compared with the simulated spectra resulting from fully periodic first principles calculations on the crystal of the triclinic polymorph of TMA (*bottom panel*). See text for details. The spectra were normalized to unity by the corresponding most intense band.

As for the orthorhombic polymorph, the intramolecular vibrational potential is also weakly perturbed by the intermolecular interactions in the triclinic polymorph of TMA, with the calculated Davidov splitting between A_g and A_u modes being similar to those found for the former crystal (mostly in the 1-3 cm^{-1} range).

The experimental data obtained for the monoclinic polymorph of TMA is shown in Figure 9, together with the results of the calculations. In this case, the face-cut of the selected crystal corresponds to the bc plane, with the laser direction making an angle of 20.8° with the a axis. The vertical (V) polarization plane of the laser beam corresponds to the direction of the b axis, and the horizontal (H) to the c axis. In the calculations, coordinates x and y correspond to the orientations of the axes a and b axes, while c makes an angle of 20.8° with the z axis. In this geometry, the VV experimental Raman spectrum correlates directly with the calculated spectra built based on the yy Raman tensors' components, and the HH and HV (or VH) spectra correlate with the Raman tensors' components xx , xz/zx and zz (HH), and xy/yx and yz/zy , respectively. For these two spectra, the combination factors measuring the contributions from each set of Raman tensors' components can be determined using simple trigonometry relations between the directions of the polarization of the excitation and collected light and those of the crystallographic and Cartesian axis according to the orientation of the crystal in the experiment and are indicated in the caption of Figure 9.

The HH spectrum has as largest component, the zz component, while the HV (or VH) spectrum is dominated by the yz component of the Raman tensors. The symmetry of the vibrations spawns the symmetry species of the C_{2h} factor group, A_g , A_u , B_g , B_u , from which only the A_g and B_g ones are Raman active. In the case of the A_g modes, the relevant components of the Raman tensors are xx , yy , zz and xz/zx , and for the B_g modes the xy and yz components. This means that in the performed experiments, the A_g modes should be observed in both the HH and VV spectra, while the B_g modes can be observed in the HV (or VH) spectrum. As seen in Figure 9 the reproduction of the experimental data by the simulated spectra based on the theoretical results is quite good, including what concerns to intensities.

The calculated Davidov splitting for this TMA polymorph follow the general rule found for those corresponding to the remaining polymorphs of this compound, being mostly in the 1-3 cm^{-1} range). Nevertheless, a few larger values for the Davidov splitting were predicted for some vibrations, noteworthy for the νNO_2 stretching modes, where values up to 11 cm^{-1} were predicted (e.g., for the most intense Raman νNO_2 symmetric stretching mode, whose A_g and B_g modes were predicted at 1369 and 1371 cm^{-1} , while the infrared active B_u and A_u modes were predicted at 1360 and 1368 cm^{-1} , respectively).

In the case of TAP, the chosen face-cut of the crystal was chosen to be the bc plane, in a similar way to what was done for the crystal of the monoclinic polymorph of TMA. The same formal treatment was then applied. However, in the case of TAP, though the crystal is monoclinic, the β angle is very close to 90° (the measured value is $91.5640(10)^\circ$), so that the coefficients of combination of the minor

Raman tensors contributing to the HH and HV (or VH) spectra became approximately zero. In the practice, this means that when considering its polarized Raman spectra, the TAP crystal can be treated as being orthorhombic.

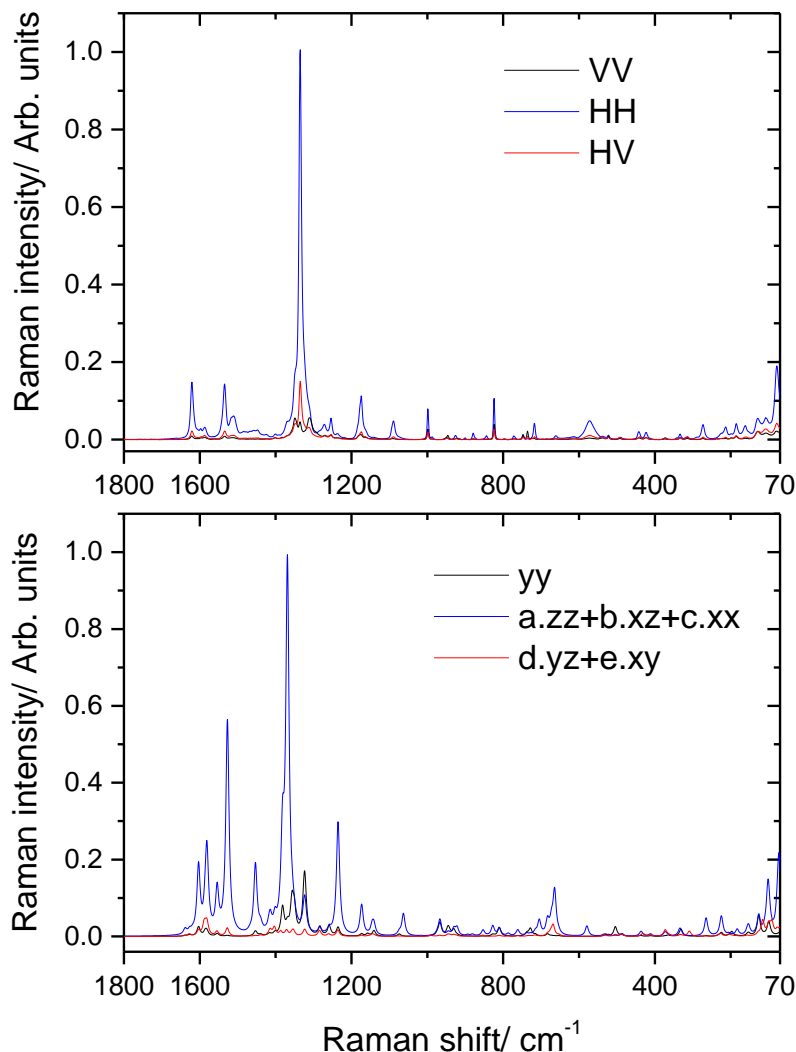


Figure 9 – Experimentally obtained single crystal polarized Raman spectra (*top panel*) compared with the simulated spectra resulting from fully periodic first principles calculations on the crystal of the monoclinic polymorph of TMA (*bottom panel*). Values of factors a, b, c, d and e are 0.874, 0.664, 0.126, 0.935 and 0.355, respectively. See text for details. The two groups of spectra were normalized to unity by the corresponding most intense band.

For TAP, according to the selected orientation of the crystal the HH, VV and HV (or VH) spectra are then obtained from the zz , yy and yz/zy Raman tensors. Like for the monoclinic crystal of TMA, the symmetry of the vibrations of the TAP crystal spawns the symmetry species of the C_{2h} factor group, A_g , A_u , B_g , B_u , the A_g and B_g modes being Raman active. The intensities of the A_g modes formally receive contributions from the Raman tensors xx , yy , zz and xz/zx , from which, as stated above, only zz is significant, while the intensity of the B_g modes formally receive contributions from the xy/yx and yz/zy

components of the Raman tensors, with those due to xy/yx being negligible in the practice. In the performed experiments, the A_g modes should be observed in both the HH and VV spectra, while the B_g modes can be observed in the HV (or VH) spectrum. The results are shown in Figure 10, where, like in the case of the TMA crystals, a good concordance between the experimental and calculated data can be noticed.

Interestingly, the calculated Davidov splitting for TAP were found to be in line with the trends observed for the monoclinic polymorph of TMA, i.e., while most of the modes were predicted to exhibit small splitting in the $1\text{-}3\text{ cm}^{-1}$ range, those estimated for the νNO_2 stretching modes were predicted to be somewhat larger, with values up to 13 cm^{-1} . For example, the two Raman intense νNO_2 symmetric stretching modes have components at $1365, 1368, 1369$ and 1371 cm^{-1} (B_u, A_u, B_g and A_g , respectively) and at 1377 (A_g), 1381 (A_u), 1383 (B_u) and 1390 (B_g) cm^{-1} .

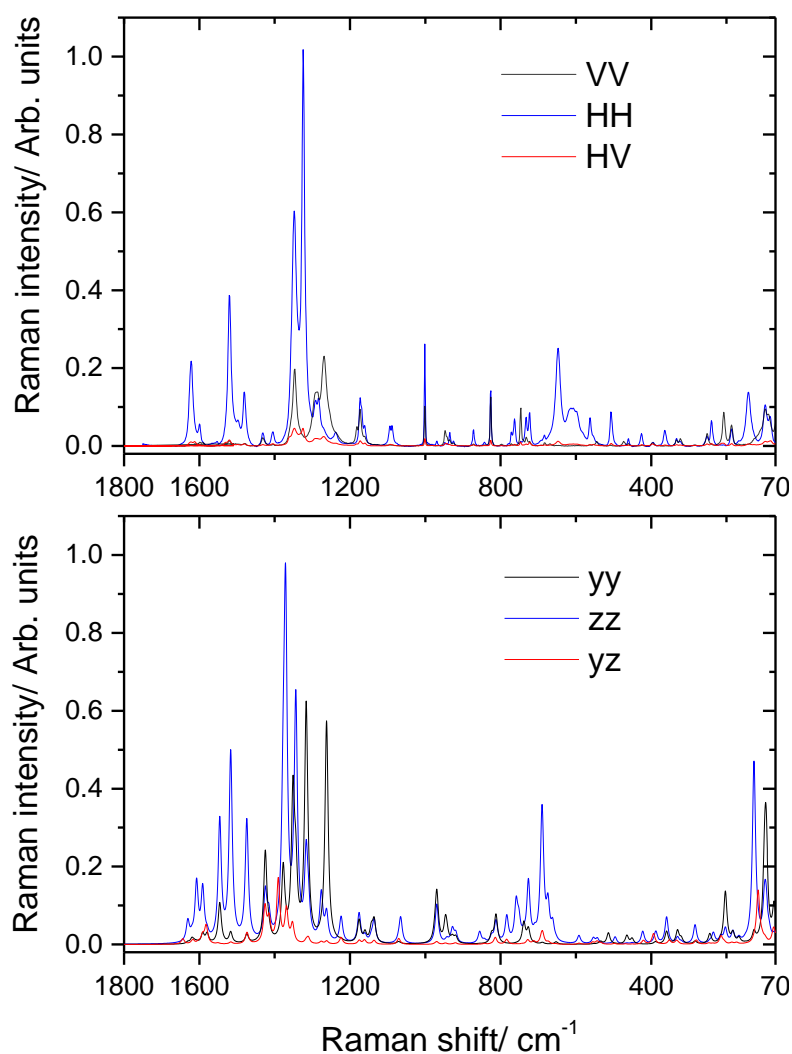


Figure 10 – Experimentally obtained single crystal polarized Raman spectra (*top panel*) compared with the simulated spectra resulting from fully periodic first principles calculations on the crystal of the TAP (*bottom panel*). See text for details. The two groups of spectra were normalized to unity by the corresponding most intense band.

The whole set of performed experimental single-crystal polarized Raman studies and fully-periodic quantum chemical calculations described above demonstrates the good ability of the used theoretical approach to provide appropriate predictions of the polarized Raman spectra for different types of crystals of formed by molecules of significant complexity, which are conformationally flexible and possess an intramolecular hydrogen bond persisting in the crystalline phases, besides participating in a variety of intermolecular interactions. Such approach increases the power of Raman spectroscopy for polymorphs' identification (and vibrational characterization of crystals in general), since it expands the amount of information that is possible to obtain in comparison with the usual Raman experiments where no advantage is taken from the polarization effects.

4. Conclusion

In this investigation, the conformational space of the isolated molecule of TAP was studied using quantum chemical electronic structure calculations undertaken at the DFT(B3LYP)/6-311++G(d,p) level. Particular emphasis was given to the characterization of the distinguishing intramolecular hydrogen bond the TAP molecule exhibits and to its influence on the stabilization of the molecule. The molecule was shown to be considerably flexible conformationally, with very interesting potential energy profiles for internal rotation around the N1–C7 bond of the amine bridge, which were shown to be dependent on the direction of the rotation. Four low-energy conformers were identified, with calculated relative energies within 0.7 kJ mol⁻¹, all of them being double-degenerated by symmetry. In all conformers, an N–H··O intramolecular hydrogen bond exists, which is established between the bridging amine moiety and one of the nitro groups of the picryl fragment, and an average angle between the two rings of ca. 55°. This intramolecular hydrogen bond is kept in the crystalline phase, whose structure was solved by single crystal XRD. The plate-shape dark-orange TAP crystals were found to monoclinic, P2₁/n space group, with $a = 11.8098(3)$, $b = 6.5706(2)$ and $c = 16.5172(4)$ Å, $\beta = 91.5640(10)^\circ$, $Z = 4$ and $Z' = 1$, and is constituted by molecules assuming a geometry similar to that of the second most stable conformer of the isolated molecule. In the crystal, besides the N–H··O intramolecular hydrogen bond present in the isolated molecule, a strong intermolecular H-bond exists where the OH group works as proton donor. It is suggested that the geometric constrains resulting from the establishment of this strong intermolecular H-bond is the main factor precluding the existence of easily-obtainable additional crystalline phases, contrarily to what has been found for similar molecules, like *N*-picryl-*p*-toluidine and TMA.^{7,8}

A throughout investigation of the single crystal polarized Raman spectra of TAP and of the three polymorphs exhibiting different colors of its analogue TMA (where the phenol OH group is replaced by a methyl group) was also undertaken. This investigation demonstrated in a clear way the power of this experimental approach for fast spectroscopic identification of polymorphs and vibrational characterization of organic crystals in general, when used complementary with theoretical calculations

on the crystals undertaken using fully periodic first principles calculations. One of the advantages of the applied strategy of investigation is the fact that it allows expanding the amount of information that is possible to obtain, compared to Raman spectroscopy used without taking advantage from polarization effects. The obtained results also clearly reveal the good prediction ability of the used theoretical approach for interpreting single crystal Raman polarization data.

Supporting Information

Figures S1 and S2, with the ^1H and ^{13}C NMR spectra and the IR-ATR spectrum of the synthesized TAP material. Figure S3, with the HH, VV, HV and VH polarized Raman spectra of the single crystal of the triclinic polymorph of TMA. And calculated spectra based on individual Raman tensors' components. Table S1, with the comparison between the experimental and the computed unit cell parameters of TAP and TMA crystals. Tables with the structural X-Ray data for TAP crystal. The CIF file containing the supplementary crystallographic data was deposited at the Cambridge Crystallographic Data Centre, with reference CCDC 2116365.

Acknowledgements

The CQC-IMS is financially supported by the Portuguese Science Foundation (“Fundação para a Ciência e a Tecnologia” - FCT) – Projects CQC UIDB/00313/2020 and UIDP/00313/2020 (National Funds). CFisUC is funded by FCT through the projects UIDB/04564/2020 and UIDP/04564/2020. Access to instruments from Laser-Lab Coimbra and TAIL-UC (ICT_2009_02_012_1890) facilities funded under QREN-Mais Centro is gratefully acknowledged. We acknowledge the Nuclear Magnetic Resonance Laboratory of the Coimbra Chemistry Centre (www.nmrccc.uc.pt), University of Coimbra for obtaining the NMR spectroscopic data. The authors are also grateful to Prof. Teresa Duarte and Dr. Vânia André, from Centro de Química Estrutural-IMS, Instituto Superior Técnico, for the preliminary X-ray experiments performed on TAP. B.A.N. acknowledges FCT for the SFRH/BD/129852/2017 PhD Scholarship.

References

1. M. Busch and E. Pungs, Über isomere Verschiedenfarbige Pikrylamine, *J. für Prakt. Chemie*, 1909, **79**, 546–554.
2. N. M. Cullinane, O. E. Embrey and D. R. Davis, Investigation of the Differently Colored Forms of Certain Derivatives of Diphenylamine, *J. Phys. Chem.*, 1932, **36**, 1434–1448.
3. R. G. Wood, S. H. Ayliffe and N. M. Cullinane, XXXIII. A crystallographic and X-Ray Investigation of Some Diphenylamine Derivatives *London, Edinburgh, Dublin Philos. Mag. J. Sci.*, 1935, **19**, 405–416.
4. M. Yasui, K. Taguchi and F. Iwasaki, Dynamic Behavior of *N*-(2,4-Dinitrophenyl)-*o*-Anisidine Crystals, *Mol. Cryst. Liq. Cryst. Sci. Technol. Sect. A. Mol. Cryst. Liq. Cryst.*, 1996, **277**, 167–

- 176.
5. D. E. Braun, T. Gelbrich, R. K. R. Jetty, V. Kahlenberg, S. L. Price and U. J. Griesser, Colored Polymorphs: Thermochemical and Structural Features of *N*-Picryl-*p*-toluidine Polymorphs and Solvates, *Cryst. Growth Des.*, 2008, **8**, 1977–1989.
 6. I. G. Ilyina, O. V. Mikhalev, K. P. Butin, B. N. Tarasevich and B. M. Uzhinov, Differently Coloured Crystalline Modifications of Organic Autocomplexes of the Nitroaromatic Types, *Synth. Met.*, 2001, **120**, 1067–1068.
 7. B. A. Nogueira, S. M. M. Lopes, S. Lopes, T. Nikitin, A. C. B. Rodrigues, M. E. S. Eusébio, J. A. Paixão, T. M. V. D. Pinho e Melo, A. Milani, C. Castiglioni and R. Fausto, 2,4,6-Trinitro-*N*-(*m*-tolyl)aniline: A New Polymorphic Material Exhibiting Different Colors, *Cryst. Growth Des.*, 2021, **21**, 7269–7284.
 8. B. A. Nogueira, C. Castiglioni and R. Fausto, Color Polymorphism in Organic Crystals, *Commun. Chem.*, 2020, **3**, 1–12.
 9. R. A. Fletton, R. W. Lancaster, R. K. Harris, A. M. Kenwright, K. J. Packer, D. N. Waters and A. Yeadon, A Comparative Spectroscopic Investigation of Two Polymorphs of 4'-Methyl-2'-nitroacetanilide Using Solid-state Infrared and High-resolution Solid-state Nuclear Magnetic Resonance Spectroscopy, *J. Chem. Soc. Perkin Trans. 2*, 1986, 1705–1709.
 10. C. Kitamura, Y. Abe, T. Ohara, A. Yoneda, T. Kawase, T. Kobayashi, H. Naito and T. Komatsu, Synthesis and Crystallochromy of 1,4,7,10-Tetraalkyltetracenes: Tuning of Solid-state Optical Properties of Tetracenes by Alkyl Side-chain Length, *Chem. - A Eur. J.*, 2010, **16**, 890–898.
 11. C. Dohmen, H. Ihmels, R. Kreienmeier and B. O. Patrick, Synthesis of a Crystallochromic Indolizine Dye by a Base- and Catalyst-free Photochemical Route, *Chem. Commun.*, 2019, **55**, 11071–11074.
 12. Y. Imai, T. Kinuta, K. Nagasaki, T. Harada, T. Sato, N. Tajima, Y. Sasaki, R. Kuroda and Y. Matsubara, Conformational and Color Polymorphism of Achiral 2-Methyl-3-(2-naphthalenylthio)-1,4-naphthalenedione, *CrystEngComm*, 2009, **11**, 1223–1226.
 13. M. F. Richardson, Q.-C. Yang, E. Novotny-Bregger and J. D. Dunitz, Conformational Polymorphism of Dimethyl 3,6-Dichloro-2,5-dihydroxyterephthalate. II. Structural, Thermodynamic, Kinetic and Mechanistic Aspects of Phase Transformations Among the Three Crystal Forms, *Acta Crystallogr. Sect. B*, 1990, **46**, 653–660.
 14. G. A. Stephenson, T. B. Borchardt, S. R. Byrn, J. Bowyer, C. A. Bunnell, S. V. Snorek and L. Yu, Conformational and Color Polymorphism of 5-Methyl-2-[(2-nitrophenyl)amino]-3-thiophenecarbonitrile, *J. Pharm. Sci.*, 1995, **84**, 1385–1386.
 15. L. Yu, Polymorphism in Molecular Solids: An Extraordinary System of Red, Orange, and Yellow Crystals, *Acc. Chem. Res.*, 2010, **43**, 1257–1266.
 16. X. He, U. J. Griesser, J. G. Stowell, T. B. Borchardt and S. R. Byrn, Conformational Color Polymorphism and Control of Crystallization of 5-Methyl-2-[(4-methyl-2-nitrophenyl)amino]-3-thiophenecarbonitrile, *J. Pharm. Sci.*, 2001, **90**, 371–388.
 17. H. Li, J. G. Stowell, X. He, K. R. Morris and S. R. Byrn, Investigations on Solid-solid Phase Transformation of 5-Methyl-2-[(4-methyl-2-nitrophenyl)amino]-3-thiophenecarbonitrile, *J. Pharm. Sci.*, 2007, **96**, 1079–1089.
 18. K. M. Lutker, Z. P. Tolstyka and A. J. Matzger, Investigation of a Privileged Polymorphic Motif: a Dimeric ROY Derivative., *Cryst. Growth Des.*, 2008, **8**, 136–139.
 19. H. Li, J. G. Stowell, T. B. Borchardt and S. R. Byrn, Synthesis, Conformational Polymorphism, and Construction of a G-T Diagram of 2-[(2-nitrophenyl)amino]-3-thiophenecarbonitrile, *Cryst. Growth Des.*, 2006, **6**, 2469–2474.
 20. J. D. Dunitz and A. Gavezzotti, Toward a Quantitative Description of Crystal Packing in Terms of Molecular Pairs: Application to the Hexamorphic Crystal System, 5-Methyl-2-[(2-nitrophenyl)amino]-3-thiophenecarbonitrile, *Cryst. Growth Des.*, 2005, **5**, 2180–2189.
 21. B. A. Nogueira, M. Carvalho, J. A. Paixão, M. E. S. Eusébio, S. M. M. Lopes, T. M. V. D. Pinho e Melo and R. Fausto, Portrayal of the Color Polymorphism in the 5-Acetyl-derivative of ROY, *CrystEngComm*, 2022, **24**, 1459–1474.
 22. D. Gentili, M. Gazzano, M. Melucci, D. Jones and M. Cavallini, Polymorphism as an Additional Functionality of Materials for Technological Applications at Surfaces and Interfaces, *Chem. Soc.*

- Rev.*, 2019, **48**, 2502–2517.
23. M. Cavallini, A. Calò, P. Stoliar, J. C. Kengne, S. Martins, F. C. Maticotta, F. Quist, G. Gbabode, N. Dumont, Y. H. Geerts and F. Biscarini, Lithographic Alignment of Discotic Liquid Crystals: A New Time-temperature Integrating Framework, *Adv. Mater.*, 2009, **21**, 4688–4691.
 24. D. Gentili, M. Durso, C. Bettini, I. Manet, M. Gazzano, R. Capelli, M. Muccini, M. Melucci and M. Cavallini, A Time-temperature Integrator Based on Fluorescent and Polymorphic Compounds, *Sci. Rep.*, 2013, **3**, 2581.
 25. Z. Lin, X. Mei, E. Yang, X. Li, H. Yao, G. Wen, C.-T. Chien, T. J. Chow, Q. Ling, Polymorphism-dependent Fluorescence of Bisthiénylmaleimide With Different Responses to Mechanical Crushing and Grinding Pressure, *CrystEngComm*, 2014, **16**, 11018–11026.
 26. S. Šašić, Ed., *Pharmaceutical Applications of Raman Spectroscopy*, John Wiley & Sons, 2007.
 27. T. Kojima, S. Onoue, N. Murase, F. Katoh, T. Mano and Y. Matsuda, Crystalline Form Information from Multiwell Plate Salt Screening by Use of Raman Microscopy, *Pharm. Res.*, 2006, **23**, 806–812.
 28. T. F. Haebele and K. Paulus, Confocal Raman Microscopy in Pharmaceutical Development, *Springer Ser. Opt. Sci.*, 2010, **158**, 165–202.
 29. D. I. Bower, Investigation of Molecular Orientation Distributions by Polarized Raman Scattering and Polarized Fluorescence, *J. Polym. Sci. Polym. Phys. Ed.*, 1972, **10**, 2135–2153.
 30. M. Tanaka and R. J. Young, Review Polarised Raman Spectroscopy for the Study of Molecular Orientation Distributions in Polymers, *J. Mater. Sci.*, 2006, **413**, 963–991.
 31. J. M. Benevides, S. A. Overman and G. J. Thomas, Raman, Polarized Raman and Ultraviolet Resonance Raman Spectroscopy of Nucleic Acids and Their Complexes, *J. Raman Spectrosc.*, 2005, **36**, 279–299.
 32. J. Kim, J.-U. Lee and H. Cheong, Polarized Raman Spectroscopy for Studying Two-dimensional Materials, *J. Phys. Condens. Matter*, 2020, **32**, 343001.
 33. B. A. Nogueira, A. Milani, C. Castiglioni and R. Fausto, The Correlation Between Experimental Polarized Raman Spectra and Their Density Functional Theory Prediction in the LCAO Framework: The R3c LiNbO₃ Crystal as a Test Case, *J. Raman Spectrosc.*, 2021, **52**, 995–1010.
 34. R. Dovesi, A. Erba, R. Orlando, C. M. Zicovich-Wilson, B. Civalleri, L. Maschio, M. Rérat, S. Casassa, J. Baima, S. Salustro and B. Kirtman, Quantum-mechanical Condensed Matter Simulations with CRYSTAL, *Wiley Interdiscip. Rev. Comput. Mol. Sci.*, 2018, **8**, e1360.
 35. B. S. Rathore, V. Gupta, R. R. Gupta and M. Kumar, Synthesis of 7-Chloro-9-trifluoromethyl-7-fluorophenothiazines, *Heteroat. Chem.*, 2007, **18**, 81–86.
 36. G. M. Sheldrick, Crystal Structure Refinement with SHELXL, *Acta Crystallogr., Sect. C: Struct. Chem.*, 2015, **71**, 3–8.
 37. G. M. Sheldrick, SHELXT – Integrated Space-Group and Crystal-Structure Determination, *Acta Crystallogr., Sect. A*, 2015, **71**, 3–8.
 38. A. D. Becke, Density-functional Exchange-energy Approximation with Correct Asymptotic Behavior, *Phys. Rev. A*, 1988, **38**, 3098–3100.
 39. C. Lee, W. Yang and R. G. Parr, Development of the Colle-Salvetti Correlation-energy Formula into a Functional of the Electron Density, *Phys. Rev. B*, 1988, **37**, 785–789.
 40. A. D. McLean and G. S. Chandler, Contracted Gaussian Basis Sets for Molecular Calculations. I. Second Row Atoms, Z=11–18, *J. Chem. Phys.*, 1980, **72**, 5639–5648.
 41. M. J. Frisch, G. W. Trucks, H. B. Schlegel, G. E. Scuseria, M. A. Robb, J. R. Cheeseman, G. Scalmani, V. Barone, B. Mennucci, G. A. Petersson, H. Nakatsuji, M. Caricato, X. Li, H. P. Hratchian, A. F. Izmaylov, J. Bloino, G. Zheng, J. L. Sonnenberg, M. Hada, M. Ehara, K. Toyota, R. Fukuda, J. Hasegawa, M. Ishida, T. Nakajima, Y. Honda, O. Kitao, H. Nakai, T. Vreven, J. A. Montgomery, J. E. Peralta, F. Ogliaro, M. Bearpark, J. J. Heyd, E. Brothers, K. N. Kudin, V. N. Staroverov, R. Kobayashi, J. Normand, K. Raghavachari, P. G. Rendell, J. C. Burant, S. S. Iyengar, J. Tomasi, M. Cossi, N. Rega, J. M. Millam, M. Klene, J. E. Knox, J. B. Cross, V. Bakken, C. Adamo, J. Jaramillo, R. Gomperts, R. E. Stratmann, O. Yazyev, A. J. Austin, R. Cammi, C. Pomelli, J. W. Ochterski, R. L. Martin, K. Morokuma, V. G. Zakrzewski, G. A. Voth, P. Salvador, J. J. Dannenberg, S. Dapprich, A. D. Daniels, O. Farkas, J. B. Foresman, J. V. Ortiz, J. Cioslowski and D. J. Fox, Gaussian 09 (revision D.01),

42. C. Adamo and V. Barone, Toward Reliable Density Functional Methods Without Adjustable Parameters: The PBE0 Model, *J. Chem. Phys.*, 1999, **110**, 6158–6170.
43. J. P. Merrick, D. Moran and L. Radom, An Evaluation of Harmonic Vibrational Frequency Scale Factors, *J. Phys. Chem. A*, 2007, **111**, 11683–11700.
44. L. Maschio, B. Kitman, M. Rerat, R. Orlando and R. Dovesi, Ab Initio Analytical Raman Intensities for Periodic Systems Through a Coupled Perturbed Hartree-Fock/Kohn-Sham Method in an Atomic Orbital Basis. II. Validation and Comparison with Experiments, *J. Chem. Phys.*, 2013, **139**, 164102.
45. A. Domenicano, G. Schultz, I. Hargittai, M. Colapietro, G. Portalone, P. George and C. W. Bock, Molecular Structure of Nitrobenzene in the Planar and Orthogonal Conformations, *Struct. Chem.*, 1990, **1**, 107–122.

4. ROY Analogues

ROY (IUPAC name: 5-methyl-2-((2-nitrophenyl)amino)thiophene-3-carbonitrile, $C_{12}H_9N_3O_2S$, also known as 5-methyl-2-[(2-nitrophenyl) amino]-3-thiophenecarbonitrile) is a widely known compound that was named after its red, orange and yellow polymorphs. Apart from the remarkable color polymorphism phenomenon that it presents, ROY is also famous for being, at the present days, the compound with more reported polymorphs, twelve, and also the compound with more crystallographic structures determined, eleven.¹⁻¹⁰ For these reasons, ROY is, indeed, the most famous and most studied compound from all the families of compounds exhibiting color polymorphism.

As already mentioned in this Thesis, ROY was firstly reported in 1995 by Stephenson *et al.*¹ and, since then, it has been receiving a great amount of interest from the scientific community. In the original work,¹ five different ROY polymorphs were reported, three of which had their structures described. These three first identified polymorphic structures were also studied by Smith and co-workers, in 1998,² and, in the year 2000, Yu *et al.* disclosed the structure of three polymorphs of ROY, the two already known polymorphs with no solved structure and a sixth, new polymorph of the compound.³ In 2001, Mitchell *et al.* reported the evidence of a seventh ROY polymorphic form and, in 2005, Chen *et al.*⁵ discovered two additional new ROY polymorphs, reporting the structure of one of them (increasing the number of determined ROY polymorphic structures at that time to seven). In the same year, the same research group discovered a tenth ROY polymorph,⁶ whose structure was not described until 2018, when Tan *et al.* published a paper reporting its structure.⁷ In 2019, Gushurst *et al.*⁸ published a paper reporting the structure of the eleventh polymorph of ROY (the ninth with resolved structure at that time), which the authors claimed to have observed for the first time in 2013 (the required time to confirm the nature of this polymorph shows the effort that has been done over the recent years in the study of ROY). Also in 2019, Nyman *et al.*,⁹ using crystal structure prediction algorithms, proposed a structure for the polymorph identified in 2001 by Mitchell *et al.* whose structure could not be determined experimentally at that time. Finally, in 2020, Tyler and co-workers¹⁰ identified a twelfth ROY polymorph and reported its crystallographic structure, reckoning ROY as the molecule with more crystal structures described, with a total number of eleven.

The described rich color polymorphism of ROY is the result of a combination of favorable thermodynamics and kinetics. However, such abundance of molecular crystals of ROY mainly arises

from the conformational flexibility associated with average angle, θ , between the nitrophenyl-amino and thiophene ring-moieties of the molecule. Very interestingly, the color of ROY polymorphs and the respective θ values can be correlated as follows:

- Red polymorphs of ROY have θ angle values between 0° to 45° ;
- Orange polymorphs, present θ values between 45° and 60° ;
- Yellow polymorphs, exhibit θ values higher than 60° .

These data clearly indicate the primary factor responsible for the color of the ROY polymorphs as being the degree of conjugation between the nitrophenyl-amino and thiophene rings, which determines the relative energies of the electronic states of the molecule. Indeed, a more effective conjugation correlates with an angle between the planes of the two rings approaching to zero. However, intermolecular forces also play an important role in determining the color of the different polymorphs of ROY, as referred in Section 1.2 of this Thesis. In fact, ROY is an extraordinary case of both conformer and packing polymorphisms, which was one of the reasons it was chosen as one of the systems to develop analogue compounds to be studied in this project.

The selected ROY analogue compounds were, 5-acetyl-2-((2-nitrophenyl)amino)thiophene-3-carbonitrile (AcROY, $C_{13}H_9N_3O_3S$ – Section 4.1), which presents an acetyl group where ROY has a methyl group substituent; 2-((4-hydroxy-2-nitrophenyl)amino)thiophene-3-carbonitrile (ROY-ol, $C_{11}H_7N_3O_3S$ – Section 4.2), which does not present the methyl group in the thiophene ring but has a hydroxyl group in the nitro-substituted phenyl ring; and 2-(4-((3-cyanothiophen-2-yl)amino)-3-nitrophenyl)acetic acid (ROY-CAM, $C_{13}H_9N_3O_4S$ – Section 4.3), which, compared to ROY-ol, has an acetic acid group linked to the nitro-substituted phenyl ring instead of having and hydroxyl substituent.

References

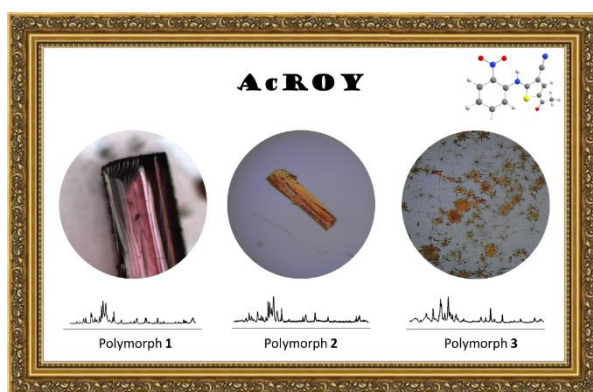
- 1 G. A. Stephenson, T. B. Borchardt, S. R. Byrn, J. Bowyer, C. A. Bunnell, S. V. Snorek and L. Yu, Conformational and color polymorphism of 5-methyl-2-[(2-nitrophenyl)amino]-3-thiophenecarbonitrile, *J. Pharm. Sci.*, 1995, **84**, 1385–1386.
- 2 J. Smith, E. MacNamara, D. Raftery, T. Borchardt and S. Byrn, Application of two-dimensional ^{13}C solid-state NMR to the study of conformational polymorphism, *J. Am. Chem. Soc.*, 1998, **120**, 11710–11713.
- 3 L. Yu, G. A. Stephenson, C. A. Mitchell, C. A. Bunnell, S. V. Snorek, J. J. Bowyer, T. B. Borchardt, J. G. Stowell and S. R. Byrn, Thermochemistry and Conformational Polymorphism of a Hexamorphic Crystal System, *J. Am. Chem. Soc.*, 2000, **122**, 585–591.
- 4 C. A. Mitchell, L. Yu and M. D. Ward, Selective nucleation and discovery of organic polymorphs through epitaxy with single crystal substrates, *J. Am. Chem. Soc.*, 2001, **123**, 10830–10839.
- 5 S. Chen, I. A. Guzei and L. Yu, New polymorphs of ROY and new record for coexisting

ROY analogues

- polymorphs of solved structures, *J. Am. Chem. Soc.*, 2005, **127**, 9881–9885.
- 6 S. Chen, H. Xi and L. Yu, Cross-nucleation between ROY polymorphs, *J. Am. Chem. Soc.*, 2005, **127**, 17439–17444.
- 7 M. Tan, A. G. Shtukenberg, S. Zhu, W. Xu, E. Dooryhee, S. M. Nichols, M. D. Ward, B. Kahr and Q. Zhu, ROY revisited, again: the eighth solved structure, *Faraday Discuss.*, 2018, **211**, 477–491.
- 8 K. S. Gushurst, J. Nyman and S. X. M. Boerrigter, The PO13 crystal structure of ROY, *CrystEngComm*, 2019, **21**, 1363–1368.
- 9 J. Nyman, L. Yu and S. M. Reutzel-Edens, Accuracy and reproducibility in crystal structure prediction: the curious case of ROY, *CrystEngComm*, 2019, **21**, 2080–2088.
- 10 A. R. Tyler, R. Ragbirsingh, C. J. McMonagle, P. G. Waddell, S. E. Heaps, J. W. Steed, P. Thaw, M. J. Hall and M. R. Probert, Encapsulated Nanodroplet Crystallization of Organic-Soluble Small Molecules, *Chem*, 2020, **6**, 1755–1765.

4.1. Ac-ROY

The paper that constitutes this section is entitled *Portrayal of the Color Polymorphism in the 5-Acetyl-derivative of ROY* and was published in the Royal Society of Chemistry's CrystEngComm (Vol. 24; Issue 7; Pages 1459-1474) on January 10th, 2022. Until the date of the submission of this Thesis, taking into consideration the information from Google Scholar, the article has one citation by peer-reviewed published works, and it has received 55 reads in Research Gate.



Supporting Information:

<https://pubs.rsc.org/en/content/articlelanding/2022/ce/d1ce01601f>.

Authors: Bernardo A. Nogueira, Maria Carvalho, José A. Paixão, M. Ermelinda S. Eusébio, Susana M. M. Lopes, Teresa M. V. D. Pinho e Melo and Rui Fausto

Corresponding author: Bernardo A. Nogueira

Author contributions: Bernardo A. Nogueira conceptualized the study, wrote a preliminary version of the manuscript, and participated in most of the experimental work and in theoretical studies. Maria Carvalho worked on the polymorphs screening and performed part of the DFT calculations and spectroscopic measurements. Rui Fausto contributed to the conceptualization of the study and data curation, took responsibility for its supervision, and wrote the final version of the manuscript. Susana M. M. Lopes and Teresa M. V. D. Pinho were responsible for the development of the synthetic route and its implementation. M. Ermelinda S. Eusébio participated in the design of the DSC studies and in the writing of the corresponding section of the manuscript. José A. Paixão performed the XRD studies

and wrote the first version of the corresponding section of the manuscript. All authors have participated in the discussion of the results and agreed with the final version of the manuscript.

Synopsis:

In this work, the first ROY analogue compound that we have studied in the context of this Thesis was described. 5-Acetyl-2-((2-nitrophenyl)amino)thiophene-3-carbonitrile, or simply AcROY, which bears an acetyl group where ROY has a methyl group (bonded to the thiophene ring), was synthesized for the first time and three different color polymorphs were identified. These polymorphs, one burgundy, one orange and one orange-yellowish, were characterized by X-ray diffraction, Raman and infrared spectroscopies, differential scanning calorimetry and polarized light thermal microscopy. Additionally, computational studies on the molecular structures of the different possible conformers of AcROY were performed, as well as Hirshfeld surface analysis for the two polymorphs whose crystal structure was obtained.

Portrayal of the Color Polymorphism in the 5-Acetyl-derivative of ROY

Bernardo A. Nogueira,^{*,1} Maria Carvalho,¹ José A. Paixão,² M. Ermelinda S. Eusébio,¹

Susana M. M. Lopes,¹ Teresa M. V. D. Pinho e Melo¹ and Rui Fausto¹

¹ University of Coimbra, CQC-IMS, Department of Chemistry, P-3004-535 Coimbra, Portugal.

² University of Coimbra, CFisUC, Department of Physics, P-3004-516 Coimbra, Portugal.

Abstract

A novel derivative of the prominent ROY compound, 5-acetyl-2-((2-nitrophenyl)amino)thiophene-3-carbonitrile (AcROY), was synthesized in a two-steps procedure by the nucleophilic aromatic substitution reaction between 1-fluoro-2-nitrobenzene and 2-aminothiophene-3-carbonitrile, followed by Friedel–Crafts acylation at position 5 of the thiophene ring. The conformational space of the compound (isolated molecule) was studied computationally, rendering 4 low-energy intramolecularly hydrogen-bonded conformers. The compound exhibits color polymorphism, with 3 different polymorphs identified. The crystal structures of two of the polymorphs were solved by single-crystal X-ray diffraction crystallography: polymorph **1** (burgundy) is monoclinic ($P2_1/n$; $a = 5.3354(2)$ Å, $b = 14.2344(4)$ Å, $c = 17.1709(6)$ Å, $\beta = 96.567(2)^\circ$, $Z = 4$, $Z' = 1$), and polymorph **2** (orange) is monoclinic ($P2_1/c$; $a = 25.451(3)$ Å, $b = 14.4966(14)$ Å, $c = 7.1113(7)$ Å, $\beta = 95.795(6)^\circ$, $Z = 8$, $Z' = 2$). It was not possible to determine the crystal structure of the third polymorph (**3**, orange-yellowish), but the obtained powder X-ray diffraction, infrared and Raman spectroscopy data clearly demonstrate the existence of this additional polymorphic form. Indexation of its powder diffraction pattern showed that it is a monoclinic variety with lattice parameters $a = 11.383(3)$ Å, $b = 13.6609(3)$ Å, $c = 25.247(7)$ Å, $\beta = 101.75(1)^\circ$, thus exhibiting a more complex supramolecular structure compared to polymorphs **1** and **2**. All polymorphs were characterized spectroscopically (by infrared and Raman spectroscopies) and by thermal analysis (by differential scanning calorimetry and polarized light thermomicroscopy). Interestingly, among the 4 predicted low energy conformers of the AcROY molecule, only the most stable form was found to be present in the crystals of the two structurally characterized polymorphs of the compound. The dominant intermolecular interactions in polymorphs **1** and **2** were investigated (also using Hirshfeld surface analysis) and were found to be significantly different. The observed polymorphism of AcROY is then an interesting case of packing-determined color polymorphism.

Keywords: 5-acetyl-2-((2-nitrophenyl)amino)thiophene-3-carbonitrile, ROY, color polymorphism, molecular structure, crystal structure, thermal analysis, infrared, Raman and NMR spectroscopies.

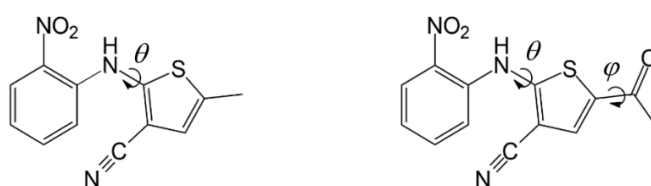
* Corresponding author e-mail: ban@qui.uc.pt

Introduction

5-Methyl-2-((2-nitrophenyl)amino)-3-thiophenecarbonitrile, better known as ROY due to the red, orange and yellow colors of its different crystalline varieties, is the most polymorphic organic material on record, with thirteen polymorphs already described.¹⁻⁶ Interestingly, most of these differently colored polymorphs owe their chromaticity diversity to the different molecular conformations assumed by the molecules in the crystals.⁷ The ROY molecule comprises two essentially rigid fragments (nitrophenyl and methyl-thiophenecarbonitrile) connected by an amine bridge (Scheme 1). The soft potential for internal rotation around the N–C bond connecting the substituted thiophene ring to the bridge provides the molecule a rich conformational landscape, which can be easily affected by intermolecular interactions in crystalline phase.¹⁻⁷ When the two rings of the molecule are nearly coplanar (*i.e.*, when the dihedral angle θ in Scheme 1 is closer to 180° or 0°), ROY crystals tend to be reddish, due to the large π electron conjugation taking place in these cases. On the other hand, when the θ dihedral is close to 90°, the two rings became nearly perpendicular, thus reducing the extent of the π electron conjugation, and the crystals have the propensity to present yellow tones. The orange colors are mostly exhibited by crystals where this dihedral angle assumes intermediate values.⁶⁻⁸ Nevertheless, at least two polymorphs of ROY have been shown to present remarkably different colors despite the conformation of their constituting molecules being nearly identical,⁹ indicating that dissimilar intermolecular forces *per se* can give rise to polymorphs of ROY showing notoriously diverse colors. As it has been recognized,⁷ ROY is in fact a comprehensive case of a compound exhibiting both conformational and packing color polymorphisms.

In the continuation of our recent investigations in systems exhibiting color polymorphism,^{7,10} in this article we report the results of our studies on a novel compound belonging to the ROY family that also exhibits color polymorphism: 5-acetyl-2-((2-nitrophenyl)amino)thiophene-3-carbonitrile (from now on designated as AcROY). The newly synthesized compound differs from ROY by replacement of the methyl substituent present in the thiophene ring of ROY by an acetyl group (see Scheme 1). The study included the structural and conformational characterization of the isolated molecule of the compound using density functional theory (DFT) calculations, as well as the synthesis of the compound, screening of its polymorphs, and their characterization using X-ray diffraction, infrared (IR) and Raman spectroscopies, differential scanning calorimetry (DSC), and polarized light thermal microscopy (PLTM). Our main motivation for studying this chemical system resulted from the fact that there are not many examples of ROY-related compounds described in the literature,^{6,11-14} in spite of the appealing properties of this type of compounds. By including the conformationally flexible acetyl substituent in the molecule (instead of the methyl group present in ROY), our general goal was to contribute to the understanding of how modifications in the basic ROY structure impact polymorphism, with emphasis on the mechanisms responsible for the different colors of the polymorphs. As described in detail below, and according to our expectations, AcROY was found to exhibit 3 different polymorphs of different

colors: **1**, burgundy; **2**, orange; **3**, orange-yellowish. The crystal structure of polymorphs **1** and **2** could be determined by single crystal X-ray crystallography, and all polymorphs were characterized spectroscopically (IR, Raman) and by thermal analysis (DSC/PLTM). Interestingly, among the 4 predicted low energy conformers of the molecule, only the most stable form was found to be present in the crystals of the two structurally characterized polymorphs of the compound. On the other hand, polymorph **1** has a single independent molecule per crystal unit cell ($Z' = 1$) and 4 molecules in the cell ($Z = 4$), while in polymorph **2** $Z' = 2$ and $Z = 8$, and the dominant intermolecular interactions were found to be substantially different in the two polymorphs (as noticed also in the performed Hirshfeld analysis of the two crystalline structures). The observed polymorphism of AcROY is then an interesting case of packing-determined color polymorphism.



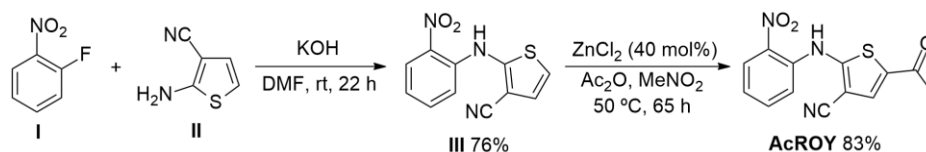
Scheme 1 – Molecular structures of ROY (*left*) and AcROY (*right*), with indication of the conformationally relevant internal rotations (θ , φ). In all low energy conformers of the two molecules, the nitrophenyl fragment is kept nearly co-planar with the NH bridging bond and oriented as depicted, due to the presence of a stabilizing intramolecular N–H \cdots O hydrogen bond that blocks the conformational flexibility around the C–N bond connecting these two fragments.¹⁻¹⁰

Below, the presentation of the results is organized in the following manner: (*i*) first, the synthesis of the compound is described and its general characterization provided; (*ii*) then, the structure of the isolated molecule of the compound, preferred conformations and their relative energies and barriers of interconversion are presented, and the major intramolecular interactions determining the structural and energetic features of the molecule of AcROY are discussed; these results provide the basis for the subsequent structural analysis of the polymorphs and effects of intermolecular interactions on the intramolecular potentials and structure of individual molecules in the crystals; (*iii*) the polymorph screening experiments are then presented; these were done using optical microscopy and Raman and infrared spectroscopies; (*iv*) following the spectroscopic identification of the three different polymorphs, X-ray diffraction data is presented for detailed structural characterization of polymorphs **1** and **2**, for which suitable crystals for single crystal experiments were obtained, and a general characterization of the unit cell of polymorph **3**, by X-ray powder diffraction, is provided; for polymorphs **1** and **2**, intermolecular interactions present in the crystals are analyzed in details by means of Hirshfeld analysis; (*v*) finally, the thermal analysis of the polymorphs is presented, which includes DSC, PLTM and temperature variation Raman spectroscopy studies.

Materials and Methods

Synthesis and polymorphs screening

General information: AcROY was synthesized in a two-step procedure by the nucleophilic aromatic substitution reaction between 1-fluoro-2-nitrobenzene (**I**) and 2-aminothiophene-3-carbonitrile (**II**) followed by Friedel–Crafts acylation at position 5 of the thiophene ring, as outlined in Scheme 2. The reaction of 1-fluoro-2-nitrobenzene (**I**) with 2-aminothiophene-3-carbonitrile (**II**) gave compound **III** in high yield (76%). Zinc chloride-catalyzed Friedel–Crafts acylation of compound **III**, using acetic anhydride as the acylating agent, afforded the target AcROY in 83% yield. The reagents and solvents were obtained commercially analytical grade.



Scheme 2 – Synthetic route to AcROY.

Synthesis of 2-((2-nitrophenyl)amino)thiophene-3-carbonitrile (III): a solution of 2-aminothiophene-3-carbonitrile (10 mmol, 1.24 g) and 1-fluoro-2-nitrobenzene (10 mmol, 1.05 mL) in dimethylformamide (15 mL) were added dropwise to a suspension of KOH (15 mmol, 0.842 g) in dimethylformamide (2.5 mL). After the addition was complete, the reaction mixture was stirred at room temperature for 6 h and an additional portion of KOH (5 mmol, 0.281 g) was added at once, and the reaction mixture was stirred for another 16 h. The reaction mixture was poured into a mixture of water/ice and extracted with dichloromethane (3 x 20 mL). The combined organic phases were washed with HCl 1M (2 x 30 mL) and brine (2 x 20 mL), dried and the solvent evaporated off. The compound was obtained as a red solid (7.59 mmol, 76%) by crystallization from ethanol, filtered and dried under vacuum. mp 129.5-131.0 °C (from ethanol). IR (ATR) ν 710, 735, 771, 814, 841, 879, 947, 969, 1053, 1068, 1093, 1146, 1217, 1235, 1275, 1319, 1344, 1378, 1403, 1440, 1456, 1501, 1549, 1589, 1610, 2211, 3106, 3167, 3204 cm^{-1} . ^1H NMR δ (CDCl_3): 7.01 (ddd, $J = 8.4, 7.2$ and 1.2 Hz, 1H), 7.10 (d, $J = 6.0$ Hz, 1H), 7.14 (d, $J = 6.0$ Hz, 1H), 7.28 (dd, $J = 8.8$ and 1.2 Hz, 1H), 7.53-7.57 (m, 1H), 8.27 (dd, $J = 8.4$ and 1.6 Hz, 1H), 9.80 (s, 1H). ^{13}C NMR δ (CDCl_3): 104.0, 113.6, 116.2, 120.4, 120.7, 126.8, 126.9, 134.5, 136.3, 140.6, 151.7. HRMS (ESI) m/z for $\text{C}_{11}\text{H}_8\text{N}_3\text{O}_2\text{S}$ [$\text{M} + \text{H}^+$] calcd. 246.0332, found 246.0329.

Synthesis of 5-acetyl-2-((2-nitrophenyl)amino)thiophene-3-carbonitrile (AcROY): zinc chloride anhydrous (40 mol%, 1.30 mmol, 0.18 g) and acetic anhydride (8.15 mL) were added to a solution of compound **III** (3.26 mmol, 0.80 g) in nitromethane (16.3 mL). The reaction mixture was stirred in a bath at 50 °C for 65 h. After this time, the reaction was allowed to cool to room temperature and dichloromethane (30 mL) and saturated aqueous NaHCO_3 (50 mL) were added. The phases were

separated, the organic phase was washed with saturated aqueous NaHCO₃ (2 x 50 mL), dried and the solvent evaporated off. AcROY was obtained as an orange solid (2.71 mmol, 83%) by crystallization from ethanol, filtered and dried under vacuum. mp 181.7-183.0 °C (from ethanol). IR (ATR) ν 708, 744, 761, 775, 787, 847, 856, 878, 1021, 1146, 1162, 1214, 1257, 1318, 1359, 1455, 1494, 1527, 1546, 1582, 1665, 1721, 2213, 2969, 3150, 3232 cm⁻¹. ¹H NMR δ (CDCl₃): 2.53 (s, 3H), 7.21 (ddd, J = 8.4, 7.2 and 1.2 Hz, 1H), 7.63 (s, 1H), 7.67-7.74 (m, 1H), 7.79 (dd, J = 8.4 and 1.2 Hz, 1H), 8.34 (dd, J = 8.5 and 1.5 Hz, 1H), 10.78 (s, 1H). ¹³C NMR δ (CDCl₃): 25.7, 97.1, 113.0, 117.5, 122.9, 127.2, 131.9, 132.9, 136.0, 136.4, 136.5, 159.4, 189.4. HRMS (ESI) m/z for C₁₃H₁₀N₃O₃S [M + H⁺] calcd. 288.0437, found 288.0434.

Polymorphs screening: the different polymorphs of AcROY were obtained by slow evaporation recrystallization from different solvent solutions, at room temperature. The solutions were prepared by dissolving 10-30 mg of AcROY in 5-20 mL of solvent. All solutions were filtered to prevent the crystallization from crystalline seeds that were not possible to solubilize.

Instrumental methods

For the initial characterization of the synthesized compounds, the ¹H and ¹³C NMR spectra (Figures S1 and S2 in the Supporting Information) were recorded on a Bruker Avance III instrument, operating at 400 MHz and at 100 MHz, respectively. The solvent used was deuteriochloroform (CDCl₃). High-resolution mass spectroscopy (HRMS) was performed by electrospray ionization (ESI) on an orbitrap q-exactive focus mass spectrometer. Melting point (uncorrected) was determined in an open glass capillary. Thin-layer chromatography (TLC) analyses were performed using precoated silica gel plates.

The Raman spectra were obtained using a micro-Raman Horiba LabRam HR Evolution system, with excitation provided by a 532 nm solid-state laser, using an approximate power of 0.5 mW at the sample, to prevent photodegradation of the compound. A 50 \times long working distance objective was used, with a laser spot diameter of around 1 μ m in the sample. The equipment was calibrated using a Si crystal (reference band at 520.5 cm⁻¹). The final spectra were the average of 100-500 accumulations of spectra obtained with an acquisition-time of 0.5-1.0 s and resolution of 0.5 cm⁻¹. For the temperature variation Raman experiments, a hot stage THMS 600 (Linkam Scientific Instruments), controlled by a T95-PE Linkpad controlling unit, was used.

The infrared spectra were collected in the attenuated total reflectance (ATR) mode, on a Thermo Scientific FT-IR Nicolet iS5 system, with an iD7 ATR accessory (angle of incidence: 45°; crystal: diamond). The spectra were recorded with spectral resolution of 1 cm⁻¹, in the wavenumber range of 400–4000 cm⁻¹, being the average of 512 scans.

The single crystal X-ray diffraction experiments were performed at room temperature using graphite monochromated MoK α (λ = 0.71073 Å) radiation in a Bruker APEX II diffractometer. The

structures were solved by the dual-space algorithm implemented in SHELXT-2018/2,¹⁵ and full-matrix least-squares refinement of the structural models were performed using SHELXL-2018/3.¹⁵ All non-hydrogen atoms were refined anisotropically. Hydrogen atoms were placed at calculated idealized positions and refined as riding using SHELXL-2018/3 default values,¹⁵ except for those of the amine groups that were refined isotropically with a displacement parameter constrained to 1.2× the U_{iso} value of the parent atom. Structure validation, ORTEP figures and drawing of packing diagrams were performed with PLATON.¹⁶ Full details on data collection and structure refinement are provided in the Supporting Information (Crystallographic Tables). A summary of the data collection and refinement details is given in Table 1. CIF files containing the supplementary crystallographic data were deposited at the Cambridge Crystallographic Data Centre, with references CCDC 2110241 and 211242.

Table 1 – Summary of the single-crystal X-ray data collections and crystal structure refinements.

	Polymorph 1	Polymorph 2
Chemical formula	C ₁₃ H ₉ N ₃ O ₃ S	=
Formula weight	287.29	=
Color	Burgundy	Orange
Space group	<i>P2₁/n</i>	<i>P2₁/c</i>
Cell volume (Å ³)	1295.51(8)	2610.4(4)
Crystal system	monoclinic	monoclinic
<i>a</i> (Å)	5.3354(2)	25.451(3)
<i>b</i> (Å)	14.2344(4)	14.4966(14)
<i>c</i> (Å)	17.1709(6)	7.1113(7)
α (deg)	90	90
β (deg)	96.567(2)	95.795(6)
γ (deg)	90	90
<i>Z</i> / <i>Z'</i>	4/1	8/2
<i>D_c</i> (Mg m ⁻³)	1.473	1.462
Radiation (Å) (graphite monochromated)	0.71073	0.71073
Max. crystal dimensions (mm)	0.32×0.25×0.22	0.50×0.13×0.12
Θ range (deg)	3.729 – 27.498	2.413 – 24.999
Range of <i>h, k, l</i>	–6,6;–18,18;–22,22	–30,30;–17,17;–8,8
Reflections measured/independent	122630/2963	207226/4598
Reflections observed (<i>I</i> > 2 σ)	2292	4598/3090
Data/restraints/parameters	2963/0/185	4598/0/369
GOF	1.062	1.099
<i>R</i> ₁ (<i>I</i> > 2 σ)	0.0417	0.0584
<i>wR</i> ₂	0.11181	0.1582
Function minimized	$\Sigma w (F_o ^2 - S F_c ^2)$	$\Sigma w (F_o ^2 - S F_c ^2)$
Diff. density final max/min (<i>e</i> Å ⁻³)	0.273, –0.192	0.374, –0.260

X-ray powder diffraction data was collected on a Bruker D8 Advance diffractometer equipped with a LYNXEYE linear position sensitive detector and using Ni-filtered Cu K α radiation ($\lambda = 1.54059$ Å). The data was measured in Bragg-Brentano geometry covering the 2θ range 5–60°, using an angular

step of 0.01° and counting 5 s/step. Indexation of the powder diffraction pattern of polymorph 3 of AcROY was done using the LP-search algorithm¹⁷ as implemented in the TOPAS V software,¹⁸ consisting of a set of Monte-Carlo searches for the lattice parameters, followed by a Pawley refinement at the end of each Monte-Carlo search. This algorithm uses a suitable figure of merit to find local minima robust to small deviations from the correct lattice parameters, which is also used as a penalty in the initial cycles of the non-linear least-squares Pawley refinement to ensure proper convergence.

The differential scanning calorimetry (DSC) experiments were performed using a Perkin Elmer Pyris-1 power compensation calorimeter, equipped with a 1:1 v/v ethylene glycol:water cooler at -25°C and a 20 mL min^{-1} nitrogen purge flow. Hermetically-sealed aluminum pans were used (samples weighting between 1 and 2 mg), with an empty pan used as reference. The temperature and enthalpy calibrations were performed with indium (Perkin Elmer, 99.99%, $T_{\text{fus}} = 156.6^\circ\text{C}$; $\Delta_{\text{fus}}H_{\text{m}} = 3286 \pm 13\text{ J}\cdot\text{mol}^{-1}$) and caffeine (Mettler Toledo calibration substance, ME 18872, $T_{\text{fus}} = 235.6 \pm 0.2^\circ\text{C}$). The samples were scanned from 25 to 210°C at a scan rate of $10^\circ\text{C min}^{-1}$.

Polarized light thermal microscopy (PLTM) experiments were performed using a Linkam DSC600 hot stage, with a Leica DMRB microscope and a Sony CCD-IRIS/RGB video camera. Images at $50\times$ magnification were collected in heating runs carried out at a scan rate of $10^\circ\text{C min}^{-1}$ and analyzed with LinkSys software by Linkam.

Density Functional Theory (DFT) calculations and Hirshfeld analysis

The DFT calculations were performed using the Gaussian 09 program (version D.01)¹⁹ on the isolated molecule of the compound, and included the geometry optimization of each low-energy intramolecularly H-bonded conformer, energy scans associated with the conformationally relevant torsional coordinates, and calculation of the vibrational spectra (IR and Raman) of the AcROY molecule. The three-parameter B3LYP density functional, with the Becke's gradient exchange correction²⁰ and the Lee, Yang and Parr correlation functional was used,²¹ together with the 6-311++G(2d,p) basis set.²²

The Hirshfeld analysis was performed with CrystalExplorer 17.5,²³ using as input the CIF files of the two polymorphs whose crystal structure could be solved. The mapping that summarizes the Hirshfeld analysis results were built from the normalized contact distances, d_{norm} , which is calculated from the distances of a given point of the Hirshfeld surface to the nearest atom outside, d_e , and inside, d_i , the surface, as defined by Equation 1, where r^{vdW} represent the van der Waals radii:^{24–28}

$$d_{\text{norm}} = \frac{d_i - r_i^{\text{vdW}}}{r_i^{\text{vdW}}} + \frac{d_e - r_e^{\text{vdW}}}{r_e^{\text{vdW}}} \quad (1)$$

Results and Discussion

Conformational analysis of the isolated AcROY molecule

As mentioned in the introduction section, AcROY molecule has essentially two internal degrees of freedom that are conformationally relevant, θ and φ , which correspond to the rotations around the N–C(thiophene) and C(thiophene)–C(acetyl) bonds, respectively (see Scheme 1). As for other structurally related molecules including ROY,¹⁻¹⁰ the nitrophenyl fragment in the low-energy conformers of AcROY is kept nearly co-planar with the NH bridging bond as a result of the presence in these forms of a stabilizing intramolecular N–H \cdots O hydrogen bond, which blocks the conformational flexibility around the C–N bond connecting these two fragments. In turn, the acetyl substituent can assume 3 equivalent geometries, corresponding to a 3-fold rotor, but this rotation does not contribute to increase the number of distinct conformers of the molecule (though it multiplies the number of minima on the potential energy of the molecule by 3). The conformational search was then performed scanning along both the θ and φ coordinates.

Four different low-energy intramolecularly H-bonded conformers were identified, which are presented in Figure 1. All conformers are C_1 symmetry and have a symmetry equivalent form (as mentioned, each structure correspond to 3 degenerate minima resulting from the 3 possible orientations of the methyl group, so that the total number of minima on the potential energy surface of AcROY associated with the 4 conformers is 24). The four conformers are here designated as **A**, **B**, **C** and **D**, following an increasing order of energy.

The two most stable conformers (**A** and **B**) present the oxygen atom of the acetyl substituent turned to the same side of the sulfur atom of the thiophene ring (φ , as defined by the C3–C4–C5=O1 dihedral angle, being equal to 178.6 and 178.9°, respectively; see Figure 1 for atom numbering, and Table 2), and differ from each other regarding the conformation defined by the θ coordinate: in the most stable conformer **A**, the sulfur atom of the thiophene ring is turned to the opposite side of the N–H bridging bond ($\theta = 169.5^\circ$, as defined by the C8–N2–C1=C2 dihedral angle), while in conformer **B** it is turned the opposite direction ($\theta = 46.0^\circ$). Conformer **A** is 6 kJ mol⁻¹ lower in energy than **B**, mostly because of the presence in conformer **B** of the unfavorable steric interaction between the cyano substituent of the thiophene ring and the closely located hydrogen atom (H9) of the nitrophenyl ring. Conformers **C** and **D** are the counterparts of forms **A** and **B**, respectively, having the acetyl group turned to the opposite side of the sulfur atom of the thiophene ring. In these conformers, θ and φ are equal to 170.0 and 1.7° (**C**) and 49.8 and 4.1° (**D**). Conformer **C** is more stable than **D** by 2.5 kJ mol⁻¹. Compared to the most stable conformer **A**, the relative energies of conformers **C** and **D** are 9.8 and 12.3 kJ mol⁻¹, respectively. The lower energy of the two conformers, **A** and **B**, compared to **C** and **D**, results mostly from the existence in the first two forms of a stabilizing O \cdots S interaction (see Figure 1), following the

trend observed previously for other molecules where this type of interaction was found to be relevant in structural terms.²⁹⁻³¹

It is interesting to point out that in all the four conformers, the intramolecular hydrogen bond connecting the N–H bridging group to the nitro substituent of the phenyl ring shares identical structural features, the O \cdots HN hydrogen bond distance and the O \cdots H–N angle varying in the short ranges of being 1.798-1.805 Å and 132.9-133.7°.

Table 2 – Values of the C8–N2–C1=C2 (θ) and C3–C4–C5=O1 (φ) dihedral angles and relative energies (ΔE) of the four low-energy conformers of AcROY.

Conformer	C8–N2–C1=C2 (θ)/°	C3–C4–C5=O1 (φ)/°	ΔE / kJ mol ⁻¹
A	169.5	178.6	0.0
B	46.0	178.9	6.0
C	170.0	1.7	9.8
D	49.8	4.1	12.3

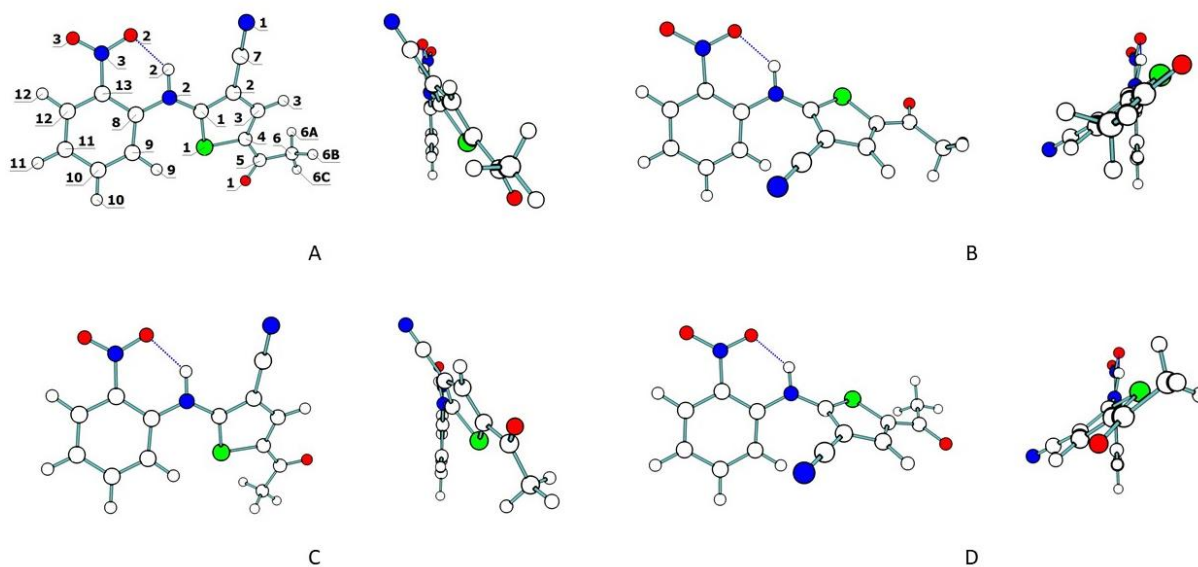


Figure 1 – Geometries of the four low-energy intramolecularly H-bonded conformers of AcROY with the adopted atom numbering (two images are presented for each conformer, corresponding to views from two different perspectives). Each of the represented structures has a symmetry-equivalent form (considering also the 3 degenerated minima resulting of the internal rotation of the methyl group for each symmetry-equivalent structure, the number of minima associated to each one of the conformers represented in the figure is in fact 6, on a total of 24 minima). For relative energies and values of the conformationally relevant dihedral angles, see Table 2.

Figures 2 and 3 show the calculated potential energy profiles for the interconversion between the AcROY conformers. Figure S4 (Supporting Information) presents in a compact form the relevant data regarding relative energies and interconversion barriers for the low energy conformers of AcROY.

In Figure 2, the scan coordinate is θ , which is associated with the interconversions between two different pairs of conformers: **A** and **B** (with the acetyl substituent in one orientation), and **C** and **D** (with the alternative orientation of the acetyl group). The two obtained energy curves show similar profiles. When considering the interconversion between **A** and **B** forms, we started the scan at the geometry of **A'** (*i.e.*, the equivalent-by-symmetry structure of that representing conformer **A** in Figure 1) and varied the scan coordinate in increments of 10° , while optimizing all the remaining structural parameters. Form **A'** first converts into **B'**, through an energy barrier of only 11.1 kJ mol^{-1} . Subsequently, the energy increases progressively while the molecule tends to co-planarity of the two rings (nitrophenyl and substituted-thiophene). However, the putative co-planar structure is highly strained due to the close contact it implies between the cyano substituent of the thiophene ring and the phenyl moiety, so that at a certain point (when θ is $\sim 30^\circ$) inversion at the bridging nitrogen atom takes place. This inversion at the N atom of the bridge leads to an abrupt decrease in energy, and takes the molecule to the potential energy well of conformer **B**. The maximum energy reached along the scan from **B'** to **B** was *ca.* 28 kJ mol^{-1} . From **B**, the molecule can then be converted into **A** through a barrier of 5.1 kJ mol^{-1} , the transition state for this transformation being equivalent-by-symmetry to that of the conversion of **A'** into **B'**. Finally, the interconversion between the two symmetry-related **A** and **A'** structures takes place through a small barrier of only 0.7 kJ mol^{-1} . In practical terms, the global format of the potential energy profile allows to conclude that interconversion between the 4 structures **A**, **B**, **B'**, **A'** can take place easily through barriers that are not larger than 11.1 kJ mol^{-1} , demonstrating the flatness of the torsional potential of AcROY along θ . The same conclusions can be extracted by taking into account the potential energy profile interconnecting forms **C**, **D**, **D'** and **C'** (see Figure 2). In this case, the barrier for **C**→**D** conversion is 6.6 kJ mol^{-1} (4.1 kJ mol^{-1} in the reverse direction) and that between the two equivalent **C** forms is 0.8 kJ mol^{-1} , while the maximum energy value for the **D'**→**D** conversion obtained along the performed scan was $\sim 25 \text{ kJ mol}^{-1}$.

Figure 3 shows the potential energy profiles for rotation of the acetyl substituent obtained when the conformation around the N–C(thiophene) bond was kept at values characteristic of the conformers of AcROY. The two curves represent the interconversion paths between conformers **A** and **C** and conformers **B** and **D**. Because the geometry around the N–C(thiophene) bond is skewed, for both A–C and B–D conversions, the internal rotation of the acetyl group can take place by two different pathways, which correspond to rotation of the acetyl group in the two possible directions. As it can be seen in Figure 3, however, all the four pathways (the two interconverting **A** and **C** and the two interconverting **B** and **D**) are very similar, with the barriers separating **A** and **C** being slightly higher than those separating **B** and **D** (43.6 and 42.3 kJ mol^{-1} , *vs.* 38.2 and 36.7 kJ mol^{-1} , respectively, taken from the corresponding lower energy conformer). It is worth noticing that these barriers are larger than those associated with the rotation around the N–C(thiophene) bond (see Figures 2,3 and S4).

ROY analogues

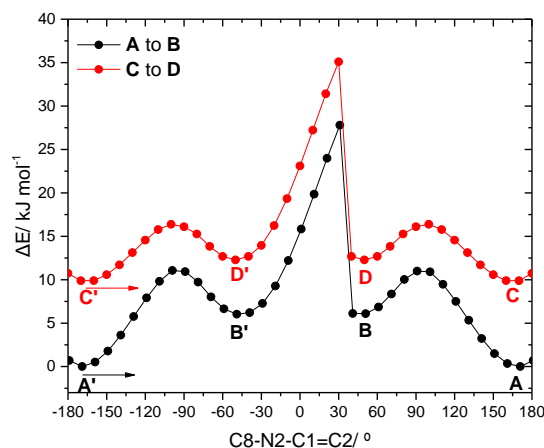


Figure 2 – Potential energy profiles associated with the internal rotation θ , as defined by the dihedral angle C8–N2–C1=C2, in keeping the conformation of the acetyl group in two different orientations. The arrows indicate the direction of the performed scans; A', B', C' and D' are the symmetry-equivalent structures of A, B, C and D, respectively (see text for details).

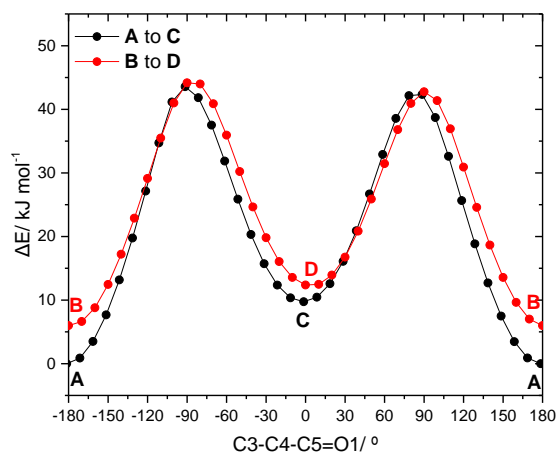


Figure 3 – Potential energy profiles associated with the internal rotation φ , as defined by the dihedral angle C3–C4–C5=O1, in keeping the conformation around the N–C(thiophene) in two different orientations (see text for details).

Polymorphs screening

After the synthesis of the compound, accomplished as described in the Materials and Methods section, the search for different polymorphs was undertaken. Two different approaches were used: the first one consisted in the recrystallization of the compound from solvents of different polarity, by slow evaporation of the solvent at room temperature; the second was by slow cooling of the melted compound. However, the latter resulted in the production of an amorphous phase, possibly due to partial degradation of the sample, which inhibited further investigation.

The solvents used are listed in Table S1 (Supporting Information), together with the corresponding obtained AcROY crystalline materials. Solids of three different morphologies and colors were obtained, which points out to three different polymorphs that are depicted in Figure 4. The

burgundy elongated-plate shape crystals labeled as **1** in Figure 4 were obtained from all used solvents. On the other hand, the orange needle shape crystals **2** were only obtained from recrystallization from acetone, always in concomitant mixtures, and the agglomerates formed by the small-sized orange-yellowish needles **3** were obtained from both acetone and DMSO, also in concomitant mixtures.

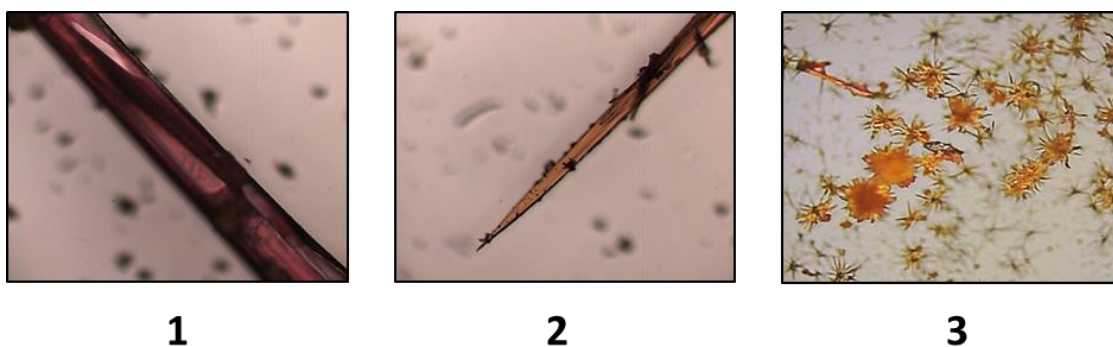


Figure 4 – The three different AcROY crystalline materials obtained in the polymorph screening experiments. Images are 10× amplified.

Infrared and Raman spectroscopy characterization of the AcROY polymorphs

The three different polymorphs of AcROY were morphology-based selected and characterized by both infrared (in ATR mode) and Raman spectroscopies. Figures 5 and 6 show the room temperature Raman and IR spectra of the three polymorphs, which show clearly distinctive vibrational signatures, in spite of the general resemblance of the spectra. Table S2 lists the major observed bands together with their tentative assignments made with help of the results of theoretical calculations of the spectra performed for the isolated molecule of the compound (conformer **A**, the conformer that is present in the crystals, according to the performed X-ray diffraction studies described in the next section).

The molecule of AcROY is C_1 symmetry, and the correlation method applied to the vibrations of the crystals of polymorphs **1** and **2**, whose structure could be obtained by single crystal X-ray diffraction crystallography (see next section), renders the representations $81A_g+81B_g+81A_u+81B_u$ (polymorph **1**) and $162A_g+162B_g+162A_u+162B_u$ (polymorph **2**) for the symmetry of the intramolecular vibrations. Besides, 24 and 48 modes, respectively for **1** and **2**, are intermolecular in nature, with the 3 acoustic modes being A_u+2B_u symmetry for both crystals and the intermolecular optical modes $6A_g+6B_g+5A_u+4B_u$ and $12A_g+12B_g+11A_u+10B_u$, respectively. This means that under the crystal symmetry, the rule of mutual exclusion applies to the vibrational spectra of both polymorphs **1** and **2**, and the modes active in IR (A_u and B_u) are silent in Raman, while those active in Raman (A_g , B_g) are not observable in infrared, so that a total of 162 modes are expected to contribute to the IR and Raman spectra of polymorph **1** and 324 modes to the spectra of polymorph **2**. Despite of the non-coincidence of vibrations in IR and Raman predicted by the symmetry analysis, one can expect the Davydov splitting

to be small for most of the modes, and thus the bands of related vibrations active in IR or Raman shall be nearly coincident. The same can also be expected for most of the related modes active either in IR and Raman belonging to different symmetry species, *i.e.*, A_u and B_u modes associated with the same coordinates in the one side and A_g and B_g modes associated with the same coordinates in the other side. As a whole, the number of expected bands in the spectra of the two polymorphs shall not be much larger than the number of vibrations of the isolated molecule of the compound (81). Since the crystal structure of polymorph **3** could not be solved, the symmetry analysis of the vibrations of this polymorph could not also be undertaken. In any case, the number of quasi-degenerated modes can also be expected to be large for this crystal, by the same reasons mentioned above, so that as for polymorphs **1** and **2**, the number of observable bands in the vibrational spectra of polymorph **3** can also be predicted not to be much larger than that for the isolated molecule of the compound. In Table S2, the vibrational spectra of the AcROY polymorphs are interpreted based on these assumptions, and the calculated spectrum of the isolated molecule of the compound (conformer **A**) was used as reference. Though being a rough simplification, this approach seems to be reasonable in the present case, also because the intermolecular interactions in the crystals can be expected to be relatively weak (no strong hydrogen bonds are present) and, thus, should perturb only in a very small extent the intramolecular vibrational potential.

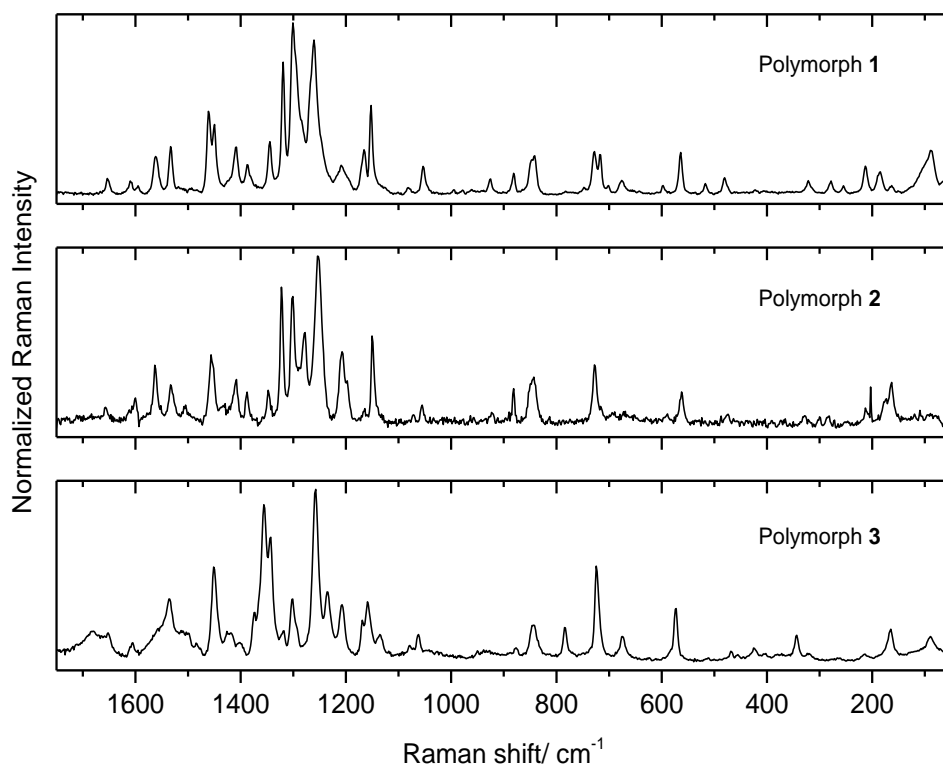


Figure 5 – Room temperature Raman spectra of the three observed AcROY polymorphs, in the 50-1750 cm^{-1} range.

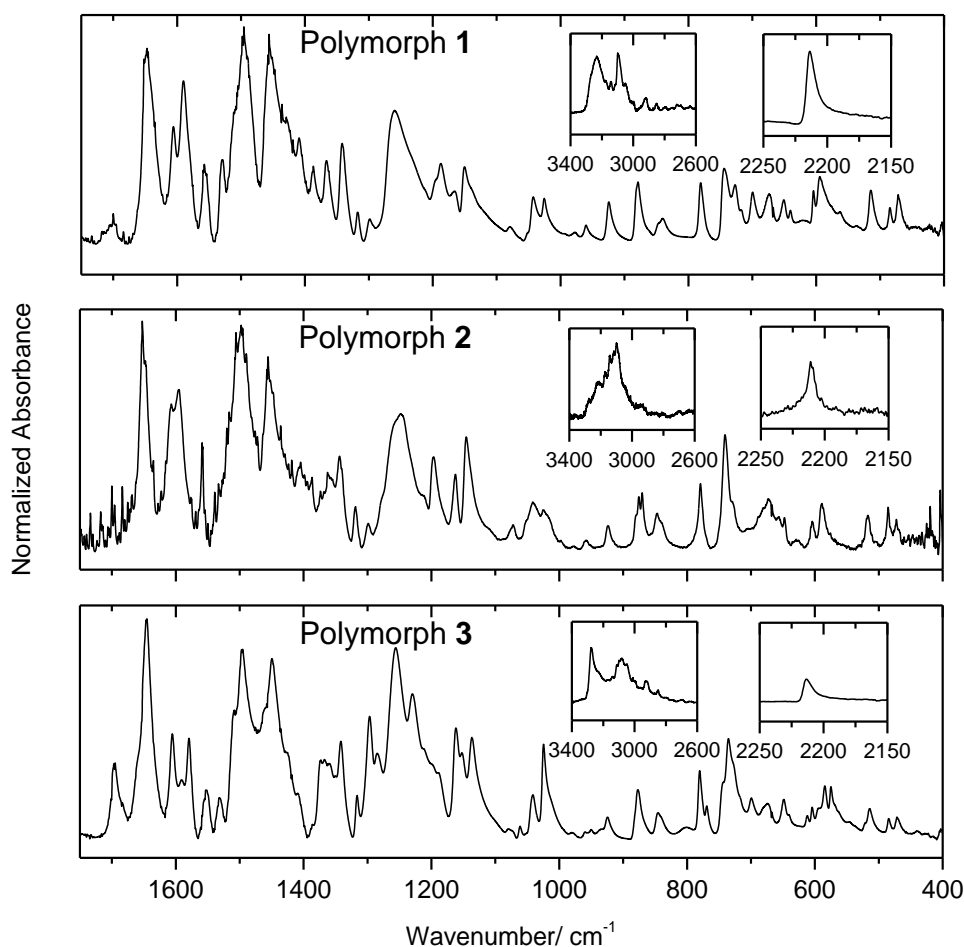


Figure 6 – FTIR spectra (ATR mode) of the three observed AcROY polymorphs, in the 1750-400 cm^{-1} range; the 3400-2600 and 2250-2150 cm^{-1} regions are shown as in-sets.

In the context of the present work, the identification of band-marks of each of the polymorphs is of particular interest. The intense bands observed in the 1100-1400 cm^{-1} range in both the IR and Raman spectra of the polymorphs appear particularly suitable for this goal. In the case of the Raman spectra, the most intense bands in this spectral region appear at 1319, 1301 and 1261 cm^{-1} , for polymorph **1**, at 1322, 1302, 1278 and 1253 cm^{-1} , for polymorph **2**, and 1356, 1344 and 1258 cm^{-1} for polymorph **3**, and can be used for fast identification of the polymorphs by using this technique. In infrared, bands at 1260, 1188 and 1150 cm^{-1} (**1**), 1248, 1196, 1162 and 1146 cm^{-1} (**2**) and 1256, 1230, 1162 and 1137 cm^{-1} (**3**) appear as good identifiers of the polymorphs.

Though a detailed discussion of the vibrational spectra of the materials is not to be done here, it is interesting to note that the frequencies at which the $\nu(\text{C}\equiv\text{N})$ stretching vibration is observed in the three polymorphs of AcROY are consistent with a small angle between the two rings of the molecules in the crystals, and also with their colors, according to the relationship between these properties recently presented by Tang and co-workers.³² Those authors have found that in the red and most of the orange polymorphs of ROY the $\nu(\text{C}\equiv\text{N})$ stretching mode appears in the 2205-2220 cm^{-1} wavenumber range,

while in the yellow polymorphs this mode gives rise to a band in the 2220-2235 cm^{-1} wavenumber range. In AcROY, this mode is observed at 2214 (in **1**), 2211 (**2**) and 2213 (**3**) cm^{-1} (see Table S2) as expected considering the burgundy, orange and orange-yellowish colors they exhibit. This is also in consonance with the small angles between the planes of the two rings observed in the crystals of polymorphs **1** and **2** [28.32(9) $^\circ$ in polymorph **1**, and 5.55(13) $^\circ$ and 13.63(14) $^\circ$ in the two different types of molecules found in the crystal of polymorph **2**, as detailed in the next section].

Crystallographic structures (polymorphs **1** and **2**)

Suitable crystals for single crystal X-ray diffraction structural studies were obtained for polymorphs **1** and **2**. Unfortunately, in the case of polymorph **3** the obtained crystals were not of good enough quality for this type of experiments. The X-ray data showed that both polymorphs **1** and **2** crystallize in the monoclinic, centrosymmetric space group N $^\circ$ 14, the unit cell used in the data-collections corresponding to the space-group settings $P2_1/n$ for polymorph **1** and $P2_1/c$ for polymorph **2**. Polymorph **1** has one symmetry independent molecule in the unit cell ($Z = 4$; $Z' = 1$) whereas the unit cell of polymorph **2** has a volume twice as large as that of polymorph **1** and corresponds to a structure with two symmetry independent molecules in the unit cell ($Z = 8$; $Z' = 2$). A thorough check with the tools available in PLATON¹⁶ did not reveal any missing symmetry in the larger unit cell. The two symmetry independent molecules in the unit cell of polymorph **2** are enantiomorph pairs that can closely match after inversion followed by a (non-crystallographic) pseudo glide-plan. ORTEP plots showing the anisotropic displacement ellipsoids and depicting the molecular conformation in the crystals of polymorphs **1** and **2** are presented in Figure S5.

For both polymorphs of AcROY studied using single crystal X-ray diffraction crystallography, the determined bond distances and valence angles in the molecules fall within the range of expected values of similar compounds (see Table S3 in Supporting Information). The N–O bond distances are in the range 1.208–1.225 Å, the longer values corresponding to those bonds involved in the intramolecular hydrogen-bonding with the N–H bridging group, as expected. The N–C bond distances of the amine bridge are significantly asymmetric [1.358(3)/1.385(3) Å], the shorter distance being towards the thiophene ring, in line with the calculated values for the isolated molecule of the compound (1.367 and 1.385 Å). The thiophene C–S–C angle is slightly larger than 90 $^\circ$, also in agreement with the calculated data for the isolated molecule (91.46 $^\circ$).

The two rings, that are strictly planar within experimental error, are not coplanar, the angle between their least-squares planes being larger for the molecule in polymorph **1** [28.32(13) $^\circ$] than for the two distinct AcROY molecules in polymorph **2** [5.55(9) $^\circ$ and 13.63(14) $^\circ$]. In fact, both molecules in polymorph **2** are more planar than in polymorph **1**, with the angle between the planes of the phenyl group and of the nitro substituent being 17.0(3) $^\circ$ in polymorph **1** and only 2.7(2) and 1.1(4) $^\circ$ in polymorph **2**, those between the planes of the thiophene ring and the acetyl group being 176.0(2) $^\circ$ (**1**)

and 177.9(4) and $-179.4(5)^\circ$ (**2**), and the C1–N2–C8–C9 dihedral angle being $-24.6(4)^\circ$ in **1** and $-5.6(6)$ and $-15.3(6)^\circ$ in **2**. The strong intramolecular hydrogen bond established between the nitro group and the amine bridge is preserved in the crystals, restricting the conformational flexibility of the nitro substituent and around the N2–C8(phenyl) bond, but like for the isolated molecule, significant deviations from planarity of the O₂N–Phe–NH fragment are observed in both polymorphs mostly due mostly to steric hindrance between the two rings (Table 3). It is interesting to note that, compared to the isolated molecule of AcROY (conformer **A**), where according to the performed DFT calculations the C1–N2–C8–C9 dihedral angle is -19.5° , this dihedral angle increases in polymorph **1** and decreases in polymorph **2** due to intermolecular packing. The same trend is observed for the deviation of the nitro group from the ring plane (as measured by the C8–C13–N3–O2 dihedral), which increases in polymorph **1** and reduces in polymorph **2** compared to the isolated molecule, where the C8–C13–N3–O2 dihedral predicted by the DFT calculations is 11.4° (in conformer **A**). Note that recent studies in ROY^{33,34} have concluded that DFT approaches provide reliable molecular geometries for this type of compounds (though not so precise conformational energy differences, tending to over-stabilize the more planar structures). As for ROY,^{33,34} the present study indicates that both the small deviations from the nitro group from the plane of the ring and the non-coplanarity of the fragments around the N2–C8 bond are not solely due to intermolecular packing, though they are modulated in some extent by intermolecular interactions in the crystals.

Table 3 – Relevant dihedral and torsion angles for the two polymorphs. The second column corresponds to the molecule of polymorph **2** with unprimed atomic labels, the third column to the molecule with primed labels in the figures.

Dihedral/torsion angle/ $^\circ$	Polymorph 1	Polymorph 2	
$\langle (S1C1\dots C4)/(C8C9\dots C13) \rangle$	28.32(9)	5.55(13)	13.63(14)
$\langle (C8C9\dots C13)/N3O_2 \rangle$	17.0(3)	2.7(2)	1.1(4)
$\langle (S1C1\dots C4)/(C4C5C6O1) \rangle$	5.11(16)	1.74(18)	4.04(12)
C8–N2–C1=C2 (θ)	177.7(2)	$-171.1(4)$	$-175.5(4)$
C3–C4–C5–O1 (φ)	176.0(2)	177.9(4)	$-179.4(5)$
C1–N2–C8–C9	$-24.6(4)$	$-5.6(6)$	$-15.3(6)$
C8–C13–N3–O2	18.6(3)	2.2(6)	$-0.4(6)$

Inspection of close contact distances and angles shows the presence of an extensive 3D network of intermolecular hydrogen bonds in both polymorphs, which are depicted in Figure 7 (polymorph **1**) and Figure 8 (polymorph **2**). The only strong donor group in the molecule is the amine group that is involved in the above-mentioned intramolecular interaction with the nitro group. All the other intermolecular short contacts can be classified as weak non-classic hydrogen bonds of the C_{aryl}–H \cdots O, C_{aryl}–H \cdots N, C_{aryl}–H \cdots S or C_{methyl}–H \cdots O types. These interactions are detailed in Tables 4 and 5 for polymorphs **1** and **2**, respectively. In polymorph **1**, every possible acceptor atom is involved in one such

interaction, while in polymorph **2** only atom O3 is not involved in the hydrogen bond network. In both polymorphs, the molecules pack in layers, the hydrogen bonds being established mainly within the layers. Cohesion between the layers is achieved by van der Waals interactions and interactions between the π -electron clouds of nearly stacked rings. In the case of polymorph **2**, in addition to these ring interactions, one C–H \cdots O hydrogen bond also interconnects the layers as shown in Figure 8b. A remarkable difference between the molecular packing in the two polymorphs is the occurrence of a somewhat short S \cdots S contact [3.585 Å] in polymorph **2**, that can be observed in Figure 8b, and that is absent in the structure of polymorph **1**. Noteworthy, the S \cdots S contact found in the polymorph **2** of AcROY is considerably shorter than all S \cdots S distances found in the different polymorphs of the parent compound ROY whose structure has been solved, which vary within 3.945 Å (in the so called ON – orange needle – polymorph) and 5.582 Å (in the Y – yellow – polymorph).^{2,5,14,35}

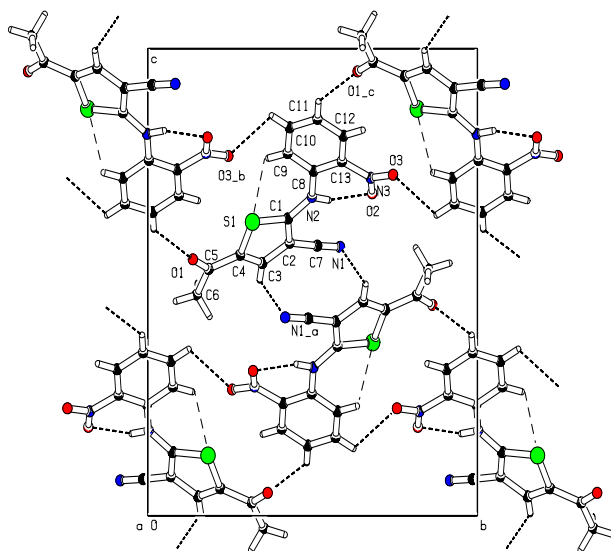


Figure 7 – Hydrogen-bonding network in polymorph **1**. The view is a projection along the crystallographic a -axis. Intramolecular C–H \cdots S short contacts are shown as long dashes.

Table 4 – Hydrogen bonds and short intermolecular contacts in polymorph **1**. Distances and angles are given in Å and degrees, respectively; D and A represent the hydrogen bond donor and acceptor atoms, respectively.

D–H \cdots A	D–H	H–A	D \cdots A	\angle D–H \cdots A
N2–H2 \cdots O2	0.82(3)	1.94(3)	2.612(2)	139(3)
C9–H9 \cdots S1	0.93	2.50	3.319(3)	147
C3–H3 \cdots N1 ^a	0.93	2.53	3.132(2)	123
C10–H10 \cdots O3 ^b	0.93	2.52	3.061(3)	117
C11–H11 \cdots O1 ^c	0.93	2.45	3.213(3)	139

Symmetry codes: a) $-1-x, 1-y, 1-z$; b) $3/2-x, -1/2+y, 3/2-z$; c) $3/2-x, 1/2+y, 3/2-z$.

ROY analogues

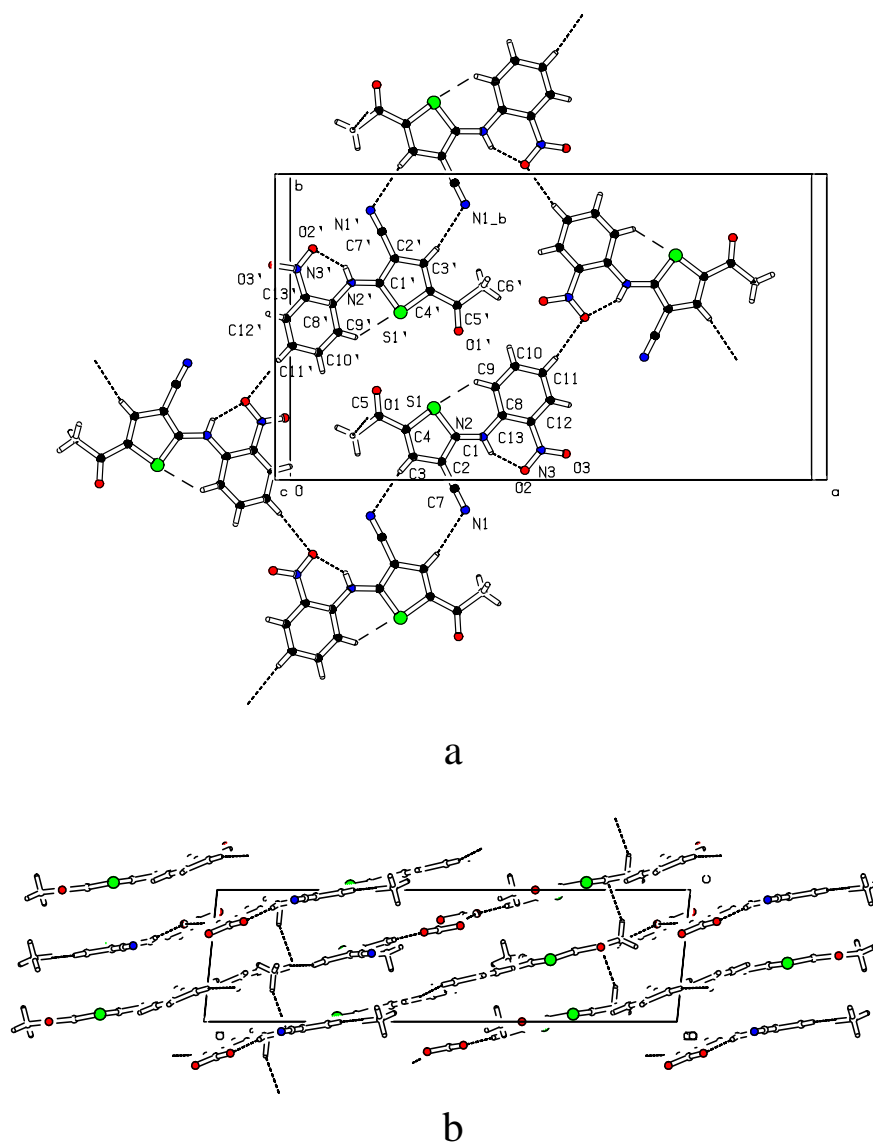


Figure 8 – Hydrogen-bonding network in polymorph 2. (a) Projection along the crystallographic *c*-axis; (b) projection along the crystallographic *b*-axis. Intramolecular C–H...S short contacts are shown as long dashes.

Table 5 – Hydrogen bonds and short intermolecular contacts in polymorph 2. Distances and angles are given in Å and degrees, respectively.

D–H...A	D–H	H–A	D...A	< D–H...A
N2–H2...O2	0.83(4)	1.87(4)	2.588(4)	145(4)
N2'–H2'...O2'	0.78(4)	1.94(4)	2.591(4)	142(4)
C9–H9...S1	0.93	2.43	3.147(4)	134
C9'–H9'...S1'	0.93	2.46	3.153(4)	132
C3–H3...N1 ^a	0.93	2.55	3.461(5)	165
C3'–H3'...N1 ^b	0.93	2.53	3.448(6)	169
C11–H11...O2 ^c	0.93	2.51	3.426(5)	170
C11'–H11'...O2' ^d	0.93	2.55	3.467(5)	170
C6–H6B...O1 ^e	0.96	2.48	3.323(6)	146

Symmetry codes: a) $x, -1+y, z$; b) $x, 1+y, z$; c) $1-x, 1/2+y, 1/2-z$; d) $-x, -1/2+y, 3/2-z$; e) $x, 1/2-y, 1/2+z$.

For polymorph **3** it was not possible to obtain suitable crystals for single crystal X-ray diffraction structure determination. Nevertheless, powder X-ray measurements were undertaken for this polymorph. The powder diffraction pattern obtained for polymorph **3** is compared with the simulated powder patterns of polymorphs **1** and **2** derived using the corresponding X-ray structural data in Figure 9. Indexing of the powder pattern of polymorph **3** resulted in a solution with lattice parameters $a = 11.383(3) \text{ \AA}$, $b = 13.6609(3) \text{ \AA}$, $c = 25.247(7) \text{ \AA}$, $\beta = 101.75(1)$ (monoclinic) that could successfully index all peaks in the diffractogram (see Figure S6 in the Supporting Information). The molar volume of polymorphs **1** and **2** is approximately 325 \AA^3 per molecule, while the volume of the unit cell found for polymorph **3** is 3843 \AA^3 , giving a total of 12 molecules per unit cell, assuming the same molar volume. As the most likely space group of polymorph **3** is $n^\circ 14 (P2_1/c)$, with $Z = 4$, this would correspond to a structure with $Z' = 12/4 = 3$. No satisfactory solution was found with unit cells of lower volume during many Monte-Carlo runs, and other indexing methods failed due to the strong overlap of diffraction peaks. Even if one cannot exclude that the unit cell found is a supercell of the true cell of polymorph **3**, as the local minimum found by the Monte-Carlo may not be the global minimum, the larger unit cell found points to a more complex supramolecular structure of polymorph **3** compared to those of polymorph **1** and **2**.

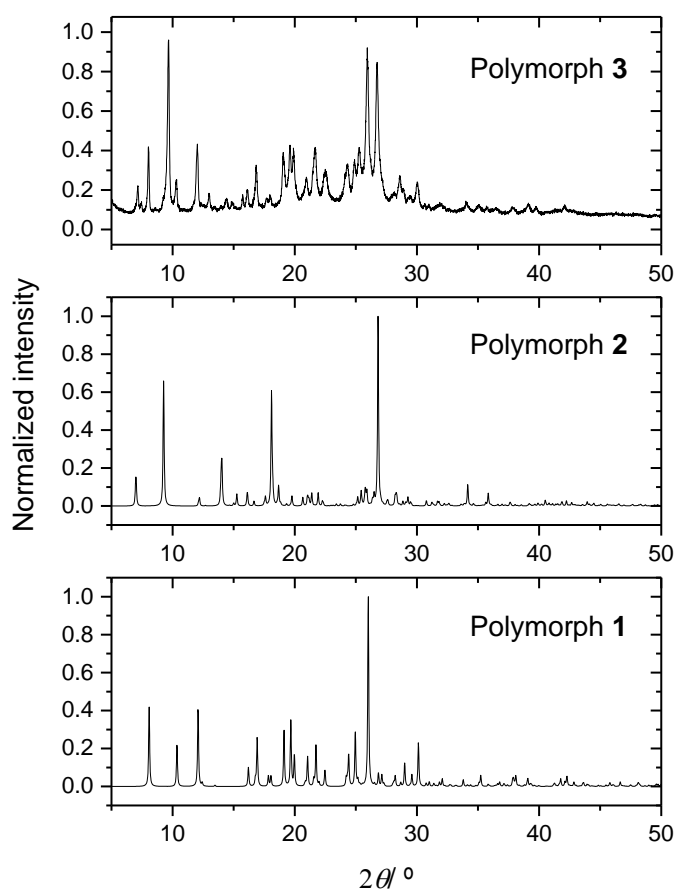


Figure 9 – Powder X-ray diffractograms for the polymorphs of AcROY. Data for polymorphs **1** and **2** were simulated using the solved crystal structure of the polymorphs; data for polymorph **3** were obtained experimentally.

Hirshfeld surfaces analysis

The study of crystallographic structures based on Hirshfeld surfaces, developed by Spackman and co-workers is an elegant effective approach to understand intermolecular interactions in a crystal and to evaluate crystal packing.³⁶ Hence, to characterize the intermolecular environments in polymorphs **1** and **2**, the Hirshfeld surface analysis of these structures was performed. Figure 10 presents the calculated Hirshfeld surfaces for the two polymorphs, with the intermolecular contacts given by the d_{norm} values, which range from -0.20 to 1.29 for polymorph **1** and from -0.19 to 1.34 for polymorph **2**. For polymorph **2**, the dimeric unit represented by the two molecules in the asymmetric unit of the crystal is considered in this analysis. Within the dimer, the most important interactions are the two pairs of non-classical hydrogen bond interactions C9–H9···O1 and C10–H10···O1. The red areas shown in the plots presented in Figure 10 represent the most important intermolecular interactions (shorter contacts) for each structure, which correspond to O3···H10–C10, O1···H11–C11, O1···H6_A–C6 and N1···H3–C3 intermolecular interactions in the case of polymorph **1**, and O3···H6_A–C6, O2···H11–C11, O3···H6_C–C6, O1···H6_B–C6 and N1···H3–C3 interactions in the case of polymorph **2**.

Table 6 presents the relative fractional areas (in %) of the Hirshfeld surfaces that are assigned to the different types of intermolecular interactions. The corresponding d_e vs d_i 2D-fingerprint plots are presented in the Supporting Information (Figures S6 and S7), together with the corresponding d_{norm} mapping on the Hirshfeld surfaces.

Considering the areas of the Hirshfeld surfaces assigned to the H···O/O···H contacts (29.1% for polymorph **1** and 22.1% for polymorph **2**), it is clear that the contribution of the non-classical intermolecular hydrogen bonds of the CH···O type to the stabilization of the crystal structure of polymorph **1** is more important than for polymorph **2**. On the other hand, the contribution of hydrogen bonds of the CH···N type to the stabilization of the crystal structure of polymorph **2** is considerably more significant than in polymorph **1** (H···N/N···H contacts fractional areas are 7.1% and 14.5% in polymorphs **1** and **2**, respectively). Interestingly, in consonance with the structural information directly extracted from the XRD data, the Hirshfeld surface analysis also reveals that, while in polymorph **1** there is no contribution of S···S intermolecular interactions to the stabilization of the crystalline lattice, in polymorph **2** there is a small, but still significant in structural terms, contribution of disulfide intermolecular contacts to the stabilization of the three-dimensional crystalline structure.

The data shown in Table 6 also show that dispersive interactions (as described in terms of short H···H and H···C/C···H contacts) are most probably also significant in stabilizing the two crystals, considering that the H···C/C···H contacts account on total for 32.2% and 32.3% of the Hirshfeld surface areas of polymorph **1** and **2**, respectively. In polymorph **1**, the first type of interaction occurs essentially between the hydrogen atoms of the methyl group and the four phenyl hydrogen atoms of neighboring molecules, while the H···C/C···H interactions refer to phenyl/phenyl stacking-type contacts between the partially superimposed rings of molecules in adjacent layers. Noteworthy, the C···C interactions occur

essentially between the carbon atoms of the thiophene ring that do not bear any hydrogen atom (C1, C2) and that of the cyano group (C7) of each molecule and the same atoms of the neighboring molecules of adjacent layers, where the interacting moieties are oriented in an anti-parallel fashion relative to the reference molecule. In polymorph **2**, H \cdots H contacts involve mostly the methyl hydrogens and the phenyl hydrogen atom H11, which are not involved in interactions with oxygens, while the H \cdots C/C \cdots H interactions are associated with the same type of stacking contacts found in polymorph **1**. On the other hand, in polymorph **2** the C \cdots C interactions are associated with the phenyl moiety of one of the molecules in the asymmetric unit, and predominantly with the carbon atom of the cyano group in the case of the second molecule. The different pattern found for the H \cdots H and C \cdots C interactions in the two polymorphs, clearly reveal the different arrangement of the molecules, in particular the neighborhoods of the phenyl and cyano substituent (for example, in the latter case, the anti-parallel orientation of the group in adjacent layers of molecules in the crystal of polymorph **1** is not preserved in polymorph **2**, where, otherwise, they are nearly perpendicular).

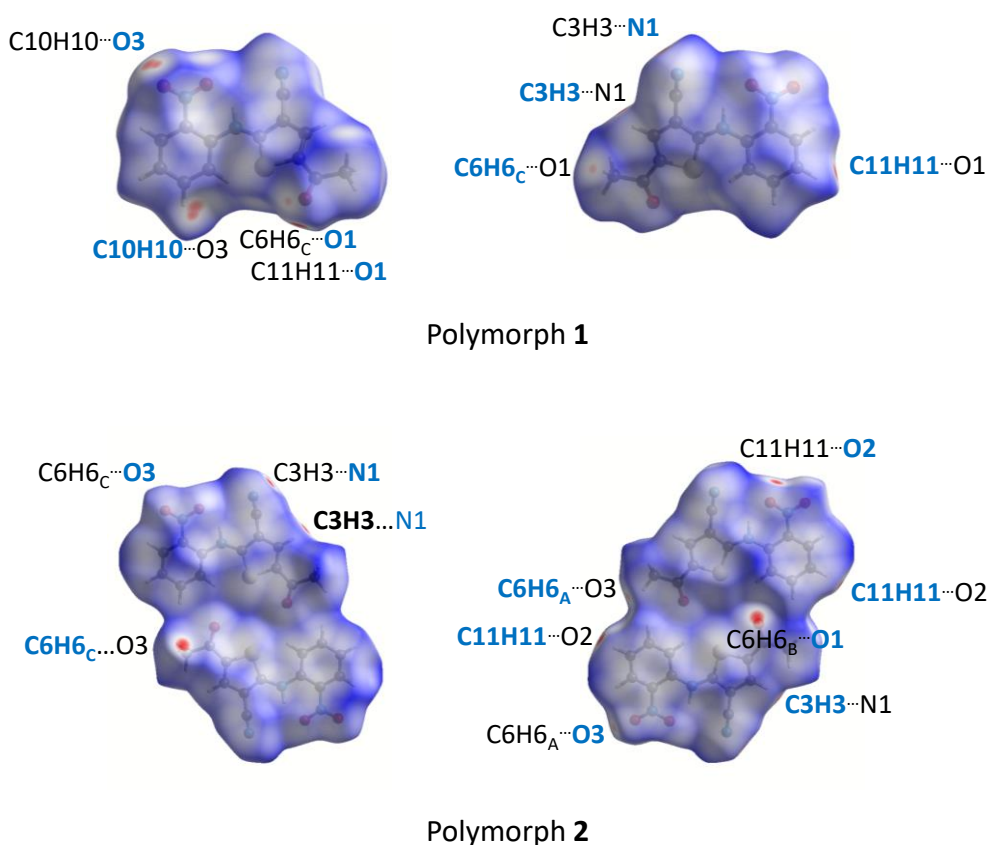


Figure 10 – d_{norm} mapping on the Hirshfeld surfaces of the molecules in polymorphs **1** and **2** of AcROY. Two different viewpoints are shown for each molecule, in the left column with the nitrobenzene group on the left-hand side (top molecule in the case of the $Z' = 2$ polymorph **2**), and in the right column with the nitrobenzene group on the right-hand side. Atoms participating in the indicated interactions that belong to neighboring molecules are notated in black.

Table 6 – Fractional areas (in %) of the Hirshfeld surface assigned to the different intermolecular interactions in AcROY polymorphs **1** and **2**.

Intermolecular interaction	Polymorph 1	Polymorph 2
H··O/O··H	29.1	22.1
H··H	20.9	18.6
H··C/C··H	11.3	13.7
C··N/N··C	7.2	4.8
H··N/N··H	7.1	14.5
C··C	7.1	8.2
H··S/S··H	4.4	2.3
C··O/O··C	3.7	4.9
N··N	2.4	0.9
C··S/S··C	1.8	3.5
N··O/O··N	1.4	2.8
O··S/S··O	1.4	0.4
N··S/S··N	1.3	0.5
O··O	1.0	2.2
S··S	0.0	0.7

Thermal analysis of the polymorphs

In order to study the thermal behavior of the identified polymorphs, crystal forms **1** and **3** were firstly investigated by differential scanning calorimetry (DSC). The melting of these polymorphs was observed at 200.3 ± 0.4 °C (polymorph **1**) and 189.9 ± 1.4 °C (polymorph **3**), as shown in Figure 11). The measured enthalpy of fusion was 32.7 ± 2.2 kJ mol⁻¹, for polymorph **1**, and 16.3 ± 2.0 kJ mol⁻¹, for polymorph **3**, which, according to the heat of fusion rule,³⁷⁻³⁹ reveals that these two polymorphs are monotropically related, with polymorph **1** being the stable form and polymorph **3** the metastable crystal structure.

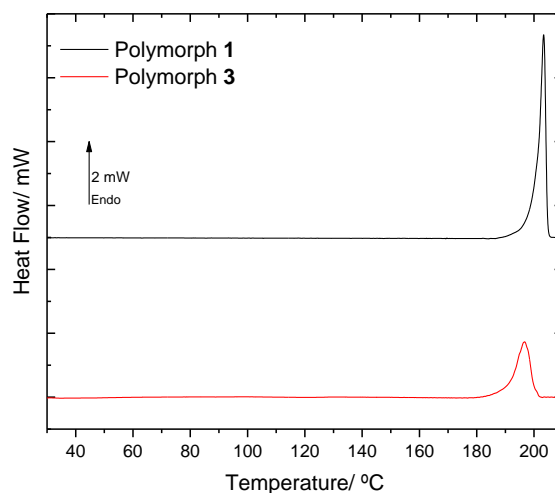


Figure 11 – DSC heating curves of polymorphs **1** and **3** of AcROY (heating rate: 10 °C min⁻¹; masses: 1.10 mg, polymorph **1**; 1.11 mg, polymorph **3**).

Due to the lack of sufficient quantity of polymorph **2** to perform a DSC analysis, this crystallographic form was studied by temperature variation Raman spectroscopy and PLTM.

The temperature variation Raman spectroscopy experiments showed evidence of a solid-solid transformation, starting at *ca.* 140 °C, in which polymorph **2** converts into polymorph **1** (see Figure 12). In these experiments, a single crystal of polymorph **2** of AcROY was used as starting material, and a first spectrum was collected at 30 °C. Then, the temperature was increased in steps of 10 °C min⁻¹, and a spectrum was collected after each step from the initially probed sample spot. At 130°, noticeable changes in the relative band intensities start to be observed and, at 140 °C, the collected spectrum was different from the previous, indicating a phase transition. Comparing this spectrum with the ones collected for each polymorph (see Figure 5 and Table S2) it becomes clear that the observed phase transition corresponds to the conversion of polymorph **2** into polymorph **1**. However, at 140 °C, Raman spectra obtained from other spots of the sample still rendered the characteristic spectrum of polymorph **2**, indicating that the observed solid-solid transition is slow and takes place in a relatively broad range of temperature. In order to better understand this event and, in particular, the range of temperatures in which it occurs, as well as to confirm the behavior of polymorphs **1** and **3** studied by DSC analysis, a PLTM study of all polymorphs was undertaken. The results are shown in the PLTM video sent as Supporting Information (see also Figure S9).

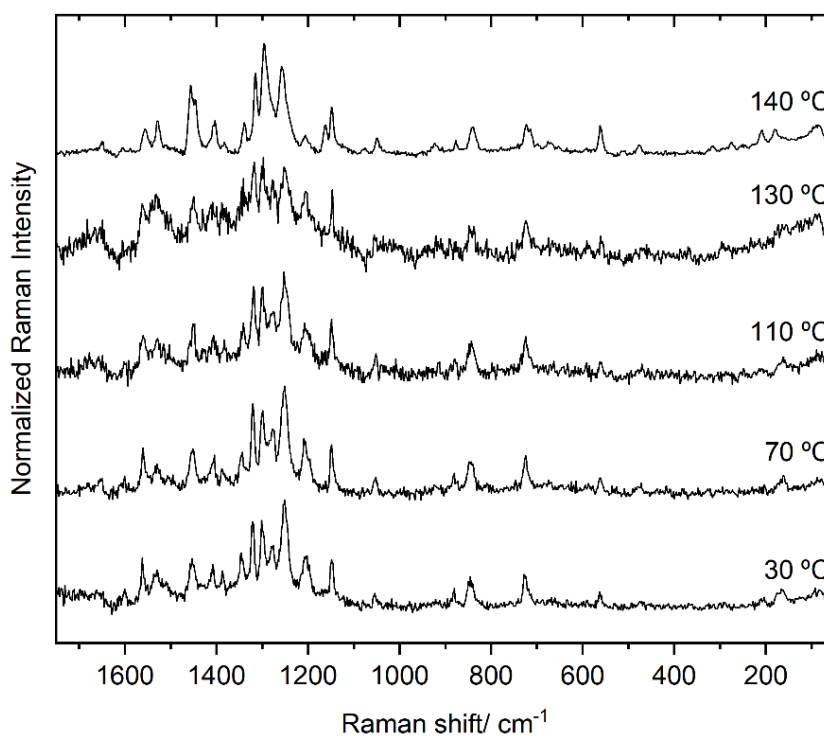


Figure 12 – Temperature variation Raman spectra obtained for a sample of polymorph **2** of AcROY (50-1750 cm⁻¹ spectral region).

In the PLTM experiments (Figures S9 and PLTM video), temperature increase from 25 to 132 °C did not lead to any visible changes in the sample (apart from the fact that some crystals moved out of the view area of the experiment due to air convection, as frequently seen in the type of experimental apparatus used). The rectangular shape crystal labelled as 2b in Figure S9 was the first crystal of polymorph **2** to undergo the solid-solid transition to polymorph **1**, between *ca.* 144 and 145 °C. The same transition was observed for crystal **2a** between 149 and 150 °C (see Figure 13 and PLTM video) and, for crystal **2c** from 152 to 153 °C, thus confirming that the **2** → **1** solid-solid transition occurs in a significantly wide range of temperature. The crystal marked as polymorph **3** in Figure S9 melts between 178 and 193 °C, validating the DSC experiments for this polymorph. The non-labelled crystals in Figure S9 are crystals of polymorph **1**. Together with the crystals of polymorph **2** that first evolved into polymorph **1**, these crystals start to melt at *ca.* 195 °C, the melting being complete at around 204 °C, a result that is also in accordance with the obtained DSC data.

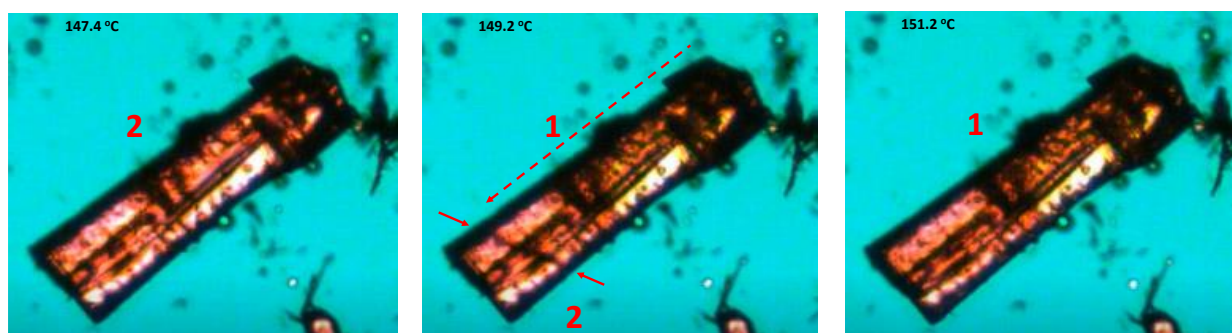


Figure 13 – PLTM images (3 consecutive frames extracted from the PLTM video submitted as Supporting Information) showing the **2** → **1** solid-solid transition for the crystal that in Figure S9 is labelled as 2a. In the middle frame, the transition is occurring. The solid arrows mark the front of the transition wave, while the dashed line indicate the direction of the transformation.

Conclusion

In this study, the synthesis and portrayal of the color polymorphism exhibited by the acetyl-derivative of ROY was undertaken. The structure and conformational landscape of the isolated molecule of the compound were investigated using DFT calculations. Four low-energy intramolecularly hydrogen-bonded conformers were located on the molecule's potential energy surface. The calculations revealed that the torsional potential of AcROY along θ is flat and allows easy interconversion between the conformers differing in the conformation around this coordinate (**A** and **B**, in one side, and **C** and **D**, in the other). The flatness of this potential also allows easy adjustment of the geometry of the molecule upon formation of a crystal, when intermolecular interactions and packing also dictate the molecular conformations that better suits the energetic demands of a given crystalline phase.

The compound was found to exhibit color polymorphism, with 3 different polymorphs identified. The crystal structures of two of the polymorphs were solved by X-ray diffraction: polymorph **1** (burgundy) and polymorph **2** (orange). It was not possible to determine the crystal structure of the third polymorph (**3**, orange-yellowish), but the obtained powder X-ray diffraction, infrared and Raman spectroscopy, and DSC and PLTM data clearly demonstrate the existence of this additional polymorphic form. Indexation of its powder diffraction pattern showed that it is a monoclinic variety with lattice parameters $a = 11.383(3) \text{ \AA}$, $b = 13.6609(3) \text{ \AA}$, $c = 25.247(7) \text{ \AA}$, $\beta = 101.75(1)$, and exhibiting a more complex supramolecular structure compared to polymorphs **1** and **2** (most probably with belonging to the $P2_1/c$ space group, with $Z = 4$ and $Z' = 3$).

In the structurally characterized polymorphs (**1** and **2**), the AcROY molecules assume conformations corresponding to the lowest energy conformer predicted for the isolated molecule of the compound, slightly modified due to intermolecular forces and packing. These two polymorphs were found to be monotropically related, with polymorph **1** being the stable form and polymorph **2** the metastable crystal structure.

The dominant intermolecular interactions in polymorphs **1** and **2** were evaluated from the crystallographic structural data and also using Hirshfeld surface analysis, and were found to be significantly different: the contribution of the non-classical intermolecular hydrogen bonds of the $\text{CH}\cdots\text{O}$ type to the stabilization of the crystal structure of polymorph **1** is more important than for polymorph **2**, while the hydrogen bonds of the $\text{CH}\cdots\text{N}$ type play a more significant role in the stabilization of the crystal structure of polymorph **2** than in polymorph **1**. Another relevant structural difference between the two polymorphs concerns the presence in polymorph **2** of short $\text{S}\cdots\text{S}$ contacts which are absent in polymorph **1**. Furthermore, while dispersive intermolecular interactions are important in both polymorphs, they are established between different fragments of the molecules in the two polymorphs. All these differences in the intermolecular interactions and packing influence the electronic properties of the AcROY molecules present in the crystals and, ultimately, determine their different colors, so that the observed polymorphism in AcROY is a case of packing-determined color polymorphism, somehow in contrast to ROY where the color polymorphism is mostly (but not exclusively, as mentioned in the Introduction) conformationally determined.¹⁻⁹

Supporting Information

Figures S1-S9, with the ^1H and ^{13}C NMR spectra of AcROY, IR-ATR spectrum of the synthesized material, relative energy plot of the four conformers of AcROY showing the energy of the transition states for conformational isomerization, ORTEP plot depicting the anisotropic displacement ellipsoids, drawn at the 50% probability level, for polymorphs **1** and **2**, results of indexing of the powder diffractogram of polymorph **3**, results of Hirshfeld analysis of these polymorphs, and PLTM images of

the heating of the polymorphs; Tables S1-S3, with results of polymorph screening, assignment of the infrared and Raman spectra of the AcROY polymorphs, and selected valence angles in the molecules present in polymorphs **1** and **2** of AcROY; Crystallographic data Tables with the structural X-Ray data for polymorphs **1** and **2**; PLTM video. CIF files containing the supplementary crystallographic data were deposited at the Cambridge Crystallographic Data Centre, with references CCDC 2110241 (polymorph **1**) and 211242 (polymorph **2**).

Acknowledgements

The CQC-IMS is financially supported by the Portuguese Science Foundation (“Fundação para a Ciência e a Tecnologia” - FCT) – Projects CQC UIDB/00313/2020 and UIDP/00313/2020 (National Funds). CFisUC is funded by FCT through the projects UIDB/04564/2020 and UIDP/04564/2020. Access to instruments from Laser-Lab Coimbra and TAIL-UC (ICT_2009_02_012_1890) facilities funded under QREN-Mais Centro is gratefully acknowledged. B.A.N. also acknowledges FCT for the SFRH/BD/129852/2017 PhD Scholarship.

References

- 1 X. Li, X. Ou, H. Rong, S. Huang, J. Nyman, L. Yu and M. Lu, The Twelfth Solved Structure of ROY: Single Crystals of Y04 Grown from Melt Microdroplets, *Cryst. Growth Des.*, 2020, **20**, 7093–7097.
- 2 K. S. Gushurst, J. Nyman and S. X. M. Boerrigter, The PO13 crystal structure of ROY, *CrystEngComm*, 2019, **21**, 1363–1368.
- 3 L. Yu, Polymorphism in Molecular Solids: An Extraordinary System of Red, Orange, and Yellow Crystals, *Acc. Chem. Res.*, 2010, **43**, 1257–1266.
- 4 A. R. Tyler, R. Ragbirsingh, C. J. McMonagle, P. G. Waddell, S. E. Heaps, J. W. Steed, P. Thaw, M. J. Hall and M. R. Probert, Encapsulated Nanodroplet Crystallization of Organic-Soluble Small Molecules, *Chem*, 2020, **6**, 1755–1765.
- 5 M. Tan, A. G. Shtukenberg, S. Zhu, W. Xu, E. Dooryhee, S. M. Nichols, M. D. Ward, B. Kahr and Q. Zhu, ROY revisited, again: the eighth solved structure, *Faraday Discuss.*, 2018, **211**, 477–491.
- 6 A. Lévesque, T. Maris and J. D. Wuest, ROY reclaims its crown: new ways to increase polymorphic diversity, *J. Am. Chem. Soc.*, 2020, **142**, 11873–11883.
- 7 B. A. Nogueira, C. Castiglioni and R. Fausto, Color polymorphism in organic crystals, *Commun. Chem.*, 2020, **3**, 1–12.
- 8 Z. Chen, Y. Gui, K. Cui, J. R. Schmit and L. Yu, Prolific Polymorph Generator ROY in Its Liquid and Glass: Two Conformational Populations Mirroring the Crystalline-State Distribution, *J. Phys. Chem. B*, 2021, **125**, 10304–10311.
- 9 L. R. Warren, E. McGowan, M. Renton, C. A. Morrison and N. P. Funnell, Direct evidence for distinct colour origins in ROY polymorphs, *Chem. Sci.*, 2021, **12**, 12711–12718.
- 10 B. A. Nogueira, S. M. M. Lopes, S. Lopes, T. Nikitin, A. C. B. Rodrigues, M. E. S. Eusébio, J. A. Paixão, T. M. V. D. Pinho e Melo, A. Milani, C. Castiglioni and R. Fausto, 2,4,6-Trinitro-*N*-(*m*-tolyl)aniline: A New Polymorphic Material Exhibiting Different Colors, *Cryst. Growth Des.*,

- 2021, **21**, 7269–7284.
- 11 X. He, U. J. Griesser, J. G. Stowell, T. B. Borchardt and S. R. Byrn, Conformational color polymorphism and control of crystallization of 5-methyl-2-[(4-methyl-2-nitrophenyl) amino]-3-thiophenecarbonitrile, *J. Pharm. Sci.*, 2001, **90**, 371–388.
 - 12 H. Li, J. G. Stowell, T. B. Borchardt and S. R. Byrn, Synthesis, Conformational Polymorphism, and Construction of a *G–T* Diagram of 2-[(2-Nitrophenyl)amino]-3-thiophenecarbonitrile, *Cryst. Growth Des.*, 2006, **6**, 2469–2474.
 - 13 H. Li, J. G. Stowell, X. He, K. R. Morris and S. R. Byrn, Investigations on solid–solid phase transformation of 5-methyl-2-[(4-methyl-2-nitrophenyl) amino]-3-thiophenecarbonitrile, *J. Pharm. Sci.*, 2007, **96**, 1079–1089.
 - 14 K. M. Lutker, Z. P. Tolstyka and A. J. Matzger, Investigation of a Privileged Polymorphic Motif: A Dimeric ROY Derivative, *Cryst. Growth Des.*, 2008, **8**, 136–139.
 - 15 G. M. Sheldrick, Crystal structure refinement with SHELXL, *Acta Crystallogr., Sect. C: Struct. Chem.*, 2015, **71**, 3–8.
 - 16 A. L. Spek, Single-crystal structure validation with the program PLATON, *J. Appl. Cryst.*, 2003, **36**, 7–13.
 - 17 A. A. Coelho, An indexing algorithm independent of peak position extraction for X-ray powder diffraction patterns, *J. Appl. Crystallogr.*, 2017, **50**, 1323–1330.
 - 18 A. A. Coelho, *TOPAS* and *TOPAS-Academic*: an optimization program integrating computer algebra and crystallographic objects written in C++, *J. Appl. Crystallogr.*, 2018, **51**, 210–218.
 - 19 Gaussian 09, Revision A.02, M. J. Frisch, G. W. Trucks, H. B. Schlegel, G. E. Scuseria, M. A. Robb, J. R. Cheeseman, G. Scalmani, V. Barone, G. A. Petersson, H. Nakatsuji, X. Li, M. Caricato, A. Marenich, J. Bloino, B. G. Janesko, R. Gomperts, B. Mennucci, H. P. Hratchian, J. V. Ortiz, A. F. Izmaylov, J. L. Sonnenberg, D. Williams-Young, F. Ding, F. Lipparini, F. Egidi, J. Goings, B. Peng, A. Petrone, T. Henderson, D. Ranasinghe, V. G. Zakrzewski, J. Gao, N. Rega, G. Zheng, W. Liang, M. Hada, M. Ehara, K. Toyota, R. Fukuda, J. Hasegawa, M. Ishida, T. Nakajima, Y. Honda, O. Kitao, H. Nakai, T. Vreven, K. Throssell, J. A. Montgomery, Jr., J. E. Peralta, F. Ogliaro, M. Bearpark, J. J. Heyd, E. Brothers, K. N. Kudin, V. N. Staroverov, T. Keith, R. Kobayashi, J. Normand, K. Raghavachari, A. Rendell, J. C. Burant, S. S. Iyengar, J. Tomasi, M. Cossi, J. M. Millam, M. Klene, C. Adamo, R. Cammi, J. W. Ochterski, R. L. Martin, K. Morokuma, O. Farkas, J. B. Foresman, and D. J. Fox, Gaussian, Inc., Wallingford CT, 2016.
 - 20 A. D. Becke, Density-functional exchange-energy approximation with correct asymptotic behavior, *Phys. Rev. A*, 1988, **38**, 3098–3100.
 - 21 C. Lee, W. Yang and R. G. Parr, Development of the Colle-Salvetti correlation-energy formula into a functional of the electron density, *Phys. Rev. B*, 1988, **37**, 785–789.
 - 22 A. D. McLean and G. S. Chandler, Contracted Gaussian basis sets for molecular calculations. I. Second row atoms, $Z=11–18$, *J. Chem. Phys.*, 1980, **72**, 5639–5648.
 - 23 S. K. Wolff, D. J. Grimwood, J. J. McKinnon, M. J. Turner, D. Jayatilaka, and M. A. Spackman, Crystal Explorer17 (version 17.5), University of Western Australia, Crawley (AUS), 2017.
 - 24 J. J. McKinnon, A. S. Mitchell and M. A. Spackman, Hirshfeld Surfaces: A New Tool for Visualising and Exploring Molecular Crystals, *Chem. Eur. J.*, 1998, **4**, 2136–2141.
 - 25 M. A. Spackman and J. J. McKinnon, Fingerprinting intermolecular interactions in molecular crystals, *CrystEngComm*, 2002, **4**, 378–392.
 - 26 A. Parkin, G. Barr, W. Dong, C. J. Gilmore, D. Jayatilaka, J. J. McKinnon, M. A. Spackman and C. C. Wilson, Comparing entire crystal structures: structural genetic fingerprinting, *CrystEngComm*, 2007, **9**, 648–652.
 - 27 A. L. Rohl, M. Moret, W. Kaminsky, K. Claborn, J. J. McKinnon and B. Kahr, Hirshfeld Surfaces Identify Inadequacies in Computations of Intermolecular Interactions in Crystals: Pentamorphic 1,8-Dihydroxyanthraquinone, *Cryst. Growth Des.*, 2008, **8**, 4517–4525.
 - 28 M. A. Spackman and D. Jayatilaka, Hirshfeld surface analysis, *CrystEngComm*, 2009, **11**, 19–32.
 - 29 K. J. Thorley and I. McCulloch, Why are S–F and S–O non-covalent interactions stabilising?, *J. Mater. Chem. C*, 2018, **6**, 12413–12421.
 - 30 Y. Nagao, T. Hirata, S. Goto, S. Sano, A. Kakehi, K. Iizuka and M. Shiro, Intramolecular

- Nonbonded S...O Interaction Recognized in (Acylimino)thiadiazoline Derivatives as Angiotensin II Receptor Antagonists and Related Compounds, *J. Am. Chem. Soc.*, 1998, **120**, 3104–3110.
- 31 L. I. L. Cabral, E. M. Brás, M. S. C. Henriques, C. Marques, L. Frija, L. Barreira, J. A. Paixão, R. Fausto and M. L. S. Cristiano, Synthesis, Structure, and Cytotoxicity of a New Sulphonyl-Bridged Thiadiazolyl-Saccharinate Conjugate: The Relevance of S...N Interaction, *Chem. Eur. J.*, 2018, **24**, 3251–3262.
- 32 S. Tang, A. Yusov, Y. Li, M. Tan, Y. Hao, Z. Li, Y.-S. Chen, C. T. Hu, B. Kahr and M. D. Ward, ROY confined in hydrogen-bonded frameworks: coercing conformation of a chromophore, *Mater. Chem. Front.*, 2020, **4**, 2378–2383.
- 33 S. P. Thomas and M. A. Spackman, The Polymorphs of ROY: A Computational Study of Lattice Energies and Conformational Energy Differences, *Austr. J. Chem.*, 2018, **71**, 279–284.
- 34 J. Nyman, L. Yu and S. M. Reutzel-Edens, Accuracy and reproducibility in crystal structure prediction: the curious case of ROY, *CrystEngComm*, 2019, **21**, 2080–2088.
- 35 S. Chen, I. A. Guzei, and L. Yu, New polymorphs of ROY and new record for coexisting polymorphs of solved structures, *J. Am. Chem. Soc.*, 2005, **127**, 9881–9885.
- 36 M. A. Spackman and P. G. Byrom, A novel definition of a molecule in a crystal, *Chem. Phys. Lett.*, 1997, **267**, 215–220.
- 37 A. Burger and R. Ramberger, On the polymorphism of pharmaceuticals and other molecular crystals. I, *Microchim. Acta*, 1979, **72**, 259–271.
- 38 A. Burger and R. Ramberger, On the polymorphism of pharmaceuticals and other molecular crystals. II, *Microchim. Acta*, 1979, **72**, 273–316.
- 39 L. Yu, Inferring thermodynamic stability relationship of polymorphs from melting data, *J. Pharm. Sci.*, 1995, **84**, 966–974.

4.2. ROY-ol

The present subchapter is constituted by the manuscript entitled *The color polymorphs of ROY-ol*, which has been submitted to publication on April 19th, 2022.



Supporting Information:

Annex – Part 1

Authors: Bernardo A. Nogueira, Susana M. M. Lopes, Alberto Milani, Vânia André, José A. Paixão, M. Ermelinda S. Eusébio, Teresa M. V. D. Pinho e Melo, Teresa Duarte, Chiara Castiglioni and Rui Fausto

Corresponding author: Bernardo A. Nogueira

Authors' contributions: B.A.N. conceptualized the study, wrote a preliminary version of the manuscript, and participated in most of the experimental work and in theoretical studies. R.F. contributed to the conceptualization of the study, took responsibility for supervision and data analysis, and wrote the final draft of the manuscript; S.M.M.L. and T.M.V.D.P.M. were responsible for the development of the synthetic route and its implementation; M.E.S.E. participated in the design of the DSC studies and in the writing of the corresponding section of the manuscript; A.M. and C.C. performed the fully-periodic DFT calculations. V.A., T.D. and J.A.P. performed the XRD studies and wrote the corresponding section of the manuscript. All authors have participated in the discussion of the results and agreed with the final version of the manuscript.

Synopsis:

In the present manuscript, the second ROY analogue compound of the current Thesis is reported. ROY-ol (2-((4-hydroxy-2-nitrophenyl)amino)thiophene-3-carbonitrile), which compared to ROY lacks the methyl group on the thiophene ring and presents a hydroxyl group in a *meta* position in relation to the nitro group of the nitrophenyl ring, was synthesized and studied for the first time in this work. Four color polymorphs of ROY-ol were identified. The crystal structures of two of them were determined by single crystal X-ray diffraction and their intermolecular interactions were subsequently evaluated, using the Hirshfeld surface analysis method. Additionally, these two polymorphs were characterized vibrationally (by infrared and Raman spectroscopies and supported by fully-periodic DFT calculations) and thermal analysis studies were performed (by DSC, PLTM and temperature-variation Raman spectroscopy), which allowed to identification of ROY-ol polymorphs 3 and 4.

The color polymorphs of ROY-ol

Bernardo A. Nogueira,^{*,1,2} Susana M. M. Lopes,¹ Alberto Milani,² Vânia André,³
José A. Paixão,⁴ M. Ermelinda S. Eusébio,¹ Teresa M. V. D. Pinho e Melo,¹
M. Teresa Duarte,³ Chiara Castiglioni² and Rui Fausto¹

¹ *University of Coimbra, CQC-IMS, Department of Chemistry, P-3004-535 Coimbra, Portugal.*

² *CMIC, Dipartimento di Chimica, Materiali e Ingegneria Chimica "G. Natta", Politecnico di Milano, 20133 Milano, Italy.*

³ *Centro de Química Estrutural-IMS, Instituto Superior Técnico, Universidade de Lisboa, Av. Rovisco Pais, 1049-001 Lisboa, Portugal*

⁴ *University of Coimbra, CFisUC, Department of Physics, P-3004-516 Coimbra, Portugal.*

Abstract

Color polymorphism is a fascinating property exhibited by compounds that have polymorphs of different colors. The most famous family of substances forming molecular organic color polymorphs is the ROY family of compounds. ROY, which states for the Red, Orange and Yellow colors of the polymorphs of 5-methyl-2-((2-nitrophenyl)amino)thiophene-3-carbonitrile, is currently the compound exhibiting the largest number of known polymorphs (twelve), all of them with crystallographic structures determined. In this study, the color polymorphism exhibited by a novel member of the ROY family, 2-((4-hydroxy-2-nitrophenyl)amino)thiophene-3-carbonitrile (ROY-ol) has been investigated. Four color polymorphs of ROY-ol were identified (one bright-burgundy and the others dark-burgundy), from which the crystal structures of two (polymorphs 1 and 2) were solved by single crystal X-ray diffraction, the intermolecular interactions in these crystals being subsequently evaluated using the Hirshfeld analysis method. These two polymorphs were also characterized vibrationally by infrared and Raman spectroscopies, supported by fully-periodic density functional theory (DFT) calculations. The performed thermal analysis studies, undertaken by differential scanning calorimetry (DSC), polarized light thermomicroscopy (PLTM), and temperature-variation Raman spectroscopy, allowed to identify two additional polymorphs of ROY-ol (polymorphs 3 and 4). Investigation of the conformational space of the ROY-ol isolated molecule within the DFT framework (together with similar calculations on similar molecules, including ROY) allowed to establish a series of correlations between the conformational landscapes of the molecules and some relevant characteristics of the polymorphism the compounds exhibit. As a whole, a detailed description of the color polymorphism exhibited by ROY-ol has been achieved, which is an additional contribution to the understanding of this phenomenon.

Keywords: ROY-ol, color polymorphism, crystal structures, infrared and Raman spectra, thermal analysis, DFT calculations.

* Corresponding author e-mail: ban@qui.uc.pt

1. Introduction

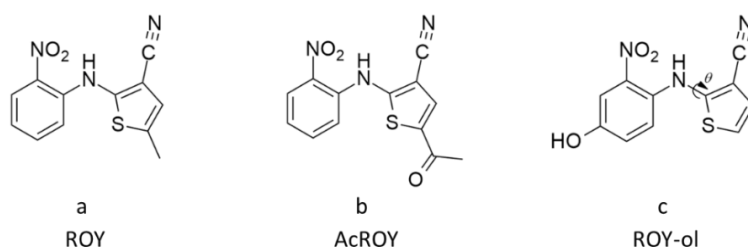
Color polymorphism is an interesting property of chemical systems that present polymorphs with different colors.¹ Despite the potential applications for these systems as time-temperature sensors and photoelectronic devices with multiplex capabilities, for example,²⁻⁵ there are only a few families of compounds that have the ability of forming molecular organic color polymorphs. One of the most famous is the ROY family of compounds. ROY, firstly described in 1995,⁶ is the common designation of 5-methyl-2-((2-nitrophenyl)amino)thiophene-3-carbonitrile (Scheme 1a), which states for the Red, Orange and Yellow colors of its polymorphs. ROY is currently the compound exhibiting the largest number of known polymorphs (twelve), the crystallographic structures of all of them having already been determined.⁶⁻¹²

The different colors of the ROY polymorphs have been attributed mainly to structural variations associated with the conformational flexibility around the N-C_(thiophene) bond (θ in Scheme 1), which determines the relative orientation of the two rings present in the molecule (phenyl and thiophene) that, in turn, determines the extent of the π -electron delocalization in the molecule. Interestingly, the red and orange polymorphs were found to be formed by one of the conformers of the molecule (where the two rings are closer to co-planarity), while the yellow polymorphs are formed by a different conformer. Nevertheless, at least one of the yellow polymorphs of the compound is constituted by the conformer present in the red and orange forms, so that ROY is a chemical system that exhibits both conformation- and packing-determined color polymorphism.¹

More recently, other compounds of the ROY family have been reported to also present polymorphs of different color, such as 2-((2-nitrophenyl)amino)thiophene-3-carbonitrile, also showing red, orange and yellow polymorphs,¹³ 5-methyl-2-((4-methyl-2-nitro-phenyl)amino)thiophene-3-carbonitrile, which had three different red polymorphs (of different tones) and one orange polymorph identified,¹⁴ 2,2'-((ethyne-1,2-diylbis(2-nitro-4,1-phenylene))bis(azanediyl))bis(5-methylthiophene-3-carbonitrile) (or simply el-ROY), with three identified polymorphs, with red and orange shades,¹⁵ and 2-((2-nitrophenyl)amino)furan-3-carbonitrile (FuROY), for each three polymorphs were structurally characterized, one orange-yellow, one red and one orange-red.¹⁶ Earlier this year, we have synthesized a new derivative of ROY, 5-methyl-2-((4-methyl-2-nitro-phenyl)amino)thiophene-3-carbonitrile, which we named AcROY (Scheme 1b), and that presents orange, yellow and burgundy polymorphs.¹⁷

In the present study, the color polymorphism exhibited by the newest member of the ROY family, 2-((4-hydroxy-2-nitrophenyl)amino)thiophene-3-carbonitrile (Scheme 1c), or ROY-ol, was investigated. Comparing to ROY, ROY-ol lacks the methyl group on the thiophene ring and presents a hydroxyl group in a *meta* position in relation to the nitro group of the nitrophenyl ring. The compound was prepared in a three-steps synthetic route, and characterized by ¹H and ¹³C NMR spectroscopy, melting point determination, infrared spectroscopy and high-resolution mass spectrometry with electrospray ionization (HRMS-ESI). Polymorph screening was then performed by the slow Generation and Characterization of Novel Materials Exhibiting Color Polymorphism

evaporation recrystallization method, using a large number of solvents with different characteristics, which rendered two color polymorphs (one bright-burgundy and the other dark-burgundy). The structures of the two polymorphs were determined by single crystal X-ray diffraction, and the polymorphs were also characterized vibrationally by both infrared and Raman spectroscopies, supported by fully-periodic density functional theory (DFT) calculations. The dominant intermolecular interactions in the crystals were evaluated using the Hirshfeld analysis method. Finally, the thermal analysis of the compound was undertaken by differential scanning calorimetry (DSC), polarized light thermomicroscopy (PLTM), and temperature-variation Raman spectroscopy. From these studies, two additional polymorphs of ROY-ol were discovered. In the last section of this article, DFT calculations undertaken for the isolated ROY-ol molecule are presented and used together with similar calculations on ROY and AcROY molecules to establish a series of correlations between the conformational landscapes of the molecules and some relevant characteristics of the polymorphism they exhibit.

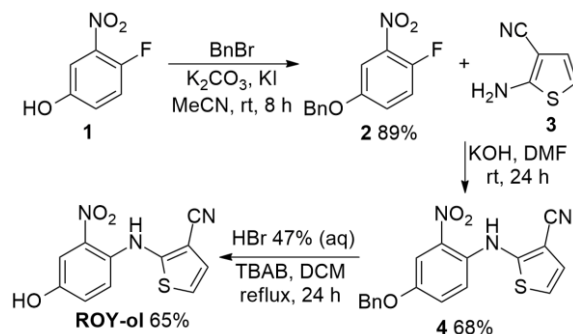


Scheme 1 – Molecules of ROY (*left*), AcROY (*middle*) and ROY-ol (*right*).

2. Materials and methods

2.1. Synthesis and instrumental methods

The synthesis of ROY-ol was achieved in a three-steps sequence (Scheme 2). First, the hydroxyl group of the commercially available 4-fluoro-3-nitrophenol (**1**) was protected with a benzyl group by reaction with benzyl bromide in presence of base, affording compound **2** in high yield. The nucleophilic aromatic substitution reaction between compound **2** and 2-aminothiophene-3-carbonitrile (**3**) gave compound **4** in 68 % yield. Finally, ROY-ol was obtained in 65 % yield by cleavage of the benzyl group using HBr 47 % (aq) in refluxing dichloromethane.



Scheme 2 – Synthetic strategy to ROY-ol.

Synthesis of 4-benzyloxy-1-fluoro-2-nitrobenzene (2): potassium carbonate (6 mmol, 0.829 g) and catalytic potassium iodide (4 mg) were added to a solution of 4-fluoro-3-nitrophenol (**1**) (4 mmol, 0.628 g) and benzyl bromide (4.4 mmol, 0.532 mL) in acetonitrile (25 mL). The reaction mixture was stirred at room temperature for 8 h. After this time, ethyl acetate (25 mL) was added and the mixture was washed with water (2 × 25 mL) and brine (25 mL), dried and the solvent evaporated off. The compound was obtained as a white solid (3.58 mmol, 89 %) by crystallization from petroleum ether, filtered and dried under vacuum. M.p. 85.4-86.9 °C. IR (ATR) ν 746, 834, 1007, 1222, 1319, 1350, 1493 and 1535 cm^{-1} . ^1H NMR δ (CDCl_3): 5.10 (s, 2H), 7.17-7.23 (m, 3H), 7.35-7.43 (m, 5H), 7.61-7.63 (m, 1H). ^{13}C NMR δ (CDCl_3): 71.1, 110.7 (d, $J = 2.7$ Hz), 119.1 (d, $J = 22.6$ Hz), 122.9 (d, $J = 7.7$ Hz), 127.6, 128.5, 128.8, 135.5, 137.2 (d, $J = 8.4$ Hz) 150.2 (d, $J = 258.7$ Hz), 154.5 (d, $J = 2.6$ Hz). HRMS (ESI) m/z for $\text{C}_{13}\text{H}_9\text{NO}_3\text{F}$ [$\text{M} - \text{H}^+$] calcd. 246.0572, found 246.0575.

Synthesis of 2-((4-benzyloxy-2-nitrophenyl)amino)thiophene-3-carbonitrile (4): a solution of 2-aminothiophene-3-carbonitrile (**3**) (2 mmol, 0.248 g) and 4-benzyloxy-1-fluoro-2-nitrobenzene (**2**) (2 mmol, 0.495 g) in dimethylformamide (14 mL) was added dropwise to a suspension of KOH (3 mmol, 0.168 g) in dimethylformamide (6 mL). After the addition was complete, the reaction mixture was stirred at room temperature for 6 h and an additional portion of KOH (1 mmol, 0.056 g) was added at once, and the reaction mixture was stirred for another 16 h. The reaction mixture was poured into a mixture of water/ice and extracted with dichloromethane (3 × 30 mL). The combined organic phases were washed with HCl 1M (2 × 30 mL) and brine (2 × 20 mL), dried and the solvent evaporated off. The compound was obtained as a red solid (1.36 mmol, 68 %) by crystallization from ethanol, filtered and dried under vacuum. M.p. 134.2-135.7 °C. IR (ATR) ν 752, 1007, 1142, 1222, 1262, 1524, 1588 and 2213 cm^{-1} . ^1H NMR δ (CDCl_3): 5.09 (s, 2H), 6.99 (d, $J = 5.6$ Hz, 1H), 7.08 (d, $J = 5.6$ Hz, 1H), 7.26 (dd, $J = 9.2$ and 3.2 Hz, 1H), 7.31 (d, $J = 9.2$ Hz, 1H), 7.35-7.38 (m, 1H), 7.39-7.45 (m, 4H), 7.80 (d, $J = 2.8$ Hz, 1H), 9.63 (s, 1H). ^{13}C NMR δ (CDCl_3): 70.9, 102.0, 109.7, 113.9, 118.0, 119.1, 126.8, 127.7, 128.4, 128.8, 134.7, 135.8, 152.3, 152.9. HRMS (ESI) m/z for $\text{C}_{18}\text{H}_{14}\text{N}_3\text{O}_3\text{S}$ [$\text{M} + \text{H}^+$] calcd. 352.0750, found 352.0744.

Synthesis of 2-((4-hydroxy-2-nitrophenyl)amino)thiophene-3-carbonitrile (ROY-ol): HBr 47 % aq. (3 mL) and tetrabutylammonium bromide (0.036 mmol, 11.4 mg) were added to a solution of compound **4** (0.142 mmol, 50 mg) in dichloromethane (5 mL). The reaction mixture was stirred under reflux for 24 h. After this time, the mixture was diluted with dichloromethane (20 mL), washed with water (2 × 20 mL) and brine (20 mL), dried and the solvent evaporated off. The crude product was purified by flash chromatography [ethyl acetate/hexane (1:2)] giving compound ROY-ol as an orange solid (0.093 mmol, 65 %). M.p. 167.9-169.1 °C (from CHCl_3). IR (ATR) ν 798, 950, 1142, 1217, 1403, 1517, 1593, 2218, 3269 and 3354 cm^{-1} . ^1H NMR δ ($\text{DMSO}-d_6$): 7.06 (d, $J = 6.0$ Hz, 1H), 7.13 (d, $J = 6.0$ Hz, 1H), 7.16 (dd, $J = 8.8$ and 2.8 Hz, 1H), 7.25 (d, $J = 8.8$ Hz, 1H), 7.43 (d, $J = 2.8$ Hz, 1H), 9.45

(s, 1H), 10.16 (br s, 1H). ^{13}C NMR δ (DMSO- d_6): 94.7, 110.6, 114.9, 116.7, 123.6, 126.5, 130.1, 139.3, 153.0, 158.3. HRMS (ESI) m/z for $\text{C}_{11}\text{H}_8\text{N}_3\text{O}_3\text{S}$ [$\text{M} + \text{H}^+$] calcd. 262.0281, found 262.0279.

For the initial characterization of the synthesized compounds, ^1H and ^{13}C NMR and infrared (IR) spectra were obtained (Figures S1-S6 the Supporting Information), as well as high-resolution mass spectra (HRMS) and melting point determination. The NMR spectra were recorded on a Bruker Avance III instrument operating at 400 MHz (^1H) or 100 MHz (^{13}C). The solvents used were deuteriochloroform (CDCl_3) or hexadeuterodimethyl sulfoxide (DMSO- d_6). The IR spectra were recorded in the attenuated total reflection (ATR) mode in an Agilent Cary 630 FTIR Fourier transform spectrometer, with a diamond-based ATR cell (Smart Orbit). HRMS were performed by electrospray ionization (ESI) in an orbitrap q-exactive focus mass spectrometer. Melting point (uncorrected) was determined in an open glass capillary.

The polymorph screening was performed by slow evaporation recrystallization (5-25 mg) with different solvents (4-20 mL), at room temperature.

Single crystal X-ray diffraction (XRD) measurements were performed in a Bruker APEX II diffractometer, at room temperature, using graphite monochromated $\text{MoK}\alpha$ ($\lambda = 0.71073 \text{ \AA}$) radiation. The structure was solved by the dual-space algorithm implemented in SHELXT-2018/2,¹⁸ and full-matrix least-squares refinement of the structural model was performed using SHELXL-2018/3.¹⁹ All non-hydrogen atoms were refined anisotropically. Hydrogen atoms were placed at calculated idealized positions and refined as riding using SHELXL-2018/3 default values,¹⁹ except for those of the hydroxyl and amine groups that were refined isotropically with a displacement parameter constrained to $1.5\times$ (hydroxyl) or $1.2\times$ (amine) of the U_{iso} value of the parent atom. Full details of the data collection and structure refinement procedures are provided in the Supporting Information (Crystallographic Data). A summary of the data collection and refinement is provided in Table 1. The CIF files containing the supplementary crystallographic data for the two polymorphs of ROY-ol were deposited at the Cambridge Crystallographic Data Centre, with the references CCDC 2160983 (polymorph-1) and CCDC 2160984 (polymorph-2).

The IR spectra (400-4000 cm^{-1} wavenumber region; spectral resolution 1 cm^{-1} ; 512 accumulations) of the purified polymorphs were obtained in a Thermo Scientific FT-IR Nicolet iS5 system, using an iD7 ATR accessory with a diamond crystal (incidence angle: 45°). The Raman spectra were collected in a Raman Horiba LabRam HR Evolution equipment, using an excitation light of 633 nm (HeNe laser) with an approximate power of 0.5 mW at the sample, to prevent photodegradation. The system was calibrated using a silicon crystal wafer (reference peak: 520.5 cm^{-1}). The spot area of the laser was approximately $100 \mu\text{m}^2$, which was focused on the sample through a $50\times$ long working distance objective. The final spectra were the average of 500 accumulations of individual spectra collected during 1 second, with a spectral resolution of 0.5 cm^{-1} .

The differential scanning calorimetry (DSC) experiments were carried out in a Perkin Elmer Pyris-1 power compensation calorimeter, equipped with a 1:1 v/v ethylene glycol:water cooler (-25 °C) and a 20 mL min^{-1} nitrogen purge flow. Aluminum pans (hermetically sealed) were used (sample weight: 0.8 to 2 mg), with an empty pan used as reference. The temperature and enthalpy calibrations were performed with indium (Perkin Elmer, 99.99 %, $T_{\text{fus}} = 156.6$ °C; $\Delta_{\text{fus}}H_{\text{m}} = 3286 \pm 13 \text{ J mol}^{-1}$) and caffeine (Mettler Toledo, ME 18872, $T_{\text{fus}} = 235.6 \pm 0.2$ °C). The samples were scanned from 25 to 200 °C at a scan rate of 10 °C min^{-1} . Polarized light thermal microscopy (PLTM) analyses were performed using a Linkam DSC600 hot stage, with a Leica DMRB microscope and a Sony CCD-IRIS/RGB video camera. Images at $50\times$ magnification were collected throughout the experiments, by combined use of polarizers and wave compensators, and occasionally using crossed polarizers. The samples were heated at a rate of 10 °C min^{-1} , from 25 to 200 °C.

Table 1 – Summary of the single-crystal X-ray data collections and crystal structure refinements.

	Polymorph-1	Polymorph-2
Chemical formula	$\text{C}_{11}\text{H}_{17}\text{N}_3\text{O}_3\text{S}$	$\text{C}_{11}\text{H}_{17}\text{N}_3\text{O}_3\text{S}$
Formula weight	261.26	261.26
Color, shape	Bright-burgundy/plate	Dark-burgundy/block
Space group	$P2_1/n$	$P2_1/n$
Temperature (K)	292(2)	293(2)
Cell volume (Å^3)	1129.0(6)	2265.9(3)
Crystal system	monoclinic	monoclinic
a (Å)	7.867(2)	8.6557(7)
b (Å)	13.046(3)	12.9351(12)
c (Å)	11.519(4)	20.2404(18)
α (deg)	90	90
β (deg)	107.26(3)	90.806(4)
γ (deg)	90	90
Z, Z'	4, 1	8, 2
D_c (Mg m^{-3})	1.537	1.532
Radiation (Å) (graphite; monochromated)	0.71073	0.71073
Max. crystal dimensions (mm)	0.23×0.20×0.08	0.06×0.04×0.04
θ range (deg)	2.422 – 27.493	2.546 – 27.499
Range of h, k, l	-10,10;-16,16;-14,14	-11,11;-16,16;-26,26
Reflections measured/independent	70874 / 2602	68321 / 5211
Reflections observed ($I > 2 \sigma$)	1873	3161
Data/restraints/parameters	2602/0/169	5211/0/338
GOF	1.053	1.020
R_1 ($I > 2 \sigma$)	0.0375	0.0574
wR_2	0.1087	0.1619
Function minimized	$\sum w (F_o ^2 - S F_c ^2)$	$\sum w (F_o ^2 - S F_c ^2)$
Diff. density final max/min ($e \text{ Å}^{-3}$)	0.174, -0.264	0.266, -0.350

2.2. Computational details

The DFT calculations performed on isolated molecules, including geometry optimizations and calculations of the potential energy profiles, were carried out using the Gaussian 09 program (version D.01).²⁰ The three-parameter B3LYP functional, which includes the Becke's gradient exchange

correction²¹ and the Lee, Yang and Parr correlation functional,²² was used together with the 6-311++G(2d,p) basis set.²³

Fully-periodic calculations on the crystalline structures were performed using the CRYSTAL17 code,^{24,25} and include geometries and cell parameters optimizations as well as calculation of infrared and Raman spectra (at the Γ point, by the diagonalization of the numerically calculated Hessian matrices) of the ROY-ol polymorphs. The input structures were those experimentally determined in this work by XRD. The calculations were performed within the DFT theoretical framework with the PBE0 functional²⁶ and the 6-31G(d,p) basis set.²⁷ Calculated frequencies were scaled by the factor 0.9512,²⁸ to allow a better comparison with the experimental data.

3. Results and discussion

3.1. Polymorph screening and IR and Raman band-marks of the polymorphs 1 and 2 of ROY-ol

The synthesized ROY-ol material was subjected to polymorph screening through recrystallization from different solvents using the solvent room-temperature slow-evaporation technique. The solvents used included apolar, polar-aprotic and polar-protic solvents. Two different polymorphs exhibiting different color, were identified (Figure 1; see also Figure S7 in Supporting Information): polymorph-1 (bright-burgundy), which was obtained from recrystallization in methanol (together with polymorph-2), and polymorph-2 (dark-burgundy), which was found upon recrystallization in all used solvents (mixed with polymorph-1 in the case of recrystallization from methanol).

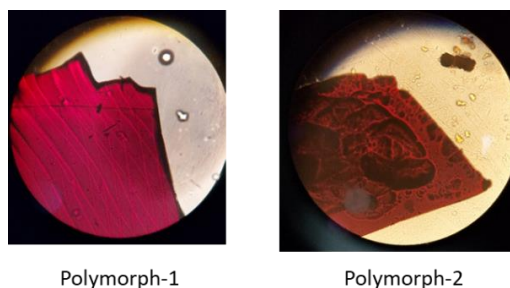


Figure 1 – ROY-ol polymorphs-1 (*left*) and -2 (*right*). Images are amplified 50 \times .

The identity of the polymorphs was first confirmed by IR-ATR and Raman spectroscopies. The spectra of the two polymorphs are shown in Figure 2 and present clear distinct profiles. Marker-bands for fast differentiation of the two polymorphs could be identified. In the IR spectra, polymorph-1 exhibits intense bands at 1584, 1506 and 1339 cm^{-1} , whereas in polymorph-2 the corresponding bands are observed at 1592, 1516 and 1356 cm^{-1} , respectively. Noteworthy, the spectral signature of the $\text{C}\equiv\text{N}$ stretching mode is clearly different for the two polymorphs. In the IR spectrum of polymorph-1, this mode gives rise to a single band 2228 cm^{-1} , while in the case of polymorph-2 a doublet of bands at 2224 and 2218 cm^{-1} is observed. Additionally, the 3500-2900 cm^{-1} spectral region (where the bands due to the CH, NH and OH stretching vibrations are observed) is also clearly distinctive for both polymorphs,

as seen in Figure 2. In the Raman spectra, the most intense peak appears at the same frequency (816 cm^{-1}) in the spectra of both polymorphs. However, characteristic Raman bands of polymorph-1 are observed at 1277, 1265 and 1150 cm^{-1} , while in the spectrum of polymorph-2 band-marks are observed at 1239, 1210 and 1142 cm^{-1} . The Raman spectra of the two polymorphs is particularly distinguishable in the 1000-1600 cm^{-1} , region where the Raman bands in the spectrum of polymorph-2 are considerably more intense than those in the Raman spectrum of polymorph-1 (Figure 2).

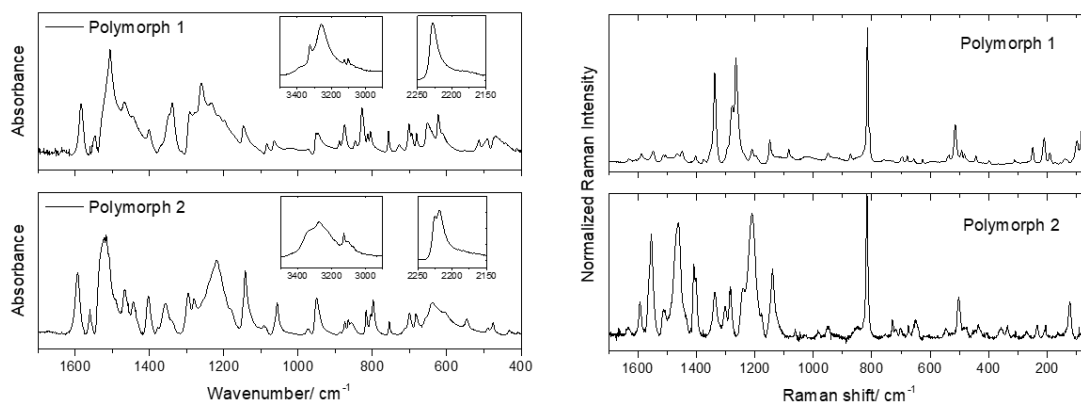


Figure 2 – IR (left) and Raman (right) spectra of polymorphs 1 and 2 of ROY-ol, respectively in the 400-1700 cm^{-1} wavenumber and 50-1700 cm^{-1} Raman shift range.

To better understand the vibrational features in both the IR and Raman spectra of polymorphs 1 and 2 of ROY-ol, fully periodic DFT calculations were performed for these two crystalline structures. These involved the crystallographic structure optimization and the calculation of the correspondent vibrational spectra at the PBE0/6-31G(d,p) level of theory. The experimentally observed and calculated vibrational frequencies are provided in Tables S1 and S2, while the calculated spectra are compared with the experimental ones in Figure S8 and S9.

The calculations show a good general agreement with the experimental data and allowed a characterization of the above-mentioned marker-bands. Hence, the calculations indicate that the IR marker-bands of polymorph-1 observed at 1584, 1506 and 1339 cm^{-1} correspond to the anti-symmetric stretching mode of the NO_2 moiety, a CC stretching vibration delocalized throughout the two rings of the molecule, and a CC stretching localized mode of the thiophene ring, respectively. In turn, the IR marker-bands of polymorph-2 observed at 1592, 1516 and 1356 cm^{-1} are assigned to the NO_2 anti-symmetric stretching mode, the same CC stretching vibration delocalized throughout the two rings of the molecule that in polymorph-1 is observed at 1506 cm^{-1} , and to a vibration containing large contributions of both the OH and NH bending modes. On the other hand, Raman marker-bands of polymorph-1 observed at 1277, 1265 and 1150 cm^{-1} correspond to a mixed NH/OH bending vibration, and two different CH bending modes of the nitrophenyl ring. These bands have counterparts in the Raman marker-bands of polymorph-2 observed at 1239, 1210 and 1142 cm^{-1} .

3.2. Crystal structure of the polymorphs 1 and 2 of ROY-ol and Hirshfeld surface analysis

The X-ray crystallographic studies determined that the two polymorphs of ROY-ol crystallize in the monoclinic system, $P2_1/n$ ($n^\circ 14$) space group, with $a = 7.867(2) \text{ \AA}$, $b = 13.046(3) \text{ \AA}$, $c = 11.519(4) \text{ \AA}$, $\beta = 107.26(3)^\circ$, $V = 1129.0(6) \text{ \AA}^3$, $Z = 4$, $Z' = 1$ for polymorph-1, and $a = 8.6557(7) \text{ \AA}$, $b = 12.9351(12) \text{ \AA}$, $c = 20.2404(18) \text{ \AA}$, $\beta = 90.806(4)^\circ$, $V = 2265.9(3) \text{ \AA}^3$, $Z = 8$, $Z' = 2$ for polymorph-2. Thus polymorph-2 distinguishes from polymorph-1 in that the unit cell has twice the volume of polymorph-1 and accommodates two symmetry independent molecules in the unit cell. In addition, as described below, the molecular conformation of the molecules in the two polymorphs differs significantly, as well as the hydrogen bonding scheme responsible for cohesion of the structures in the crystalline state.

Figure 3 depicts the molecular geometry found in the crystals of the two polymorphs, where, in both cases, the OH substituent of the nitrophenyl ring and the cyano substituent of the thiophene ring point away from and towards the nitro group, respectively.

In both polymorphs, a strong intramolecular hydrogen bond is present between the amine N–H group and an O atom from the neighbor nitro group acting as proton acceptor. It is notorious that both symmetry independent molecules present in the unit cell of polymorph-2 are almost strictly planar, with torsion angles around the rotational degrees of freedom present in the molecule being close to $0/180^\circ$, the C–N–C–S dihedral angle being $-6.7(5)^\circ$ in one of the molecules and $7.9(5)^\circ$ in the other. In contrast, the molecule in polymorph-1 is found to have a significant deviation from planarity, with the C–N–C–S dihedral angle being $-31.6(3)^\circ$. In polymorph-1, the nitro group is also significantly tilted ($23.1(2)^\circ$) from the plane of the phenyl ring (see Figure 3). Bond lengths and valence angles are similar in the two polymorphs and fall within the range of values observed in similar compounds.^{1,5-17}

Molecular packing and the associated set of intermolecular interactions is distinct in the two polymorphs, even if in both the major role is played by a strong N–H \cdots O hydrogen bond between the cyano and hydroxyl groups of neighbor molecules. In polymorph-1, these hydrogen bonds interconnect the molecules forming chains running parallel to the crystallographic b -axis. Parallel sets of chains are further weakly linked by non-classic C–H \cdots O hydrogen bonds between the thiophene rings and the hydroxyl groups, forming an extensive hydrogen bond network, as depicted in Figure 4. In polymorph-2, the N–H \cdots O hydrogen bond between the cyano and hydroxyl groups is established between the two symmetry independent molecules, forming chains running along the $[1\ 1\ 0]$ and $[1\ -1\ 0]$ crystallographic directions and, in addition, a weaker C–H \cdots O interaction between a C–H group of the phenyl ring and the O2 atom that participates as well in the intramolecular N–H \cdots O bond is also present. These chains are further interlinked by weaker C–H \cdots O between the thiophene rings and the hydroxyl groups, as depicted in Figure 5. Notoriously, one of the O atoms of the nitro group does not participate in the hydrogen bond network in neither of the polymorphs. Inspection of the short contacts present in the two polymorphs discloses a more extensive set for polymorph-2 (Table 4). In polymorph-1, only one such

ROY analogues

contact adds to those of the hydrogen bonds discussed above, that occurs between the S atom and the H atom of a close C–H group of the nitrophenyl ring (a similar C–H···S intramolecular contact is also present in polymorph-2).

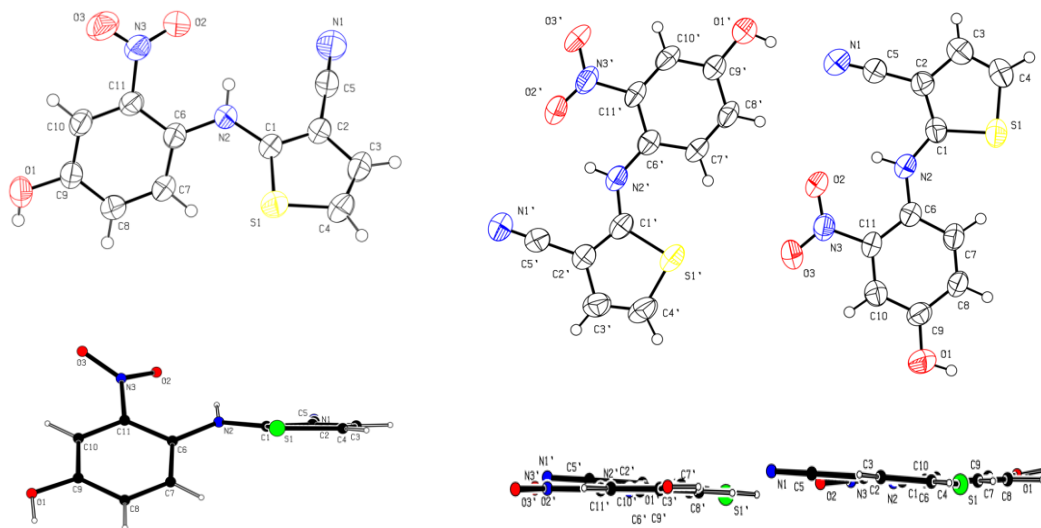


Figure 3 – ORTEP plots depicting the anisotropic displacement ellipsoids drawn at the 50 % probability level and the atom numbering schemes for polymorph-1 (*left*) and polymorph-2 (*right*). In the bottom panel, a profile view of the molecules is shown (viewing direction parallel to the thiophene ring plane).

Table 2 – Valence angles (°) in the thiophene and nitrophenyl rings of polymorphs 1 and 2 of ROY-ol.

Angle	Polymorph-1	Polymorph-2
C1–C2–C3	112.92(18)	114.1(3) / 113.6(3)
C2–C3–C4	112.16(18)	111.4(3) / 111.7(3)
C3–C4–S1	112.85(15)	113.4(3) / 113.6(3)
C4–S1–C1	91.46(10)	91.62(16) / 91.74(17)
S1–C1–C2	110.56(14)	109.5(2) / 109.5(2)
C6–C7–C8	122.01(17)	121.9(3) / 122.8(3)
C7–C8–C9	120.70(18)	123.1(3) / 121.6(3)
C8–C9–C10	118.93(18)	116.9(3) / 118.1(3)
C9–C10–C11	120.07(17)	120.4(3) / 120.7(3)
C10–C11–C6	122.34(17)	122.4(3) / 121.9(3)
C11–C6–C7	115.92(17)	115.4(3) / 114.9(3)

Table 3 – Relevant dihedral and torsion angles (°) for polymorphs 1 and 2 of ROY-ol.

Dihedral/torsion angle	Polymorph-1	Polymorph-2
< (C1...S1)/(C6–C11)	46.52(7)	4.2(2) / 4.4(2)
< (C6...C11)/N3O2O3	23.1(2)	0.8(6) / 1.8(6)
C6–C11–N3–O2	24.0(3)	–1.3(5) / –0.3(5)
C6–C11–N3–O3	–157.6(2)	179.0(3) / 178.6(3)
C6–N2–C1–S1	–31.6(3)	–6.7(5) / 7.9(5)
C1–N2–C6–C11	156.9(2)	–177.3(3) / 177.2(3)
C6–N2–C1–C2	155.4(2)	174.9(3) / –174.5(3)

Table 4 – Hydrogen bonds and short intermolecular contact distances and angles for polymorphs 1 and 2 of ROY-ol.

D-H...A	D-H	H-A	D...A	<D-H...A
<i>Polymorph-1</i>				
O1–H1...N1 ^a	0.79(3)	1.98(3)	2.769(3)	170(3)
N2–H2...O2	0.82(3)	2.03(2)	2.653(2)	132(2)
C3–H3...O1 ^b	0.93	2.50	3.184(3)	130.4
C7–H7...S1	0.93	2.73	3.220(2)	113.6
<i>Polymorph-2</i>				
O1–H1...N1 ^c	0.89(5)	1.99(5)	2.874(4)	177(5)
N2–H2...O2	0.86(4)	1.90(4)	2.597(4)	137(3)
C3–H3...O1 ^d	0.93	2.49	3.157(4)	128.6
C7–H7...S1	0.93	2.47	3.194(3)	134.3
C8–H3...O2 ^c	0.93	2.51	3.295(4)	142.4
N2'–H2'...N3'	0.82(4)	2.49(4)	2.922(4)	114(3)
N2'–H2'...O2'	0.82(4)	1.91(4)	2.608(3)	142(3)
C4'–H4'...O1	0.93	2.65	3.412(4)	139.3
C7'–H7'...S1'	0.93	2.43	3.156(3)	135.3
C8'–H8'...O2	0.93	2.43	3.233(4)	144.3
O1'–H1'...N1	0.82(5)	2.01(5)	2.816(4)	170(5)

^a Distances and angles are given in Å and degrees, respectively. Symmetry codes: a) $3/2-x, -1/2+y, 1/2-z$; b) $x, y, -1+z$; c) $1+x, 1+y, z$; d) $1/2-x, 1/2+y, 3/2-z$.

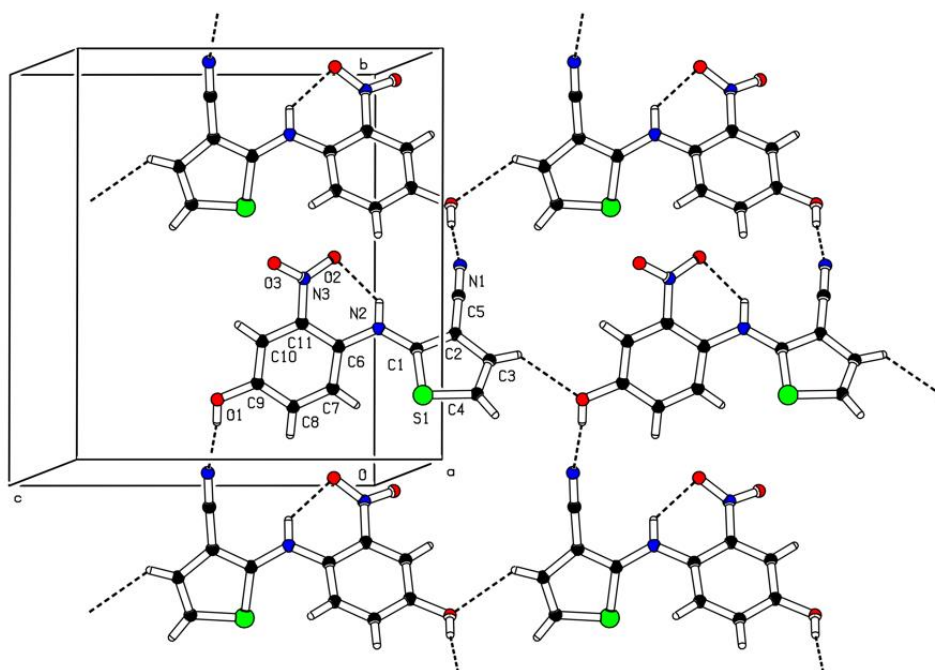


Figure 4 – Hydrogen-bonding network in polymorph-1 of ROY-ol showing the 1D-chains running along the crystallographic direction *b*-axis with molecules joined by strong N–H...O hydrogen bonds. These chains are linked to identical chains in the unit cell *via* weaker C–H...O hydrogen bonds. For clarity, not all molecules present in the unit cell are shown.

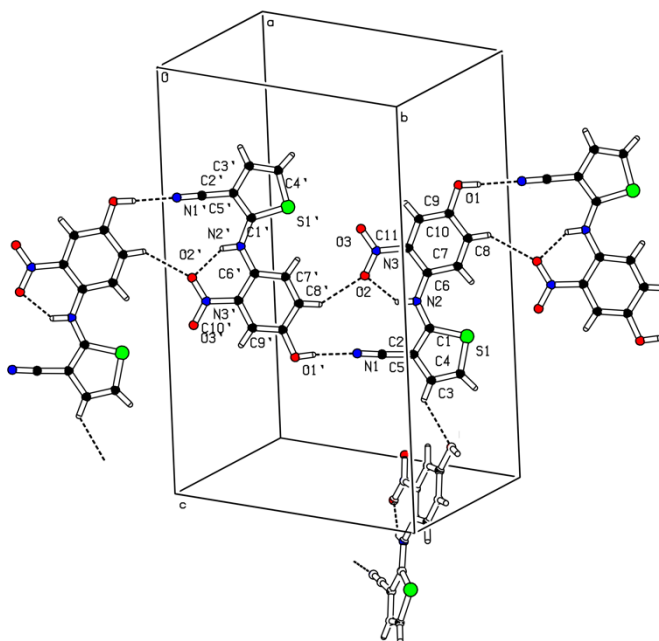


Figure 5 – Hydrogen-bonding network in polymorph-2 of ROY-ol showing the 1D-chains running along the [1 1 0] and [1 -1 0] crystallographic direction joined by strong N–H···O hydrogen bonds. These chains are interlinked *via* weaker C–H···O hydrogen bonds. For clarity, not all molecules present in the unit cell are shown, only one chain running along [1 1 0] and the interconnection to a single molecule of another chain that runs along [1 -1 0] is depicted.

In order to characterize in detail the dominant intermolecular interactions in the crystals of polymorphs 1 and 2 or ROY-ol, the Hirshfeld surface analysis method developed by Spackman and co-workers was used.^{29,30} The analyses were done using Crystal Explorer 17.5,³¹ using as input the crystal structures obtained in the XRD studies.

Maps of the normalized contact distance, d_{norm} , on the calculated Hirshfeld surfaces, and the respective 2D-fingerprint plots were obtained (Figure 6 and Figures S10-S12 in the Supporting Information). d_{norm} is calculated from the distances to the surface of the nearest atom outside, d_e , and inside, d_i , the surface, as defined in the Eq. 1, where r^{vdW} are the van der Waals radii of the atoms.

$$d_{\text{norm}} = \frac{d_i - r_i^{\text{vdW}}}{r_i^{\text{vdW}}} + \frac{d_e - r_e^{\text{vdW}}}{r_e^{\text{vdW}}} \quad (1)$$

The d_{norm} maps allow the identification of the regions of the molecule in the crystal where intermolecular interactions are more relevant,^{30,32} while the 2D-fingerprint plots summarize the information about the relative importance of the different types of contacts (combinations of d_e and d_i ,

expressed as percentages of the surface area allocated to each combination of atoms) throughout the Hirshfeld surface of the molecule (Table 5).^{33–35}

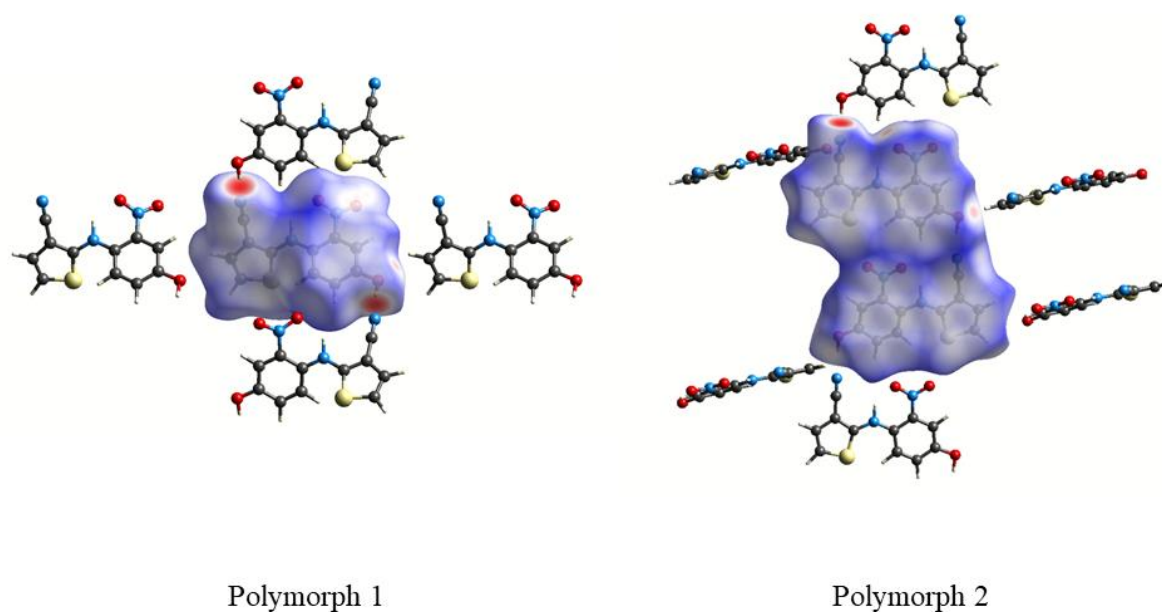


Figure 6 – Maps of d_{norm} on the Hirshfeld surfaces of the crystallographic asymmetric units of polymorphs 1 (*left*) and 2 (*right*) of ROY-ol, showing also the neighboring molecules which account for the strongest interactions (shorter contacts).

Table 5 – Fractional areas (in %) of the Hirshfeld surface assigned to the different intermolecular contacts in ROY-ol polymorphs 1 and 2.

Intermolecular contact	Polymorph-1	Polymorph-2			
	Asymmetric unit ($Z' = 1$)	Asymmetric unit ($Z' = 2$)	Independent molecule 1	Independent molecule 2	Independent molecules Average
H \cdots O/O \cdots H	23.2	25.6	26.4	28.6	27.5
H \cdots H	18.4	16.2	13.7	15.2	14.5
H \cdots N/N \cdots H	14.1	11.8	14.0	16.3	15.2
C \cdots C	10.6	10.4	9.5	9.4	9.5
H \cdots C/C \cdots H	8.2	13.3	12.2	11.3	11.8
H \cdots S/S \cdots H	5.4	3.2	2.9	3.4	3.2
C \cdots N/N \cdots C	5.2	3.7	3.2	3.3	3.3
O \cdots S/S \cdots O	5.1	1.3	2.4	2.8	2.6
N \cdots O/O \cdots N	3.7	3.4	4.0	2.0	3.0
C \cdots O/O \cdots C	3.4	3.6	3.5	2.8	3.2
C \cdots S/S \cdots C	1.1	4.6	6.0	2.4	4.2
O \cdots O	0.9	0.6	0.6	0.5	0.6
N \cdots S/S \cdots N	0.6	1.2	0.9	1.2	1.1
S \cdots S	0.1	0.0	0.0	0.0	0.0
N \cdots N	0.0	0.9	0.7	0.8	0.8

Figure 6 shows the maps of d_{norm} on the Hirshfeld surfaces of the crystallographic asymmetric units of polymorphs 1 and 2 of ROY-ol, showing also the neighboring molecules which account for the strongest interactions (shorter contacts, indicated by the red spots on the Hirshfeld surfaces). The d_{norm} values vary from -0.646 to 1.361 in polymorph-1 and from -0.573 to 1.327 in polymorph-2. For polymorph-1, the shortest intermolecular contacts are related with the H-bonds established between the OH substituent of the nitrophenyl moiety and the N atom of the cyano substituent of the thiophene ring, while the second most relevant intermolecular interactions are associated with the weak non-classical H-bonds formed between the thiophene ring (through the *m*-hydrogen atom) and the oxygen atom of the hydroxyl group. In the case of the polymorph-2, while the most important interactions between the two molecules that constitute the asymmetric unit of the crystal involve the OH group and the cyano N atom, on one side, and the oxygen atoms of the nitro group and the hydrogen atom of the nitrophenyl group in *p*-position to the NO₂ moiety, on the other side (see Figure S10 in the Supporting Information), the most important interactions between the asymmetric unit of crystal as a whole and the adjacent molecules are similar to those existing in polymorph-1 (see Figure 6): (i) the H-bond interactions established by the OH groups and the cyano N atoms that do not participate in the intermolecular H-bond interaction inside the asymmetric unit dimer (which are established respectively with the cyano N atom and the OH group of adjacent molecules), and (ii) weak non-classical H-bonds formed between thiophene rings (through the *m*-hydrogen atom) of neighboring molecules and the oxygen atom of the hydroxyl groups of the molecules forming the asymmetric unit dimer (and vice-versa).

Table 5 displays the percentages of the Hirshfeld surfaces assigned to the different types of contacts (d_e vs. d_i), which are also shown graphically in the 2D-fingerprint d_e vs. d_i plots provided as Supporting Information (Figures S11-S12). H \cdots O/O \cdots H contacts are prevalent in both polymorphs, representing 23.2 and 25.6 % of the total surface areas of polymorphs 1 and 2 respectively when for polymorph-2 the full asymmetric unit is considered, and are mostly related with the C–H \cdots O non-classical hydrogen-bond interactions referred to above. When the individual molecules in asymmetric unit of polymorph-2 are considered, the percentage of total surface area assigned to the H \cdots O/O \cdots H contacts increase, as expected, because between the two molecules one of the dominant interactions involves the oxygen atoms of the nitro group and the hydrogen atom of the nitrophenyl group in *p*-position to the NO₂ moiety, as mentioned above. The second and third most relevant types of contacts are the H \cdots H contacts (18.4 and 16.2 % in polymorphs 1 and 2, respectively; somewhat lower, i.e., 14.5 % in average, if individual molecules in the unit cell of polymorph-2 are considered), which are associated to intermolecular interactions of dispersive type, and the H \cdots N/N \cdots H contacts (14.1 and 11.8 %), which are essentially related with the strong O–H \cdots N hydrogen-bond interactions established between the OH groups and the cyano N atoms (also as expected considering the O–H \cdots N interaction within the two molecules of the asymmetric unit of polymorph-2, the H \cdots N/N \cdots H contacts percentage increase to 15.2 % in average when the individual molecules are taken in separate). Interestingly, the

most significant difference between the major intermolecular interactions in the crystals of the polymorphs 1 and 2 of ROY-ol is observed for the $\text{H}\cdots\text{C}/\text{C}\cdots\text{H}$ contacts, which correspond to 8.2 % of the surface area in polymorph-1 and to almost twice this value (13.3 %) in polymorph-2 (11.8 % in average when the two molecules of its asymmetric unit are taken in separate). In polymorph-1, the close $\text{H}\cdots\text{C}/\text{C}\cdots\text{H}$ contacts are related with the parallel stacking of the nitrophenyl and thiophene rings of adjacent molecules (i.e., nitrophenyl...thiophene stacking interactions), while in the case of polymorph-2, these contacts result from parallel stacking between the same type of ring in adjacent molecules (i.e., nitrophenyl...nitrophenyl and thiophene...thiophene ring staking interactions). The sum of the areas related to the principal hydrogen-bond intermolecular interactions ($\text{H}\cdots\text{O}/\text{O}\cdots\text{H}$, $\text{H}\cdots\text{N}/\text{N}\cdots\text{H}$ and $\text{H}\cdots\text{S}/\text{S}\cdots\text{H}$) are 42.7 % for polymorph-1 and 45.9 % (average values for the two independent molecules) for polymorph-2, which suggest that H-bonding might be globally more relevant in the packing of polymorph-2 than in polymorph-1.

3.3. Thermal studies (DSC, PLTM and temperature dependent Raman spectroscopy)

The thermal behavior of ROY-ol polymorphs 1 and 2 was firstly investigated by DSC. Since it was not possible to isolate the sufficient amount of polymorph-1 to conduct an experiment with this polymorph alone (polymorph-1 always co-form with polymorph-2 from recrystallization in methanol, as already pointed out), the DSC experiments were done with a sample of pure polymorph-2 and a sample containing a mixture of the two polymorphs obtained from recrystallization from methanol. The obtained DCS heating curves are shown in Figure 7.

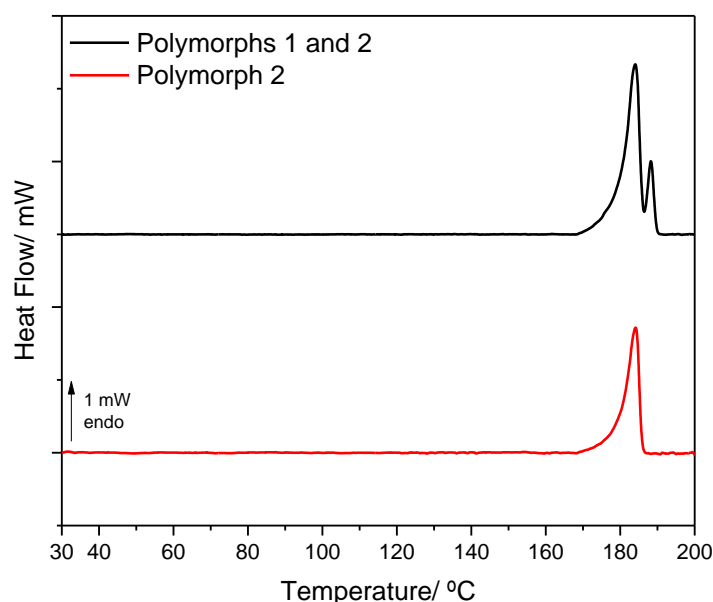


Figure 7 – DSC heating curves of two samples of ROY-ol, one corresponding to pure polymorph-2 and the other to a mixture of polymorphs 1 and 2 (heating rate: 10 °C min^{-1} ; masses: 0.85 mg, polymorph-1 + polymorph-2 mixed sample; 0.8 mg, pure polymorph-2 sample).

As seen in the figure, the pure sample of polymorph-2 exhibits an endothermic peak at 176.2 ± 0.8 °C, with an enthalpy of fusion of 36.4 ± 1.0 kJ mol⁻¹, which corresponds to the melt of this polymorph. In the curve of the sample containing the mixture of the two polymorphs, the melting of polymorph-2 is also observed as a first endothermic process, followed by a second melting process, which takes place at 187 °C. It was tempting to ascribe the second melting peak to the melting of polymorph-1, but, as shown below, the reality is considerably more complex.

Since low-enthalpy processes occurring before the melting processes are frequently undetectable in DSC experiments (in particular when they take place in a wide range of temperature), and also because we wanted to observe the thermal behavior of polymorph-1 as an isolated species, the two polymorphs of ROY-ol were subjected to investigation by PLTM.

In the PLTM analysis of polymorph 2, which is illustrated in Figure 8, the only visible thermodynamic event was, as suggested by the DSC data, the melting of the crystal, starting at 165 °C and finishing at 187 °C, in accordance with the DSC information recorded for the sample of this polymorph.

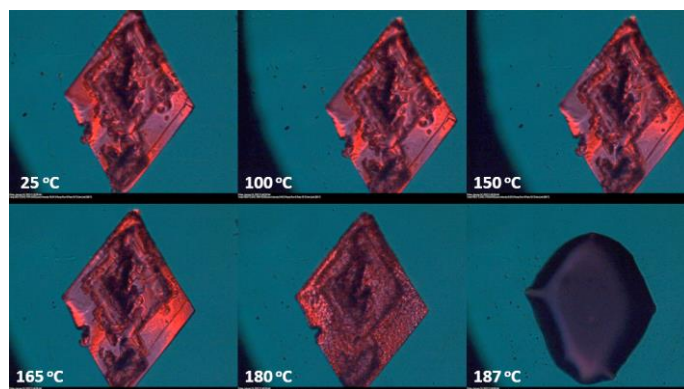


Figure 8 – PLTM images obtained along the heating of a crystal of the polymorph-2 of ROY-ol (heating rate: 10 °C min⁻¹).

On the other hand, in the PLTM images of a crystal of polymorph-1 (Figure 9), one can clearly observe a solid-solid transition, from polymorph-1 to another solid form, which starts at ca. 100 °C and is completed at around 135 °C. After this transformation, the melting process starts at around 175 °C, with the first drops of the melted material being formed, as seen in the center of the image shown in Figure 9. At 196 °C, the melting of the whole sample is complete. The first steps of this latter transition are better observed in the PLTM video submitted as Supporting Information. These results mean that, upon heating, polymorph-1 converts into a new polymorph that melts at higher temperatures than polymorph-2 (polymorph-3), and that the melting process observed at higher temperature in the DSC experiments (see Figure 7 – black curve) is not the melting of polymorph-1, but that of polymorph-3. The solid-solid transition between polymorph-1 and polymorph-3 is not detected in the DSC experiments because of the broad range of temperature where it occurs and, presumably also of its low enthalpy.

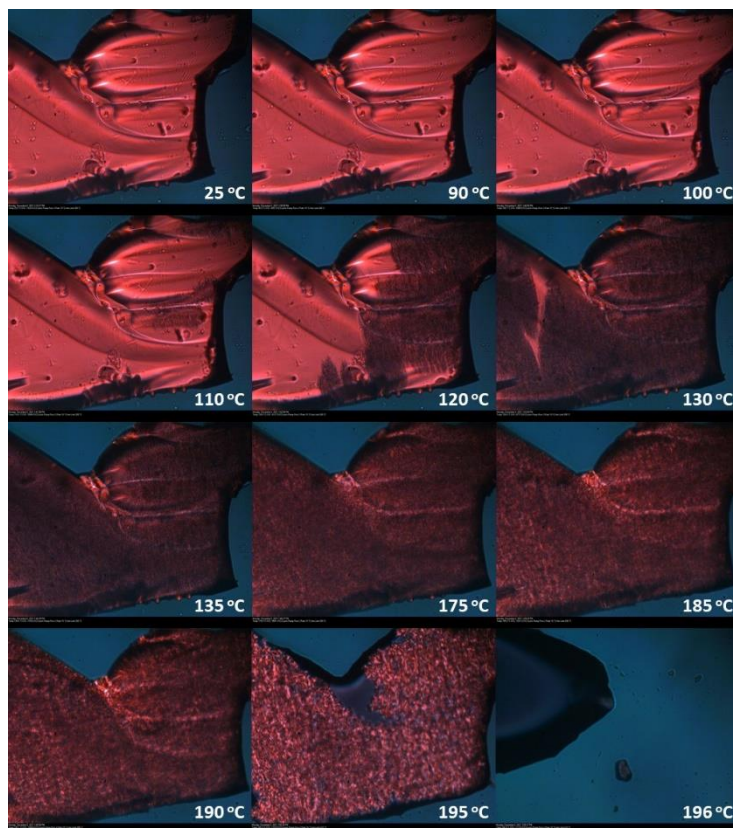


Figure 9 – PLTM images obtained along the heating of a crystal of the polymorph-1 of ROY-ol (heating rate: 10 °C min^{-1}). These pictures were extracted from the PLTM video submitted as Supporting Information.

This solid-solid transition between polymorphs 1 and 3 was also investigated by temperature variation Raman spectroscopy, where the same temperature variation programme used in the PLTM experiment was applied. Monitoring of the optical image of the crystal selected for the Raman experiments at the microscope was concordant with the results of PLTM, with observation of changes in the morphology of the crystal compatible with the solid-solid transition, including its color that changes from bright-burgundy to dark-burgundy. The Raman spectra obtained before and after the solid-solid transition are presented in Figure 10.

As seen in Figure 10, the Raman spectrum of polymorph-3 is clearly distinct from that of polymorphs 1 and 2, in particular in the low frequency region. This spectral region is in general more sensitive to rearrangements of the intermolecular environment than the higher frequency spectroscopic regions, which are more related with the structure of individual molecules in the crystal. Nevertheless, also in the higher frequency region (above 1300 cm^{-1}) the Raman spectrum of polymorph-3 of ROY-ol is rather distinct from those of polymorphs 1 and 2 of the compound. Particularly noticeable are the intense bands at 99 and 60 cm^{-1} appearing in the spectrum of polymorph-3, which can act as marker-bands of this form. In addition, the most intense band of the Raman spectra of all polymorphs, which appear in the spectra of both polymorphs 1 and 2 at 816 cm^{-1} , is observed at 812 cm^{-1} in the case of polymorph-3.

ROY analogues

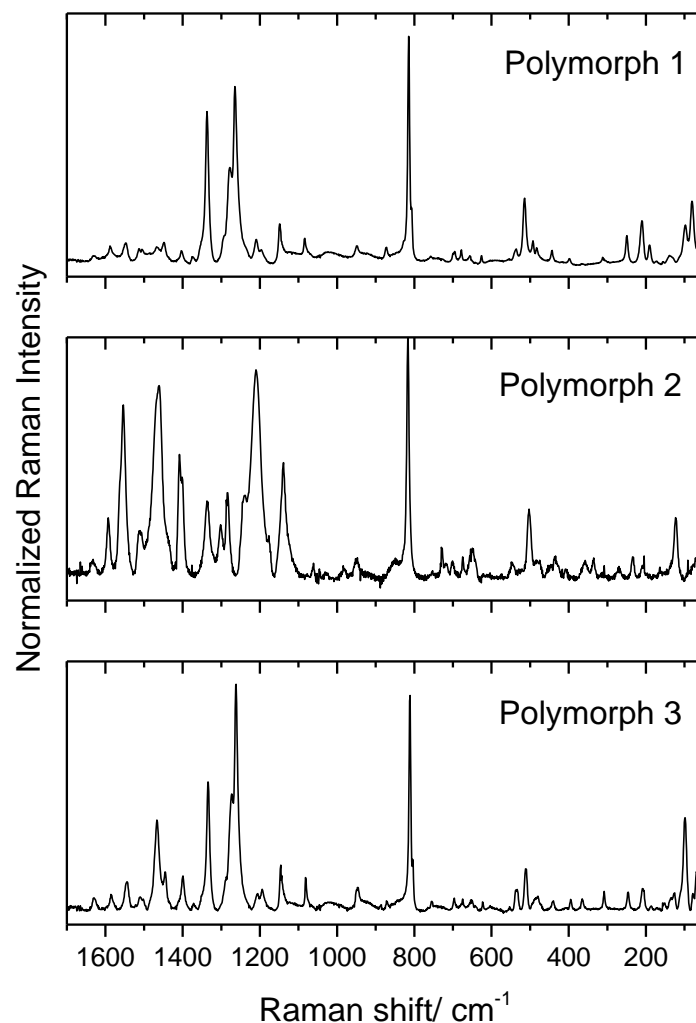


Figure 10 – Raman spectra of ROY-ol polymorphs 1, 2 and 3 in the 50-1700 cm^{-1} Raman shift range.

In some samples, optically isotropic material, amorphous ROY-ol, could be identified. Being isotropic, amorphous material was clearly in the images obtained using crossed polarizers (see Figure S12), where it is not distinguishable from the black background. In some PLTM experiments an interesting thermal behavior was observed. Figure 11 shows the heating of a crystal of polymorph-2 with a small amount of this amorphous material on it. As seen in this figure (see also PLTM video2 submitted as Supporting Information) crystallization of the isotropic material starts at approximately 80 °C. The formed crystalline material then melts at ca. 150 °C, which is a melting temperature that does not correspond to those of either polymorph-2 or polymorph-3. This crystalline phase is most likely not also polymorph-1, as in all experiments carried out on form 1, at the same scanning rate, a solid-solid transition to polymorph 3 was always observed, starting at ca. 100 °C. The existence of another ROY-ol polymorph (polymorph-4; also dark-burgundy) is then proposed. Unfortunately, further characterization of this polymorph was not yet possible, considering that its generation proved to be very difficult to control. Indeed, the formation of the amorphous phase (which was the precursor of

polymorph-4 in our experiments) from the melted compound is not possible because decomposition takes place immediately after melting, while the generation of amorphous material using the solvent evaporation method was found to be fortuitous and, when it is observed, it constitutes only a residual fraction of the obtained material.

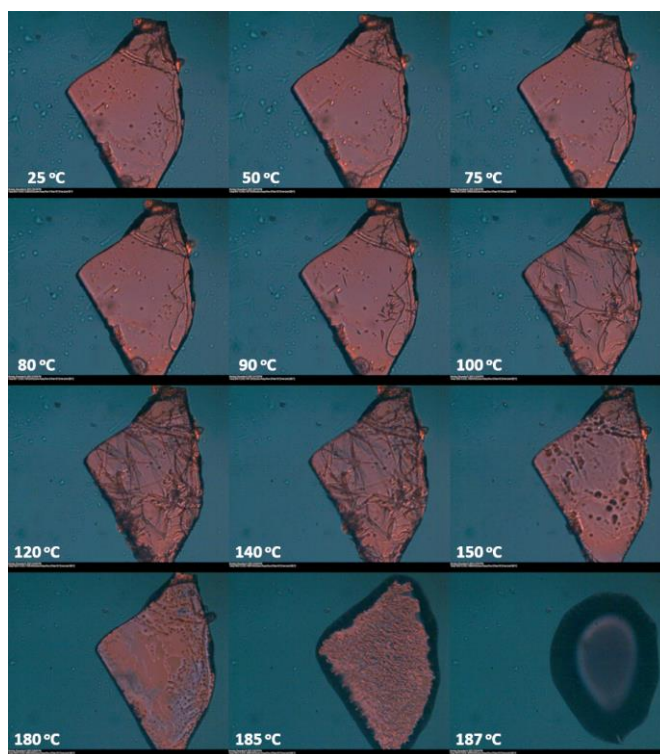


Figure 11 – PLTM images obtained along the heating of ROY-ol amorphous material on a crystal of polymorph-2 (heating rate: 10 °C min⁻¹). The PLTM video2, submitted as Supporting Information, shows the entire experiment.

3.4. DFT calculations for the isolated molecule (ROY-ol vs. AcROY vs. ROY): correlating the intramolecular potentials for internal rotation about the N–C_(thiophene) bond and polymorphism

As observed before for ROY, AcROY and other similar molecules bearing an NH bridging group (connecting two ring moieties) in the *ortho*-position to a nitro substituent in a phenyl ring,^{1,5-17} the low-energy conformers of the isolated ROY-ol molecule have an intramolecular H-bond established between the NH bridging group and the *ortho*-nitro group. This structural characteristic limits the conformational space of this type of molecules, and gives exceptional relevance to other internal degrees of conformational flexibility. A search on the DTF(B3LYP)/6-311++G(2d,p) potential energy surface of ROY-ol allowed to identify four distinct low-energy conformers of the molecule, which are represented in Figure 12. Conformer A is the most stable one, followed by conformers B, C and D, which are predicted to be 1.4, 3.5 and 4.3 kJ mol⁻¹ higher in energy than A, respectively. The conformers differ in the orientation of the OH substituent present in the nitrophenyl ring (which may exist in two

stable arrangements, pointing towards the nitro group – in A and B forms – or against this group – in C and D forms) and/or in the relative orientation of the two rings (with the cyano group pointing to the side of the nitro group – in B and D forms – or to the opposite direction – in A and C forms), and all conformers have a symmetry-equivalent form.

The C–N–C–S dihedral angle values in conformers A to D are, by this order, 126.2, 35.1, 129.8 and 33.9°. Interestingly, the highest energy conformer of the isolated molecule of ROY-ol (conformer D) is the one existing in both polymorphs 1 and 2 of the compound. In polymorph-1, the C–N–C–S dihedral angle is -31.6° , i.e., the conformation assumed by the molecule in the crystal is very much close to that of isolated conformer D. On the other hand, in polymorph-2, the C–N–C–S dihedral angle in the two different molecules in the asymmetric unit is $-6.7(5)^\circ$ and $7.9(5)^\circ$, i.e., in this crystal the molecules correspond to a strongly distorted conformer D where the two rings are almost coplanar.

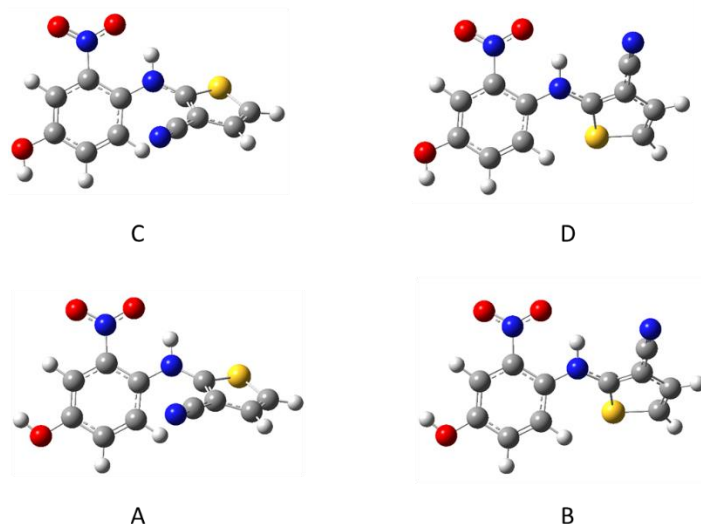


Figure 12 – Geometries of the four low-energy conformers of ROY-ol. Each of the represented structures has a symmetry-equivalent form.

Like in the previously studied analogue molecules, the most relevant torsional coordinate in terms of its impact on the optical properties of the ROY-ol molecule is precisely that defined the N–C_(thiophene) bond (θ in Scheme 1, related with the C–N–C–S dihedral angle), which determines in large amount the extension of the π -electron delocalization in the molecule. When the two rings are co-planar, the π -electron delocalization reaches its maxima and the energy gap between the ground and excited electronic states reaches its minimum values. In the case of ROY and the known ROY derivatives,^{1,6-17} the general rule is that for small angles between the two ring planes, the maximum of absorption appears in the green region of the electromagnetic spectrum, so that the compound appears in tones of red/burgundy, while large angles between the ring planes lead to shift the absorption maximum to the blue, and the compound appears in yellow. For intermediate values of the angle between the two ring

planes, the compound is perceived as orange. The N–C_(thiophene) torsional coordinate is also known to be quite flexible, with low energy barriers separating the conformers that differ in the spatial arrangement about this bond. For example, in the case of ROY-ol, the lowest energy barrier separating conformers A and B has a height of only 2.9 kJ mol⁻¹ when taken in the A→B direction (1.5 kJ mol⁻¹ in the opposite direction), according to the performed DFT calculations, and that between conformers C and D is similar (3.0 kJ mol⁻¹ in the C→D direction; 2.2 kJ mol⁻¹ in the reverse direction). The low energy barriers, together with the small energy differences between the conformers, justify the fact that different conformers have been found to be present as structural units of the different polymorphs of this type of compounds, noteworthy in the case of the parent ROY compound.^{1,6-12}

The barrier to internal rotation of the OH group of ROY-ol, which leads to interconversion between the pairs of conformers A and C, on the one side, and B and D, on the other side, are comparatively higher than those associated with the rotamerization about the N–C_(thiophene) bond. Nevertheless, they are still small in absolute terms, with the A→C barrier predicted by the calculations being 14.1 kJ mol⁻¹ (10.7 kJ mol⁻¹ in the reverse direction) and that associated with the B→D transformation being 12.2 kJ mol⁻¹ (9.3 kJ mol⁻¹ in the opposite direction).

Figure 13 shows the calculated potential energy profile for internal rotation around the N–C_(thiophene) bond in the isolated molecule of ROY-ol, as defined by the C–N–C–S dihedral angle. The corresponding potential energy profiles for ROY and AcROY have also been calculated and are plotted in the figure, for comparison. Symbols representing the different polymorphs of the three compounds are superposed to the corresponding energy curves, with their color representing the color of the polymorph (classified in a simple way only as red, orange and yellow). The symbols are placed at the values of the C–N–C–S dihedral angle observed in the crystals (see Table S3, in the Supporting Information; for crystals with more than one molecule in the asymmetric unit, as in the case of polymorph-2 of ROY-ol, the value of the dihedral angle in the different molecules is indicated, so that the symbol corresponding to these polymorphs appears repeated in the plot).

Before comparing the results for the 3 compounds, a brief explanation of the general profile of the energy curves is required. A detailed analysis of the curve shown in the figure for AcROY can be found in our recent publication on that compound,¹⁵ and that analysis apply equally to the energy profiles for ROY and ROY-ol. The first thing to highlight is that the precise shape of the curve in the region corresponding to values of the C–N–C–S dihedral angle around 180° depends on the direction of the performed scan. Around this value of the dihedral angle, repulsion between the rings is maximal due to the close proximity of the cyano substituent of the thiophene ring and the closely located *meta*-hydrogen atom of the nitrophenyl ring. In the scans shown in Figure 13, the scanning direction was performed anti-clockwise, as indicated in the figure, starting at the geometry of conformer D in the case of ROY-ol or the related conformer of the other two molecules. After crossing the D→C energy barrier, when the dihedral angle approaches 180°, the energy increases strongly due to the above mention

repulsive interaction. In fact, in this region, the scan conducts to geometries which are highly strained, so that at a certain point (when θ is ca. -150°) inversion at the bridging nitrogen atom takes place, leading to an abrupt decrease in energy, while bringing the molecule to the potential energy well C', which corresponds to the symmetry-equivalent form of conformer C. Then, the conversions C' \rightarrow D' and D' \rightarrow D, both involving crossing of low energy barriers, take place.

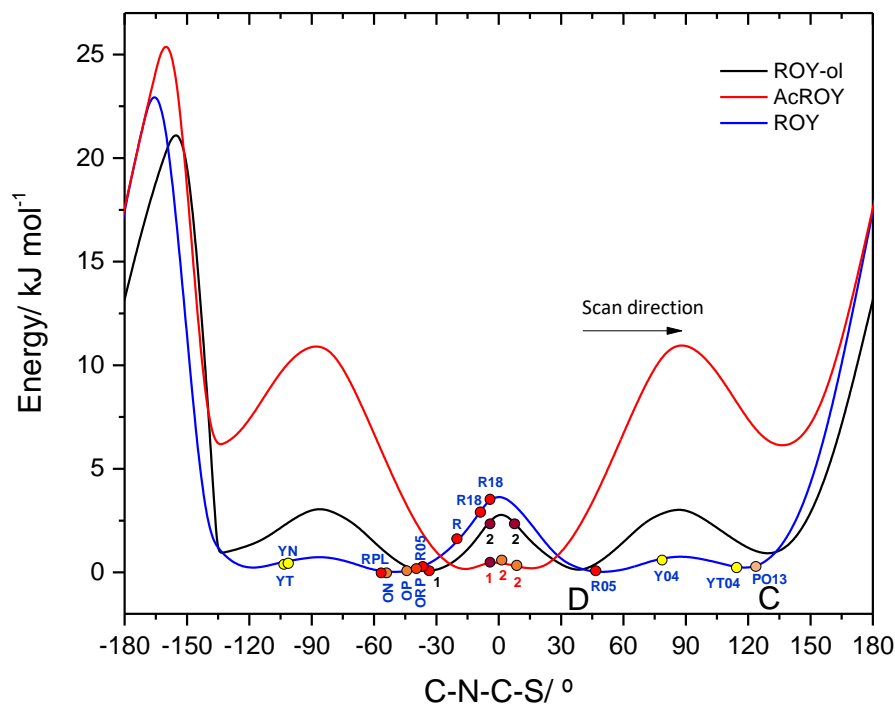


Figure 13 – DFT calculated potential energy profiles (gas phase) associated with the internal rotation θ , as defined by the dihedral angle C–N–C–S, for ROY-ol, AcROY and ROY compounds, and corresponding dihedral angles observed experimentally for the different polymorphs (indicated by the circles, colored according to the color of the polymorph). See text for details. In the case of ROY polymorphs YN, YT, YT04 and PO13, whose C–N–C–S dihedral angle is larger than 90° , the angles between the planes of the ring correspond to the absolute value of the difference between 180° and the value of the dihedral angle, i.e., 76.0 , 75.3 , 67.2 and 57.9° , the latter value thus being similar to those found for the remaining orange polymorphs of ROY. The exceptions to the “color vs. angle between the ring planes” general rule are only the RPL red polymorph of ROY, whose angle stays in the range of those appearing in the orange polymorphs of the compound, and the orange polymorph-2 of AcROY, whose angle stays in the range observed for red/burgundy polymorphs.

As it can be seen in Figure 13, the scan profiles of the three compounds are, as expected, similar. However, it is interesting to note that the flatness of the potential energy profiles in the relevant potential energy region, defined by values of the C–N–S–C dihedral angle ranging from about -120° to $+120^\circ$, correlates with the number of polymorphs identified for the three compounds hitherto. According to the performed calculations, the profile for ROY is that exhibiting the lowest energy barriers in the relevant potential energy region, this compound having the largest number of known polymorphs, while ROY-ol, with 4 different polymorphs reported in the present study, has intermediate energy barriers, and AcROY, with only two polymorphs discovered until now, has the potential energy curve with the

highest barriers among the three compounds. This correlation between the relative flatness of the potential energy profiles in the three compounds and the number of polymorphs discovered for each one seems to be significant, because it can be expected that if less energy is required to adjust the structure of individual molecules to specific packing requirements the number of energy-accessible stable crystalline structures should tend to be larger. It shall be noticed that the exact form of potential energy profiles for the three considered molecules are still to be determined by using higher-level computational tools (or appropriate experimental techniques, if possible) and that our conclusions are based only on their general features, in particular the relative flatness of the potential for a C–N–S–C dihedral angle in the -120° to $+120^\circ$ region in the three molecules as mentioned above. Note also that in this potential energy surface region the energy profiles shown in Figure 13 are not influenced by the effects due to the scan procedure (that otherwise, as referred to above, affect the region in the vicinity of a C–N–S–C dihedral angle close to $\pm 180^\circ$).

Lower energy intrinsic torsional barriers may also be correlated with the accessibility of polymorphs where the structural molecular unit is composed by a different conformer. In accordance with this conclusion, and as depicted in Figure 13, among the three molecules now being compared, ROY exhibits 4 polymorphs formed by one conformer and 8 polymorphs formed by a second conformer, and AcROY 2 polymorphs formed by the same conformer. In the case of ROY-ol, both polymorphs 1 and 2 are composed by conformer D, but for polymorph-2 the molecule is strongly distorted compared to its geometry in the gas phase, as it has been highlighted above. Moreover, the conformer(s) present in polymorphs 3 and 4 is(are) not known, since the determination of the structure of these two polymorphs was not yet undertaken. In the case of polymorph-3, since it can be easily obtained from polymorph-1 without requiring a large amount of energy and also because it is formed in a process that does not require destruction of the crystals (as shown in the PLTM experiments described in Section 3.3), it can be expected that conformer D is also present in this polymorph (to be confirmed). On the other hand, no clues on the nature of the constituting conformer of polymorph-4 can be extracted from the experiments performed in our investigation, so that this stays as a completely open question to further investigation.

4. Conclusion

In this study, the color polymorphism in ROY-ol, a novel member of the ROY family of compounds, has been investigated. In total, four polymorphs were identified, with polymorph-1 being bright-burgundy and polymorphs 2, 3 and 4 dark-burgundy. The crystal structures of polymorphs 1 and 2 were determined by single crystal XRD, both forms being monoclinic, space group $P2_1/n$ ($n^\circ 14$), with $a = 7.867(2)$, $b = 13.046(3)$, $c = 11.519(4)$ Å, $\beta = 107.26(3)^\circ$, $V = 1129.0(6)$ Å³, $Z = 4$, $Z' = 1$ for

polymorph-1, and $a = 8.6557(7), 12.9351(12), 20.2404(18) \text{ \AA}$, $\beta = 90.806(4)$, $V = 2265.9(3) \text{ \AA}^3$, $Z = 8$, $Z' = 2$ for polymorph-2.

In the crystals, the molecular conformation of the molecules differs significantly, as well as the hydrogen bonding network. In the case of polymorph-1, the molecules exist in a conformation very closely resembling that of the conformer D predicted for the gas-phase, thus having a significant deviation from planarity, with the C–N–C–S dihedral angle being $-31.6(3)^\circ$ (similar to that of conformer D for the isolated molecule: $\pm 33.9^\circ$). In polymorph-1, the nitro group is also significantly tilted ($23.1(2)^\circ$) from the plane of the phenyl ring. On the other hand, in polymorph-2 both symmetry independent molecules are almost strictly planar, with the C–N–C–S dihedral angle being $-6.7(5)^\circ$ in one of the molecules and $7.9(5)^\circ$ in the other. The conformation of the molecules is still related to that of conformer D for the isolated molecule, but strongly disturbed due to intermolecular interactions.

In both polymorphs 1 and 2, a strong N–H \cdots O hydrogen bond between the cyano and hydroxyl groups of neighbor molecules exist, which play the major structural role in the crystal. Another common structural element to both polymorphs is the fact that one of the O atoms of the nitro group does not participate in the hydrogen bond network. However, the additional intermolecular interactions are distinct and result in markedly different tridimensional arrangements. Short contacts were found to be more abundant in polymorph-1, while the sum of the fractional areas assigned to the principal hydrogen-bond-related contacts (H \cdots O/O \cdots H, H \cdots N/N \cdots H and H \cdots S/S \cdots H) in the Hirshfeld analysis (d_{norm} maps on the Hirshfeld surface) suggest that H-bonding interactions are globally more relevant in the packing of polymorph-2 than in polymorph-1. Polymorphs 1 and 2 were also characterized vibrationally by infrared and Raman spectroscopies, supported by fully-periodic density functional theory (DFT) calculations, which allowed for spectra assignment. Marker-bands for fast identification of the polymorphs were proposed.

The performed thermal analysis studies, undertaken by DSC, PLTM, and temperature-variation Raman spectroscopy, allowed to identify one additional polymorph of ROY-ol (polymorph 3). Polymorph-3 is formed upon heating of polymorph-1, *via* a solid-solid, low-enthalpy, transition that starts at ca. 100 °C and is completed at around 135 °C, at a 10 °C min $^{-1}$ scanning rate. Raman marker-bands for fast spectroscopic identification of this polymorph were also offered. An additional polymorphic form, polymorph-4, is proposed, which melts at about 150 °C, and was obtained upon recrystallization of the amorphous material upon heating (at about 80 °C).

Investigation of the conformational space of the isolated ROY-ol molecule within the DFT framework (together with similar calculations on ROY and AcROY) allowed to establish a “color of the polymorph vs. angle between the ring planes” empirical rule, while the global profile of the potential energy curves related with the C–N–C–S torsional coordinate in the molecules belonging to ROY family were also correlated with the trend of the compound to form polymorphs, the more flat the

torsional potential in the relevant potential energy region, defined by values of the C–N–S–C dihedral angle ranging from about -120° to $+120^\circ$, the higher the number of easily accessible polymorphs.

As a whole, in this study, a detailed description of the color polymorphism exhibited by ROY-ol has been performed, which is an additional contribution to the understanding of this phenomenon, in particular in what concerns to the captivating ROY family of compounds.

Supporting Information

Figures S1-S6, with the ^1H and ^{13}C NMR and IR spectra of 4-benzyloxy-1-fluoro-2-nitrobenzene, 2-((4-benzyloxy-2-nitrophenyl)amino)thiophene-3-carbonitrile and ROY-ol; Figure S7 with the visible absorption spectrum of polymorph 2 and the position of the color obtained from this spectrum in the CIE color map. Figures S8-S9, with the comparison between the DFT calculated IR and Raman spectra for polymorphs 1 and 2 and the corresponding experimental spectra; Figures S10-S12, with results of Hirshfeld analysis; Figure S13, with polarized-light and cross-polarized light photographs of a sample showing small crystals of polymorph-2 and an amount of amorphous ROY-ol; Tables S1-S2, with observed infrared and Raman bands of ROY-ol polymorphs 1 and 2 and their respective DFT calculated frequencies, with proposed assignments; Table S3, with C–N–C–S dihedral angles in the different polymorphs of ROY, AcROY and ROY-ol; Crystallographic data Tables with the structural X-Ray data for ROY-ol polymorphs 1 and 2; PLTM video, showing the transformation of polymorph-1 into polymorph-3; PLTM2 video, showing formation of polymorph-4; CIF files containing the supplementary crystallographic data were deposited at the Cambridge Crystallographic Data Centre, with references CCDC 2160983 (polymorph-1) and 2160984 (polymorph-2).

Acknowledgments

The CQC-IMS is financially supported by the Portuguese Science Foundation (“Fundação para a Ciência e a Tecnologia” - FCT) – Projects CQC UIDB/00313/2020 and UIDP/00313/2020, and CQE-IMS is funded by UIDB/00100/2020, UIDP/00100/2020 and LA/P/0056/2020 (National Funds). CFisUC is funded by FCT through the projects UIDB/04564/2020 and UIDP/04564/2020. The authors also want to acknowledge to Roberto Dovesi, Fabien Pascale, Michel Rerat and Matteo Tommasini for their help in solving some technical problems related to the periodic calculations. Access to instruments from Laser-Lab Coimbra, the Nuclear Magnetic Resonance Laboratory of CQC-IMS (www.nmrccc.uc.pt), and TAIL-UC (ICT_2009_02_012_1890) facilities (funded under QREN-Mais Centro), is gratefully acknowledged. B.A.N. also acknowledges FCT for the SFRH/BD/129852/2017 PhD Scholarship. V.A. acknowledges FCT for contract under CEECIND program - CEECIND/00283/2018.

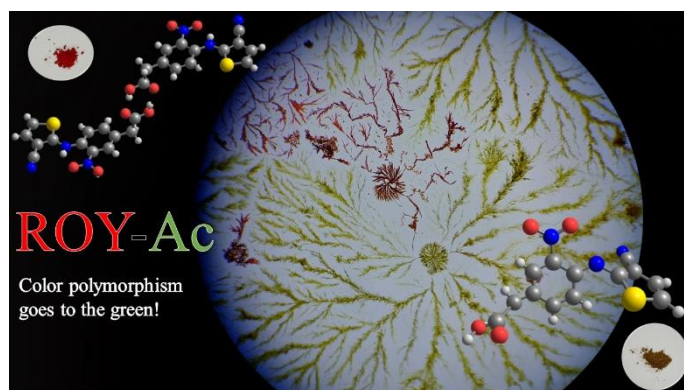
References

1. B. A. Nogueira, C. Castiglioni and R. Fausto, Color Polymorphism in Organic Crystals, *Commun. Chem.*, 2020, **3**, 1–12.
2. D. Gentili, M. Gazzano, M. Melucci, D. Jones and M. Cavallini, Polymorphism as an Additional Functionality of Materials for Technological Applications at Surfaces and Interfaces, *Chem. Soc. Rev.*, 2019, **48**, 2502–2517.
3. M. Cavallini, A. Calò, P. Stoliar, J. C. Kengne, S. Martins, F. C. Maticotta, F. Quist, G. Gbabode, N. Dumont, Y. H. Geerts and F. Biscarini, Lithographic Alignment of Discotic Liquid Crystals: A New Time-temperature Integrating Framework, *Adv. Mater.*, 2009, **21**, 4688–4691.
4. D. Gentili, M. Durso, C. Bettini, I. Manet, M. Gazzano, R. Capelli, M. Muccini, M. Melucci and M. Cavallini, A Time-temperature Integrator Based on Fluorescent and Polymorphic Compounds, *Sci. Rep.*, 2013, **3**, 2581
5. Z. Lin, et al., Polymorphism-dependent Fluorescence of Bisthiénylmaleimide With Different Responses to Mechanical Crushing and Grinding Pressure, *CrystEngComm*, 2014, **16**, 11018–11026.
6. G. A. Stephenson, T. B. Borchardt, S. R. Byrn, J. Bowyer, C. A. Bunnell, S. V. Snorek and L. Yu, Conformational and Color Polymorphism of 5-Methyl-2-[(2-nitrophenyl) amino]-3-thiophenecarbonitrile, *J. Pharm. Sci.*, 1995, **84**, 1385–1386.
7. L. Yu, G. A. Stephenson, C. A. Mitchell, C. A. Bunnell, S. V. Snorek, J. J. Bowyer, T. B. Borchardt, J. G. Stowell and S. R. Byrn, Thermochemistry and Conformational Polymorphism of a Hexamorphic Crystal System, *J. Am. Chem. Soc.*, 2000, **122**, 585–591.
8. S. Chen, I. A. Guzei and L. Yu, New Polymorphs of ROY and New Record for Coexisting Polymorphs of Solved Structures, *J. Am. Chem. Soc.*, 2005, **127**, 9881–9885.
9. M. Tan, A. G. Shtukenberg, S. Zhu, W. Xu, E. Dooryhee, S. M. Nichols, M. D. Ward, B. Kahr and Q. Zhu, ROY Revisited, Again: The Eighth Solved Structure, *Faraday Discuss.*, 2018, **211**, 477–491.
10. K. S. Gushurst, J. Nyman and S. X. M. Boerrigter, The PO13 Crystal Structure of ROY, *CrystEngComm*, 2019, **21**, 1363–1368.
11. A. R. Tyler, R. Ragbirsingh, C. J. McMonagle, P. G. Waddell, S. E. Heaps, J. W. Steed, P. Thaw, M. J. Hall and M. R. Probert, Encapsulated Nanodroplet Crystallization of Organic-Soluble Small Molecules, *Chem*, 2020, **6**, 1755–1765.
12. X. Li, X. Ou, H. Rong, S. Huang, J. Nyman, L. Yu and M. Lu, The Twelfth Solved Structure of ROY: Single Crystals of Y04 Grown from Melt Microdroplets, *Cryst. Growth Des.*, 2020, **20**, 7093–7097.
13. H. Li, J. G. Stowell, T. B. Borchardt and S. R. Byrn, Synthesis, Conformational Polymorphism, and Construction of a G-T Diagram of 2-[(2Nitrophenyl)amino]-3-thiophenecarbonitrile, *Cryst. Growth Des.*, 2006, **6**, 2469–2474.
14. X. He, U. J. Griesser, J. G. Stowell, T. B. Borchardt and S. R. Byrn, Conformational color Polymorphism and Control of Crystallization of 5-Methyl-2-[(4-methyl-2-nitrophenyl)amino]-3-thiophenecarbonitrile., *J. Pharm. Sci.*, 2001, **90**, 371–88.
15. K. M. Lutker, Z. P. Tolstyka and A. J. Matzger, Investigation of a Privileged Polymorphic Motif: a Dimeric ROY Derivative., *Cryst. Growth Des.*, 2008, **8**, 136–139.
16. A. Levesque, T. Maris and J. D. Wuest, ROY Reclaims Its Crown: New Ways to Increase Polymorphic Diversity, *J. Am. Chem. Soc.*, 2020, **142**, 11873–11883.
17. B. A. Nogueira, M. Carvalho, J. A. Paixão, M. E. S. Eusébio, S. M. M. Lopes, T. M. V. D. Pinho e Melo and R. Fausto, Portrayal of the Color Polymorphism in the 5-Acetyl-derivative of ROY, *CrystEngComm*, 2022, **24**, 1459–1474.
18. G. M. Sheldrick, Crystal Structure Refinement with SHELXL, *Acta Crystallogr., Sect. C: Struct. Chem.*, 2015, **71**, 3–8.
19. G. M. Sheldrick, SHELXT – Integrated Space-Group and Crystal-Structure Determination, *Acta Crystallogr., Sect. A*, 2015, **71**, 3–8.
20. M. J. Frisch, G. W. Trucks, H. B. Schlegel, G. E. Scuseria, M. A. Robb, J. R. Cheeseman,

- G. Scalmani, V. Barone, B. Mennucci, G. A. Petersson, H. Nakatsuji, M. Caricato, X. Li, H. P. Hratchian, A. F. Izmaylov, J. Bloino, G. Zheng, J. L. Sonnenberg, M. Hada, M. Ehara, K. Toyota, R. Fukuda, J. Hasegawa, M. Ishida, T. Nakajima, Y. Honda, O. Kitao, H. Nakai, T. Vreven, J. A. Montgomery, J. E. Peralta, F. Ogliaro, M. Bearpark, J. J. Heyd, E. Brothers, K. N. Kudin, V. N. Staroverov, R. Kobayashi, J. Normand, K. Raghavachari, P. G. Rendell, J. C. Burant, S. S. Iyengar, J. Tomasi, M. Cossi, N. Rega, J. M. Millam, M. Klene, J. E. Knox, J. B. Cross, V. Bakken, C. Adamo, J. Jaramillo, R. Gomperts, R. E. Stratmann, O. Yazyev, A. J. Austin, R. Cammi, C. Pomelli, J. W. Ochterski, R. L. Martin, K. Morokuma, V. G. Zakrzewski, G. A. Voth, P. Salvador, J. J. Dannenberg, S. Dapprich, A. D. Daniels, O. Farkas, J. B. Foresman, J. V. Ortiz, J. Cioslowski and D. J. Fox, Gaussian 09 (revision D.01),
21. A. D. Becke, Density-functional Exchange-energy Approximation with Correct Asymptotic Behavior, *Phys. Rev. A*, 1988, **38**, 3098–3100.
 22. C. Lee, W. Yang and R. G. Parr, Development of the Colle-Salvetti Correlation-energy Formula into a Functional of the Electron Density, *Phys. Rev. B*, 1988, **37**, 785–789.
 23. A. D. McLean and G. S. Chandler, Contracted Gaussian basis sets for molecular calculations. I. Second row atoms, Z=11–18, *J. Chem. Phys.*, 1980, **72**, 5639.
 24. R. Dovesi, A. Erba, R. Orlando, C. M. Zicovich-Wilson, B. Civalleri, L. Maschio, M. Rérat, S. Casassa, J. Baima, S. Salustro and B. Kirtman, Quantum-mechanical Condensed Matter Simulations with CRYSTAL, *Wiley Interdiscip. Rev. Comput. Mol. Sci.*, 2018, **8**, e1360.
 25. R. Dovesi, V. R. Saunders, C. Roetti, R. Orlando, C. M. Zicovich-Wilson, F. Pascale, B. Civalleri, K. Doll, N. M. Harrison, I. J. Bush, P. D’Arco, M. Llunell, M. Causà, Y. Noël, L. Maschio, A. Erba, M. Rerat and S. Casassa, CRYSTAL17 User’s Manual. 2018.
 26. C. Adamo and V. Barone, Toward Reliable Density Functional Methods Without Adjustable Parameters: The PBE0 Model, *J. Chem. Phys.*, 1999, **110**, 6158–6170.
 27. R. Ditchfield, W. J. Hehre, and J. A. Pople, Self-Consistent Molecular Orbital Methods. 9. Extended Gaussian-type basis for molecular-orbital studies of organic molecules, *J. Chem. Phys.*, 1971, **54**, 724–728.
 28. J. P. Merrick, D. Moran and L. Radom, An Evaluation of Harmonic Vibrational Frequency Scale Factors, *J. Phys. Chem. A*, 2007, **111**, 11683–11700.
 29. M. A. Spackman and P. G. Byrom, A Novel Definition of a Molecule in a Crystal, *Chem. Phys. Lett.*, 1997, **267**, 215–220.
 30. M. A. Spackman and D. Jayatilaka, Hirshfeld Surface Analysis, *CrystEngComm*, 2009, **11**, 19–32.
 31. S. K. Wolff, D. J. Grimwood, J. J. McKinnon, M. J. Turner, D. Jayatilaka and M. A. Spackman, Crystal Explorer17 (version 17.5), University of Western Australia, Crawley (AUS), 2017.
 32. J. J. McKinnon, A. S. Mitchell and M. A. Spackman, Hirshfeld Surfaces: A New Tool for Visualising and Exploring Molecular Crystals, *Chem. - A Eur. J.*, 1998, **4**, 2136–2141.
 33. M. A. Spackman and J. J. McKinnon, Fingerprinting Intermolecular Interactions in Molecular Crystals, *CrystEngComm*, 2002, **4**, 378–392.
 34. A. L. Rohl, M. Moret, W. Kaminsky, K. Claborn, J. J. McKinnon and B. Kahr, Hirshfeld Surfaces Identify Inadequacies in Computations of Intermolecular Interactions in Crystals: Pentamorphic 1,8-Dihydroxyanthraquinone, *Cryst. Growth Des.*, 2008, **8**, 4517–4525.
 35. A. Parkin, G. Barr, W. Dong, C. J. Gilmore, D. Jayatilaka, J. J. McKinnon, M. A. Spackman and C. C. Wilson, Comparing Entire Crystal Structures: Structural Genetic Fingerprinting, *CrystEngComm*, 2007, **9**, 648–652.

4.3. ROY-CAM

This section consists of the manuscript entitled *The ROY family goes to the green! The red and green polymorphs of ROY-CAM*, which is ready for submission to publication.



Supporting Information:

Annex – Part 2

Authors: Bernardo A. Nogueira, Susana M. M. Lopes, M. Ermelinda S. Eusébio, Vânia André, Teresa Duarte, José A. Paixão, Teresa M. V. D. Pinho e Melo and Rui Fausto

Corresponding author: Bernardo A. Nogueira

Author contributions

B.A.N. and R.F. conceptualized the study. B.A.N. wrote a preliminary version of the manuscript and performed the theoretical studies as well as the vibrational spectroscopy and the thermal studies experimental work. R.F. took responsibility for supervision, analysed and interpreted the data and wrote the final version of the manuscript; S.M.M.L. and T.M.V.D.P.M. were responsible for the development of the synthetic route and its implementation; V.A., T.D and J.A.P performed the XRD studies and wrote the corresponding part of the manuscript. M.E.S.E. supervised the thermal experiments undertaken in this work.

Synopsis:

In this study, color polymorphism in ROY-CAM (2-(4-((3-cyanothiophen-2-yl)amino)-3-nitrophenyl)acetic acid), the third ROY analogue compound investigated in this Thesis, is described. Synthesized for the first time, this compound presents a carboxymethyl group in the same ring position where the aforementioned ROY-ol compound bears a hydroxyl group. Two color polymorphs of ROY-CAM were identified: one red and one green. This is the first time that a color polymorph which does not belong to the triad red-orange-yellow was identified for a member of the ROY family of compounds. A comprehensive study of the conformational landscape of the monomeric molecule is reported (obtained through quantum-chemical calculations), together with a detailed spectroscopic (IR and Raman) and thermal analysis characterization of the studied system.

The ROY family goes to the green!

The red and green polymorphs of ROY-CAM

Bernardo A. Nogueira,^{*,1} Susana M. M. Lopes,¹ M. Ermelinda S. Eusébio,¹
Vânia André,² Teresa Duarte,² J. A. Paixão,³ Teresa M. V. D. Pinho e Melo¹ and Rui Fausto¹

¹ *University of Coimbra, CQC-IMS, Department of Chemistry, P-3004-535 Coimbra, Portugal.*

² *Centro de Química Estrutural-IMS, Instituto Superior Técnico, Universidade de Lisboa, Av. Rovisco Pais, 1049-001 Lisboa, Portugal*

³ *University of Coimbra, CFisUC, Department of Physics, P-3004-516 Coimbra, Portugal.*

Abstract

Polymorphism has been the subject of many studies in the last decades, including a particular type of polymorphism where the colors exhibited by the polymorphs differ. However, only relatively limited/narrow differences in color were observed in color polymorphs of the same compound. Indeed, to this date, the most common cases of color polymorphism exhibit red, orange or yellow tones, as it is the case of the well-known ROY molecule (5-methyl-2-((2-nitrophenyl)amino)thiophene-3-carbonitrile), which is the compound with more polymorphs reported and structurally characterized hitherto. In this work, we report a new color polymorphic material derived from ROY, (2-(4-((3-cyanothiophen-2-yl)amino)-3-nitrophenyl)acetic acid; or ROY-CAM), which exhibits a red and a green polymorph. This is the first time a member of the ROY family of compounds exhibiting a green polymorph was observed. The isolated molecule of ROY-CAM has 11 low-energy conformers, which were accessed by DFT calculations, with two of these conformers being identified in the observed polymorphs of the compound: in the green polymorph, the most stable conformer exists, while the red polymorph is composed of molecules assuming a conformation similar to that of the third most stable conformer. In the latter polymorph, the intramolecularly disfavored conformation assumed by the molecules is stabilized in the crystal lattice through interactions between carboxylic acid groups of neighboring molecules, resulting in dimeric units formed between pairs of the two distinct molecules that constitute the asymmetric unit of the crystal. The two identified polymorphs were characterized vibrationally (by both IR and Raman spectroscopies), and a thermal study is also presented (based on DSC, PLTM and TGA measurements).

Keywords: color polymorphism, ROY-CAM, ROY, red and green polymorphs, crystal structure, DFT calculations

* Corresponding author e-mail: ban@qui.uc.pt

1. Introduction

Polymorphism, whose term was firstly coined by McCrone,¹ is now commonly described as the ability of certain compounds to exist in more than one crystallographic form that have different physical, chemical and mechanical properties due to the different molecular arrangements and intermolecular interactions presented in the different crystals.^{2,3} Although the first polymorphic systems have been described as early as the 1800s, following the discovery of different crystals of the same phosphate salts by Mitscherlich,⁴ the relevance of these systems only reached the contemporary importance in the second half of the 20th century.⁵ Currently, apart from its importance in fundamental research, polymorphism is a key aspect in many industries, such as pharmaceutical, agrochemical, of pigments and dyes, and of energetic materials, for example.^{2,6,7} Despite the numerous studies in this field worldwide, the processes that give rise to the different crystals and the ability of the compounds to originate different polymorphs are still poorly understood, making the constant investigation on this domain one of the most important topics in solid-state chemistry.⁶⁻¹²

One of the properties that can vary in the different polymorphs of the same substance is the color they exhibit,¹³ although the variation in color is rather uncommon in the case of organic molecular crystals. Up to now, only a few families of organic compounds have been shown to exhibit polymorphs of different color, the most prominent one being the ROY family of compounds. The parent compound of this family is 5-methyl-2-((2-nitrophenyl)amino)thiophene-3-carbonitrile, whose acronym ROY derives from the Red, Orange and Yellow colors of its polymorphs. Presently, ROY is the compound possessing the largest number of identified and structurally characterized polymorphs, with a total number of twelve.¹⁴⁻²⁴

Color polymorphism results from different electronic properties of the molecules of the compound in the different crystalline phases, which results mostly from different intermolecular interactions in the crystals between molecules exhibiting the same conformational state (packing polymorphism) or due to the presence of distinct conformers in the different crystals (conformational polymorphism).¹³ Compounds may exhibit both conformational and packing polymorphism, with ROY being a paradigmatic example of a substance that exhibits the two types of polymorphism.¹⁶⁻²⁶

In our research group, we have been developing a research program on ROY derivatives,^{25,26} and other organic compounds presenting color polymorphism.^{13,27,28} New compounds have been synthesized and studied using a multidisciplinary approach, which involves the concerted use of spectroscopic, diffraction, thermal and computational methods, in the latter case including contemporary fully-periodic quantum chemical calculations on the crystals (in addition to the theoretical study of the conformational landscapes of the isolated molecules).

One common feature of the different color polymorphs of the compounds belonging to the ROY family investigated until now (that is shared with the other families of organic molecules known to

exhibit color polymorphs)¹⁵ is the range of colors exhibited by their different polymorphs, which has been restricted to the Red-Orange-Yellow triad. In this article, we report the fascinating case of a new ROY derivative for which two different polymorphs could be obtained and characterized, one exhibiting the traditional red color, and the second showing a green color. This is the first report on a member of the ROY family of compounds showing a green polymorph.

The new ROY derivative, 2-(4-((3-cyanothiophen-2-yl)amino)-3-nitrophenyl)acetic acid (or simply ROY-CAM) was synthesized by the nucleophilic aromatic substitution reaction between 2-(4-fluoro-3-nitrophenyl)acetic acid and 2-aminothiophene-3-carbonitrile, and the subsequent polymorph screening was carried out. As shown below, ROY-CAM is a typical case of conformational polymorphism with a red and, notoriously, a green polymorph, but the molecular packing in the two polymorphs is also substantially distinct. The thermal behavior of the two materials was also found to differ considerably. In the last section of this article, results of DFT calculations undertaken for the isolated ROY-CAM molecule are presented, and relevant features of the determined conformational landscape of the molecule are used to help understanding the colors exhibited by the discovered polymorphs of the compound.

2. Materials and Methods

Computational details

The computational calculations performed to investigate the conformational space of the studied compound were carried out within the density functional theory (DFT) framework, using the Gaussian 09 program (Revision A.02).²⁹ The three-parameter B3LYP density functional, which includes the Becke's gradient exchange correction³⁰ and the Lee, Yang and Parr correlation functional,³¹ together with the 6-311++G(2d,p) basis set³² were employed in the calculations.

The analysis of molecular crystal structures based on Hirshfeld surfaces was performed using CrystalExplorer 17.5,³³ with the structure input files of the two polymorphs (in CIF format). The results were summarized in the form of maps of the normalized contact distances, d_{norm} , to the calculated Hirshfeld surfaces, and the respective 2D-fingerprint plots. d_{norm} is calculated from the distances of a given point of the surface to the nearest atom outside, d_e , and inside, d_i , the surface, as $d_{norm} = \frac{d_i - r_i^{vdW}}{r_i^{vdW}} + \frac{d_e - r_e^{vdW}}{r_e^{vdW}}$, (where r_i^{vdW} are the van der Waals radii), allowing the identification of the most important intermolecular contacts.^{34,35} The 2D-fingerprint plots are used to condense the information about the different types of contacts and enables to access their relative importance.³⁶⁻³⁸

Synthesis

The studied compound was synthesized as described in Results and Discussion's Synthesis Section and characterized by nuclear magnetic resonance (NMR; in DMSO- d_6) and infrared (IR)

spectroscopies, high-resolution mass spectrometry (HRMS) and melting point determination. The ^1H - and ^{13}C -NMR spectra (Figure S1) were recorded on a Bruker Avance III instrument, operating at 400 MHz and at 100 MHz, respectively. The IR spectrum (Figure S2) was recorded on an Agilent Cary 630 Fourier transform IR (FTIR) spectrometer, in the attenuated total reflection (ATR) mode, using a Smart Orbit ATR diamond-based cell. The HRMS experiments were carried out using the electrospray ionization (ESI) method on an Orbitrap q-Exactive Focus mass spectrometer. Melting point (uncorrected) was determined in an open glass capillary.

Polymorph screening

The polymorph screening was done by the room-temperature evaporation/recrystallization (10-25 mg) method, using different solvents (4-10 mL, depending on the solubility).

Vibrational spectroscopy

The IR-ATR spectra of the polymorphs were collected in the wavenumber region of 400-4000 cm^{-1} (spectral resolution: 1 cm^{-1} ; 512 accumulations) using a Thermo Scientific FTIR Nicolet iS5 spectrometer, with an iD7 ATR accessory (angle of incidence of 45° into a diamond crystal).

Raman spectra were obtained in a Raman Horiba LabRam HR Evolution system, with excitation at $\lambda = 532$ nm. The spot diameter of the laser was approximately 1 μm , which was focused on the sample through a $50\times$ long-working-distance objective. A laser power of ~ 0.05 mW (at the sample) was used in order to prevent photodegradation of the compound. The final spectra were the average of 1000 accumulations of individual spectra collected during 1 second, with the spectral resolution of 0.5 cm^{-1} . The calibration of the system was performed using as reference the silicon crystal Raman peak at 520.5 cm^{-1} .

Single crystal X-ray diffraction

In the single crystal X-ray diffraction studies, crystals of the ROY-CAM polymorphs were mounted with Fomblin[®] in a cryoloop. Data were collected on a Bruker AXS-KAPPA APEX II diffractometer with graphite-monochromated radiation (Mo K_α , $\lambda = 0.71073$ Å) at 293 K. The X-ray generator was operated at 50 kV and 30 mA and the X-ray data collection was monitored using the APEX2³⁹ program. All data were corrected for Lorentzian, polarization and absorption effects using the SAINT and SADABS programs.³⁹ SHELXT 2014/4⁴⁰ was used for structure determination and SHELXL 2014/7⁴⁰ for full matrix least-squares refinement on F^2 . These programs are included in the package of the program WINGX-Version 2014.1.⁴¹ Non-hydrogen atoms were refined anisotropically. A full-matrix least-squares refinement was used for the non-hydrogen atoms with anisotropic thermal parameters. All the hydrogen atoms were inserted in idealized positions and allowed to refine riding in the parent carbon atom.

Thermal analysis

The differential scanning calorimetry (DSC) experiments were carried out in a Perkin Elmer Pyris-1 power compensation calorimeter, equipped with a 1:1 v/v ethylene glycol:water cooler at -25 °C and a 20 mL min^{-1} nitrogen purge flow. Hermetically sealed aluminium pans were used (sample weight between 1 and 2 mg), and an empty pan was used as reference. Temperature and enthalpy calibrations were performed using caffeine (Mettler Toledo calibration substance, ME 18872, $T_{\text{fus}} = 235.6 \pm 0.2$ °C) and indium (Perkin Elmer, 99.99%, $T_{\text{fus}} = 156.6$ °C; $\Delta_{\text{fus}}H_{\text{m}} = 3286 \pm 13 \text{ J mol}^{-1}$). The samples were scanned from 25 to 200 °C at a rate of 10 °C min^{-1} .

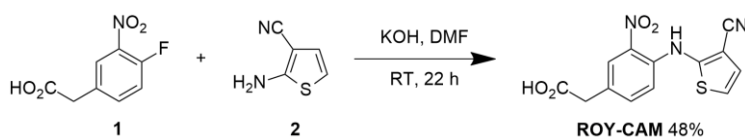
Polarized light thermal microscopy (PLTM) studies were conducted using a Linkam DSC600 hot stage, with a Leica DMRB microscope and a Sony CCD-IRIS/RGB video camera. The images ($50\times$ magnification) were collected, by the combined use of polarizers and wave compensator, in heating runs carried out at a scan rate of 10 °C min^{-1} and analyzed with the LinkSys software (Linkam).

The thermogravimetric analysis (TGA) was performed with a Perkin-Elmer STA 6000 apparatus, with a cooling unit stabilized at 15 °C and a nitrogen flow of 20 mL min^{-1} . The temperature and enthalpy calibrations were performed with indium (Perkin Elmer, 99.99%, $T_{\text{fus}} = 156.6$ °C; $\Delta_{\text{fus}}H_{\text{m}} = 3286 \pm 13 \text{ J mol}^{-1}$) and zinc (Perkin Elmer, reference material, $T_{\text{fus}} = 419.47$ °C). The samples were heated from 25 to 900 °C, at a temperature rate of 10 °C min^{-1} , in alumina crucibles.

3. Results and Discussion

3.1 Synthesis

ROY-CAM was synthesized by the nucleophilic aromatic substitution reaction between 2-(4-fluoro-3-nitrophenyl)acetic acid (**1**) and 2-aminothiophene-3-carbonitrile (**2**), as outlined in Scheme 1.



Scheme 1 – Synthesis of ROY-CAM.

A solution of 2-(4-fluoro-3-nitrophenyl)acetic acid (**1**) (4.03 mmol, 0.5 g) and 2-aminothiophene-3-carbonitrile (**2**) (4.03 mmol, 0.802 g) in dimethylformamide (DMF; 28 mL) were added dropwise to a suspension of KOH (8.06 mmol, 0.452 g) in DMF (12 mL). After the addition was complete, the reaction mixture was stirred at room temperature for 6 h and an additional portion of KOH (4.03 mmol, 0.226 g) was added, the reaction mixture being stirred for another 16 h. The reaction mixture was poured into a mixture of HCl 1M/ice and extracted with ethyl acetate (3×20 mL). The combined organic phases were washed with HCl 1M (2×30 mL) and brine (2×20 mL), dried and the solvent evaporated off. The compound was obtained as a red solid (1.95 mmol, 48%) by crystallization from ethanol, filtered and dried under vacuum. m.p.: $185.7\text{--}187.5$ °C. IR (ATR): ν 711, 813, 926, 1155,

1250, 1336, 1401, 1527, 1702, 2216 cm^{-1} . $^1\text{H-NMR}$ δ ($\text{DMSO-}d_6$): 3.65 (s, 2H), 7.09 (d, $J = 8.4$ Hz, 1H), 7.32 (d, $J = 6.0$ Hz, 1H), 7.45 (d, $J = 6.0$ Hz, 1H), 7.53 (d, $J = 8.4$ Hz, 1H), 8.07 (s, 1H), 9.70 (s, 1H), 12.48 (br s, 1H). $^{13}\text{C NMR}$ δ ($\text{DMSO-}d_6$): 102.5, 114.2, 117.8, 122.0, 126.5, 126.8, 127.7, 134.9, 137.6, 138.8, 153.8, 172.3. HRMS (ESI) m/z for $\text{C}_{13}\text{H}_{10}\text{N}_3\text{O}_4\text{S}$ $[\text{M}+\text{H}^+]$: calcd. 304.0386, found 304.0382.

3.2 Polymorph screening

Different polymorphs of ROY-CAM were searched by recrystallization of the compound from a series of solvents with different characteristics (polar protic and aprotic, and non-polar, with different dielectric constants ranging from 2.6 – dichloromethane, to 45.0 - DMSO) at different temperatures, between 0 °C and 25 °C, to modulate the solvent evaporation rate. Two different crystals were obtained, which were easily distinguished by their characteristic red and green colors (Figure 1). Very interestingly, the nature of the polymorph obtained in the different recrystallizations was found not to depend on the particular type of solvent used but, otherwise, on the time required by the solvent to evaporate. When the evaporation of the solvent was fast, the red polymorph was primarily obtained, whereas a long evaporation process was found to generally lead to generation of the green polymorph.



Figure 1 – Top panel: Crystals of Red (left) and green (right) polymorphs of ROY-CAM (10x amplified images) obtained from the polymorph screening experiments. Bottom panel: red and green bulk polymorph images.

3.3 Vibrational spectroscopy

The two polymorphs of ROY-CAM were characterized vibrationally by both infrared (ATR) and Raman spectroscopies. The spectra are presented in Figures 2 and 3 and are clearly distinguishable. In the IR spectra (Figure 2), the most prominent difference is observed in the $\nu(\text{CN})$ stretching region, where the green polymorph gives rise to a single band at 2225 cm^{-1} , while in the red polymorph originates a doublet at $2219/2207\text{ cm}^{-1}$. Other band-markers of the polymorphs are assigned to the $\nu(\text{C=O})$ stretching vibration, which is observed at 1700 and 1692 cm^{-1} in the green and red polymorph, respectively, to the two stretching vibrations and the rocking mode of the NO_2 group [$\nu_{\text{as}}(\text{NO}_2)$, $\nu_{\text{s}}(\text{NO}_2)$ and $\gamma(\text{NO}_2)$, observed in the green polymorph at 1573 , 1529 and 763 cm^{-1} and in the red polymorph at 1591 , 1525 and 757 cm^{-1} , respectively], to the carboxyl OH bending mode (green: 1224 cm^{-1} , vs. red: 1239 cm^{-1}), and to two deformational vibrations originated in the aromatic rings (observed at 1157 and 665 cm^{-1} in the green polymorph and at 1149 and 655 cm^{-1} in the red). These bands can act (separately or in group) as fast-identifiers of the ROY-CAM polymorphs.

In the Raman spectra (Figure 3), there are also significant differences in the vibrational signatures of the two polymorphs, especially in the regions between 1600 and 1200 cm^{-1} and below 200 cm^{-1} . The $\nu_{\text{as}}(\text{NO}_2)$ stretching vibration gives rise to a pair of bands in the spectra of both polymorphs, which are observed at 1578 and 1545 cm^{-1} in spectrum of the green polymorph and at 1599 and 1549 cm^{-1} in that of the red polymorph. In turn, the $\delta(\text{NH})$ and $\gamma(\text{NH})$ modes are assigned to the bands appearing at 1401 and $1282/1248\text{ cm}^{-1}$, in the case of the green polymorph, and at 1405 and $1254/1222\text{ cm}^{-1}$, for the red form, while two ring modes that are mostly located in the thiophene ring and in the nitrophenyl ring, respectively, give rise to bands at 1338 and 1096 cm^{-1} in the Raman spectrum of the green polymorph and at 1350 and 1101 cm^{-1} in that of the red polymorph. A tentative assignment for the observed IR and Raman bands of the two polymorphs of ROY-CAM is presented in Tables S1 and S2, and was made based on literature data for analogous compounds.^{25,26}

3.4 X-ray diffraction

Crystals for single crystal X-ray diffraction structure determination were obtained for the red polymorph and the green polymorph of ROY-CAM, which were deposited at the Cambridge Crystallographic Data Centre, with the references CCDC 2174469 (red polymorph) and CCDC 2177884 (green polymorph).

The obtained X-ray data showed that the red polymorph crystallizes in the monoclinic, centrosymmetric space group $P2_1/n$, with two symmetry independent molecules in the unit cell ($Z' = 2$; $Z = 8$), while the green polymorph is triclinic, crystallizing in the centrosymmetric $P\bar{1}$ space group, with one symmetry independent molecule in the unit cell ($Z' = 1$; $Z = 2$). A summary of the data-collection and structural refinement data is given in Table 1.

ROY analogues

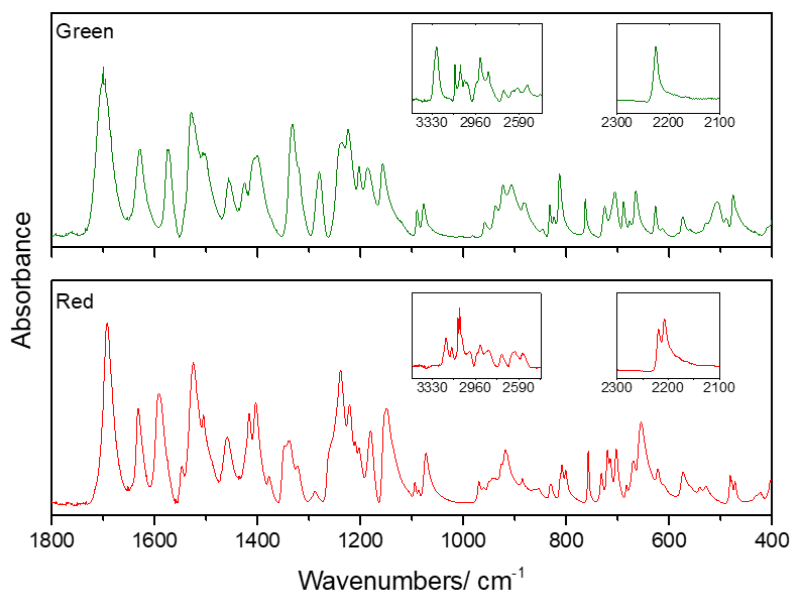


Figure 2 – IR-ATR spectra of ROY-CAM green (top) and red (bottom) polymorphs in the 3400-2400 and 2300-2100 and 1800-400 cm⁻¹ regions.

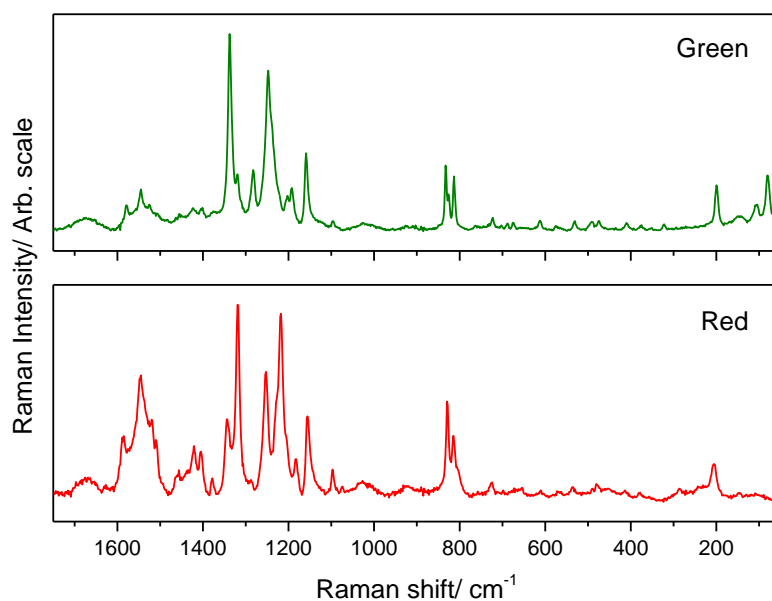


Figure 3 – Raman spectra of ROY-CAM green (top) and red (bottom) polymorphs in the 1750-50 cm⁻¹ region.

Bond lengths and valence angles of the ROY-CAM molecules in both polymorphs are unexceptional, but inspection of the dihedral and torsion angles (Table 2) shows that the conformation of the molecules differs significantly in the red and green polymorphs, being notorious that the dihedral angle between the two rings in the green polymorph ($65.0(2)^\circ$) is much larger than in either of the two symmetry independent molecules of the red polymorph ($4.4(1)^\circ$; $7.2(1)^\circ$). This is due to the rotational flexibility around the C1–N2 bond (see Figure 4 for atom numbering), with the rotation around N2–C6 being hindered by the presence of an intramolecular hydrogen bond between the amine N–H group

acting as donor and a close O atom of the nitro group, which is present in both polymorphs. The dihedral angle between the two rings is known to be a key factor for the determination of the color of the different polymorphs in ROY family members,^{13,25,26} and the significant difference in the value of this angle in the molecules constituting the two polymorphs of ROY-CAM can be also expected to play a major role in determining their remarkably different colors. Additionally, in the red polymorph the carboxylic group of both symmetry independent molecules are close to being orthogonal to the ring of the nitrophenyl group ($86.2(2)^\circ$; $88.6(2)^\circ$), while the correspondent angle in the molecule of the green polymorph is much smaller ($63.5(6)^\circ$), which shall also contribute to the steep color difference of the two ROY-CAM polymorphs. The distinct molecular conformations are enlightened in Figure 4.

Both polymorphs feature an extensive network of hydrogen bonds that contribute to the cohesive energy of the crystalline structures (Table 3). These hydrogen-bond networks are described in detail below. Here, we provide only a brief overall description of the hydrogen-bond interactions and how they impact on the distinct molecular packing observed in the red and green polymorphs of ROY-CAM.

In the red polymorph, the two symmetry independent molecules are strongly connected in pairs via a typical carboxylic cyclic $O-H\cdots O/O\cdots H-O$ bonding. Molecular packing is such that the molecules are laying in parallel layers where they are interconnected via weaker $C-H\cdots O$ and $C-H\cdots N$ hydrogen bonds, the connection between adjacent molecular layers being provided through the stronger hydrogen bond between the carboxylic groups (Figure 5). In the green polymorph, the dimeric motif connected via the cyclic carboxylic hydrogen bonding is still found, but the molecular packing is notoriously distinct and is no longer a layered one. Here, the bare carbonyl O atom of the carboxylic groups is involved, as acceptor, in an extra and weaker hydrogen bond of the $C-H\cdots O$ type, as depicted in Figure 6.

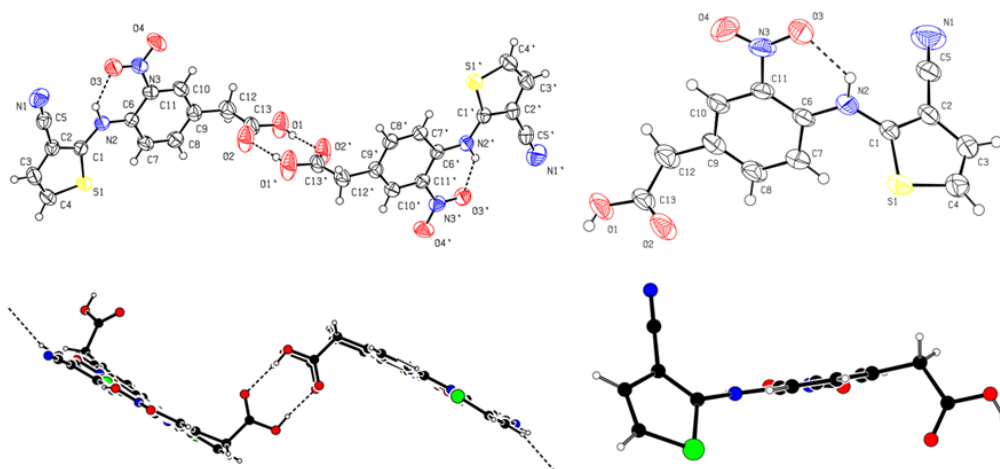


Figure 4 ORTEP plots depicting the anisotropic displacement ellipsoids drawn at the 50 % probability level and the atom numbering schemes for the red (left) and green (right) polymorphs of ROY-CAM. In the bottom panels, a profile view of the molecules is shown.

Table 1 – Summary of the single-crystal X-ray data collections and crystal structure refinements.

	Red polymorph C ₁₃ H ₉ N ₃ O ₄ S	Green Polymorph C ₁₃ H ₉ N ₃ O ₄ S
Chemical formula	C ₁₃ H ₉ N ₃ O ₄ S	C ₁₃ H ₉ N ₃ O ₄ S
Formula weight	303.29	303.29
Color, shape	red/needle	green/plate
Space group	<i>P</i> 2 ₁ / <i>n</i>	<i>P</i> -1
Temperature (K)	293 (2)	293(2)
Cell volume (Å ³)	2636.4(3)	662.0(18)
Crystal system	monoclinic	triclinic
<i>a</i> (Å)	4.9760(3)	4.1707(3)
<i>b</i> (Å)	25.8727(17)	6.9281(5)
<i>c</i> (Å)	20.5662(13)	22.9364(15)
<i>α</i> (deg)	90	89.355(3)
<i>β</i> (deg)	95.307(3)	92.345(3)
<i>γ</i> (deg)	90	91.290(3)
<i>Z</i> , <i>Z'</i>	8, 2	2, 1
<i>D</i> _c (Mg m ⁻³)	1.528	1.522
Radiation (Å) (graphite; monochromated)	0.71073	0.71073
Max. crystal dimensions (mm)	0.04×0.04×0.18	0.16×0.06×0.02
<i>θ</i> range (deg)	1.989 – 25.698	2.666 – 24.999
Range of <i>h</i> , <i>k</i> , <i>l</i>	-6,6;-31,31;-24,25	-4,4;-8,8;-27,27
Reflections measured/independent	39709 / 4983	6452 / 2120
Reflections observed (<i>I</i> > 2 <i>σ</i>)	3474	1511
Data/restraints/parameters	4983/0/381	2120/0/191
GOF	1.008	1.782
<i>R</i> ₁ (<i>I</i> > 2 <i>σ</i>)	0.0415	0.1360
<i>wR</i> ₂	0.1077	0.4369
Function minimized	Σ <i>w</i> (<i>F</i> _o ² - <i>S</i> <i>F</i> _c ²)	Σ <i>w</i> (<i>F</i> _o ² - <i>S</i> <i>F</i> _c ²)
Diff. density final max/min (e Å ⁻³)	0.276, -0.233	0.645, -0.749

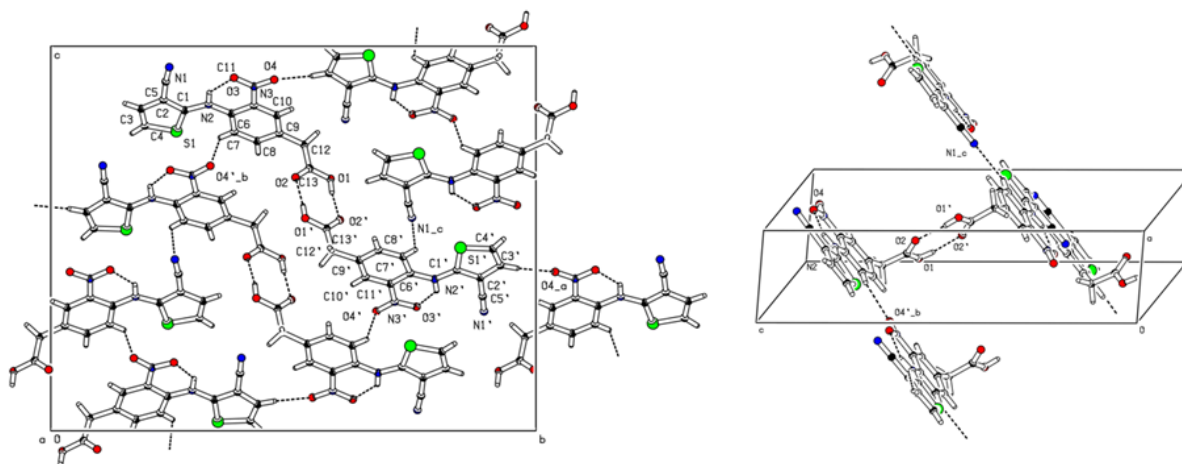


Figure 5 – Hydrogen-bonding network in the red polymorph of ROY-CAM showing the stacking of molecular planes joined via weak C–H···O and C–H···N hydrogen bonds. Molecules of adjacent planes are interconnected via the O–H···O hydrogen bonds involving the carboxylic groups. Left panel: projection of the structure along the reciprocal *a**-axis; right panel: perspective view of the structure showing the stacking of molecular planes. For clarity, not all molecules present in the unit cell are shown in the right panel.

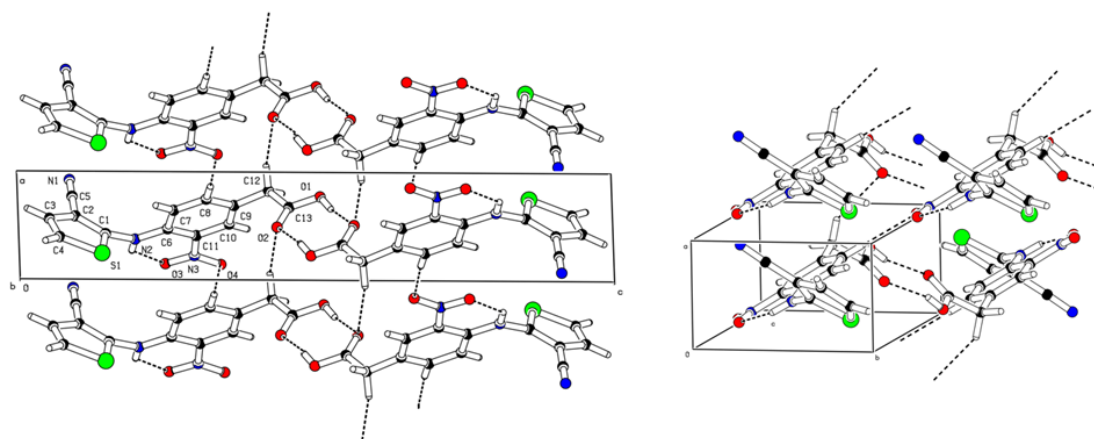


Figure 6 – Hydrogen-bonding network in the green polymorph of ROY-CAM showing the main hydrogen bond interactions. Left panel: projection of the structure along the reciprocal b^* -axis; right panel: perspective view of the structure showing the 3D nature of the hydrogen bond network. For clarity, not all molecules present in the unit cell are shown in the right panel.

Table 2 – Relevant dihedral and torsion angles ($^\circ$) for the red and green polymorphs of ROY-CAM.

Angle ($^\circ$)	<i>Red</i> (unprimed molecule)	<i>Red</i> (primed molecule)	<i>Green</i>
\angle (C1...S1)/(C6–C11)	4.43(14)	7.21(14)	65.0(2)
\angle (C6...C11)/N3O3O4	4.4(2)	7.66(17)	9.1(14)
\angle (C6...C11)/C13O1O2	86.2(2)	88.6(2)	63.5(6)
C6–N2–C1–C2	176.0(2)	–175.9(2)	120.4(10)
C11–C6–N2–C1	–176.4(2)	173.8(2)	179.1(8)
O3–N3–C11–C6	3.2(4)	–5.3(3)	7.9(13)
C8–C9–C12–C13	–83.7(3)	86.6(3)	72.3(12)
C9–C12–C13–O2	–3.8(4)	11.0(4)	–11.2(15)
O2–C13–O1–H1	4.98	0.03	15

Table 3 – Hydrogen bonds and short intermolecular contact distances and angles for ROY-CAM polymorphs.

<i>Red</i>				
D–H...A	D–H	H...A	\angle D–H...A	D–A
N2–H2...O3	0.860	1.907	137.18	2.604(2)
N2'–H2'...O3'	0.860	1.899	136.80	2.593(2)
O1–H1...O2'	0.820	1.833	169.90	2.644(3)
O1'–H1'...O2	0.820	1.814	173.59	2.631(3)
C7–H7...S1	0.930	2.379	135.57	3.112(3)
C7'–H7'...S1	0.930	2.422	134.24	3.143(2)
C7–H7...O4 ^{a)}	0.930	2.466	138.30	3.220(3)
C7'–H7'...N1 ^{b)}	0.930	2.512	130.55	3.196(3)
<i>Green</i>				
D–H...A	D–H	H...A	\angle D–H...A	D–A
N2–H2...O3	0.860	1.978	129.48	2.611(9)
O1–H1...O2 ^{c)}	0.820	1.958	162.48	2.751(9)
C7–H7...S1	0.930	2.802	120.93	3.376(8)
C12–H12...O2 ^{d)}	0.970	2.502	145.21	3.345(12)

a) $-x, -y + 1, -z + 1$; b) $-x + 5/2, y + 1/2, -z + 3/2$; c) $-x + 1, -y + 2, -z + 1$; d) $x + 1, y, z$

3.5 Thermal studies

In order to investigate the thermal behavior and stability relationship between the two polymorphs of ROY-CAM, DSC analyses were performed on samples of the individual polymorphs and also on a sample containing a mixture of the two forms. The DSC curves are presented in Figure 7.

According to the DSC experiments, the red polymorph melts at 183.9 ± 0.7 °C, with an enthalpy of fusion of 35.2 ± 2.1 kJ mol⁻¹, while the green polymorph melts at 190.4 ± 0.3 °C, with an enthalpy of fusion of 44.4 ± 0.7 kJ mol⁻¹. From the heat of fusion rule,⁴²⁻⁴⁴ the green polymorph is the stable polymorph and the red form is a metastable form. The DSC curve representing the heating of the mixture of the two polymorphs suggests that there is no other thermodynamic event apart from the melting of the two forms.

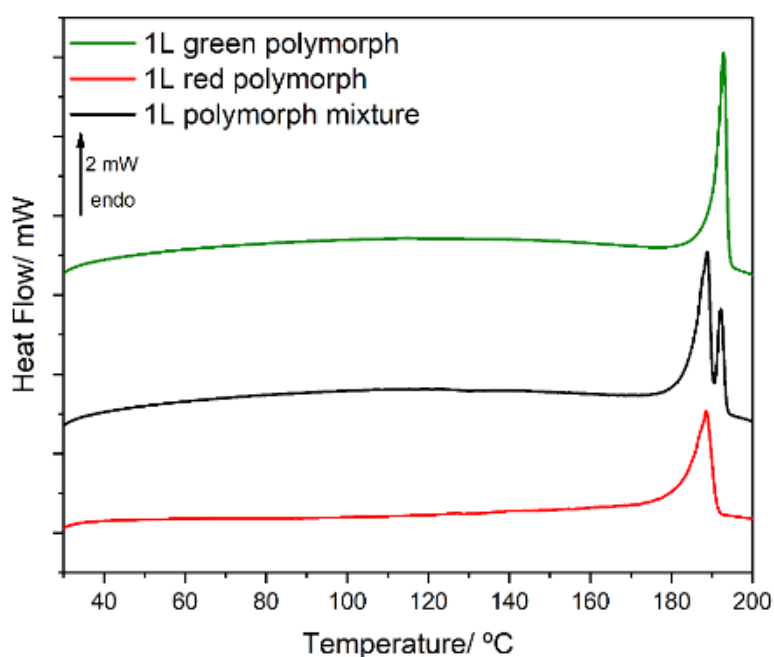


Figure 7 – DSC heating curves of ROY-CAM red and green polymorphs and of a sample containing both forms (heating rate: 10 °C min⁻¹; masses: 1.06 mg, red polymorph – recrystallized from acetic acid solution; 1.05 mg, green polymorph – recrystallized from ethyl acetate solution; 1.14 mg, total mass of the mixture – recrystallized from acetonitrile solution).

The heating of both polymorphs was also followed by PLTM. In agreement with the DSC data, in the case of the red polymorph (Figure 8; see also the PLTM video1 submitted as Supporting Information) only the melting was observed, which starts to be perceived at ca. 175 °C, being completed at ~190 °C. In turn, the images obtained during the heating of the green polymorph in the open PLTM pan (Figure 9) did not show evidence of any event until 150 °C, temperature at which a few bubbles started to be formed at the surface of the crystals (see also the PLTM video2 submitted as Supporting Information). These bubbles became more prominent in the temperature range 180-190 °C, immediately before the melting of the polymorph, which takes place between 192 °C and 195 °C.

ROY analogues

Interestingly, when the experiment was performed under nitrogen atmosphere (see PLTM video3 in the Supporting Information), the number of bubbles formed reduced significantly, suggesting that the thermal degradation of the green polymorph of ROY-CAM is hindered in the absence of atmospheric oxygen. To get some additional clues about this phenomenon, a thermogravimetric analysis of ROY-CAM was undertaken.



Figure 8 – PLTM images obtained from the heating of the red ROY-CAM polymorph – recrystallized from acetone solution (heating rate: 10 °C min^{-1}). These pictures were extracted from the PLTM video1 submitted as Supporting Information.

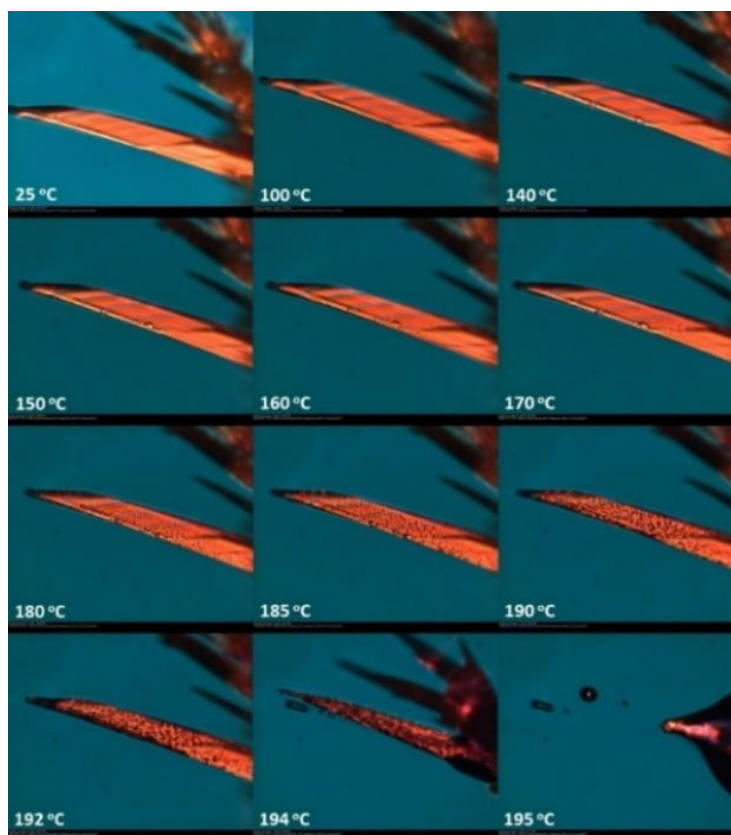


Figure 9 – PLTM images obtained from the heating of green ROY-CAM polymorph – recrystallized from acetonitrile solution (heating rate: 10 °C min^{-1}). These pictures were extracted from the PLTM video2 submitted as Supporting Information.

The TGA experiment confirmed that the sample starts to lose weight at a temperature below that of melting, as seen in Figure S3. Indeed, at a temperature increasing rate of $10\text{ }^{\circ}\text{C min}^{-1}$, around 1% of the sample mass was lost at the melting temperature. In the closed-pan DSC experiment, this event is expected to occur in a smaller extent than in the open pan TGA investigation. For this reason, this result is not in contradiction with the stability relationship between the two polymorphs established above.

Within the temperature range probed in the TGA experiments, the degradation of the sample takes place in two steps (with the second one still going on at the maximum temperature reached). The first degradation step starts at ca. $150\text{ }^{\circ}\text{C}$ (in accordance with the PLTM results) and ends at a temperature of ca. $270\text{ }^{\circ}\text{C}$, involving a mass reduction of about 15-18%, which is roughly the mass percentage of CO_2 in the ROY-CAM molecule. The results suggest ROY-CAM undergoes thermal decarboxylation before melting, which starts at a temperature of about $150\text{ }^{\circ}\text{C}$. The decarboxylation process also explains why the solid-state degradation of ROY-CAM is the first reported case of such event in ROY compound family, since ROY-CAM is the first ROY analogue compound to present a carboxylic group in its structure.

3.6 Hirshfeld surface analysis

The Hirshfeld surface analysis method, developed by Spackman and co-workers,^{34,45} was used to better characterize the dominant intermolecular interactions in the crystals of the ROY-CAM green and red polymorphs. Maps of the normalized contact distance on the calculated Hirshfeld surfaces (d_{norm}), which vary from -0.6260 to 1.2374 in the green polymorph and from -0.2056 to 1.3038 in the red polymorph, and the respective 2D-fingerprint plots are presented in the Figures S4-S7. As shown in Figure S4, the strongest intermolecular interactions (shortest contacts) between the lattice asymmetric unit of the green polymorph and the neighbor molecules are established via (i) the $\text{H}\cdots\text{O}/\text{O}\cdots\text{H}$ contact formed by the carboxylic acid moieties, making a dimer, (ii) the $\text{H}\cdots\text{O}/\text{O}\cdots\text{H}$ contact formed between the carboxylic acid carbonyl oxygen atom and a hydrogen atom of the CH_2 group of an adjacent molecule, and the reciprocal interaction with a second adjacent molecule, forming a chain in the a crystallographic axis, and (iii) the $\text{H}\cdots\text{O}/\text{O}\cdots\text{H}$ contact between one of the oxygen atoms of the nitro group and the hydrogen atom of the nitro ring in the para position. Conversely, for the red polymorph, the strongest intermolecular interactions of the crystal asymmetric unit and the neighbor molecules exist, for one of the independent molecules, via the $\text{H}\cdots\text{O}/\text{O}\cdots\text{H}$ contacts formed between the oxygen atoms of the nitrophenyl group and one hydrogen atom of the thiophene ring, on the one side, and one of the m -position hydrogen atoms of the nitro ring of the same adjacent molecule on the other side; for the other independent molecule an $\text{H}\cdots\text{O}/\text{O}\cdots\text{H}$ bifurcated contact is formed between only one of the oxygen atoms of the nitro group and two thiophene hydrogen atoms belonging to two different adjacent molecules, while the second oxygen atom from the nitro ring is involved in a short contact interaction with a sulfur

atom. Additionally, in the latter described independent molecule of the red polymorph, there is a further strong intermolecular N \cdots H interaction between the nitrogen atom of the cyanide group and one of the hydrogen atoms placed in the *m*-position relatively to the nitro group, while for the first described independent molecule, the reciprocal interaction takes place.

Table 4 – Fractional areas (in %) of the Hirshfeld surface assigned to the different intermolecular contacts in ROY-CAM green and red poly-morphs.

Intermolecular contact	Green Polymorph		Red Polymorph		
	Asymmetric unit ($Z' = 1$)	Asymmetric unit ($Z' = 2$)	Independent molecule 1	Independent molecule 2	Independent molecules Average
H \cdots O/O \cdots H	29.5	25.2	28.0	29.3	28.7
H \cdots H	14.0	19.9	18.9	18.9	18.9
H \cdots N/N \cdots H	13.8	11.9	11.9	10.9	11.4
H \cdots C/C \cdots H	13.4	12.4	12.1	11.8	12.0
C \cdots C	5.3	2.6	2.4	2.7	2.6
H \cdots S/S \cdots H	4.6	2.5	2.6	2.1	2.4
C \cdots N/N \cdots C	3.9	6.6	6.0	6.6	6.3
O \cdots O	3.7	0.7	0.9	0.5	0.7
C \cdots O/O \cdots C	3.2	8.4	8.1	7.9	8.0
C \cdots S/S \cdots C	3.1	2.8	2.5	2.8	2.7
N \cdots S/S \cdots N	2.4	1.6	1.6	1.4	1.5
O \cdots S/S \cdots O	2.0	3.7	3.5	3.6	3.6
N \cdots O/O \cdots N	1.2	1.4	1.4	1.3	1.4
N \cdots N	0.0	0.3	0.3	0.3	0.3
S \cdots S	0.0	0.0	0.0	0.0	0.0

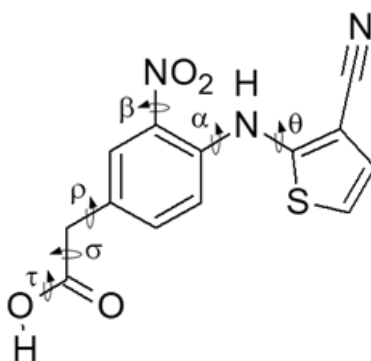
Table 4 presents the percentages of the Hirshfeld surfaces assigned to the different types of contacts (d_e vs. d_i), which are also shown graphically in the 2D-fingerprint plots (Figures S6-S7). Though H \cdots O/O \cdots H contacts are prevalent in both polymorphs, comprising 29.5 and 25.2 % of the total surface areas of the green and the red polymorphs, respectively, (considering the full asymmetric unit for the red polymorph; $Z' = 2$), this type of hydrogen bonding is clearly more important in the stabilization of the crystal lattice of the green polymorph than in the red one. Interestingly, in the case of the red polymorph, the comparison of the percentage of the H \cdots O/O \cdots H contacts obtained for the average of the two independent molecules (28.7%) and for the asymmetric unit (25.2%) confirms that the dimer between the two independent molecules, formed via the acetic acid substituent, is the main source of these contacts. Additionally, the referred difference also points out that this strong interaction between the two independent molecules is the main reason why the H \cdots O/O \cdots H contacts are weaker in the stabilization of the lattice network since the dimeric interaction reduces the potential of creating additional strong hydrogen bonds with other neighbor molecules.

The sum of the areas related to the principal hydrogen-bond intermolecular interactions (H \cdots O/O \cdots H, H \cdots N/N \cdots H and H \cdots S/S \cdots H) is 47.9% for the green polymorph and 42.5% (average values

for the two independent molecules) for the red polymorph, which suggests that H-bonding is significantly more relevant in the packing of the green polymorph, being in accordance with the monotropic relationship obtained from the thermal studies, where the green polymorph was found to be the stable crystal form.

3.7 DFT calculations on the ROY-CAM isolated molecule

The conformational landscape of the molecule of ROY-CAM was investigated at the DFT(B3LYP)/6-311++G(2d,p) level of theory. The molecule has 6 internal rotation axes that can *a priori* originate different conformers (Scheme 2). However, as found previously for ROY derivatives^{25,26} and also for other molecules with an amine group bridging two aromatic rings that is ortho to a nitrophenyl-substituent,^{13,27,28} all low energy conformers of the isolated molecule of ROY-CAM can be expected to have the characteristic stabilizing N–H··O intramolecular hydrogen bond, which was also found to be present in the structural units of its crystals. This H-bond locks the conformation around both C–N(O₂) and C–N(H) bonds, so that the internal rotation axes α and β in Scheme 2 become irrelevant in practical terms when considering the possible conformers of the molecule. In addition, the expected minimum energy conformations defined around the rotation axis τ , which defines the conformation within the carboxylic acid group, are those corresponding to the *cis* and *trans* carboxylic acid typical geometries, where the O=C–O–H dihedral angle is ca. 0 and 180°, respectively. It is well-known that the *cis* carboxylic acid geometry is intrinsically more stable than the *trans* form by ca. 20 kJ mol⁻¹.^{46,47} Hence, the conformationally relevant internal rotation axes in the ROY-CAM molecule become reduced to only 3, which are those designated by θ , ρ and σ in Scheme 2. A conformational search was then undertaken taking into account these 3 internal rotational degrees of freedom.



Scheme 2 – Internal rotation axes in the isolated molecule of ROY-CAM.

As it can be seen in Table 5, 11 pairs of symmetry-equivalent low-energy conformers bearing a *cis* carboxylic acid moiety were located on the potential energy surface of the ROY-CAM molecule, in which the θ angle assumes values around $\pm 60^\circ$ or $\pm 150^\circ$, and the two values assumed by ρ correspond

to geometries where the CH₂CO₂H substituent is nearly perpendicular to the phenyl ring (in the range ± 100 to $\pm 120^\circ$). Note that when the θ and ρ values have different signs, the cyano group and the acid acetic moiety face different directions regarding the main plane of the molecule, while for θ and ρ of the same sign these two groups are oriented to the same side of the main molecular plane.

Table 5 – Dihedral angle values and relative energies of the different ROY-CAM optimized conformers.^a

Conformer	Dihedral angles				Relative energies kJ mol ⁻¹
	θ C _{ph} -N-C-C	ρ C ^b -C-C-C(=O)	σ C-C-C=O	τ O=C-O-H	
1	146.8	-117.1	-17.1	-0.6	-
2	60.3	-116.4	-15.5	-0.6	0.27
3	150.0	117.7	18.0	0.6	0.79
4	147.0	113.5	78.0	-1.0	1.50
5	60.9	-114.2	-68.7	0.4	1.55
6	61.7	118.0	83.3	-1.7	2.16
7	67.9	120.4	25.9	0.7	2.88
8	59.8	-98.9	102.9	-1.4	2.90
9	146.3	-98.5	104.3	-1.4	2.95
10	146.8	95.9	-104.5	1.6	3.20
11	58.3	97.7	-105.6	2.5	3.25

^a For each conformer, a symmetry-equivalent form exists where the angles have the symmetrical value. ^b Carbon atom in the phenyl ring *ortho* to the nitro substituent.

For each geometric arrangement defined by the θ and ρ angles, the angle σ assumes either 2 or 3 different values that define minimum energy structures. Reduction of one unit in the number of minima results from steric repulsions between the thiophene ring and carboxylic acid group which take place for the θ and ρ angles characteristic of the most stable conformer of the molecule (around 150 and -120° , respectively; or, in the symmetry-equivalent form, ca. -150 and 120°). For θ and ρ angles around these values, the σ dihedral angle only assumes the values $\pm 17.1^\circ$ (in the most stable form **1** and its equivalent-by-symmetry form) and $\pm 104.3^\circ$ (in conformer **9** and its symmetry-equivalent structure). This can be clearly seen in Figure 10, which depicts the potential energy profile for internal rotation about the rotational axis σ , in keeping the θ and ρ angles around 150 and 120° , respectively. On the other hand, for the remaining combinations of values of θ and ρ , three different minima are observed along the σ coordinate (Table 5). As an example, the potential energy profile along the σ coordinate calculated for θ and ρ values $\sim 150^\circ$ and 118° , respectively, has minima for σ equal to 18.0° , 78.0° and 104.5° (in conformers **3**, **4** and **10**, respectively; Figure 10). The same happen for the triads formed by conformers **2**, **5** and **8**, on the one hand, and conformers **6**, **7** and **11**, on the other.

The 11 conformers of ROY-CAM are shown in Figure 11, while their relative energies are given in Table 5. It shall be highlighted that the energies of the conformers are very similar, with that of the less stable form shown in Table 5 and Figure 11 being only 3.25 kJ mol⁻¹ higher than that of the lowest energy form.

ROY analogues

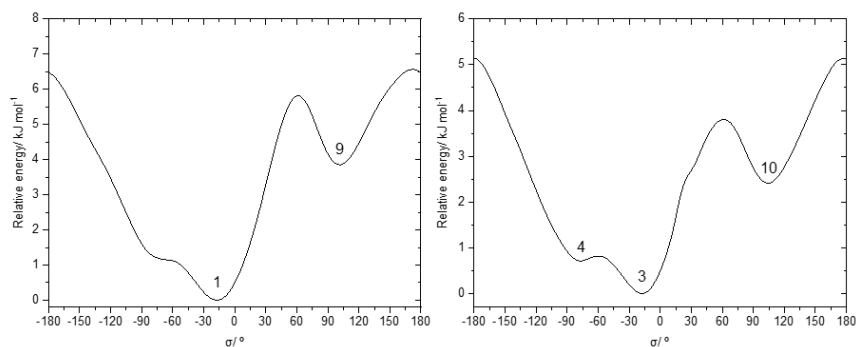


Figure 10 – B3LYP/6-311++G(2d,p) calculated relaxed potential energy scan corresponding to the rotation around the σ internal rotation axis (as defined by the C–C–C=O dihedral angle), keeping the θ and ρ angles around 150° and -120° , respectively (left), and around 150° and 120° , respectively (right). For conformers structures see Figure 11.

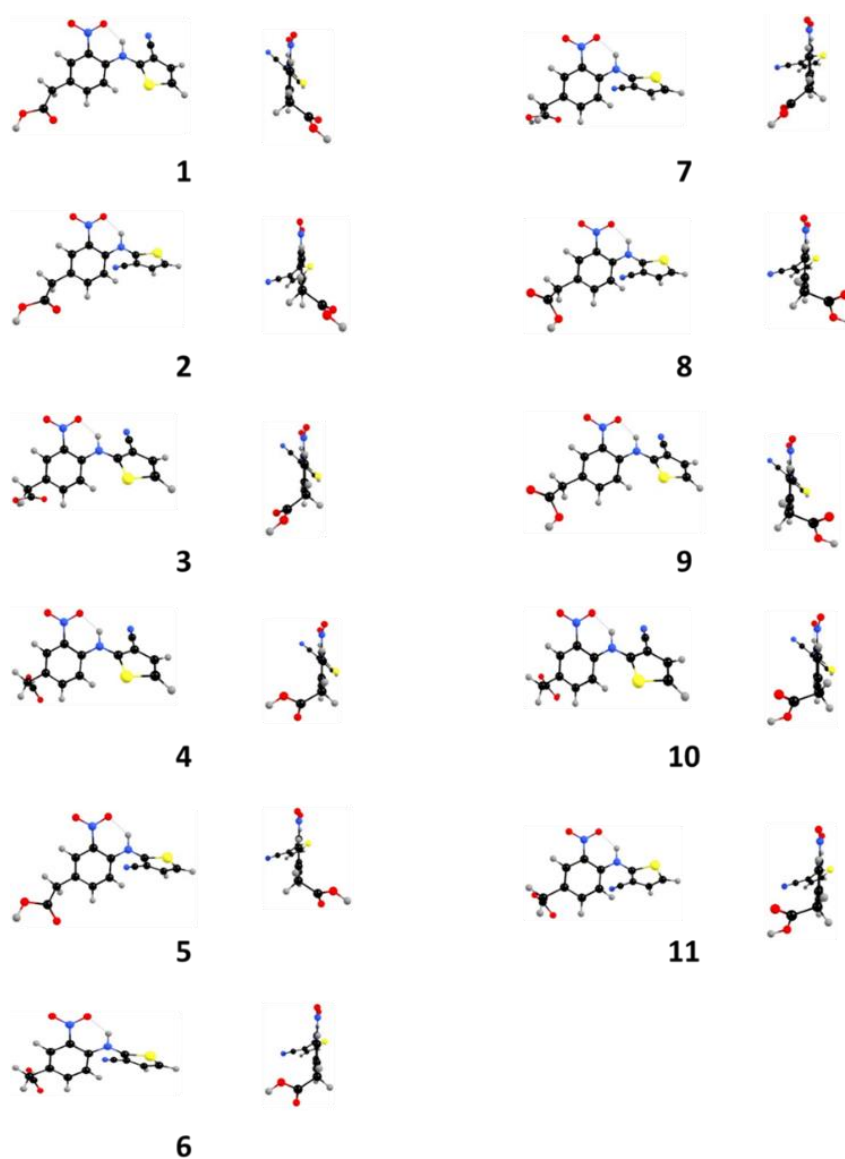


Figure 11 – Geometry representation of the 11 low-energy carboxylic acid *cis* conformers of ROY-CAM (two different perspectives). Carbon atoms are shown in black, hydrogens in grey, nitrogen in blue, oxygen in red, and sulphur in yellow.

The two different polymorphs of ROY-CAM present different conformers in their crystal lattice, being therefore conformational color polymorphs. The green polymorph is composed by ROY-CAM molecules assuming a conformation close to that predicted for the isolated molecule lowest energy conformer **1**, though the θ dihedral angle in the crystal is smaller than obtained for the isolated molecule ($120.4(10)^\circ$ vs. 146.8°). On the other hand, the two molecules present in the asymmetric unit of the red polymorph assume geometries resembling that of conformer **3** and its symmetry-equivalent form (**3'**), which have a calculated energy (as isolated molecule) 0.79 kJ mol^{-1} higher than that of the most stable conformer **1** (Table 3).

Interestingly, in the crystal, the θ dihedral angle is considerably larger ($176.0(2)^\circ$ and $175.9(2)^\circ$, for the two molecules in the asymmetric unit), than that calculated for the isolated molecule (150°), i.e., the crystal packing in the red polymorph makes the two rings of the ROY-CAM individual molecules to become considerably more planar, when compared to conformer **3** (Figure 12). Hence, it can be concluded that the main structural differences in the molecules in the two polymorphs are: (i) the relative degree of co-planarity of the two rings, which strongly increase in the red polymorph compared to the green polymorph, as expected taking into account the color exhibited by the two crystalline phases, the red color requiring a higher degree of π -electron delocalization in the molecule; (ii) the relative orientation of the cyano and carboxylic acid substituents, which in the green polymorph point to different directions from the main plane of the molecule (as in the case of conformer **1** in the isolated molecule situation), while in the red polymorph they are nearly perpendicular to each other, since the cyano group is located nearly in the main molecular plane (in the isolated conformer **3** these groups face the same side of the main plane of the molecule).

It shall also be pointed out that the only slightly higher energy difference between the conformer existing in the red polymorph compared to that existing in the green polymorph (0.79 kJ mol^{-1} , as calculated for the isolated conformers **1** and **3**) can be expected to be easily superseded by crystal packing forces, justifying the occurrence of different conformers in the polymorphs of ROY-CAM. For the isolated molecule, the calculations predict that the conversion of conformer **1** into conformer **3** requires only ca. 3.1 kJ mol^{-1} (2.3 kJ mol^{-1} in the opposite direction) (Figure 12), but these barriers in the crystalline state are expected to represent only a small fraction of energy for the putative (non-observed) conversion between the two polymorphs, which, as pointed out above, possess a significantly different molecular packing.

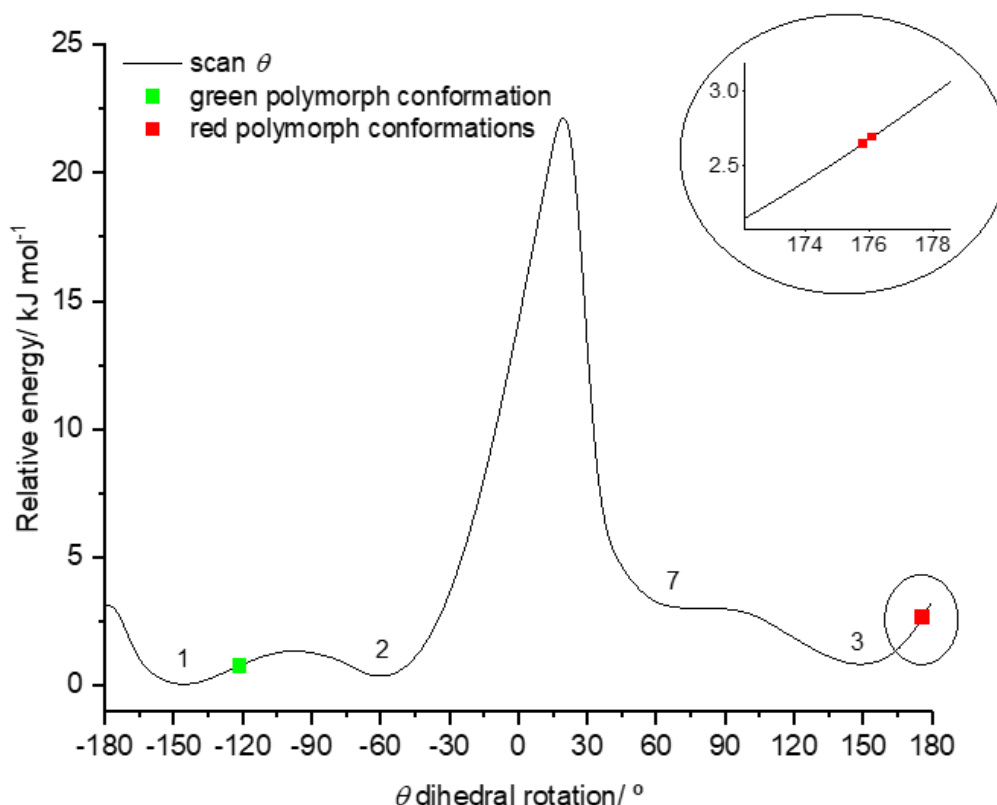


Figure 12 – B3LYP/6-311++G(2d,p) calculated relaxed potential energy scan corresponding to the rotation around the θ dihedral angle, as defined by the 6C–2N–1C–2C torsion angle, corresponding to the curve of conformers **1**, **2**, **3** and **7**, as indicated in the graph. The angles of the green and red polymorphs asymmetric molecules are also presented, in the respective color, in the potential curve.

4. Conclusions

In this article we reported on the first member of the ROY family of compounds that exhibits a green polymorph, thus expanding the color spectrum of the polymorphs of this type of compounds from the usual red, yellow and orange wavelengths to shorter ones.

The synthesis of the new color polymorphic material (ROY-CAM) was described, and the two polymorphs found (one red and one green) were structurally, vibrationally and thermodynamically characterized. Band-markers in the IR and Raman spectra were identified that allow the fast identification of the polymorphs, and band assignments were proposed. The crystal structures of the polymorphs were determined, and the main intermolecular interactions characteristic of each crystal were identified from the structural data and also with help of Hirshfeld analysis. The obtained data showed that the intramolecular hydrogen bonding network between the asymmetric units of the crystal lattice of the green polymorph is somewhat stronger than that in between the asymmetric units of the crystal lattice of the red polymorph. These results are in agreement with the found thermodynamic relationship between the two polymorphs in the temperature range studied, which allowed to conclude that the green polymorph is the stable form, while the red polymorph is metastable.

In line with previous results on similar compounds,^{13,25-28} the different colors of the two polymorphs, which are constituted by molecules exhibiting conformations similar to the most stable conformer **1** and to the third most stable conformer **3** predicted by the DFT calculations performed on the isolated molecule of the compound, respectively, were explained as being mostly determined by the different degree of co-planarity between the two rings of the ROY-CAM molecule, which is considerably higher in the case of the red polymorph than in the green polymorph, i.e., a higher degree of π -electron delocalization in the molecule exists in the red compared to the green polymorph.

Supporting Information

Figure S1, with the ¹H- and ¹³C-NMR spectra of ROY-CAM, and Figure S2, with the IR-ATR spectrum of ROY-CAM. Figure S3 present the TGA curve of ROY-CAM green polymorph. Figures S4-S7 comprise information regarding the Hirshfeld surface analysis of the green and red polymorph of ROY-CAM. Tables S1-S2, with the proposed assignments of the Raman and IR spectra for the two polymorphs.

Acknowledgments

The CQC-IMS is financially supported by the Portuguese Science Foundation (“Fundação para a Ciência e a Tecnologia” - FCT) – Projects CQC UIDB/00313/2020 and UIDP/00313/2020 (National Funds). Access to instruments from Laser-Lab Coimbra is gratefully acknowledged. The authors also thank the Nuclear Magnetic Resonance Laboratory of the Coimbra Chemistry Centre (www.nmrccc.uc.pt), University of Coimbra for obtaining the NMR spectroscopic data. B.A.N. acknowledges FCT for the SFRH/BD/129852/2017 PhD Scholarship.

References

- 1 W. C. McCrone, *Polymorphism*, in *Physics and Chemistry of the Organic Solid State*, (ed. D. Fox, M. M. Labes and A. Weissberger), Wiley-Interscience, 1965, 725–767.
- 2 J. Bernstein, *Polymorphism in Molecular Crystals. Polymorphism in Molecular Crystals*, Oxford University Press, 2010.
- 3 J. Bernstein, Polymorphism - A perspective, *Cryst. Growth Des.*, 2011, **11**, 632–650.
- 4 E. Mitscherlich, Sur la relation qui existe entre la forme cristalline et les proportions chimiques. I. Mémoire sur les arsenates et les phosphates, *Ann. Chim. Phys.*, 1822, **19**, 350–419.
- 5 K. Kersten, R. Kaur and A. Matzger, Survey and analysis of crystal polymorphism in organic structures, *IUCrJ*, 2018, **5**, 124–129.
- 6 B. R. Chen, W. Sun, D. A. Kitchaev, J. S. Mangum, V. Thampy, L. M. Garten, D. S. Ginley, B. P. Gorman, K. H. Stone, G. Ceder, M. F. Toney and L. T. Schelhas, Understanding crystallization pathways leading to manganese oxide polymorph formation, *Nat. Commun.*, 2018, **9**, 1–9.
- 7 S. Jiang, P. J. Jansens and J. H. Ter Horst, Control over polymorph formation of o-aminobenzoic acid, *Cryst. Growth Des.*, 2010, **10**, 2541–2547.
- 8 W. Du, Q. Yin, J. Gong, Y. Bao, X. Zhang, X. Sun, S. Ding, C. Xie, M. Zhang and H. Hao, Effects of solvent on polymorph formation and nucleation of prasugrel hydrochloride, *Cryst. Growth Des.*, 2014, **14**, 4519–4525.
- 9 A. Llinàs and J. M. Goodman, Polymorph control: past, present and future, *Drug Discov. Today*,

- 2008, **13**, 198–210.
- 10 A. Mattei and T. Li, Polymorph formation and nucleation mechanism of tolfenamic acid in solution: An investigation of pre-nucleation solute association, *Pharm. Res.*, 2012, **29**, 460–470.
- 11 L. M. C. Luong, M. A. Malwitz, V. Moshayedi, M. M. Olmstead and A. L. Balch, Role of Anions and Mixtures of Anions on the Thermochromism, Vapochromism, and Polymorph Formation of Luminescent Crystals of a Single Cation, [(C₆H₁₁NC)₂Au]⁺, *J. Am. Chem. Soc.*, 2020, **142**, 5689–5701.
- 12 Y. Xu and N. A. J. M. Sommerdijk, Aragonite formation in confinements: A step toward understanding polymorph control, *PNAS*, 2018, **115**, 8469–8471.
- 13 B. A. Nogueira, C. Castiglioni and R. Fausto, Color Polymorphism in Organic Crystals, *Commun. Chem.*, 2020, **3**, 1–12.
- 14 G. A. Stephenson, T. B. Borchardt, S. R. Byrn, J. Bowyer, C. A. Bunnell, S. V. Snorek and L. Yu, Conformational and Color Polymorphism of 5-Methyl-2-[(2-nitrophenyl) amino]-3-thiophenecarbonitrile, *J. Pharm. Sci.*, 1995, **84**, 1385–1386.
- 15 J. Smith, E. MacNamara, D. Raftery, T. Borchardt and S. Byrn, S. Application of two-dimensional ¹³C solid-state NMR to the study of conformational polymorphism. *J. Am. Chem. Soc.*, 1998, **120**, 11710–11713.
- 16 L. Yu, G. A. Stephenson, C. A. Mitchell, C. A. Bunnell, S. V. Snorek, J. J. Bowyer, T. B. Borchardt, J. G. Stowell and S. R. Byrn, Thermochemistry and Conformational Polymorphism of a Hexamorphic Crystal System. *J. Am. Chem. Soc.*, 2000, **122**, 585–591.
- 17 C. A. Mitchell, L. Yu and M. D. Ward, Selective nucleation and discovery of organic polymorphs through epitaxy with single crystal substrates. *J. Am. Chem. Soc.*, 2001, **123**, 10830–10839.
- 18 S. Chen, I. A. Guzei and L. Yu, New polymorphs of ROY and new record for coexisting polymorphs of solved structures. *J. Am. Chem. Soc.*, 2005, **127**, 9881–9885.
- 19 S. Chen, H. Xi and L. Yu, Cross-nucleation between ROY polymorphs. *J. Am. Chem. Soc.*, 2005, **127**, 17439–17444.
- 20 M. Tan, A. G. Shtukenberg, S. Zhu, W. Xu, E. Dooryhee, S. M. Nichols, M. D. Ward, B. Kahr and Q. Zhu, ROY revisited, again: the eighth solved structure. *Faraday Discuss.*, 2018, **211**, 477–491.
- 21 K. S. Gushurst, J. Nyman and S. X. M. Boerrigter, The PO13 crystal structure of ROY. *CrystEngComm*, 2019, **21**, 1363–1368.
- 22 J. Nyman, L. Yu and S. M. Reutzel-Edens, Accuracy and reproducibility in crystal structure prediction: the curious case of ROY, *CrystEngComm*, 2019, **21**, 2080–2088.
- 23 A. R. Tyler, R. Ragbirsingh, C. J. McMonagle, P. G. Waddell, S. E. Heaps, J. W. Steed, P. Thaw, M. J. Hall and M. R. Probert, Encapsulated Nanodroplet Crystallization of Organic-Soluble Small Molecules, *Chem*, 2020, **6**, 1755–1765.
- 24 X. Li, X. Ou, H. Rong, S. Huang, J. Nyman, L. Yu and M. Lu, The Twelfth Solved Structure of ROY: Single Crystals of Y04 Grown from Melt Microdroplets, *Cryst. Growth Des.*, 2020, **20**, 7093–7097.
- 25 B. A. Nogueira, M. Carvalho, J. A. Paixão, M. E. S. Eusébio, S. M. M. Lopes, T. M. V. D. Pinho e Melo and R. Fausto, Portrayal of the Color Polymorphism in the 5-Acetyl-derivative of ROY, *CrystEngComm*, 2022, **24**, 1459–1474.
- 26 B. A. Nogueira, S. M. M. Lopes, A. Milani, V. André, J. A. Paixão, M. E. S. Eusébio, T. M. V. D. Pinho E Melo, T. Duarte, C. Castiglioni and R. Fausto, The color polymorphs of ROY-ol, *submitted*.
- 27 B. A. Nogueira, S. M. M. Lopes, S. Lopes, T. Nikitin, A. C. B. Rodrigues, M. E. S. Eusébio, J. A. Paixão, T. M. V. D. Pinho e Melo, A. Milani, C. Castiglioni and R. Fausto, 2,4,6-Trinitro-*N*-(*m*-tolyl)aniline: A New Polymorphic Material Exhibiting Different Colors, *Cryst. Growth Des.*, 2021, **21**, 7269–7284.
- 28 B. A. Nogueira, S. M. M. Lopes, T. M. V. D. Pinho E Melo, J. A. Paixão, A. Milani, C. Castiglioni and R. Fausto, Molecular and Crystal Structures of *N*-Picryl-*m*-phenolidine and Investigation of Single Crystal Polarized Raman Spectra, *J. Mol. Struct.*, 2022, **1262**, 133111.
- 29 Gaussian 09, Revision A.02, M. J. Frisch, G. W. Trucks, H. B. Schlegel, G. E. Scuseria, M. A.

- Robb, J. R. Cheeseman, G. Scalmani, V. Barone, G. A. Petersson, H. Nakatsuji, X. Li, M. Caricato, A. Marenich, J. Bloino, B. G. Janesko, R. Gomperts, B. Mennucci, H. P. Hratchian, J. V. Ortiz, A. F. Izmaylov, J. L. Sonnenberg, D. Williams-Young, F. Ding, F. Lipparini, F. Egidi, J. Goings, B. Peng, A. Petrone, T. Henderson, D. Ranasinghe, V. G. Zakrzewski, J. Gao, N. Rega, G. Zheng, W. Liang, M. Hada, M. Ehara, K. Toyota, R. Fukuda, J. Hasegawa, M. Ishida, T. Nakajima, Y. Honda, O. Kitao, H. Nakai, T. Vreven, K. Throssell, J. A. Montgomery, Jr., J. E. Peralta, F. Ogliaro, M. Bearpark, J. J. Heyd, E. Brothers, K. N. Kudin, V. N. Staroverov, T. Keith, R. Kobayashi, J. Normand, K. Raghavachari, A. Rendell, J. C. Burant, S. S. Iyengar, J. Tomasi, M. Cossi, J. M. Millam, M. Klene, C. Adamo, R. Cammi, J. W. Ochterski, R. L. Martin, K. Morokuma, O. Farkas, J. B. Foresman, and D. J. Fox, Gaussian, Inc., Wallingford CT, 2016.
- 30 A. D. Becke, Density-functional exchange-energy approximation with correct asymptotic behavior, *Phys. Rev. A*, 1988, **38**, 3098–3100.
- 31 C. Lee, W. Yang and R. G. Parr, Development of the Colle-Salvetti correlation-energy formula into a functional of the electron density, *Phys. Rev. B*, 1988, **37**, 785–789.
- 32 A. D. McLean and G. S. Chandler, Contracted Gaussian Basis Sets for Molecular Calculations. I. Second Row Atoms, $Z = 11-18$, *J. Chem. Phys.*, 1980, **72**, 5639–5648
- 33 S. K. Wolff, D. J. Grimwood, J. J. McKinnon, M. J. Turner, D. Jayatilaka and M. A. Spackman, Crystal Explorer17 (version 17.5), University of Western Australia, Crawley (AUS), 2017.
- 34 M. A. Spackman and D. Jayatilaka, Hirshfeld Surface Analysis, *CrystEngComm*, 2009, **11**, 19–32.
- 35 J. J. McKinnon, A. S. Mitchell and M. A. Spackman, Hirshfeld Surfaces: A New Tool for Visualising and Exploring Molecular Crystals, *Chem. - A Eur. J.*, 1998, **4**, 2136–2141.
- 36 M. A. Spackman and J. J. McKinnon, Fingerprinting Intermolecular Interactions in Molecular Crystals, *CrystEngComm*, 2002, **4**, 378–392.
- 37 A. Parkin, G. Barr, W. Dong, C. J. Gilmore, D. Jayatilaka, J. J. McKinnon, M. A. Spackman and C. C. Wilson, Comparing Entire Crystal Structures: Structural Genetic Fingerprinting, *CrystEngComm*, 2007, **9**, 648–652.
- 38 A. L. Rohl, M. Moret, W. Kaminsky, K. Claborn, J. J. McKinnon and B. Kahr, Hirshfeld Surfaces Identify Inadequacies in Computations of Intermolecular Interactions in Crystals: Pentamorphic 1,8-Dihydroxyanthraquinone, *Cryst. Growth Des.*, 2008, **8**, 4517–4525.
- 39 APEX2, SAINT and SADABS. Bruker AXS Inc.: Madison, Wisconsin, USA 2006.
- 40 G. M. Sheldrick, Crystal Structure Refinement with SHELXL, *Acta Crystallogr., Sect. C: Struct. Chem.*, 2015, **71**, 3–8.
- 41 L. J. Farrugia, WinGX suite for small-molecule single-crystal crystallography, *J. Appl. Cryst.*, 1999, **32**, 837–838.
- 42 A. Burger and R. Ramberger, On the Polymorphism of Pharmaceuticals and Other Molecular Crystals. I - Theory of Thermodynamic Rules, *Mikrochim. Acta*, 1979, **72**, 259–271.
- 43 A. Burger and R. Ramberger, On the Polymorphism of Pharmaceuticals and Other Molecular Crystals. II - Applicability of Thermodynamic, Rules, *Mikrochim. Acta*, 1979, **72**, 273–316.
- 44 L. Yu, Inferring Thermodynamic Stability Relationship of Polymorphs from Melting Data, *J. Pharm. Sci.*, 1995, **84**, 966–974.
- 45 M. A. Spackman and P. G. Byrom, A novel definition of a molecule in a crystal, *Chem. Phys. Lett.*, 1997, **267**, 215–220.
- 46 J. J. C. Teixeira-Dias and R. Fausto, A Molecular Mechanics Force Field for Conformational Analysis of Simple Acyl Chlorides, Carboxylic Acids and Esters, *J. Mol. Struct.*, 1986, **144**, 199–214.
- 47 R. Fausto, Bonding in Carbonyl and Thiocarbonyl Compounds: An Ab Initio Charge Density Study of $H_2C=X$ and $HC(=X)YH$ ($X, Y = O$ or S), *J. Mol. Struct. (Theochem.)*, 1994, **315**, 123–136.

5. Conclusions and Perspectives for the Future

In this Thesis, a comprehensive study of a series of organic compounds exhibiting color polymorphism has been reported. Firstly, a thorough review on the chemical organic molecular systems showing color polymorphism previously described has been presented, and a clarification on the definition of the different types of polymorphism (conformational and packing), which was frequently inappropriately used in the literature, has been provided. The clarification of the major driven forces which determine the different color of the polymorphs of the previously reported molecular systems has also been presented, highlighting the roles of conformational and packing polymorphism.

Five compounds with potential for exhibiting color polymorphism were investigated in this work, including their design, synthesis, polymorph screening and physical and chemical determination of several properties of their identified polymorphs. The studied compounds were: 2,4,6-Trinitro-*N*-(*m*-tolyl)aniline (TMA), 3-((2,4,6-Trinitrophenyl)amino)phenol (TAP), 5-Acetyl-2-((2-nitrophenyl)amino) thiophene-3-carbonitrile (AcROY), 2-((4-Hydroxy-2-nitrophenyl)amino)thiophene-3-carbonitrile (ROY-ol) and 2-(4-((3-Cyanothiophen-2-yl)amino)-3-nitrophenyl)acetic Acid (ROY-CAM). From these compounds, four have been shown to give rise to color polymorphs, while for one of the compounds (TAP) only a crystalline phase could be obtained, which, nevertheless, was also studied in detail in a comparative basis with the remaining compounds (in particular, with TMA).

An extensive series of single molecule and fully periodic quantum-chemical calculations on the studied compounds has also been undertaken in this investigation.

The color polymorphism exhibited by TMA, where 3 polymorphs were identified (one yellow, one orange and one red) is an interesting case where both conformational and packing polymorphs exist. The yellow polymorph is formed by TMA molecules assuming the conformation of the most stable conformer (A) observed for the isolated molecule of the compound, while both the orange and red polymorphs are formed by another conformer (B). From the analysis of the structural data obtained for the isolated molecule and for the crystals, it was possible to conclude that packing appears to be the decisive cause determining the different colors of all polymorphs, modulating the electronic properties of the chromophore, in particular the electron donation from the amine bridge nitrogen atom to the picryl moiety. Such conclusion resulted evident from the analysis of the structural data obtained for the isolated molecule and for the crystals, in particular the N–C(picryl) bond length, which is a measure of

the electron delocalization from the bridging N atom to the picryl ring: this bond length correlates inversely with the electron delocalization and it follows the expected order in the polymorphs, $R < O < Y$, but it is longer in the isolated conformer B than in conformer A. Accordingly, the structural data show that the electron delocalization involving the tolyl moiety and the bridge is modest and that the angle between the two rings (picryl and tolyl) is nearly the same in all crystals. The Hirshfeld surface analysis for TMA crystals suggests that the more relevant dispersive forces in the yellow polymorph and the stronger hydrogen bonds in the orange and red polymorphs might be the origin of the different influence of the crystal packing on the electronic properties of the chromophore in the various polymorphs. It was also concluded that the three TMA polymorphs are enantiotropically related, with the orange polymorph being the most stable crystal at the lower temperatures studied (including room temperature), and the red and yellow forms being the most stable forms in intermediate and high temperature ranges, respectively. Interestingly, due to kinetic restrictions, no solid-solid transformations were observed for the different polymorphic samples of the compound in more than two years of storage.

From the analysis of the potential energy surface of the isolated molecule of TAP, performed by quantum chemical electronic structure calculations, this molecular system revealed to be considerably flexible conformationally, showing a very interesting potential energy profiles for internal rotation around the N1–C7 bond of the amine bridge, which were shown to be dependent on the direction of the performed scans. Four low-energy TAP conformers were identified, with calculated relative energies within to 1 kJ mol^{-1} . However, despite its *a priori* potential for exhibiting polymorphism, only one TAP crystal type was identified, whose structure was determined and found to be constituted by molecules assuming a geometry similar to the second most stable conformer of the isolated molecule. It was suggested that the geometric constrains resulting from the establishment of a strong intermolecular H-bond, where the OH group of the molecule works as proton donor, is the main factor precluding the existence of easily obtainable additional crystalline phases, contrarily to what has been found for similar molecules, like *N*-picryl-*p*-toluidine and TMA. Furthermore, a throughout investigation of the single crystal polarized Raman spectra of TAP and of the three polymorphs exhibiting different colors of its analogue TMA was undertaken.

The color polymorphism exhibited by the acetyl-derivative of ROY (AcROY) was also investigated and, from the performed analysis of the conformational landscape of the isolated molecule of the compound, studied by DFT calculations, four low-energy intramolecularly hydrogen-bonded conformers were discovered. Three different color polymorphs of AcROY were identified and the structures of polymorph 1 (burgundy) and polymorph 2 (orange) were obtained. In AcROY polymorphs 1 and 2, the molecular conformations correspond to the lowest energy conformer predicted for the isolated molecule of the compound, slightly adjusted due to intermolecular forces and packing. The differences in the intermolecular interactions and packing, which were evaluated from the

crystallographic structural data and also using Hirshfeld surface analysis, were concluded to influence the electronic properties of the AcROY molecules present in the crystals and determine their different colors, demonstrating that the observed polymorphism in AcROY is a case of packing-determined color polymorphism.

In the case of ROY-ol, other of the novel members of the ROY family of compounds considered in this Thesis, four different polymorphs were identified, with polymorph-1 being bright-burgundy and polymorphs 2, 3 and 4 dark-burgundy. The crystal structures of polymorphs 1 and 2 were determined and it was found that the conformation of ROY-ol molecules differs significantly in the two forms (though belonging to the same molecular conformer), while the hydrogen bonding networks are also substantially distinct in the two polymorphs. In both polymorphs 1 and 2, there is a strong N–H··O hydrogen bond between the cyano and hydroxyl groups of neighbor molecules, which play the major structural role in the crystals. However, the remaining intermolecular interactions are distinct and result in markedly different three-dimensional arrangements, which were thoroughly studied by Hirshfeld surface analysis. Short contacts were found to be more abundant in polymorph-1, while hydrogen-bond-related intermolecular forces are more relevant in polymorph-2. Both polymorphs were also characterized vibrationally by infrared and Raman spectroscopies. The performed fully periodic density functional theory (DFT) calculations allowed for detailed spectra assignment, and identification of marker-bands for these polymorphs. The thermal analysis investigation on ROY-ol allowed the identification of two additional polymorphs of the compound (polymorphs 3 and 4).

ROY-CAM, the third member of the ROY family of compounds investigated in this Thesis, was also shown to present a rich conformational landscape, which, in this case, comprehends the existence of 11 different low-energy conformers and 7 high-energy forms. Two of these 18 conformers were found to be present in the two identified polymorphs of the compound. The two polymorphs exhibit the most significant color difference of all color polymorphs of a ROY derivative known to this date: one is green and the other red. As for the remaining compounds, the polymorphs of ROY-CAM were investigated in detail by X-ray single crystal diffraction, vibrational spectroscopy, and thermodynamics methods. Due to wide color difference of the investigated polymorphs, the uncovering of ROY-CAM might unlock new paths for the development of color polymorphic materials suitable for practical and industrial applications.

The analysis of the information available in the literature of the ROY compound and the computational and experimental data acquired for the AcROY, ROY-ol and ROY-CAM systems throughout this Thesis led to the identification of the angle formed between the two rings constituting the core of the ROY system as the major factor influencing the colors exhibited by the different polymorphs. The angle between the nitrophenyl and the thiophene rings, can be measured from the C–N–C–S torsional coordinate. The potential energy curves for all four compounds as a function of this

dihedral angle are presented in Figure 1. In this graphical representation, the dihedral angle values observed experimentally for the different polymorphs are also given. The angle between the rings corresponds directly to the C–N–C–S torsional angle if this value is inferior to 90°, whereas it corresponds to 180° *minus* the indicated value of the C–N–C–S dihedral angle, if the latter is > 90°. Hence, and as can be seen in Figure 1, the angle between the two aromatic rings in ROY's polymorphs is: 5.0° and 10.3° (R18), 21.7° (R), 34.0° and 44.9° (R05), 39.4° (ORP), 46.1° (OP), 52.0° (ON), 55.0° (RPL), 57.9° (PO13), 67.2° (YT04), 75.3° (YT), 76.0° (YN) and 76.9° (Y04). It becomes evident that, in general, when the two rings are close to coplanarity the polymorphs tend to exhibit reddish tones, while the increase of the angle between the rings leads first to the appearance of orange polymorphs and finally to yellow polymorphs, in this latter case when the aromatic rings are approaching perpendicularity.

There are, however, a few red and orange polymorphs with a similar C–N–C–S torsional angle, and even a few inconsistencies to the general rule for some red and orange polymorphs. These facts suggest that the color exhibited is not just regulated by the conformational features, but also by intermolecular packing (whose relative importance may vary from case to case).

The investigation of AcROY, ROY-ol and ROY-CAM confirmed the establishment of the empirical rule “color of the polymorph *vs.* angle between the ring planes”, as observed in Figure 1. Moreover, it also became clear that when the system presents lower energy barriers for the interconversion of the conformers differing in the C–N–C–S dihedral angle, the probability of a high number of different colored polymorphs increases, so that a second general thumb-rule can thus be stated: the flatter the C–N–C–S torsional potential in ROY systems, the higher the number of easily accessible polymorphs and the more distinct colors are likely to be exhibited by those polymorphs.

In fact, the conformational conversion barrier for ROY is ca. 0.75 kJ mol⁻¹ and this system has 11 characterized polymorphs, whereas for the remaining compounds the barriers are higher, and the number of polymorphs is smaller. In ROY-CAM, where the identified polymorphs present angles formed between the rings of 3.3° and 4.5° (red polymorph) and 65.6° (green polymorph), and which is the only studied compound where the rotation of the CNCS angle does not give rise to 2 pairs of symmetric conformers present in the crystals, the conversion energy barriers between the conformers are 1.4, 1.4 and 4.8 kJ mol⁻¹. The two polymorphs that were identified exhibit the most different colors of all known molecular organic color polymorphs (red and green). ROY-ol, depending on the position of the hydroxyl hydrogen atom, has energy barriers of 2.9 and 3.2 kJ mol⁻¹ for the interconversion of the conformers that differ in the value of the CNCS angle. In the ROY-ol polymorphs, the angle between the two rings is 5.1° and 5.8°, in the dark burgundy polymorph 2, and 31.2° in the bright-burgundy polymorph 1. Finally, for AcROY, the conversion between the most stable conformer (the one presented in the two structurally characterized polymorphs) and the conformer where the angle between the rings is larger (which is ca. 6 kJ mol⁻¹ higher in energy than the most stable one) is approximately

Conclusions and Perspectives for the Future

11 kJ mol⁻¹. The relatively higher conformational energy differences for AcROY make the existence of polymorphs composed by the higher-energy conformer less probable. In AcROY, the angle between the rings is 5.7° in the burgundy polymorph 1 and 2.7 and 10.0° in the two asymmetric unit monomers of the orange polymorph 2, making this a more complex case where packing plays a major role in determining the colors of the polymorphs.

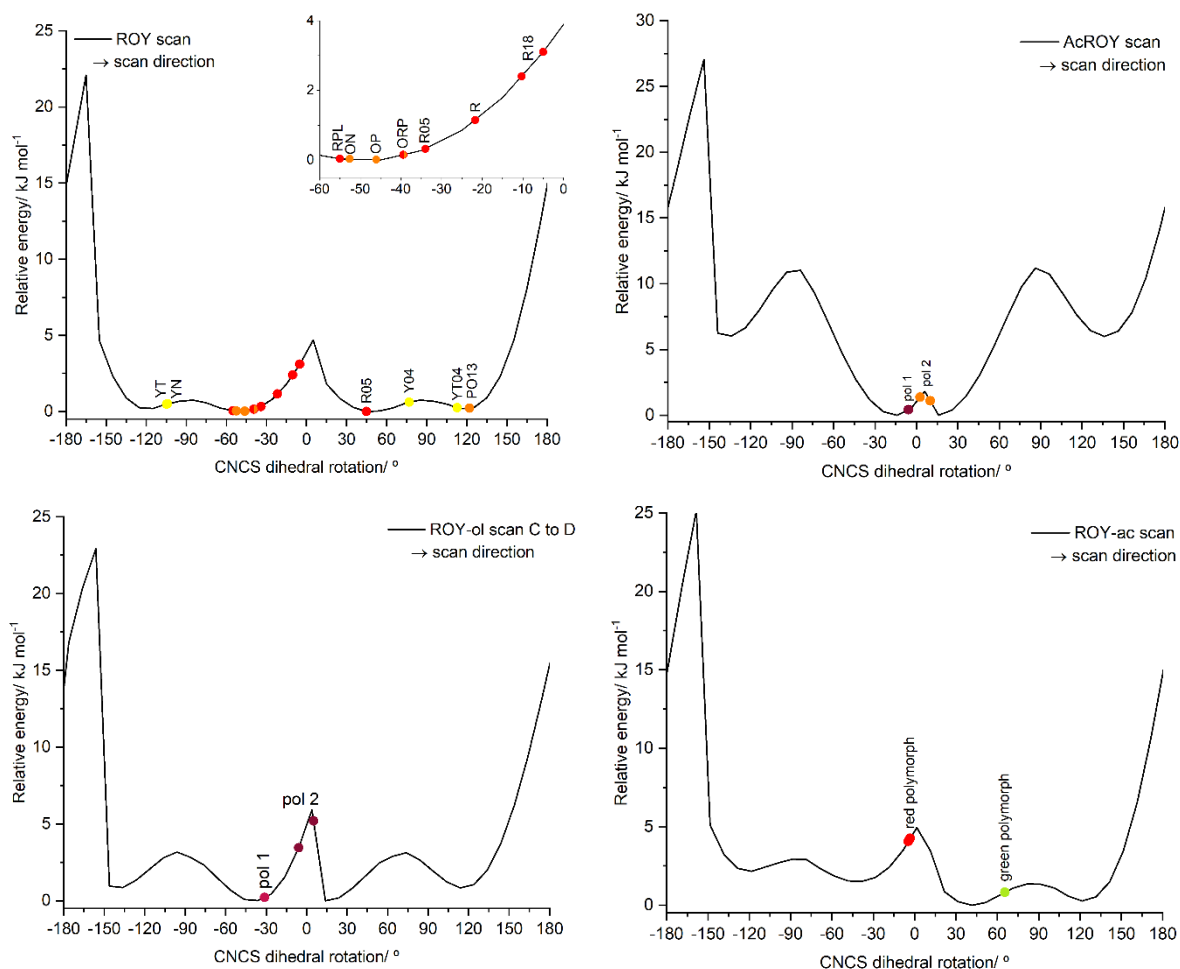


Figure 1 – CNCS dihedral energy scans for ROY (top, left), AcROY (top, right), ROY-ol (bottom, left) and ROY-CAM (bottom, right), with the corresponding dihedral angles observed experimentally for the different polymorphs (indicated by the circles, colored according to the color of the polymorph). A thorough interpretation of the AcROY, ROY-ol and ROY-CAM potential energy profiles is provided in Sections 4.1, 4.2 and 4.3, respectively. The ROY scan curve presented here can be understood analogously.

Contrarily to what succeeds for the ROY family of compounds, the study of the *N*-picryl-*p*-toluidine analogue compounds indicated that, in this case, the color of the polymorphs is not firstly determined by the angle between the two ring moieties present in their molecules. Indeed, as it is shown in Figure 2, the value of the angle formed between the rings is similar for all the crystallographic structures: 43.1° for the *N*-picryl-*p*-toluidine red polymorph, 49.1° for the *N*-picryl-*p*-toluidine orange

Conclusions and Perspectives for the Future

polymorph, 30.8° for the TMA yellow polymorph, 36.3° for the TMA red polymorph, 38.0° for the TMA orange polymorph and 34.7° for TAP dark-orange single crystal structure. Indeed, the conformers of all three molecules (as isolated species) also present a similar angle between the two rings: 41.3° in the case of *N*-picryl-*p*-toluidine, 40.4° and 40.6° in the case of TMA's conformer 1 and 2, and 39.4°, 39.5°, 40.7° and 38.1° for conformers A, B, C and D of TAP, respectively. Hence, the molecules potential to present different structures with dissimilar angle values between the two moiety rings is substantially low.

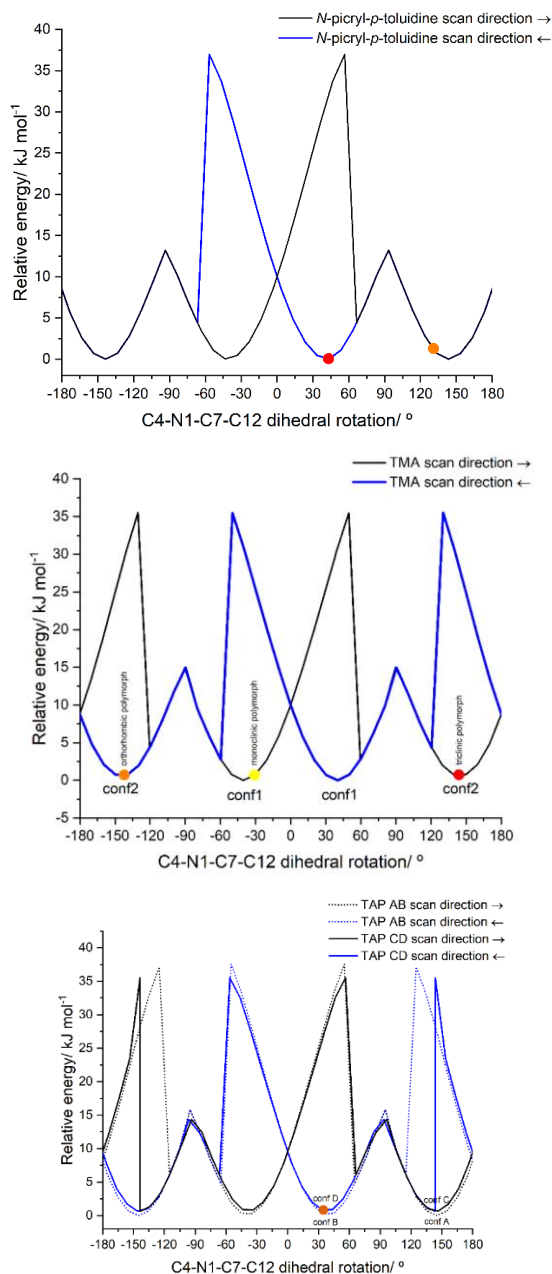


Figure 2 – C4-N1-C7-C12 dihedral energy scans of *N*-picryl-*p*-toluidine (top), TMA (centre) and TAP (bottom), with the corresponding dihedral angles observed experimentally for the different polymorphs (indicated by the circles, colored according to the color of the polymorph). See Figure 2 – Section 3.1, for atom numbering.

The scans of the dihedral angle between the two rings, illustrated in Figure 2 by the dihedral angle comprising the atoms C4-N1-C7-C12 (see Figure 2 – Section 3.1, for atom numbering), is significantly more complex than the ones of the ROY family compound, due to the presence of one nitro group in a position that sterically hinders the rotation of the scanned torsional coordinate. However, it is still possible to clearly see the small differences in energy of the several conformers and the barriers for their interconversions, which correspond to approximately 15 kJ mol⁻¹ for all the cases, in the stereochemically most favorable direction of the scan.

As the observed angles between the rings of the TMA polymorphs suggest, this structural feature is not the main characteristic that contribute to the difference of colors of the polymorphs of this compound. In fact, the yellow polymorph has the lowest angle value, which is contrary to the empirical rule formulated for the ROY family of compounds. As detailed above, an angle between the rings closer to zero corresponds to a higher conjugation between the rings, which in turn corresponds to a red-shifted in the color exhibited by the material. This means that another fundamental feature (or even a series of other factors) is differently contributing to the electronic delocalization of the polymorphs, outrunning the ring planarity angle value contribution.

It has been suggested before, in the study of the parent compound *N*-picryl-*p*-toluidine that the main reason for the color difference in this type of systems is the N–H···O intramolecular distance. In the 2008's study of Braun *et al.* (D. E. Braun, T. Gelbrich, R. K. R. Jetti, V. Kahlenberg, S. L. Price and U. J. Griesser, Colored Polymorphs: Thermochemical and Structural Features of *N*-Picryl-*p*-toluidine Polymorphs and Solvates, *Cryst. Growth Des.*, 2008, 8, 1977–1989.), it is proposed that a shorter hydrogen bond (2.611 Å, in the case of the orange polymorph) results in a hypsochromic, or blue shift, relative to a greater distance between the nitrogen and oxygen atoms defining this intramolecular H-bond (as in the *N*-picryl-*p*-toluidine dark-red polymorph: 2.632 Å). However, the N–H···O intramolecular distances observed for the three-color polymorphs of TMA (3.634 Å in the red polymorph, 3.646 Å in the orange one and 2.702 Å in the yellow case), seem to invalidate this mechanistic suggestion.

In the considered case, the main characteristics influencing the color of the polymorphs can be correlated with the N–C(picryl) bond length and are certainly very much influenced by the different packing of the polymorphs. The N–C(picryl) bond length is a measure of the electron delocalization from the ring-anchor nitrogen atom to the picryl ring, the bond length being inversely proportional to the electron delocalization. In TMA, the N–C(picryl) bond length is 1.344 Å for the TMA red polymorph, 1.348 Å for TMA orange polymorph and 1.355 Å for the TMA yellow polymorph. Additionally, the crystal lattices of the three polymorphs are stabilized differently by dispersion forces. Indeed, this type of intermolecular forces (contacts corresponding to H···H, O···O, C···O, C···C, O···N and C···N) comprises 51% of the total for the yellow polymorph, 46% for the orange polymorph and only

40% for the red polymorph. Since the higher the contribution of dispersive forces, the higher the distortion on the electronic distribution is expected, in particular regarding the π electronic system of the aromatic rings, it is suggested that the distortion of the electronic distribution by the referred intermolecular contacts may be one of the main causes of the color exhibited by the *N*-picryl-*p*-toluidine family compounds' polymorphs, making this a case of packing-determined color polymorphism.

Besides the detailed studies on the color polymorphism exhibited by the selected compounds, an evaluation of the computational predicted results of the polarization Raman modes for the model system LiNbO_3 (*R3c* crystal) obtained *via* CRYSTAL software (using the LCAO approach) was performed, by comparing the calculated data with the different back-scattering experimental polarized Raman spectra. This comparison demonstrated the remarkable ability of the mentioned theoretical approach to calculate the frequency and the relative intensity of the vibrational modes in crystalline materials. Once validated, this approach allowed to obtain expanded spectroscopic information for TMA and TAP crystals.

As a whole, the work developed in the context of this PhD Thesis led to 7 articles (two of them still in the process of publication).

In the continuation of this work, some additional compounds will be considered for investigation. The four ROY isomeric compounds 2-((2-methyl-6-nitrophenyl)amino)thiophene-3-carbonitrile, 2-((3-methyl-2-nitrophenyl)amino)thiophene-3-carbonitrile, 2-((4-methyl-2-nitrophenyl)amino)thiophene-3-carbonitrile and 2-((5-methyl-2-nitrophenyl)amino)thiophene-3-carbonitrile, where the thiophenic methyl group of ROY is transferred to different positions of the nitrophenyl ring, appear very interesting to be study in a comparative basis, due to their expected similar C-N-C-S potential energy profiles. The search for color polymorphs of the ROY family with blue and violet colors may also be pursued, following our discovery of the green polymorph of ROY-CAM. Additionally, applications of the systems already investigated will be explored, particularly in the cases where thermal (inter)conversion between the polymorphs with different colors were observed. The potential applications of these materials still require a thorough kinetic and thermodynamic investigation performed on the specific solid-solid reaction. One can foresee applications of these systems as thermo-sensors or thermo-adaptable optical filters/paints for uses in different types of functional materials.

PART 1

Supporting Information for The color polymorphs of ROY-ol

Bernardo A. Nogueira,^{*,1,2} Susana M. M. Lopes,¹ Alberto Milani,² Vânia André,³ José A. Paixão,⁴ M. Ermelinda S. Eusébio,¹ Teresa M. V. D. Pinho e Melo,¹ M. Teresa Duarte,³ Chiara Castiglioni² and Rui Fausto¹

¹ University of Coimbra, CQC-IMS, Department of Chemistry, P-3004-535 Coimbra, Portugal.

² CMIC, Dipartimento di Chimica, Materiali e Ingegneria Chimica "G. Natta", Politecnico di Milano, 20133 Milano, Italy.

³ Centro de Química Estrutural-IMS, Instituto Superior Técnico, Universidade de Lisboa, Av. Rovisco Pais, 1049-001 Lisboa, Portugal

⁴ University of Coimbra, CFisUC, Department of Physics, P-3004-516 Coimbra, Portugal.

Supporting Information

INDEX	page
Figure S1 – ¹ H and ¹³ C NMR spectra 4-benzyloxy-1-fluoro-2-nitrobenzene in CDCl ₃	244
Figure S2 – IR-ATR spectrum of 4-benzyloxy-1-fluoro-2-nitrobenzene.....	245
Figure S3 – ¹ H and ¹³ C NMR spectra of 2-((4-benzyloxy-2-nitrophenyl)amino)thiophene-3-carbonitrile in CDCl ₃	246
Figure S4 – IR-ATR spectrum of 2-((4-benzyloxy-2-nitrophenyl)amino)thiophene-3-carbonitrile..	247
Figure S5 – ¹ H and ¹³ C NMR spectra of ROY-ol in DMSO- <i>d</i> ₆	248
Figure S6 – IR-ATR spectrum of ROY-ol.....	249
Figure S7 – Comparison between the experimental and calculated IR and Raman spectra of polymorph-1.....	250
Figure S8 – Comparison between the experimental and calculated IR and Raman spectra of polymorph-2.....	250
Figure S9 – <i>d</i> _{norm} mapping on the Hirshfeld surface representing the intermolecular contacts between the two molecules forming the crystallographic asymmetric unit in polymorph-2.....	251
Figure S10 – Two-dimensional <i>d</i> _e vs. <i>d</i> _i fingerprint plots for ROY-ol polymorph-1 crystal.....	252
Figure S11 – Two-dimensional <i>d</i> _e vs. <i>d</i> _i fingerprint plots for ROY-ol polymorph-2 crystal.....	253
Figure S12 – Polarized light and cross-polarized light photographs of a sample showing small crystals of polymorph-2 and amorphous of ROY-ol.....	254
Table S1 – Raman frequencies (experimental and calculated) of ROY-ol polymorphs 1 and 2.....	255
Table S2 – Infrared frequencies (experimental and calculated) of ROY-ol polymorphs 1 and 2.....	256
Table S3 – C–N–C–S dihedral angles in the different polymorphs of ROY, AcROY and ROY-ol.....	257

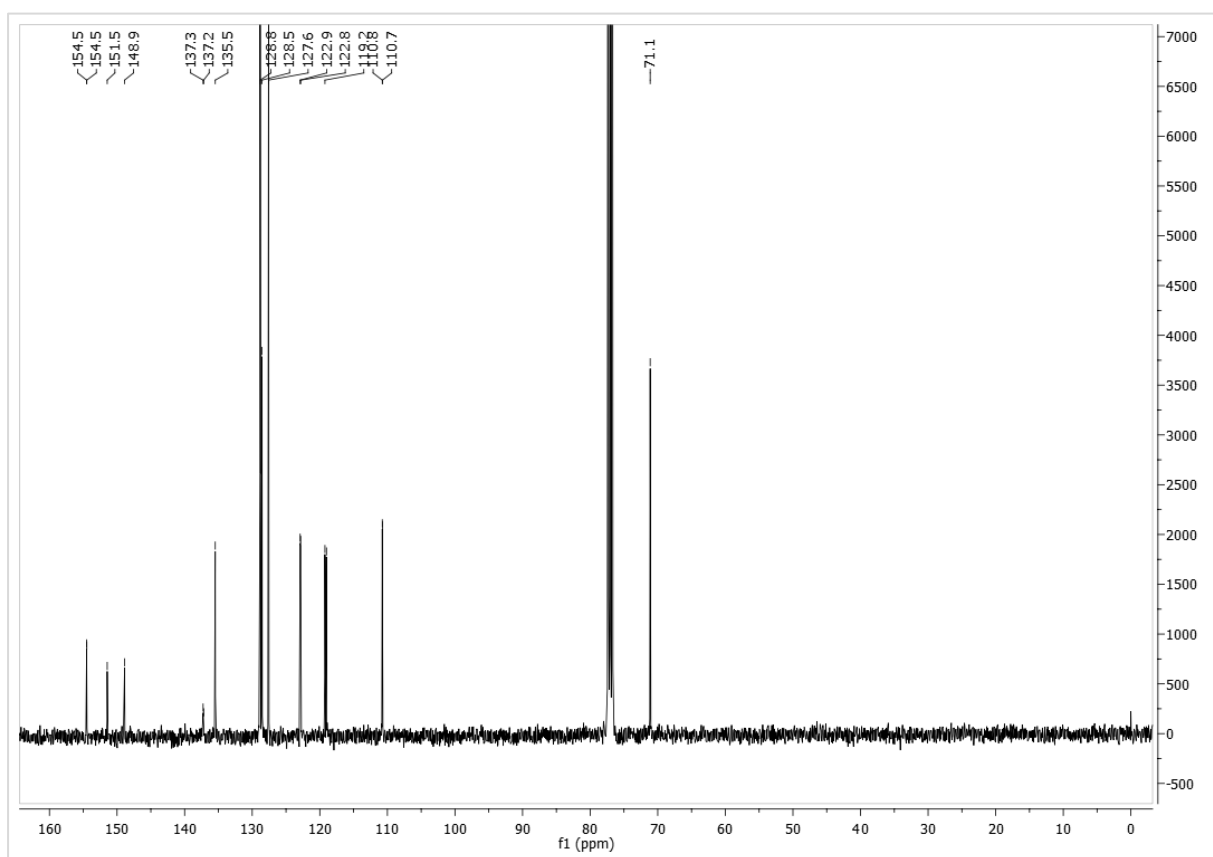
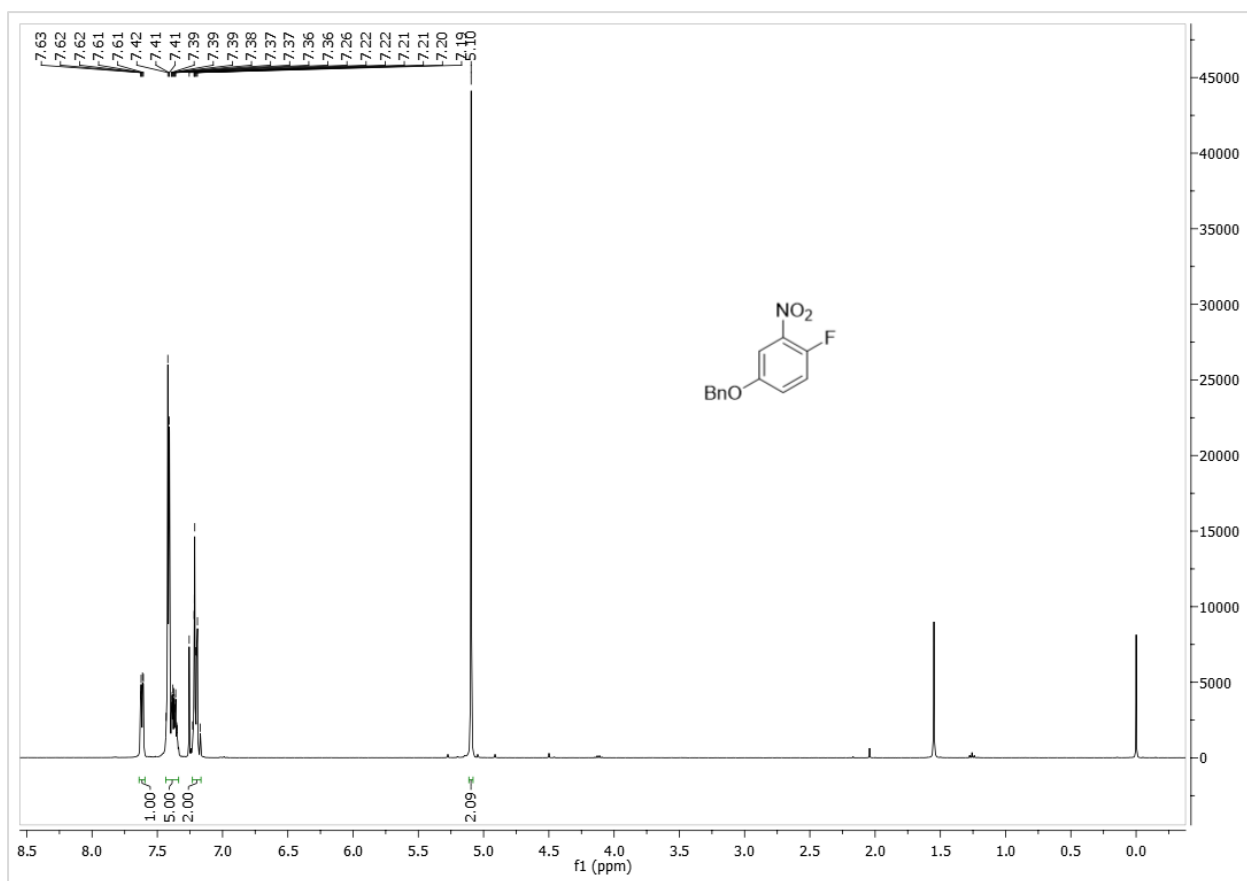


Figure S1. ^1H and ^{13}C NMR spectra of 4-benzyloxy-1-fluoro-2-nitrobenzene (**2**) in CDCl_3 .

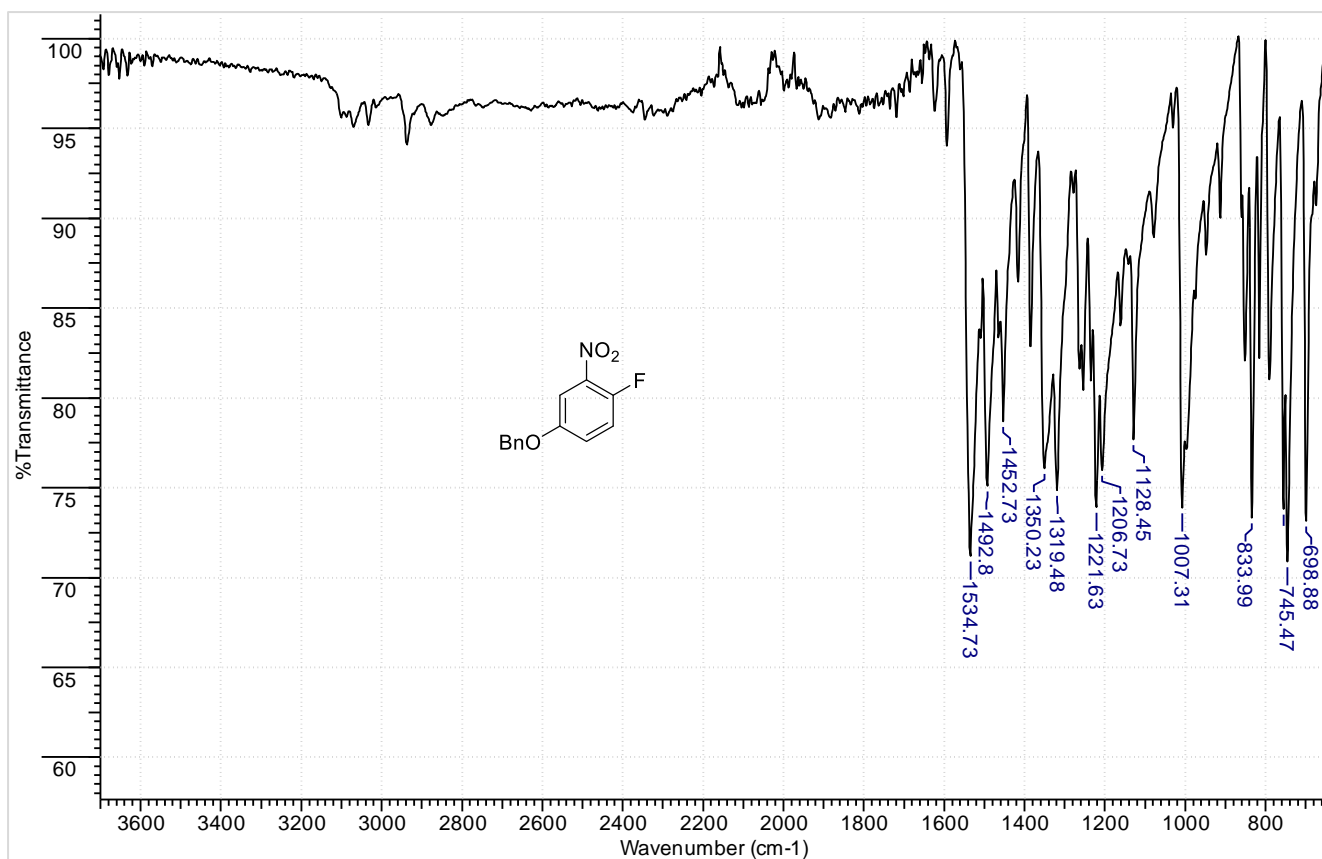


Figure S2. IR-ATR spectrum of 4-benzyloxy-1-fluoro-2-nitrobenzene (2).

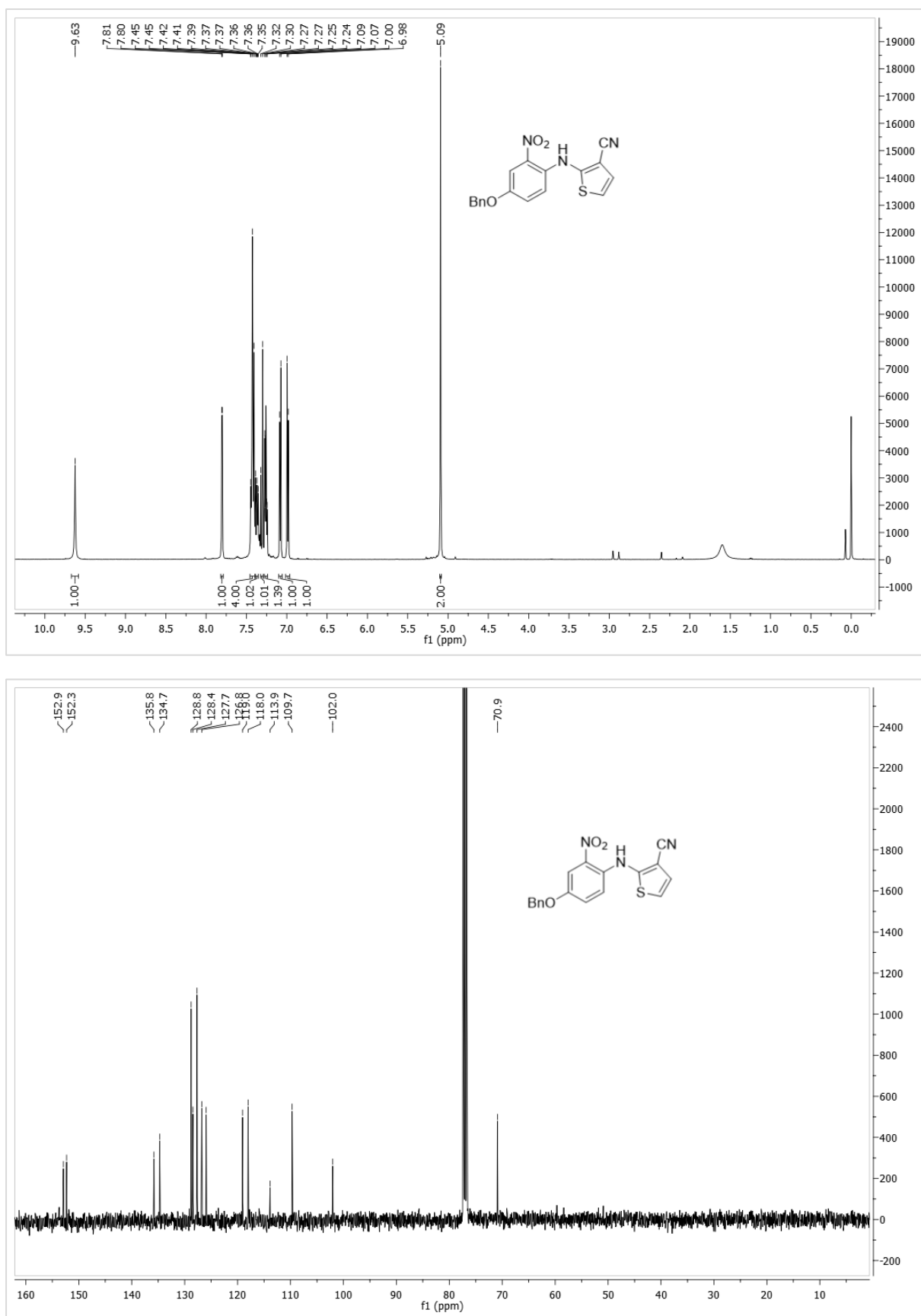


Figure S3. ¹H and ¹³C NMR spectra of 2-((4-benzyloxy-2-nitrophenyl)amino)thiophene-3-carbonitrile (**4**) in CDCl₃.

Annexes

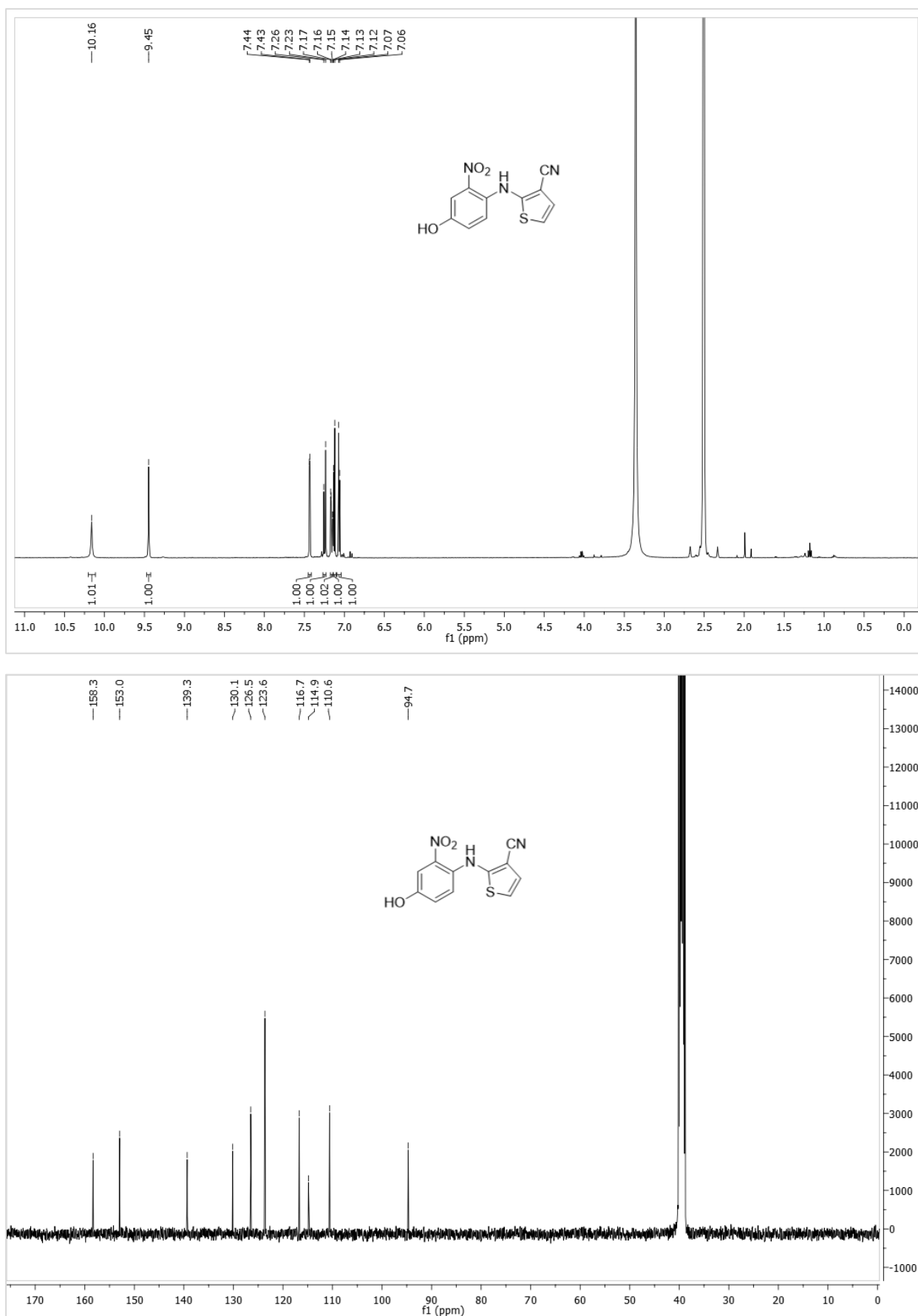


Figure S5. ¹H and ¹³C NMR spectra of ROY-ol in DMSO-*d*₆.

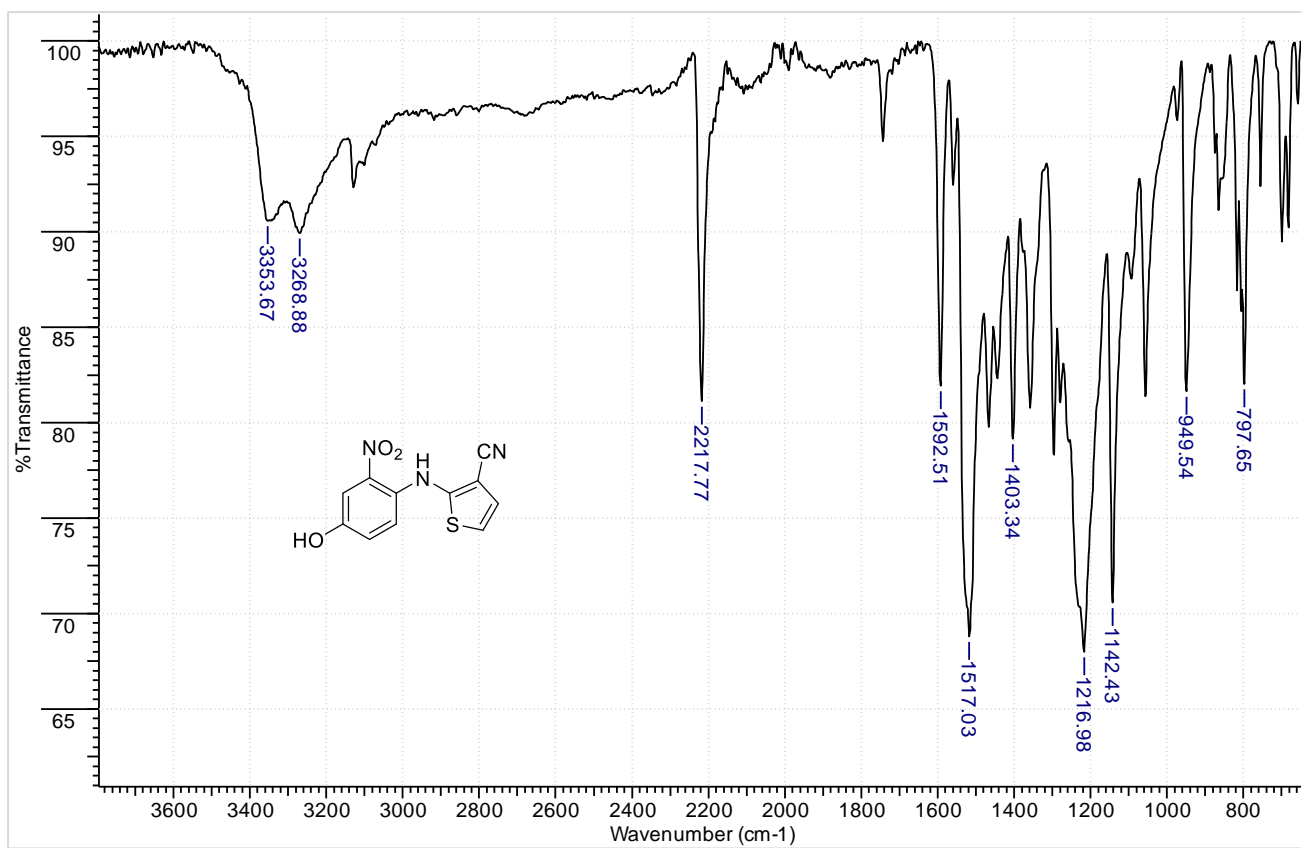


Figure S6. IR-ATR spectrum of ROY-ol.

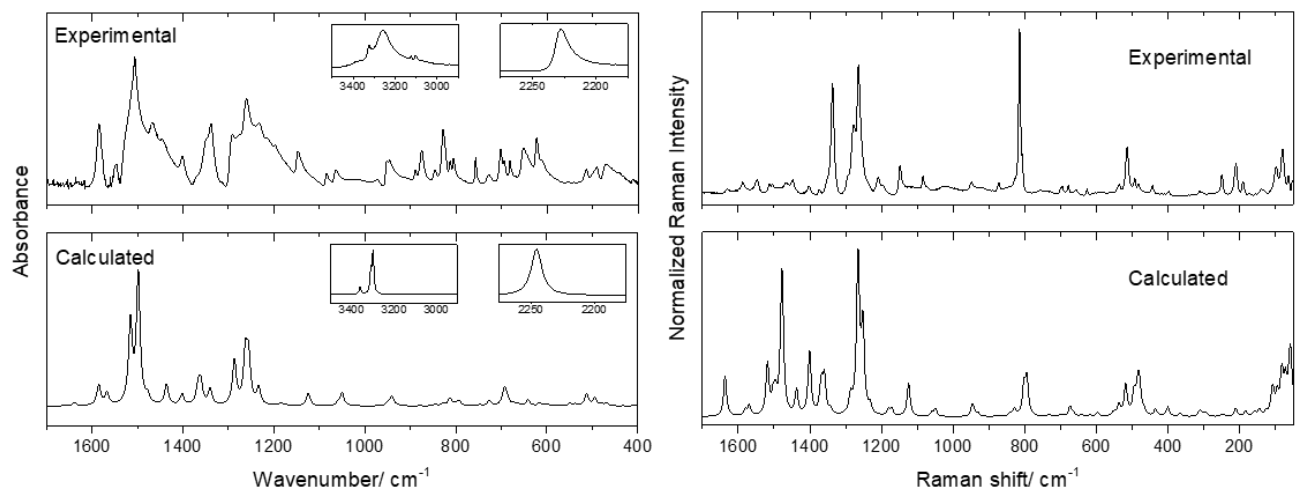


Figure S7. Comparison between the experimental and the calculated IR spectra (*left*) and Raman spectra (*right*) of polymorph-1 of ROY-ol.

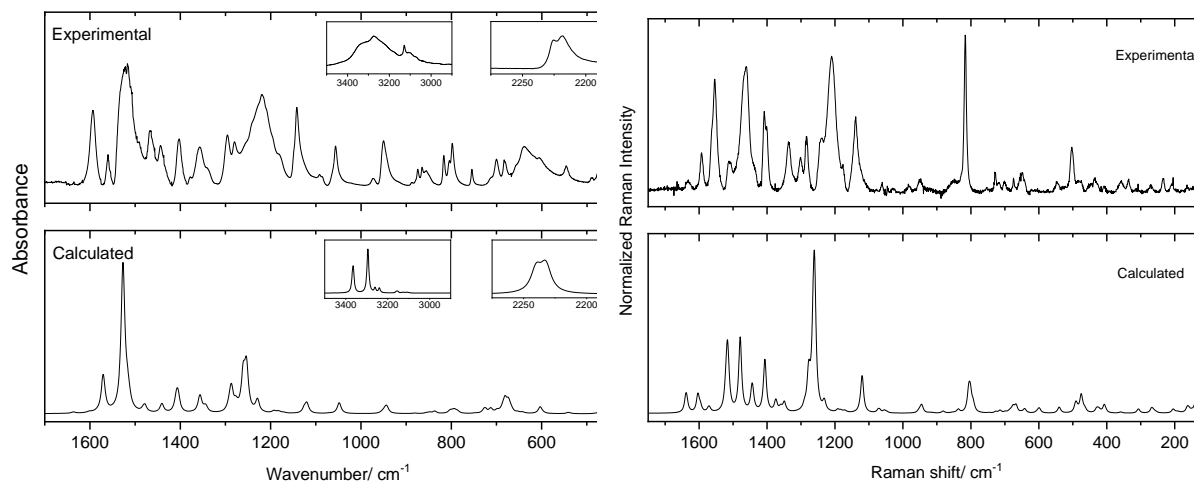


Figure S8. Comparison between the experimental and the calculated IR spectra (*left*) and Raman spectra (*right*) of polymorph-2 of ROY-ol.

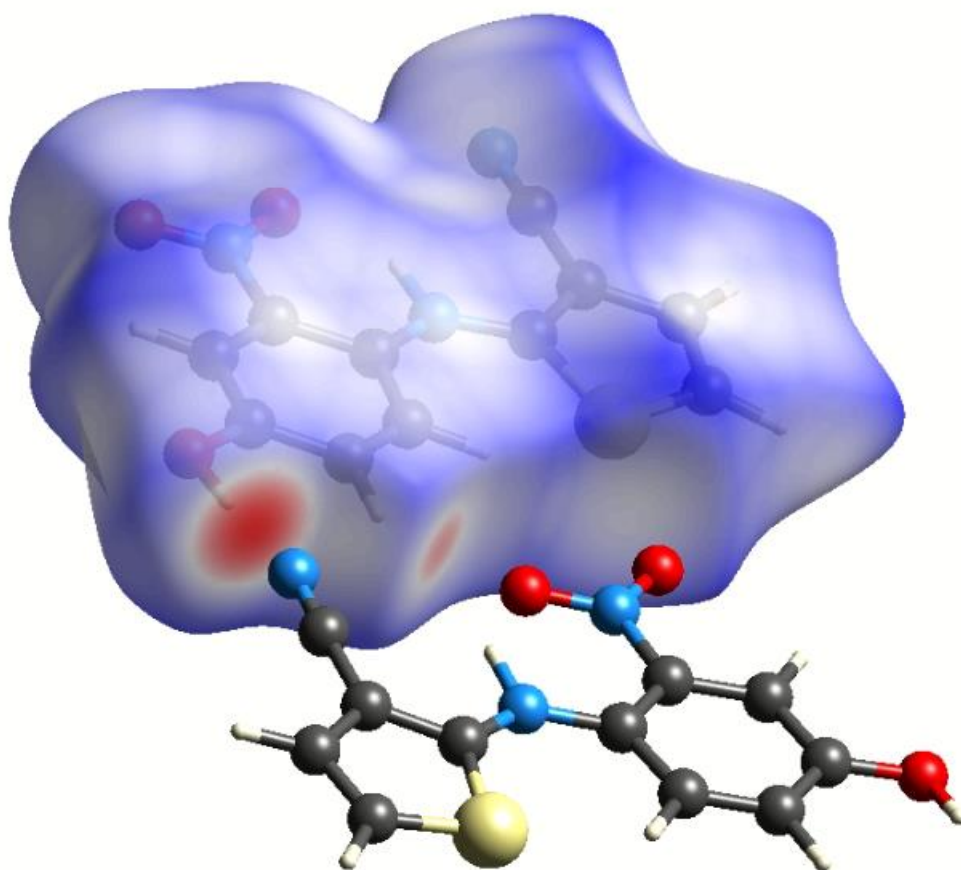


Figure S9. d_{norm} mapping on the Hirshfeld surface representing the intermolecular contacts between the two molecules forming the crystallographic asymmetric unit in polymorph-2 of ROY-ol.

Annexes

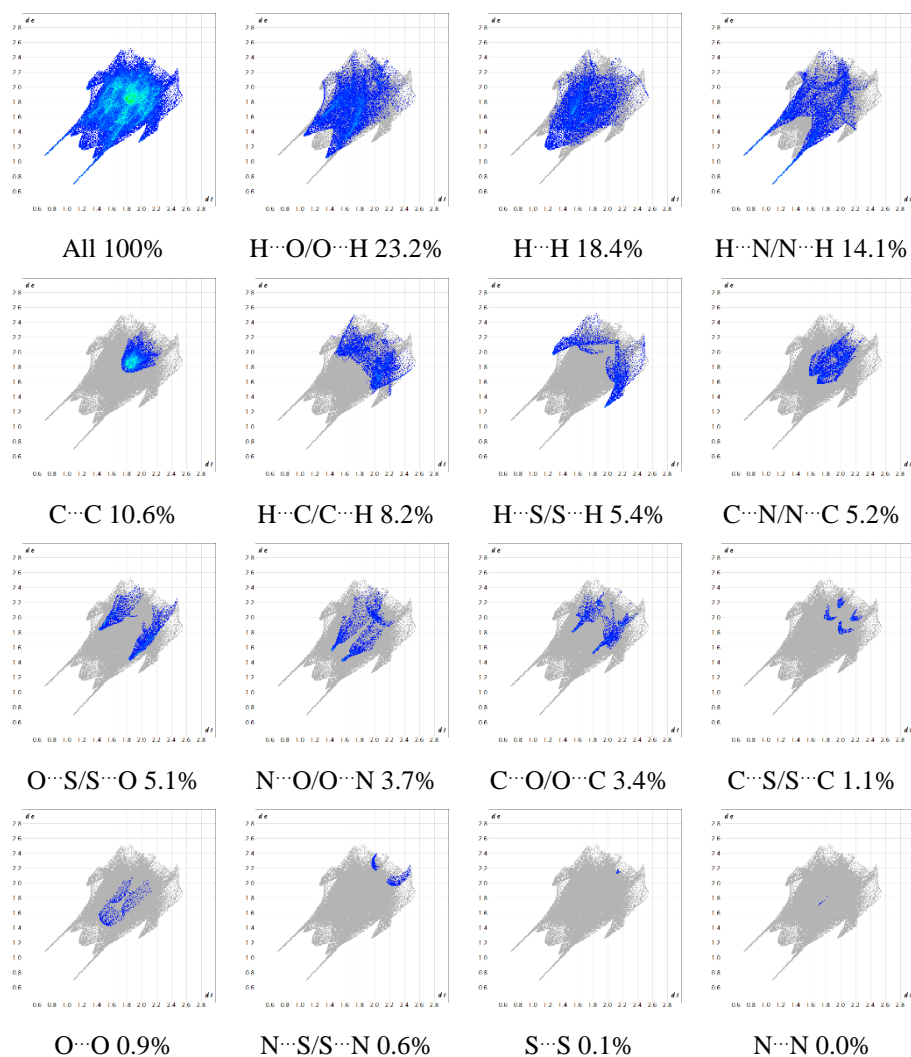


Figure S10. Two-dimensional d_e vs. d_i fingerprint plots for ROY-ol polymorph-1 crystal. The colored areas represent the contributions of the referred interacting pair of atoms, whereas the non-colored grey areas represent the whole set of interactions. Colors are determined by the fraction of surface points in 0.01 \AA bin in both d_e and d_i . The real colors span a continuous range and are mapped using the HSV (Hue, Saturation, Value) scheme, where $S \approx V \approx 1.0$ and $H \sim 0.66$ (240° , blue) for minimum relative area, and $H \approx 0.0$ (0° , red) for more than 0.1% of surface points in the bin.

Annexes

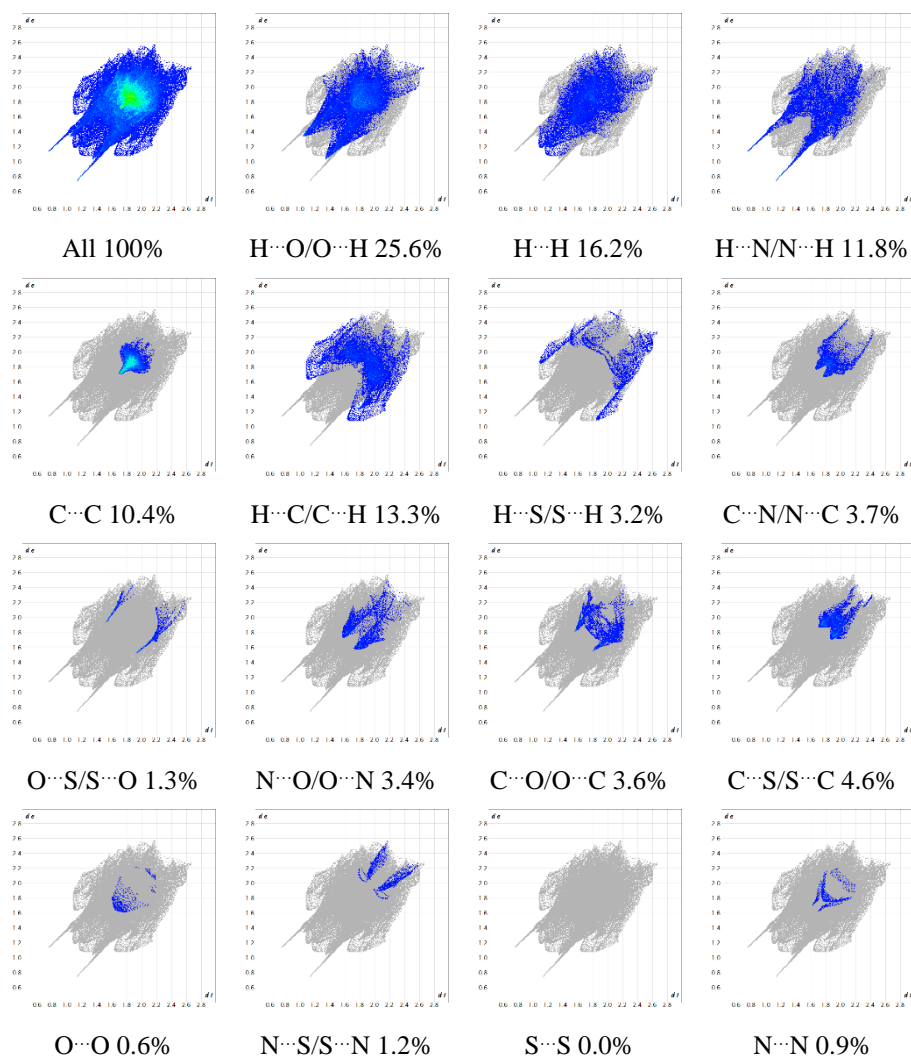


Figure S11. Two-dimensional d_e vs. d_i fingerprint plots for ROY-ol polymorph-2 crystal. The colored areas represent the contributions of the referred interacting pair of atoms, whereas the non-colored grey areas represent the whole set of interactions. Colors are determined by the fraction of surface points in 0.01 \AA bin in both d_e and d_i . The real colors span a continuous range and are mapped using the HSV (Hue, Saturation, Value) scheme, where $S \approx V \approx 1.0$ and $H \sim 0.66$ (240° , blue) for minimum relative area, and $H \approx 0.0$ (0° , red) for more than 0.1% of surface points in the bin.

Annexes

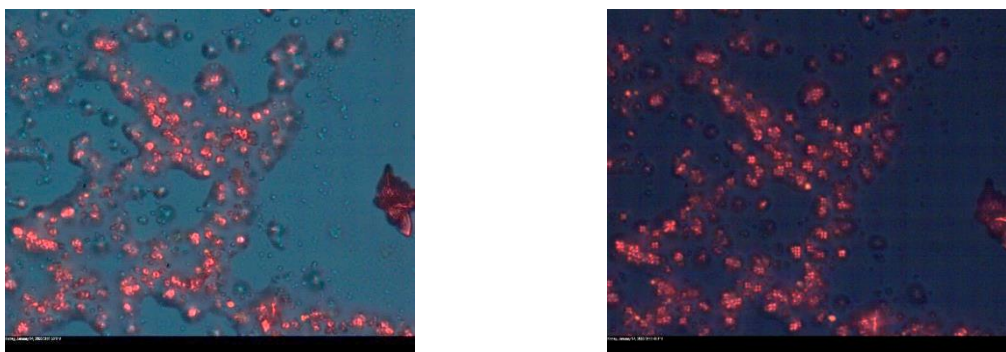


Figure S12. Polarized light (*left*) and cross-polarized light (*right*) photographs (200x amplified) of the same sample of ROY-ol, where it is possible to see small crystals of polymorph-2 and an amorphous material of the same compound.

Annexes

Table S1 – Observed Raman bands of ROY-ol polymorphs 1 and 2 and their respective PBE0/6-31G(d,p) calculated (scaled) frequencies (in cm^{-1}), with proposed assignments.

Polymorph 1		Polymorph 2		Approximate description ^b
Exp.	Calc ^a	Exp.	Calc ^a	
1631	1637	1634	1638	vCC ring1
1588	1580	1593	1603	vNO ₂
	1570		1571	δNH
1547	1518	1554	1568	vCC ring2
1513	1501	1512	1517	vCC ring2 + vCC ring1
1505	1496	1507	1514	vCC ring1 + δCH ring1
1468	1478	1461	1479	vCC ring2
1448	1437	1436	1444	δNH + δOH
1403	1401	1408	1406	δNH
1374	1366	1375	1374	δOH
	1360		1359	vCC ring2
1337	1344	1336	1350	δNH + δOH
1292	1285	1302	1291	δCH ring1
1278	1266	1283	1276	δNH + δOH
1264	1253	1239	1261	δNH
1243	1233		1232	δOH + δCH ring1
1209	1180	1210	1192	δNH + δCH ring2 + δCH ring1
1195	1172	1178	1183	δCH ring2 + δCH ring1
1150	1125	1142	1120	δCH ring1
1084	1058	1061	1071	δCH ring2 + δCH ring1
	1050	1045	1055	δCH ring2
	946		945	vCC ring1 + vCC ring2
948	931	947	923	γCH ring1
872	880	849	882	γCH ring2
	839		847	γCH ring1
827	829		834	vCC ring1 (breathing)
	801	816	804	vCC ring2 (breathing)
815	795		793	vCC ring1 (breathing) + vCC ring2 (breathing)
757	752	753	747	γNO ₂
728	732	729	726	γCH ring2
695	698	701	714	γOH
	673		675	vCC ring2 (breathing)
678	665	674	668	vCC ring1 (breathing)
656	641	654	642	γCC ring1
626	619	648	599	γCC ring2
600	597	604	597	δCC≡N
554	553	548	545	γNH + γCH ring1
536	539	528	540	γNH + δCC≡N
515	518	503	492	γNH
493	494	452	489	γNH + δCC≡N
483	482	435	475	γCH ring2 + γCC≡N
443	435	416	428	δCC ring1
398	400	407	407	δCC ring1
367	366	357	359	γCC ring1
312	311	336	307	δCC ring2 + δCC ring1
303	295	313	268	δCC ring1 + δCC ring2
250	247	270	255	δCC ring2 + δCC ring1
210	211	234	204	γCC ring2 + δCC ring1
190	184	205	193	δCC ring1
156	157	164	161	γCC ring1
139	145	147	135	γC≡N
130	126		132	δC≡N
115	107	123	116	γCNO ₂
98	95	90	95	lattice vibration
80	81		92	lattice vibration
64	72	62	73	lattice vibration
53	59		58	lattice vibration

^a Only calculated modes predicted with a Raman activity of at least $5 \text{ \AA}^4 \text{ amu}^{-1}$ and Raman shifts equal or larger than 50 cm^{-1} are presented. A scaling factor of 0.9512 was used for the theoretical frequency values. ^b Abbreviations: v, stretching; δ, in-plane bending; γ, out-of-plane bending. Ring1 and ring2 refer to the nitro and thiophene ring, respectively.

Annexes

Table S2 – Observed infrared bands of ROY-ol polymorphs 1 and 2 and their respective PBE0/6-31G(d,p) calculated (scaled) frequencies (in cm^{-1}), with proposed assignments.

Polymorph 1		Polymorph 2		Approximate description ^b
Exp.	Calc ^a	Exp.	Calc ^a	
3376	3361	3381	3260/3240	vNH
3324	3308	3330	3365	vOH
3258	3299	3264	3294	vOH
3124	3158	3128	3153	vCH ring2
3102	3120	3109	3128	vCH ring2
3072	3084	2921	3120	vCH ring1
3032	3071	2851	3109	vCH ring1
2228	2246	2224/2218	2239/2233	vC≡N
1634	1638	1633	1637	vCC ring1
1584	1584	1592	1602	vNO ₂
1547	1567	1559	1570	δNH + vCC ring1
1506	1515	1516	1526	vCC ring2
	1498		1513	vCC ring1
1468	1479	1464	1479	vCC ring2 + vCC ring1
1445	1436	1443	1441	δOH
1401	1402	1402	1407	δNH
1350	1362	1356	1356	vCC ring2
1339	1340	1338	1346	δOH + δNH
1291	1287	1295	1287	δCH ring1
1276	1262	1279	1278	vCC ring1
1261	1257	1241	1254	δNH + δCH ring1
1234	1234	1229	1229	δOH + δCH ring1
1198	1184	1216	1183	δCH ring2
1147	1124	1141	1120	δCH ring1
1084	1060	1091/1085	1048	δCH ring1
1065	1050	1055	1070	δCH ring2
946	941	948/973	944	δCH ring2 + vCC ring2
875	880	887/874	881	γCH ring2
846	845	865	848	γCH ring1
828	828	855	837	δCCring2
813	813	816	802	γCH ring1
805	793	804/798	794	vCC ring2 (breathing) + δCCring1
757	748	755	748	γNO ₂
728	727	736	726/713	γCH ring2
702	693	700	697	γOH
694	675	683	680	vCC ring2 (breathing)
682	667	680	675	vCC ring1 (breathing)
652	642	667	654	δCC ring1 + δCC ring2
623	617	635	643	γCC ring2
612	601	604	603	δCC ring2
552	549	545	540	δCC≡N
541	538	525	538	γNH
514	512	502	492	γNH
490	495	490	484	vCC ring2 (breathing)
470	481	475	474	γC≡N
	469		466	γCC ring2
441	432	428/422	426	γCC ring1
411	401	409	407	γCC ring1

^a Only calculated modes predicted with an IR intensity higher of 2 km mol^{-1} and with frequency equal or larger than 400 cm^{-1} are presented. A scaling factor of 0.9512 was used for the theoretical frequency values. ^b Abbreviations: v, stretching; δ, in-plane bending; γ, out-of-plane bending. Ring1 and ring2 refer to the nitro and thiophene ring, respectively.

Table S3. C–N–C–S dihedral angles (°) in the different polymorphs of ROY, AcROY and ROY-ol.^a

Molecule	Polymorph	Color	Z'	C–N–C–S angle	Conformer (relative energy)	
ROY	R18	red	2	-5.01 -10.28	1 (0.0)	
	R	red	1	-21.74	1 (0.0)	
	R05	red	2	-34.00 44.88	1 (0.0)	
	ORP	orange-red	1	-39.40	1 (0.0)	
	OP	orange	1	-46.08	1 (0.0)	
	ON	orange	1	-52.57	1 (0.0)	
	RPL	red	1	-55.03	1 (0.0)	
	YN	yellow	1	-104.03 ^b	2 (0.2)	
	YT	yellow	1	-104.72 ^b	2 (0.2)	
	YT04	yellow	1	112.84 ^b	2 (0.2)	
	PO13	pumpkin-orange	1	122.06 ^b	2 (0.2)	
	AcROY	Polymorph-1	burgundy	1	- 5.73	A (0.0)
		Polymorph-2	orange	2	9.98 2.72	A (0.0)
ROY-ol	Polymorph-1	bright-burgundy	1	-31.22	D (3.5)	
	Polymorph-2	dark-burgundy	2	-5.84 5.09	D (3.5)	

^a The relative energy of the conformers (in kJ mol⁻¹) are presented relative to the most stable conformer of each molecule (DFT(B3LYP)/6-311++G(2d,p) data). Z' is the number of molecules in the asymmetric unit of the crystal. ^b The angle between the planes of the rings for polymorphs YN, YT, YT04 and PO13 are given by 180° *minus* the indicated value of the C–N–C–S dihedral angle, i.e., 75.97, 75.28, 67.16 and 57.94°, respectively.

PART 2

Supporting Information for
The ROY family goes to the green!
The red and green polymorphs of ROY-CAM

Bernardo A. Nogueira,^{*1} Susana M. M. Lopes,¹ M. Ermelinda S. Eusébio,¹
 Vânia André,² Teresa Duarte,² J. A. Paixão,³ Teresa M. V. D. Pinho e Melo¹ and Rui Fausto¹

¹ *University of Coimbra, CQC-IMS, Department of Chemistry, P-3004-535 Coimbra, Portugal.*

² *Centro de Química Estrutural-IMS, Instituto Superior Técnico, Universidade de Lisboa, Av. Rovisco Pais, 1049-001 Lisboa, Portugal.*

³ *University of Coimbra, CFisUC, Department of Physics, P-3004-516 Coimbra, Portugal.*

Supporting Information

Index	<i>Page</i>
Figure S1 - ¹ H- and ¹³ C-NMR spectra of ROY-CAM	259
Figure S2 - IR-ATR spectrum of ROY-CAM	260
Figure S3 - Thermogravimetric weight-loss curve of the ROY-CAM green polymorph recrystallized from ethyl acetate solution.	261
Figure S4 - Maps of d_{norm} on the Hirshfeld surfaces for both ROY-CAM polymorphs	262
Figure S5 - d_{norm} mapping on the Hirshfeld surface representing the intermolecular contacts between the two molecules forming the crystallographic asymmetric unit in ROY-CAM red polymorph.....	263
Figure S6 - Two-dimensional d_e vs. d_i fingerprint plots for ROY-CAM green polymorph.....	264
Figure S7 - Two-dimensional d_e vs. d_i fingerprint plots for ROY-CAM red polymorph	265
Table S1 - Observed Raman bands of ROY-CAM green and red polymorphs with proposed assignments	266
Table S2 – Observed IR bands of ROY-CAM green and red polymorphs with proposed assignments	267

* Corresponding author e-mail: ban@qui.uc.pt

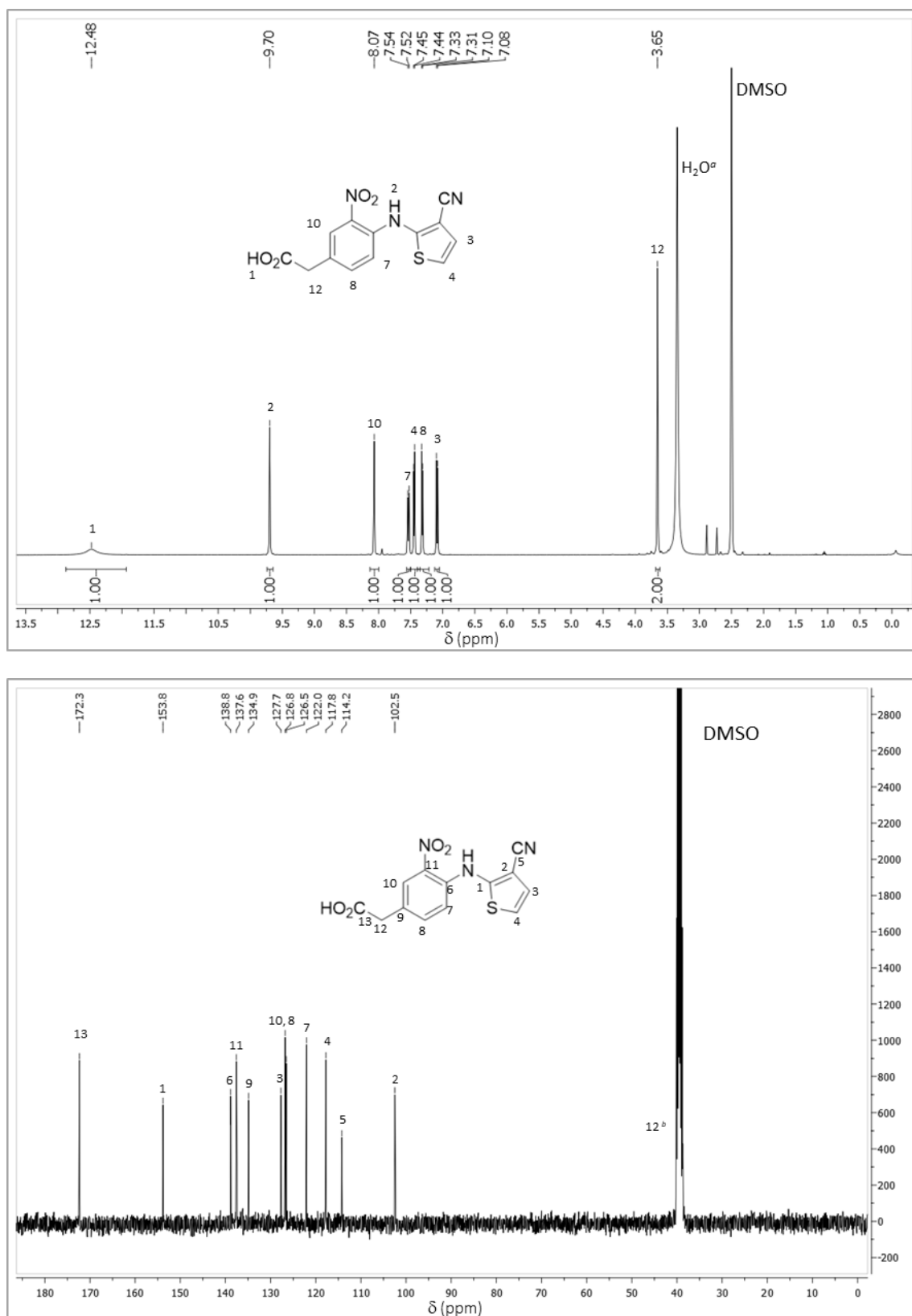


Figure S1 – ¹H- (*top panel*) and ¹³C-NMR (*bottom*) spectra of ROY-CAM in DMSO-*d*₆. ^a band of water traces contamination of the solvent; ^b the peak of the methylene carbon atom (C12) are underneath the solvent peak.

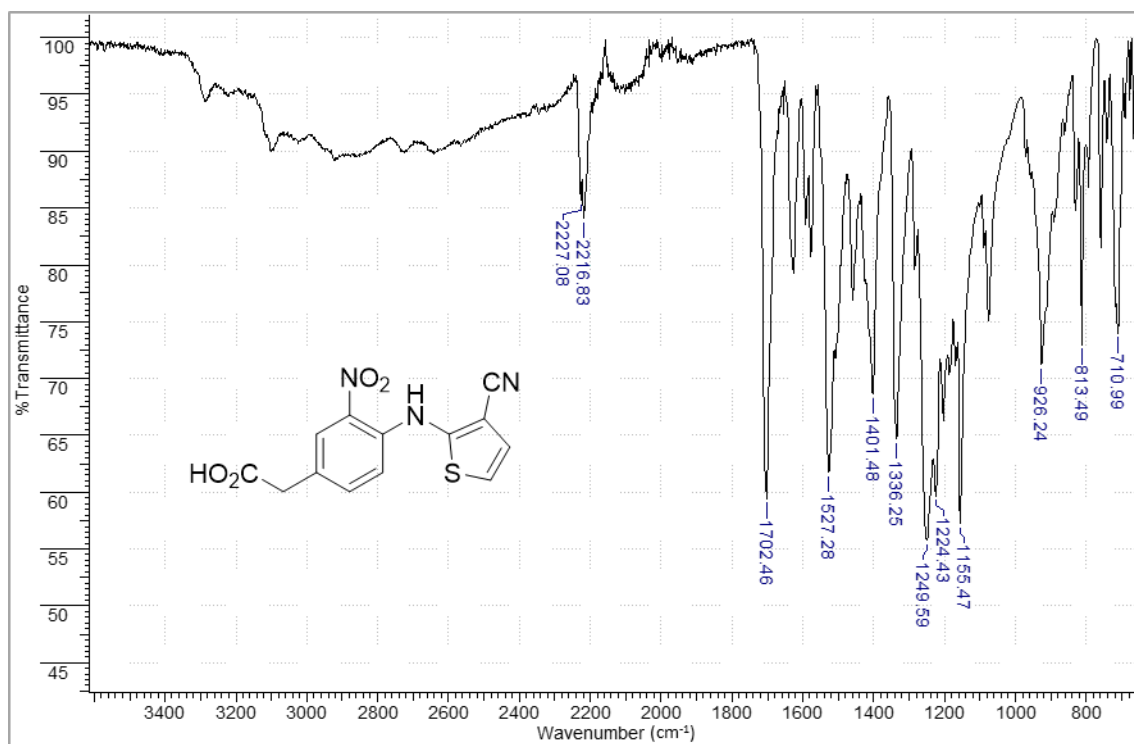


Figure S2 – ATR-IR spectrum of ROY-CAM.

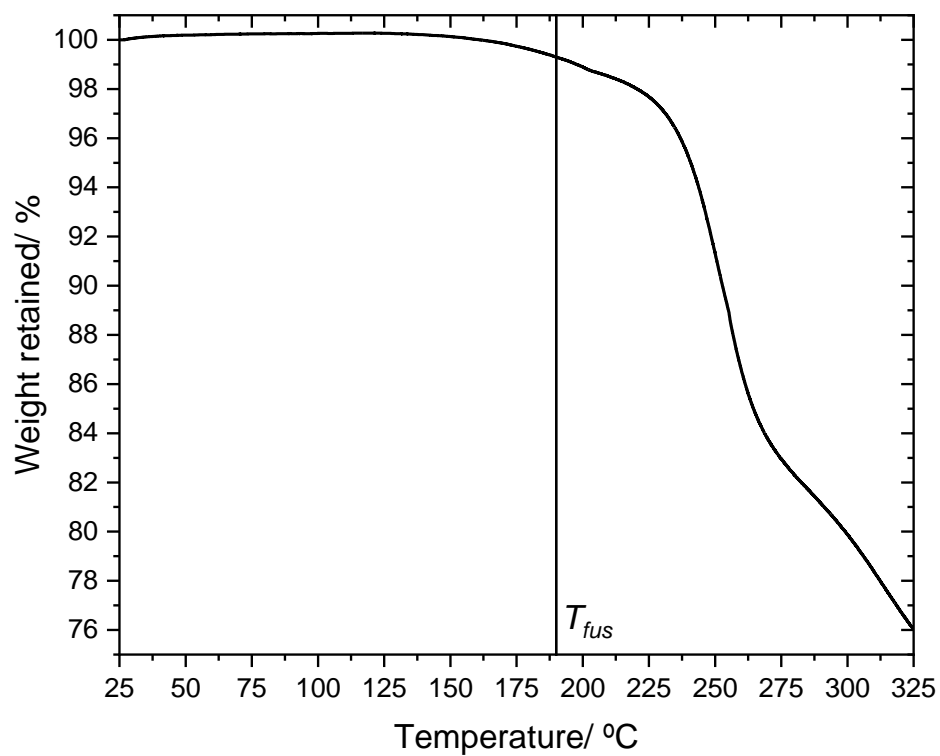


Figure S3 – Thermogravimetric weight-loss curve of the ROY-CAM green polymorph recrystallized from ethyl acetate solution (heating rate: 10 °C min⁻¹), from 25 °C until 325 °C.

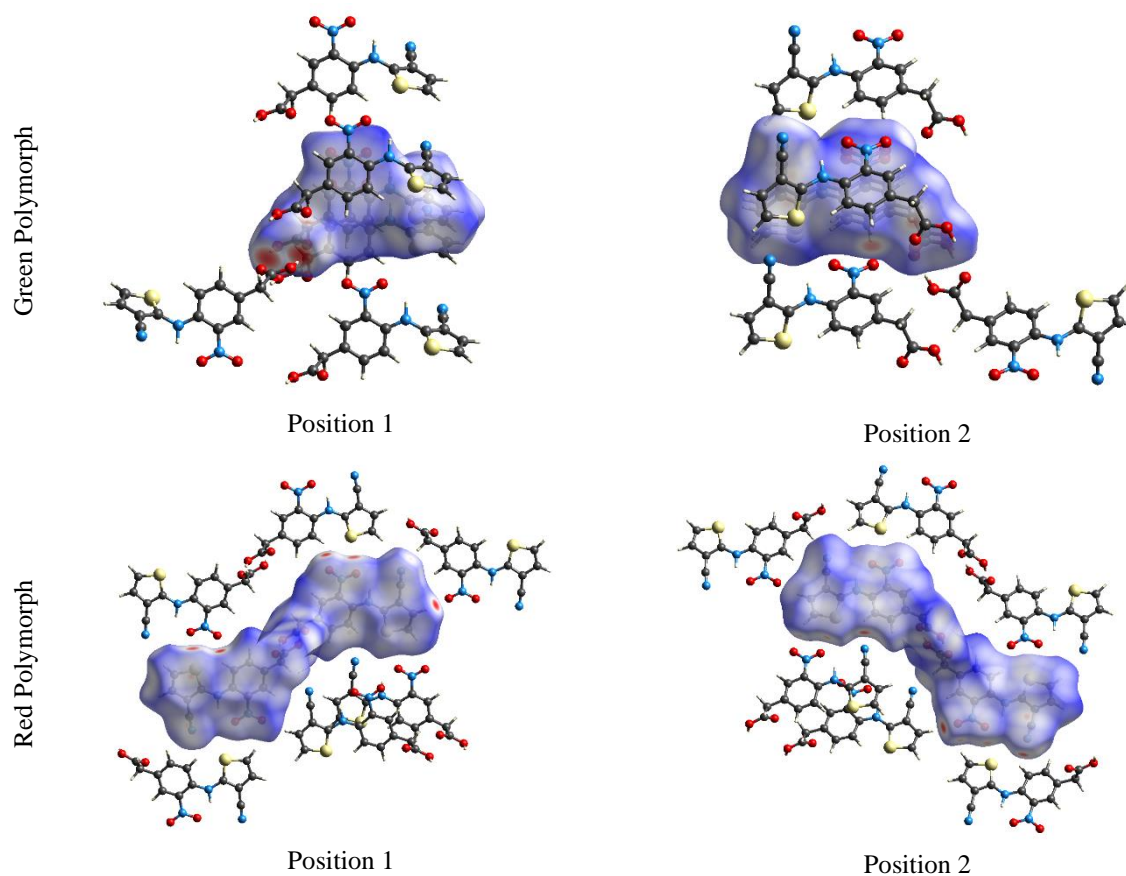


Figure S4 – Maps of d_{norm} on the Hirshfeld surfaces (two different spatial positions) of the crystallographic asymmetric units of green polymorph (*on top*) and red polymorph (*bottom*) of ROY-CAM, showing the neighboring molecules which account for the strongest interactions (shorter contacts).

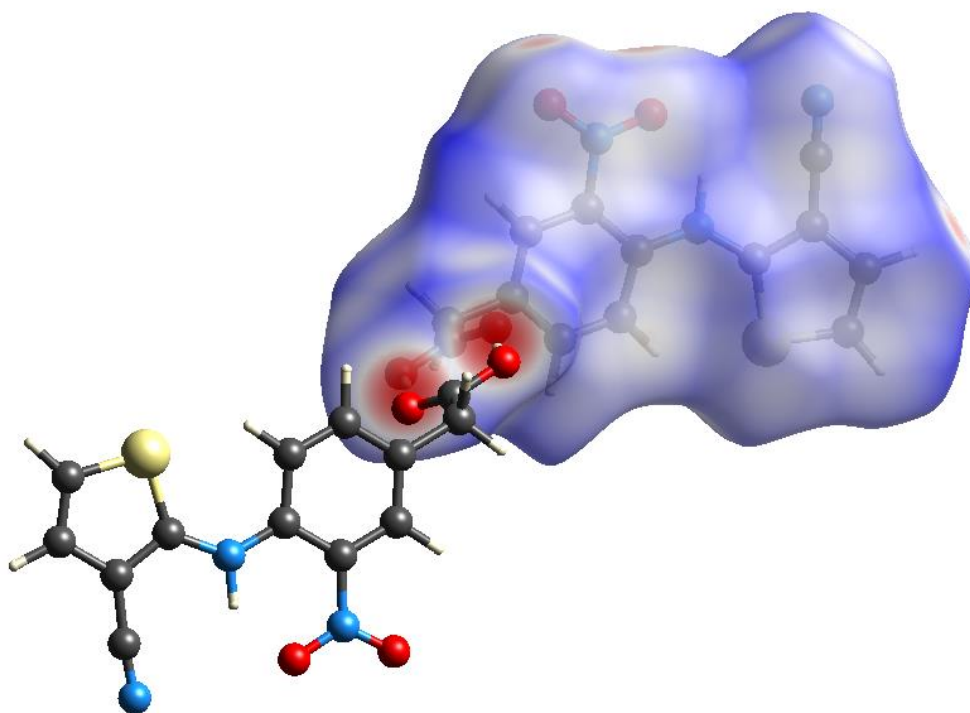


Figure S5 – d_{norm} mapping on the Hirshfeld surface representing the intermolecular contacts between the two independent molecules forming the crystallographic asymmetric unit in the red polymorph of ROY-CAM.

Annexes

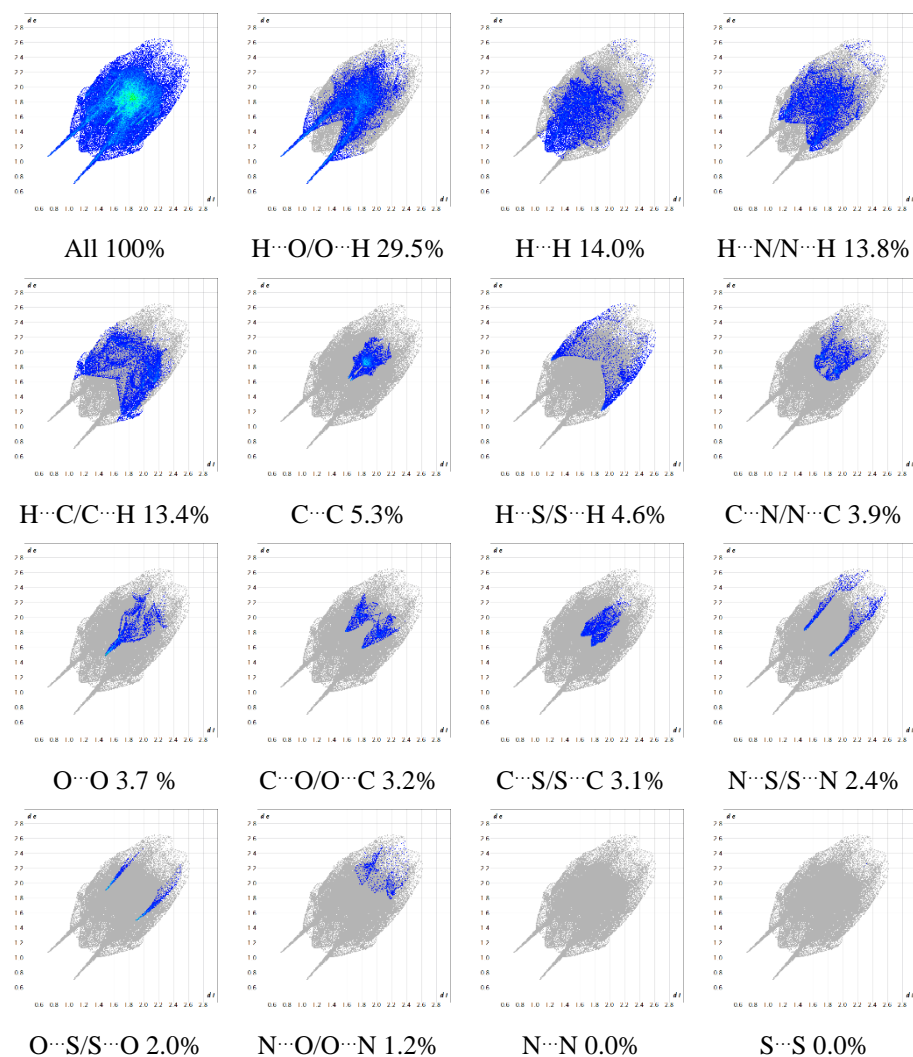


Figure S6 – Two-dimensional d_e vs. d_i fingerprint plots for ROY-CAM green polymorph. The colored areas represent the contributions of the referred interacting pair of atoms, whereas the non-colored grey areas represent the whole set of interactions. Colors are determined by the fraction of surface points in 0.01 \AA bin in both d_e and d_i . The real colors span a continuous range and are mapped using the HSV (Hue, Saturation, Value) scheme, where $S \approx V \approx 1.0$ and $H \sim 0.66$ (240° , blue) for minimum relative area, and $H \approx 0.0$ (0° , red) for more than 0.1% of surface points in the bin.

Annexes

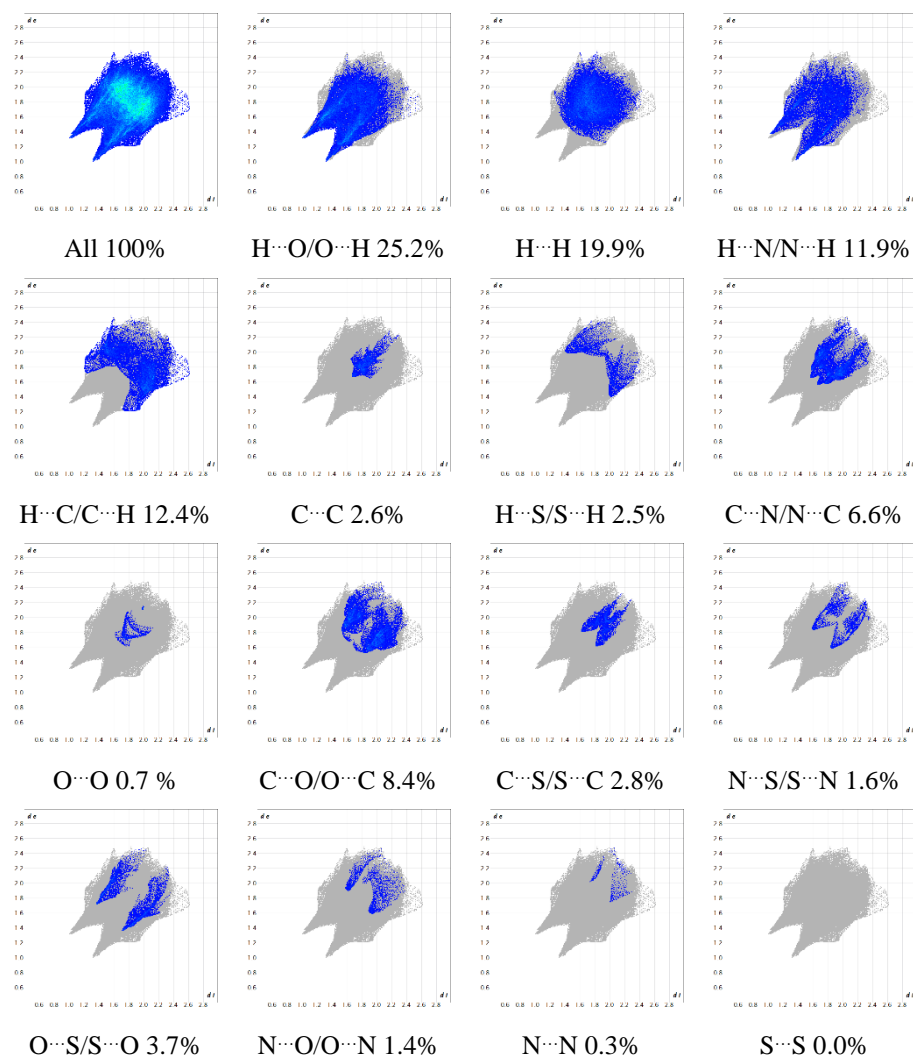


Figure S7 – Two-dimensional d_e vs. d_i fingerprint plots for ROY-CAM red polymorph. The colored areas represent the contributions of the referred interacting pair of atoms, whereas the non-colored grey areas represent the whole set of interactions. Colors are determined by the fraction of surface points in 0.01 Å bin in both d_e and d_i . The real colors span a continuous range and are mapped using the HSV (Hue, Saturation, Value) scheme, where $S \approx V \approx 1.0$ and $H \sim 0.66$ (240°, blue) for minimum relative area, and $H \approx 0.0$ (0°, red) for more than 0.1% of surface points in the bin.

Table S1 – Observed Raman bands of ROY-CAM green and red polymorphs (frequencies in cm^{-1}), with proposed assignments.

Green polymorph	Red polymorph	Approximate description
1674	1669	vCC ring1
1578	1599	vNO ₂
1545	1549	vNO ₂
1525	1520	vCC ring2 + vCC ring1
1507	1509	vCC ring1 + δ CH ring1
1455	1456	vCC ring2
1424	1421	δ OH
1401	1405	δ NH
1375	1378	δ OH
1338	1350	vCC ring2
1320	1319	δ CH ring1
1282	1254	δ NH
1248	1222	δ NH + δ OH
1202		
1193	1183	δ NH + δ CH ring2 + δ CH ring1
1159	1156	δ CH ring1
1096	1101	δ CH ring1
1081	1074	δ CH ring2
1026	1027	vCC ring1 + vCC ring2
927	931	γ CH ring1
903	899	γ CH ring2
890	890	γ CH ring1
833		vCC ring1 (breathing)
826	829	vCC ring2 (breathing)
813	815	vCC ring1 (breathing) + vCC ring2 (breathing)
763	758	γ NO ₂
723	725	γ CH ring2
703	713	γ OH
688	698	vCC ring2 (breathing)
675	673	vCC ring1 (breathing)
612	610	γ CC ring1 + γ CC ring2 + δ CC \equiv N
576	572	γ NH + γ CH ring1
531	535	γ NH + δ CC \equiv N
492	489	γ NH + δ CC \equiv N
474	480	γ CH ring2 + γ CC \equiv N
436	453	δ CC ring1
410	414	δ CC ring1
375	378	γ CC ring1
351	357	δ CC ring2 + δ CC ring1
322	287	δ CC ring1 + δ CC ring2
199	205	δ CC ring1
145	144	γ C \equiv N
80	90	lattice vibration

Abbreviations: v, stretching; δ , in-plane bending; γ , out-of-plane bending. Ring1 and ring2 refer to the nitro and thiophene ring, respectively.

Table S2 – Observed IR bands of ROY-CAM green and red polymorphs (frequencies in cm^{-1}), with proposed assignments.

Green polymorph	Red polymorph	Approximate description
3399	3390	vNH
3294	3213	vOH
3136	3164	vCH ring2
3090	3110/3095	vCH ring2
3056	3010	vCH ring1
2921	2921	vCH ring1
2852	2847	vCH ₂
2225	2219/2207	vC≡N
1700	1692	vC=O
1629	1632	vCC ring1
1573	1591	vNO ₂
1529	1547/1525	vNO ₂
1507	1505	vCC ring2 + vCC ring1
1456	1458	vCC ring2 + vCC ring1
1426	1416	δOH
1401	1404/1378	δNH
1332	1347/1338	vCC ring2
1321	1323	δOH + δNH
1280	1288	δCH ring1
1237	1239	δOH
1224	1221	δOH
1203	1210/1203	δOH + δCH ring1
1186	1180	δCH ring2
1157	1149	δCH ring1 + δCH ring2
1090	1094/1087	δCH ring1
1077	1073	δCH ring2
981	970	δCH ₂
959/937	960/943	δCH ring2 + vCC ring2
923/907	925/919	γCH ₂
883	885	γCH ring2
846	854	γCH ring1
832	830	δCCring2
824	808	γCH ring1
813	801	vCC ring2 (breathing) + δCCring1
763	757	γNO ₂
725	732/720	γCH ring2
706	714/703	γOH
689	683	vCC ring2 (breathing)
677	669	vCC ring1 (breathing)
665	655	δCC ring1 + δCC ring2
627	622	γCC ring2
613	612	δCC ring2
584/574	573	δCC acetic acid
560	540	γNH
528	529	γNH
506	506	γNH
489	481/478	γNH
476	472	γC≡N
434	430	γCC ring2
423	423	γCC ring1

Abbreviations: v, stretching; δ, in-plane bending; γ, out-of-plane bending. Ring1 and ring2 refer to the nitro and thiophene ring, respectively.